Characterization of CDC14 and NAGK in model systems of development

By

Leif Richard Neitzel

Dissertation

Submitted to the Faculty of the

Graduate School of Vanderbilt University

in fulfillment of the requirements

for the degree of

DOCTOR OF PHILOSOPHY

In

Cell and Developmental Biology

August 31st, 2018

Nashville, Tennessee

Approved:

Ethan Lee, M.D., Ph.D.

Andrea Page-McCaw, Ph.D.

Ken S. Lau, Ph.D.

Rebecca S. Cook, Ph.D.

Sandra S. Zinkel, M.D., Ph.D.

“The pursuit of knowledge is hopeless and eternal.”

-Hubert Farnsworth

Dedicated to my Grandfather Richard Neitzel

Abstract

Cell division cycle 14 (Cdc14) is an evolutionarily conserved phosphatase originally identified in *Saccharomyces cerevisiae* as a cell cycle regulator. In *Drosophila melanogaster*, Cdc14 is encoded by a single gene, thus facilitating its study. I characterized a null mutation of *cdc14* in *D. melanogaster*, and found that the animals were viable, with no obvious defects in the cell cycle or DNA damage repair. However, the *cdc14* null mutants have defects in chemosensation, mechanosensation, lipid metabolism and resistance to starvation. Additionally, the *cdc14* null males exhibit decreased sperm competitiveness, which was not the result of decreased mating behavior from motor defects or decreased fertility. This is the first characterization of Cdc14 in *D. melanogaster* and demonstrates several novel roles for Cdc14 in metazoans.

N-acetyl-*D*-glucosamine kinase (NAGK) is a sugar kinase and first step in the UDP-GlcNAc salvage pathway of glycosylation. The UDP-GlcNAc salvage pathway is responsible for approximatly 80% of the free UDP-GlcNAc pool that is required for protein glycosylation. I demonstrate that overexpression of NAGK, the UDP-GlcNAc salvage pathway enzymes (Phosphoglucomutase 3 (PGM3) and UDP-*N*-acetyl-*D*-glucosamine Pyrophosphorylase 1 (UAP1)), the first enzyme in the *N*-glycosylation pathway (Dolichyl-Phosphate (UDP-*N*-Acetylglucosamine) *N*-Acetylglucosaminephosphotransferase 1 (DPAGT1)) or injection of the UDP-GlcNAc salvage pathway sugars (*N*-acetyl-*D*-glucosamine (GlcNAc), GlcNAc-1-Phosphate (GlcNAc-1-P), GlcNAc-6-Phosphate (GlcNAc-6-P), and Uridine diphosphate GlcNAc (UDP-GlcNAc)) posteriorized *Xenopus laevis* embryos and inhibited eye formation in *Danio rerio*.

Conversely, inhibition of NAGK, PGM3, UAP1, and DPAGT1 anteriorized *X. laevis* embryos and resulted in cyclopia in *D. rerio*. Injection of *N*-glycanase 1 (NGLY1) mRNA, which removes *N*-linked glycans from glycoproteins, anteriorized *X. laevis* embryos and resulted in cyclopia in *D. rerio*. qRT-PCR data suggests NAGK, PGM3, UAP1, and DPAGT1 specifically affect Wnt signaling in the early embryo, likely through the control of the Wnt ligand and/or the receptors Frizzled (Fz) and Low-density lipoprotein 6 (LRP6). This is the first work to link NAGK, PGM3, UAP1, and DPAGT1 to Wnt signaling.

Acknowledgements

First and most importantly, I would like to recognize my mentor Dr. Ethan Lee, who has guided and supported me throughout my graduate career. His door was always open and he never hesitated to offer advice and guidance no matter where my projects took me. His enthusiasm for science and amenable demeanor made him a joy to work with.

I would like to thank the members of the Lee lab. Especially, Dr. Kenyi Saito Diaz who always answered my questions, Dr. Tony Chen who would talk science with me for hours, Eddie Ross who made lab interesting, and especially Emily Crispi whose help was essential for me to publish many of my papers. I would like to thank Leah Marie Sawyer who kept the lab running and helped with image acquisition. I would like to thank my trainees and co-authors, William Conor Rork, Alya Zouaoui, and CheyAnne Youngblood. Thank you Dr. Brian Hang, Dr. Rubin Baskir, Dr. Matthew Broadus, Dr. Amanda Hansen, Dr. Annastasia Hyde, Arrush Choudhary, Victoria Ng, and Trevor Hann for the many great memories of lab.

I would like to extend a special thank you to my committee chair Dr. Andrea Page-McCaw. Without Andrea's help I would never have published my Cdc14 paper. I would also like to thank the rest of my wonderful and supportive committee; Dr. Ken Lau, Dr. Rebecca Cook, and Dr. Sandra Zinkel. I would also like to thank Dr. Christopher V. E. Wright and the Training Program in Developmental Biology for supporting me. I would like to thank those without whose help I would not have made it this far, including, but not limited to: Margaret Calhoun, Amy P. Morrison, Kathrin Lawrence, Dr. Peter Van Laarhoven, Dr. Tamim Shaikh, Dr. Maria

Couppis, Dr. David Stock, Dr. Alexander Cruz, Dr. Jennifer Knight, Dr. Joaquin Espinosa, Dr. Sarah Hainline, Dr. Laura A. Lee, Dr. Jim G. Patton, Dr. Kristen B. Artinger, Dr. Bruce Appel, Dr. Jia Shi and Qiang Guan. Lastly, I would like to thank my mother, Kathleen Neitzel-Hewes, my father, Richard Neitzel, my step mom, Teresa Boulay, my sisters, Katrina Neitzel and Kyra Hewes, and the rest of my family. Thank you everyone!

Table of contents

Title page i

Copyright ii

Dedication iii

Abstract iv

Acknowledgements vi

Table of contents viii

List of tables xii

List of figures xiii

List of abbreviations xv

Chapter 1: Introduction and overview 1

Chapter 2: Cdc14: a review of the known function and phenotypes 5

Structure of Cdc14 5

Cdc14 is essential in the cell cycle of the budding yeast, *Saccharomyces cerevisiae,* but not the fusion yeast, *Saccharomyces pombe* 6

Studies in *Phytophthora infestans* suggests an ancestral function in flagella 8

Fungal Cdc14 plays a conserved role in the cell cycle 9

Cdc14 in *Caenorhabditis elegans* regulates formation of vulval progenitor cells 9

Xenopus laevis Cdc14A is required in the abscission step of cytokinesis 10

Danio rerio Cdc14 control cilia formation and left-right body asymmetry 11

Cdc14 controls DNA damage repair in *Gallus gallus* 11

Mus musculus Cdc14 controls fertility and auditory function 12

Homo sapiens Cdc14 regulates auditory function and male fertility 13

Drosophila melanogaster Cdc14 controls sperm competitiveness, chemosensation, mechanosensation, metabolism, and resistance to starvation 14

Cdc14 is a highly conserved gene with a wide array of functions 15

Chapter 3: Characterization of a *cdc14* null allele in *Drosophila melanogaster* 18

Abstract 18

Introduction 19

Materials and methods 23

Generation of *cdc14* null by homologous recombination 23

DNA constructs 24

Drosophila stocks 24

Quantitative PCR 25

Immunoblotting 26
Assessment of female fertility 26
Progeny survival assay 27
Assessment of progeny sex 27
Male fertility assay 27
Sperm competition assay 28
Assessment of spermatids and mature sperm 28
Immunostaining 28
Microscopy 29
Egg aspect ratio 29
Larval path-length 30
Body wall contraction assay 30
Adult climbing assay 31
DNA damage assays 31
Mechanosensation assay 32
Larval yeast feeding assay 32
Larval quinine preference assay 32
Chemosensation test of adults 33
Phototaxis assay 34
Fat body staining 34
Assessment of starvation resistance 35
Statistics 35
Results 36
cdc14 expression is highest in the testis 36
Generation of *cdc14* knockout lines in D. melanogaster 36
Knockout of cdc14 is well tolerated 39
Overexpression of Cdc14-Myc 39
cdc14 knockdown does not affect the ratio of male-to-female progeny 40
Cdc14 is not required for Drosophila spermatogenesis 45
Loss of *cdc14* does not affect Drosophila oogenesis or embryogenesis 49
Cdc14 is not required for cell cycle checkpoint activation or DNA damage repair 49
Sperm competiveness is decreased in cdc14 null flies 53
Loss of cdc14 does not affect Drosophila path-length, coordination, or locomotion 59
Drosophila cdc14 null larvae have decreased mechanosensation 62
Gustation in Drosophila larvae is modulated by cdc14 66

Photoreception is unaffected in the *cdc14* null larvae 67
cdc14 confers resistance to starvation and modulation of lipid metabolism 72
Discussion 75
Chapter 4: The role of Glycosylation in Metazoan development 77
N-linked glycosylation 77
O-linked glycosylation 81
Glycosylation in development 84
Congenital Disorders of Glycosylation and *N*-glycosylation 89
Complex glycosylation and non-glycosylation pathways lead to CDGs 93
Treatment of CDGs 93
The UDP-GlcNAc salvage pathway recycles GlcNAc from degraded glycoproteins 95
Glycosylation is essential for proper metazoan development 96
Chapter 5: Wnt signaling and implications of glycosylation 97
The canonical Wnt/β-catenin pathway 97
The non-canonical Wnt pathway 101
Wnt signaling and *N*-glycosylation 101
NAGK and *N*-glycosylation modulate Wnt signaling possibly through LRP6 102
Chapter 6: *N*-acetyl-*D*-glucosamine kinase controls Wnt signaling in the early embryo 103
Abstract 103
Introduction 104
Materials and methods 106
Kinase screen 106
DNA constructs, mRNA and protein 111
Sugars and Morpholinos 111
Animals care 112
Xenopus embryo injections 112
Embryo soaking 113
Zebrafish embryo injections 113
Generation of cDNA and quantitative-PCR 114
Microscopy 115
Statistics 118
Results 119
Genome-scale human kinase screen identifies NAGK as a regulator of axiation in *Xenopus* 119
NAGK overexpression posteriorizes *Xenopus* embryos and NAGK inhibition anteriorizes *Xenopus* embryos 120
Posteriorization of *Xenopus* embryos by NAGK occurs via its role in glycosylation 126

Overexpression of UDP-GlcNAc salvage pathway posteriorizes *Xenopus* embryos; conversely, inhibition of the pathway and *N*-glycosylation anteriorizes embryos 131

Inhibition of *DPAGT1* or overexpression of *NGYL1* anteriorizes *Xenopus* embryos, while *DPAGT1* overexpression posteriorizes embryos. 141

Axis duplications from overexpression of UDP-GlcNAc salvage pathway enzymes, *DPAGT1*, and GlcNAc-1-P suggests Wnt specificity 142

NAGK expression in zebrafish results in a Wnt like phenotype 145

NAGK expression in zebrafish results in a convergent extension phenotype 151

qRT-PCR of early *Xenopus* embryos suggests NAGK is Wnt specific 154

NAGK regulates Wnt signaling in *Xenopus* ectodermal explants likely via cell surface receptors 157

Discussion 162

Chapter 7: Future directions 166

Cdc14 167

Feeding behavior, fat body metabolism, and longevity 167

Chemosensory reception, mechanosensory reception, sperm competitiveness, and cilia formation 169

NAGK 173

The salvage pathway, DPAGT1 and CDGs 173

The salvage pathway, DPAGT1 and cancer 174

Final thought on kinases and phosphatase 175

References 176

Appendix 1: References for NAGK phenotypes 210

Appendix 2: published works completed during graduate school that are not discussed in the main text 219

The Drosophila MCPH1-B isoform is a substrate of the APCCdh1 E3 ubiquitin ligase complex 220

The Small Molecule IMR-1 Inhibits the Notch Transcriptional Activation Complex to Suppress Tumorigenesis 230

Identification of a Paralog-Specific Notch1 Intracellular Domain Degron 267

The MAPK Pathway Regulates Intrinsic Resistance to BET Inhibitors in Colorectal Cancer 293

Comparative genetic screens in human cells reveal new regulatory mechanisms in WNT signaling 332

Differential abundance of CK1α provides selectivity for pharmacological CK1α activators to target WNT-dependent tumors 373

Phosphorylation of XIAP at threonine 180 controls its activity in Wnt signaling 406

List of tables

Table 2-1: Overview of possible known functions of Cdc14 in metazoa 17

Table 3-1: Representative metazoan Cdc14 orthologs identified across phyla 22

Table 4-1: Diseases of *N*-linked glycosylation identified in humans 92

List of figures

1-1: Diagram of Kinase and phosphatase activity....4

3-1: High expression of *cdc14* in the testes and generation of Drosophila *cdc14* null mutants by homologous recombination....37

3-2: *cdc14* is not required for female fertility or animal development....41

3-3: *cdc14* does not affect the ratio of male-to-female offspring, and nos-gal4 > UASp-cdc14-myc results in Cdc14-Myc protein expression....43

3-4: Cdc14-Myc localizes to the sperm bundle heads, but loss of *cdc14* does not affect male fertility or spermatid/sperm number or result in overt morphological changes of the testis....47

3-5: Cdc14-Myc is diffusely localized in the embryo and is not required for embryogenesis, apoptosis, or DNA damage repair....51

3-6: *cdc14* null males exhibit decreased sperm competition....55

3-7: *cdc14* null males mate overnight at the same rate as controls....57

3-8: *cdc14* nulls do not show impaired path-length or locomotion....60

3-9: Larval touch sensitivity assay....63

3-10: *cdc14* null larvae exhibit decreased sensitivity to mechanical stimuli....64

3-11: *cdc14* null larvae show decreased but indiscriminate feeding and loss of chemosensory responses....68

3-12: Adult chemosensation and larval phototaxis is unaffected by loss of *cdc14*....70

3-13: *cdc14* is required for normal lipid metabolism and survival during starvation conditions....73

4-1: Simplified scheme of the *N*-glycosylation pathway....79

4-2: The basics of *O*-glycosylation of proteins....82

4-3: The role of DPAGT1 in Wnt signaling....85

4-4: Discovery of glycosylation disorders....87

4-5: Diagram detailing known molecular and metabolic defects associated with CDGs....91

5-1: The current model of canonical Wnt/β-catenin signaling....99

6-1: Genome-scale human kinase screen identification of NAGK in *Xenopus* embryos....107

6-2: A GFP control for the screen shows robust expression of the kinase constructs in *Xenopus*....109

6-3: The qRT-PCR primers sets amplify a single product....116

6-4: NAGK overexpression posteriorizes *Xenopus* embryos, conversely NAGK inhibition anteriorizes *Xenopus* embryos....122

6-5: Examples of *Xenopus* phenotypes....124

6-6: Diagram of the UDP-GlcNAc salvage pathway and DPAGT1....127

6-7: Soaking *Xenopus* embryos in GlcNAc results in posteriorization, while soaking embryos in Tunicamycin results in anteriorization....129

6-8: Inhibition of NAGK, PGM3, UAP1, DPAGT1, or overexpression of NGLY1 anteriorize *Xenopus* embryos; conversely, overexpression of UDP-GlcNAc pathway enzymes, sugars, and DPAGT1 posteriorize embryos....133

6-9: Inhibition of the endogenous UDP-GlcNAc salvage pathway enzymes rescues the overexpression of pathway enzymes 135

6-10: Co-injection of downstream UDP-GlcNAc salvage pathway sugars rescues the inhibition of the pathway enzymes 137

6-11: Co-injection of downstream MO rescues overexpression of the UDP-GlcNAc salvage pathway sugars 139

6-12: Over expression of UDP-GlcNAc salvage pathway components promotes axis duplication in *Xenopus* 143

6-13: Overexpression of glycosylation salvage pathway enzymes, sugars and DPAGT1 inhibit eye formation in zebrafish 147

6-14: Inhibition of NAGK and *N*-glycosylation in zebrafish caused cyclocephaly 149

6-15: Inhibition and overexpression of NAGK, UDP-GlcNAc salvage pathway components, DPAGT1, and NGYL1 result in a short anterior-posterior body axis 152

6-16: qRT-PCR suggest the UDP-GlcNAc salvage pathway and DPAGT1 specifically control the Wnt signaling pathway in the early *Xenopus* embryo 155

6-17: Expression of *Xnr3* in Stage 10.5 animal caps suggests the UDP-GlcNAc salvage pathway works at the level of the ligand and/or receptor 158

6-18: Expression of *chordin* in Stage 10.5 animal caps suggests the salvage pathway works at the level of the ligand and/or receptor 160

7-1: The chordotonal organ of *cdc14* null larvae shows morphological changes in size, number, and length of scolopidia 171

Appendix-1: Examples of post-midblastula transition Wnt signaling phenotypes in the early *Xenopus laevis* embryo 211

Appendix-2: Examples of pre-midblastula transition Wnt signaling phenotypes in the early *Xenopus laevis* embryo 213

Appendix-3: Examples of Wnt signaling phenotypes in the early *Danio rerio* embryo 215

Appendix-4: Examples of Wnt mediated posteriorization of *Danio rerio* embryos 217

List of abbreviations

Cell Division Cycle 14 (CDC14)

N-Acetylglucosamine Kinase (NAGK)

Asparagine-linked glycosylation (ALG)

Congenital Disorders of Glycosylation (CDGs)

Cyclin-dependent kinase 1 (CDK1)

Dickkopf1 (Dkk1)

Dolichyl-phosphate *N*-acetylglucosamine-1-phosphate-transferase (DPAGT1)

Dishevelled (Dsh)

Endoplasmic reticulum (ER)

Frizzled (Fz)

N-acetylglucosamine (GlcNAc)

N-glycanase 1 (NGLY1)

GlcNAc-1-Phosphate (GlcNAc-1-P)

GlcNAc-6-Phosphate (GlcNAc-6-P)

Glycosylphos-phatidylinositol (GPI)

Kupffer's vesicle (KV)

Lipid-linked oligosaccharide (LLO)

Low-density lipoprotein receptor-related protein (LRP5/6)

Phosphoglucomutase 3 (PGM3)

Phospho-Histone H3 (pH3)

Phosphatidylinositol (4,5)-bispho-sphate (PIP2)

Quantitative reverse transcription polymerase chain reaction (qRT-PCR)

RNA interference (RNAi)

Reverse transcription polymerase chain reaction (RT-PCR)

Sex peptide (SP)

Terminal deoxynucleotidyl transferase dUTP nick end labeling (TUNEL)

UDP-*N*-Acetylglucosamine Pyrophosphorylase 1 (UAP1)

Uridine diphosphate N-acetylglucosamine (UDP-GlcNAc)

Ultra-violet (UV)

Chapter 1:

Introduction and overview

Five percent of the proteome comprises enzymes that perform more than two hundred different types of posttranslational modifications (Duan and Walther, 2015). Posttranslational modifications are essential for regulating activity, maturation, intracellular localization, stability, secretion, solubility, and preparation of substrates for additional modification. Modifications can be the addition or removal of chemical groups, such phosphate (phosphorylation), acetyl (acetylation), methyl (methylation), or hydroxyl (hydroxylation). They can also be polypeptides, such as ubiquitin (ubiquitylation), or complex molecules, such as carbohydrates (glycosylation), lipid (palmitylation), isoprenoid lipids (prenylation), adenosine diphosphate ribose (ADP-ribosylation), or adenosine monophosphate (adenylylation). In this work I will focus on two posttranslational modifications. First, I will focus on the addition and removal of phosphate (phosphorylation and dephosphorylation). Second, I will discuss modification with carbohydrates (glycosylation; discussed in chapter 4)

The human genome encodes about 147 protein phosphatases and 518 kinases (Alonso et al., 2004; Manning et al., 2002). Protein kinases and protein phosphatases have opposing catalytic activities (Fig. 1-1). Protein kinases catalyze the addition of phosphate to the hydroxyl group of Ser, Thr, or Tyr residues. Conversely, phosphatases catalyze the hydrolysis of phosphate from these residues. Other kinases and phosphatases catalyze the addition or removal of phosphates from sugars or lipids.

Protein kinases are derived from a single common ancestor (Tonks, 2006). The core of all known kinases share a large number of conserved sequence motifs (Hanks and Hunter, 1995; Taylor and Korney, 2010). In contrast to this, phosphatases evolved independently from several evolutionary progenitors and are considered to be promiscuous (Tonks, 2006). Therefore, the activity of these kinases and phosphatases needs to be precisely targeted to the appropriate substrates through temporal and spatial regulation, the use of alternative promoters to control their expression, the presence of multiple splicing variants, post-translational modifications, and formation of various holoenzyme complexes consisting of catalytic and regulatory subunit(s) (Andreassen et al., 1998; Davezac et al., 2000; Liu et al., 2010; Takizawa and Morgan, 2000; Tonks, 2006; Trinkle-Mulcahy et al., 2003; Virshup and Shenolikar, 2009).

In this work, I will describe my characterization of the protein phosphatase, Cell Division Cycle 14 (CDC14) during *Drosophila melanogaster* development. Specifically, I will describe the generation and analysis of the phenotype of a *cdc14* null line in *Drosophila*. The *cdc14* null flies are were both viable and fertile. However, I will show that Drosophila *cdc14* plays a role in ciliated sperm competitiveness, chemosensory reception, mechanosensory reception, fat body metabolism, and longevity during starvation conditions.

I will also describe my analysis of the sugar kinase, *N*-Acetylglucosamine Kinase (NAGK), which converts the amino sugar *N*-acetylglucosamine into N-acetylglucosamine-1-Phosphate. I will describe how we identified NAGK in a screen for novel kinases regulating development. I will also show the NAGK misregulation in *Xenopus laevis* leads to anteroposterior defects, and inhibition of eye formation or cyclopia in *Danio rerio*. I will show that the UDP-GlcNAc salvage

pathway and enzymes controlling *N*-glycosylation phenocopy this finding. Finally, I will show that these changes are the result of changes in Wnt signalling.

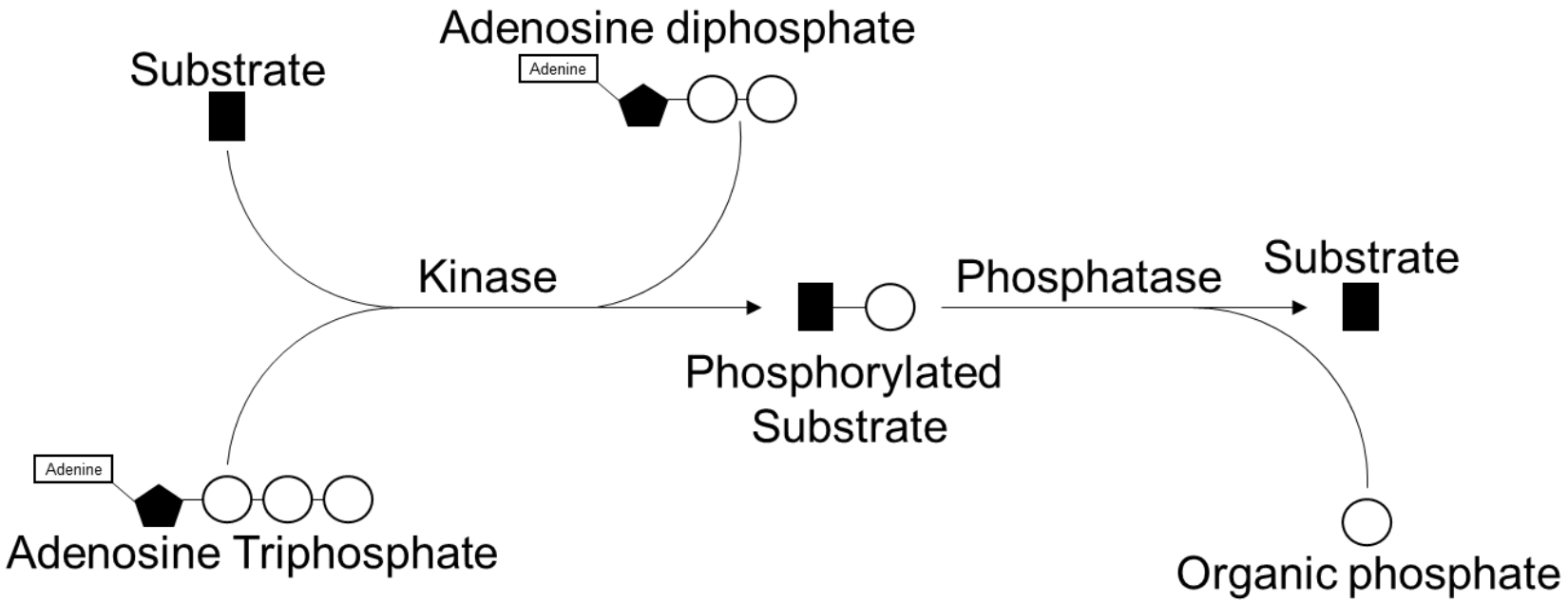

Figure 1-1: Diagram of Kinase and phosphatase activity.

Chapter 2:

Cdc14: a review of the known function and phenotypes[1]

Cdc14 was first identified in a genetic screen in the budding yeast, *Saccharomyces cerevisiae,* to identify novel loci that control the cell cycle (Hartwell et al., 1974). Cdc14 is a protein phosphatase and a member of the dual specificity phosphatase family of phosphatases, a subgroup of the larger protein tyrosine phosphatase super family (Taylor et al., 1997). Therefore, Cdc14 is possess the catalytic ability to dephosphorylate both phosphotyrosine and phosphoserine/phosphothreonine. Cdc14 Is one of the best characterized and most studied dual specificity phosphatases because of its essential role in *S. cerevisiae* (Mocciaro and Schiebel, 2010).

Structure of Cdc14

All known orthologs of Cdc14 share a highly conserved N-terminal core of ~350 amino acids (Mocciaro and Schiebel, 2010). Analysis of Cdc14's crystal structure suggests a conserved core that contains two domains (Gray et al., 2003). The first is the N-terminal A-domain which is proposed to contribute to substrate specificity and the second is the catalytic C-terminal B-domain encompassing the signature Protein tyrosine phosphatase motif (Gray et al., 2003). The

[1] Table 2-1, a summary of phenotypes is provided at the end of the chapter.

carboxyl-terminal region of Cdc14, which is variable in length and sequence, contains a nuclear export sequence and may be important for subcellular localization (Mocciaro and Schiebel, 2010). Yeast orthologs have an additional nuclear localization sequence, while a unique the N-terminal KKIR motif in vertebrate Cdc14B targets Cdc14 to the nucleolus (Berdougo et al., 2008; Cho et al., 2005; Kaiser et al., 2002; Mailand et al., 2002; Mocciaro and Schiebel, 2010; Rosso et al., 2008).

Cdc14 is essential in the cell cycle of the budding yeast, *Saccharomyces cerevisiae,* but not the fusion yeast, *Saccharomyces pombe*

Pioneering work in *S. cerevisiae* demonstrated that ScCdc14 is essential for opposing Cdk1 activity to promote mitotic exit and cytokinesis (Visintin et al., 1998). Subsequent studies in other organisms suggest this cell cycle function is specific to *S. cerevisiae* (Berdougo et al. 2008; Mocciaro and Schiebel 2010). Studies on Cdc14 substrate specificity indicates that it only acts on a subset of Cdk substrates and plays a specialized role in antagonizing Cdk phosphorylation (Powers and Hall, 2017; Ubersax et al., 2003). Genetic and biochemical studies in *S. cerevisiae* suggest that ScCdc14 is involved in nearly all aspects of the cell cycle and is involved in the metaphase-to-anaphase transition, meiosis I to meiosis II transition, anaphase spindle stabilization, preventing anaphase bridges, resetting replication origins, mitotic spindle elongation, mitotic exit, septum formation, and cytokinesis (Bembenek and Yu, 2001; Chin et al., 2010; Fox et al., 2017; García-Luis et al., 2014; Higuchi and Uhlmann, 2005; Hatano et al., 2016; Holt et al., 2008; Jaspersen and Morgan, 2000; Khmelinskii et al., 2007; Khmelinskii et al.,

2009; Kao et al., 2014; Konig et al., 2010; Lippincott et al., 2001; Machín et al., 2016; Meitinger et al., 2010; Menssen et al., 2001; Miller et al., 2015; Palani et al., 2012; Pereira and Schiebel, 2003; Quevedo et al., 2015; Raspelli et al., 2015; Roccuzzo et al., 2015; Stegmeier et al., 2002; Sanchez-Diaz, et al. 2012; Tzeng et al., 2011; Varela et al., 2010; Visintin et al., 1998). The cell-cycle dependent release of ScCdc14 from the nucleus to the cytoplasm is controlled through oscillations of Cdk activity, largely driven by periodic synthesis and destruction of mitotic cyclins, and a negative feedback loop (Lu and Cross, 2010; Manzoni et al., 2010). Even brief and reversible inhibition of ScCdc14 can induce multiple gross chromosomal rearrangements and changes in ploidy (Quevedo et al., 2015). Additionally, ScCdc14 inhibits transcription of ribosomal DNA (rDNA) in anaphase, targets condensin to rDNA to accurately segregate rDNA and telomeric regions (D'Amours et al., 2004; Fox et al., 2017; Sullivan et al., 2004; Clemente-Blanco et al., 2009; Clemente-Blanco et al., 2011; Matos-Perdomo and Machin, 2018). Recently, ScCdc14 has been implicated DNA damage repair and in autophagy induction (Eissler et al., 2014; Kondo et al., 2018; Villoria et al., 2017).

In contrast to *S. cerevisiae,* the *Saccharomyces pombe* orthologue, Cdc14-like phosphatase (Clp1; also known as Flp1) is not essential (Cueille et al., 2001; Trautmann et al., 2001). Clp1 is released into the nucleolus at the G–M transition and subsequently localizes to the mitotic spindle and to kinetochores (Chen et al., 2006). While both ScCdc14 and Clp1 antagonize Cdk1 activity, Clp1 regulates mitotic entry and cytokinesis but not mitotic exit (Cueille et al., 2001; Trautmann et al., 2001). Clp1 may ensure accurate chromosome segregation and regulate the formation of the septum during cytokinesis (Clifford et al., 2008; Cueille et al., 2001; Simanis, 2003; Trautmann et al., 2001; Trautmann et al., 2004). However,

Clp1 is not essential for cytokinesis or septation (Clifford et al., 2008; Cueille et al., 2001; Simanis, 2003; Trautmann et al., 2001).

Studies in *Phytophthora infestans* suggests an ancestral function in flagella

Interestingly, Cdc14 is rarely found in species lacking flagella (Ah-Fong and Judelson, 2011). The primitive eukaryote, *Phytophthora infestans*, lacks a classical cell cycle. Instead, *P. infestans* grows by extending a filamentous coenocytic hyphae (Whittaker et al., 1991). The coenocytic hyphae is a multinucleate cell in which the nuclei divide asynchronously, without the accompanying cytokinesis (Whittaker et al., 1991). This growth continues until metabolic and environmental factors trigger sporulation (Marks, 1965; Maltese et al., 1995). PiCdc14 is only expressed during asexual sporulati on, its expression is essential (Ah-Fong and Judelson, 2003). PiCdc14 is not expressed in the vegetative hyphae, where most mitosis takes place (Ah-Fong and Judelson, 2003; Ah-Fong and Judelson, 2011). PiCdc14 is suggested to synchronize nuclear behavior during sporulation and maintain dormancy in spores until germination (Ah-Fong and Judelson, 2003). PiCdc14 is enriched at flagella-basal body complexes, the site from which flagella develop, suggesting an ancestral role of Cdc14 in the flagella of eukaryotes (Ah-Fong and Judelson, 2011). These studies suggest Cdc14 may have originated to control the formation and/or activity of flagella and acquired additional roles in other eukaryotes (e.g., the cell cycle).

Fungal Cdc14 plays a conserved role in the cell cycle

Cdc14 is present in animals and fungi but is not found in plants (Li et al., 2015). In the fungus *Beauveria bassiana*, BbCdc14 phosphatase is localized to the nuclei and regulates cytokinesis, asexual development, thermotolerance, UV-resistance, and virulence (Wang et al., 2013). In *Fusarium graminearum*, FgCdc14 is required for cell division, nuclear division, cytokinesis, septum formation, conidiation, ascosporogenesis, and virulence (Li et al., 2015). In *Magnaporthe oryzae,* a typical foliar pathogen, MoCdc14 plays an essential role in nuclear distribution, pathogenesis, and septum formation during conidiogenesis and appressorium, critical steps in the infection cycle (Li et al. 2018). In *Aspergillus flavus,* a common agricultural pest, AflCdc14 is localized to the cytoplasm and vesicles during coidial germination and mycelial development stages and is essential for septum formation, sclerotia generation, conidium morphology, osmotic sensitivity, aflatoxin production, and virulence (Yang et al., 2018). These studies suggest cdc14 has a conserved role in the cell cycle between fungi and yeast.

Cdc14 in *Caenorhabditis elegans* regulates formation of vulval progenitor cells

While relatively little is known about Cdc14 in vertebrates, it is highly conserved amongst all metazoan. Work on *Caenorhabditis elegans* (CeCdc14) suggest localization is regulated by nucleocytoplasmic shuttling to the spindle midzone in anaphase, midbody in telophase, cytoplasm in interphase cells, on centrosomes, and spindle microtubules (Gruneberg et al., 2002; Roy et al., 2011; Saito et al., 2004). In post-mitotic cells, CeCdc14 localizes to the

nucleus and the nucleolus (Saito et al., 2004). RNA interference experiments suggest CeCdc14 plays a role in cytokinesis, with depletion leading to multi-nucleated cells and embryonic lethality (Gruneberg et al., 2002). A second study was unable to replicate these results, and found that animals were viable and did not exhibit observable mitotic or cytokinetic defects (Saito et al., 2004). Instead, Saito et al., and later Roy et al., observed defects in the duplication of vulval progenitor cells (Roy et al., 2010; Saito et al., 2004). It has been suggested that high concentrations of small interfering RNA may have resulted in off target effect in the initial study by Gruneberg (Kipreos, 2004; Saito et al., 2004).

Xenopus laevis Cdc14A is required in the abscission step of cytokinesis

Two Cdc14 isoforms, XCdc14A and XCdc14B, exist in *Xenopus laevis* (Kaiser et al., 2004; Krasinska et al., 2007). XCdc14A has been suggested to localize to the midbody during cytokinesis and the centrosome during interphase (Krasinska et al., 2007). While no studies have tested the role of XCdc14B, XCdc14A has been shown to be required in abscission, the final step of cytokinesis during the cell cycle (Krasinska et al., 2007). XCdc14A may also regulate the G1/S and G2/M transitions (Krasinska et al., 2007). Overexpression of XCdc14A is suggested to inhibit the recruitment of soluble N-ethylmaleimide-sensitive factor (NSF) attachment protein receptor (SNARE) and exocyst complexes to the midbody, but did not interfere with central spindle formation, re-localization of passenger proteins, or central spindlin complexes to the midbody (Krasinska et al., 2007). These data suggest a novel role for Cdc14 in vesicle trafficking during the abscission step of cytokinesis.

Danio rerio Cdc14 control cilia formation and left-right body asymmetry

Danio rerio have two Cdc14 orthologues (zCdc14A1 and zCdc14B). Knockdown of either zCdc14A1 or zCdc14B inhibited ciliogenesis in Kupffer's vesicle (KV) and other ciliated tissues, independent of its cell cycle function (Clement et al., 2011; Clement et al., 2012). KV is a transient embryonic organ of asymmetry (Essner et al., 2005). The movement of cilia in KV establishes a directional flow of fluid, which directs left-right asymmetrical patterning in the early embryo (Essner et al., 2005). Consistent with inhibition of cilia in the KV, both zCdc14A1 and zCdc14B knockdowns exhibit left-right asymmetry defects (Clement et al., 2011; Clement et al., 2012; Delmaghani et al., 2016; Imtiaz et al., 2017). In addition, embryos had ventrally curved bodies, hydrocephaly, kidney cysts, and the kinocilia length in inner-ear hair cells may be reduced (Clement et al., 2011; Clement et al., 2012; Delmaghani et al., 2016; Imtiaz et al., 2017). These data suggest that zCdc14A1 and zCdc14B are both required and essential for the formation and function of cilia. Taken with the data in *P. infestans*, this suggests Cdc14 has retained its ancestral role in ciliogenesis vertebrates.

Cdc14 controls DNA damage repair in *Gallus gallus*

Two orthologs, cCdc14A and cCdc14B have been identified in *Gallus gallus* cells (Mocciaro et al., 2010). cCdc14A localizes to the centrosome in interphase, while cCdc14B shows nuclear localization similar to human orthologs (Mocciaro et al., 2010; Mailand et al., 2002). *In vitro* knockouts of cCdc14A and cCdc14B are viable, but exhibit impaired DNA damage

repair (Mocciaro et al., 2010). This finding is consistent with data in human cell lines and suggests a novel role for Cdc14 in vertebrate DNA damage repair (Mocciaro et al., 2010).

Mus musculus Cdc14 controls fertility and auditory function

Work on *Mus musculus* cell lines suggest the two orthologues (mCdc14a and mCdc14b) play a redundant role in DNA damage repair (Lin et al., 2015). *In vivo* homozygous recessive mutations of mCdc14A result in significant levels of perinatal lethality (Imtiaz et al., 2018). However, in surviving animals, mCdc14a mutations have been found to cause progressive, moderate-to-profound deafness and male infertility (Imtiaz et al., 2018; Delmaghani et al., 2016). This recapitulates the phenotypes identified in humans homozygous for mutations in Cdc14A (Imtiaz et al., 2018; Delmaghani et al., 2016).

In the kinocilia of the inner ear, endogenous mCdc14A was found to localize to the basal bodies and as puncta concentrated towards the tips of stereocilia (Imtiaz et al., 2018). When taken with the data in zebrafish and *P. infestans*, this suggests a role for mCdc14 in the cilia of *M. musculus*. Interestingly, the auditory hair and seminiferous tubules of mCdc14a mutants form normally, but then degenerate (Imtiaz et al., 2018). Furthermore, mutation of mCdc14 resulted in a loss of spermatogenic cells and mature sperm, as well abnormal sperm. These data suggest that mCdc14 plays a role in maintaining the auditory hair and spermatogenic cells, possible through cilia maintenance or function.

***Homo sapiens* Cdc14 regulates auditory function and male fertility**

Most mammals have two Cdc14 homologues (Cdc14A and Cdc14B) (Lin et al., 2015). However, hominoids have a third (Cdc14C) due to a gene retro-duplication event, whose expression is specific to the brain and testis (Rosso et al., 2008). Functional studies in *S. pombe* show that both hCdc14A and hCdc14B rescue Clp1-deficiency, and hCdc14B can rescue ScCdc14 deficiency, suggesting conserved function (Vazquez-Novelle et al., 2005). While hCdc14A or hCdc14B knockout cells do not exhibit obvious growth or mitotic defects, knockdown and overexpression studies have suggested several phenotypes (Berdougo et al., 2008; Mocciaro et al., 2010). The role of Cdc14c is unknown, but overexpression studies suggest it localization to the endoplasmic reticulum and microtubules (Rosso et al., 2008).

Localized to the cytoplasm and on centrosomes in interphase, hCdc14A has been implicated in centrosome separation, chromosome segregation, and cytokinesis (Kaiser et al., 2002; Mailand et al., 2002). Furthermore, hCdc14A has been found to regulate cell migration and cell adhesion in cancer cell lines (Chen et al., 2016; Chen et al., 2017). hCdc14B is predominantly nucleolar, though it may be localized to centrioles, long nuclear filaments, microtubules, the spindle midzone, and the midbody and may play a role in nuclear organization, mitotic-spindle assembly, centriole duplication, mitotic exit, regulation of the M-to-G1 transition and/or in G2 DNA damage checkpoint activation (Bassermann et al., 2008; Berdougo et al., 2008; Cho et al., 2005; Dryden et al., 2003; Kaiser et al., 2002; Mailand et al., 2002; Nalepa and Harper, 2004; Rodier et al., 2008; Rosso et al., 2008; Tanguay et al., 2010; Wu et al., 2008).

In 2016, Delmaghani et al. reported the first know mutation of hCdc14A in a large consanguineous Iranian family. Eleven affected individuals were presented with severe or profound congenital deafness resulting from an autosomal-recessive nonsense mutation of Cdc14. A subsequent screen of individuals with severe deafness identified an additional nonsense mutation. In 2018, Imtiaz et al. identified families with an additional four novel truncating and three missense alleles associated with progressive, moderate-to-profound deafness. Deaf males in five of these families were infertile, while deaf females were fertile. This data agrees with mutations in mCdc14A, which exhibit deafness and male infertility (Imtiaz et al., 2018).

Drosophila melanogaster Cdc14 controls sperm competitiveness, chemosensation, mechanosensation, metabolism, and resistance to starvation

Drosophila melanogaster encode a single Cdc14 gene. The function of the *Drosophila* Cdc14 has not been previously reported. In the next chapter of I will demonstrate that the single *Drosophila* Cdc14 gene plays a role in sperm competitiveness, chemosensory reception, mechanosensory reception, fat body metabolism, and longevity during starvation conditions. These phenotypes are distinct from those identified in any other organism. Though, they suggest a conserved function in ciliated structures, similar to that seen in *Phytophthora infestans*. Furthermore, they suggest a conserved function in sperm that may have implications in the study of mutations of human Cdc14A.

Cdc14 is a highly conserved gene with a wide array of functions

Cdc14 has been implicated in many cellular processes, including mitotic entry, cytokinesis, chromosome segregation, DNA damage repair, and ciliogenesis (Table 2-1). While Cdc14 is only known to be essential in *S. cerevisiae*, all metazoans and fungi have at least a single ortholog. In *H. sapiens* and *M. musculus* Cdc14 is important for male fertility and auditory function. Previous work in *D. rerio, P. infestans*, and *M. musculus* has suggested that the observed phenotypes in humans may be due to a conserved role of Cdc14 in cilia.

While Cdc14 is highly conserved, its function is poorly understood. Data in *H. sapiens*, *D. rerio, P. infestans*, and *M. musculus* models suggests a role in cilia that may have been conserved throughtout evolution. However, Cdc14 has not been implicated in ciliation of *C. elegans*, *X. laevis*, *G. gallus*, *B. bassiana*, *F. graminearum*, *M. oryzae*, or *A. flavus*, suggesting that this could be an atavism (an ancestral trait lost through evolution that reappears). As I will show in the next chapter, Cdc14 plays a role in the ciliated cells of *D. melanogaster*. This suggests that Cdc14 is not atavistic, but may play a role in the cilia of *C. elegans*, *X. laevis*, *G. gallus* that has not yet been identified.

In *B. bassiana*, *F. graminearum*, *M. oryzae*, or *A. flavus, S. cerevisiae, S. pombe, C. elegans, X. laevis, D. rerio, M. musculus, and H. sapiens* Cdc14 plays a role in the cell cycle. However, the role varies between organisms. For example, in *X. laevis* Cdc14 only plays a role in abscission, while in *S. pombe* cdc14 controls earlier events, such as chromosome segregation. This suggests that Cdc14 may have gained or lost roles in the cell cycle throughtout evolution. This is further supported by the fact that Cdc14 is essential in *S. cerevisiae*, but not in any other

organism studied so far. It is possible that Cdc14 has become redundant with additional phosphatases, as phosphatases are considered to be promiscuous enzymes. Furthermore, studies have suggested the activity of Cdc14 is controlled by temporal and spatial expression. It is possible that Cdc14 has evolved new functions in the cell cycle dependant upon when and where it is expressed. Therefore, Cdc14 likely works on many substrates that may vary between organisms. Moreover, multiple Cdc14 orthologues may work redundantly, confounding studies of Cdc14's function and evolutionary conservation.

The use of *D. melanogaster* to study Cdc14 is important for several reasons. First, it is the closet model system to *H. sapien* evolutionarily that has a single Cdc14 orthologue. This removes the possibility of redundancy confounding the results. *D. melanogaster* has only two ciliated cell types (Sensilla and sperm) and a large number of tools (transgenics, stains, cell lines, mutants, etc.) exist to study cilia and the cell cycle. The speed with which Cdc14 can be investigated and the lack of redundancy make *D. melanogaster* ideal for studies of molecular function in the sperm and cell cycle, which can be followed up by investigation in the *M. musculus* and *H. sapiens.*

	Proposed Function(s)
Saccharomyces cerevisiae (budding yeast)	• Mitotic exit • Cytokinesis • Spindle elongation and stabilization • Resetting of replication origins • Antagonism of Cdk phosphorylation • Septum formation • rDNA transcription and segregate • Segregation of telomeric regions • DNA damage repair • Autophagy
Saccharomyces pombe *(fission yeast)*	• Cytokinesis • Chromosome segregation • Septum formation
Phytophthora infestans	• Formation and/or activity of flagella
Caenorhabditis elegans	• Cytokinesis • Vulval progenitor cells proliferation
Xenopus laevis	• Abscission during cytokinesis
Danio rerio (zebrafish)	• Ciliogenesis • Establishing Left-right body asymmetry
Gallus gallus (Chicken)	• DNA damage repair
Mus musculus *(mouse)*	• DNA damage repair • Auditory hair cell maintenance • Male fertility
Homo sapien *(Human)*	• Centrosome separation • Chromosome segregation • Cytokinesis • Nuclear organization • Mitotic-spindle assembly • Centriole duplication • Mitotic exit • DNA damage repair • Auditory hair cell maintenance • Male infertility

Table 2-1: Overview of possible known functions of Cdc14 in metazoa.

Chapter 3:

Characterization of a *cdc14* null allele in *Drosophila melanogaster*

The work described herein this chapter has been published:

Leif R. Neitzel, Matthew R. Broadus, Nailing Zhang, Leah Sawyer, Heather A. Wallace, Julie A. Merkle, Jeanne N. Jodoin, Poojitha Sitaram, Emily E. Crispi, William Rork, Laura A. Lee, Duojia Pan, Kathleen L. Gould, Andrea Page-McCaw, Ethan Lee. (2018) *Biology Open*

doi: 10.1242/bio.035394

Abstract

Cdc14 is an evolutionarily conserved serine/threoninephosphatase. Originally identified in *S. cerevisiae* as a cell cycle regulator, its role in other eukaryotic organisms remains unclear. In *Drosophila melanogaster*, Cdc14 is encoded by a single gene, thus facilitating its study. We found that Cdc14 expression is highest in the testis of adult flies and that *cdc14* null flies are viable. *cdc14* null female and male flies do not display altered fertility. *cdc14* null males, however, exhibit decreased sperm competitiveness. Previous studies have shown that Cdc14 plays a role in ciliogenesis during zebrafish development. In Drosophila, sensory neurons are ciliated. We found that the Drosophila *cdc14* null mutants have defects in chemosensation and mechanosensation as indicated by decreased avoidance of repellant substances and decreased response to touch. In addition, we show that *cdc14* null mutants have defects in lipid metabolism and resistance to starvation. These studies highlight the diversity of Cdc14 function in eukaryotes despite its structural conservation.

Introduction

Cdc14 phosphatases are a well conserved family of proline-directed serine/threonine phosphatases (Mocciaro et al., 2010). Initially identified in *Saccharomyces cerevisiae* as an essential cell cycle protein (Stegmeier and Amon, 2004), Cdc14 functions to antagonize cyclin-dependent kinase (CDK)-mediated phosphorylation events (Machin et al., 2016; Mocciaro et al., 2010; Queralt and Uhlmann, 2008; Stegmeier and Amon, 2004). Despite its conservation, Cdc14 orthologs are not essential for cell division in all organisms, although they play important roles in an array of biological processes, including chromosome segregation (Clemente-Blanco et al., 2011; Machin et al., 2016; Mocciaro et al., 2010; Stegmeier and Amon, 2004), cytokinesis (Clifford et al., 2008), centrosome duplication (Mocciaro et al., 2010; Rüthnick and Schiebel, 2016), mitotic exit (Wolfe and Gould, 2004), transcription (Clemente-Blanco et al., 2009, 2011; Guillamot et al., 2011; Papadopoulou et al., 2010), the DNA damage response (Mocciaro et al., 2010), and ciliogenesis (Clément et al., 2011, 2012). Although they have been much studied, a comprehensive understanding of Cdc14 phosphatases in higher eukaryotes in particular is still lacking.

A thorough dissection of the role(s) of Cdc14 phosphatases in metazoans is complicated by the existence of multiple Cdc14 paralogs in vertebrates (Table 3-1) (Clément et al., 2011; Kaiser et al., 2004; Krasinska et al., 2007; Li et al., 2000; Mocciaro et al., 2010). For example, human Cdc14 phosphatases are encoded by three different genes, *CDC14A*, *CDC14B*, and *CDC14C* (Clément et al., 2011; Kaiser et al., 2004; Krasinska et al., 2007; Li et al., 2000; Mocciaro et al., 2010). Knockout studies of individual human CDC14 genes failed to demonstrate growth

or mitotic defects, possibly reflecting functional redundancy between the paralogs (Berdougo et al., 2008; Mocciaro et al., 2010). However, it is still unclear whether the cellular functions of Cdc14 paralogs are fully redundant or simply overlapping. It is clear that they have distinct intracellular locations with CDC14A at centrosomes and CDC14B in the nucleolus of interphase cells (Clément et al., 2011; Kaiser et al., 2004; Krasinska et al., 2007; Li et al., 2000; Mocciaro et al., 2010), and they have been assigned some distinct functions. While CDC14A has been implicated in cytokinesis, transcriptional repression, and DNA damage repair, CDC14B is implicated in G1-phase length, centriole duplication, spindle stability, zygotic genome activation, DNA damage repair and checkpoint response (Buffone et al., 2014; Cho et al., 2005; Clemente-Blanco et al., 2011; Rodier et al., 2008; Wu et al., 2008). The biological role of CDC14C is currently unknown (Rosso et al., 2008).

Like yeast, the roundworm, *Caenorhabditis elegans*, has only one identified Cdc14 orthologue. The lack of multiple paralogs makes the roundworm an attractive organism to gain a comprehensive understanding of Cdc14 phosphatase function in a higher eukaryote. However, in *C. elegans*, Cdc14 functions in a manner unrelated to that in any other organism reported to date – to promote cellular quiescence of specific precursor cells (Cueille et al., 2001; Saito et al., 2004).

The common fruit fly, *Drosophila melanogaster* also has a single gene that encodes Cdc14 (*Dmel**cdc14*), the role of which has not yet been reported (Fisher et al., 2012). Herein, we demonstrate that the Drosophila *cdc14* gene plays a role in sperm competitiveness, chemosensory reception, mechanosensory reception, fat body metabolism, and longevity

during starvation conditions. This array of phenotypes associated with loss of *cdc14* function is once again distinct from those identified in any other organism, thereby highlighting a remarkable functional versatility for such a conserved protein.

Species	Cdc14 Orthologs
S. cerevisiae	*CDC14*
S. pombe	*clp1/flp1*
C. elegans	*cdc-14*
D. melanogaster	*cdc14*
D. rerio	*cdc14A,cdc14B*
X. laevis	*cdc14A,cdc14B*
G. gallus	*CDC14A,CDC14B*
M. musculus	*Cdc14A,Cdc14B*
H. sapiens	*CDC14A,CDC14B,CDC14C*

Table 3-1: Representative metazoan Cdc14 orthologs identified across phyla.

Materials and methods

Generation of *cdc14* null by homologous recombination

For recombination, the homologous arms for *cdc14* were cloned into the pW25 vector. The left homologous arm was generated using the forward primer CG7134-NotI (5'-AGCAGCGGCCGCTACATCGCGGTTCGTGTCACCG-3' and the reverse primer CG7134-ACC65I 5'-TACCGGTACCCAGGAGCACGGGAGACTTCGAC-3'). The right homologous arm was generated using the forward primer CG7134-AscI (5'-AGCAggcgcgccATTTTGGCCAGTTCGGGGAGCAG-3') and the reverse primer CG7134-BsiWI (5'-TACCCGTACGTCTCCACCAATTTGTAGGTGGG-3'). The construct covers a 9035-bp region of chromosome 2L where the left arm ends 13 bp upstream of the ATG and the right arm starts immediately after the coiled-coil domain encoded by *cdc14*. This construct was used to excise the 5'-UTR and exons 1 through 6 of *cdc14*-RA and *cdc14*-RD and the 5'-UTR, exons 1 through 5, and 3'-UTR of *cdc14*-RB, *cdc14*-RC, and *cdc14*-RE (2L:7802415 to 7810697) and replace it with the *white*$^{+}$ cDNA via ends-out-homologous recombination (Gong and Golic, 2003; Maggert et al., 2008).

Knockout lines were verified by PCR of *r2d2* and *cdc14* using the forward 5'-TTGATAGAGCGCTCTCTCGT-3' and reverse 5'-CGGATGGATGGAAGTATGTA-3' primers for *r2d2* (Liu et al., 2006) and the forward 5'-CATCGCTGTATTTCCACCCAC-3' and reverse 5'-AAGGCATCACTCGCGATCC-3' primers for *cdc14*. For PCR and sequencing of the boundaries of the *cdc14* mutation, the forward 5'-CGAAGTCTCCCGTGCTCCTG-3' and reverse 5'-CGACGAAGCGCCTCTATTTA-3' primers were used for the left recombination boundary and the

forward 5′-TCCGGTTGTTTTCGTGCTCA-3′ and reverse 5′-CTCCCCGAACTGGCCAAAAT-3′ primers were used for the right recombination boundary.

DNA constructs

cDNA clone GH01148 encoding *cdc14*-B was obtained from the Drosophila Gene Collection (Stapleton et al., 2002). *UASp-cdc14-myc* was created by subcloning the amplified coding sequence from GH01148 into a modified version of UASp that confers a C-terminal Myc tag (Rørth, 1998).

Drosophila stocks

Stocks were maintained at 25°C using standard techniques (Greenspan, 2004). The y^1 w^{1118}, w^{1118}, $mei\text{-}41^{RT1}$ (FlyBase ID: FBal0046106), and red-eyed control [*y w*; *FLAG-Mcm4* (*BAC#1 attP40*): from the Nordman lab, Vanderbilt University] lines were used as controls. The *UASp-cdc14-myc* transgenic line was generated by *P*-element mediated insertion via embryo injection in the *y w* background using standard methods (Rubin and Spradling, 1982). Overexpression of *UASp-cdc14-myc* was driven by crossing with *nanos-Gal4* (FlyBase ID: FBst0032563) or *tubP-Gal4* (FlyBase ID: FBtp0002651) flies. The *UASp-cdc14-myc,* $cdc14^{\Delta 1}$ line was established by recombination using standard methods. The $cdc14^{\Delta 1}$; *nanos-gal4* line was established by performing standard genetic crosses. $cdc14^{\Delta 1}$ null larvae with maternally

contributed *cdc14* (*cdc14*$^{\Delta 1\text{-}Maternal}$) were obtained by crossing *cdc14*$^{\Delta 1}$/*CyO* females to *cdc14*$^{\Delta 1}$ homozygous males. All transgenic lines were isogenic.

The *cdc14* gene is located on chromosome 2L:7,801,668 to 7,810,703 (FlyBase ID: FBgn0031952, FlyBase build: FB2018_02) and has five alternative transcripts, the longest of which encodes a 1052 amino acid protein (Fig. 3-1B) (Gramates et al., 2017). The *cdc14* gene is flanked by the housekeeping gene *r2d2* (2L:7,800,147 to 7,802,098).

Quantitative PCR

cDNA was generated from adult carcasses, late third instar larvae, and excised gonads. Samples were homogenized in 1 ml RNA Stat-60 and cleaned up by chloroform extraction. cDNA was prepared using the High Capacity cDNA Reverse Transcription Kit (Applied Biosystems, Foster City, USA) with the supplied random primers. qPCR was performed using the GoTaq® qPCR Master Mix (Promega, Madison, USA) on a CFX96 qPCR machine from Bio-Rad. cDNA was prepared in triplicate using samples from separate crosses, and qPCR was performed using three technical replicates. The forward 5'-GAGATGCAGGAAGACCGATTAT-3' and reverse 5'-CTCATCGACGCTGAAGTAGTG-3' primers were used to assess relative *cdc14* mRNA levels, which were normalized to Dmel*Rp49* expression levels using the 5'-GAGATAGAGGCCCTTGGAAATG-3' forward and 5'-CAGATCACCCACAGTCGAATC-3' reverse primer.

Immunoblotting

Embryo lysates for immunoblotting were generated as previously described (Hainline et al., 2014). For late third instar larvae, pools of ten were collected and homogenized in 200 µl of running buffer (Fig. 3-1F, Fig. 3-3B,C), and protein equivalent to one-half of a larva (10 µl) was used. All samples were run on ExpressPlus™ PAGE gels 4–20% from GenScript. Membranes were probed with mouse anti-Myc (9E10, 1:100; Santa Cruz Biotechnology, catalog #sc-40) and mouse anti-alpha tubulin (DM1α, 1:2500; Sigma-Aldrich, catalog #T6199) primary antibodies and anti-mouse horseradish peroxidase (1:5000) secondary antibody followed by visualization of signal on a LI-COR C-DiGit® Blot Scanner using SuperSignal™ West Femto Maximum Sensitivity Substrate or HyGLO™ Quick Spray.

Assessment of female fertility

Males were allowed to mate with virgin females for 3 or 7 days within chambers on grape juice plates (3% agar, 25% grape juice, 0.3% sucrose). Individual females were then transferred to a standard culture vial and allowed to lay eggs for 24 h followed by assessment of the number of eggs per vial. The average number of eggs per female was determined by counting the total number of eggs collected and dividing by the number of females that laid eggs.

Progeny survival assay

Males were allowed to mate with virgin females for 3 days within chambers on grape juice plates (3% agar, 25% grape juice, 0.3% sucrose). Groups of ten females were then transferred to a single standard culture vial and allowed to lay eggs for 24 h followed by the removal of adults and determination of the number of eggs collected per vial. Eggs were allowed to develop through larval stages to adulthood, and the number of adults alive at 3 days post-eclosion was assessed. The percentage of eggs that survived to 3-day-old adults was determined by dividing the number of 3-day-old adults by the number of eggs laid.

Assessment of progeny sex

Mendelian inheritance assays were performed by mating equal numbers of 3-day-old males and virgin females under standard conditions. Parental flies were removed 9 days after setting up the cross. Adult progeny were collected daily and counted from day 10 to day 20.

Male fertility assay

Fertility assays were performed by mating equal numbers of 0–5- or 6–11-day-old males (control or *cdc14* nulls) with control virgin females under standard conditions. Parental flies were removed 9 days after setting up the cross. Adult progeny were collected and counted daily from day 10 to day 20.

Sperm competition assay

Sperm competition was performed based on a modification of a previously described assay (Yeh et al., 2013). Virgin males and females were collected and aged for 3 days on standard food supplemented with extra yeast paste. Single mating pairs were transferred to new vials and allowed to mate for 24 h. The first male was then removed, and a second 3-day-old virgin male was added to the vial and allowed to mate for 24 h. The female was then transferred to a fresh standard culture vial and allowed to lay eggs at 25°C for 9 days, at which point the female was removed. Eclosed adult progeny were collected and counted daily over the next 10 days and eye color was assessed. The experiments were blinded to the genotypes of the red-eyed males used in these experiments.

Assessment of spermatids and mature sperm

Testes were isolated from 1–3-day-old males as previously described (Zamore and Ma, 2011). Testes were snipped and squashed as previously described (Sitaram et al., 2014). Spermatids and mature sperm were observed using bright field microscopy.

Immunostaining

Testes were collected from 1–3-day-old males as previously described (Zamore and Ma, 2011). Testes were snipped at level 2 and immunostained as previously described (Sitaram et

al., 2014). Anti-Myc (9E10, 1:100; Santa Cruz Biotechnology, catalog #sc-40) and anti-tubulin (DM1α, 1:200; Sigma-Aldrich, catalog #T6199) primary antibodies were used in combination with goat anti-mouse Cy2 secondary (1:400; Invitrogen, catalog #A-11004).

Localization of Myc-tagged Cdc14 protein in 0–2 embryos laid by females carrying the *UASp-cdc14-myc* and *nanos-Gal4* transgenes was assessed by immunofluorescence using standard conditions. Anti-Myc (9E10, 1:100; Santa Cruz Biotechnology, catalog #sc-40) and rat anti-alpha tubulin (1:200; Accurate Chemical & Scientific, Westbury, USA, catalog #MCA77G) primary antibodies were used in combination with goat anti-mouse Cy2 (1:400; Invitrogen, catalog #A-11004) and goat anti-rat Cy3 (1:400; Abcam, catalog #ab6953) secondary antibodies.

Microscopy

Bright field images were obtained using a Stemi 2000-CS microscope (Zeiss, Oberkochen, Germany) with an Olympus DP72 camera. Fluorescent images were obtained using a Nikon Eclipse 80*i* microscope with a Cool SNAP ES camera (Photometrics, Tucson, USA). Images were analyzed in Fiji or Photoshop.

Egg aspect ratio

Adults were placed in egg-laying chambers over a grape juice plate (3% agar, 25% grape juice, 0.3% sucrose) and allowed to lay for 1 h. Plates were collected, imaged, and assessed by a

blinded experimenter. The measuring tool in Fiji was used to determine the ratio of the anteroposterior to sagittal axes of imaged 0–1 h embryos.

Larval path-length

Analysis of larval path-length was based on a modification of a previously described assay (Anreiter et al., 2016). Early third instar larvae were washed in PBS and placed on a 1% agarose plate. Larvae were allowed to move freely for 1 min. Plates were imaged, and the length of the path taken was assessed in Fiji as previously described (Anreiter et al., 2016).

Body wall contraction assay

Determination of body wall contraction was based on a modification of a previously described assay (Nichols et al., 2012). Early third instar larvae were washed in PBS and placed on a 1% agarose plate. Larvae were observed for 1 min under a dissection microscope, and the number of peristalsis contractions was scored. A single contraction was defined as a full anterior to posterior movement.

Adult climbing assay

Analysis of adult climbing was based on a modification of a previously described assay (Crowther et al., 2005). Up to 30 animals at 7–10 days post eclosion were placed at the bottom of a 3 inch vial. A second vial was placed on top of the first vial, and flies were allowed to climb for 20 s. The vials were then separated, and the number of flies in the top vial were counted. The percentage of flies climbing was determined by dividing the number of animals in the top vial by the total number of animals in both vials.

DNA damage assays

Third instar larvae were collected, washed in PBS, and left untreated or exposed to 40 Gy of ultraviolet radiation using a UV Stratalinker 1800 from Stratagene. Larvae were incubated at room temperature and dissected for wing or eye discs as previously described (Purves and Brachmann, 2007). Discs were stained with terminal deoxynucleotidyl transferase dUTP nick end labeling (TUNEL) or anti-phospho-Histone H3 (pH3) as previously described (Brodsky et al., 2000; Sarkissian et al., 2014). TUNEL- and pH3-stained samples were assessed by a blinded experimenter using Fiji. TUNEL-stained samples were assessed by measuring the fluorescence of the entire sample. pH3-stained samples were assessed by counting the number of stained cells in each sample.

Mechanosensation assay

Touch insensitivity of larvae was assessed using a previously described assay (see Fig. 3-9) (Kernan et al., 1994). A human eyelash is affixed to the end of a dowel rod with tape to make an eyelash brush. Larvae were washed with PBS, placed on a 1% agarose plate, tested four times by a blinded experimenter, and assigned a scored between 0 to 4. Scores were added together to determine the final score (0–16).

Larval yeast feeding assay

Test plates and yeast paste were prepared using blue or red food coloring as previously described (Wu et al., 2005). Early third instar larvae were washed in copious amounts of PBS, placed on the yeast paste, and allowed to feed or roam freely for 30 min. Wu et al. (2005) found that larvae feed in a bimodal fashion, either feeding persistently with substantial coloration of the gut or roaming across the plate without feeding. Larvae were scored by a blinded experimenter as feeding (>50% of the midgut full of colored yeast paste) or non-feeding (≤10% of gut filled with colored yeast past).

Larval quinine preference assay

The quinine chemosensory assay was performed as previously described with minor alterations (Apostolopoulou et al., 2014). Plates were prepared by filling a 60 mm petri dish

with 5 ml of autoclaved 0.5% agarose (minus or plus 7.5 mM sucrose) and allowed to solidify. Agarose was then removed from one-half of the plate and replaced by 2.5 ml of media (cooled to 50°C) containing quinine (minus or plus 7.5 mM sucrose). Plates were allowed to cool to room temperature and then stored in the dark at 4°C. Early third instar larvae were collected, washed in PBS, and placed near the center of the plate. Larvae were placed perpendicular to the boundary between the quinine-containing and quinine-free halves of the plate with the anterior end of each larva facing the quinine-containing half of the plate. Larvae were left undisturbed for 5 min and then scored by a blinded experimenter for location in either the quinine-containing or quinine-free side of the plate. Preference for quinine was determined as follows as previously described (Apostolopoulou et al., 2014): Preference=[(Larvae on quinine)−(Larvae on agarose)]/Total number of larvae. Preferences can range from −1 to 1, with negative values indicating avoidance of quinine and positive values indicating no avoidance of quinine.

Chemosensation test of adults

A modified version of the previously described two-way choice behavioral assay was used (Shim et al., 2015). Virgin 3-day-old adult flies were starved for 18 h and then placed in the dark with a 96-well plate containing 1 mM sucrose plus brilliant blue FCF dye (blue; 0.125 mg/ml) or 1 mM sucrose+0.8% quinine plus sulforhodamine B dye (red; 0.2 mg/ml) in alternating wells. Feeding was allowed to proceed for 90 min, flies frozen, and carcasses

analyzed for the presence of ingested dye. The experiment was then repeated with the dyes reversed.

Phototaxis assay

Response of larvae to photostimulation was assessed as previously described with the following modifications (Lilly and Carlson, 1990). One-half of the plate contained no added food coloring, and the other half contained 1 ml of an equal-parts mixture of red, green, and blue food coloring added to 100 ml of 0.5% agarose to produce an opaque black-colored agarose. Larvae were placed on the light box and allowed to move freely for 5 min prior to assessment of their location by a blinded experimenter.

Fat body staining

Staining for fat bodies was performed using Oil Red O as previously described (Gutierrez et al., 2007)**.** Nile Red experiments were performed using the same protocol except for the dye substitution. Nile red stock solution (1 mg/ml) was prepared as previously described and used at a 1:100 dilution (Greenspan et al., 1985). Nile Red was visualized at an excitation wavelength of 480 nm and emission wavelength of >530 nm. Oil Red O sample images were analyzed in ImageJ by a blinded experimenter. The width of a lipid droplet was measured at its widest point and binned into large (>160 μm), medium (125-160 μm) or small (<125 μm) droplets.

Assessment of starvation resistance

Adipose cells of the larval fat body degenerate and are replaced by adult adipose cells by 3 days post-eclosion (Butterworth et al., 1965). To test adult resistance to starvation, virgin female adults were collected and incubated at 25°C for 3 days. Animals were then anesthetized with CO_2, washed in PBS, and separated into vials with a PBS-soaked cotton ball (20 flies per vial). Flies were maintained at room temperature and assessed for mortality every 3 h.

Statistics

All statistical analyses were performed in R v3.1.0. Chi-square analyses were performed using Yates and corrected for continuity. Fisher's exact test, one-way ANOVA, and *t*-test (two tailed, equal variance) were used as indicated in figure legends. Post hoc analysis of ANOVA was performed with Tukey HSD. Post hoc analysis of Chi-square and Fisher's exact tests used the Bonferroni correction when applicable. The following critical *P* values were used for all analyses prior to correction: 0.05, 0.01, and 0.001.

Results

cdc14 expression is highest in the testis

Tissue expression data from the FlyAtlas indicate differential expression of *cdc14* with a sevenfold higher level of *cdc14* mRNA in the testis compared to the next highest expressing organ, the brain. To verify organ-specific levels of expression, we performed quantitative-PCR of whole adult carcasses, ovaries, and testes. Consistent with FlyAtlas, we found testis-specific expression of *cdc14* to be approximately eleven times higher than whole male carcass expression (Fig. 3-1A).

Generation of *cdc14* knockout lines in *D. melanogaster*

Homologous recombination was used to generate a *cdc14* null allele, designated $cdc14^{\Delta 1}$, in a *y w* line by replacing a portion of the *cdc14* gene (spanning from the 5'-UTR to just downstream of exon 6) with the $white^{+}$ gene (Fig. 3-1B). We then generated a stable homozygous knockout line (hereafter referred to as *cdc14* null) with confirmation of knockout by genomic PCR (Fig. 3-1C). The housekeeping gene, *r2d2*, adjacent to *cdc14* served as a control (Fig. 3-1C). Additionally, while *cdc14* mRNA was detected in wild-type flies by quantitative PCR (Fig. 3-1D,E), there was no detectable *cdc14* mRNA in the *cdc14* null flies (Fig. 3-1E). Further confirmation of the knockout was performed by sequencing the boundaries of the *cdc14* gene mutation (Fig. 3-1F).

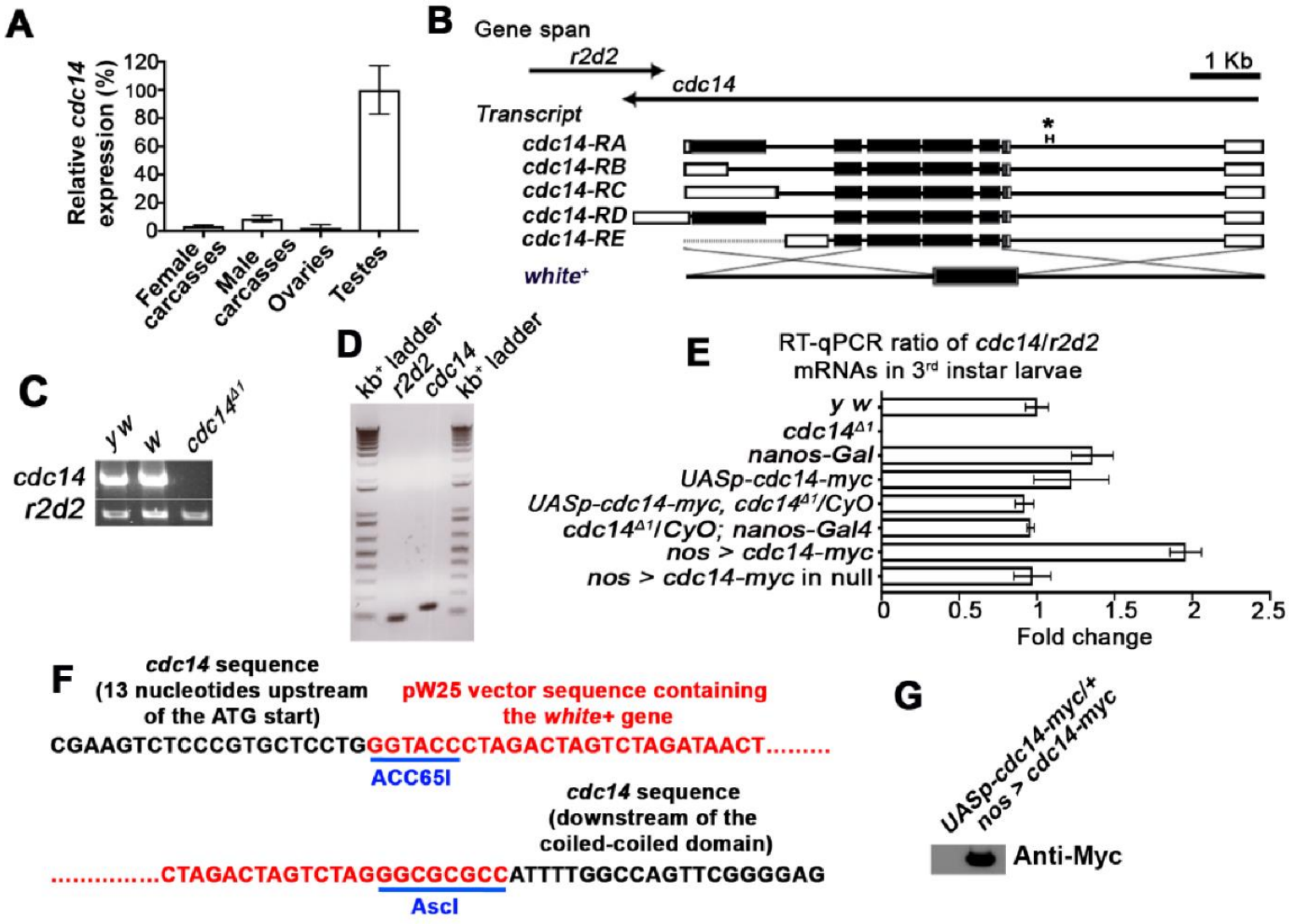
A
Relative cdc14 expression (%)
120
100
80
60
40
20
0
Female carcasses
Male carcasses
Ovaries
Testes
B
Gene span
r2d2
cdc14
1 Kb
Transcript
cdc14-RA
cdc14-RB
cdc14-RC
cdc14-RD
cdc14-RE
white+
H
C
y w
w
cdc14Δ1
cdc14
r2d2
D
kb+ ladder
r2d2
cdc14
kb+ ladder
E
RT-qPCR ratio of cdc14/r2d2 mRNAs in 3rd instar larvae
y w
cdc14Δ1
nanos-Gal
UASp-cdc14-myc
UASp-cdc14-myc, cdc14Δ1/CyO
cdc14Δ1/CyO; nanos-Gal4
nos > cdc14-myc
nos > cdc14-myc in null
0
0.5
1
1.5
2
2.5
Fold change
F
cdc14 sequence (13 nucleotides upstream of the ATG start)
pW25 vector sequence containing the white+ gene
CGAAGTCTCCCGTGCTCCTGGGTACCCTAGACTAGTCTAGATAACT.....
ACC65I
cdc14 sequence (downstream of the coiled-coiled domain)
.....CTAGACTAGTCTAGGGCGCGCCATTTTGGCCAGTTCGGGGAG
AscI
G
UASp-cdc14-myc/+
nos > cdc14-myc
Anti-Myc

Figure 3-1: High expression of *cdc14* in the testes and generation of Drosophila *cdc14* null mutants by homologous recombination. (A) Relative expression of endogenous *cdc14* in adult flies as determined by RT-PCR. The highest level of expression is in the testes. *cdc14* expression was normalized to *Rp49*. cDNA was generated from adult carcasses (N≥50) or excised gonads (N≥200, N=3 independent biological replicates with N=3 technical replicates). (B) Structure of the Drosophila *cdc14* and its five alternative transcripts. Black boxes are exons, white boxes are UTRs, and lines are introns. Ends-out homologous recombination of *cdc14* was used to replace *cdc14* with the *white*$^{+}$ gene. Asterisk (*) indicates the 371 bp (2L:7,807,273 to 7,87,543) region of *cdc14* used for PCR depicted in (C). A region (2 kb; not shown) of the overlapping housekeeping gene, *r2d2*, was used as a positive PCR control. Control *r2d2* PCR product is 2 kb. *r2d2* is upstream of *cdc14* (PCR region not depicted). *White*$^{+}$ gene is not to scale. (C) A *cdc14* null line was generated in a *y w* background and verified by PCR amplification of genomic DNA. The control lines, *y w* and *w1118*, and the adjacent housekeeping gene, *r2d2*, were used as positive controls. The *cdc14* $^{\Delta 1}$ null allele was used for all subsequent experiments and for generation of the rescue line. Gel is representative result from N=3 replicates. (D) Final products from the RT-qPCR reaction of *y w* third instar larvae run on a 1% agarose DNA gel. Only a single product was amplified, suggesting high specificity of the primers used in (E). (E) Fold changes of *cdc14* mRNA normalized to *r2d2* mRNA. The level of expression is normalized to the *y w* control. No *cdc14* expression was detectable in the *cdc14 null* line, but *r2d2* expression was equivalent to that of the *y w* control line. cDNA was generated from late third instar larvae (N≥30, N=3 independent biological replicates with N=3 technical replicates). (F) Nucleotide sequence of the boundaries of the *cdc14* null mutation. Two of the restriction endonuclease sites (ACC65I and AscI) used for cloning the two homologous arms of *cdc14* into the pW25 vector for recombination are shown. (G) Anti-Myc immunoblot of 0-2 hr old embryos demonstrates expression of *UASp-cdc14-myc* using the *nanos-Gal4* driver.

Knockout of *cdc14* is well tolerated

cdc14 null flies are viable and reach adulthood. Female *cdc14* nulls crossed to male *cdc14* nulls lay eggs at the same rate as the *y w* control line, regardless of the age of the females (Fig. 3-2A,B). The average number of eggs produced per laying female is not significantly different (Fig. 3-2A,C). The progeny of female *cdc14* nulls crossed to male *cdc14* nulls are viable. An equivalent proportion of eggs developed into 3-day-old adults when compared to the control line (Fig. 3-2D,E,F,G). Finally, no difference in the ratio of male to female progeny was observed (Fig. 3-3C). Our data suggests that Cdc14 is not an essential gene in Drosophila.

Overexpression of Cdc14-Myc

To determine whether overexpression of Cdc14 could provide insight into its function, we generated an inducible cMyc-tagged Cdc14 expression line (*UASp-cdc14-myc*) and verified expression of Cdc14-Myc by immunoblot analysis; this transgenic line was used for overexpression and rescue experiments (Fig. 3-1G; Fig. 3-3A,B). Nanos is active in germline formation, oocyte maturation, and early embryogenesis (Forbes and Lehmann, 1998; Kobayashi et al., 1996; Wang and Lehmann, 1991), making a *nanos* (*nos*) driver appropriate to rescue *cdc14* loss, especially in the germ line. We found that introduction of *nos>cdc14-myc* in a *y w* background resulted in a twofold increase in *cdc14* mRNA levels compared to the *y w* control line at the late third instar stage of larval development and very closely approximated wild-type

levels of expression in a *cdc14* null background (Fig. 3-1E). Immunoblotting confirmed expression of Cdc14-Myc in *nos>cdc14-myc* in third instar larvae (Fig. 3-3A,B). All rescue experiments described herein were performed using the *cdc14* null line with *nos>cdc14-myc* expression ('rescue line').

cdc14 knockdown does not affect the ratio of male-to-female progeny

The relatively high expression of *cdc14* in the Drosophila testis compared with other tissues raised the possibility that knockout or overexpression may specifically affect the health of males. However, no significant differences between the ratios of male-to-female offspring were observed (Fig. 3-3C,D). This finding indicates that neither the insertion/expression of *UASp-cdc14-myc* nor the loss of *cdc14* affect the viability of male offspring.

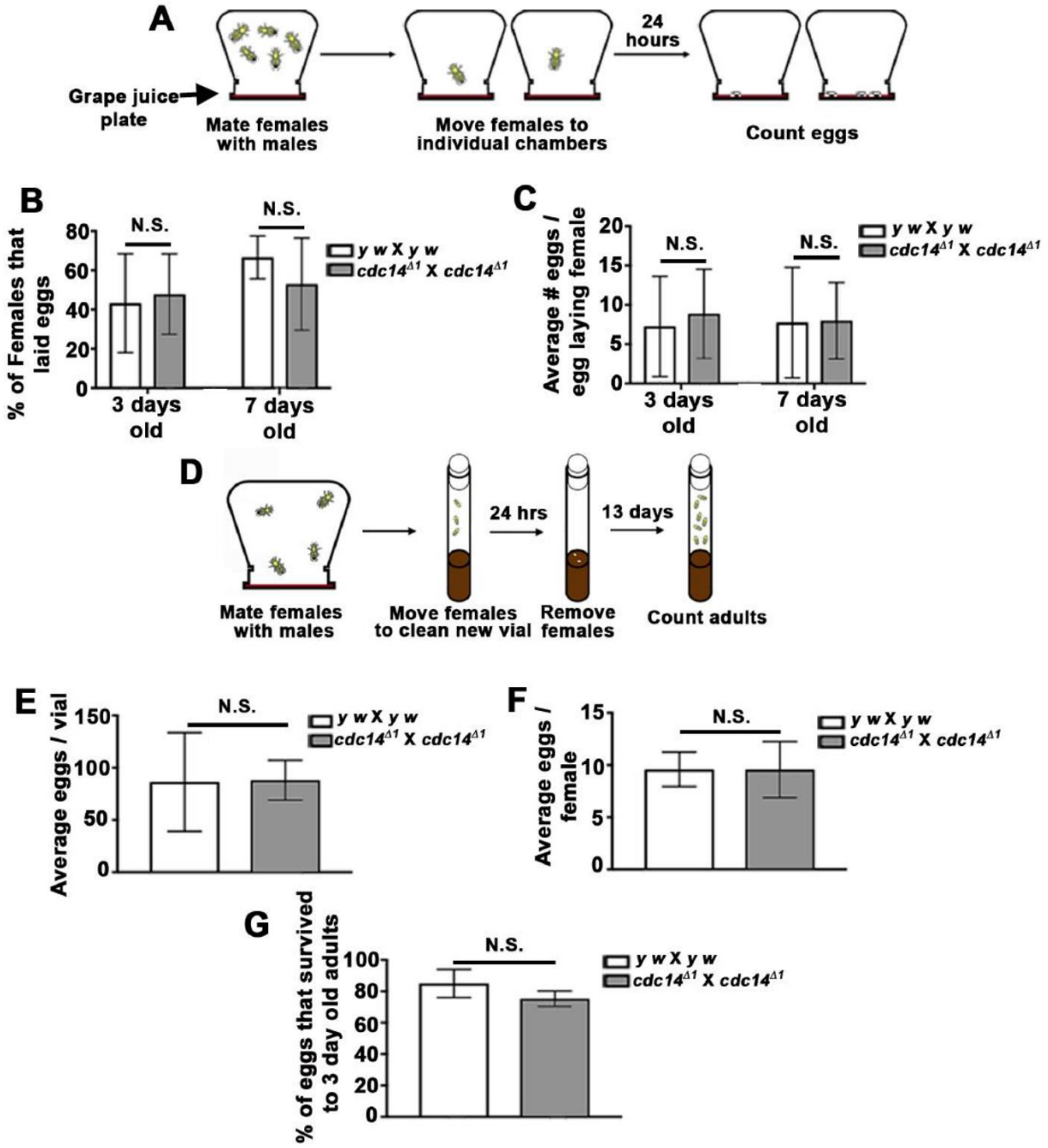
A
Grape juice plate
Mate females with males
Move females to individual chambers
24 hours
Count eggs
B
% of Females that laid eggs
N.S.
N.S.
3 days old
7 days old
y w X y w
cdc14Δ1 X cdc14Δ1
C
Average # eggs / egg laying female
N.S.
N.S.
3 days old
7 days old
y w X y w
cdc14Δ1 X cdc14Δ1
D
Mate females with males
Move females to clean new vial
24 hrs
Remove females
13 days
Count adults
E
Average eggs / vial
N.S.
y w X y w
cdc14Δ1 X cdc14Δ1
F
Average eggs / female
N.S.
y w X y w
cdc14Δ1 X cdc14Δ1
G
% of eggs that survived to 3 day old adults
N.S.
y w X y w
cdc14Δ1 X cdc14Δ1

Figure 3-2: *cdc14* is not required for female fertility or animal development. (A) Three or seven days old females were placed in individual egg laying chambers and allowed to lay eggs for 24 h. (B,C) No significant differences in the percentage of females laying eggs (B) or the number of embryos laid per female (C) were observed. Only females that laid eggs were included in the analysis in (C). Results were aggregated from females (N≥53) in N≥3 repetitions in (A), (B), and (C). (D) Ten females per vial were allowed to lay for 24 h. Females were then removed, and the number of eggs in each vial were counted and compared between vials (E) and by the total number of females (F). No differences in the number of eggs per vial (E) or eggs per female (F) were observed. (G) Eggs were allowed to hatch and larvae grown to adulthood. No differences in the number of eggs that survived to three days old adult animals were observed. Eggs (N≥200) were assessed from N=5 vials from N=3 repetitions in (E), (F), and (G). In (B), (C), (E), (F), and (G) both parental lines were *cdc14* nulls ($cdc14^{\Delta 1}/cdc14^{\Delta 1}$), and the *cdc14* nulls were compared to their genetic background line (*y w*). Results shown in (B), (C), (E), (F), and (G) were analyzed by Chi-squared test.

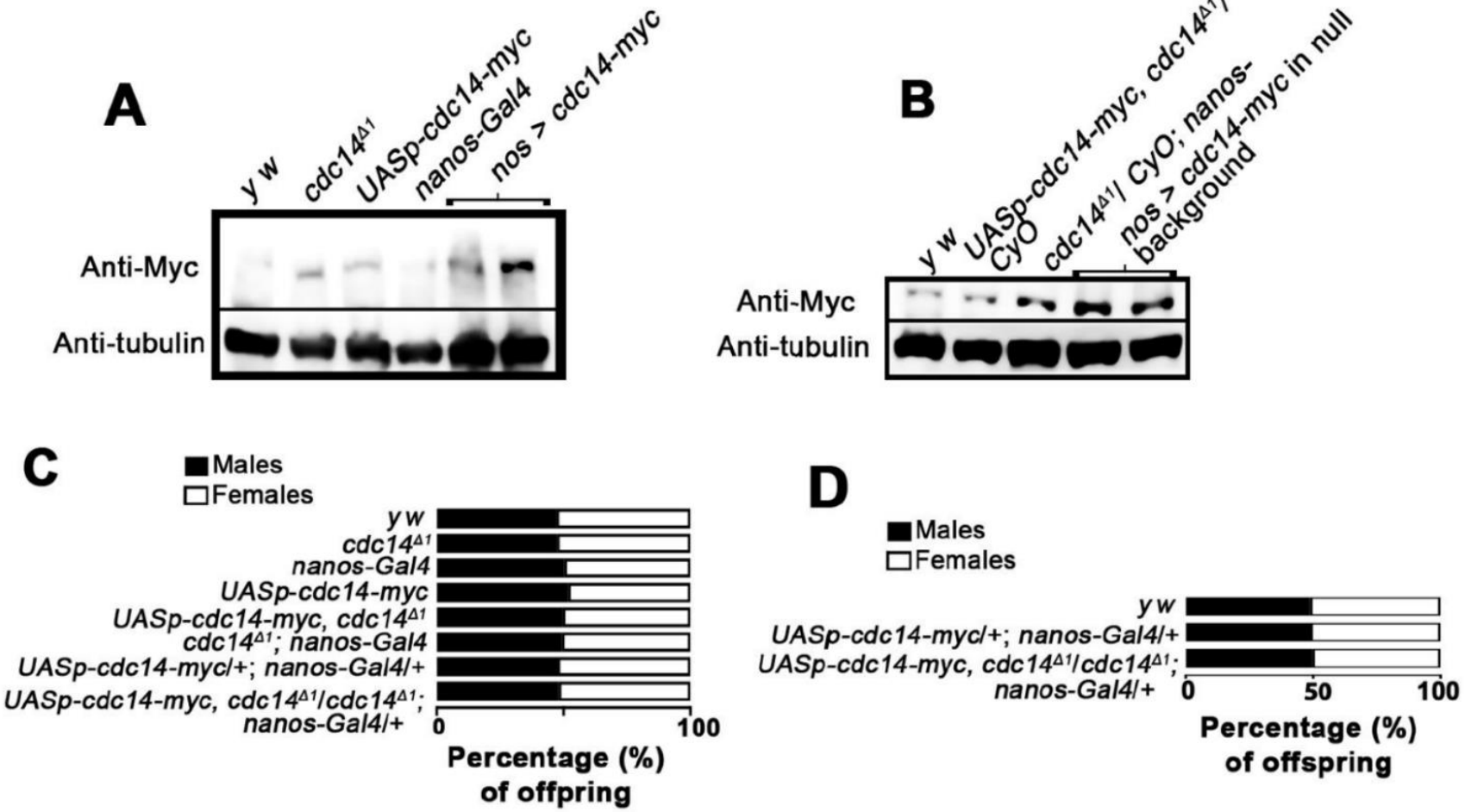
A
y w
cdc14Δ1
UASp-cdc14-myc
nanos-Gal4
nos > cdc14-myc
Anti-Myc
Anti-tubulin
B
y w
UASp-cdc14-myc, cdc14Δ1/ CyO
cdc14Δ1/ CyO; nanos-
nos > cdc14-myc in null background
Anti-Myc
Anti-tubulin
C
Males
Females
y w
cdc14Δ1
nanos-Gal4
UASp-cdc14-myc
UASp-cdc14-myc, cdc14Δ1
cdc14Δ1; nanos-Gal4
UASp-cdc14-myc/+; nanos-Gal4/+
UASp-cdc14-myc, cdc14Δ1/cdc14Δ1;
nanos-Gal4/+
0
100
Percentage (%)
of offpring
D
Males
Females
y w
UASp-cdc14-myc/+; nanos-Gal4/+
UASp-cdc14-myc, cdc14Δ1/cdc14Δ1;
nanos-Gal4/+
0
50
100
Percentage (%)
of offspring

Figure 3-3: *cdc14* does not affect the ratio of male-to-female offspring, and *nos-gal4 > UASp-cdc14-myc* results in Cdc14-Myc protein expression. (A) Immunoblot analysis of Cdc14-Myc levels in third instar larvae expressing *UASp-cdc14-myc* under the control of *nanos-Gal4* (*nos-Gal4*) in a *y w* background. (B) Immunoblot analysis of Cdc14-Myc levels in third instar larvae expressing *UASp-cdc14-myc* under the control of *nos-Gal4* in a *cdc14* null background. (A) and (B) are representative gels of N=3 replicates. Tubulin was used as loading control. (C) The ratio of male to female offspring for lines used in this paper. Comparisons of different parental genotypes show no differences in the ratios of male to female offspring. Results were aggregated from offspring (N≥261) in N≥3 replicates. (D) Male offspring from the cross in (C) mated to a *y w* control female. Comparisons of male offspring from the different parental genotypes show no differences in the ratios of male to female offspring. Results were aggregated from offspring (N≥121) in N≥3 replicates.

Cdc14 is not required for Drosophila spermatogenesis

To test the fertility of *cdc14* null flies, we crossed male *cdc14* nulls to control females and assessed the number of offspring. We observed no significant differences in the number of progeny produced by *cdc14* null versus control males at either 0–5 or 6–11 days of age (Fig. 3-4A). These data suggest that *cdc14* loss does not affect male fertility.

Given that *cdc14* expression is highest in Drosophila testes relative to other tissues and that Cdc14A and Cdc14B are involved in ciliogenesis in zebrafish (Clément et al., 2011, 2012), we tested whether Cdc14 is involved in Drosophila spermatogenesis. Primary cilia first form in apolar spermatocytes and persist through the early spermatid stage, disassembling only partially at the end of spermatogenesis when the centriole at the cilium forms the base of the flagella axoneme (Riparbelli et al., 2012). These primary cilia are therefore thought to be precursors of the spermatid flagellum, although their role in spermatogenesis is unclear (Riparbelli et al., 2012). The majority of cells in the testis are ciliated; however, the function of the cilia during the meiotic prophase is unknown.

We initially examined the testis as a whole for potential gross morphological defects. Examination of bright-field images revealed no observable morphological differences between *cdc14* null and control testes (Fig. 3-4B). Immunostaining of testes for alpha-tubulin showed no notable differences in sperm morphology or number during spermatogenesis (Fig. 3-4C). Additionally, using *nos>cdc14-myc* animals, we observed localization of Cdc14-Myc protein primarily to the head of mature sperm bundles in the testes (Fig. 3-4D). Analysis of spermatids and mature sperm revealed no observable differences between *cdc14* nulls and controls (Fig. 3-

4E,F). Thus, we conclude that *cdc14* is not essential for formation of mature sperm in Drosophila.

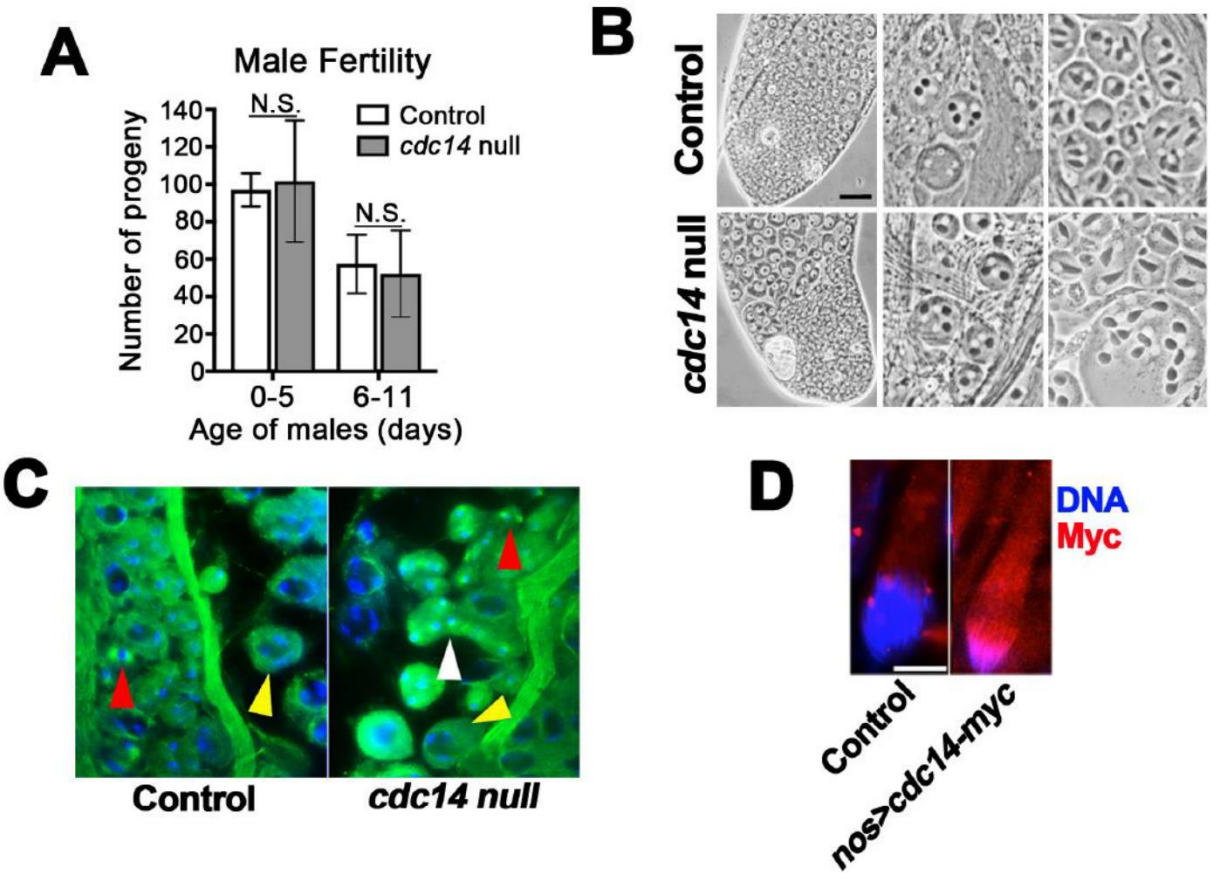
A
Male Fertility
N.S.
N.S.
Control
cdc14 null
Number of progeny
140
120
100
80
60
40
20
0
0-5
6-11
Age of males (days)
B
Control
cdc14 null
C
Control
cdc14 null
D
DNA
Myc
Control
nos>cdc14-myc
E
Number of spermatids / cyst
70
65
60
55
50
N.S.
y w
cdc14Δ1
F
Number of mature sperm
70
65
60
55
50
N.S.
y w
cdc14Δ1

Figure 3-4: Cdc14-Myc localizes to the sperm bundle heads, but loss of *cdc14* does not affect male fertility or spermatid/sperm number or result in overt morphological changes of the testis. (A) Comparison of the number of progeny from a single control female crossed to 0-5 or 6-11 days old *cdc14* null versus control males. Results were analyzed by T-test (two tailed, equal variance; ρ>0.05). N.S. = not significant. Animals (N≥782) from N=15 crosses were assessed in (A). (B) and (C) Testes mutant for *cdc14* appear to exhibit normal spermatogenesis and cell divisions. (B) Bright-field images of control and *cdc14* null testes showed no consistent or significant gross morphological differences between groups. Three separate cross sections from different animals are shown. Left panels display early 2-16 cell stage spermatogonial cysts. The smaller cells are part of 2-4 cell cysts, whereas the larger cells are part of 8-16 cell cysts. Middle panels display round onion-stage spermatids. The right panels show early onion stage elongating spermatids that will form mature sperm. (C) Testes stained for tubulin (green) and DNA (blue, DAPI) showed no overt differences between *cdc14* null and control flies. Panels show a mixture of primary (yellow arrowheads) and secondary (red arrowheads) spermatocytes. The latter are shown undergoing and completing the second meiotic division. White arrowhead marks clearly observed early onion stage spermatids in the *cdc14* null testes. (D) Sperm bundles from control and *nos-Gal4 > cdc14-myc* male flies show localization of Cdc14-Myc to the head of the sperm bundle. Red is Myc and blue (DAPI) is DNA. Magnification, 100x. (B-D) are representative figures from N≥20 testes from N≥6 replicates. Scale bars, 10 µm. Testes from *y w* and *cdc14* null males were assessed for number of spermatids in the spermatogenic cyst (E) and number of mature sperm per bundle (F). No significant differences were observed in the number of spermatids (N=3 cysts from N=3 males in (E)) or sperm (N=3 mature sperm bundles from N=3 males in (F)). Results shown in (E) and (F) were analyzed by Chi-squared test.

Loss of *cdc14* does not affect Drosophila oogenesis or embryogenesis

Previous studies indicated that Drosophila *cdc14* is maternally contributed with diffuse localization in early larvae (Fisher et al., 2012; Keil, 1997). We performed immunolocalization studies using the *UASp-cdc14-myc* transgenic line under the control of a maternal *nos-Gal4* driver. Consistent with the *in situ* studies, we found that the cMyc-tagged Cdc14 protein is diffusely localized around mitotic nuclei in the early embryo (Fig. 3-5A).

We tested the effects of Cdc14 on viability and early development. We found that male and female *cdc14* null flies are fertile and the offspring of *cdc14* null parents are viable (Figs 3-2B,G, 3-4A). We found no significant effects of Cdc14 loss on the embryo's aspect ratio (length:width) (Fig. 3-5B). Thus, we conclude that Cdc14 does not play an essential role in early oogenesis or embryogenesis of Drosophila.

Cdc14 is not required for cell cycle checkpoint activation or DNA damage repair

Cdc14 phosphatases are reported to play a role in DNA damage repair and the checkpoint response in human cells (Mocciaro et al., 2010). We observed no increase in single or double strand DNA breaks in response to ionizing radiation as determined by the amount of TUNEL staining in wing discs from *cdc14* null third instar null larvae (Fig. 3-5C). To determine whether Drosophila Cdc14 is involved in DNA checkpoint regulation, we assessed the mitotic index of eye discs from irradiated larvae of *cdc14* null animals by immunostaining for the mitosis specific marker phospho-histone H3 (pH3). Eye discs from *cdc14* null flies showed a

reduction in pH3 similar to that of control flies following irradiation (Fig. 3-5D), suggesting normal activation of a DNA damage checkpoint. As positive control, discs from homozygous animals that are null for an allele of the checkpoint gene, *mei-41*^{RT}, showed no reduction in proliferation. These results suggest that *cdc14* is not required for mitotic checkpoint activation or DNA damage repair in Drosophila.

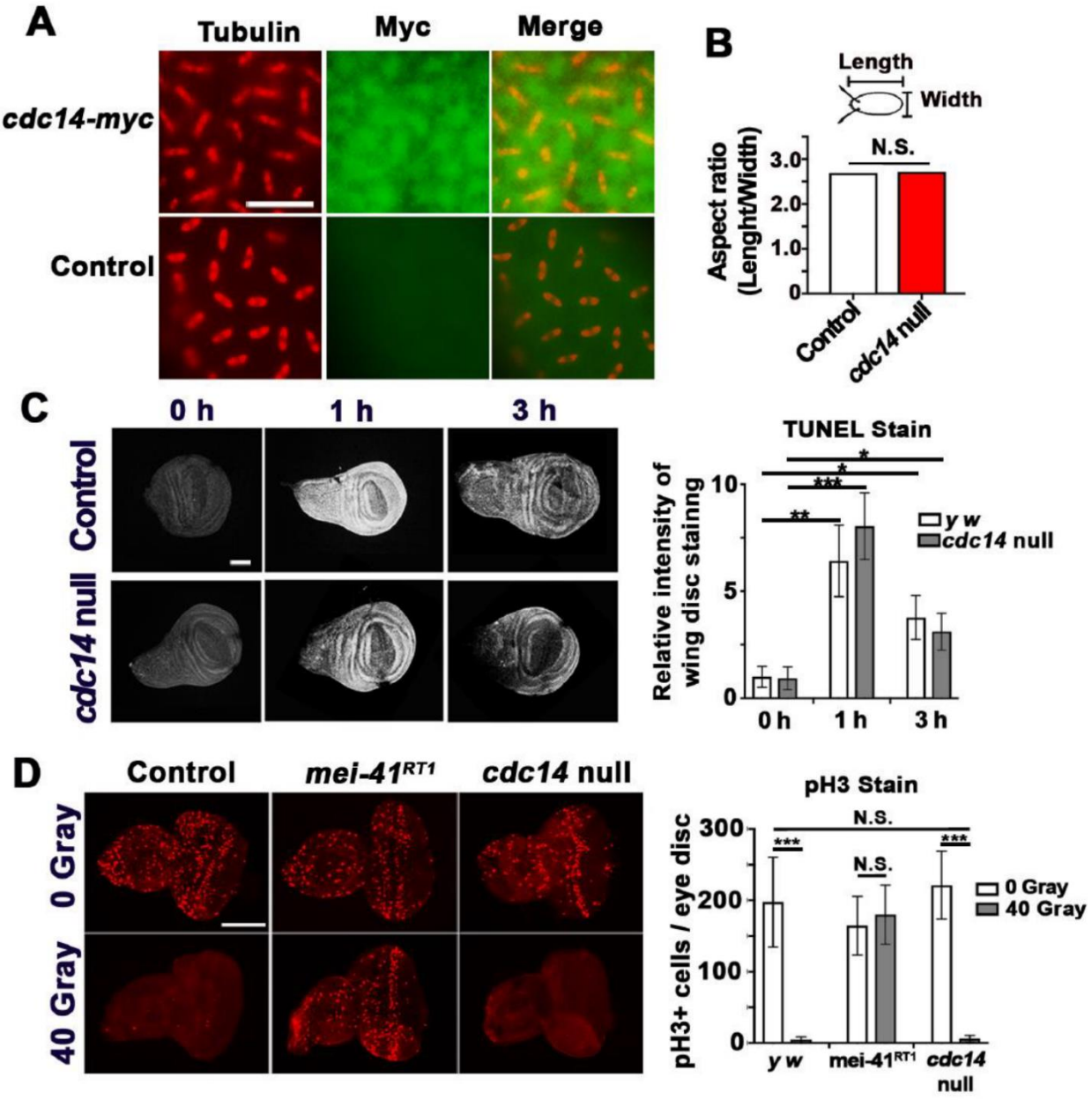
A
Tubulin
Myc
Merge
cdc14-myc
Control
B
Length
Width
N.S.
Aspect ratio (Lenght/Width)
3.0
2.0
1.0
0
Control
cdc14 null
C
0 h
1 h
3 h
Control
cdc14 null
TUNEL Stain
Relative intensity of wing disc stainng
10
5
0
0 h
1 h
3 h
y w
cdc14 null
D
Control
mei-41RT1
cdc14 null
0 Gray
40 Gray
pH3 Stain
pH3+ cells / eye disc
300
200
100
0
N.S.
y w
mei-41RT1
cdc14 null
0 Gray
40 Gray

Figure 3-5: Cdc14-Myc is diffusely localized in the embryo and is not required for embryogenesis, apoptosis, or DNA damage repair. (A) Precellularized 0-2 h embryos showed diffuse localization of Cdc14-Myc that had been expressed under the control of *nanos-Gal4*. Tubulin is red and Myc is green. Magnification, 40x. Scale bar, 20 µm. Embryos (N≥75) from N=2 replicates. (B) The ratio of the length to width of 1 hr post fertilization embryos showed no difference between control and *cdc14* null embryos. Results were analyzed by t-test (two tailed, equal variance). Eggs (N≥61) were aggregated from N≥3 replicates were assessed. (C) TUNEL-stained wing discs showed no difference between control and *cdc14* null third instar larvae upon exposure to ionizing radiation (40 Gray). Scale bars, 50 µm. Images were assessed in Fiji by measuring fluorescence of the entire sample. Treatments were normalized to the *y w* 0 h control. 0, 1, and 3 h time points were compared to each other as well as control to *cdc14* null at each time point. Results were analyzed by t-test (two-tailed, equal variance with Bonferroni correction) (Wing discs (N≥7) from N≥3 replicates). (D) Images of eye discs from third instar larvae stained with anti-phospho-Histone H3 to mark cells in mitosis. No changes in the mitotic index were observed between the *cdc14* null and control line upon irradiation. As a control, the $mei\text{-}41^{RT1}$ eye discs (defective in DNA damage repair) continued to undergo mitosis. Scale bars, 50 µm. Comparisons were made between 0 and 40 Gray treatments between genotypes. Results were analyzed by t-test (two-tailed, equal variance with Bonferroni correction). Experiments were performed using N≥25 eye discs in N≥3 replicates. *ρ<0.008, **ρ<0.002, ***ρ<0.0002.

Sperm competiveness is decreased in *cdc14* null flies

The fertility experiments performed above reflect reproduction in an optimized and controlled laboratory environment. In the wild, Drosophila males compete with each other by promoting removal or inactivation of the previous male's sperm (Price et al., 1999). Therefore, we performed a sperm competition assay to assess 'sperm fitness'. By sequentially mating a white-eyed male and red-eyed male to a white-eyed female, competitiveness was determined by counting the number of red-eyed (heterozygous for red pigment genes) or white-eyed offspring. The *cdc14* null, rescue, and overexpression lines are all homozygous for a gene that produces red pigment in the eye. The *y w* line has white eyes, as it is homozygous for a loss of function allele of the *white* gene and does not produce red pigment.

When mated to a white-eyed female, the percentage of offspring produced by the *cdc14* null was significantly less than that of the control groups, regardless of whether the *cdc14* null male was the first or second male to mate (Figs. 3-6, 3-7B). This result suggests that, in spite of the lack of notable morphological differences between *cdc14* null and control sperm, *cdc14* null sperm are less efficient than wild-type sperm in conferring reproductive competitiveness.

It is possible that seminal fluid proteins could induce changes in female behavior and physiology, such as sexual receptivity, ovulation, and egg-laying rates, and these changes could confound a sperm competition assay (Avila et al., 2011). We found that the cdc14 stock had a normal egg-laying rate (Fig. 3-2B,C,E,F). The proportion of *cdc14* null males that mated at least

once in the sperm competition assay was comparable to controls (Fig. 3-7A). However, we cannot rule out that *cdc14* nulls mated fewer times than controls within the 24 h period.

The seminal fluid protein, sex peptide (SP), is transferred with the sperm to the female reproductive tract, where it is bound to the tail of the sperm and plays a role in sperm storage (Avila et al., 2010; Avila and Wolfner, 2009; Peng et al., 2005; Rogers et al., 2009). SP null males have been reported to give rise to more progeny compared to controls when mated first in specific competition assays (Avila et al., 2010). In contrast, we found that *cdc14* null males gave rise to fewer progeny compared to controls when they were mated first (Fig. 3-6; Fig. 3-7B). Thus, it is possible that Cdc14 may function to inhibit SP release or the association of SP with the ciliary tail of the sperm.

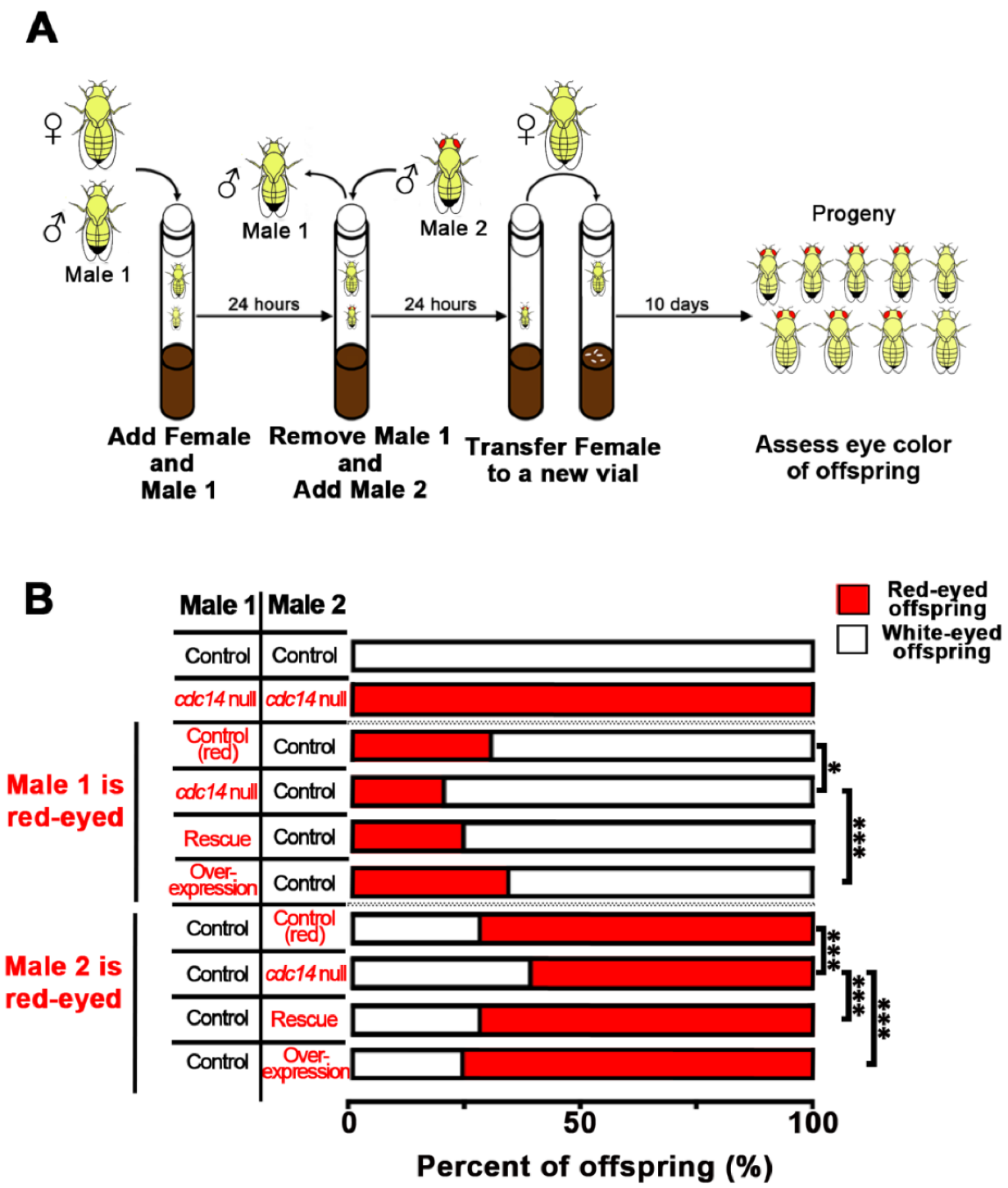
A
Male 1
Male 1
Male 2
Progeny
24 hours
24 hours
10 days
Add Female and Male 1
Remove Male 1 and Add Male 2
Transfer Female to a new vial
Assess eye color of offspring
B
Male 1
Male 2
Red-eyed offspring
White-eyed offspring
Control
Control
cdc14 null
cdc14 null
Control (red)
Control
cdc14 null
Control
Rescue
Control
Over-expression
Control
Male 1 is red-eyed
Control
Control (red)
Control
cdc14 null
Control
Rescue
Control
Over-expression
Male 2 is red-eyed
*
***
***
***
***
0
50
100
Percent of offspring (%)

Figure 3-6: *cdc14* null males exhibit decreased sperm competition. (Top) An example of a sperm competition assay in which a single *y w* virgin female (white-eyed) is mated to a single male (white-eyed) for 24 h. The male is then removed and the female is mated to a second male with red-eyes for 24 h. The female is then transferred to a fresh vial and allowed to lay eggs. The female is removed, and offspring are allowed to develop and assessed for eye color (red or white). The assay is repeated using a red-eyed male first and then a white-eyed male. (Bottom) A control experiment was performed using white-eyed *y w* males for both the first and second males. A second control experiment was performed using red-eyed *cdc14* null males for both the first and second males. The *cdc14* null males are less competitive compared to control males regardless of whether they are the first or second male to mate. Results for a single representative replicates (N≥15 vials per cross) are shown. Additional data can be found in Fig. 3-7B. Data were analyzed using a Chi-squared test with Bonferroni correction. Six pairwise comparisons were made. Red-eyed control males were compared to the *cdc14* null, rescue, or overexpression males; *cdc14* null males were compared to rescue or overexpression male; and rescue males were compared to overexpression males. * $\rho<0.009$ and *** $\rho<0.0002$.

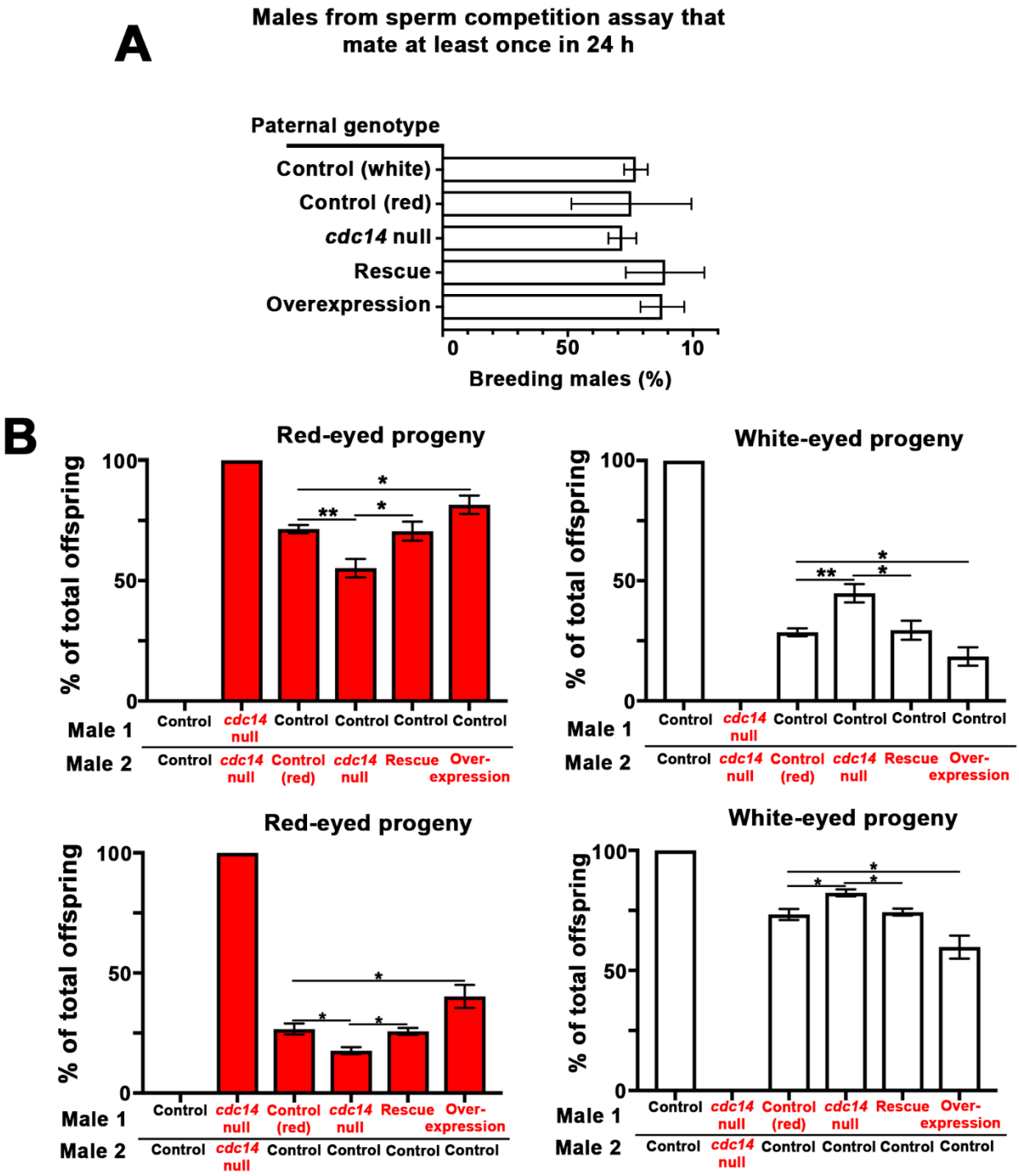
A
Males from sperm competition assay that mate at least once in 24 h
Paternal genotype
Control (white)
Control (red)
cdc14 null
Rescue
Overexpression
0
50
10
Breeding males (%)
B
Red-eyed progeny
White-eyed progeny
% of total offspring
100
50
0
Male 1
Male 2
Control
cdc14 null
Control (red)
Rescue
Over-expression

Figure 3-7: *cdc14* null males mate overnight at the same rate as controls. (A) Vials from all sperm competition assays (see Figure 3-6) were assessed for progeny from each male. No significant differences were observed in the number of mating males of each genotype. Vials in which no progeny were observed for either the first or second male were excluded from all analyses of sperm competition. Data were analyzed by Chi-squared test with Bonferroni correction. (B) Eye color of offspring from all replicates of the sperm competition assay. The proportion of offspring from *cdc14* null males was significantly lower than the control (red). This decrease was rescued by expression of *nos* > *myc-cdc14*. Data were analyzed by Chi-squared test with Bonferroni correction. Control (red) was compared to the *cdc14* null, rescue, and overexpression. The *cdc14* null was compared to the rescue. * $\rho<0.02$, ** $\rho<0.003$, *** $\rho<0.0003$. In (A) and (B), $N\geq48$ vials aggregated in $N\geq3$ experiments.

Loss of *cdc14* does not affect Drosophila path-length, coordination, or locomotion

The decrease in sperm competitiveness may be the result of coordination or locomotion defects inhibiting mating behaviors. Drosophila are negatively geotactic, and the adult climbing assay is a motor assay that takes coordination into account (Ali et al., 2011; Nichols, 2015; Nichols et al., 2012). When coordination is disrupted, flies should climb slower and/or fewer flies should rapidly climb the chamber walls (Nichols, 2015). We found that the climbing behavior of *cdc14* nulls was not significantly different than that of control *y w* control (Fig. 3-8A). Furthermore, path-length (distance traveled by a larva on yeast within a defined period) and the number of body wall contractions, both measures of locomotion (Anreiter et al., 2016; Nichols et al., 2012), did not significantly differ between *cdc14* null and control larvae (Fig. 3-8B,C). These results suggest that Cdc14 does not play a role in path-length, coordination, or locomotion in Drosophila.

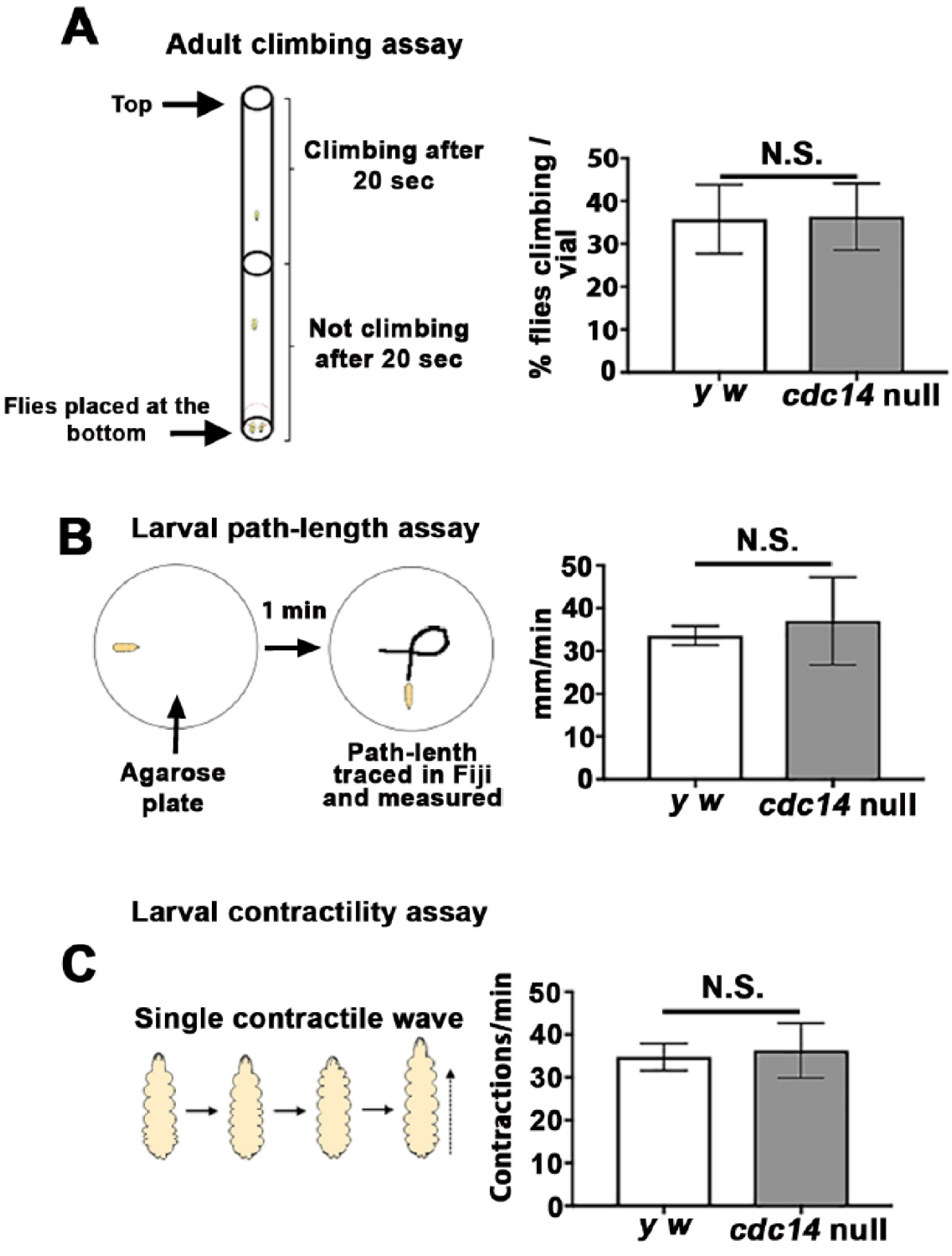
A
Adult climbing assay
Top
Climbing after 20 sec
Not climbing after 20 sec
Flies placed at the bottom
% flies climbing / vial
N.S.
y w
cdc14 null
B
Larval path-length assay
1 min
Agarose plate
Path-lenth traced in Fiji and measured
mm/min
N.S.
y w
cdc14 null
C
Larval contractility assay
Single contractile wave
Contractions/min
N.S.
y w
cdc14 null

Figure 3-8: *cdc14* nulls do not show impaired path-length or locomotion. (A) In the adult climbing assay (left), flies were allowed to climb for 20 seconds, followed by assessment of the number of flies in the top vial ("climbing" flies). The number of climbing adults was not significantly different between the control and *cdc14* null line. Results were aggregated from N>150 flies in N=3 replicates. (B) Third instar larvae were allowed to move freely for 1 min on an agarose plate (left). The larval path was traced and measured in Fiji. The average path-length traveled per larva per minute was not significantly different between the control and *cdc14* null line. (C) Larvae were observed under a brightfield microscope, and the number of full contractile waves (left) were counted for 1 min. No difference was observed between the control and *cdc14* null line. N=30 larvae were tested in (B) and (C). (A), (B), and (C) were analyzed by t-test (two tailed, equal variance; $\rho>0.05$).

Drosophila *cdc14* null larvae have decreased mechanosensation

In Drosophila, spermatozoa and sensory neurons are the only ciliated cells (Ma and Jarman, 2011). Type I sensory neurons (sensilla) have modified cilia that act as a site for sensory reception and transduction (Field and Matheson, 1998; Keil, 1997; Laurençon et al., 2007; Lee et al., 2008; Ma and Jarman, 2011; Riparbelli et al., 2012). In accordance with a role in zebrafish ciliogenesis (Clément et al., 2011, 2012), we tested whether *cdc14* null sensory neurons have decreased function compared to that of control flies. Mechanosensation and chemosensation are the two primary functions of Type I sensory neurons (Brody, 1999). To test the functionality of the mechanosensory neurons, we used a touch insensitivity assay in third instar larvae (Fig. 3-9). Control larvae demonstrated a normal distribution of touch response scores (Fig. 3-10A). In contrast, *cdc14* larvae showed a broad distribution of touch response scores and a decreased average score, suggesting a distinct loss of touch sensitivity (Fig. 3-10A,B). The loss of touch sensitivity in *cdc14* null larvae was partially rescued by maternally contributed *cdc14* ($cdc14^{\Delta 1\text{-}Maternal}$; Fig. 3-10B). These data suggest a role for *cdc14* in the function and/or formation of ciliated Type I sensory neurons controlling mechanosensation.

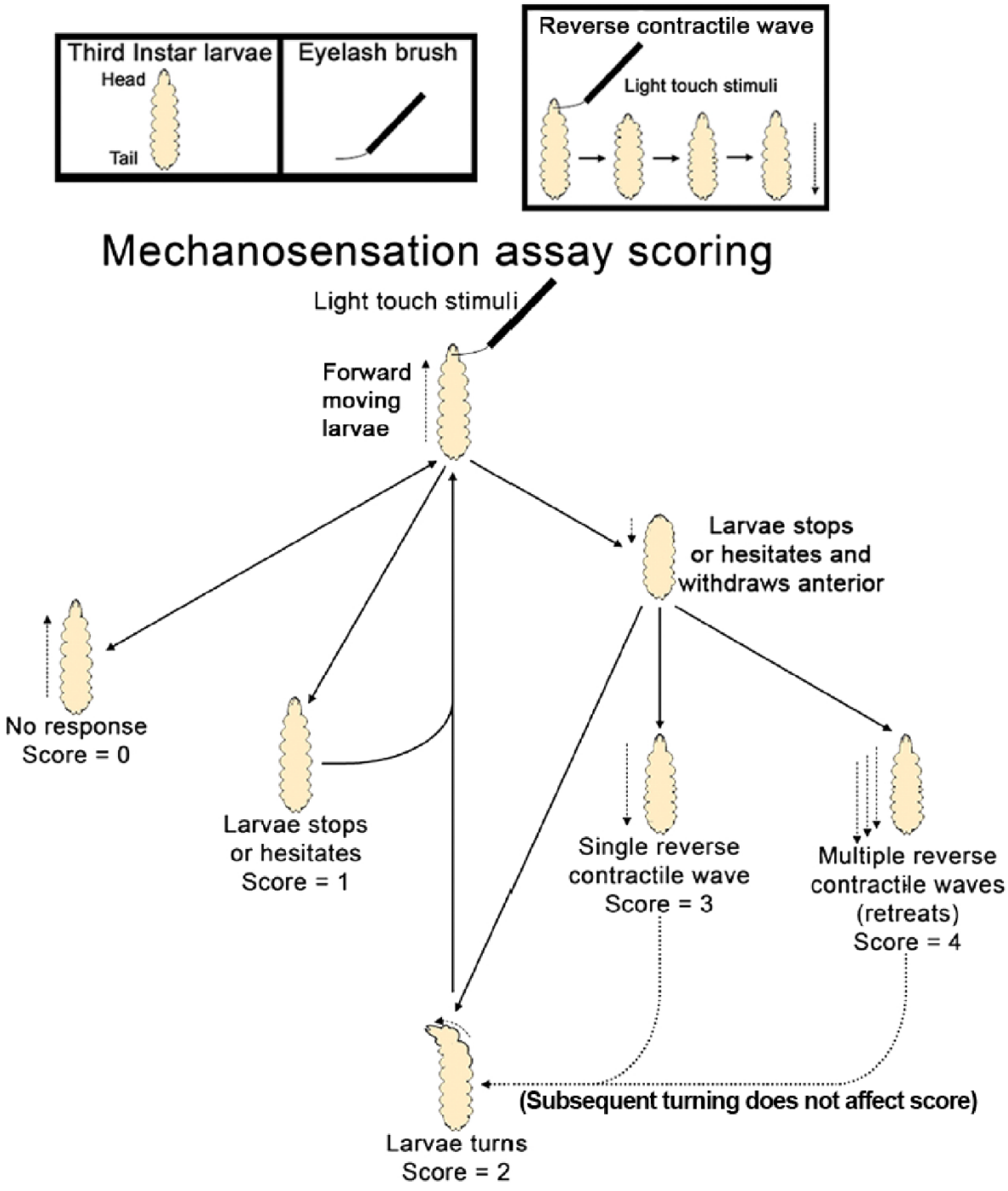

Figure 3-9: Larval touch sensitivity assay. Modified from (Kernan et al., 1994).

A

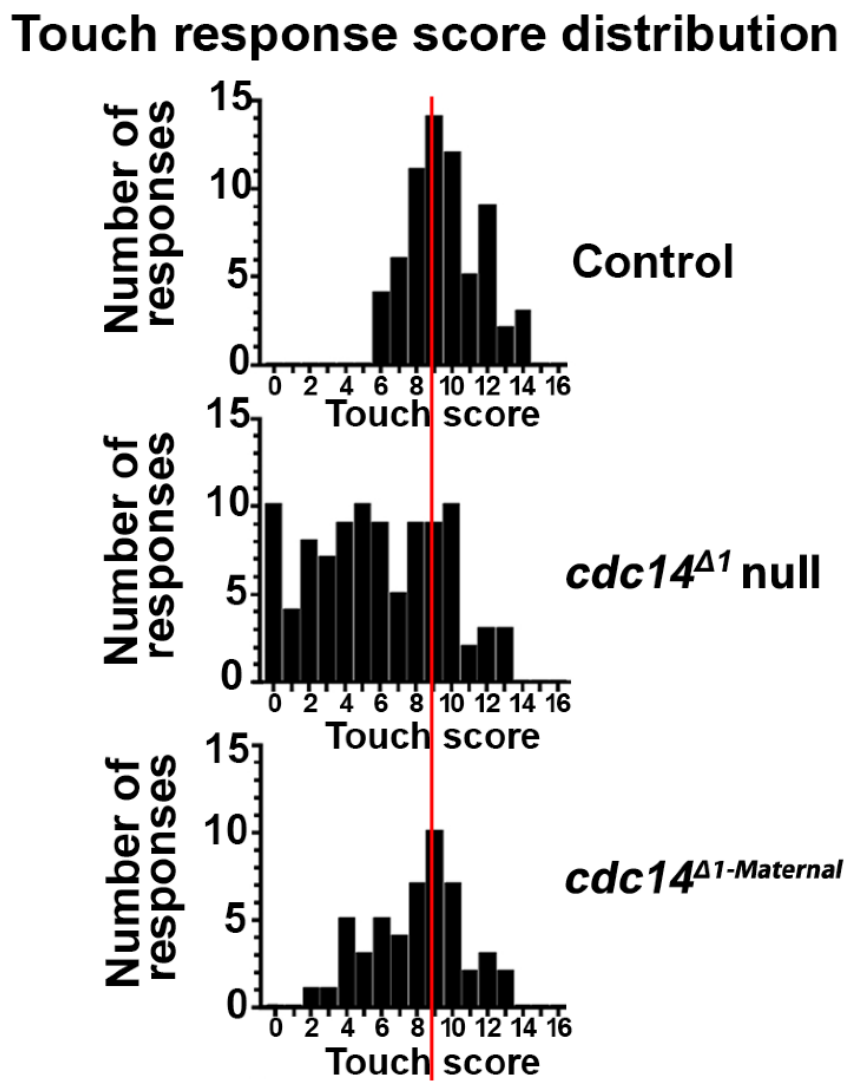

B

Genotype	Median	Standard deviation
Control	9	2.0
cdc14$^{\Delta 1}$ null	6	3.6
cdc14$^{\Delta 1\text{-Maternal}}$	8	2.6

Figure 3-10: *cdc14* null larvae exhibit decreased sensitivity to mechanical stimuli. (A) Distribution of touch response scores (see Figure 3-9). $cdc14^{\Delta 1}$ null larvae with maternally contributed *cdc14* ($cdc14^{\Delta 1\text{-}Maternal}$) exhibited an approximately normal distribution of scores relative to control with a peak at 9, whereas the *cdc14* null larvae exhibited a flat distribution. The mean score for *cdc14* null larvae was significantly lower than controls ($\rho<0.001$) and $cdc14^{\Delta 1\text{-}Maternal}$ ($\rho<0.001$). Data sets were analyzed by one-way ANOVA with Tukey HSD post hoc analysis. Red vertical line delineates the mean touch response score for control. (B) Mean touch response scores with standard deviation for control, *cdc14* null, and $cdc14^{\Delta 1\text{-}Maternal}$ larvae. Results were aggregated from $N\geq50$ larvae in $N\geq5$ repetitions.

Gustation in Drosophila larvae is modulated by *cdc14*

Drosophila gustatory neurons are also Type I sensory neurons. Drosophila larvae have more than 81 external chemosensory gustatory neurons (including 37 neurons in the head) (Stewart et al., 2015). In order to test the functionality of the chemosensory neurons, we assessed the ability of larvae to detect and avoid the bitter substance, quinine (Wu et al., 2005). Larvae were placed for 5 min on a nutritious yeast paste containing food coloring, and the number of larvae with dyed food in >50% of their intestines were scored as feeding (Fig. 3-11A). In the absence of quinine, three times fewer *cdc14* null larvae had fed compared to control larvae (Fig. 3-11A). In the presence of quinine, only 5% of control larvae had fed, whereas the percentage of fed *cdc14* null larvae remained unchanged at 15–17% (Fig. 3-11A). These findings indicate that loss of *cdc14* results in both a loss of chemosensation and reduced but indiscriminate feeding.

A second test was used to verify the changes in gustatory sensation and to test the ability of the animals to discriminate between attractive (sucrose) and repellant (quinine) substances (Fig. 3-11B,C,D). In the absence or presence of sucrose across an entire plate, *cdc14* null larvae demonstrated a significant decrease in aversion to quinine when compared to controls (Fig. 3-11B,D). Furthermore, this discrimination against quinine returned to nearly wild-type levels in $cdc14^{\Delta 1\text{-}Maternal}$ larvae. When given the choice between sugar and quinine, no statistically significant differences were found between the *cdc14* null larvae and controls (Fig. 3-11C). No differences between the sexes were observed under these testing conditions.

In contrast to larvae, no difference in quinine avoidance was observed between *cdc14* null and control adults (Fig. 3-12A). Our results suggest that *cdc14* null larvae have the capacity to identify certain attractive substances (sucrose), but not repellant substances (quinine), possibly due to a defect in the functionality of the gustatory sensilla.

Photoreception is unaffected in the *cdc14* null larvae

To test if the mechanosensory and chemosensory behaviors in *cdc14* null larvae were specific to ciliary function (rather than non-ciliary-mediated functions such as mobility), we tested photoreception, which is not mediated by ciliated neurons. Drosophila are negatively phototactic (Lilly and Carlson, 1990). Late third instar larvae were exposed to light with a choice between opaque-black and clear agarose backgrounds. We observed no differences between the *cdc14* null, control, and rescue larvae (Fig. 3-12B). These results suggest the observed defects in *cdc14* null animals are specific to ciliated cell types (e.g. Type I sensory neurons and sperm).

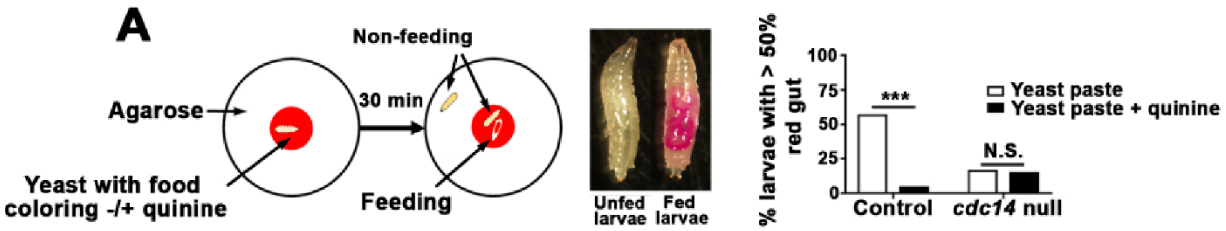
A
Non-feeding
Agarose
30 min
Yeast with food coloring -/+ quinine
Feeding
Unfed larvae
Fed larvae
% larvae with > 50% red gut
100
75
50
25
0
***
N.S.
Yeast paste
Yeast paste + quinine
Control
cdc14 null

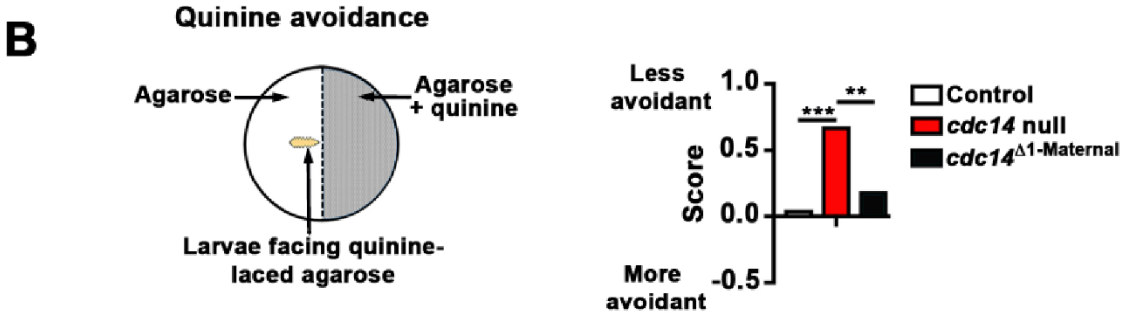
B
Quinine avoidance
Agarose
Agarose + quinine
Larvae facing quinine-laced agarose
Less avoidant
More avoidant
Score
1.0
0.5
0.0
-0.5
***
**
Control
cdc14 null
cdc14Δ1-Maternal

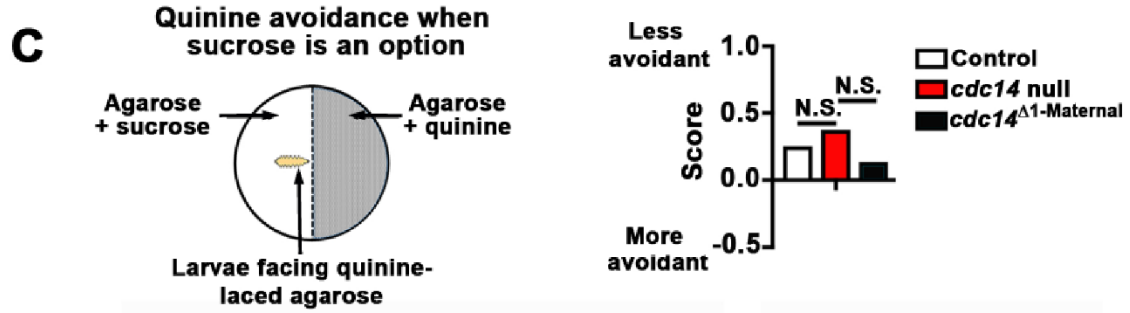
C
Quinine avoidance when sucrose is an option
Agarose + sucrose
Agarose + quinine
Larvae facing quinine-laced agarose
Less avoidant
More avoidant
Score
1.0
0.5
0.0
-0.5
N.S.
N.S.
Control
cdc14 null
cdc14Δ1-Maternal

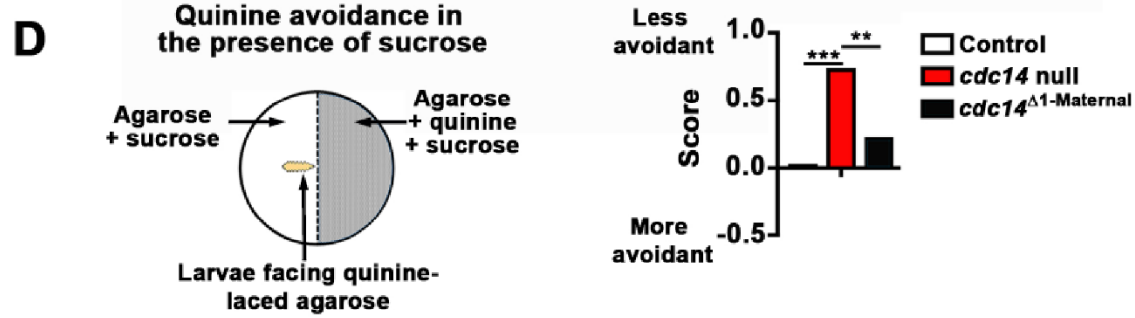
D
Quinine avoidance in the presence of sucrose
Agarose + sucrose
Agarose + quinine + sucrose
Larvae facing quinine-laced agarose
Less avoidant
More avoidant
Score
1.0
0.5
0.0
-0.5
***
**
Control
cdc14 null
cdc14Δ1-Maternal

Figure 3-11: c*dc14* null larvae show decreased but indiscriminate feeding and loss of chemosensory responses. (A) Diagram of yeast feeding assay (left). *cdc14* null larvae fed at the same rate in the absence or presence of quinine in contrast to controls (right). Furthermore, in the absence of quinine, *cdc14* null larvae fed at a significantly lower rate than control larvae (***). Data were aggregated from N≥40 larvae in N≥3 repetitions. Data was analyzed by Chi-squared test with Bonferroni correction; ** ρ<0.004, *** ρ<0.0004. All possible comparisons were made. (B), (C), and (D) Diagrams of quinine preference assays used are shown to the left. (B) *cdc14* null larvae showed reduced avoidance of quinine. (C) No difference was observed between *cdc14* null and control larvae when sucrose was present in one-half of the plate and quinine present in the other half. (D) *cdc14* null larvae did not avoid quinine in the presence of sucrose. Results were aggregated from N≥51 larvae in N≥15 replicates and analyzed by Chi-squared test with Bonferroni correction in (B), (C), and (D). Control larvae were compared to *cdc14* null and $cdc14^{\Delta 1\text{-}Maternal}$. *cdc14* null larvae were also compared to $cdc14^{\Delta 1\text{-}Maternal}$. ** ρ<0.004, *** ρ<0.0004, N.S. = not significant.

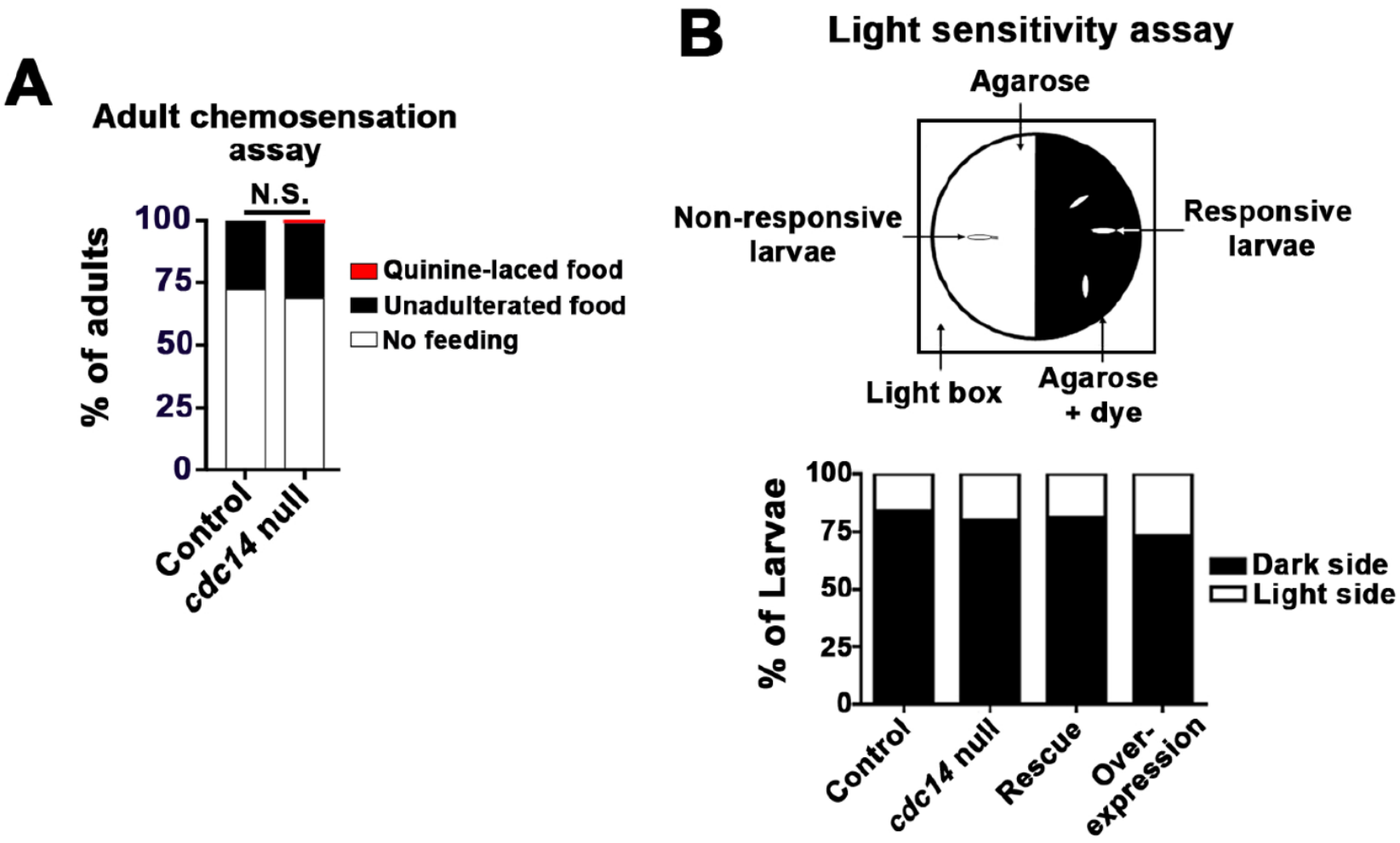
A
Adult chemosensation assay
N.S.
100
75
50
25
0
% of adults
Quinine-laced food
Unadulterated food
No feeding
Control
cdc14 null
B
Light sensitivity assay
Agarose
Non-responsive larvae
Responsive larvae
Light box
Agarose + dye
100
75
50
25
0
% of Larvae
Dark side
Light side
Control
cdc14 null
Rescue
Over-expression

Figure 3-12: Adult chemosensation and larval phototaxis is unaffected by loss of *cdc14*. (A) Adult flies (three days old) were starved for 18 h, transferred to the dark, and given the choice between regular versus quinine-laced food. Flies were allowed to feed for 90 minutes, frozen, and assessed for feeding. No difference in the rate of feeding or preference for quinine was observed in adult flies. N≥423 animals from N=6 replicates were tested. (B) Diagram of light sensitivity assay (top). Light sensitivity was not significantly different between any groups. Results were aggregated from N≥100 larvae in N=3 repetitions. Results shown in (A) and (B) were analyzed by Chi-squared test with Bonferroni correction.

***cdc14* confers resistance to starvation and modulation of lipid metabolism**

In a Drosophila genome-wide RNAi screen for genes involved in adiposity, *cdc14* was previously identified as a potential regulator of triglyceride metabolism (Pospisilik et al., 2010). Drosophila store energy in the form of triglycerides and glycogen; growth, reproduction, and normal energy expenditure under extended non-feeding periods (e.g. starvation) are dependent upon proper lipid metabolism (Arrese and Soulages, 2010). Alterations in fat metabolism manifest as changes in the size of the fat body or the abundance of lipid droplets (Figueroa-Clarevega and Bilder, 2015).

We dissected and analyzed the larval fat body, the major triglyceride storage organ (Figueroa-Clarevega and Bilder, 2015; Gutierrez et al., 2007). Staining with Oil Red O revealed large and abnormally shaped fat bodies in the *cdc14* null larvae in contrast to the controls (Fig. 3-13A,B). Staining with Nile Red showed a similar effect (Fig. 3-13C).

Previous studies have demonstrated that female flies are more resistant to starvation and have a higher lipid content than males (Huey et al., 2004; Jang et al., 2014). Thus, defects in triglyceride regulation may affect the resistance of the animals to nutrient deprivation. We found that control females have a slightly longer lifespan (>4.25 h) compared to *cdc14* null females under starvation conditions (Fig. 3-13D). The decrease in lifespan under starvation conditions and alterations in lipid droplet morphology observed in *cdc14 null* flies suggest that Cdc14 may play a role in the regulation of metabolism in Drosophila.

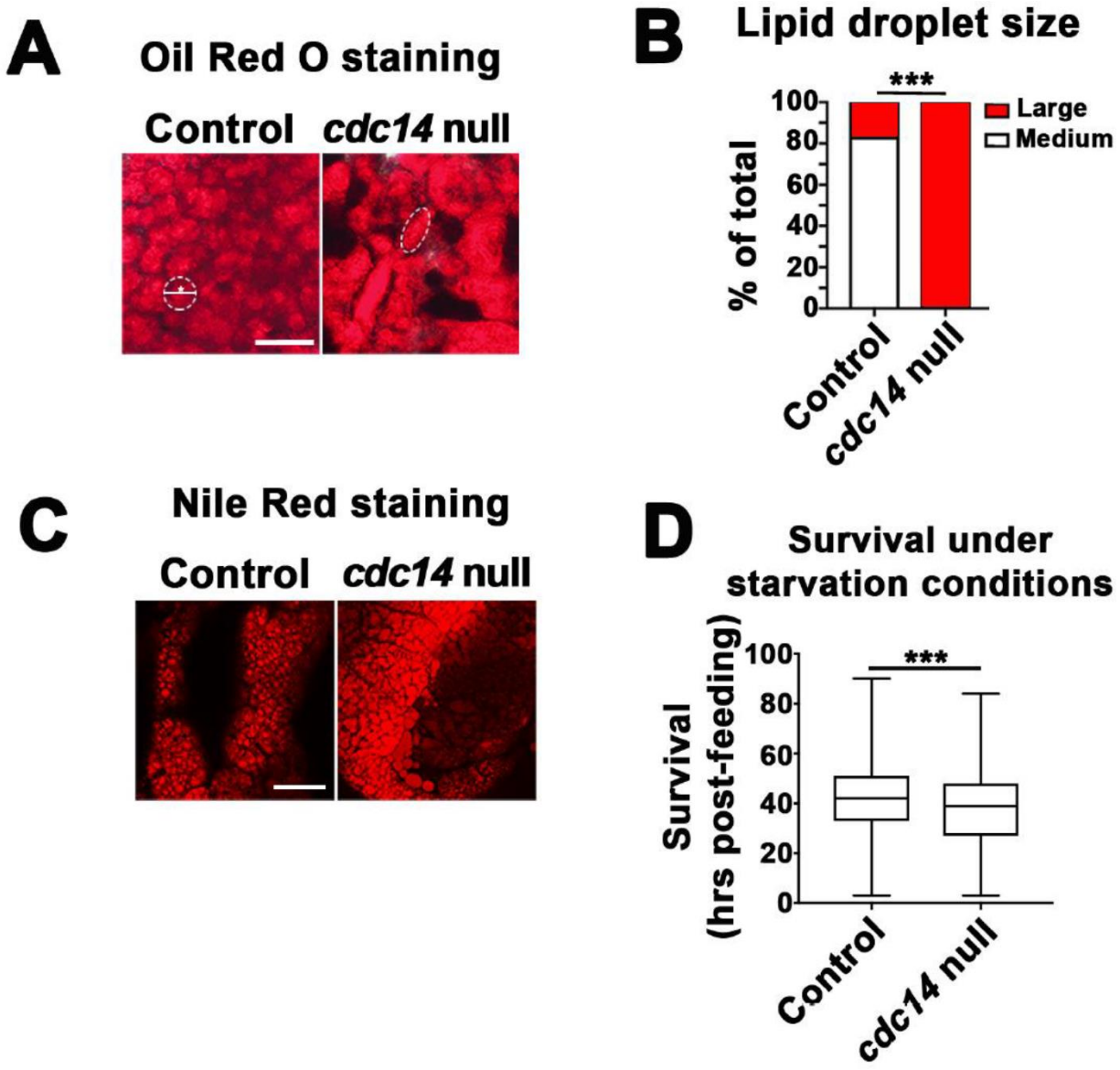
A
Oil Red O staining
Control
cdc14 null
B
Lipid droplet size
***
Large
Medium
% of total
100
80
60
40
20
0
Control
cdc14 null
C
Nile Red staining
Control
cdc14 null
D
Survival under
starvation conditions
Survival
(hrs post-feeding)
***
100
80
60
40
20
0
Control
cdc14 null

Figure 3-13: *cdc14* is required for normal lipid metabolism and survival during starvation conditions. (A) Oil Red O stained anterior fat bodies from segments T3 and A1 of late third instar larvae. Lipid droplets in fat bodies of *cdc14* null larvae were larger and more irregular in shape compared to controls. A regular shape droplet is outlined by a dotted white line in the control, and an irregular droplet is outlined in the null. Scale bar, 50 μm. N≥5 pelts were assessed. (B) Quantification of Oil Red O stained fat body cross-sections. *cdc14* null larvae lipid droplets were significantly larger than that of control larvae. Droplets from pelts were measured across their widest point; see asterisk (*) in (A). Droplets >2 standard deviations larger (≥160 μm) than the average droplet were classified as large. Samples were scored blind. N≥60 droplets were assessed from N≥5 pelts per genotype. Fisher's exact test was used to determine significance. ***ρ<0.001. (C) Larval fat bodies from the inner surface of the cuticle of abdominal segment A2-A4 stained with Nile Red. Large and irregularly shaped lipid droplets were observed in *cdc14* null larvae. Scale bar, 50 μm. N≥5 pelts were assessed per genotype. (D) Resistance to starvation of *cdc14* null and control adult females. Box and whisker plot shows that control animals lived modestly longer (> 4.25 h) than the *cdc14* null adult. Results were aggregated from N≥347 animals in N≥15 experiments using a t-test (two tailed, equal variance). *** ρ<.001.

Discussion

In the current study, we used ends-out homologous recombination to knock out the single Drosophila *cdc14* gene (Fisher et al., 2012; Gong and Golic, 2003). We have found that Drosophila Cdc14 confers several competitive advantages. Despite the fact that *cdc14* null males are fertile, they have a decreased capacity to compete with other males for mating. Loss of larval gustatory chemosensation and mechanosensation results in reduced and indiscriminate feeding behaviors, presumably leading to inadvertent feeding on a toxic food source. Our findings suggest that in times of food scarcity, *cdc14* nulls have a shorter lifespan than wild-type flies, possibly due to altered lipid metabolism and/or feeding behaviors. This constellation of defects associated with loss of *cdc14* in Drosophila may provide an explanation for its conservation in metazoans.

To our knowledge, the present study is the first characterization of a Drosophila *cdc14* null mutation. Similar to *S. pombe* and *C. elegans*, *D. melanogaster cdc14* is not an essential gene. Flies lacking *cdc14* are viable, and they do not display phenotypes that have been observed in other organisms (Mocciaro and Schiebel, 2010). For example, we were unable to demonstrate that *cdc14* participates in the DNA damage repair response, and loss of *cdc14* did not alter growth or lead to any obvious perturbations in mitosis or more generally in cell proliferation. Specifically, we did not observe any centrosomal or mitotic spindle defects or any defects in chromosome segregation or cytokinesis (data not shown).

We did not detect morphological differences in sperm formation between *cdc14* null and wild-type males. However, we show that sperm competiveness is decreased in *cdc14* null flies, suggesting an effect on sperm ciliary function (Brody, 1999). These findings merit further detailed molecular study of the role of *cdc14* in sperm ciliary function.

Chapter 4:

The role of Glycosylation in Metazoan development

At least 1% of all proteins encoded in the human genome are glycosylated or modify glycosylated proteins (Ohtsubo and Marth, 2006). Greater than 50% of all human proteins will undergo glycosylation during their lifetime (Apweiler, 1999). The addition of carbohydrate moieties can control localization, maturation, secretion, activity, and stability of proteins (Varki and Chrispeels, 1999). There are five classes of glycosylation: *N*-linked, *O*-linked, *C*-linked, *P*-linked (phosphoglycans), and *G*-linked (glypiation) (Chauhan et al., 2013). In this chapter I will primarily discuss the two most common classes of glycosylation, *N*-linked and *O*-linked, with a focus on *N*-linked. I will also discuss glycosylation in signaling pathways, and specifically highlight the role of *N*-glycosylation in Wnt signaling. Finally, I will discuss disorders of glycosylation in humans and their treatments.

N-linked glycosylation

In *N*-linked glycosylation, a lipid-linked oligosaccharide (LLO) attached by a diphosphate linkage to a dolichol lipid is transferred onto a protein (Fig. 4-1) (Varelas et al., 2014). The LLO consists of two *N*-acetyl-*D*-glucosamine moieties (GlcNAc), three glucose moieties (Glc_3), and nine mannose moieties added in a branched chain pattern (Varelas et al., 2014). The LLO forms on the cytoplasmic face of the endoplasmic reticulum (ER) membrane and is subsequently

flipped into the ER lumen by the flippase RFT1 (Varelas et al., 2014). The LLO is then transferred to asparagine residues within the consensus sequence Asn-X-Thr/Ser of proteins trafficked through the ER (Aebi, 2013). The LLO is further modified by enzymes as the protein matures in the ER and Golgi (Varelas, et al. 2014). As *N*-glycosylated proteins are found in the ER, they are commonly secreted or membrane bound, but may also be ER-resident proteins (Gupta and Brunak, 2002; Heine et al., 2004).

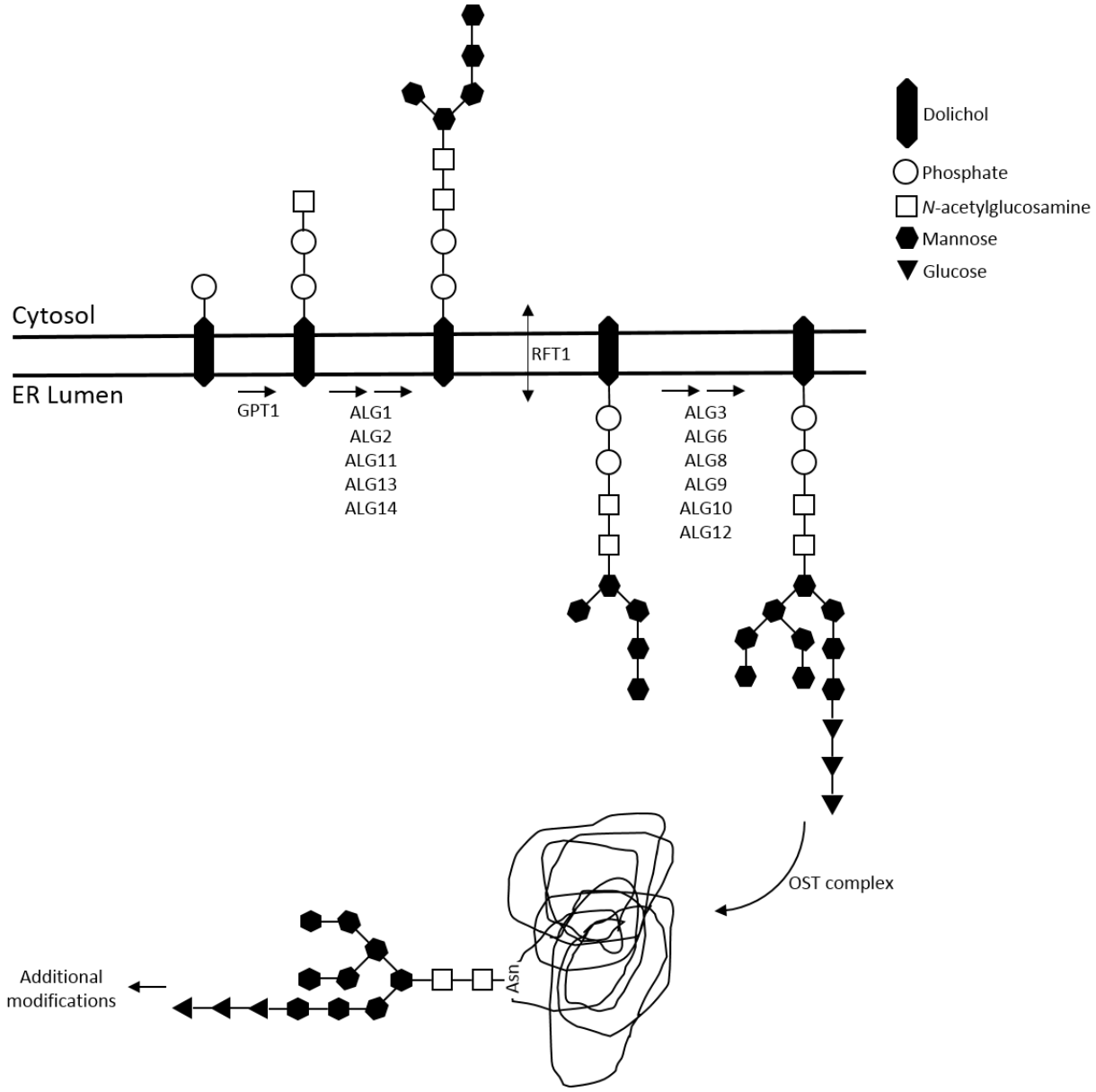
Dolichol
Phosphate
N-acetylglucosamine
Mannose
Glucose
Cytosol
ER Lumen
GPT1
ALG1
ALG2
ALG11
ALG13
ALG14
RFT1
ALG3
ALG6
ALG8
ALG9
ALG10
ALG12
OST complex
Asn
Additional
modifications

Figure 4-1: Simplified scheme of the *N*-glycosylation pathway. *N*-Glycosylation is initiated by GPT, encoded by the DPAGT1 gene. GPT catalyzes the transfer of GlcNAc from UDP-GlcNAc to dolichol-phosphate to produce dolichol-PP-GlcNAc, which is the first step in the synthesis of the LLO precursor. ALG13/ALG14, ALG1, ALG2, and ALG11 add carbohydrate moieties to produces the LLO depicted. The flippase RFT1 flips the dolichol-LLO structure into the ER lumen. ALG3, ALG9, ALG12, ALG6, ALG8, and ALG10 further modify the LLO in the ER to produce a mature LLO. Subsequently, the LLO is transferred co-translationally to newly synthesized polypeptides by the OST complex. After initial processing steps in the ER, glycoproteins will transit to the Golgi, where *N*-glycans are further modified to produce mature *N*-glycoproteins. ALG; asparagine-linked glycosylation. DPAGT1; Dolichyl-Phosphate *N*-Acetylglucosamine phosphotransferase 1. Asn; Asparagine.

_O_-linked glycosylation

In the simplest form of *O*-linked glycosylation a single GlcNAc moiety is transferred onto a serine or threonine residue (Brockhausen et al., 2009). However, eight 'core' structures exist that may be modified into longer much more complex chains (Fig. 4-2) (Brockhausen et al., 2009). Core 1 is the most common form of *O*-linked glycosylation (Brockhausen et al., 2009). Cores 5-8 are rare with highly restricted expression (Brockhausen et al., 2009). *O*-linked glycosylation in the ER and/or Golgi is common among proteoglycans, a major component of the extracellular matrix (Brockhausen et al., 2009). The addition of a single GlcNAc moiety to a serine or threonine residue can occur in the cytoplasm and nucleus, where it will not be modified into a carbohydrate oligomer (Brockhausen et al., 2009). Rather, this single GlcNAc moiety is a transient protein modification similar to phosphorylation or ubiquitination, such as transient inactivation of β-catenin by *O*-glycosylation (Ha et al., 2014; Sayat, 2008).

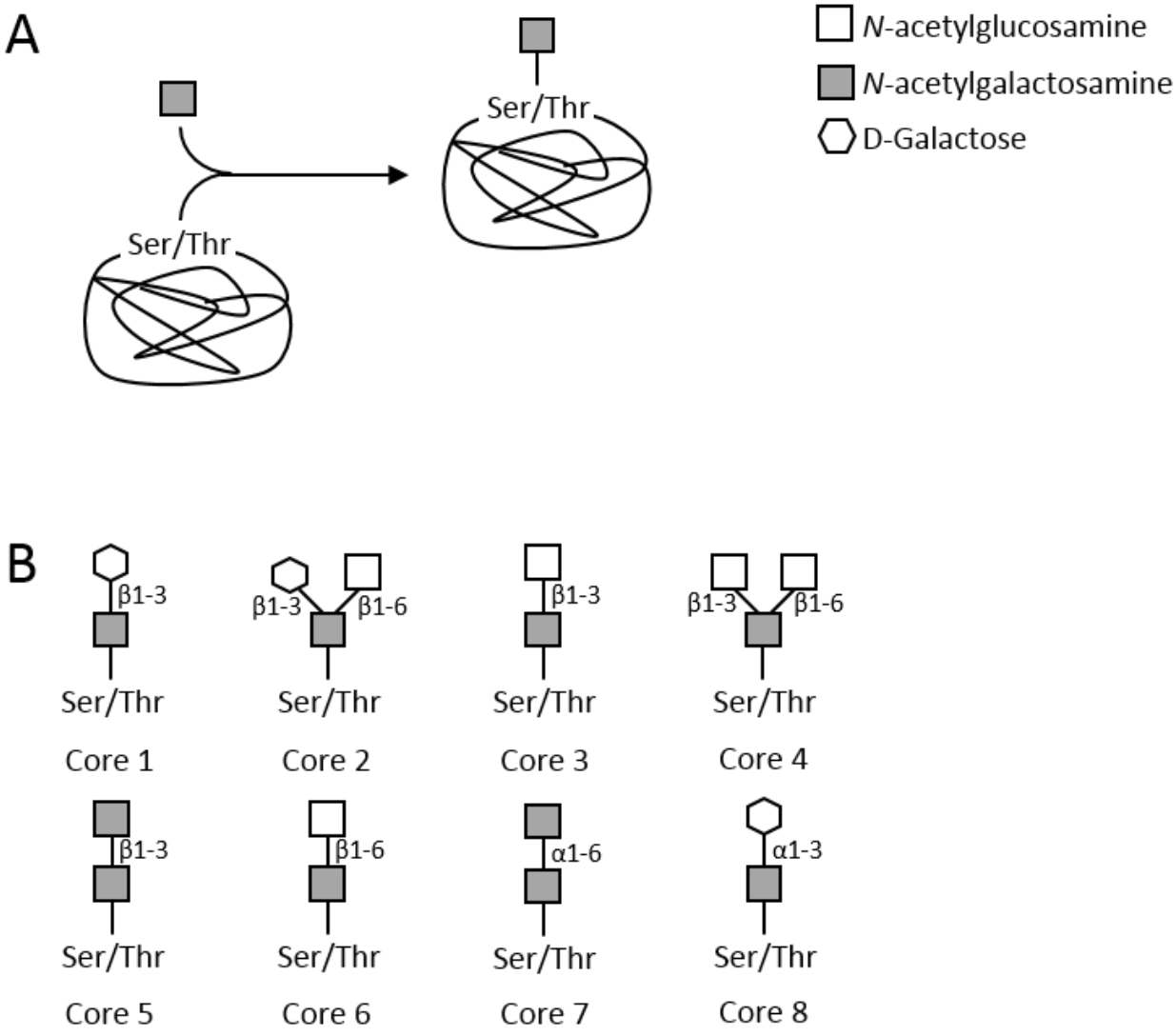
A
N-acetylglucosamine
N-acetylgalactosamine
D-Galactose
Ser/Thr
Ser/Thr
B
β1-3
Ser/Thr
Core 1
β1-3
β1-6
Ser/Thr
Core 2
β1-3
Ser/Thr
Core 3
β1-3
β1-6
Ser/Thr
Core 4
β1-3
Ser/Thr
Core 5
β1-6
Ser/Thr
Core 6
α1-6
Ser/Thr
Core 7
α1-3
Ser/Thr
Core 8

Figure 4-2: The basics of *O*-glycosylation of proteins. (A) The simplest form of *O*-Glycosylation is a single *N*-acetylgalactosamine moiety attached to a protein. (B) The eight identified core structures of *O*-Glycosylation. The glycosidic bonds of the sugar moieties is shown next to the bonds. Core 1 is the most commonly observed form of *O*-glycosylation. Cores 5-8 are rarely observed. Each core may be further modified.

Glycosylation in development

Multiple studies have analyzed developmental phenotypes resulting from loss-of-function of components of the glycosylation pathway and demonstrated that their loss of function are associated with changes in specific cell signaling pathways (Haltiwanger and Lowe, 2004). In Drosophila mutation of β1,3-*N*-acetylglucosaminyl-transferase in the *O*-Linked glycosylation of fucose results in defects of Notch through inhibition of *O*-fucosylated Notch ligands (Moloney et al., 2000). In mice FGF signaling is specifically inhibited by mutation of UDP-glucose dehydrogenase, which leads to loss of all extracellular matrix GAGs (Garcia-Garcia and Anderson, 2003). In human cell lines and oral cancers the glycosyltransferase dolichol-P-dependent *N*-acetylglucosamine-1-phosphate-transferase (DPAGT1) has been shown to work in a positive feedback loop through *N*-glycosylation with the canonical Wnt/β-catenin as well as non-canonical Wnt signaling (Fig. 4-3) (Varelas et al., 2014; Vargas et al., 2016).

Mutations in genes of glycosylation are not limited to loss-of-function, but a number of pathologic mutations in humans create ectopic glycosylation sites leading to disease. In 2005, Vogt et al. identified a missense mutation in IFNGR2 which created a novel *N*-glycosylation site in the IFNγR2 chain and abolished the cellular response to IFNγ (Vogt et al., 2005). Patients with this mutation lose resistance to illness caused by moderately virulent mycobacterial species (Vogt et al., 2005; Vogt et al., 2008). The identification of diseases caused by mutations in human glycosylation genes continues to increase each year (Fig. 4-4) (Cylwik et al., 2013; Ng and Freeze, 2018; Jaeken and Péanne, 2017).

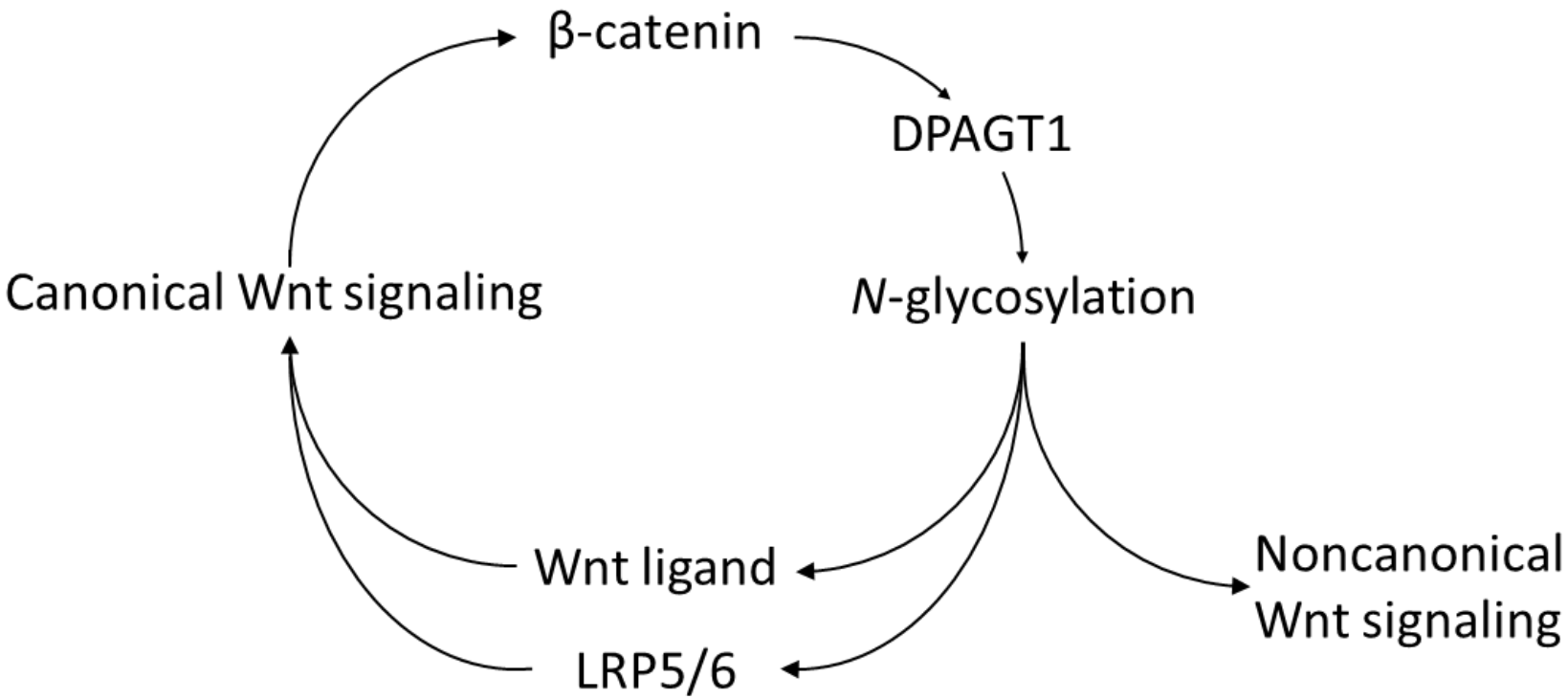
β-catenin
DPAGT1
Canonical Wnt signaling
N-glycosylation
Wnt ligand
Noncanonical
Wnt signaling
LRP5/6

Figure 4-3: The role of DPAGT1 in Wnt signaling. DPAGT1 is transcriptional target of canonical Wnt signaling. DPAGT1 expression increases *N*-glycosylation of proteins. Higher expression of DPAGT1 leads to a subsequent increase in protein *N*-glycosylation, including Wnt ligands and the LRP5/6 receptor. Thus, activation of canonical Wnt signaling leads to a positive feedback loop with DPAGT1 and *N*-glycosylation. In addition, increased *N*-glycosylation of Collagen Triple Helix Repeat Containing 1, a component of the noncanonical Wnt pathway, leads to an increase of noncanonical Wnt signaling.

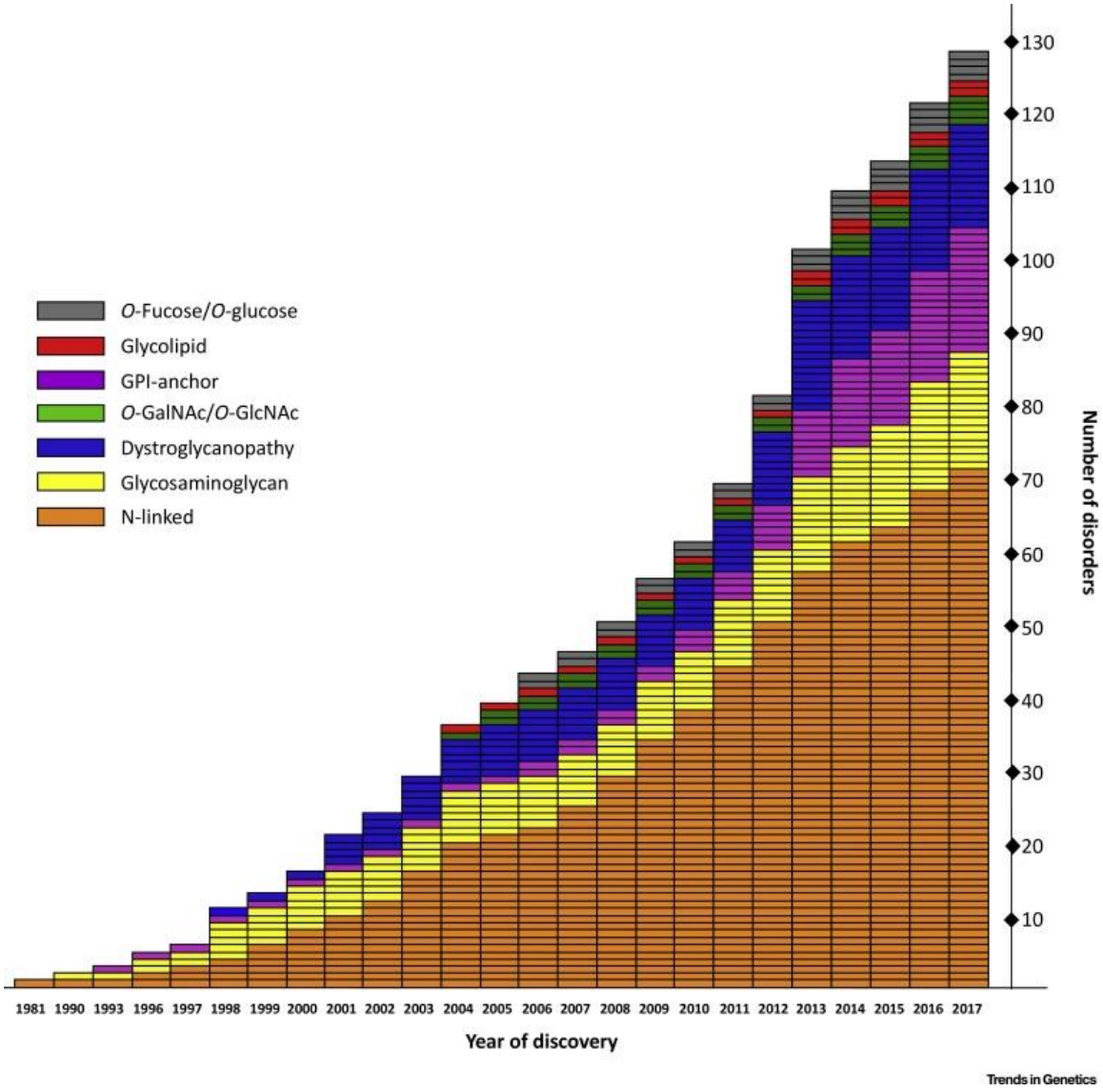
O-Fucose/O-glucose
Glycolipid
GPI-anchor
O-GalNAc/O-GlcNAc
Dystroglycanopathy
Glycosaminoglycan
N-linked
130
120
110
100
90
80
70
60
50
40
30
20
10
Number of disorders
1981 1990 1993 1996 1997 1998 1999 2000 2001 2002 2003 2004 2005 2006 2007 2008 2009 2010 2011 2012 2013 2014 2015 2016 2017
Year of discovery
Trends in Genetics

Figure 4-4: Discovery of glycosylation disorders (Copied from Ng and Freeze, 2018). The distribution of glycosylation-related disorders by the year they were identified. They are grouped according to the glycosylation pathway which they affect and while most fall within a clear specific pathway, there are those that can affect multiple glycosylation disorders. This describes disorders identified up to the end of 2017.

Congenital Disorders of Glycosylation and *N*-glycosylation

Disorders affecting glycosylation are classified as Congenital Disorders of Glycosylation (CDGs) (Fig. 4-5) (Ng and Freeze, 2018). Forty-two different mutations in *N*-linked glycosylation or multiple glycosylation pathways including *N*-linked glycosylation have been identified alone (Table 4-1) (Sparks and Krasnewich, 2017). Type 1 CDGs affect synthesis or transfer of the LLO onto the asparagine residue, while type 2 CDGs affect processing of the LLO in the ER and Golgi (Blau et al., 2014; Eklund and Freeze, 2006).

One would expect that mutations in similar pathways would lead to similar phenotypic outcomes. For example, in *O*-glycosylation, mutation of any one of the twelve genes involved in alpha-dystroglycan lead to muscular dystrophy (Endo, 2015). As mutations in any of the fourteen enzymes involved in LLO synthesis lead to incomplete *N*-glycosylation of nascent proteins, they would be expected to present with similar phenotypes. However, this is not the case. For example, defects in UDP-GlcNAc synthesis (e.g. as in GFPT1-CDG), addition of the first GlcNAc to the LLO (DPAGT1-CDG), or addition of the second GlcNAc to the LLO (ALG14-CDG) lead to myasthenic syndrome (Cossins et al., 2013; Senderek et al., 2011; Wu et al., 2003). However, defects in addition of the fourth and fifth mannoses LLO (ALG11-CDG) or flipping of the LLO into the lumen of the ER (RFT1-CDG) cause sensorineural hearing loss, a rare CDG phenotype (Regal et al., 2014; Rind et al., 2010; Vleugels et al., 2009). Once in the ER lumen, mutations in the addition of the last four mannoses (ALG3-CDG, ALG9-CDG and ALG12-CDG), result in skeletal phenotypes not observed in other CDGs; specifically mesomelic brachymelia, round pelvis, shortened sacrosciatic notch and ovoid ischia, hypomineralization of the skull, cervical vertebral

bodies, pubic rami and a thick occipital bone (Tham et al., 2016). Lastly, defects in the addition of the first (ALG6-CDG) and second (ALG8-CDG) Glc to the LLO lead to brachydactyly (Höck et al., 2015; Morava et al., 2016). While the first identified and most common CDG (PMM2-CDG) exhibits the opposite phenotype of long and slender fingers and toes (Ferreira et al., 2018; Jaeken et al., 1980; Matthijs et al., 1997; Van Schaftingen and Jaeken, 1995).

As this clustering of phenotypes occurs prior to the transfer of the LLO to the protein, hypoglycosylation cannot be the sole cause of the phenotypes. It is possible that accumulated LLOs or modified LLOs could be toxic (Ferreira et al., 2018). However, it is also possible that both hypoglycosylation and misglycosylation with truncated LLOs contribute to pathogenesis, as truncated LLOs can indeed be transferred to nascent proteins with decreased efficiency (Krasnewich et al., 1995; Panneerselvam and Freeze, 1996; Vleugels et al., 2009).

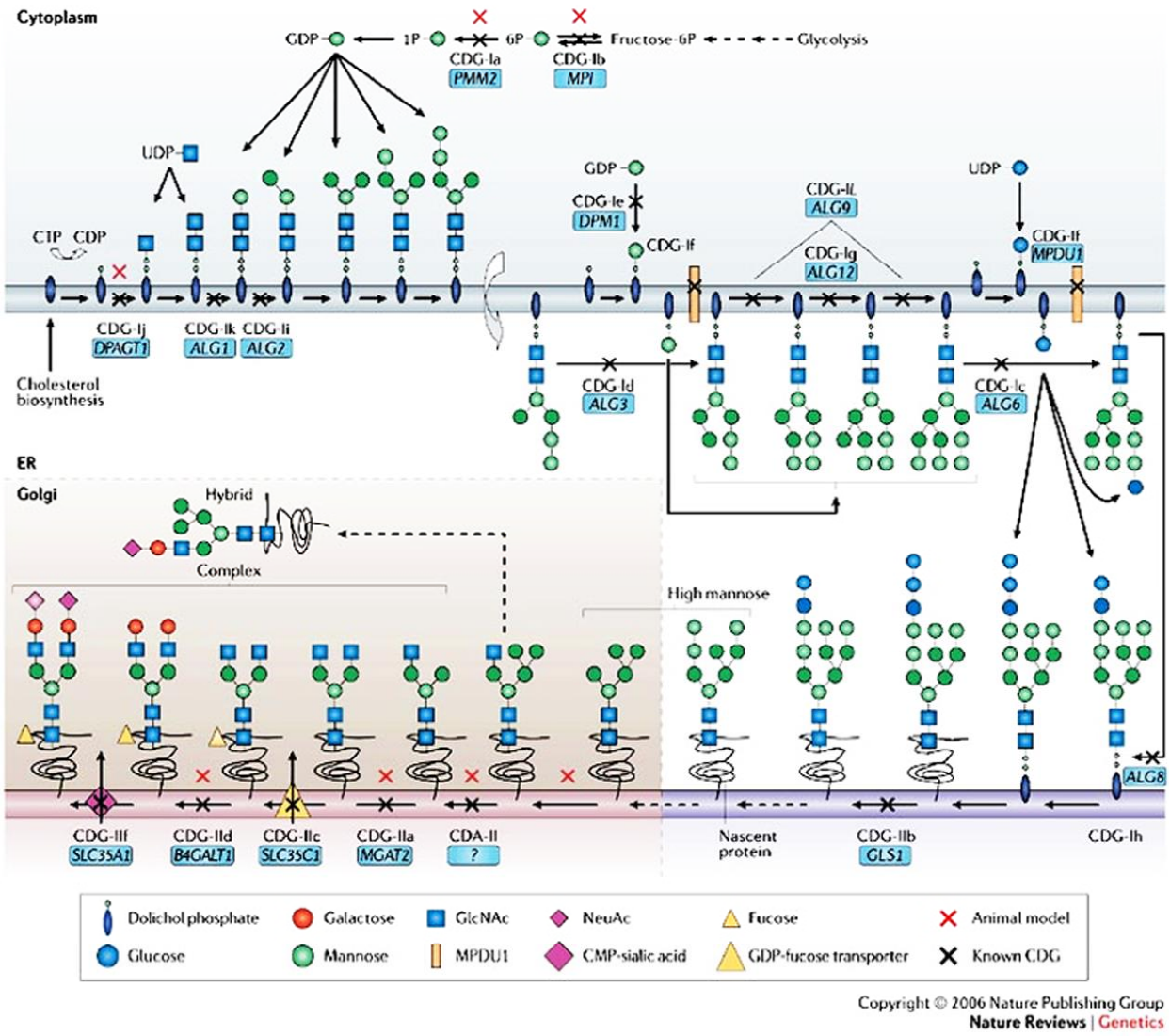

Figure 4-5: Diagram detailing known molecular and metabolic defects associated with CDGs (Copied from Freeze et al., 2006).

***N*-linked Glycosylation**		
	# of Cases Reported	**Gene**
PMM2-CDG (*CDG-Ia*)	700	*PMM2*
MPI-CDG (*CDG-Ib*)	20	*MPI*
ALG6-CDG (*CDG-Ic*)	89	*ALG6*
ALG3-CDG (*CDG-Id*)	11	*ALG3*
DPM1-CDG (*CDG-Ie*)	9	*DPM1*
MPDU1-CDG (*CDG-If*)	5	*MPDU1*
ALG12-CDG (*CDG-Ig*)	7	*ALG12*
ALG8-CDG (*CDG-Ih*)	5	*ALG8*
ALG2-CDG (*CDG-Ii*)	≤2	*ALG2*
DPAGT1-CDG (*CDG-Ij*)	5	*DPAGT1*
ALG1-CDG (*CDG-Ik*)	57	*ALG1* (*HMT-1*)
ALG9-CDG (*CDG-IL*)	≤2	*ALG9*
DOLK-CDG (*CDG-Im*)	≤2	*DOLK (DK1)*
RFT1-CDG (*CDG-In*)	6	*RFT1*
DPM3-CDG (*CDG-Io*)	≤2	*DPM3*
ALG11-CDG (*CDG-Ip*)	4	*ALG11*
SRD5A3-CDG (*CDG-Iq*)	15	*SRD5A3*
DDOST-CDG (*CDG-Ir*)	1	*DDOST*
MAGT1-CDG	4	*MAGT1*
TUSC3-CDG	12	*TUSC3*
ALG13-CDG	1	*ALG13*
PGM1-CDG	2	*PGM1*
MGAT2-CDG (*CDG-IIa*)	4	*MGAT2*
STT3A-CDG, STT3B-CDG	2	*STT3A, STT3B*
SSR4-CDG	<2	*SSR4*
MOGS-CDG (*CDG-IIb*)	≤2	*MOGS (GCS1)*
SLC35C1-CDG (*CDG-IIc*)	≤2	*SLC35C1*
B4GALT1-CDG (*CDG-IId*)	≤2	*B4GALT1*
SLC35A2-CDG	<2	SLC35A2
GMPPA-CDG	<2	*GMPPA*
Multiple-Pathway Disorders		
COG7-CDG (*CDG-IIe*)	≤2	*COG7*
SLC35A1-CDG (*CDG-IIf*)	≤2	*SLC35A1*
COG1-CDG (*CDG-IIg*)	≤2	*COG1*
COG2-CDG	1	*COG2*
COG8-CDG (*CDG-IIh*)	≤2	*COG8*
COG5-CDG (*CDG-IIi*)	7	*COG5*
COG4-CDG (*CDG-IIj*)	≤2	*COG4*
TMEM165-CDG (*CDG-IIk*)	5	*TMEM165*
COG6-CDG (*CDG-IIL*)	17	*COG6*
DPM2-CDG	<2	*DPM2*
DHDDS-CDG	<2	*DHDDS*
MAN1B1-CDG	<2	*MAN1B1*
PGM3-CDG	8	*PGM3*

Table 4-1: Diseases of *N*-linked glycosylation identified in humans. MOI: Mode of inheritance. XL: X-linked. AR: Autosomal recessive.

Complex glycosylation and non-glycosylation pathways lead to CDGs

Defects in any one of six of the eight subunits of the conserved oligomeric Golgi (COG) demonstrate that mutations in proteins not specifically or exclusively involved in glycosylation can result in CDGs (Foulquier, 2009; Lübbehusen et al., 2010; Morava et al., 2007; Ng et al., 2007; Paesald-Burda et al., 2009; Reynders et al., 2009; Wu et al., 2004; Zeevaert et al., 2009). Furthermore, congenital dyserythropoietic anemia type II, a type of genetic anemia, is caused by a defect in the SEC23B gene (SEC23B-CDG), which codes for a secretory COPII coat component (Denecke and Marquardt, 2009; Bianchi et al., 2009; Schwarz et al., 2009).

Four mutations in glycosylphos-phatidylinositol (GPI) anchor glycosylation, such as in the second mannosyltransferase (PIGV-CDG), have been identified (Jaeken, 2011; Krawitz et al., 2010). Furthermore, a number of patients have presented with defects in both *N*- and *O*-linked glycosylation (Jaeken and Matthijs, 2007). For example, defects in the a2 subunit of the vacuolar H^+-ATPase (V-ATPase), a multi-subunit, ATP-dependent proton pump located in cell and organelle membranes and implicated in Wnt signaling, results in a combined defect in *N*- and *O*-glycosylation (Bryan Ray, 2010; Guillard et al., 2009; Kornak et al., 2008; Morava et al., 2005; Morava et al., 2008; Van Maldergem et al., 2008).

Treatment of CDGs

As some CDGs are metabolic enzymes, supplementation with the downstream product of the enzyme should ameliorate the loss-of-function phenotypes. However, because these

disorders are often quite rare and difficult to diagnose, this therapeutic strategy has rarely been attempted. Therefore, effective treatment is only available for two CDGs: MPI-CDG (oral mannose) and CAD-CDG (oral uridine) (Koch et al., 2017; Niehues et al., 1998). Partial treatments are available for CDGs that can present as a congenital myasthenic syndrome (DPAGT1-CDG, ALG2-CDG, ALG14-CDG, GFPT1-CDG and GMPPB-CDG; cholinesterase inhibitors), as well as for PIGM-CDG (oral butyrate controls seizures), SLC35C1-CDG (oral fucose controls infections), DOLK-CDG (heart transplantation), PGM1-CDG (galactose), SLC35A2-CDG and SLC39A8-CDG (galactose), PGM3-CDG (haematopoietic stem cell transplantation) (Dörre et al., 2015; Marquardt et al., 1999; Morava, 2014; Park et al., 2015; Stray-Pedersen et al., 2014). Supplementation with sialic acid may stabilize muscle strength in GNE-CDG (Argov et al., 2016).

As CDGs are rare and difficult to treat in humans, animal models are needed to further develop and test treatments. Certain CDGs, such as PMI have been knocked-out in mice, however the null mutation often causes embryonic lethality making it a poor model system (DeRossi et al., 2006). Rather than generating a null mutations, hypomorphic or antimorphic alleles could be used to interrogate the molecular cause of the diseases and potential treatments. Furthermore, partial loss-of-function can more analyzed more quickly in other vertebrate organisms such as *Xenopus* or zebrafish using Morpholino oligonucleotides.

The UDP-GlcNAc salvage pathway recycles GlcNAc from degraded glycoproteins

Glycoproteins are commonly endocytosed and degraded in the lysosome (Freeze et al., 2015). The transport or diffusion of free GlcNAc moieties from the lysosomal lumen to the cytosol is poorly understood. However, in the cytosol *N*-Acetylglucosamine Kinase (NAGK), the first enzyme of the UDP-GlcNAc salvage pathway converts GlcNAc into GlcNAc-6-P (Bergeret al., 2002). GlcNAc-6-P is then converted into GlcNAc-1-P by Phosphoglucomutase 3 (PGM3) (Bergeret al., 2002). Finally, UDP-*N*-Acetylglucosamine Pyrophosphorylase 1 (UAP1) converts GlcNAc-1-P into UDP-GlcNAc (Bergeret al., 2002). Once GlcNAc has been salvaged but conversion in UDP-GlcNAc, it can be used by DPAGT1 mediated *N*-linked glycosylation (Bergeret al., 2002; Freeze et al., 2015).

Lysosomal degradation of glycoproteins is an important step in glycosylation, as nearly half of all amino sugars from endocytosed glycans are reused for glycoprotein synthesis (Freeze et al., 2015). Approximately 80% of GlcNAc salvaged from degraded glycoproteins is converted into Uridine diphosphate *N*-acetylglucosamine (UDP-GlcNAc) (Freeze et al., 2015). At least 30% of this “salvaged” UDP-GlcNAc is used to synthesize secreted glycoproteins (Freeze et al., 2015). Therefore, salvage of GlcNAc from degraded *N*-glycosylated proteins is important for the availability of UDP-GlcNAc and DPAGT1 one function.

Glycosylation is essential for proper metazoan development

Glycosylation is an essential post-translational modification regulating more than half of the proteome. Cell signaling pathways, such as Fgf and Wnt, are regulated by glycosylation of component proteins (e.g. ligands and receptors). Of the five classes of glycosylation, *N*-linked and *O*-linked glycosylation are the most common. Both gain-of-function and loss-of-function mutations lead to congenital disorders of glycosylation (CDG), through alterations of protein glycosylation states. However, only two loss-of-function CDGs can be effectively treated, through supplementation with the downstream carbohydrate.

To date, forty-two mutations in proteins involved in *N*-linked glycosylation have been identified. In chapter 6, I will discuss three enzymes involved in the salvage of UDP-GlcNAc from glycosylated proteins, the first enzyme in *N*-linked glycosylation, and how they work to regulate the glycosylation state of Wnt signaling pathway components. Two of these enzymes (PGM3 and DPAGT1) are known to result in CDGs. Our results suggest supplementation with the final carbohydrate of the pathway (UDP-GlcNAc) may be an effective treatment for these CDGs.

Chapter 5:

Wnt signaling and implications of glycosylation

The canonical Wnt/β-catenin pathway

Wnt signaling plays an essential role in cell fate, proliferation, polarity, and cell death during embryonic development. Canonical Wnt signaling uses the essential downstream transcriptional effector, β-catenin, to facilitate alterations in transcriptional targets. When the pathway is not active, β-catenin is continually synthesized and destroyed by the β-catenin destruction complex in a futile cycle. Activation of the pathway inhibits the formation of the destruction complex and stabilizes β-catenin. β-catenin can then enter the nucleus to modulate transcription (Fig. 5-1).

Extracellularly secreted Wnts bind to members of the Frizzled (Fz) family of transmembrane receptors (Bhanot et al., 1996; Hsieh et al., 1999). The Wnt-Fz complex binds the functionally redundant co-receptors: low-density lipoprotein receptor-related protein 5 (LRP5) or 6 (LRP6) (Pinson et al., 2000; Tamai et al., 2000; Wehrli et al., 2000). This interaction induces production of phosphatidylinositol (4,5)-bispho-sphate (PIP2), which induces oligomerization and clustering of LRP5/6 (Pan et al., 2008). Dishevelled (Dsh) is then recruited to the receptor complex where it binds to Fz and activates PI4KIIa and PIP5KI to promote further synthesis of PIP2 (Pan et al., 2008; Rothbacher et al., 2000; Semenov and Snyder, 1997; Tauriello et al., 2012; Wong et al., 2000; Wong et al., 2003; Yanagawa et al., 1995). However,

Dsh alone is sufficient to activate β-catenin signaling, independently of the Wnt-receptor complex (Salic et al., 2000; Wehrli et al., 2000).

The Wnt-Fz-LRP5/6 complex recruits Axin to LRP5/6, resulting in further recruitment of Glycogen Synthase Kinase 3 (GSK3) and Casein Kinase (CK1) to phosphorylate LRP5/6 (Baig-Lewis et al., 2007; Davidson et al., 2005; Zeng et al., 2005). Phosphorylation of LRP5/6 promotes recruitment of cytoplasmic Axin-bound GSK3 complexes to the cell surface in a positive feedback loop promoting further the phosphorylation of additional LRP5/6 (Baig-Lewis et al., 2007; Mao et al., 2001; Zeng et al., 2008). Axin is the limiting component of the destruction complex. The recruitment of Axin to the membrane inhibits the formation of the destruction complex and stabilizes β-catenin (in a mechanism that has yet to be defined) (Saito-Diaz et al., 2013). Cytoplasmic β-catenin accumulates in the cytosol and nucleus, where it associates with the TCF/LEF family of DNA-bound transcription factors to mediate transcription of target genes (Behrens et al., 1996; Goentoro and Kirschner, 2009; Molenaar et al., 1996; Saito-Diaz et al., 2013).

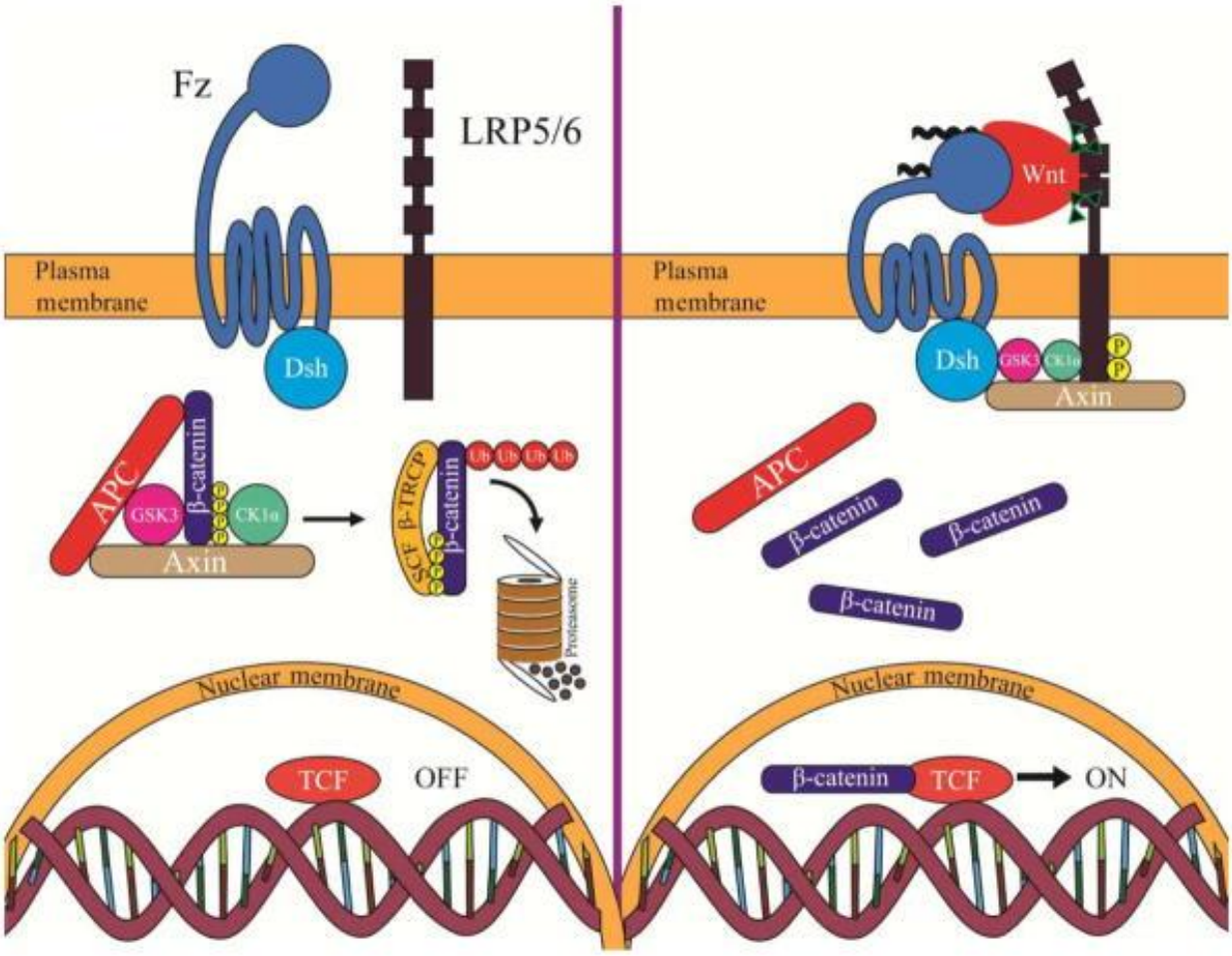
Fz
LRP5/6
Plasma membrane
Dsh
APC
β-catenin
GSK3
CK1α
Axin
SCF β-TRCP
Ub
Proteasome
Nuclear membrane
TCF
OFF
Wnt
P
ON

Figure 5-1: The current model of canonical Wnt/β-catenin signaling (Copied here from Saito-Diaz et al., 2013). (Left panel) In the absence of Wnt, cytoplasmic β-catenin forms a complex with APC, Axin, GSK3, and CK1α. β-Catenin is phosphorylated by CK1α and subsequently phosphorylated by GSK3. The phosphorylated form of β-catenin is recognized by the E3 ubiquitin ligase $SCF^{\beta\text{-}TRCP}$, which targets β-catenin for proteasomal degradation. In the absence of nuclear β-catenin, Wnt target genes are repressed. APC, adenomatous polyposis coli; GSK3, glycogen synthase kinase 3; CK1α, casein kinase 1 alpha. (Right panel) In the presence of Wnt ligand, a receptor complex forms between Fz, LRP5/6, and Wnt. The recruitment of Dsh by Fz leads to LRP5/6 phosphorylation by CK1α and GSK3 followed by recruitment of Axin to LRP5/6. The latter disrupts Axin-mediated phosphorylation/degradation of β-catenin, leading to accumulation of β-catenin in the cytoplasm and its translocation to the nucleus, where it acts as a transcriptional co-activator with TCF to activate Wnt-responsive target genes. Fz, Frizzled; Dsh, Dishevelled; TCF, T-cell factor. Copied here from Saito-Diaz et al. 2013.

The non-canonical Wnt pathway

Non-transcriptional Wnt pathways are known as noncanonical Wnt signaling, and include planar cell polarity, convergent extension, Wnt-Ca^{2+}, and Wnt-atypical protein kinase C pathways (Amerongen, 2012; Kikuchi et al., 2009; Lai et al., 2009; Semenov et al., 2007; Simons and Mlodzik, 2008; Thrasivoulou et al., 2013). Noncanonical Wnt signalling is initiated by Wnt or Fz and is independent of the β-catenin transcriptional element (Semenov et al., 2007). Unlike canonical Wnt/β-catenin signaling, the mechanisms underlying activation of noncanonical Wnt pathways are poorly understood. Noncanonical activity of Wnt3a, Wnt4, Wnt5a, and Wnt11 have been identified and may use Dvl, axin, and GSK3 to activate LRP6 and other co-receptor in addition to Fz (Angers and Moon, 2009; Green et al., 2008; Grumolato et al., 2010; Kumawat and Gosens, 2016; Lai et al., 2009; Qian et al., 2007; Wang et al., 2006; Yamamoto et al., 2008).

Wnt signaling and *N*-glycosylation

All of the secreted Wnt ligands are *N*-linked glycosylated (Saito-Diaz et al., 2013). However, the role(s) of glycosylation in Wnt are not well conserved, as the number and position of glycosylation sites within the Wnt family differ (Tang et al., 2012). In Wnt1, *N*-glycosylation has been suggested to be dispensable for autocrine and paracrine signaling (Doubravska et al., 2011; Mason et al., 1992). In the *Drosophila* the Wnt orthologue, Wingless, is secreted and retains activity when Glycosylation-deficient (Tang et al., 2012). However, studies by the Kikuchi lab found that *N*-glycosylation of Wnt3a and Wnt5a precedes lipid modification and is

important for Wnt secretion, but not for Wnt activity (Komekado et al., 2007; Kurayoshi et al., 2007; Takada et al., 2006; Tanaka et al., 2002; Willert et al., 2003). The exit of LRP5/6 from the ER is dependent on *N*-linked glycosylation for maturation and membrane localization (Jung et al., 2011; Kahn et al., 2007). Furthermore, binding of the Wnt antagonist Dkk1 Is Regulated by *N*-glycosylation of LRP6 (Matoba et al., 2017). Shisa has been suggested to retain Fz protein in the ER, by binding immature Fz8 which has not been fully glycosylated (Yamamoto et al., 2005). Therefore, the role of glycosylation in Wnt remains unclear. In addition to glycosylation of Wnt, LRP5/6 and Fz, β-catenin is stabilized by the addition of an *O*-linked GlcNAc (*O*-GlcNAcylation) (Ha et al., 2014; Olivier-Van Stichelen et al., 2014).

NAGK and *N*-glycosylation modulate Wnt signaling possibly through LRP6

In the next chapter of this work we will show that Wnt signaling is regulated by the UDP-GlcNc glycosylation salvage pathway in *Xenopus laevis* and zebrafish. Overexpression of key components of the salvage pathway (particularly, NAGK) promotes Wnt signaling, and, conversely, downregulating NAGK inhibits Wnt signaling. qRT-PCR analysis of ectodermal explants suggest that the effect of the salvage pathway on the Wnt pathway is at the level of Wnt receptor activation. Finally, we show that both the canonical and the noncanonical Wnt pathways are affected by the UDP-GlcNc salvage pathway.

Chapter 6:

N-acetyl-*D*-glucosamine kinase controls Wnt signaling in the early embryo

The work described herein is a completed but unpublished manuscript by:

Leif R. Neitzel, Christopher S. Cselenyi, Cheyanne Q. Youngblood, Alya Zouaoui, and Ethan Lee

Abstract

The UDP-GlcNAc glycosylation salvage pathway is responsible for nearly 80% of the UDP-GlcNAc pool required for glycosylation. In a novel screen for human kinases that regulate early *Xenopus laevis* development, we identified *N*-acetyl-*D*-glucosamine kinase (NAGK), a key enzyme in the UDP-GlcNAc salvage pathway, as a regulator of vertebrate anteroposterior pattering. Overexpression of *NAGK* posteriorized and knockdown anteriorized *Xenopus* embryos. Inhibition of the UDP-GlcNAc glycosylation salvage pathway enzymes, PGM3 and UAP1, as well as the DPAGT1, the first enzyme in *N*-linked glycosylation, anteriorized *Xenopus* embryos. Conversely, overexpression of PGM3, UAP1, or DPAGT1 posteriorized *Xenopus* embryos. The sugars of the UDP-GlcNAc glycosylation salvage pathway (GlcNAc, GlcNAc-6-P, GlcNAc-1-P, and UDP-GlcNAc) were sufficient to posteriorize *Xenopus* embryos. Inhibition of NAGK in *Danio rerio* resulted in cyclopia. Overexpression of NAGK, PGM3, UAP1, DPAGT1, GlcNAc, GlcNAc-6-P, GlcNAc-1-P, or UDP-GlcNAc inhibited eye formation in *D. rerio*. The observed phenotypes in *Xenopus* and *D. rerio* are consistent with Wnt phenotypes. qRT-PCR of target genes demonstrates that the salvage pathway affected Wnt signaling, but not Notch, Shh, BMP, or Fgf. Moreover, studies of ectodermal explants indicate that alterations of the salvage pathway effect the Wnt pathway at the level of the receptor and/or ligand. These results demonstrate that altering the *N*-glycosylation pathway specifically regulates the Wnt signaling pathway.

Introduction

At least 1% of all proteins encoded in the human genome are involved in or modify glycosylated proteins, and >50% of all proteins will undergo glycosylation during their lifetime (Apweiler, 1999; Ohtsubo and Marth, 2006). *N*-acetyl-*D*-glucosamine (GlcNAc) moieties are key monomers of *N*-/*O*-glycans, glycolipids, glycosaminoglycans and the glycosyl phosphatidylinositol anchor of membrane bound glycoproteins (Esko and Lindahl, 2001; Hakomori, 2000; Hwa, 2001; Kornfeld and Kornfeld, 1976; Schachter, 2000; Van den Steen et al., 1998). Approximately 80% of GlcNAc salvaged from degraded glycoproteins is converted into Uridine diphosphate *N*-acetylglucosamine (UDP-GlcNAc) (Freeze et al., 2015). At least 30% of this "salvaged" UDP-GlcNAc is used to synthesize secreted glycoproteins (Freeze et al., 2015). It has been estimated that nearly half of all amino sugars from endocytosed glycans are reused for glycoprotein synthesis in cells (Freeze et al., 2015).

N-acetylglucosamine kinase (NAGK; GlcNAc kinase, E.C. 2.7.1.59) is a member of the sugar kinase/heat shock protein70/actin superfamily (Berger et al., 2002). NAGK is a key enzyme in both the production of UDP-GlcNAc and *N*-linked glycosylation. NAGK converts GlcNAc into GlcNAc 6-phosphate (GlcNAc-6-P), the first step in the UDP-GlcNAc salvage pathway.

In the current study, we show that enzymes and sugar products of the UDP-GlcNAc glycosylation salvage pathway play a critical role in selectively regulating Wnt signaling in *Xenopus* and zebrafish embryos. qRT-PCR analysis of target genes suggest that the effects of the

salvage pathway is specific for the Wnt pathway and not Notch, Shh, BMP, or Fgf. We show that control of Wnt signaling by the salvage pathway is likely via its effect at the level of the Wnt receptors. These data identify the UDP-GlcNAc salvage pathway as a conserved and selective regulator of Wnt signaling in early development.

Materials and methods

Kinase screen

We obtained 232 cDNAs from the Harvard Institute of Proteomics (HIP) FLEXGene human kinase cDNA collection (pDNR-dual complete set). Primers designed to facilitate *in vitro* transcription were used to generate PCR constructs. First, a fragment of the pCS2 Poly(A) sequence was first obtained using: 5' GACCATTCGTTTGGCGCGCGGGCCTGAGATCCAGACATGATAAGATAC 3' and 5' GAATTAAAAAACCTCCCACACCTCCCCCTGAACCTG 3'. The human kinase was amplified with an 3' oligonucleotide sequence designed to overlap with the 5' oligonucleotide sequence of the CS2 Poly(A) fragment, using 5' GGCCCGCGCGCCAAACGAATGGTC 3' and 5' CCAAGCCTTCTAATACGACTCACTATAGGGAGACAGTGAGCGAGGAAGCGGCCGC 3'. Both constructs were stitched together in a third PCR reaction to produce a single fragment with a 5' human kinase and a 3' poly(A) tail. RNA was then generated using the MEGAscript T7 Transcription Kit from Ambion (Catalog number: AM1333). Pools of 8 human kinases mRNAs were injected equatorially in the dorsal blastomere four-cell stage *Xenopus laevis* embryos. Pools were assed for perturbation of development. Single mRNAs were injected from pools that perturbation of development to identify the causal kinase (Fig. 6-1). Screen efficiency was verified with injection of GFP constructs (Fig. 6-2).

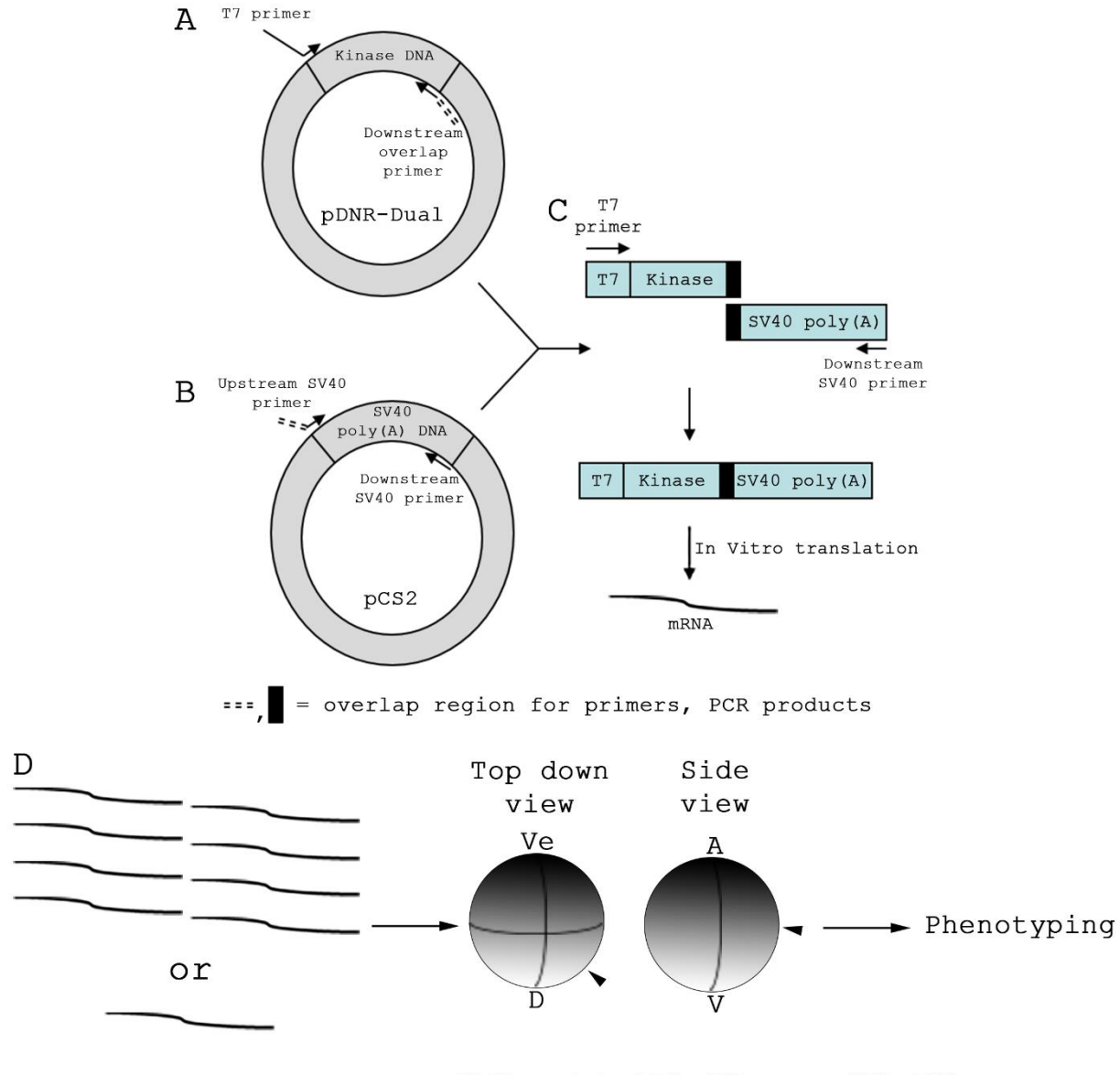
A
T7 primer
Kinase DNA
Downstream overlap primer
pDNR-Dual
B
Upstream SV40 primer
SV40 poly(A) DNA
Downstream SV40 primer
pCS2
C
T7 primer
T7
Kinase
SV40 poly(A)
Downstream SV40 primer
T7
Kinase
SV40 poly(A)
In Vitro translation
mRNA
===, = overlap region for primers, PCR products
D
or
Top down view
Ve
D
Side view
A
V
Phenotyping
E
WT
NAGK protein
BLK mRNA
HCK mRNA

Figure 6-1: Genome-scale human kinase screen identification of NAGK in *Xenopus* embryos. Diagram of the human kinase screen. (A) Human cDNAS in pDNR-dual were amplified by primers designed to introduce a T7 promoter to the 5' end of the amplicon and a 3' primer with an introduced overlap to the 5' of the CS2 poly(A) fragment. (B) The poly(A) sequence from pCS2 amplified by PCR with an introduced 5' fragment to overlap with the 3' of the construct from (A). (C) The amplicons from (A) and (B) were then stitched together in a third PCR to constitute a 5' T7-human kinase-poly(A) tail 3' sequence. mRNA was then synthesized in vitro. (D) Pools of eight mRNAs were injected into the marginal zone of the dorsal blastomeres of four-cell stage Xenopus laevis embryos. Kinases from pools with identified phenotypes were then injected individually to identify specific kinases. (E) Overexpression of NAGK protein (*n*=5/40), BLK mRNA (*n*=5/31), and HCK mRNA (*n*=4/27) resulted in posteriorization of *Xenopus* embryos. Posteriorized embryos were not observed in the WT controls (*n*=0/47). Embryos were injected in each blastomere with 20 pg MBP-tagged human NAGK, 0.1 ng of BLK mRNA, or 0.17 ng of HCK mRNA, in a volume of 2.5 nl. Numbers were aggregated from $n \geq 3$ replicates. V; vegetal pole. A, animal pole. Ve, ventral. D, dorsal.

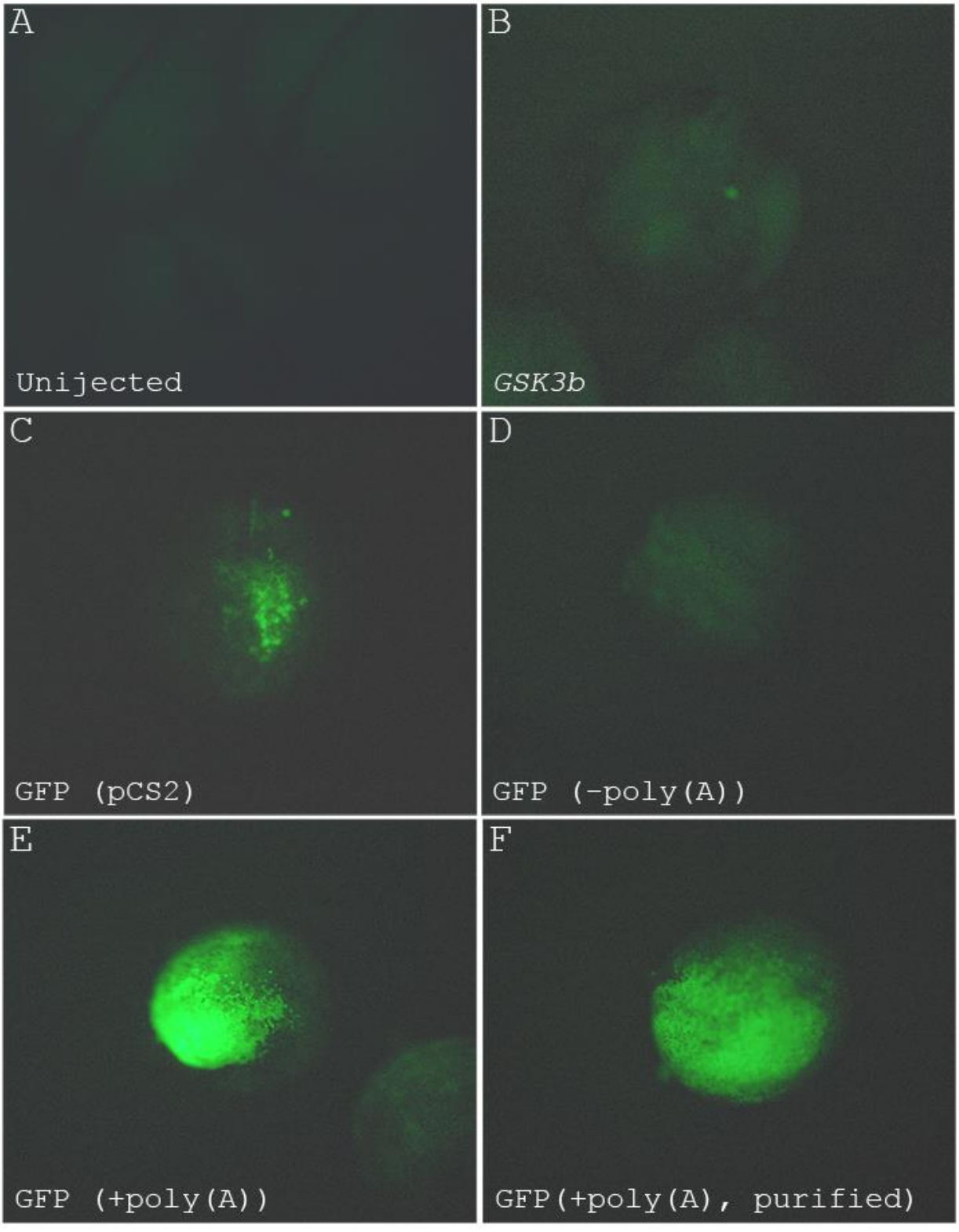
A
Unijected
B
GSK3b
C
GFP (pCS2)
D
GFP (-poly(A))
E
GFP (+poly(A))
F
GFP(+poly(A), purified)

Figure 6-2: A GFP control for the screen shows robust expression of the kinase constructs in *Xenopus*. (A) An uninjected control embryo (*n*=0/46). Xenopus embryos were injected mRNA and *in vtiro* transcribed with (B) GSK3β control amplified from pDNR-Dual with an introduced 5' T7 promotor and 3' poly(A) tail (*n*=0/21), (C) A GFP control was amplified from a pCS2-GFP construct (*n*=23/23), (D) GFP amplified from pDNR-Dual with an introduced 5' T7 promotor (*n*=20/22). (E) GFP amplified from pDNR-Dual with an introduced 5' T7 promotor and 3' poly(A) tail (*n*=29/35). (F) The product from (E) cleaned up on with a PCR Purification Kit before *in vitro* translation (*n*=36/36). No fluorescence was observed (A), (B) or (D). In (C) a small number of GFP positive cells are observed (green). The product from (E) and (F) show robust GFP expression. (A) - (F) Each dorsal blastomere was injected or co-injected with 1 ng of mRNA in a volume of 2.5 nl. Embryos are aggregate from *n*≥3 biological replicates for (A) – (F).

DNA constructs, mRNA and protein

Identified kinases, were sub-cloned into pCS2, and the pCS2 constructs were used for all further experiments. A kinase-dead NAGK mutant was created by inducing a threonine to methionine at nucleotide 128 ($NAGK^{T128M}$) using site directed mutagenesis. cDNA encoding full-length human *PGM3* (Catalog Number: OHS1770-202324198), human *UAP1* (Catalog Number: OHS1770-202321404), human *DPAGT1* (Catalog Number: OHS1770-202315445), and mouse *NGYL1* (Catalog Number: MMM1013-202769864) were obtained from Open Biosystems and subcloned into pCS2. *Drosophila* CG6218 was obtained from the Drosophila Genomics Resource Center (Stock number: 6497) and subcloned into pCS2. *Xenopus* Wnt8, *Xenopus* Wnt8-human frizzled 5 fusion (Fz), VSV-G-LRP6 (LRP6), and *Xenopus* Dishevelled (DSH) in pCS2 were used for co-injection experiments. mRNA was generated from the pCS2 constructs using the mMESSAGE mMACHINE SP6 transcription kit (Catalog number: AM1340) from Invitrogen. *NAGK* was subcloned into pMAL and used to generate recombinant MBP-tagged human protein as previously described (Saito-Diaz, Benchabane et al. 2018).

Sugars and Morpholinos

3-O-methyl-GlcNAc (*CAS* Number: 94825-74-8) and UDP-GlcNAc (CAS Number: 91183-98-1) were *obtained from Cayman Chemical Company.* GlcNAc-6-P was obtained from Carbosynth (CAS Number: 102029-88-9). GlcNAc *(*CAS Number: 7512-17-6) and GlcNac-1-P (CAS Number: 31281-59-1) were obtained from Sigma-Aldrich. Morpholinos were designed using J-

Strain 9.2 and acquired from Gene Tools, LLC. The MO sequences were *NAGK* 5' CCCCCATACACAGCAGCCATCTC 3', *PGM3* 5' ATTCAGCACTGCTTCCATCTTCATC 3', *UAP1* 5' TGACGAACAACTGCCACATCCATAC 3', and *DPAGT1* 5' CCGGCATGTTTGCCAATAGTTTACG 3'. Sugars and Morpholinos were re-suspended in pure water.

Animals care

All animals in this study (*Xenopus*, zebrafish, and *Drosophila*) were treated in accordance with Vanderbilt's Institutional Animal Care and Use Committee.

***Xenopus* embryo injections**

Fresh *Xenopus laevis* testis were excised, suspended in 1ml 1x Modified Barth's saline (MBS) with 50ul FBS, and crushed with a disposable pestle. Embryos were collected in 1x MBS, excess MBS was removed and 200 ul of the crushed testis mixture added. Embryos were immediately flooded with 0.1x MBS. After approximately 30 mins fertilized embryos were dejellied for 5 mins with 2% (w/v) L-cysteine (pH 8.0). Embryos were washed 12 times with 0.1x MBS and transferred to 4% Ficoll in 1x Marc's Modified Ringer's (MMR). Embryos were injected equatorially in both dorsal blastomeres at developmental stage 3 (4-cells) and grown at room temperate for two days (Stage 35) before phenotyping. Embryos were fixed overnight in MEMFA (1 ml of 10X MEM salts, 1 ml 37% formaldehyde, and 8 ml Milli-Q water). Washed and

stored in PBS at 4°C until imaged. Here we report only phenotypes observed in *n*≥3 biological repeats. One male and three females were used per biological repeat. *Xenopus* were grown at a density of 50 or less embryos per 100 x 20 mm petri dish with excess 1x MMR.

Embryo soaking

Xenopus embryos were fertilized and dejellied as described above. At stage 3, embryos were transferred to 2.5% (w/v) GlcNAc or Tunicamycin suspended in 1X MMR. Embryos were grown at room temperate for two days (Stage 35) before phenotyping. Embryos were fixed as described above. Here we report only phenotypes observed in *n*≥3 biological repeats. One male and three females were used per biological repeat. Embryos were grown at a density of 10 or less embryos per 60 X 15 mm petri dish.

Zebrafish embryo injections

Wild-type (AB) zygotes (1 cell) were injected in the single cell. Embryos were raised in egg water (0.03% Instant Ocean) + 0.01mg/L methylene blue at 28.5°C and a density of 50 or less embryos per 100 x 20 mm petri dish. Dead embryos were removed and fresh egg water added daily. Embryos were phenotyped at 5 days post fertilization. Embryos were fixed overnight in 4% Paraformaldehyde in PBS overnight. Washed and stored in PBS at 4°C until imaged. Here we report only phenotypes observed in *n*≥3 biological repeats. Embryos with

sever and non-specific edema were excluded from analysis. Embryos from *n*≥3 male/females pairs were collected per biological repeat.

Generation of cDNA and quantitative-PCR

Whole RNA was collected from whole embryos at stage 10.5, 13, or 16 or animal caps from stage 10.5 embryos. Samples were homogenized in 1 ml RNA Stat-60 (Amsbio) with a disposable pestle and cleaned up using chloroform extraction. The High Capacity cDNA Reverse Transcription Kit (Applied Biosystems) was used to produce cDNA using the supplied random primers. qPCR was ran using the GoTaq® qPCR Master Mix (Promega) on a CFX96 qPCR machine (Bio-rad). qPCR were run in biological and technical triplicate. mRNA levels were normalized to the house keeping gene Ornithine decarboxylase (*odc*). Fold change was calculated using $2^{-\Delta\Delta ct}$ as described in (Rao et al., 2013).

odc was amplified with the forward 5' GTCAATGATGGAGTGTATGGATC 3' and reverse 5' TCCATTCCGCTCTCCTGAGCAC 3' primers (Swain et al., 2005). *hes1* was amplified with the forward 5' AAAGTCCTCCAAGCCCATC 3' and reverse 5' CCGGGAGCTATCTTTCTTGAG 3' primers. *dusp6* was amplified with the forward 5' GTGACACCAAACTTGCCTAATC 3' and reverse 5' CGGGCTTCATCTATAAACGAGAT 3' primers. *tbxt* was amplified with the forward 5'-GGATCGTTATCACCTCTG-3' and reverse 5'-GTGTAGTCTGTAGCAGCA-3' primers (Batut et al., 2005). *ptch1* was amplified with the forward 5'-GGACAAGAATCGCAGAGCTG-3' and reverse 5'-GGATGCTCAGGGAACCTTAC-3' primers (Jin et al., 2016). *chordin* was amplified with the forward

5’-AACTGCCAGGACTGGATGGT-3’ and reverse 5’-GGCAGGATTTAGAGTTGCTTC-3’ primers (Sun et al., 2015). *Xnr3* was amplified with the forward 5’-CTTCTGCACTAGATTCTG-3’ and reverse 5’-CAGCTTCTGGCCAAGACT-3’ primers (Miyazaki et al., 2012). Only a single product was amplified by each primer pair (Fig. 6-3).

Microscopy

Bright field images were obtained using a Stemi 2000-CS microscope (Zeiss, Oberkochen, Germany) with an Olympus DP72 camera. Fluorescent images were obtained using a Nikon Eclipse 80*i* microscope with a Cool SNAP ES camera (Photometrics, Tucson, USA). Images were analyzed in Fiji or Photoshop.

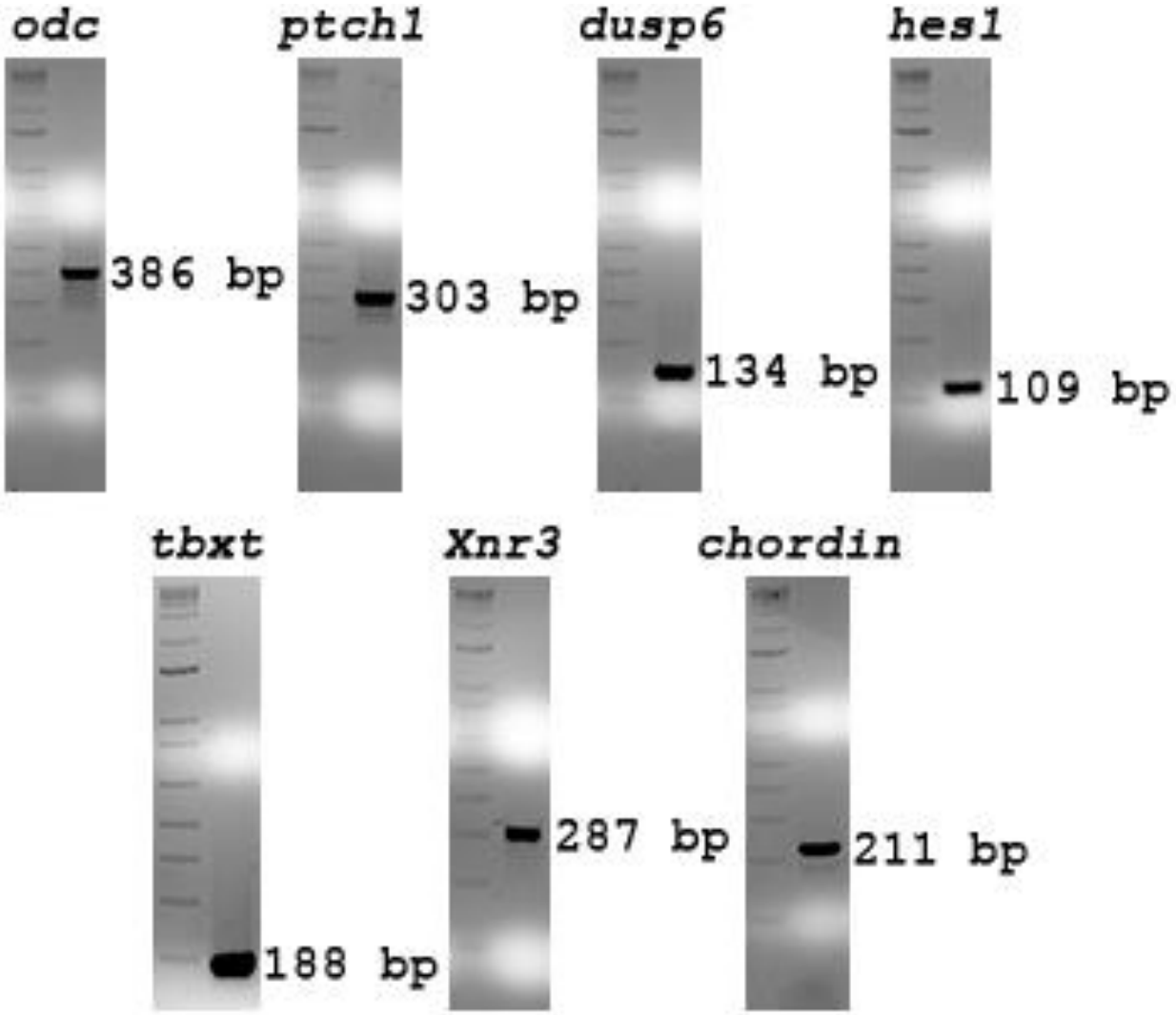
odc
386 bp
ptch1
303 bp
dusp6
134 bp
hes1
109 bp
tbxt
188 bp
Xnr3
287 bp
chordin
211 bp

Figure 6-3: The qRT-PCR primers sets amplify a single product. Final products from qRT-PCR run on a 2% Agarose gel. Products are from whole WT embryos. Size of the products are indicated (base pairs; bp). Ornithine decarboxylase 1; *odc*. Patched 1; *ptch1*. Dual specificity phosphatase 6; *dusp6*. Hes family bHLH transcription factor 1; *hes1*. T-box transcription factor T; *tbxt*. Nodal homolog 3, gene 1; *Xnr3*. Chordin, gene 1; *chordin*. *n*≥3 gels were run for each from different biological repeats.

Statistics

All statistical analyses were performed in R v3.1.0. Fisher's exact test and multiple T-test (two tailed, equal variance) were used as indicated in figure legends. Post hoc analysis of Fisher's exact test and multiple T-test tests were by Bonferroni correction. The following critical ρ values were used for all analyses: 0.05, 0.01, and 0.001. Sample sizes (n) are indicated as n= number of samples with the observed phenotype / total number of samples.

Results

Genome-scale human kinase screen identifies NAGK as a regulator of axiation in *Xenopus*

In an overexpression screen to identify novel kinases that regulate vertebrate development, an arrayed library of cDNAs encoding 230 human kinases was subjected to a series of PCR reactions that resulted in the addition a T7 promoter and an SV40 polyadenylation signal from the pCS2+ plasmid in the 5' and 3' region of the open reading frame, respectively (Turner and Weintraub, 1994) (Fig. 6-1A,B). Reactions products were then purified and subjected to *in vitro* transcription to generate capped mRNAs for injection into *Xenopus laevis* embryos (Fig. 6-1C,D). The addition of the SV40 polyadenylation signal from the pCS2+ plasmid was critical for robust expression of injected mRNAs into *Xenopus* embryos (Fig. 6-2). Although we found that unpurified *in vitro* transcribed mRNAs expressed in embryos when injected, purified mRNAs yielded more consistent results.

For screening, 29 pools of 8 mRNAs encoding human kinases were injected into the dorsal blastomeres of four-cell stage *Xenopus* embryos (Fig. 6-1D). Embryos were then analyzed for developmental defects post-neurula stage. Pools of mRNAs that perturbed development were then injected individually to identify the relevant kinase giving rise to the developmental phenotype. From the screen, five kinases were identified that perturbed early development in addition to casein kinase 1 epsilon and delta, both known regulators of Wnt signaling (Gao et al., 2002; Hino et al., 2003; Peters et al., 1999; Sakanaka et al., 1999; Swiatek et al., 2004). Of the five kinases not previously characterized as a regulator of early vertebrate development, *N*-

Acetyl-*D*-glucosamine Kinase, (NAGK), had the strongest and most penetrant phenotype and we proceeded with its further characterization.

NAGK overexpression posteriorizes *Xenopus* embryos and NAGK inhibition anteriorizes *Xenopus* embryos

Injection of *NAGK* mRNA or recombinant NAGK protein results in posteriorized *Xenopus* embryos with reduced anterior trunk and head structures (Fig. 6-1E, 6-4A, appendix-1). Injection with mRNA of the *Drosophila melanogaster* orthologue to *NAGK*, Dmel\CG6218 (CG6218), phenocopied *NAGK* mRNA (Fig. 6-4A, 6-5A). Conversely, knocking down *NAGK* by injection of a *NAGK* Morpholino Oligonucleotide (MO) results in anteriorized embryos (Fig. 6-4B, appendix-1). Previous studies with a related kinase, glucokinase, indicated that a mutation in the ATP binding region (T228M) resulted in a kinase dead protein that acted in a dominant-negative fashion (Mahalingam et al., 1999). Based on these studies, we generated a corresponding mutation (T128M) in *NAGK*, and injected mRNA into Xenopus embryos (Berger et al., 2002). Consistent with the *NAGK* MO injections, expression of the putative kinase dead mutant of *NAGK* (*NAGK*^{T128M}) results in anteriorized embryos (Fig. 6-4B, 6-5A). Similarly, injection of a small molecule competitive inhibitor of *NAGK*, 3-O-methyl *N*-acetylglucosamine (3-O-Me-GlcNAc), that mimics the substrate of *NAGK* (Zeitler et al., 1992; Miwa et al., 1994; Blume et al., 2008), also results in anteriorization of embryos (Fig. 6-4B, 6-5A). Finally, both *NAGK* MO and 3-O-Me-GlcNAc were able to suppress the posteriorized embryo phenotype of

injected *NAGK* mRNA (Fig. 6-4C). These data provide strong evidence for the role of NAGK in primary axis formation in *Xenopus* embryos.

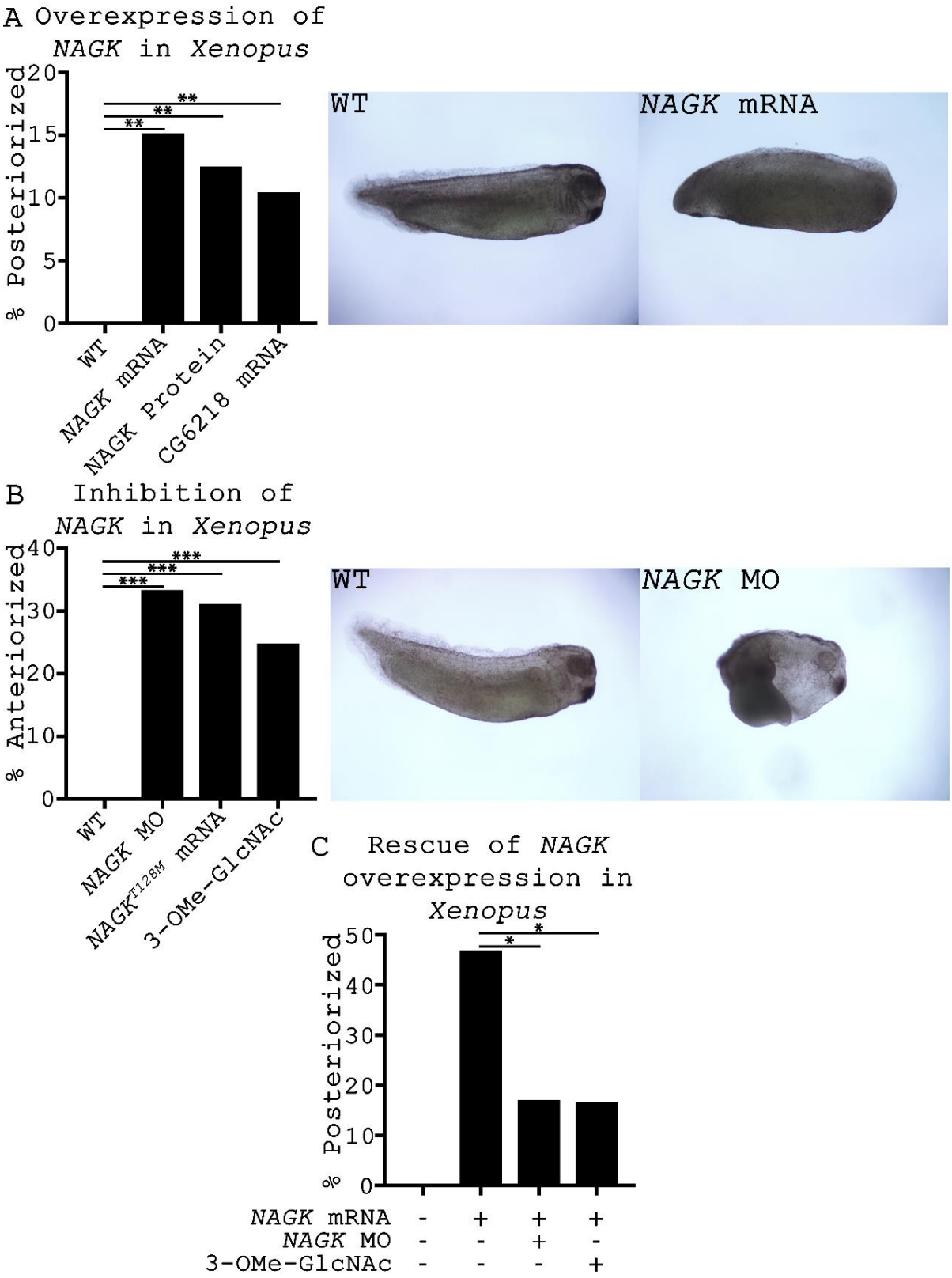
A Overexpression of NAGK in Xenopus
% Posteriorized
0
5
10
15
20
**
**
**
WT
NAGK mRNA
NAGK Protein
CG6218 mRNA
WT
NAGK mRNA
B Inhibition of NAGK in Xenopus
% Anteriorized
0
10
20
30
40
***
***
***
WT
NAGK MO
NAGKT128M mRNA
3-OMe-GlcNAc
WT
NAGK MO
C Rescue of NAGK overexpression in Xenopus
% Posteriorized
0
10
20
30
40
50
*
*
NAGK mRNA - + + +
NAGK MO - - + -
3-OMe-GlcNAc - - - +

Figure 6-4: NAGK overexpression posteriorizes *Xenopus* embryos, conversely NAGK inhibition anteriorizes *Xenopus* embryos. (A) (Left) Injection of *NAGK* mRNA (*n*=5/33), MBP-tagged NAGK protein (*n*=5/40), or CG6218 mRNA (*n*=7/67) posteriorizes *Xenopus* embryos. (Right) Example of an embryo posteriorized by injection of *NAGK* mRNA. (B) (Left) Injection of *NAGK* MO (*n*=10/30), $NAGK^{T128M}$ (*n*=23/74), or 3-O-Me-GlcNAc (*n*=31/125) anteriorizes *Xenopus* embryos. (Right) Example of an embryo anteriorized by injection of *NAGK* MO. (C) Posteriorization of embryos by *NAGK* mRNA (*n*=15/32) was rescued by co-injection of *NAGK* MO (*n*=7/41) or 3-O-Me-GlcNAc (*n*=5/30). WT embryos did not display the observed phenotypes in (A) (*n*=0/86), (B) (*n*=0/42) or (C) (*n*=0/33). (A) - (C) was aggregated from $n \geq 3$ replicates. (A) - (C) Each dorsal blastomere was injected or co-injected with 1.5 ng of mRNA, 1 pg MO, or 20 pg protein, in a volume of 2.5 nl. (A) - (C) Significance was calculated using Fisher's exact test and Bonferroni correction. (A) and (B) Treatments were compared to the WT; **$\rho<0.00334$, ***$\rho<0.000334$. (C) Co-injections were compared to the mRNA control; *$\rho< 0.0253$.

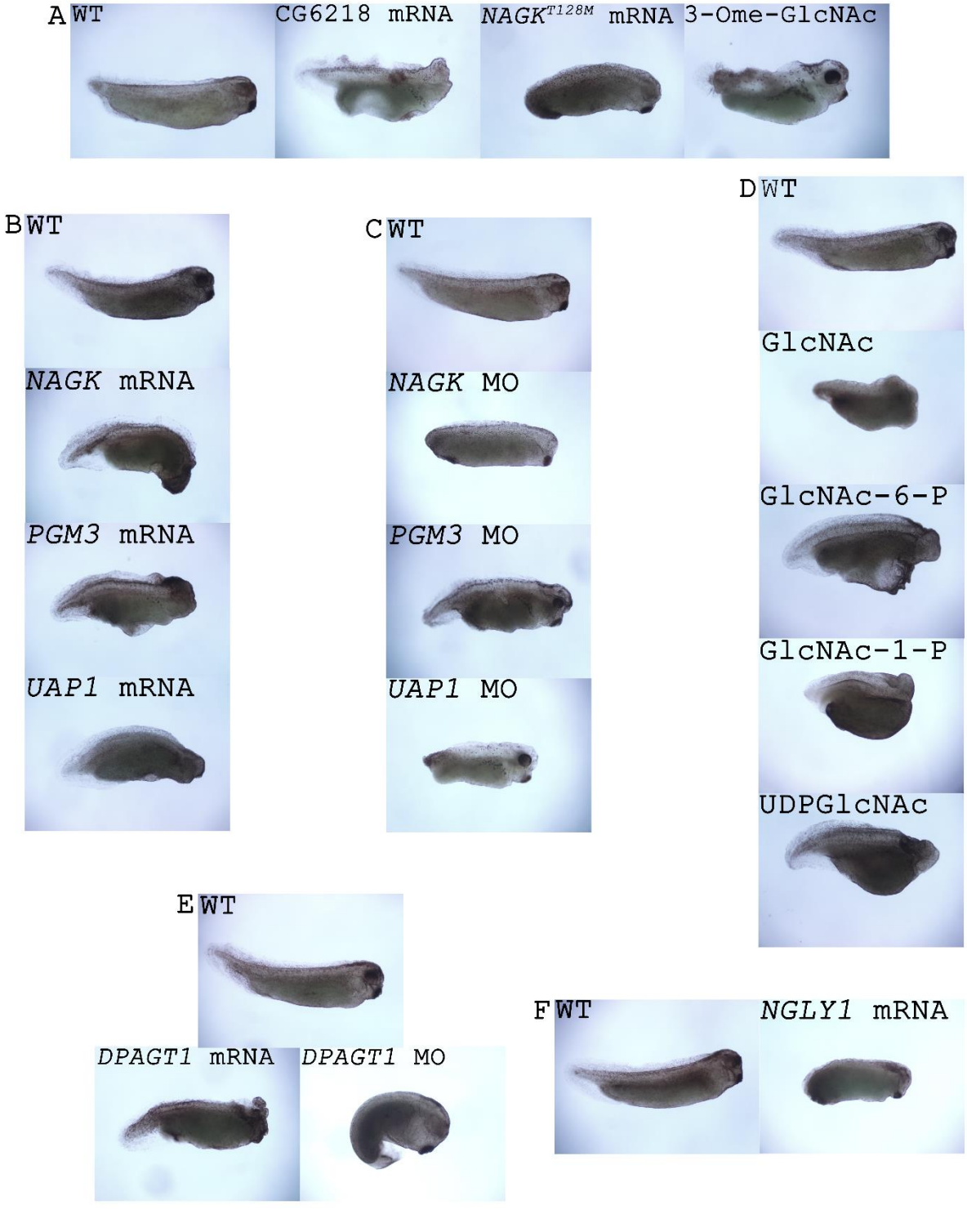
A
WT
CG6218 mRNA
NAGK T128M mRNA
3-Ome-GlcNAc
B
WT
NAGK mRNA
PGM3 mRNA
UAP1 mRNA
C
WT
NAGK MO
PGM3 MO
UAP1 MO
D
WT
GlcNAc
GlcNAc-6-P
GlcNAc-1-P
UDPGlcNAc
E
WT
DPAGT1 mRNA
DPAGT1 MO
F
WT
NGLY1 mRNA

Figure 6-5: Examples of *Xenopus* phenotypes. (A) Example of a CG6218 mRNA posteriorized embryo, and *NAGKT*^{128M} mRNA and 3-Ome-GlcNAc anteriorized animals (C) Examples of animals posteriorized by injection of mRNAs of the UDP-GlcNAc salvage pathway. (D) Examples of animals anteriorized by injection of MOs against the enzymes of the UDP-GlcNAc salvage pathway. (E) Examples of animals posteriorized by injection of the sugars of the UDP-GlcNAc salvage pathway. (F) Examples of animals posteriorized by *DPAGT1* mRNA injection and anteriorized by *DPAGT1* MO injection. (G) Example of an anteriorized embryo injected with *NGLY1*.

Posteriorization of *Xenopus* embryos by NAGK occurs via its role in glycosylation

NAGK is the first enzyme in the salvage pathway that converts free, cytoplasmic *N*-acetylglucosamine (GlcNAc) generated from degradative cellular pathways into UDP-*N*-acetylglucosamine (UDP-GlcNAc), which is then transferred onto oligosaccharides that are incorporated into glycosylated proteins and glycosaminoglycans (Hinderlich et al., 2000) (Fig. 6-6A,B). Structural studies performed with *NAGK* suggests that it is unlikely to exhibit kinase activity towards protein substrates (Berger et al., 2002). We set out to test whether the effects of altering *NAGK* expression or activity on primary axis formation were due to the effect of *NAGK* on glycosylation in the early *Xenopus* embryos. We found that soaking embryos in *N*-acetyl-*D*-glucosamine, the first substrate in the hexosamine biosynthesis pathway which produces *N*-acetylglucosamine-6-P (GlcNAc-6-P), posteriorizes *Xenopus* embryos (Fig. 6-7A,C). This suggests *NAGK* promotes posteriorization of *Xenopus* embryos through its canonical function in the UDP-GlcNAc salvage pathway.

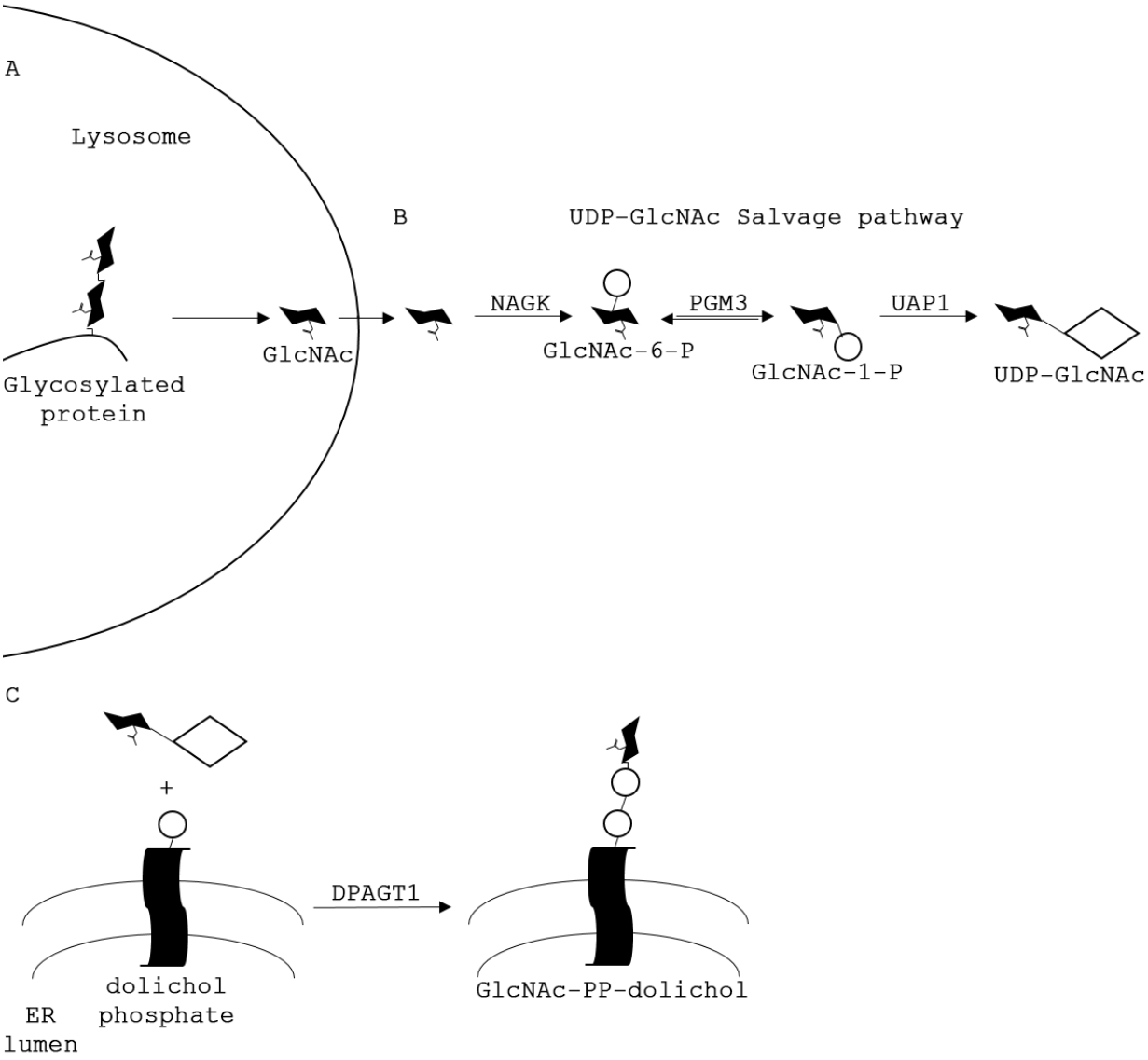
A
Lysosome
Glycosylated protein
GlcNAc
B
UDP-GlcNAc Salvage pathway
NAGK
GlcNAc-6-P
PGM3
GlcNAc-1-P
UAP1
UDP-GlcNAc
C
+
DPAGT1
dolichol phosphate
ER lumen
GlcNAc-PP-dolichol

Figure 6-6: Diagram of the UDP-GlcNAc salvage pathway and DPAGT1. (A) Glycosylated proteins are digested and free GlcNAc are released and transported to the cytosol. (B) The UDP-GlcNAc salvage pathway converts the free pool of cytosolic GlcNAc into UDP-GlcNAc. (C) Free UDP-GlcNAc is attached to dolichol phosphate in the cytosol. GlcNAc; *N*-acetyl-*D*-glucosamine. GlcNAc-1-P; *N*-acetyl-D-glucosamine-1-Phosphate. GlcNAc-1-P; *N*-acetyl-*D*-glucosamine-6-Phosphate. UDP-GlcNAc; Uridine diphosphate *N*-acetyl-*D*-glucosamine. NAGK; *N*-acetylglucosamine kinase. PGM3; *N*-Acetylglucosamine-Phosphate Mutase. UAP1; UDP-*N*-Acetylglucosamine Pyrophosphorylase 1. DPAGT1; Dolichyl-Phosphate *N*-Acetylglucosaminephosphotransferase 1.

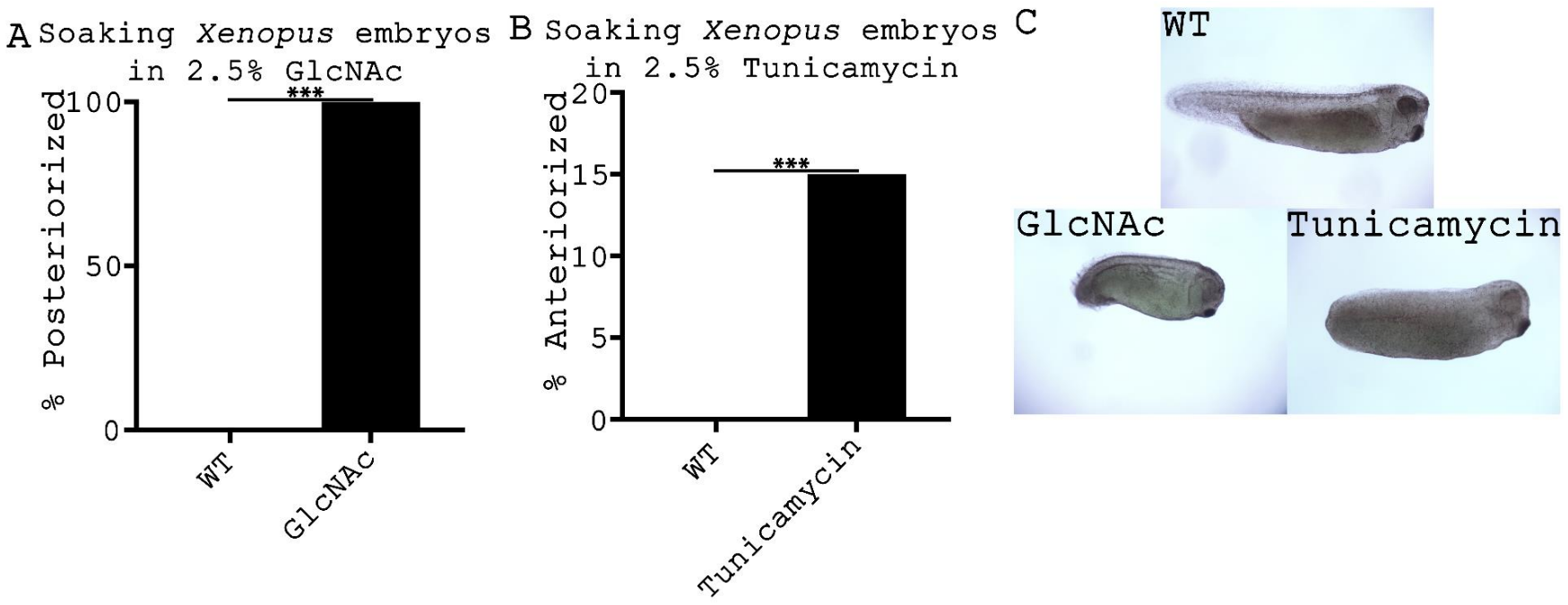
A
Soaking *Xenopus* embryos in 2.5% GlcNAc
% Posteriorized
100
50
0
***
WT
GlcNAc
B
Soaking *Xenopus* embryos in 2.5% Tunicamycin
% Anteriorized
20
15
10
5
0
***
WT
Tunicamycin
C
WT
GlcNAc
Tunicamycin

Figure 6-7: Soaking *Xenopus* embryos in GlcNAc results in posteriorization, while soaking embryos in Tunicamycin results in anteriorization. (A) Soaking *Xenopus* embryos in 2.5% (w/v) GlcNAc resulted in posteriorization (*n*=35/35). Posteriorization was not observed in the WT controls (*n*=0/40). (B) Conversely, soaking *Xenopus* embryos in 2.5% (w/v) Tunicamycin resulted in anteriorization (*n*=9/60). Anteriorization was not observed in the WT controls (*n*=0/76). (C) Examples of GlcNAc and Tunicamycin soaked animals. (A) and (B) where aggregated from *n*≥4 replicates. Significance was calculated using Fisher's exact test and Bonferroni correction. Treatments where compared to the WT; ***ρ<.001.

Overexpression of UDP-GlcNAc salvage pathway posteriorizes *Xenopus* embryos; conversely, inhibition of the pathway and *N*-glycosylation anteriorizes embryos

NAGK phosphorylates GlcNAc to GlcNAc-6-P, which is converted to GlcNAc-1-P *PGM3* (Fig. 6-6B) (Berger et al., 2002). GlcNAc-1-P is utilized by *UAP1* to synthesize UDP-GlcNAc (Fig. 6-6B) (Berger et al., 2002). To test whether the other UDP-GlcNAc salvage enzymes, similar to *NAGK*, perturbed *Xenopus* axis formation, we injected *PGM3* and *UAP1* mRNA. Both mRNAs posteriorized the animals similarly to *NAGK* mRNA injection (Fig. 6-5B, 6-8A). Conversely, injection of *PGM3* and *UAP1* MO anteriorized embryos similar to *NAGK* MO injection (Fig. 6-5C, 6-8B). Furthermore, the observed phenotypes were suppressed by co-injecting mRNAs with UDP-GlcNAc salvage pathway MOs (Fig. 6-9A,B,C). These data suggest that that the enzymes involved in the UDP-GlcNAc salvage pathway play a role in anterior-posterior patterning of the early *Xenopus* embryo.

To determine whether the products of the UDP-GlcNAc salvage pathway affected axiation, we injected GlcNAc, GlcNAc-6P, GlcNAc-1-P, and UDP-GlcNAc into *Xenopus* embryos. We found that they resulted in posteriorized embryos similar to what we observed with injection of the mRNAs encoding the UDP-GlcNAc salvage enzymes (Fig. 6-8C). Furthermore, we found that the knockdown and inhibition phenotypes of *NAGK* MO, *PGM3* MO, *UAP1* MO, $NAGK^{T128M}$, and 3-O-Me-GlcNAc could be suppressed by co-injecting the downstream sugars (Fig. 6-10A,B,C,D). Conversely, the phenotype of injected UDP-GlcNAc salvage pathway sugars could be suppressed by injecting MOs encoding the downstream enzyme in the pathway (Fig. 6-

11A,B,C,D,E). These data provide strong evidence that axiation in *Xenopus* embryos is sensitive to perturbations in the UDP-GlcNAc salvage pathway.

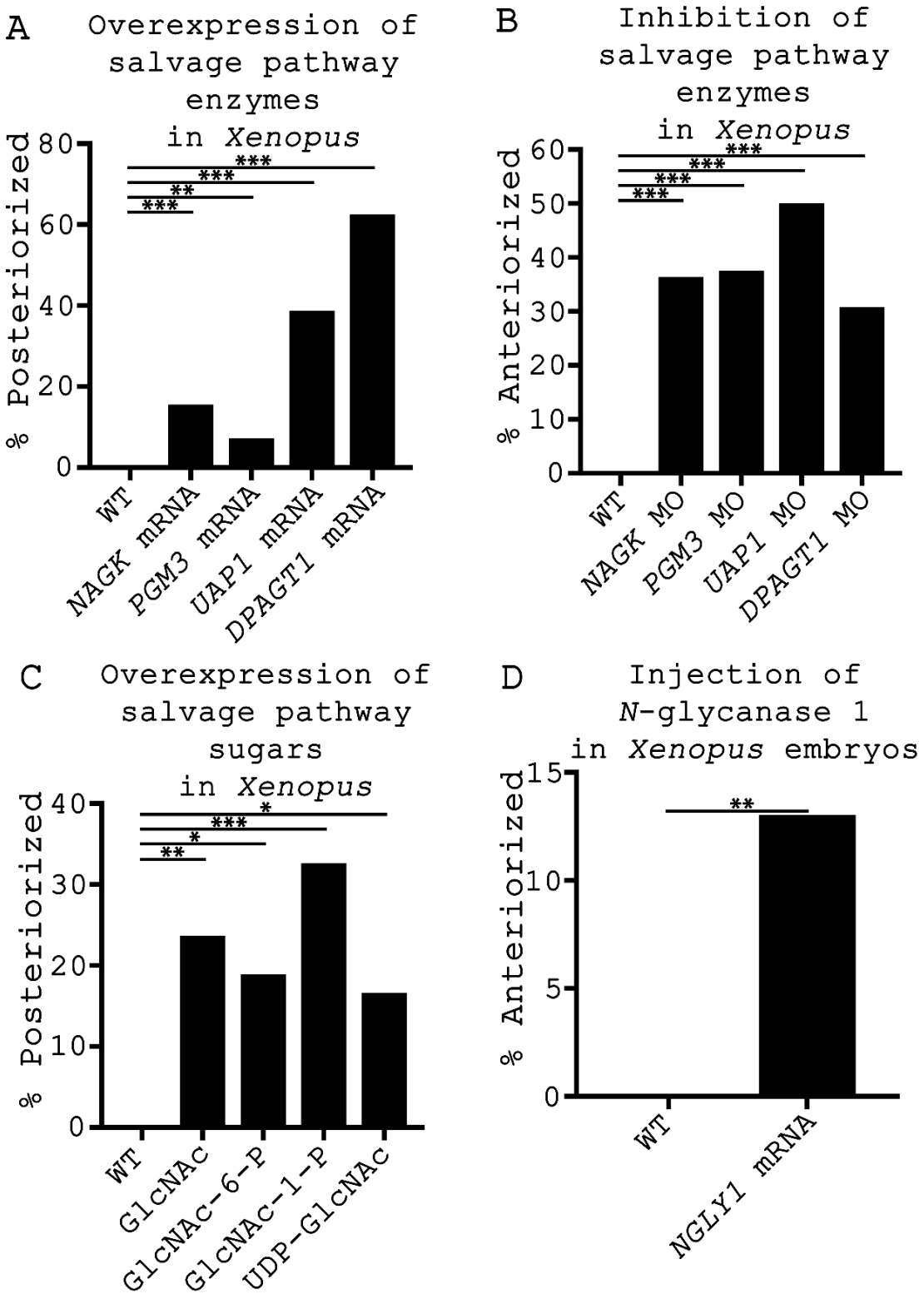
A
Overexpression of salvage pathway enzymes in Xenopus
% Posteriorized
0
20
40
60
80
***
***
**
***
WT
NAGK mRNA
PGM3 mRNA
UAP1 mRNA
DPAGT1 mRNA
B
Inhibition of salvage pathway enzymes in Xenopus
% Anteriorized
0
10
20
30
40
50
60
***
***
***
***
WT
NAGK MO
PGM3 MO
UAP1 MO
DPAGT1 MO
C
Overexpression of salvage pathway sugars in Xenopus
% Posteriorized
0
10
20
30
40
*
***
*
**
WT
GlcNAc
GlcNAc-6-P
GlcNAc-1-P
UDP-GlcNAc
D
Injection of N-glycanase 1 in Xenopus embryos
% Anteriorized
0
5
10
15
**
WT
NGLY1 mRNA

Figure 6-8: Inhibition of *NAGK*, *PGM3*, *UAP1*, *DPAGT1*, or overexpression of *NGLY1* anteriorize *Xenopus* embryos; conversely, overexpression of UDP-GlcNAc pathway enzymes, sugars, and *DPAGT1* posteriorize embryos. (A) Injection of enzymes from the UDP-GlcNAc salvage pathway of glycosylation. *NAGK* mRNA (*n*=7/45), *PGM3* mRNA (*n*=6/83), *UAP1* mRNA (*n*=19/49), and *DPAGT1* mRNA (*n*=20/32) posteriorizes *Xenopus* embryos. (B) Injection with MOs directed against the enzymes of the UDP-GlcNAc salvage pathway. *NAGK* MO (*n*=16/44), *PGM3* MO (*n*=30/80), *UAP1* MO (*n*=27/54), and *DPAGT1* MO (*n*=20/65) result in anteriorization. (C) Injection of the sugars from the UDP-GlcNAc salvage pathway. GlcNAc (*n*=9/38), GlcNAc-6-P (*n*=7/37), GlcNAc-1-P (*n*=15/46), and UDP-GlcNAc (*n*=5/30) result in posteriorization. (D) Injection of *NGLY1* mRNA (*n*=6/46) anteriorized *Xenopus* embryos. WT embryos did not display the observed phenotypes in (A) (*n*=0/132), (B) (*n*=0/120), (C) (*n*=0/40), or (D) (*n*=0/99). (A) - (D) was aggregated from *n*≥3 replicates. (A) - (D) Each dorsal blastomere was injected or co-injected with 1.5 ng of mRNA, 1 pg MO, or 125 pMols sugar, in a volume of 2.5 nl. (A) - (D) Significance was calculated using Fisher's exact test and Bonferroni correction. (A) - (C) Treatments were compared to the WT; *ρ< 0.0127, **ρ<0.00250, ***ρ<0.000250. (D) Treatment was compared to the WT; **ρ< 0.01.

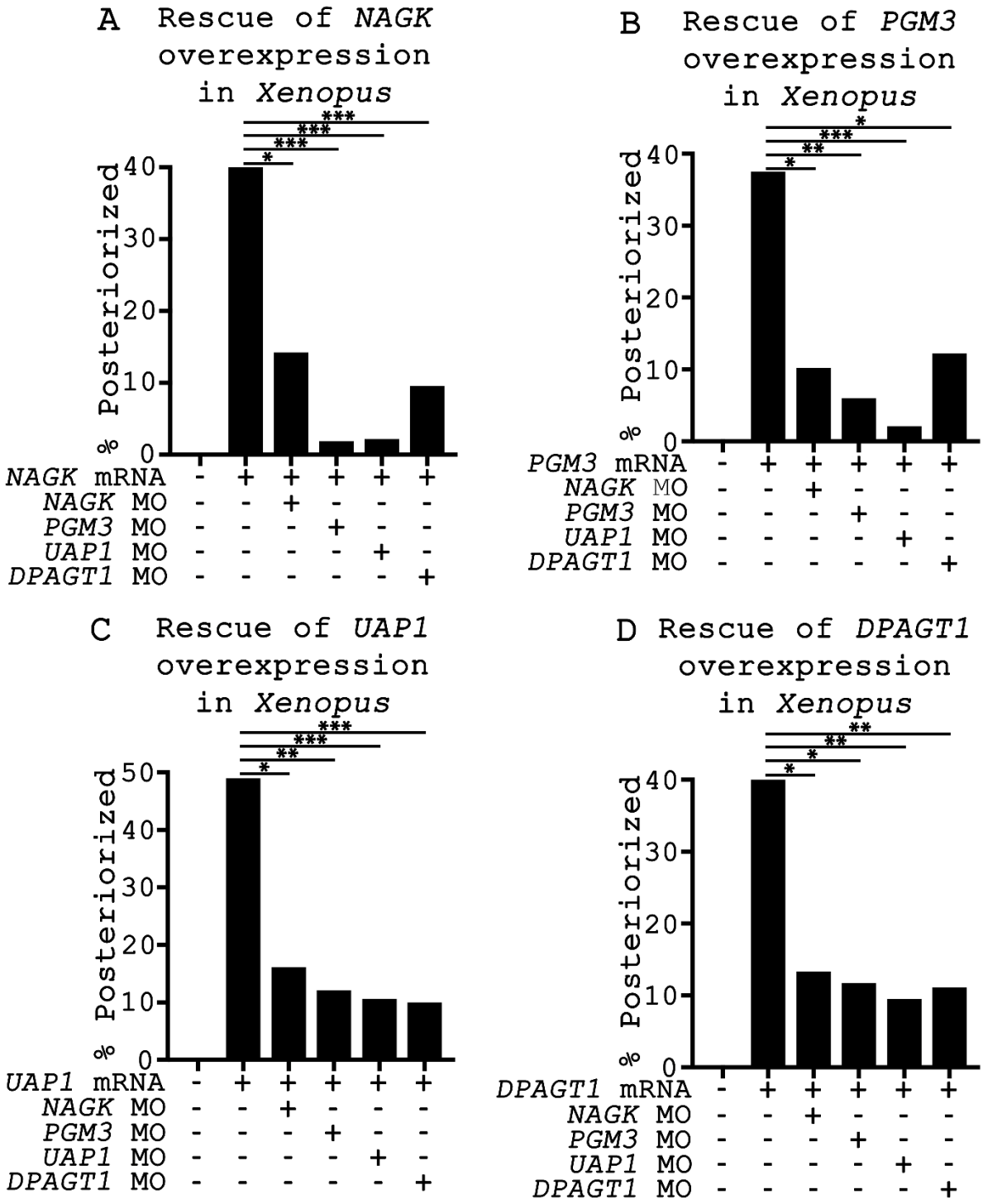
A Rescue of NAGK overexpression in Xenopus
% Posteriorized
0
10
20
30
40
***
***
***
*
NAGK mRNA - + + + + +
NAGK MO - - + - - -
PGM3 MO - - - + - -
UAP1 MO - - - - + -
DPAGT1 MO - - - - - +
B Rescue of PGM3 overexpression in Xenopus
% Posteriorized
0
10
20
30
40
*
***
**
*
PGM3 mRNA - + + + + +
NAGK MO - - + - - -
PGM3 MO - - - + - -
UAP1 MO - - - - + -
DPAGT1 MO - - - - - +
C Rescue of UAP1 overexpression in Xenopus
% Posteriorized
0
10
20
30
40
50
***
***
**
*
UAP1 mRNA - + + + + +
NAGK MO - - + - - -
PGM3 MO - - - + - -
UAP1 MO - - - - + -
DPAGT1 MO - - - - - +
D Rescue of DPAGT1 overexpression in Xenopus
% Posteriorized
0
10
20
30
40
**
**
*
*
DPAGT1 mRNA - + + + + +
NAGK MO - - + - - -
PGM3 MO - - - + - -
UAP1 MO - - - - + -
DPAGT1 MO - - - - - +

Figure 6-9: Inhibition of the endogenous UDP-GlcNAc salvage pathway enzymes rescues the overexpression of pathway enzymes. (A) Overexpression of *NAGK* mRNA results in posteriorization (*n*=32/80). Co-injection with *NAGK* MO (*n*=6/42), *PGM3* MO (*n*=1/53), *UAP1* MO (*n*=1/46), or *DPAGT1* MO (*n*=9/94) rescues the posteriorization phenotype. (B) Overexpression of *PGM3* mRNA results in posteriorization (*n*=15/40). Co-injection with *NAGK* MO (*n*=5/49), *PGM3* MO (*n*=3/50), *UAP1* MO (*n*=1/47), or *DPAGT1* MO (*n*=6/49) rescues the posteriorization phenotype. (C) Overexpression of *UAP1* mRNA results in posteriorization (*n*=24/49). Co-injection with *NAGK* MO (*n*=5/31), *PGM3* MO (*n*=4/33), *UAP1* MO (*n*=5/47), or *DPAGT1* MO (*n*=5/50) rescues the posteriorization phenotype. (D) Overexpression of *DPAGT1* mRNA results in posteriorization (*n*=26/65). Co-injection with *NAGK* MO (*n*=4/30), *PGM3* MO (*n*=4/34), *UAP1* MO (*n*=4/42), or *DPAGT1* MO (*n*=5/45) rescues the posteriorization phenotype. WT embryos did not display the observed phenotypes in (A) (*n*=0/39), (B) (*n*=0/33), (C) (*n*=0/66), or (D) (*n*=0/52). (A) - (D) was aggregated from *n*≥3 replicates. (A) - (D) Each dorsal blastomere was injected or co-injected with 1.5 ng of mRNA or 1 pg MO, in a volume of 2.5 nl. (A) - (D) Significance was calculated using Fisher's exact test and Bonferroni correction. (A) - (D) Co-injections were compared to the mRNA control; *$\rho < 0.0127$, **$\rho < 0.00251$, ***$\rho < 0.000251$.

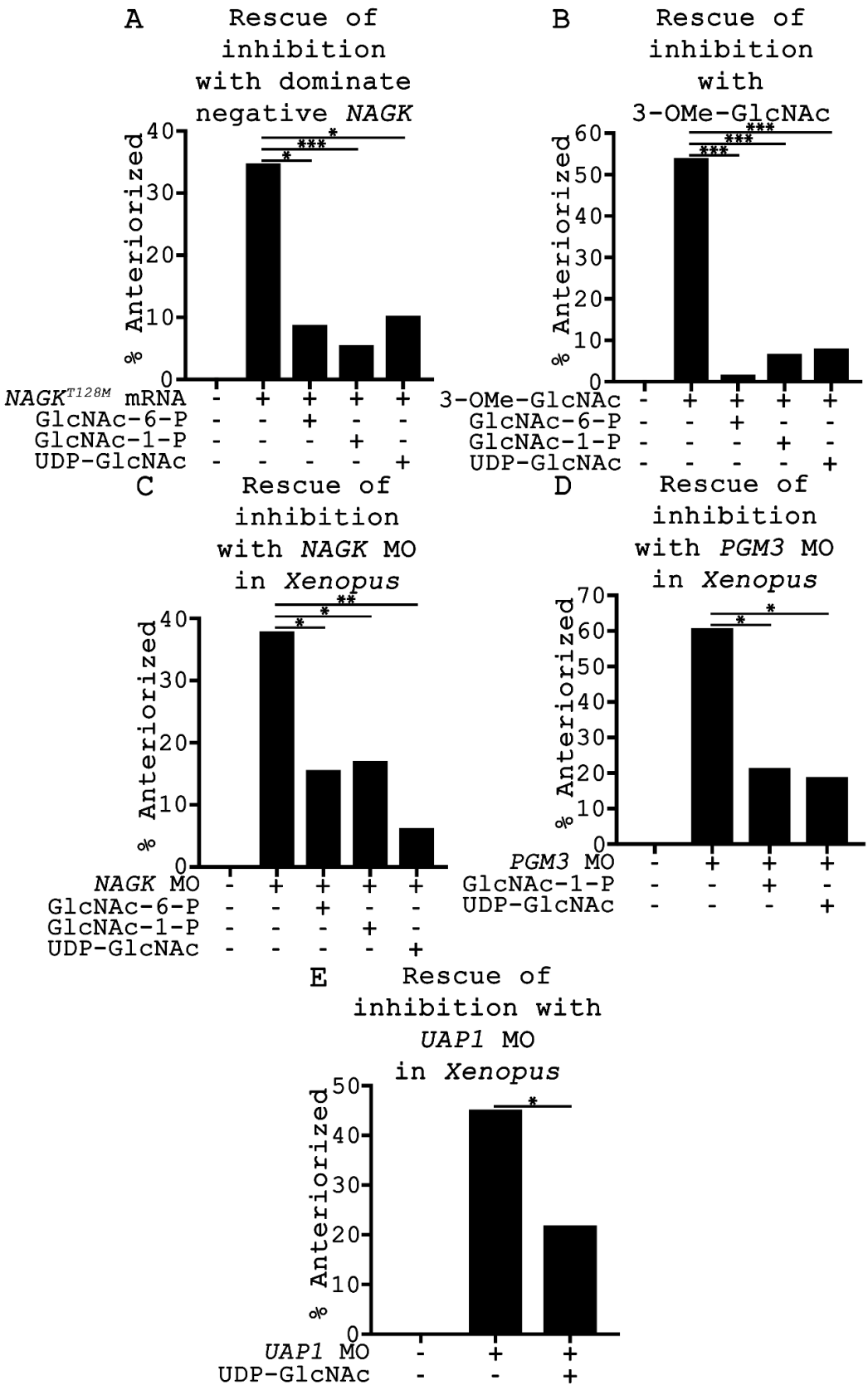
A
Rescue of inhibition with dominate negative NAGK
% Anteriorized
NAGK^T128M mRNA - + + + +
GlcNAc-6-P - - + - -
GlcNAc-1-P - - - + -
UDP-GlcNAc - - - - +
B
Rescue of inhibition with 3-OMe-GlcNAc
% Anteriorized
3-OMe-GlcNAc - + + + +
GlcNAc-6-P - - + - -
GlcNAc-1-P - - - + -
UDP-GlcNAc - - - - +
C
Rescue of inhibition with NAGK MO in Xenopus
% Anteriorized
NAGK MO - + + + +
GlcNAc-6-P - - + - -
GlcNAc-1-P - - - + -
UDP-GlcNAc - - - - +
D
Rescue of inhibition with PGM3 MO in Xenopus
% Anteriorized
PGM3 MO - + + +
GlcNAc-1-P - - + -
UDP-GlcNAc - - - +
E
Rescue of inhibition with UAP1 MO in Xenopus
% Anteriorized
UAP1 MO - + +
UDP-GlcNAc - - +

Figure 6-10: Co-injection of downstream UDP-GlcNAc salvage pathway sugars rescues the inhibition of the pathway enzymes. (A) Inhibition of the pathway with *NAGK*^{T128M} mRNA anteriorized the embryos (*n*=16/46). Co-injection with GlcNAc-6-P (*n*=3/34), GlcNAc-1-P (*n*=2/36), or UDP-GlcNAc (*n*=4/39) rescued the anteriorization phenotype. (B) Inhibition of the pathway with 3-O-Me-GlcNAc anteriorized the embryos (*n*=27/50). Co-injection with GlcNAc-6-P (*n*=1/60), GlcNAc-1-P (*n*=4/59), or UDP-GlcNAc (*n*=6/75) rescued the anteriorization phenotype. (C) Inhibition of the pathway with *NAGK* MO anteriorized the embryos (*n*=41/108). Co-injection with GlcNAc-6-P (*n*=4/32), GlcNAc-1-P (*n*=6/41), or UDP-GlcNAc (*n*=2/32) rescued the anteriorization phenotype. (D) Inhibition of the pathway with *PGM3* MO anteriorized the embryos (*n*=42/69). Co-injection with GlcNAc-1-P (*n*=12/56) or UDP-GlcNAc (*n*=7/37) rescued the anteriorization phenotype. (E) Inhibition of the pathway with *UAP1* MO anteriorized the embryos (*n*=19/42). Co-injection with UDP-GlcNAc (*n*=7/32) rescued the anteriorization phenotype. WT embryos did not display the observed phenotypes in (A) (*n*=0/36), (B) (*n*=0/30), (C) (*n*=0/61), (D) (*n*=0/46), or (E) (*n*=0/50). (A) - (E) was aggregated from *n*≥3 replicates. (A) - (E) Each dorsal blastomere was injected or co-injected with 1.5 ng of mRNA, 1 pg MO, or 125 pMols sugar, in a volume of 2.5 nl. (A) - (E) Significance was calculated using Fisher's exact test and Bonferroni correction. (A) - (C) Co-injections were compared to the control; *ρ< 0.0170, **ρ< 0.00334, ***ρ< 0.000334. (D) Co-injections were compared to the MO control; *ρ< 0.0253. (E) Co-injections were compared to the MO control; *ρ< 0.05.

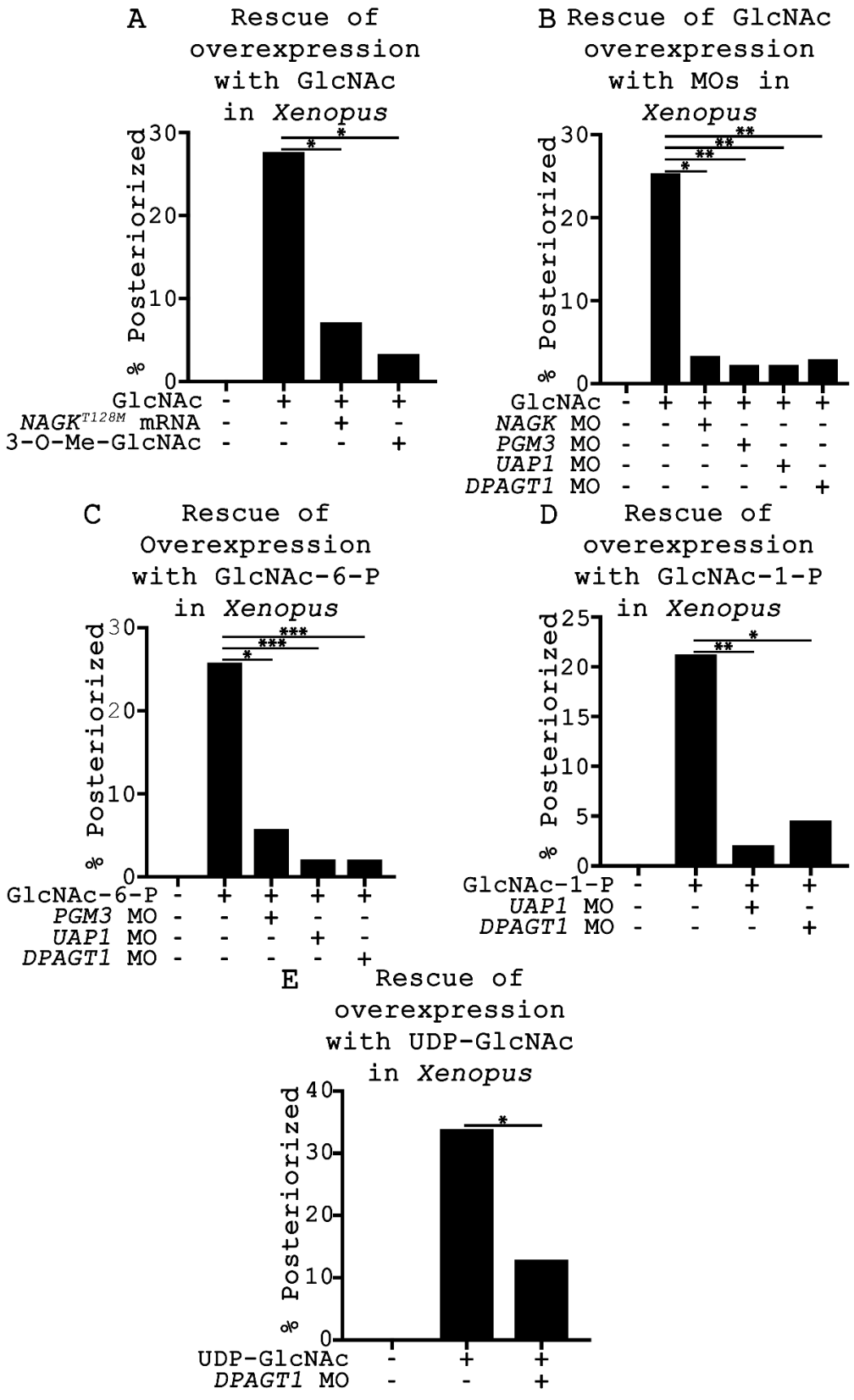
A
Rescue of overexpression with GlcNAc in Xenopus
% Posteriorized
GlcNAc
NAGK T128M mRNA
3-O-Me-GlcNAc
B
Rescue of GlcNAc overexpression with MOs in Xenopus
% Posteriorized
GlcNAc
NAGK MO
PGM3 MO
UAP1 MO
DPAGT1 MO
C
Rescue of Overexpression with GlcNAc-6-P in Xenopus
% Posteriorized
GlcNAc-6-P
PGM3 MO
UAP1 MO
DPAGT1 MO
D
Rescue of overexpression with GlcNAc-1-P in Xenopus
% Posteriorized
GlcNAc-1-P
UAP1 MO
DPAGT1 MO
E
Rescue of overexpression with UDP-GlcNAc in Xenopus
% Posteriorized
UDP-GlcNAc
DPAGT1 MO

Figure 6-11: Co-injection of downstream MO rescues overexpression of the UDP-GlcNAc salvage pathway sugars. (A) Overexpression with GlcNAc posteriorizes the embryos (*n*=13/47). Co-injection with *NAGK*^{T128M} mRNA (*n*=3/42) or 3-O-Me-GlcNAc (*n*=1/29) rescued the posteriorization phenotype. (B) Overexpression with GlcNAc posteriorizes the embryos (*n*=37/146). Co-injection with *NAGK* MO (*n*=1/30), *PGM3* MO (*n*=1/44), *UAP1* MO (*n*=1/44), or *DPAGT1* MO (*n*=1/34) rescued the posteriorization phenotype. (C) Overexpression with GlcNAc-6-P posteriorizes the embryos (*n*=8/31). Co-injection with *PGM3* MO (*n*=3/52), *UAP1* MO (*n*=1/47), or *DPAGT1* MO (*n*=1/48) rescued the posteriorization phenotype. (D) Overexpression with GlcNAc-1-P posteriorizes the embryos (*n*=17/80). Co-injection with *UAP1* MO (*n*=1/48) or *DPAGT1* MO (*n*=2/44) rescued the posteriorization phenotype. (E) Overexpression with UDP-GlcNAc posteriorizes the embryos (*n*=19/56). Co-injection with *DPAGT1* MO (*n*=4/31) rescued the posteriorization phenotype. WT embryos did not display the observed phenotypes in (A) (*n*=0/30), (B) (*n*=0/34), (C) (*n*=0/48), (D) (*n*=0/30), or (E) (*n*=0/31). (A) - (E) was aggregated from *n*≥3 replicates. (A) - (E) Each dorsal blastomere was injected or co-injected with 1.5 ng of mRNA, 1 pg MO, or 125 pMols sugar, in a volume of 2.5 nl. (A) - (E) Significance was calculated using Fisher's exact test and Bonferroni correction. (A) and (D) Co-injections were compared to the sugar control; *ρ< 0.0253, **ρ< 0.00501. (B) Co-injections were compared to the sugar control; *ρ< 0.0127, **ρ< 0.00251. (C) Co-injections were compared to the sugar control; *ρ< 0.0170, ***ρ< 0.00334. (E) Co-injections were compared to the sugar control; *ρ< 0.05.

Inhibition of *DPAGT1* or overexpression of *NGYL1* anteriorizes *Xenopus* embryos, while *DPAGT1* overexpression posteriorizes embryos.

To determine whether the salvage pathway acts on anteroposterior patterning via effects on *N*-linked glycosylation, we tested whether perturbation of *DPAGT1*, the rate-limiting enzyme in the *N*-linked glycosylation pathway, perturbed primary body axis formation. *DPAGT1* transfers the first sugar (GlcNAc) onto dolichol in the endoplasmic reticulum to initiate the synthesis of *N*-linked glycoproteins (Lehrman et al., 1988). We found that, similar to what we observed with salvage pathway components, injection of *DPAGT1* mRNA posteriorized embryos, whereas *DPAGT1* MO strongly anteriorized embryos (Fig. 6-5E, 6-8A,B). Consistent with our *DPAGT1* MO result, we found that soaking embryos in tunicamycin, a UDP-GlcNAc analog and potent inhibitor of DPAGT1 similarly anteriorizes *Xenopus* embryos (Fig. 6-7B,C) (Heifetz et al., 1979; Lehrman et al., 1988). Posteriorization with *DPAGT1* mRNA could be rescued with co-injection of UDP-GlcNAc salvage way MOs (Fig. 6-9D). Finally, we found that injection of *N*-glycanase 1 (*NGLY1*) mRNA, which removes asparagine-linked glycans from glycoproteins in the cytosol (and, thus opposing the activity of *DPAGT1*), anteriorized embryos (Fig. 6-5F, 6-8D). These results provide strong evidence that the UDP-GlcNAc salvage pathway promotes posteriorization through upregulation of protein *N*-glycosylation. Similarly, inhibition of the UDP-GlcNAc salvage pathway downregulates protein *N*-glycosylation, resulting in anteriorization.

Axis duplications from overexpression of UDP-GlcNAc salvage pathway enzymes, *DPAGT1*, and GlcNAc-1-P suggests Wnt specificity

The observed antero-posterior patterning defects are consistent with Wnt misexpression post the midblastula transition. Prior to the mid-blastula transition, overexpression of Wnt signaling components can lead to an axis duplication (McMahon and Moon, 1989). A small but significant and repeatable number of full and partial axis duplications were observed when CG6218, *NAGK*, *PGM3*, *UAP1*, or *DPAGT1* mRNA were injected in *Xenopus* embryos (Fig. 6-12A,B, appendix-2). Furthermore, injection of GlcNAc, GlcNAc-6-P, GlcNAc-1P, and UDP-GlcNAc lead to axis duplications (Fig. 6-12C). However, only GlcNAc-1-P was consistently repeatable and statistically significant. This data suggests that the observed *Xenopus* phenotypes are from misexpression of Wnt in the early embryo.

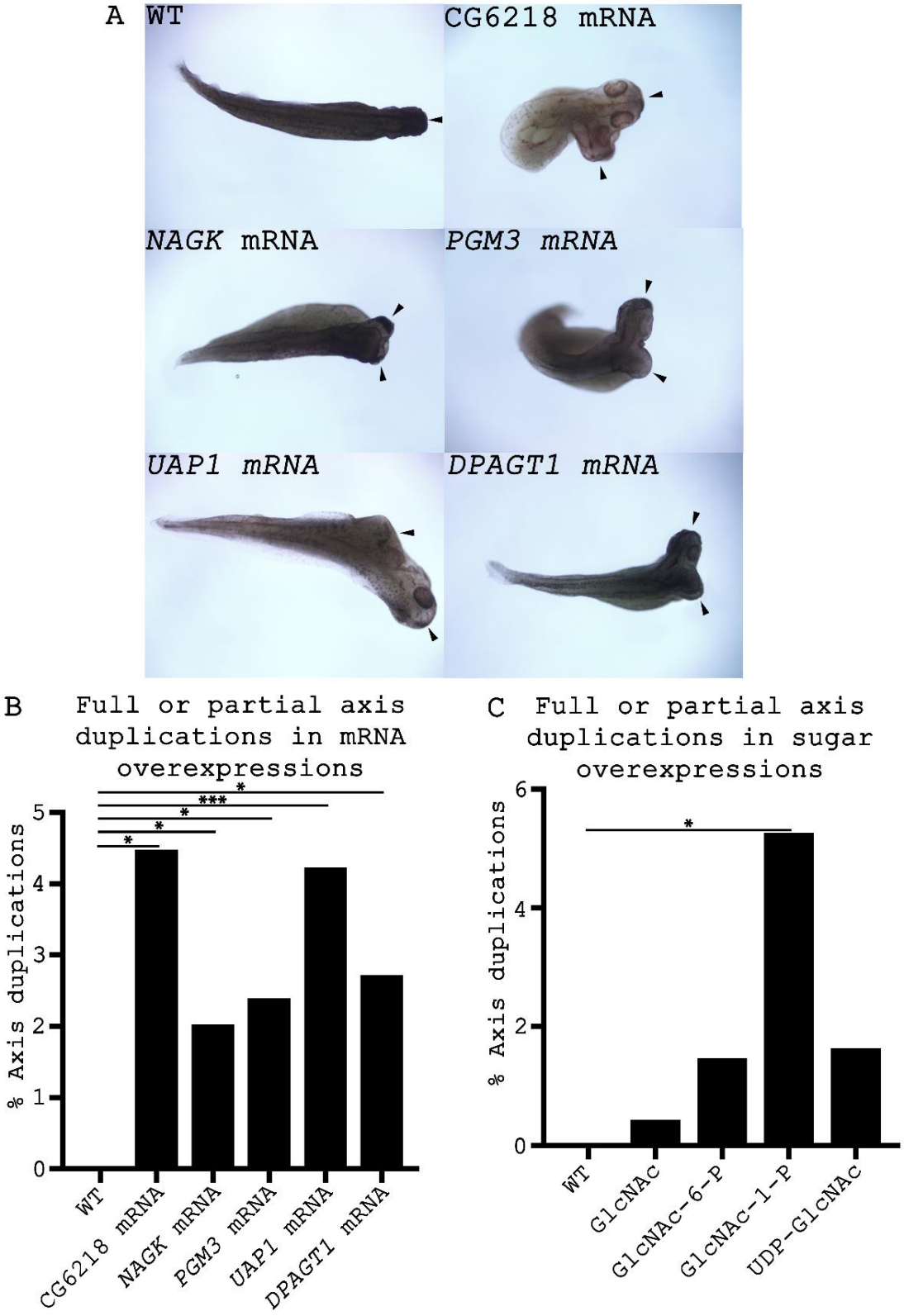
A
WT
CG6218 mRNA
NAGK mRNA
PGM3 mRNA
UAP1 mRNA
DPAGT1 mRNA
B
Full or partial axis duplications in mRNA overexpressions
% Axis duplications
0
1
2
3
4
5
*
***
*
*
*
WT
CG6218 mRNA
NAGK mRNA
PGM3 mRNA
UAP1 mRNA
DPAGT1 mRNA
C
Full or partial axis duplications in sugar overexpressions
% Axis duplications
0
2
4
6
*
WT
GlcNAc
GlcNAc-6-P
GlcNAc-1-P
UDP-GlcNAc

Figure 6-12: Over expression of UDP-GlcNAc salvage pathway components promotes axis duplication in *Xenopus*. (A) Examples of full and partial axis duplications. Black arrows indicate individual body axes. (B) When injected with mRNA axis duplications were observed in the CG6218 (*n*=3/67), *NAGK* (*n*=4/197), *PGM3* (*n*=4/167), *UAP1* (*n*=6/142), and *DPAGT1* (*n*=4/147) treated embryos, but not in the WT controls (*n*=0/441). Axis duplications were found in *n*≥3 replicate experiments. (C) Embryos injected with GlcNAc (*n*=1/231), GlcNac-6-P (*n*=1/68), GlcNAc-1-P (*n*=4/76), and UDP-GlcNAc (*n*=1/61) all exhibited axis duplications. No axis duplications were observed in the controls (*n*=0/213). Only GlcNAc-1-P was statistically significant. GlcNAc-1-P axis duplications were identified in *n*=4 experiments. (B) Injections were compared to the WT control; *ρ< 0.0102, ***ρ< 0.00020. (C) Injections were compared to the WT control; *ρ< 0.0127.

NAGK expression in zebrafish results in a Wnt like phenotype

To provide further evidence for the role of the UDP-GlcNAc salvage pathway in regulating Wnt signaling, and to determine whether its effects on antero-posterior patterning is conserved, we tested the effects of perturbing the UDP-GlcNAc salvage pathway in zebrafish. Wnt signaling has been shown to pattern the anterior-posterior neuraxis in zebrafish (Chan et al., 2009; Hikasa and Sokol, 2013). Eyes do not form in embryos upon ectopic activation of the Wnt/β-catenin pathway, and zebrafish with activating Wnt/β-catenin pathway mutations in axin (masterblind) and tcf7l1 (headless) give rise to embryos with defects in anterior structures (Cavodeassi et al., 2005; Erter et al., 2001; Heisenberg et al., 2001; Kim et al., 2000; Lekven et al., 2001; Momoi et al., 2003; van de Water et al., 2001). Inhibition of noncanonical Wnts such as *wnt4* and *wnt11* in zebrafish are characterized by midline defects of the head such as by cyclopia (Heisenberg et al., 2000; Matsui et al., 2005; Thorpe and Moon, 2004; Ungar et al., 1995). Consistent with activation of Wnt signaling, we found that injection of mRNAs encoding CG6218, *NAGK*, *PGM3*, *UAP1*, and *DPAGT1* gave rise to eyeless embryos (Fig. 6-13A,B, appendix-3). Injection of sugars of the salvage pathway (GlcNAc, GlcNAc-6P, GlcNAc-1-P, and UDP-GlcNAc) also inhibited eye formation in zebrafish embryos (Fig. 6-13C). Conversely, injection of $NAGK^{T128M}$ or 3-O-Me-GlcNAc gave rise to cycloptic embryos (Fig. 6-14A). The cycloptic phenotype of $NAGK^{T128M}$ injected embryos could be rescued by co-injection with GlcNAc, GlcNAc-6P, GlcNAc-1-P, or UDP-GlcNAc (Fig. 6-14B). Injection of *Ngly1* also gave rise to cycloptic embryos, similar to inhibition of *nagk* (Fig. 6-14C). These results suggest that the effects of perturbing the UDP-GlcNAc salvage pathway in embryonic development are

conserved in *Xenopus* and zebrafish, and the observed phenotypes are due to altered Wnt signaling.

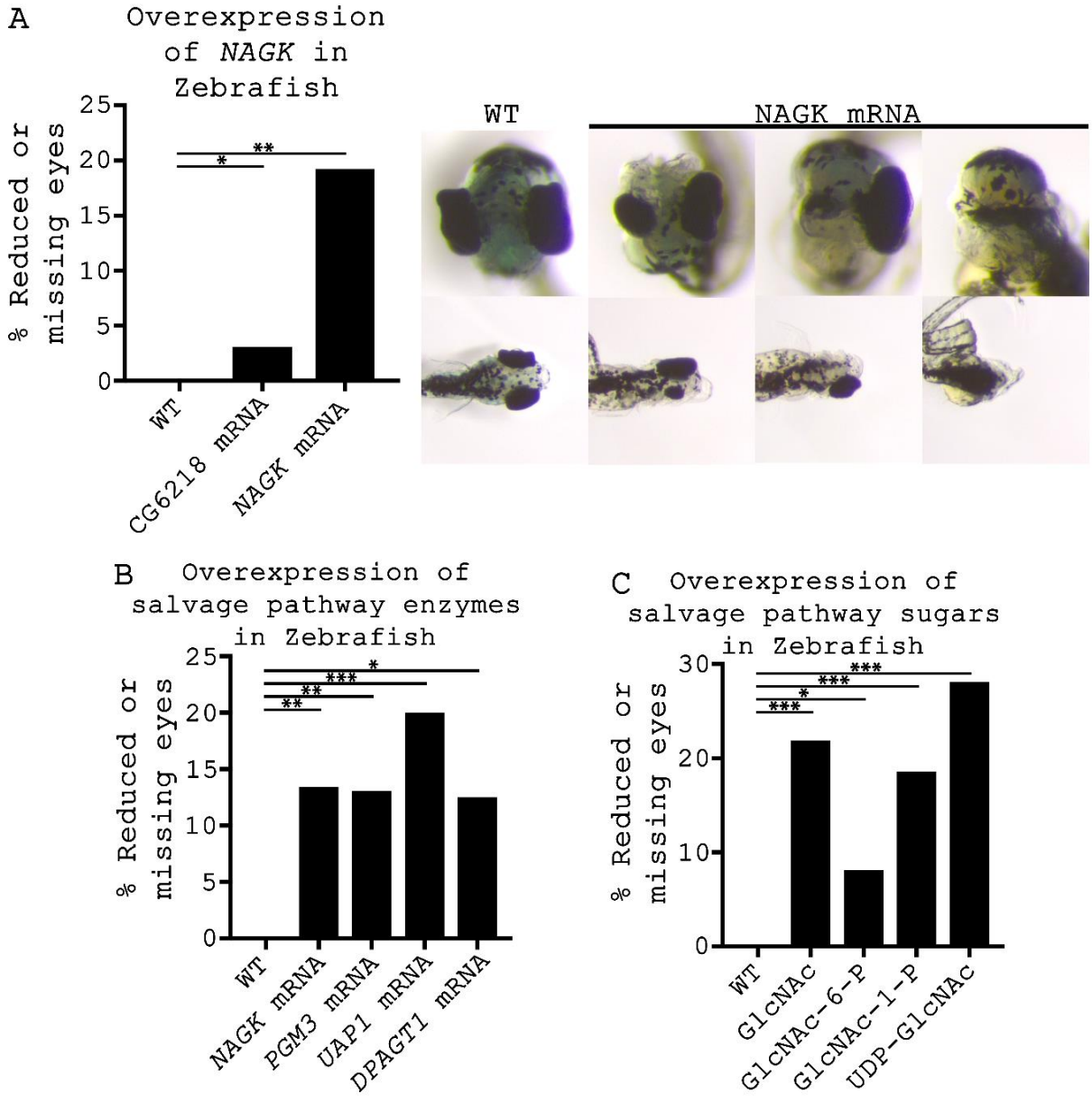
A
Overexpression of NAGK in Zebrafish
% Reduced or missing eyes
25
20
15
10
5
0
*
**
WT
CG6218 mRNA
NAGK mRNA
WT
NAGK mRNA
B
Overexpression of salvage pathway enzymes in Zebrafish
% Reduced or missing eyes
25
20
15
10
5
0
*
***
**
**
WT
NAGK mRNA
PGM3 mRNA
UAP1 mRNA
DPAGT1 mRNA
C
Overexpression of salvage pathway sugars in Zebrafish
% Reduced or missing eyes
30
20
10
0
***
***
*
***
WT
GlcNAc
GlcNAc-6-P
GlcNAc-1-P
UDP-GlcNAc

Figure 6-13: Overexpression of glycosylation salvage pathway enzymes, sugars and DPAGT1 inhibit eye formation in zebrafish. (A) (Left) Injection of CG6218 mRNA (*n*=4/129) and *NAGK* mRNA (*n*=5/31) inhibited the formation of the Zebrafish eye. (Right) Examples of eye formation in animals injected with *NAGK* mRNA at 5 days post fertilization. Phenotypes ranged from reduced eye size to one or both eyes missing. Reduced eyes were defined as less than half the size of a WT eye. (B) Injection of *NAGK* mRNA (*n*=11/82), *PGM3* mRNA (*n*=9/69), *UAP1* mRNA (*n*=9/45), or *DPAGT1* mRNA (*n*=4/32) inhibited eye formation as in (A). (C) Injection of GlcNAc (*n*=14/64), GlcNAc-6-P (*n*=6/74), GlcNAc-1-P (*n*=18/97), or UDP-GlcNAc (*n*=9/32) inhibited eye formation like (A) and (B). WT embryos did not display the observed phenotypes in (A) (*n*=0/208), (B) (*n*=0/78), or (C) (*n*=0/92). (A) - (C) was aggregated from $n \geq 3$ replicates. (A) - (C) The single cell of a zygote was injected with 0.5 ng of mRNA or 25 pMols sugar, in a volume of 1 nl. (A) - (C) Significance was calculated using Fisher's exact test and Bonferroni correction. (A) Treatments were compared to the WT; *$\rho < 0.0253$, **$\rho < 0.00501$. (B) and (C) Treatments were compared to the WT; *$\rho < 0.0127$, **$\rho < 0.00251$, *** $\rho < 0.000251$.

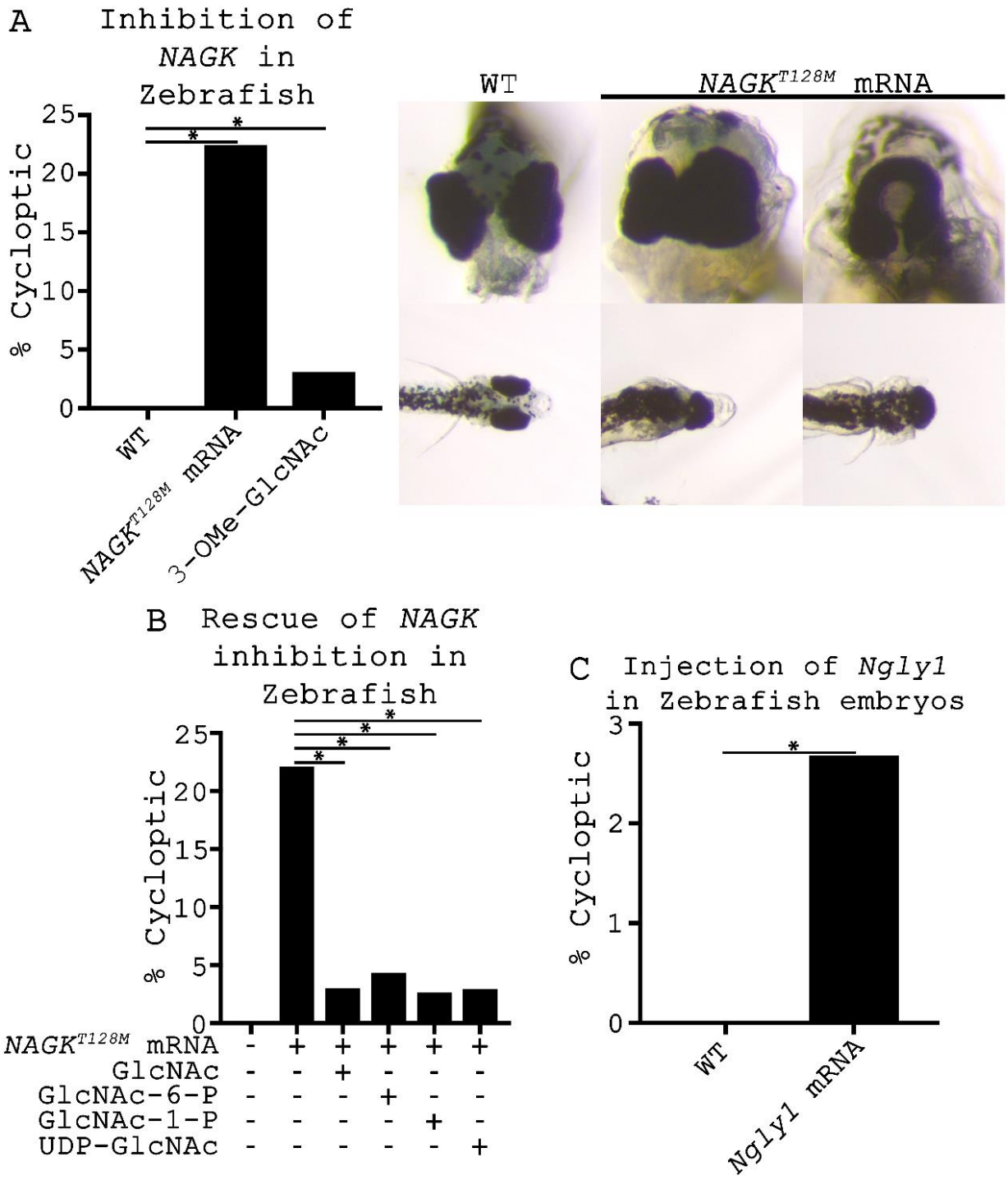
A
Inhibition of NAGK in Zebrafish
% Cyclopic
25
20
15
10
5
0
*
*
WT
NAGKT128M mRNA
3-OMe-GlcNAc
WT
NAGKT128M mRNA
B
Rescue of NAGK inhibition in Zebrafish
% Cyclopic
25
20
15
10
5
0
*
*
*
*
NAGKT128M mRNA - + + + + +
GlcNAc - - + - - -
GlcNAc-6-P - - - + - -
GlcNAc-1-P - - - - + -
UDP-GlcNAc - - - - - +
C
Injection of Ngly1 in Zebrafish embryos
% Cyclopic
3
2
1
0
*
WT
Ngly1 mRNA

Figure 6-14: Inhibition of NAGK and *N*-glycosylation in zebrafish caused cyclocephaly. (A) (Left) Injection of *NAGK*^{T128M} mRNA (*n*=20/89) and 3-O-Me-GlcNAc (*n*=3/97) resulted in cycloptic zebrafish. (Right) Examples of cyclopia from *NAGK*^{T128M} mRNA injected zebrafish embryos at 5 days post fertilization. Animals were defined as cycloptic if they were Classes III-V (according to Marlow et al. 1998). (B) Injection of *NAGK*^{T128M} mRNA (*n*=25/113) caused cyclopia. This cyclopia was partially rescued by co-injection with GlcNAc (*n*=1/33), GlcNAc-6-P (*n*=2/46), GlcNAc-1-P (*n*=1/38), or UDP-GlcNAc (*n*=1/34). (C) Injection of *Ngly1* mRNA (*n*=3/115) caused cyclopia as in (A). WT embryos did not display the observed phenotypes in (A) (*n*=0/250), (B) (*n*=0/42), or (C) (*n*=0/300). (A) - (C) was aggregated from *n*≥3 replicates. (A) - (C) The single cell of a zygote was injected or co-injected with 0.5 µg of mRNA or 25 pMols sugar, in a volume of 1 nl. (A) - (C) Significance was calculated using Fisher's exact test and Bonferroni correction. (A) Treatments were compared to the WT; *ρ< 0.0253. (B) Co-injections were compared to the mRNA control; *ρ< 0.0127. (C) Treatment was compared to the WT; *ρ<.05.

NAGK expression in zebrafish results in a convergent extension phenotype

Eye formation and cyclopia are reliable and specific phenotypes in the early formation of zebrafish that suggest Wnt signaling. Inhibition of noncanonical Wnts such as Wnt5b (*pipetail)* and Wnt11 (*silberblick*) in zebrafish are characterized by defects of convergent extension (Goudevenou et al., 2011; Heisenberg et al., 2000; Rauch et al., 1997; Stoick-Cooper et al., 2007; Xing et al., 2018). Convergent extension malformations were observed both concurrently with and independently of eye malformations. Injection of *NAGK* mRNA, *PGM3* mRNA, *UAP1* mRNA, *DPAGT1* mRNA, GlcNAc, GlcNAc-6-P, GlcNAc-1-P, UDP-GlcNAc, $NAGK^{T128M}$ mRNA, 3-O-Me-GlcNAc, and *NGLY1* mRNA caused convergent extension defects (Fig. 6-15A,B,C,D, appendix-4). Inhibition of NAGK with $NAGK^{T128M}$ mRNA, 3-O-Me-GlcNAc, and *NGLY1* mRNA was significantly more severe than over expression of the UDP-GlcNAc salvage pathway sugars and enzymes (Fig. 6-15A). These results suggest the UDP-GlcNAc salvage pathway regulates convergent extension through noncanonical Wnt signaling in the early embryo.

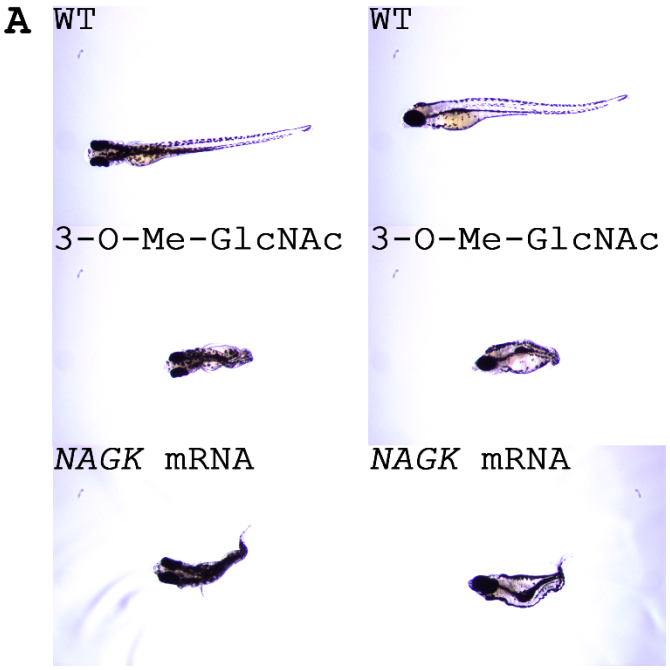
A
WT
WT
3-O-Me-GlcNAc
3-O-Me-GlcNAc
NAGK mRNA
NAGK mRNA

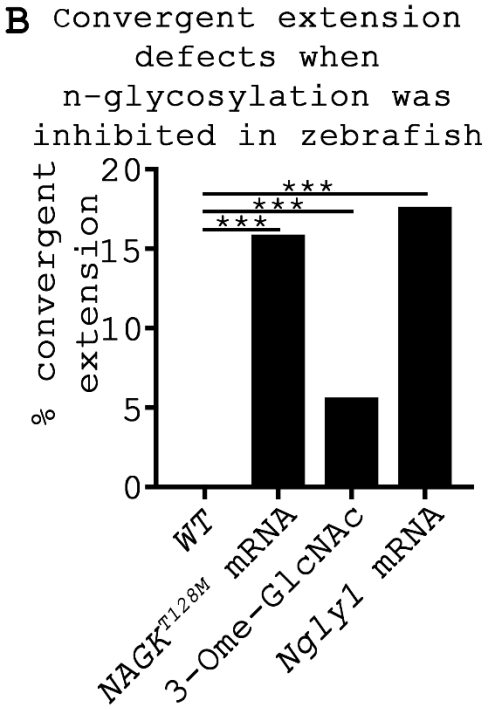
B
Convergent extension defects when n-glycosylation was inhibited in zebrafish
% convergent extension
0
5
10
15
20
***
***
***
WT
NAGK T128M mRNA
3-Ome-GlcNAc
Ngly1 mRNA

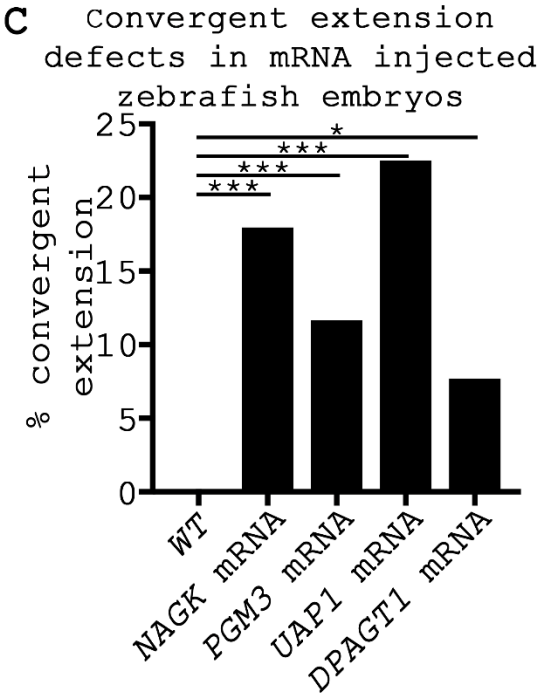
C
Convergent extension defects in mRNA injected zebrafish embryos
% convergent extension
0
5
10
15
20
25
*
***
***
***
WT
NAGK mRNA
PGM3 mRNA
UAP1 mRNA
DPAGT1 mRNA

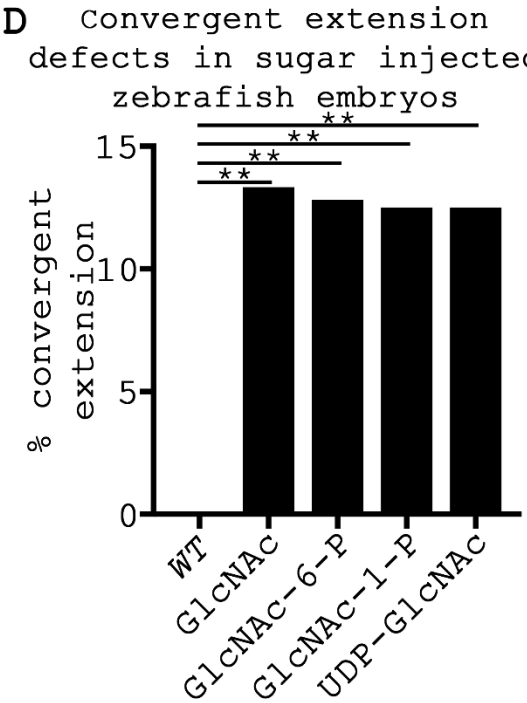
D
Convergent extension defects in sugar injected zebrafish embryos
% convergent extension
0
5
10
15
**
**
**
**
WT
GlcNAc
GlcNAc-6-P
GlcNAc-1-P
UDP-GlcNAc

Figure 6-15: Inhibition and overexpression of NAGK, UDP-GlcNAc salvage pathway components, DPAGT1, and NGYL1 result in a short anterior-posterior body axis. (A) (left) Topdown and (Right) side view of inhibition of NAGK (3-O-Me-GlcNAc) and overexpression of NAGK (*NAGK* mRNA) exhibiting defects in convergent extension. (B) Injection of $NAGK^{T128M}$ mRNA (*n*=24/151), 3-O-me-GlcNAc (*n*=7/124), or *Ngly1* mRNA (n=21/119) results in defects of convergent extension defects. Defects were not observed in WT controls (*n*=0/273). (C) Injection of *NAGK* mRNA (*n*=23/128), *PGM3* mRNA (*n*=14/120), *UAP1* mRNA (*n*=9/40), or *DPAGT1* mRNA (*n*=5/65) results in defects of convergent extension. Convergent extension defects were not observed in WT controls (*n*=0/102). (D) Injection of GlcNAc (*n*=4/30), GlcNAc-6-P (*n*=5/39), GlcNAc-1-P (*n*=4/32), UDP-GlcNAc (*n*=4/32) results in defects of convergent extension as in (C). Convergent extension defects were not observed in WT controls (*n*=0/129). (B) - (D) was aggregated from *n*≥3 replicates. (B) - (D) The single cell of a zygote was injected with 0.5 ng of mRNA or 25 pMols sugar, in a volume of 1 nl. (B) - (D) Significance was calculated using Fisher's exact test and Bonferroni correction. (B) Treatments were compared to the WT; ***ρ<0.00033. (C) and (D) Treatments were compared to the WT; *ρ< 0.0127, **ρ<0.00251, *** ρ<0.000251.

qRT-PCR of early *Xenopus* embryos suggests NAGK is Wnt specific

Our phenotypic data in *Xenopus* and zebrafish suggests Wnt specificity of NAGK in the early embryo. To verify this observation, we tested five key signaling pathways; Fgf, Hedgehog, Wnt, BMP, and Notch, known to control early embryonic patterning. These signaling pathways are expressed at different times, in different regions of the embryo, to eliciting diverse cellular responses. Various components of all of these signaling pathways are glycosylated and may therefore be perturbed by changes in the UDP-GlcNac salvage pathway and *DPAGT1*. To test this we preformed qRT-PCR on a reporter gene for each pathway. Overexpression and knockdown of the UDP-GlcNac salvage pathway and *DPAGT1* did not show significant changes in expression of the Fgf (dual specificity phosphatase 6; *dusp6*), TGFβ (T-box transcription factor T; *tbxt*), Notch (hes family bHLH transcription factor 1; *hes1*), or Shh (patched 1; *ptch1*) (Fig. 6-16) (Gu et al., 2012; Kofron et al., 2008: Mir et al., 1997; Moriishi et al., 2005; Nishimoto and Nishida, 2007; Zheng et al., 2017). When injected with *NAGK*, *PGM3*, *UAP1*, or *DPAGT1* mRNA, the expression of the Wnt reporter genes, nodal homolog 3, gene 1 (*Xnr3*) and chordin, gene 1 (*chordin*), were significantly increased (Fig. 6-16). Conversely, injection with 3-O-Me-GlcNAc, $NAGK^{T128M}$ mRNA, or *NAGK*, *PGM3*, *UAP1*, or *DPAGT1* MO reduced *Xnr3* and *chordin* expression (Fig. 6-16). These results suggest that the effects of the UDP-GlcNAc salvage pathway in early embryonic development are specific to Wnt signaling.

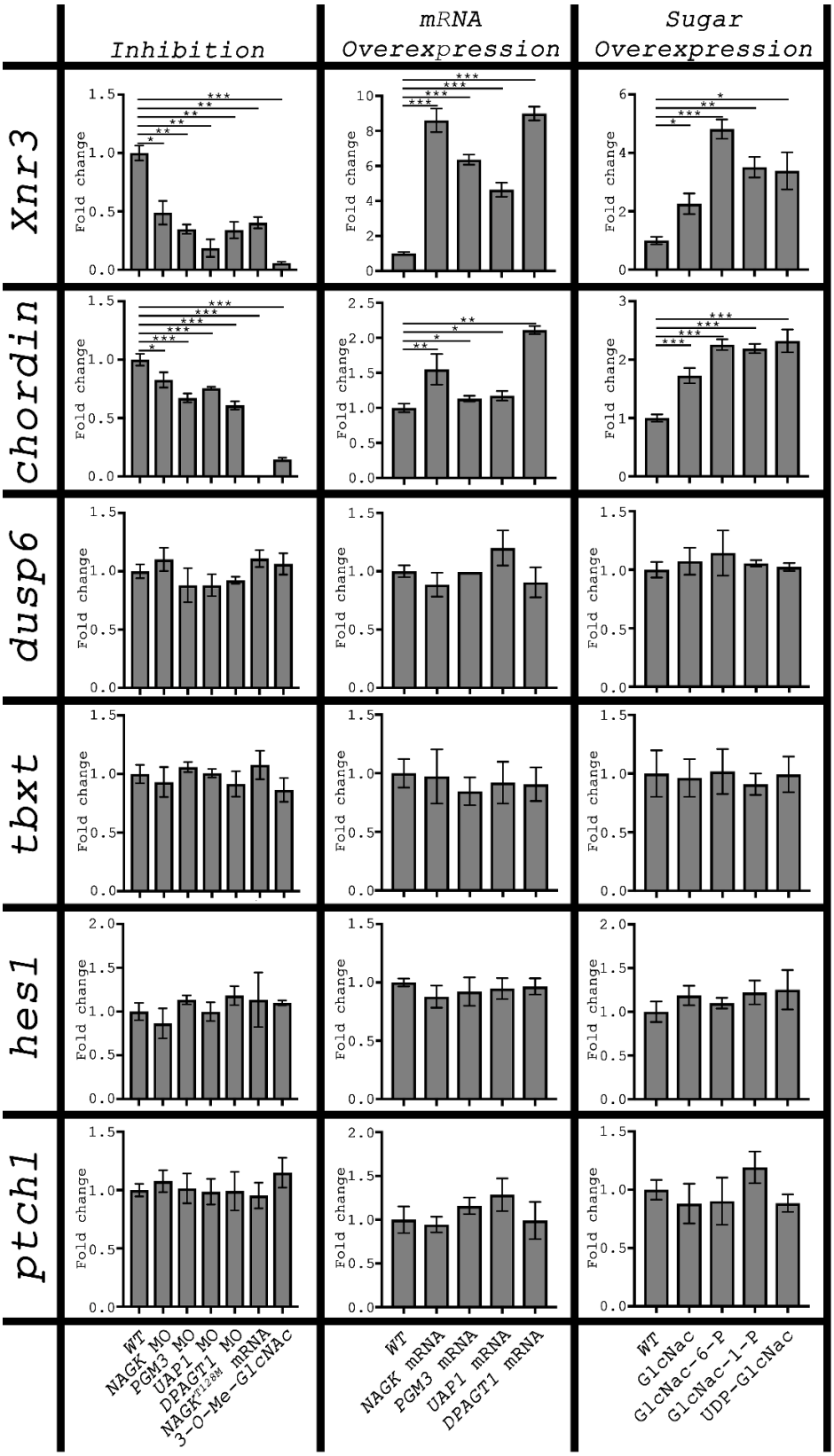
Inhibition
mRNA Overexpression
Sugar Overexpression
Xnr3
chordin
dusp6
tbxt
hes1
ptch1
Fold change
WT
NAGK MO
PGM3 MO
UAP1 MO
DPAGT1 MO
NAGK^tf12.8M mRNA
3-O-Me-GlcNAc
WT
NAGK mRNA
PGM3 mRNA
UAP1 mRNA
DPAGT1 mRNA
WT
GlcNac
GlcNac-6-P
GlcNac-1-P
UDP-GlcNac

Figure 6-16: qRT-PCR suggest the UDP-GlcNAc salvage pathway and DPAGT1 specifically control the Wnt signaling pathway in the early *Xenopus* embryo. Data from qRT-PCR on whole embryos. (Left) Knockdown or inhibition of the UDP-GlcNAc salvage pathway and DPAGT1. (Middle) Overexpression of the UDP-GlcNAc salvage pathway enzymes and DPAGT1. (Right) Overexpression of the UDP-GlcNAc salvage pathway sugars. *Xnr3* and *chordin*, are reporter gene for Wnts. In stage 10.5 embryos knockdown and inhibition of the UDP-GlcNAc salvage pathway and DPAGT1 inhibited *Xnr3* and *chordin* expression. Conversely, overexpression of the UDP-GlcNAc salvage pathway enzymes and sugars, as well as DPAGT1, increased the expression of *Xnr3* and *chordin* in whole embryos. In stage 10.5 embryos, expression of *dusp6,* a reporter gene for FGF, is unaffected by knockdown, inhibition, or overexpression of the UDP-GlcNAc salvage pathway and DPAGT1. In stage 10.5 embryos, expression of *tbxt,* a reporter gene for BMP, is unaffected by knockdown, inhibition, or overexpression of the UDP-GlcNAc salvage pathway and DPAGT1. In stage 13 embryos, expression of *hes1,* a reporter gene for Notch, is unaffected by knockdown, inhibition, or overexpression of the UDP-GlcNAc salvage pathway and DPAGT1. In stage 16 embryos, expression of *ptch1,* a reporter gene for SHH, is unaffected by knockdown, inhibition, or overexpression of the UDP-GlcNAc salvage pathway and DPAGT1. Data shown are representative of $n \geq 3$ biological replicates using $n=3$ technical replicates. Each replicate was a pool of $n=5$ whole embryos. Both cells of a stage 2 (2-cell) embryo was injected or co-injected with 2.5 ng of mRNA, 2.5 pg MO, or 125 pMols sugar, in a volume of 2.5 nl. Expression was normalized to the house keeping gene, ODC. Graphs are fold change calculated using the $2^{-\Delta\Delta Ct}$ method. Significance was calculated using T-test with equal variance and Bonferroni correction on the ΔCt values. (Left) Inhibition of the UDP-GlcNAc salvage pathway were compared to the WT control. (Middle) and (Right) overexpression of UDP-GlcNAc salvage pathway enzymes and sugars were compared to the WT control. No significant values were found. For Inhibition (left); *$\rho<0.0085$, **$\rho< 0.00167$, *** $\rho<0.000167$. For overexpressions (middle and right); *$\rho<0.01274146$, **$\rho< 0.00250943$, ***$\rho< 0.000250943$.

NAGK regulates Wnt signaling in *Xenopus* ectodermal explants likely via cell surface receptors

Wnt signaling is not detectable in the early animal cap (undifferentiated ectodermal explants) of Xenopus embryos, making it a clean system for testing the expression of Wnt components with members of the salvage pathway. We therefore co-injected mRNAs of *Wnt8*, a *Wnt8-Fz5* fusion, *LRP6*, and *Dsh* with UDP-GlcNAc salvage pathway and *DPAGT1* mRNAs and MOs. Human and rat Frizzled 5 are unable to activate Wnt signaling in *Xenopus* embryos (He et al., 1997; Holmen et al., 2002; Wodarz and Nusse, 1998). *Wnt8-Fz5* is *Xenopus XWnt8* fused to human Frizzled 5, which has been shown to interact with LRP6 to activate the canonical Wnt/β-catenin pathway (Holmen et al., 2002). Injection of *Wnt8*, *Wnt8-Fz5*, *LRP6*, or *Dsh* by themselves are sufficient to activate the Wnt pathway in animal caps (Fig. 6-17A,B,C,D, 6-18 A,B,C,D).

Co-injection of *Wnt8*, *Wnt8-Fz5*, or *LRP6* mRNA with *NAGK*, *PGM3*, *UAP1*, or *DPAGT1* mRNA resulted in higher expression of Wnt target genes, *Xnr3* and *chordin* (Fig. 6-17A,B,C, 6-18A,B,C). Conversely, lower expression of both *Xnr3* and *chordin* were observed when *Wnt8*, *Wnt8-Fz5*, or *LRP6* mRNA was co-injected with *NAGK*, *PGM3*, *UAP1*, or *DPAGT1* MOs (Fig. 6-17A,B,C, 6-18A,B,C). Co-injection of *Dsh* mRNA with *NAGK*, *PGM3*, *UAP1*, or *DPAGT1* mRNA did not alter the expression of *Xnr3* or *chordin* in the animal cap (Fig. 6-17D, 6-18D). Similarly, co-injection of *Dsh* mRNA with *NAGK*, *PGM3*, *UAP1*, or *DPAGT1* MO did not alter the expression of *Xnr3* or *chordin* in the animal cap (Fig. 6-17D, 6-18D). These data suggest that the UDP-GlcNAc salvage pathway controls Wnt signaling is at the level of the receptor or ligand in the early embryo.

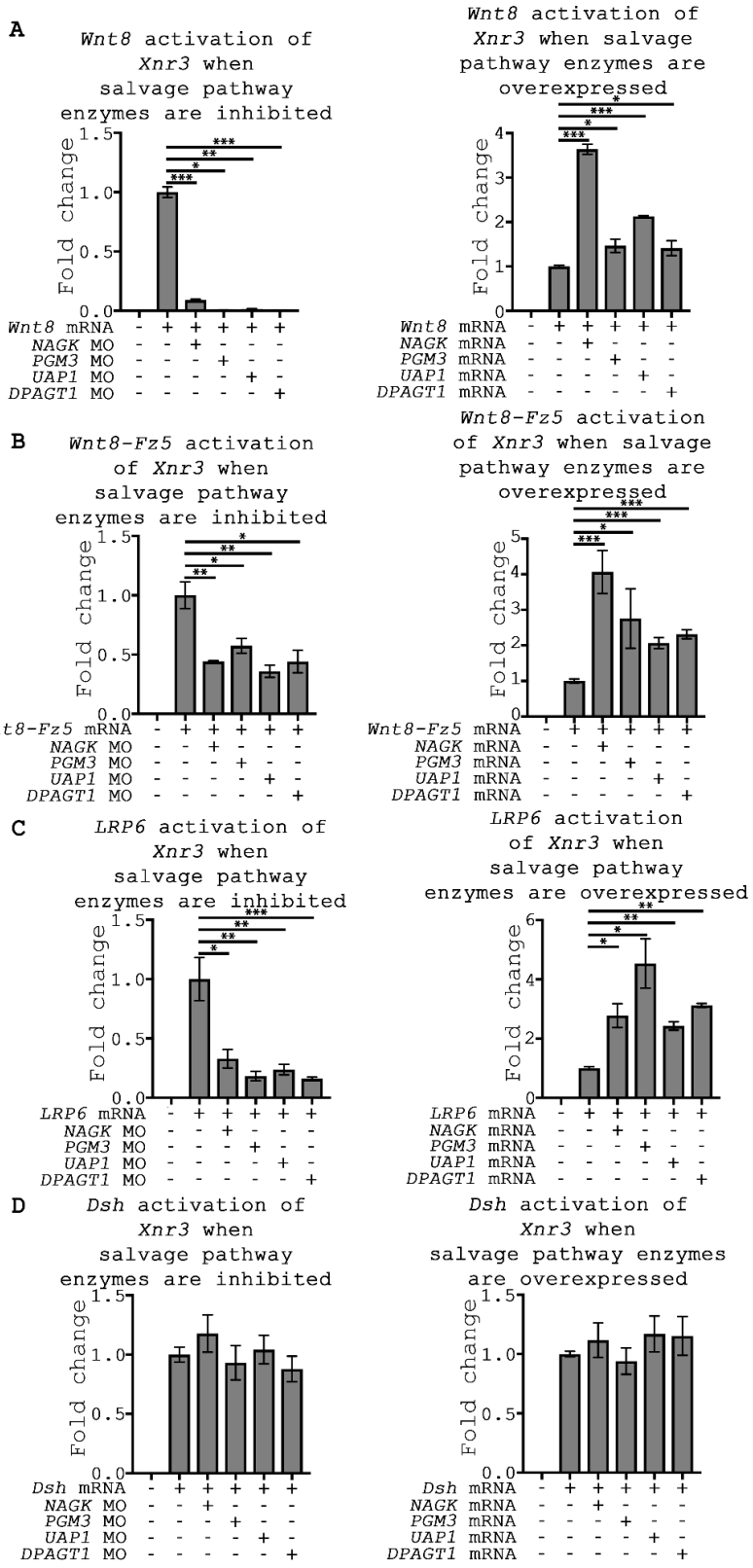
A
Wnt8 activation of Xnr3 when salvage pathway enzymes are inhibited
Fold change
Wnt8 mRNA - + + + + +
NAGK MO - - + - - -
PGM3 MO - - - + - -
UAP1 MO - - - - + -
DPAGT1 MO - - - - - +
Wnt8 activation of Xnr3 when salvage pathway enzymes are overexpressed
Fold change
Wnt8 mRNA - + + + + +
NAGK mRNA - - + - - -
PGM3 mRNA - - - + - -
UAP1 mRNA - - - - + -
DPAGT1 mRNA - - - - - +
B
Wnt8-Fz5 activation of Xnr3 when salvage pathway enzymes are inhibited
Fold change
Wnt8-Fz5 mRNA - + + + + +
NAGK MO - - + - - -
PGM3 MO - - - + - -
UAP1 MO - - - - + -
DPAGT1 MO - - - - - +
Wnt8-Fz5 activation of Xnr3 when salvage pathway enzymes are overexpressed
Fold change
Wnt8-Fz5 mRNA - + + + + +
NAGK mRNA - - + - - -
PGM3 mRNA - - - + - -
UAP1 mRNA - - - - + -
DPAGT1 mRNA - - - - - +
C
LRP6 activation of Xnr3 when salvage pathway enzymes are inhibited
Fold change
LRP6 mRNA - + + + + +
NAGK MO - - + - - -
PGM3 MO - - - + - -
UAP1 MO - - - - + -
DPAGT1 MO - - - - - +
LRP6 activation of Xnr3 when salvage pathway enzymes are overexpressed
Fold change
LRP6 mRNA - + + + + +
NAGK mRNA - - + - - -
PGM3 mRNA - - - + - -
UAP1 mRNA - - - - + -
DPAGT1 mRNA - - - - - +
D
Dsh activation of Xnr3 when salvage pathway enzymes are inhibited
Fold change
Dsh mRNA - + + + + +
NAGK MO - - + - - -
PGM3 MO - - - + - -
UAP1 MO - - - - + -
DPAGT1 MO - - - - - +
Dsh activation of Xnr3 when salvage pathway enzymes are overexpressed
Fold change
Dsh mRNA - + + + + +
NAGK mRNA - - + - - -
PGM3 mRNA - - - + - -
UAP1 mRNA - - - - + -
DPAGT1 mRNA - - - - - +

Figure 6-17: Expression of *Xnr3* in Stage 10.5 animal caps suggests the UDP-GlcNAc salvage pathway works at the level of the ligand and/or receptor. (A) (left) activation of the Wnt pathway by *Xenopus wnt8* is inhibited by co-injection with MOs against the salvage pathway enzymes. (Right) Conversely, co-injection with mRNA encoding the pathway enzymes enhanced the expression of *Xnr3*. Both *Fz* (B) and *LRP6* (C) were inhibited by co-injection with MOs and enhanced by mRNAs, as in (A). (D) Activation of the Wnt pathway by *DSH* was unaffected by inhibition (left) or overexpression (right) of the salvage pathway enzymes. (A) - (D) Data shown are representative of n≥3 biological replicates using n=3 technical replicates. Each replicate was a pool of n=5 animal caps. Each dorsal blastomere was injected or co-injected with 1 ng of mRNA or 1 pg MO, in a volume of 2.5 nl. Expression was normalized to the house keeping gene, *odc*. *Xnr3* was not detected in the WT animal caps. *odc* was detected in the WT animals caps. Graphs are fold change calculated using the $2^{-\Delta\Delta Ct}$ method. Significance was calculated using T-tests with equal variance and Bonferroni correction on the ΔCt values. Each co-injection was compared to the control mRNA. *ρ< 0.0127, **ρ<0.00251, ***ρ<0.000251.

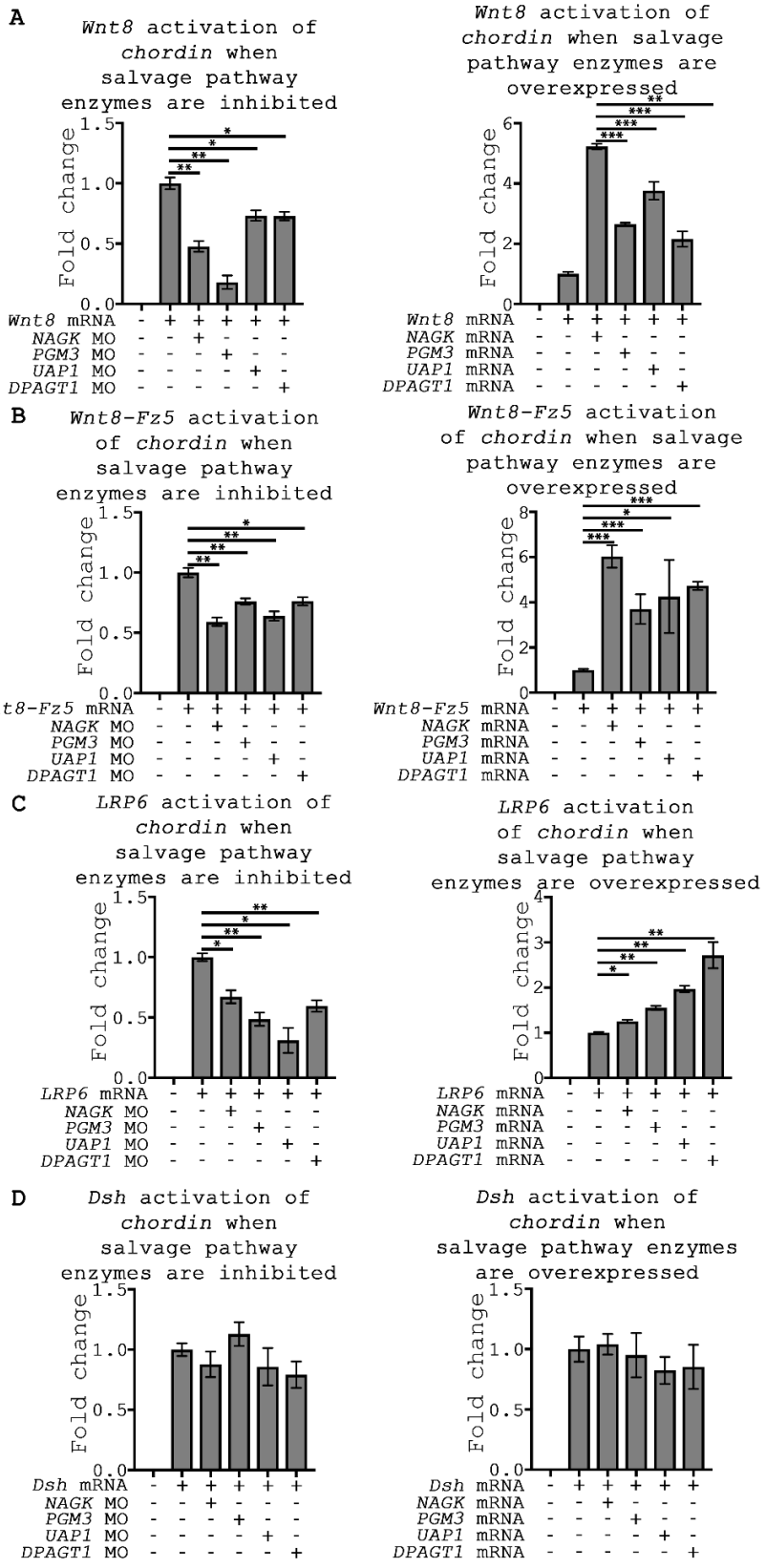
A
Wnt8 activation of chordin when salvage pathway enzymes are inhibited
Fold change
Wnt8 mRNA
NAGK MO
PGM3 MO
UAP1 MO
DPAGT1 MO
Wnt8 activation of chordin when salvage pathway enzymes are overexpressed
Wnt8 mRNA
NAGK mRNA
PGM3 mRNA
UAP1 mRNA
DPAGT1 mRNA
B
Wnt8-Fz5 activation of chordin when salvage pathway enzymes are inhibited
Wnt8-Fz5 mRNA
Wnt8-Fz5 activation of chordin when salvage pathway enzymes are overexpressed
C
LRP6 activation of chordin when salvage pathway enzymes are inhibited
LRP6 mRNA
LRP6 activation of chordin when salvage pathway enzymes are overexpressed
D
Dsh activation of chordin when salvage pathway enzymes are inhibited
Dsh mRNA
Dsh activation of chordin when salvage pathway enzymes are overexpressed

Figure 6-18: Expression of *chordin* in Stage 10.5 animal caps suggests the salvage pathway works at the level of the ligand and/or receptor. (A) (left) activation of the Wnt pathway by *Xenopus wnt8* is inhibited by co-injection with MOs against the salvage pathway enzymes. (Right) Conversely, co-injection with mRNA encoding the pathway enzymes enhanced the expression of *chordin*. Both *Fz* (B) and *LRP6* (C) were inhibited by co-injection with MOs and enhanced by mRNAs, as in (A). (D) Activation of the Wnt pathway by *DSH* was unaffected by inhibition (left) or overexpression (right) of the salvage pathway enzymes. (A) - (D) Data shown are representative of $n \geq 3$ biological replicates using $n=3$ technical replicates. Each replicate was a pool of $n=5$ animal caps. Each dorsal blastomere was injected or co-injected with 1 ng of mRNA or 1 pg MO, in a volume of 2.5 nl. Expression was normalized to the house keeping gene, *odc*. *chordin* was not detected in the WT animal caps. *odc* was detected in the WT animals caps. Graphs are fold change calculated using the $2^{-\Delta\Delta Ct}$ method. Significance was calculated using T-tests with equal variance and Bonferroni correction on the ΔCt values. Each co-injection was compared to the mRNA control. *$\rho < 0.0127$, **$\rho < 0.00251$, ***$\rho < 0.000251$.

Discussion

In this study, we show that *NAGK* regulates anterior-posterior patterning in early *Xenopus* embryos. In zebrafish, *NAGK* inhibits formation of the eye, while loss of *NAGK* results in cyclopia, suggesting effects in both canonical and noncanonical Wnt. These data are phenocopied by the UDP-GlcNAc salvage pathway enzymes and sugars, and *DPAGT1*. Data from overexpression of *NGYL1* suggests the observed phenotypes are the result of changes in *N*-glycosylation. Finally, our qRT-PCR data suggests the observed phenotypes are due to alteration in the Wnt signaling pathway at the level of the receptor and/or ligand.

Partial loss-of-function proteins regulating glycosylation leads to a group of human diseases termed Congenital Disorders of Glycosylation (CDGs) (Freeze, 2006; Haltiwanger and Lowe, 2004; Jaeken and van den Heuvel, 2014). In addition to its well-characterized role as a rate-limiting enzyme in *N*-glycosylation, DPAGT1 is mutated in CDG Type 1j (DPAGT1-CDG) (Wu et al., 2003). DPAGT1 has been suggested to regulate both cononical and noncanonical Wnt signaling through regulation of *N*-linked glycosylation (Liu et al., 2013; Varelas et al., 2014). Consistant with the literature, mutations in Wnt signaling pathway components have been shown to cause clinodactyly (Ockeloen et al., 2016; Saal et al., 2015), intellectual disability (Snijders et al., 2015), microcephaly (Buchman et al., 2011) and micrognathia (White et al., 2018), the four most common DPAGT1-CDG phenotypes, observed in over 80% of patients (Ganetzky et al., 2015; Wu et al., 2003). Recently, mutations in PGM3 (PGM3-CDG) have been identified that suggest alterations in the free pool of UDP-GlcNAc and its utilization in glycosylation may result in CDGs (Pacheco-Cuellar et al., 2017; Stray-Pedersen et al., 2014).

Patients with PGM3-CDG presented with neutropenia, B and T lymphopenia, bone marrow failure, skeletal dysplasis short stature, brachydactyly, cognitive impairment, phenotypes that have each been linked to inhibition of the Wnt signaling pathway (Akbarzadeh et al., 2008; Calaminus et al., 2010; Hiramoto et al., 2013; Malhotra and Yang, 2014; Pacheco-Cuellar et al., 2017; Ranheim et al., 2005; Snijders Blok et al., 2015; Stray-Pedersen et al., 2014; Wong et al. 2015).

As the specific developmental and molecular perturbations that link deficits in *N*-glycosylation and CDG disease symptoms have not been identified, the DPAGT1 and PGM3 (as well as NAGK and UAP1) loss-of-function phenotypes that we have identified in *Xenopus* and zebrafish embryos may provide a model system to study the molecular pathogenesis of CDGs. Furthermore, two CDGs, MPI-CDG and CAD-CDG, are treatable by oral supplementation with mannose or uridine, respectively (Harms et al., 2007; Jaeken and van den Heuvel, 2014; Jaeken and Péanne, 2017; Koch et al., 2017). Several other CDGs are partially treatable with oral butyrate, oral fucose, or galactose (Jaeken and Péanne, 2017; Witters et al., 2017). Our data suggests that these diseases may be due, in part, to alterations in Wnt signaling during development and that supplementation with UDP-GlcNAc salvage pathway sugars may benefit patients with PGM3-CDG and DPAGT1-CDG

UAP1 and *PGM3* are significantly up-regulated in clinical prostate carcinomas, controlling cancer cell viability and androgen control (Itkonen et al., 2015, Munkley et al., 2016). High expression of UAP1 in prostate cancer cell lines greatly increased UDP-GlcNAc, and conversely, inhibition significantly decreased UDP-GlcNAc levels (Itkonen et al., 2015).

Inhibition of *PGM3* in mice and human triple negative breast cancer cells greatly reduced UDP-GlcNAc levels (Greig et al., 2007, Ricciardiello et al., 2018). *PGM3* inhibition resulting in cell proliferation and survival of cancer (Ricciardiello et al., 2018). DPAGT1 overexpression is linked to oral squamous cell carcinoma through Wnt activation (Jamal et al., 2012; Nita-Lazar et al., 2009). These and our current data suggest that the UDP-GlcNAc salvage pathways' effect on the free pool of UDP-GlcNAc may play a role in cancer via the Wnt pathway.

Our data suggests that NAGK, PGM3, UAP1, and DPAGT1 promotes Wnt signaling through *N*-glycosylation of proteins. Overexpression of each gene posteriorized *Xenopus* embryos and resulted in reduced or missing eyes in zebrafish. Conversely, inhibition of NAGK, PGM3, UAP1, and DPAGT1 anteriorized *Xenopus* embryos. This suggests that the pathway, and not any individual enzyme, is important for the observed phenotypes. However, only PGM3 and DPAGT1 have been linked to CDGs. There is a possibility that changes in NAGK and UAP1 are more potent and perhaps lethal, however our data does not support this. Alternatively, only 8 cases of PGM3-CDG and 5 of DPAGT1-CDG are known. Therefore, it is possible that NAGK and UAP1 mutations are merely so rare that they have not yet been identified (Table 4-1).

Furthermore, PGM3-CDG and DPAGT1-CDG express with different constellations of phenotypes, suggesting effects on different pathways. It is possible that the effects we have observed are limited to the early embryo, but the phenotypes observed in these CDGs are due to continuous changes in the UDP-GlcNAc salvage pathway. However, soaking *Xenopus* embryos in GlcNAc for two days did not result in additional phenotypes (Fig. 6-7). Therefore, this is unlikely to be the case. The UDP-GlcNAc salvage pathway feeds into additional pathways

besides *N*-glycosylation, such as hyaluronan biosynthesis (Vigetti et al., 2014). It is therefore possible that the PGM3-CDG phenotypes are due to effects on additional pathways not affected by DPAGT1-CDG. However, PGM3 should also exhibit the same phenotypes as DPAGT1-CDG. This disparity warrants further study to elucidate why PGM3 and DPAGT1 are the same in *Xenopus* and zebrafish but not in humans.

Our data suggests NAGK, PGM3, UAP1, and DPAGT1 specifically promotes Wnt signaling in the early embryo through *N*-glycosylation. However, only a single reporter gene and time point was used to test the Fgf, Shh, Notch, and BMP pathways. It is possible that these specific genes were unaffected in the early embryo. It is also possible that additional pathways are affected later in development. Additional testing with different time points and/or reporters may further elucidate the role(s) of NAGK, PGM3, UAP1, and DPAGT1 in development.

Chapter 7:

Future directions

In this work we have discussed two distinct pathways that show the significant impact that kinase and phosphatase have on biological systems. We have shown that the loss the phosphatase Cdc14 leads to multiple phenotypic effects, all of which can be explored in depth in further works. Similarly, the Kinase NAGK is shown to control Wnt singnaling through *N*-glycosylation of its ligand and/or receptors. Below we will discuss possible future studies that can further elucidate the role and mechanism of thses enzymes.

Feeding behavior, fat body metabolism, and longevity

Our data suggest that feeding behavior of *cdc14* null animals was decreased, but indiscriminate (Fig. 11A). Staining of larval fat bodies suggested *cdc14* null had both irregular and larger lipid droplets, suggesting a defect in metabolism (Fig. 13A,B,C). In addition, the *y w* control flies live modestly longer (> 4.25 h) than *cdc14* null animals (Fig. 13D). This constellation of phenotypes has not been reported in any other animal model system. However, in 2018 Kondo et al. found evidence that *CDC14* provoked macroautophagy under starvation conditions and when overexpressed in *S. cerevisiae*, suggesting these phenotypes may be a conserved function of Cdc14. Furthermore, these phenotypes and macroautophagy have implications in human diseases such as obesity.

Under normal feeding conditions, enterocytes absorb lipids digested from dietary food in Drosophila (Warnakula et al., 2011). Lipids are then packaged into lipoprotein particles and are transported to the fat body (Warnakula et al., 2011). Loss of these enterocytes in *cdc14* nulls may be apparent and could suggest impairment of lipid absorption (Song et al., 2014). It is also possible that the reduction in feeding behavior may alter lipid droplet formation through alterations in fat consumption. The *UASp-cdc14-myc, cdc14*$^{\Delta 1}$ line could be crossed to a *cdc14* nulls with a fat body specific promoter such as *larval serum protein-2 gene* (*lsp-2*) (Aguila et al., 2007; Benes et al., 1990). Alternatively, fat body-specific RNA interference could be used to inhibit *cdc14* expression (Musselman et al., 2013). The progeny should not exhibit reduced

feeding behavior. Therefore, if the lipid droplet formation is still affected, it would suggest that feeding behavior is independent of the metabolism defects.

Continued lipid droplet malformation could suggest a defect in taste reception (Figs. 11A,B and 12A). The *UASp-cdc14-myc, cdc14*$^{\Delta 1}$ line could be crossed to a *cdc14* nulls with a cilia specific promoter such as *hemingway* (*hmw*). If rescue of *cdc14* expression in ciliated cells rescues the fat body phenotype it would suggest that fat body and possibly starvation resistance phenotypes are due to defects in feeding. Two-way choice assays using mediums containing different proportions and varieties of proteins, sugars, salts, and fat could be used to discriminate between changes in specific gustatory receptor activity, such as the Gr family of sugar receptors (Miyamoto et al., 2013). Further investigation in humans may elucidate Cdc14 role in taste and food consumption in disease, such as hypogeusia (reduced ability to taste), ageusia (loss of the ability to taste), or obesity.

During metamorphosis, lipid metabolism accounts for >80% of fuel consumption, therefore the larvae may be retaining lipids erroneously in preparation for pupation (Merkey et al., 2011). Macroautophagy in the fat bodies of *cdc14* nulls may be impaired leading to retention of lipids. The *cdc14* nulls could be crossed to nulls of *SREBP*, a lipogenesis inducing gene, to test for rescue of lipogenesis and abnormal lipid retention (Song et al., 2014). Work in yeast suggests *cdc14* dephosphorylates Atg13 in the TORC1 pathway to induce macroautophagy in yeast. Therefore, genetic and biochemical studies in Drosophila could identify a new functions of Cdc14. Conservation of this function would suggest a role for Cdc14 in higher organism such as human that may influence diseases such as obesity.

Chemosensory reception, mechanosensory reception, sperm competitiveness, and cilia formation

In zebrafish, knockdown of Cdc14 impaired ciliation, while studies in *P. infestans* suggest cdc14 is enriched at flagella-basal body complexes and may play a role I the formation or function of flagella (Ah-Fong and Judelson, 2011; Clement et al., 2011; Clement et al., 2012). As basal bodies are found in all ciliated cells and Drosophila have only two ciliated cell types (sperm and sensilla), Drosophila is an attractive model to better understand the biology of this organelle (Jana et al., 2016). We found that mechanosensation (Fig. 3-10A,B) and chemosensation (Figs. 3-11A,B,C,D and 3-12A) were both impaired in *cdc14* nulls. However, photoreception (Fig. 3-12B) was unaffected in *cdc14* nulls. As Drosophila spermatozoa and Type I sensory neurons (mechanosensory and chemosensory neurons) are ciliated, but photosensory neurons are not, our data suggests the function of *cdc14* is specific to cilia. To test this idea, we have stained the chordotonal organs, stretch receptor organs that used ciliated neurons for reception. We found the organs to be disorganized and smaller, with a decrease in the number and length of ciliated cells. However, the changes were small (~4%) with high standard deviations (Fig. 7-1). Numerous stains, counter stains, and transgenic lines that specifically mark cilia in Drosophila can be used to verify these results and study the specific molecular nature of the defect (Jana et al., 2016; Vieillard et al., 2015). For example, staining for the extracellular protein, spacemaker, and α-HRP labelling will aid in validating our results (Cook et al., 2008). Tagging-cdc14 with GFP or other marker, may demonstrate specific association with the basal body and/or additional structures. Using an inducible promotor, such as the hsp-70 heat shock

promoter, to express cdc14-myc in post eclosion *cdc14* null adults, could help distinguish between roles in ciliogenesis and cilia function.

Mutations in CDC14A in human have been liked to progressive and moderate-to-profound deafness and male infertile (Imtiaz et al., 2018). Mutation in mice recapitulate the human phenotypes, while exhibiting degeneration of seminiferous tubules and spermatogenesis defects resulting in abnormal sperm motility, morphology, and sperm count (Song et al., 2014). In our studies, we found that sperm competitiveness was impaired in *cdc14* null flies (Figs. 3-6B and 3-7B). Our data suggests this is not due to a failure to mate (Figs. 3-2B,C,E,F,G, 4A, and 3-7A), locomotion defects (Fig. 3-8A,B,C), testis malformations or reductions in sperm numbers (Figs. 3-4B,C,D,E,F). Our data suggests that *cdc14* is important in the function of *Drosophila* sperm, similar to Humans and mice. Importantly, Drosophila have a single copy of Cdc14 knockout of which does not result in degradation of the testis as it does in the mouse, making it ideal for further study of Cdc14's role in spermatogenesis.

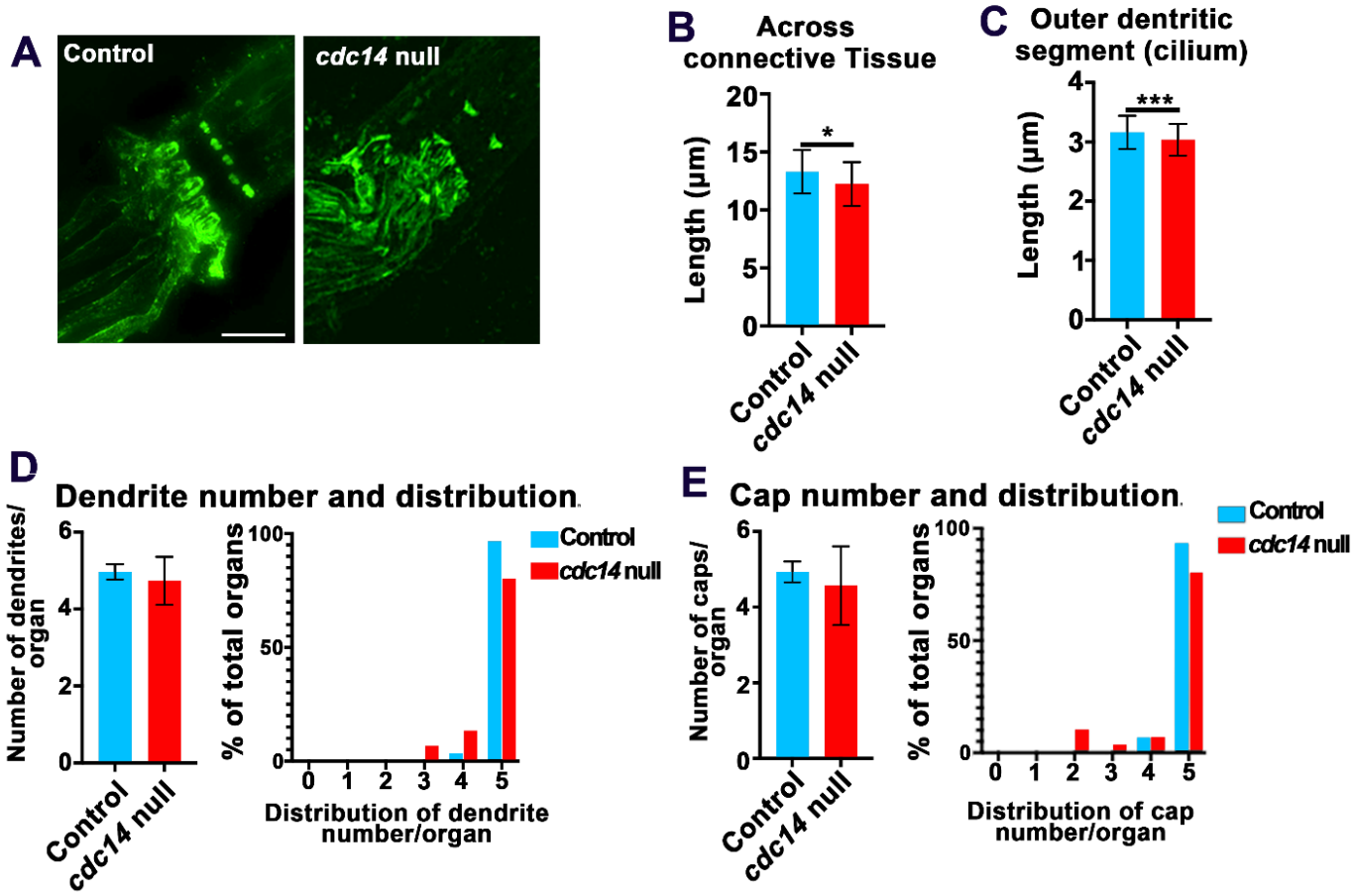
A
Control
cdc14 null
B
Across connective Tissue
Length (µm)
20
15
10
5
0
*
Control
cdc14 null
C
Outer dentritic segment (cilium)
Length (µm)
4
3
2
1
0
***
Control
cdc14 null
D
Dendrite number and distribution
Number of dendrites/ organ
6
4
2
0
Control
cdc14 null
% of total organs
100
50
0
0 1 2 3 4 5
Distribution of dendrite number/organ
Control
cdc14 null
E
Cap number and distribution
Number of caps/ organ
6
4
2
0
Control
cdc14 null
% of total organs
100
50
0
0 1 2 3 4 5
Distribution of cap number/organ
Control
cdc14 null

Figure 7-1: The chordotonal organ of *cdc14* null larvae shows morphological changes in size, number, and length of scolopidia. (A) Representative SIM images of the chordotonal organ (ChO) from control and *cdc14* null larvae. Scale bar, 5 μm. (B) The length across the connective tissue of the chordotonal organ was decreased (8.0%) in *cdc14* null larvae. (C) A decrease in length (4.0%) of the outer segment (a proxy for cilia length, measured from the tip of the dendritic cap to the top of the cap) was observed in *cdc14* null larvae. (D) The distribution of neuronal dendrites numbers per ChO showed a greater number of *cdc14* null mutant larvae with decreased dendrites per organ. (E) The distribution of cap numbers per ChO showed a greater number of *cdc14* null mutant larvae with decreased caps per organ. (C) through (F) were analyzed by T-test (two tailed, unequal variance). Chordotonal organs were imaged by Structured Illumination Microscopy (SIM) on a Nikon SIM with a 100X SR Apo TIRF lens and Andor DU-897 EMCCD camera, using 3D SIM mode. 3D reconstructions were performed within the Nikon software at the time of image capture. Reconstructed images were blinded and imported to Fiji, where "max projection" was used to create a 2D image of the Z-stack for analysis. N=30 ChOs from 15 pelts were assessed. N≥131 outer dendritic segments and N≥127 caps were measured.

NAGK

The salvage pathway, DPAGT1 and CDGs

We found that alterations in NAGK expression were phenocopied by PGM3, UAP1, and DPAGT1 in both *Xenopus* and zebrafish (Fig 6-4, 6-5, 6-8, 6-10, 6-14). This suggests a common downstream effect on *N*-glycosylation of proteins. This was further supported by expression of NGYL1, which cleaves N-glycans in the cytosol (Fig. 6-4, 6-8, 6-14) However, in the literature, only PGM3 and DPAGT1 have been linked to a congenital disorders of glycosylation (CDG) (Stray-Pedersen et al., 2014; Wu et al., 2003). As CDGs are often very rare, many with two or less know patients, it is very likely that NAGK and UAP1 cause a CDG that has not been identified (Sparks and Krasnewich, 2017). However, it is possible that mutations in either gene are not tolerated in humans. Further testing with techniques such as whole genome sequencing will be able to identify patients with mutations in NAGK or UAP1.

There are no effective treatments for PGM3-CDG or DPAGT1-CDG. However, our data supports the idea that inhibition of a UDP-GlcNAc salvage pathway enzyme can be rescued by supplementation with the downstream sugars, similar to the effective treatment of MPI-CDG and CAD-CDG (Koch et al., 2017; Niehues et al., 1998). For PGM3-CDG, supplementation with GlcNAc-1-P or UDP-GlcNAc may prove effective. GlcNAc is non-toxic and well tolerated, it is possible that the other sugars of the UDP-GlcNAc salvage pathway are well tolerated as well (Levin et al., 1961; Liu et al., 2008). Human patients could be supplemented with the UDP-GlcNAc sugars and assed for alleviation of phenotypes. For example, in the PGM3-CDG, part of

the mutant phenotype is susceptibility to infection. Therefore, A GlcNac-1-P supplement could be tested by comparing rate of infection pre and post supplementation.

Finally, our data suggests the UDP-GlcNAc salvage pathway and DPAGT1 regulate Wnt signaling in the early embryo. This is consistent with literature, which suggests DPAGT1 is in a positive feedback loop with Wnt (Fig. 6-16, 6-17, 6-18, 6-19). Inhibition of the enzymes NAGK, PGM3, UAP1, and DPAGT1 all inhibited Wnt activity in animal cap experiments. This suggest that the use of a Wnt agonist may relive the phenotype of patents with PGM3-CDG or DPAGT1-CDG. Creating a transgenic animals, with a knockout or conditional knockout (such as Cre-Lox) of these enzymes would allow for the testing of Wnt agonists in the survival and alleviation of mutant phenotypes.

The salvage pathway, DPAGT1 and cancer

Overexpression of UAP1, PGM3, and DPAGT1 have all been linked to cancer (Greig et al., 2007; Itkonen et al., 2015; Jamal et al., 2012 Munkley et al., 2016; Nita-Lazar et al., 2009; Ricciardiello et al., 2018). This suggests that PGM3, UAP1, and DPAGT1, could all be potential chemotherapy targets. Furthermore, our data suggest that the UDP-GlcNAc salvage pathways' effect on the free pool of UDP-GlcNAc may be the contributing factor in these cancers. Therefore, NAGK could also be a viable chemotherapy target. *In vitro* and *In vivo* studies could provide valuable data on the potential role of these enzymes in tumorigenesis and their viability as drug targets.

Final thought on kinases and phosphatase

In this work, I have shown that proper phosphorylation is important in *N*-glycosylation, Wnt signaling, anterior-posterior patterning, eye formation, ciliogenesis, chemosensation, mechanosensation, metabolism, and more. This wide array of phenotypes highlights the importance of both kinases and phosphatases. Precise control of these enzymes is essential for development and misregulation results in disease. It is important that the findings be expanded upon to further elucidate the functions of both Cdc14 and NAGK and their roles in human health and disease.

Reference

Aebi, M. (2013) N-linked protein glycosylation in the ER. *Biochim Biophys Acta* **1833**(11):2430-7.

Aguila, J. R., Suszko, J., Gibbs, A. G., Hoshizaki, D. K. (2007) The role of larval fat cells in adult *Drosophila melanogaster. J. Exp. Biol* **210**:956-963.

Ah-Fong, A. M., Judelson, H. S. (2003) Cell cycle regulator Cdc14 is expressed during sporulation but not hyphal growth in the fungus-like oomycete Phytophthora infestans. *Mol Microbiol* **50**(2):487-94.

Ah-Fong, A. M. V., Judelson, H. S. (2011) New Role for Cdc14 Phosphatase: Localization to Basal Bodies in the Oomycete Phytophthora and Its Evolutionary Coinheritance with Eukaryotic Flagella. *PLoS ONE* **6**(2):e16725.

Akbarzadeh, S., Wheldon, L. M., Sweet, S. M., Talma, S., Mardakheh, F. K., Heath, J. K. (2008). The deleted in brachydactyly B domain of ROR2 is required for receptor activation by recruitment of Src. *PLoS One* **3**(3):e1873.

Ali, Y. O., Escala, W., Ruan, K., Zhai, R. G. (2011). Assaying locomotor, learning, and memory deficits in Drosophila models of neurodegeneration. *J Vis Exp*.

Alonso, A., Sasin, J., Bottini, N., Friedberg, I., Osterman, A., Godzik, A., Hunter, T., Dixon, J., Mustelin, T. (2004). Protein tyrosine phosphatases in the human genome. *Cell* **117**:699-711.

Andreassen, P. R., Lacroix, F. B., Villa-Moruzzi, E., Margolis, R. L. (1998). Differential subcellular localization of protein phosphatase-1 alpha, gamma1, and delta isoforms during both interphase and mitosis in mammalian cells. *J. Cell Biol* **141**:1207-1215.

Angers, S., Moon, R. T. (2009) Proximal events in Wnt signal transduction. *Nat Rev Mol Cell Biol* **10**:468–477.

Anreiter, I., Vasquez, O. E., Allen, A. M., Sokolowski, M. B. (2016). Foraging Path-length Protocol for Drosophila melanogaster Larvae. *J Vis Exp*.

Apostolopoulou, A. A., Hersperger, F., Mazija, L., Widmann, A., Wust, A., Thum, A. S. (2014). Composition of agarose substrate affects behavioral output of Drosophila larvae. *Front Behav Neurosci* **8:**11.

Apweiler, R. (1999) On the frequency of protein glycosylation, as deduced from analysis of the SWISS-PROT database. *Biochimica et Biophysica Acta (BBA) - General Subjects* **1473**:4-8.

Argov, Z., Caraco, Y., Lau, H., Pestronk, A., Shieh, P. B., Skrinar, A., Koutsoukos, T., Ahmed, R., Martinisi, J., Kakkis, E. (2016) Aceneuramic acid extended release administration maintains upper limb muscle strength in a 48-week study of subjects with GNE myopathy: results from a phase 2, randomized, controlled study. *J Neuromuscul Dis* **3**:49–66.

Apweiler, R., Hermjakob, H., Sharon, N. (1999) On the frequency of protein glycosylation, as deduced from analysis of the SWISS-PROT database. *Biochim Biophys Acta*. **6**;1473(1):4-8.

Arrese, E. L., Soulages, J. L. (2010). Insect fat body: energy, metabolism, and regulation. *Annu Rev Entomol* **55**:207-25.

Avila, F. W., Ravi Ram, K., Bloch Qazi, M. C., Wolfner, M. F. (2010). Sex peptide is required for the efficient release of stored sperm in mated Drosophila females. *Genetics* **186**:595-600.

Avila, F. W., Sirot, L. K., LaFlamme, B. A., Rubinstein, C. D., Wolfner, M. F. (2011). Insect seminal fluid proteins: identification and function. *Annu Rev Entomol* **56**:21-40.

Avila, F. W., Wolfner, M. F. (2009). Acp36DE is required for uterine conformational changes in mated Drosophila females. *Proc Natl Acad Sci U S A* **106**:15796-800.

Bai, Y., Tan, X., Zhang, H., Liu, C., Zhao, B., Li, Y., Lu, L., Liu, Y., Zhou, J. (2014) Ror2 Receptor Mediates Wnt11 Ligand Signaling and Affects Convergence and Extension Movements in Zebrafish. *J Biol Chem* **289**(30):20664–20676.

Baig-Lewis, S., Peterson-Nedry, W., Wehrli, M. (2007) Wingless/Wnt signal transduction requires distinct initiation and amplification steps that both depend on Arrow/LRP. *Dev Biol* **306**:94–111.

Bänziger, C., Soldini, D., Schütt, C., Zipperlen, P., Hausmann, G., Basler, K. (2006) Wntless, a conserved membrane protein dedicated to the secretion of Wnt proteins from signaling cells. *Cell* **125**(3):509-22.

Bassermann, F., Frescas, D., Guardavaccaro, D., Busino, L., Peschiaroli, A., Pagano, M. (2008). The Cdc14B-Cdh1-Plk1 axis controls the G2 DNA-damage-response checkpoint. *Cell* **134**:256-267.

Batut, J., Vandel, L., Leclerc, C., Daguzan, C., Moreau, M., Neant, I. (2005) The Ca2+-induced methyltransferase xPRMT1b controls neural fate in amphibian embryo. *Proc Natl Acad Sci U S A* **102**:15128-15133.

Behrens, J., von Kries, J. P., Kühl, M., Bruhn, L., Wedlich, D., Grosschedl, R., Birchmeier, W. (1996) Functional interaction of beta-catenin with the transcription factor LEF-1. *Nature* **382**(6592):638-42.

Bembenek, J., Yu, H. (2001) Regulation of the anaphase-promoting complex by the human dual-specificity phosphatase hCdc14a. *J. Biol. Chem* **276**:48237-48242.

Benes, H., Spivey, D. W., Miles, J., Neal, K., Edmondson, R. G. (1990) Fat-body-specific expression of the Drosophila Lsp-2 gene. *SAAS Bull Biochem Biotechnol* **3**:129-33.

Berdougo, E., Nachury, M. V., Jackson, P. K., Jallepalli, P. V. (2008). The nucleolar phosphatase Cdc14B is dispensable for chromosome segregation and mitotic exit in human cells. *Cell Cycle* **7**:1184-90.

Berger, M., Chen, H., Reutter, W., Hinderlich, S. (2002) Structure and function of N-acetylglucosamine kinase. Identification of two active site cysteines. *Eur J Biochem* **269**:4212-4218.

Bhanot, P., Brink, M., Samos, C. H., Hsieh, J. C., Wang, Y., Macke, J. P., Andrew, D., Nathans, J., Nusse, R. (1996) A new member of the frizzled family from *Drosophila* functions as a Wingless receptor. *Nature* **382**:225–230.

Bianchi, P., Fermo, E., Vercellati, C., Boschetti, C., Barcellini, W., Iurlo, A., Marcello, A. P., Righetti, P. G., Zanella, A. (2009) Congenital dyserythropoietic anemia type II (CDAII) is caused by mutations in the *SEC23B* gene. *Hum Mutat* **30**:1292-1298.

Blau, N., Duran, M., Gibson, K. M., Vici, C. D. (2014) hysician's Guide to the Diagnosis, Treatment, and Follow-Up of Inherited Metabolic Diseases.

Blume, A., Berger, M., Benie, A.J., Peters, T., Hinderlich, S. (2008) Characterization of ligand binding to N-acetylglucosamine kinase studied by STD NMR. *Biochemistry* **47**:13138-13146.

Brodsky, M. H., Nordstrom, W., Tsang, G., Kwan, E., Rubin, G. M., Abrams, J. M. (2000). Drosophila p53 binds a damage response element at the reaper locus. *Cell* **101**:103-113.

Brody, T. (1999). The Interactive Fly: gene networks, development and the Internet. *Trends in Genetics* **15**:333-4.

Bryan Ray, L. (2010) Of Wnt, Prorenin Receptor, and V-ATPase. *Science Signaling* **106**(3):ec29

Bryja, V., Andersson, E. R., Schambony, A., Esner, M., Bryjová, L., Biris, K. K., Hall, A. C., Kraft, B., Cajanek, L., Yamaguchi, T. P., Buckingham, M., Arenas, E. (2009) The Extracellular Domain of Lrp5/6 Inhibits Noncanonical Wnt Signaling In Vivo. *Mol Biol Cell* **20**(3):924–936.

Buechling, T., Chaudhary, V., Spirohn, K., Weiss, M., Boutros, M. (2011) p24 proteins are required for secretion of Wnt ligands. *EMBO* **12**:1265–1272.

Buchman, J. J., Durak, O., Tsai, L. H. (2011). ASPM regulates Wnt signaling pathway activity in the developing brain. *Genes Dev* **25**(18):1909-1914.

Buffone, M. G., Schindler, K., Schultz, R. M. (2014). Over-expression of CDC14B causes mitotic arrest and inhibits zygotic genome activation in mouse preimplantation embryos. *Cell Cycle* **8**:3904-3913.

Butterworth, F. M., Bodenstein, D., King, R. C. (1965). Adipose tissue of Drosophila melanogaster. I. An experimental study of larval fat body. *Journal of Experimental Zoology* **158**:141-153.

Calaminus, S. D., Inman, G., Ghaevert, C., Sansom, O., Watson, S. P., Holyoake, T. L., Machesky, L. (2010). lterations In Wnt Signalling In the Megakaryocytic Lineage Leads to Bone Marrow Failure and Myelofibrosis. *Blood* **116**(21): 276-276.

Cavodeassi, F., Carreira-Barbosa, F., Young, R. M., Concha, M. L., Allende, M. L., Houart, C., Tada, M., Wilson, S. W. (2005) Early stages of zebrafish eye formation require the coordinated activity of Wnt11, Fz5, and the Wnt/beta-catenin pathway. *Neuron* **47**:43-56.

Chan, T. M., Longabaugh, W., Bolouri, H., Chen, H. L., Tseng, W. F., Chao, C. H., Jang, T. H., Lin, Y. I., Hung, S. C., Wang, H. D., Yuh, C. H. (2009) Developmental gene regulatory networks in the zebrafish embryo. *Biochim Biophys Acta* **1789**:279-298.

Chauhan, J. S., Rao, A., Raghava, G. P. S. (2013) In silico Platform for Prediction of N-, O- and C-Glycosites in Eukaryotic Protein Sequences. *PLoS One* **8**(6):e67008.

Chen, N. P., Uddin, B., Hardt, R., Ding, W., Panic, M., Lucibello, I., Kammerer, P., Ruppert, T., Schiebel, E. (2017) Human phosphatase CDC14A regulates actin organization through dephosphorylation of epithelial protein lost in neoplasm. *Proc Natl Acad Sci U S A* **114**(20):5201-5206.

Chen, N. P., Uddin, B., Voit, R., Schiebel, E. (2016) Human phosphatase CDC14A is recruited to the cell leading edge to regulate cell migration and adhesion. *Proc Natl Acad Sci U S A* **113**(4):990-5.

Chin, C. F., Bennett, A. M., Ma, W. K., Hall, M. C., Yeong, F. M. (2012) Dependence of Chs2 ER export on dephosphorylation by cytoplasmic Cdc14 ensures that septum formation follows mitosis. *Mol Biol Cell* **23**(1):45-58.

Cho, H. P., Liu, Y., Gomez, M., Dunlap, J., Tyers, M., Wang, Y. (2005). The dual-specificity phosphatase CDC14B bundles and stabilizes microtubules. *Mol Cell Biol* **25**:4541-51.

Chen, C. T., Peli-Gulli, M. P., Simanis, V., McCollum, D. (2006). S. pombe FEAR protein orthologs are not required for release of Clp1/Flp1 phosphatase from the nucleolus during mitosis. *J. Cell Sci* **119**:4462-4446.

Clement, A., Solnica-Krezel, L., Gould, K. L. (2011). The Cdc14B phosphatase contributes to ciliogenesis in zebrafish. *Development* **138**:291-302.

Clement, A., Solnica-Krezel, L., Gould, K. L. (2012). Functional redundancy between Cdc14 phosphatases in zebrafish ciliogenesis. *Dev Dyn* **241**:1911-21.

Clemente-Blanco, A., Mayan-Santos, M., Schneider, D. A., Machin, F., Jarmuz, A., Tschochner, H., Aragon, L. (2009). Cdc14 inhibits transcription by RNA polymerase I during anaphase. *Nature* **458**:219-22.

Clemente-Blanco, A., Sen, N., Mayan-Santos, M., Sacristan, M. P., Graham, B., Jarmuz, A., Giess, A., Webb, E., Game, L., Eick, D., Bueno, A., Merkenschlager, M., Aragón, L. (2011). Cdc14 phosphatase promotes segregation of telomeres through repression of RNA polymerase II transcription. *Nat Cell Biol* **13**:1450-6.

Clifford, D. M., Wolfe, B. A., Roberts-Galbraith, R. H., McDonald, W. H., Yates, J. R. 3rd, Gould, K. L. (2008). The Clp1/Cdc14 phosphatase contributes to the robustness of cytokinesis by association with anillin-related Mid1. *J Cell Biol* **181**:79-88.

Cook, B., Hardy, R. W., McConnaughey, W. B., Zuker C.S. (2008) Preserving cell shape under environmental stress. *Nature* **452:**361-364.

Cossins, J., Belaya, K., Hicks, D., Salih, M. A., Finlayson, S., Carboni, N., Liu, W. W., Maxwell, S., Zoltowska, K., Farsani, G. T., Laval, S., Seidhamed, M. Z.; WGS500 Consortium, Donnelly, P., Bentley, D., McGowan, S. J., Müller, J., Palace, J., Lochmüller, H., Beeson, D. (2013) Congenital myasthenic syndromes due to mutations in ALG2 and ALG14. *Brain* **136**(Pt 3):944-56.

Crowther, D. C., Kinghorn, K. J., Miranda, E., Page, R., Curry, J. A., Duthie, F. A., Gubb, D. C., Lomas, D. A. (2005). Intraneuronal Abeta, non-amyloid aggregates and neurodegeneration in a Drosophila model of Alzheimer's disease. *Neuroscience* **132**:123-35.

Cueille, N., Salimova, E., Esteban, V., Blanco, M., Moreno, S., Bueno, A., Simanis, V. (2001). Flp1, a fission yeast orthologue of the s. cerevisiae CDC14 gene, is not required for cyclin degradation or rum1p stabilisation at the end of mitosis. *J Cell Sci* **114**:2649-64.

D'Amours, D., Stegmeier, F., Amon, A. (2004). Cdc14 and condensin control the dissolution of cohesin-independent chromosome linkages at repeated DNA. *Cell* **117**:455-469.

D'Costalain, A., Shepherd, I. (2009) Zebrafish Development and Genetics: Introducing Undergraduates to Developmental Biology and Genetics in a Large Introductory Laboratory Class. *Zebrafish* **6**(2):169-77.

Datta, A. (1970) Studies on hog spleen kinase. I. Purification and properties of kinase. *Biochimica et Biophysica Acta (BBA) - Enzymology* **220**:51-60.

Davezac, N., Baldin, V., Gabrielli, B., Forrest, A., Theis-Febvre, N., Yashida, M., Ducommun, B. (2000). Regulation of CDC25B phosphatases subcellular localization. *Oncogene* **19**:2179-2185.

Davidson, G., Wu, W., Shen, J., Bilic, J., Fenger, U., Stannek, P., Glinka, A., Niehrs, C. (2005) Casein kinase 1 [gamma] couples Wnt receptor activation to cytoplasmic signal transduction. *Nature* **438**:867–872.

Delmaghani, S., Aghaie, A., Bouyacoub, Y., El Hachmi, H., Bonnet, C., Riahi, Z., Chardenoux, S., Perfettini, I., Hardelin, J. P., Houmeida, A. Herbomel, P., Petit, C. (2016) Mutations in CDC14A, encoding a protein phosphatase involved in hair cell ciliogenesis, cause autosomal-recessive severe to profound deafness. *Am. J. Hum*. *Genet* **98**:266–1270

Denecke, J., Marquardt, T. (2009) Congenital dyserythropoietic anemia type II (CDAII/HEMPAS): where are we now? *Biochim Biophys Acta* **1792**:915–920.

Dörre, K., Olczak, M., Wada, Y., Sosicka, P., Grüneberg, M., Reunert, J., Kurlemann, G., Fiedler, B., Biskup, S., Hörtnagel, K., Rust, S., Marquardt, T. (2015) A new case of UDP-galactose transporter deficiency (SLC35A2-CDG): molecular basis, clinical phenotype, and therapeutic approach. *J Inherit Metab Dis* **38**:931–940.

Doubravska, L., Krausova, M., Gradl, D., Vojtechova, M., Tumova, L., Lukas, J., Valenta, T., Pospichalova, V., Fafilek, B., Plachy, J., Sebesta, O., Korinek, V. (2011) Fatty acid modification of Wnt1 and Wnt3a at serine is prerequisite for lipidation at cysteine and is essential for Wnt signalling. *Cell Signal* **23**:837–48.

Dryden, S. C., Nahhas, F. A., Nowak, J. E., Goustin, A. S., Tainsky, M. A. (2003). Role for human SIRT2 NAD-dependent deacetylase activity in control of mitotic exit in the cell cycle. *Mol. Cell. Biol* **23**:3173-3185.

Duan, G. and Walther, D. (2015) The Roles of Post-translational Modifications in the Context of Protein Interaction Networks. *PLoS Comput Biol* **11**(2):e1004049.

Eissler, C. L., Mazón, G., Powers, B. L., Savinov, S. N., Symington, L. S., Hall, M. C. (2014) The Cdk/cDc14 module controls activation of the Yen1 holliday junction resolvase to promote genome stability. *Mol Cell* **54**(1):80-93.

Eklund, E. A., Freeze, H. H. (2006). The congenital disorders of glycosylation: a multifaceted group of syndromes. *NeuroRx* **3**:254-263.

Endo, T. (2015) Glycobiology of α-dystroglycan and muscular dystrophy. *J Biochem* **157**(1):1-12.

Erter, C., Wilm, T., Basler, N., Wright, C., Solnica-Krezel, L. (2001) Wnt8 is required in lateral mesendodermal precursors for neural posteriorization in vivo. *Development* **128**:3571-3583.

Esko, J.D., Lindahl, U. (2001) Molecular diversity of heparan sulfate. *J Clin Invest* **108**:169-173.

Essner, J. J., Amack, J. D., Nyholm, M. K., Harris, E. B., Yost, H. J. (2005) Kupffer's vesicle is a ciliated organ of asymmetry in the zebrafish embryo that initiates left-right development of the brain, heart and gut. *Development* **132**(6):1247-60.

Ferreira, C. R., Altassan, R., Marques-Da-Silva, D., Francisco, R., Jaeken, J, Morava, E. (2018) Recognizable phenotypes in CDG. *J Inherit Metab Dis* **41**(3):541-553.

Ferreira, I. G., Pucci, M., Venturi, G., Malagolini, N., Chiricolo, M., Dall'Olio, F. (2018) Glycosylation as a Main Regulator of Growth and Death Factor Receptors Signaling. *Int. J. Mol. Sci **19***(2):580.

Field, L. H., Matheson, T. (1998). Chordotonal organs of insects. *Advances in Insect Physiology* **27**:1-228.

Figueroa-Clarevega, A., Bilder, D. (2015). Malignant Drosophila tumors interrupt insulin signaling to induce cachexia-like wasting. *Dev Cell* **33**:47-55.

Fisher, K. H., Wright, V. M., Taylor, A., Zeidler, M. P., Brown, S. (2012). Advances in genome-wide RNAi cellular screens: a case study using the Drosophila JAK/STAT pathway. *BMC Genomics* **13**:506.

Forbes, A., Lehmann, R. (1998). Nanos and Pumilio have critical roles in the development and function of Drosophila germline stem cells. *Development* **125**:679-690.

Foulquier, F. (2009) COG defects, birth and rise! *Biochim Biophys Acta* **1792**:896–902.

Fox, C., Zou, J., Rappsilber, J., Marston, A. L. (2017) Cdc14 phosphatase directs centrosome re-duplication at the meiosis I to meiosis II transition in budding yeast. *Wellcome Open Res* **2**:2.

Freeze, H. H. (2006) Genetic defects in the human glycome. *Nat Rev Genet* **7**:537-551.

Freeze, H. H., Hart, G.W., Schnaar, R.L., 2015. Glycosylation Precursors, in: rd, Varki, A., Cummings, R.D., Esko, J.D., Stanley, P., Hart, G.W., Aebi, M., Darvill, A.G., Kinoshita, T., Packer, N.H., Prestegard, J.H., Schnaar, R.L., Seeberger, P.H. Essentials of Glycobiology, Third Edition ed. Cold Spring Harbor, Cold Spring Harbor (NY) pp. 51-63.

Galli, L. M., Barnes, T. L., Secrest, S. S., Kadowaki, T., Burrus, L. W. (2007) Porcupine-mediated lipid-modification regulates the activity and distribution of Wnt proteins in the chick neural tube. *Development* **134**(18):3339-48.

Ganetzky, R., Izumi, K., Edmondson, A., Muraresku, C. C., Zackai, E., Deardorff, M., Ganesh, J. (2015). Fetal akinesia deformation sequence due to a congenital disorder of glycosylation." *Am J Med Genet A* **167A**(10):2411-2417.

Gao, Z. H., Seeling, J. M., Hill, V., Yochum, A., Virshup, D. M. (2002) Casein kinase I phosphorylates and destabilizes the beta-catenin degradation complex. *Proc Natl Acad Sci U S A* **99:**1182-1187.

García-Luis, J., Clemente-Blanco, A., Aragón, L., Machín, F. (2014) Cdc14 targets the Holliday junction resolvase Yen1 to the nucleus in early anaphase. *Cell Cycle* **13**(9):1392-9.

Garcia-Garcia, M. J., Anderson, K. V. (2003). Essential role of glycosaminoglycans in Fgf signaling during mouse gastrulation. *Cell* **114**;727-737.

GindzieNski, A., Glowacka, D., Zwiez, K. (1974) Purification and Properties of N-Acetylglucosamine Kinase from Human Gastric Mucosa. *European Journal of Biochemistry* **43**:155-160.

Goentoro, L., Kirschner, M. W. (2009) Evidence that fold-change, and not absolute level, of beta-catenin dictates Wnt signaling. *Mol Cell* **36**:872–884.

Gong, W. J., Golic, K. G. (2003). Ends-out, or replacement, gene targeting in Drosophila. *Proc Natl Acad Sci U S A* **100**:2556-61.

Goudevenou, K., Martin, P., Yeh, Y., Jones, P., Sablitzky, F. (2011) Def6 Is Required for Convergent Extension Movements during Zebrafish Gastrulation Downstream of Wnt5b Signaling. *PLoS One* **6**(10):e26548.

Gramates, L. S., Marygold, S. J., dos Santos, G., Urbano, J-M., Antonazzo, G., Matthews, B. B., Rey, A. J., Tabone, C. J., Crosby, M. A., Emmert, D. B., Falls, K., Goodman, J. L., Hu, Y., Ponting, L., Schroeder, A. J., Strelets, V. B., Thurmond, J., Zhou, P.; the FlyBase Consortium. (2017). FlyBase at 25: looking to the future. *Nucleic* Acids Research **45**:D663-D671.

Gray, C. H., Good, V. M., Tonks, N. K., Barford, D. (2003) The structure of the cell cycle protein Cdc14 reveals a prolinedirected protein phosphatase. *EMBO J*, **22**(14):3524-35.

Green, J. L., Kuntz, S. G., Sternberg, P. W. (2008) Ror receptor tyrosine kinases: Orphans no more. *Trends Cell Biol* **18**:536–544.

Greenspan, P., Mayer, E. P., Fowler, S. D. (1985). Nile Red: A selective Fluorescent Stain for Intracellular Lipid Droplets. *The jouranl of Cell Biology* **100**:965-973.

Greenspan, R. J. (2004). Fly Pushing: The Theory and Practice of Drosophila Genetics. Cold Spring Harbor, NY: Cold Spring Harbor Laboratory Press.

Greig, K. T., Antonchuk, J., Metcalf, D., Morgan, P. O., Krebs, D. L., Zhang, J. G., Hacking, D. F., Bode, L., Robb, L., Kranz, C., de Graaf, C., Bahlo, M., Nicola, N. A., Nutt, S. L., Freeze, H. H., Alexander, W. S., Hilton, D. J., Kile, B. T. (2007) Agm1/Pgm3-mediated sugar nucleotide synthesis is essential for hematopoiesis and development. *Mol Cell Biol* **27**:5849-5859.

Grumolato, L., Liu, G., Mong, P., Mudbhary, R., Biswas, R., Arroyave, R., Vijayakumar, S., Economides, A. N., Aaronson, S. A. (2010) Canonical and noncanonical Wnts use a common mechanism to activate completely unrelated coreceptors. *Genes & Dev* **24**:2517-2530.

Gruneberg, U., Glotzer, M., Gartner, A., Nigg, E. A. (2002). The CeCDC-14 phosphatase is required for cytokinesis in the Caenorhabditis elegans embryo. *J. Cell Biol* **158**, 901-914.

Gu, F., Shi, H. J., Gao, L., Zhang, H. Y., Tao, Q. H. (2012) Maternal Mga is required for Wnt signaling and organizer formation in the early Xenopus embryo. *Acta Bioch Bioph Sin* **44**:939-947.

Guillamot, M., Manchado, E., Chiesa, M., Gomez-Lopez, G., Pisano, D. G., Sacristan, M. P., Malumbres, M. (2011). Cdc14b regulates mammalian RNA polymerase II and represses cell cycle transcription. *Sci Rep* **1**:189.

Guillard, M., Dimopoulou, A., Fischer, B., Morava, E., Lefeber, D. J., Kornak, U., Wevers, R. A. (2009) Vacuolar H^+ -ATPase meets glycosylation in patients with cutis laxa. *Biochim Biophys Acta* **1792**:903–914.

Gupta, R., Brunak, S. (2002) Prediction of glycosylation across the human proteome and the correlation to protein function. *Pacific Symposium on Biocomputing* **7**:310-322.

Gutierrez, E., Wiggins, D., Fielding, B., Gould, A. P. (2007). Specialized hepatocyte-like cells regulate Drosophila lipid metabolism. *Nature* **445**:275-80.

Ha, J. R., Hao, L., Venkateswaran, G., Huang, Y. H., Garcia, E., Persad, S. (2014) β-catenin is O-GlcNAc glycosylated at Serine 23: implications for β-catenin's subcellular localization and transactivator function. *Exp Cell Res* **321**(2):153-66.

Hainline, S. G., Rickmyre, J. L., Neitzel, L. R., Lee, L. A., Lee, E. (2014). The Drosophila MCPH1-B isoform is a substrate of the APCCdh1 E3 ubiquitin ligase complex. *Biol Open* **3**:669-76.

Hakomori, S. (2000) Traveling for the glycosphingolipid path. *Glycoconjugate Journal* **17**:627-647.

Haltiwanger, R. S., Lowe, J. B. (2004). Role of glycosylation in development. *Annu Rev Biochem* **73**:491-537.

Hanks, S. K., Hunter, T. Protein kinases 6. (1995) The eukaryotic protein kinase superfamily: kinase (catalytic) domain structure and classification. *Faseb J* **9**(8):576–96.

Harms, H., Zimmer, K., Kurnik, K., Bertele-Harms, R., Weidinger, S., Reiter, K. (2007) Oral mannose therapy persistently corrects the severe clinical symptoms and biochemical abnormalities of phosphomannose isomerase deficiency. *ACTA Paediatrica* **91**:1065-1072.

Hartwell, L.H., Culotti, J., Pringle, J.R. and Reid, BJ (1974). Genetic control of the cell division cycle in yeast. *Science* **183** (4120):46–51.

Hatano, Y., Naoki, K., Suzuki, A., Ushimaru, T. (2016) Positive feedback promotes mitotic exit via the APC/C-Cdh1-separase-Cdc14 axis in budding yeast. *Cell Signal* **28**(10):1545-54.

He, X., Saint, J. J., Wang, Y., Nathans, J., Dawid, I., Varmus, H. (1997) A member of the Frizzled protein family mediating axis induction by Wnt-5A. *Science* **275**:1652–54

Heifetz, A., Keenan, R. W., Elbein, A. D. (1979) Mechanism of action of tunicamycin on the UDP-GlcNAc: dolichyl-phosphate Glc-NAc-1-phosphate transferase. *Biochemistry* **18**:2186-2192.

Heine, C., Koch, B., Storch, S., Kohlschütter, A., Palmer, D. N., Braulke T. (2004) Defective endoplasmic reticulum-resident membrane protein CLN6 affects lysosomal degradation of endocytosed arylsulfatase A. *J Biol Chem* **21**:22347-52.

Heisenberg, C. P., Houart, C., Take-Uchi, M., Rauch, G. J., Young, N., Coutinho, P., Masai, I., Caneparo, L., Concha, M. L., Geisler, R., Dale, T. C., Wilson, S. W., Stemple, D. L. (2001) A mutation in the Gsk3-binding domain of zebrafish Masterblind/Axin1 leads to a fate transformation of telencephalon and eyes to diencephalon. *Genes Dev* **15**:1427-1434.

Heisenberg, C. P., Tada, M., Rauch, G. J., Saude, L., Concha, M. L., Geisler, R., Stemple, D. L., Smith, J. C., Wilson, S. W. (2000) Silberblick/Wnt11 mediates convergent extension movements during zebrafish gastrulation. *Nature* **405**:76-81.

Herr, P., Basler, K. (2011) Porcupine-mediated lipidation is required for Wnt recognition by Wls. *Dev Biol* **361**:392–402.

Higuchi, T., Uhlmann, F. (2005). Stabilization of microtubule dynamics at anaphase onset promotes chromosome segregation. *Nature* **433**:171-176.

Hikasa, H., Sokol, S. Y. (2013) Wnt signaling in vertebrate axis specification. *Cold Spring Harb Perspect Biol* **5**:a007955.

Hinderlich, S., Berger, M., Schwarzkopf, M., Effertz, K., Reutter, W. (2000) Molecular cloning and characterization of murine and human N-acetylglucosamine kinase. *Eur J Biochem* **267**:3301-3308.

Hino, S., Michiue, T., Asashima, M., Kikuchi, A. (2003) Casein kinase I epsilon enhances the binding of Dvl-1 to Frat-1 and is essential for Wnt-3a-induced accumulation of beta-catenin. *J Biol Chem* **278**.

Hiramoto, T., Ebihara, Y., Mizoguchi, Y., Nakamura, K., Yamaguchi, K., Ueno, K., Nariai, N., Mochizuki, S., Yamamoto, S., Nagasaki, M., Furukawa, Y., Tani, K., Nakauchi, H., Kobayashi, M., Tsuji K. (2013). Wnt3a stimulates maturation of impaired neutrophils developed from severe congenital neutropenia patient-derived pluripotent stem cells. *Proc Natl Acad Sci U S A* **110**(8):3023-3028.

Höck, M., Wegleiter, K., Ralser, E., Kiechl-Kohlendorfer, U., Scholl-Bürgi, S., Fauth, C., Steichen, E., Pichler, K., Lefeber, D. J., Matthjis, G., Keldermans, L., Maurer, K., Zschocke, J., Holmen, S. L., Salic, A., Zylstra, C. R., Kirschner, M. W., Williams, B. O. (2002) A novel set of Wnt-Frizzled fusion proteins identifies receptor components that activate beta -catenin-dependent signaling. *J Biol Chem* **277**:34727-35.

Holt, L. J., Krutchinsky, A. N., Morgan, D. O. (2008). Positive feedback sharpens the anaphase switch. *Nature* **454**:353-357.

Hsieh, J. C., Rattner, A., Smallwood, P. M., Nathans, J. (1999) Biochemical characterization of Wnt-frizzled interactions using a soluble, biologically active vertebrate Wnt protein. *Proc Natl Acad Sci U S A* **96**(7):3546-51.

Huey R. B., Suess, J., Hamilton, H., Gilchrist, G. W. (2004). Starvation resistance in Drosophila melanogaster: testing for a possible 'cannibalism' bias. *Functional Ecology* **18**:952-954.

Hurley, J. H. (1996) The sugar kinase/heat shock protein 70/actin superfamily: implications of conserved structure for mechanism. *Annu Rev Biophys Biomol Struct* **25**:137-162.

Hwa, K. (2001) Glycosyl Phosphatidylinositol-Linked Glycoconjugates: Structure, Biosynthesis and function. *Adv Exp Med Biol* **491**:207-214.

Imtiaz, A., Belyantseva, I. A., Beirl, A. J., Fenollar-Ferrer, C., Bashir, R., Bukhari, I., Bouzid, A., Shaukat, U., Azaiez, H., Booth, K. T., Kahrizi, K., Najmabadi, H., Maqsood, A., Wilson, E. A., Fitzgerald, T. S., Tlili, A., Olszewski, R., Lund, M., Chaudhry, T., Rehman, A. U., Starost, M. F., Waryah, A. M., Hoa, M., Dong, L., Morell, R. J., Smith, R. J. H., Riazuddin, S., Masmoudi, S., Kindt, K. S., Naz, S., Friedman, T. B. (2018) CDC14A phosphatase is essential for hearing and male fertility in mouse and human. *Hum Mol Genet* **27**(5):780-798.

Islam, M. A., Sharif, S. R., Lee, H., Moon, I. S. (2015). N-Acetyl-D-Glucosamine Kinase Promotes the Axonal Growth of Developing Neurons. *Mol Cells* **38**:876-885.

Islam, M. A., Sharif, S. R., Lee, H., Seog, D. H., Moon, I. S. (2015) N-acetyl-D-glucosamine kinase interacts with dynein light-chain roadblock type 1 at Golgi outposts in neuronal dendritic branch points. *Exp Mol Med* **47**:e177.

Itkonen, H. M., Engedal, N., Babaie, E., Luhr, M., Guldvik, I. J., Minner, S., Hohloch, J., Tsourlakis, M. C., Schlomm, T., Mills, I. G. (2015) UAP1 is overexpressed in prostate cancer and is protective against inhibitors of N-linked glycosylation. *Oncogene* **34**:3744-3750.

Jaeken, J. (2011) Congenital disorders of glycosylation (CDG): it's (nearly) all in it! *J Inherit Metab Dis* **34**(4):853-858.

Jaeken, J., Matthijs, G. (2007) Congenital disorders of glycosylation: a rapidly expanding disease family. *Annu Rev Genomics Hum Genet* **8**:261-78.

Jaeken, J., Péanne, R. (2017) What is new in CDG? *J Inherit Metab Dis* **40**(4):569–586.

Jaeken, J., van den Heuvel, L. (2014) Congenital Disorders of Glycosylation, Physician's guide to the diagnosis, treatment, and follow-up of inherited metabolic diseases. Springer-Verlag Berlin Heidelberg, New York, pp. 483-512.

Jaeken, J., van Eijk, H. G., van der Heul, C., Corbeel, L., Eeckels, R., Eggermont, E. (1984) Sialic acid-deficient serum and cerebrospinal fluid transferrin in a newly recognized genetic syndrome. Clin Chim Acta. **144**(2-3):245-7.

Jaeken, J., Matthijs, G., Lefeber, D., Wevers, R. A. (2016) ALG6-CDG: a recognizable phenotype with epilepsy, proximal muscle weakness, ataxia and behavioral and limb anomalies. J *Inherit Metab Dis* **39**(5):713-723.

Jamal, B., Sengupta, P. K., Gao, Z. N., Nita-Lazar, M., Amin, B., Jalisi, S., Bouchie, M. P., Kukuruzinska, M. A. (2012) Aberrant amplification of the crosstalk between canonical Wnt signaling and N-glycosylation gene DPAGT1 promotes oral cancer. *Oral Oncol* **48**:523-529.

Jana, S. C., Mendonça, S., Werner, S., Bettencourt-Dias, M. (2016) Methods to Study Centrosomes and Cilia in Drosophila. *Methods Mol Biol* **1454**:215-36.

Jaspersen, S. L., Morgan, D. O. (2000). Cdc14 activates Cdc15 to promote mitotic exit in budding yeast. *Curr. Biol* **10**:615-618.

Jin, Z., Schwend, T., Fu, J., Bao, Z., Liang, J., Zhao, H., Mei, W., Yang, J. (2016) Members of the Rusc protein family interact with Sufu and inhibit vertebrate Hedgehog signaling. *Development* **143**:3944-3955.

Jung, H., Lee, S. K., Jho, E. (2011) Mest/Peg1 inhibits Wnt signalling through regulation of LRP6 glycosylation. *Biochemical Journal* **436**(2):263-269.

Kadowaki, T., Wilder, E., Klingensmith, J., Zachary, K., Perrimon, N. (1996) The segment polarity gene porcupine encodes a putative multitransmembrane protein involved in Wingless processing. *Genes Dev* **10**(24):3116-28.

Kaessmann, H. (2008). Birth and rapid subcellular adaptation of a hominoid-specific CDC14 protein. *PLoS Biol* **6**:e140.

Kaiser, B. K., Nachury, M. V., Gardner, B. E., Jackson, P. K. (2004). Xenopus Cdc14 alpha/beta are localized to the nucleolus and centrosome and are required for embryonic cell division. *BMC Cell Biol* **5**:27.

Kaiser, B. K., Zimmerman, Z. A., Charbonneau, H., Jackson, P. K. (2002). Disruption of centrosome structure, chromosome segregation, and cytokinesis by misexpression of human Cdc14A phosphatase. *Mol. Biol. Cell* **13**:2289-2300.

Kao, L., Wang, Y., Chen, Y., Tseng, S., Jhang, J., Chen, Y., Teng, S. (2014) Global Analysis of Cdc14 Dephosphorylation Sites Reveals Essential Regulatory Role in Mitosis and Cytokinesis. *Mol Cell Proteomics* **13**(2):594–605.

Karall, D. (2015) ALG8-CDG: novel patients and review of the literature. *Orphanet J Rare Dis*. **10**:73.

Kategaya, L. S., Changkakoty, B., Biechele, T., Conrad, W. H., Kaykas, A., DasGupta, R., Moon, R. T. (2009) Bili Inhibits Wnt/β-Catenin Signaling by Regulating the Recruitment of Axin to LRP6. *PLoS One* **4**(7):e6129.

Keil, T. A. (1997). Functional morphology of insect mechanoreceptors. *Microsc Res Tech* **39**:506-31.

Kernan, M., Cowan, D., Zuker, C. (1994). Genetic dissection of mechanosensory transduction: mechanoreception-defective mutations of Drosophila. *Neuron* **12**:1195-206.

Khan, Z., Vijayakumar, S., de la Torre, T. V., Rotolo, S., Bafico, A. (2007) Analysis of endogenous LRP6 function reveals a novel feedback mechanism by which Wnt negatively regulates its receptor. *Mol. Cell. Biol* **27**:7291–7301.

Khmelinskii, A., Lawrence, C., Roostalu, J., Schiebel, E. (2007). Cdc14-regulated midzone assembly controls anaphase B. *J. Cell Biol* **177**:981-993.

Khmelinskii, A., Roostalu, J., Roque, H., Antony, C., Schiebel, E. (2009). Phosphorylation-dependent protein interactions at the spindle midzone mediate cell cycle regulation of spindle elongation. *Dev. Cell* **17**:244-256.

Kiecker, C., Niehrs, C. (2013) The Role of Wnt Signaling in Vertebrate Head Induction and the Organizer-Gradient Model Dualism. *Landes Bioscience.*

Kikuchi, A., Yamamoto, H., Sato, A. (2009) Selective activation mechanisms of Wnt signaling pathways. *Trends Cell Biol* **19**:119–129.

Kim, C., Oda, T., Itoh, M., Jiang, D., Artinger, K., Chandrasekharappa, S., Driever, W., Chitnis, A. (2000) Repressor activity of Headless/Tcf3 is essential for vertebrate head formation. *Nature* **407**:913-916.

Kipreos, E. T. (2004). Developmental quiescence: Cdc14 moonlighting in G1. *Nat. Cell Biol* **6**:693-695.

Kobayashi, S., Yamada, M., Asaoka, M., Kitamura, T. (1996). Essential role of the posterior morphogen nanos for germline development in Drosophila. *Nature* **380**:708-11.

Koch, J., Mayr, J. A., Alhaddad, B., Rauscher, C., Bierau, J., Kovacs-Nagy, R., Coene, K. L., Bader, I., Holzhacker, M., Prokisch, H., Venselaar, H., Wevers, R. A., Distelmaier, F., Polster, T., Leiz, S., Betzler, C., Strom, T. M., Sperl, W., Meitinger, T., Wortmann, S. B., Haack, T. B. (2017) CAD mutations and uridine-responsive epileptic encephalopathy. *Brain* **140**:279-286.

Komekado, H., Yamamoto, H., Chiba, T., Kikuchi, A. (2007) Glycosylation and palmitoylation of Wnt-3a are coupled to produce an active form of Wnt-3a. *Genes Cells* **12**(4):521-34.

Kondo, A., Mostofa, M. G., Miyake, K., Terasawa, M., Nafisa, I., Yeasmin, A. M. S. T., Waliullah, T. M., Kanki, T., Ushimaru, T. (2018) Cdc14 Phosphatase Promotes TORC1-Regulated Autophagy in Yeast. *J Mol Biol* **25**;430(11):1671-1684.

Konig, C., Maekawa, H., Schiebel, E. (2010). Mutual regulation of cyclin-dependent kinase and the mitotic exit network. *J. Cell Biol* **188**:351-368.

Kornak, U., Reynders, E., Dimopoulou, A., van Reeuwijk, J., Fischer, B., Rajab, A., Budde, B., Nürnberg, P., Foulquier, F.; ARCL Debré-type Study Group, Lefeber, D., Urban, Z., Gruenewald, S., Annaert, W., Brunner, H. G., van Bokhoven, H., Wevers, R., Morava, E., Matthijs, G., Van Maldergem, L., Mundlos, S. (2008) Impaired glycosylation and cutis laxa caused by mutations in the vesicular H^+-ATPase subunit ATP6V0A2. *Nat Genet* **40**:32–34.

Kornfeld, R., Kornfeld, S. (1976) Comparative aspects of glycoprotein structure. *Annu Rev Biochem* **45**:217-237.

Krasinska, L., de Bettignies, G., Fisher, D., Abrieu, A., Fesquet, D., Morin, N. (2007). Regulation of multiple cell cycle events by Cdc14 homologues in vertebrates. *Exp Cell Res* **313**:1225-39.

Krasnewich, D. M., Holt, G. D., Brantly, M., Skovby, F., Redwine, J., Gahl, W. A. (1995) Abnormal synthesis of dolichol-linked oligosaccharides in carbohydrate-deficient glycoprotein syndrome. *Glycobiology*. **5**(5):503-10.

Krawitz, P. M., Schweiger, M. R., Rödelsperger, C., Marcelis, C., Kölsch, U., Meisel, C., Stephani, F., Kinoshita, T., Murakami, Y., Bauer, S., Isau, M., Fischer, A., Dahl, A., Kerick, M., Hecht, J., Köhler, S., Jäger, M., Grünhagen, J., de Condor, B. J., Doelken, S., Brunner, H. G., Meinecke, P., Passarge, E., Thompson, M. D., Cole, D. E., Horn, D., Roscioli, T., Mundlos, S., Robinson, P. N. (2010) Identity-by-descent filtering of exome sequence data identifies *PIGV* mutations in hyperphosphatasia mental retardation syndrome. *Nat Genet* **42**:827–829.

Kumawat, K., Gosens, R. (2016) WNT-5A: signaling and functions in health and disease. *Cell Mol Life Sci* **73**:567–587.

Kurayoshi, M., Yamamoto, H., Izumi, S., Kikuchi, A. (2007) Post-translational palmitoylation and glycosylation of Wnt-5a are necessary for its signalling. *Biochem J* **402**:515–523.

Lai, s., Chien, A. J., Moon, R. T. (2009) Wnt/Fz signaling and the cytoskeleton: potential roles in tumorigenesis. *Cell Research* **19**:532–545.

Laurencon, A., Dubruille, R., Efimenko, E., Grenier, G., Bissett, R., Cortier, E., Rolland, V., Swoboda, P., Durand, B. (2007). Identification of novel regulatory factor X (RFX) target genes by comparative genomics in Drosophila species. *Genome Biol* **8**:R195.

Lee, E., Salic, A., Krüger, R., Heinrich, R., Kirschner, M. W. (2003) The roles of APC and Axin derived from experimental and theoretical analysis of the Wnt pathway. *PLoS Biol* **1**(1):E10.

Lee, E., Sivan-Loukianova, E., Eberl, D. F. and Kernan, M. J. (2008). An IFT-A Protein Is Required to Delimit Functionally Distinct Zones in Mechanosensory Cilia. *Current Biology* **18**:1899-1906.

Lee, H., Cho, S. J., Moon, I. S. (2014) The non-canonical effect of N-acetyl-D-glucosamine kinase on the formation of neuronal dendrites. *Mol Cells* **37**:248-256.

Lee, H., Dutta, S., Moon, I. S. (2014) Upregulation of dendritic arborization by N-acetyl-D-glucosamine kinase is not dependent on its kinase activity. *Mol Cells* **37**:322-329.

Lee, K. P., Jang, T. (2014). Exploring the nutritional basis of starvation resistance in Drosophila melanogaster. *Functional Ecology* **28**:1144-1155.

Lehrman, M. A., Zhu, X. Y., Khounlo, S. (1988) Amplification and molecular cloning of the hamster tunicamycin-sensitive N-acetylglucosamine-1-phosphate transferase gene. The hamster and yeast enzymes share a common peptide sequence. *J Biol Chem* **263**:19796-19803.

Lekven, A., Thorpe, C., Waxman, J., Moon, R. (2001) Zebrafish wnt8 encodes two wnt8 proteins on a bicistronic transcript and is required for mesodermand neurectoderm patterning *Dev Cell* 103-114.

Li, C., Cao, S., Zhang, C., Zhang, Y., Zhang, Q., Xu, J. R., Wang, C. (2018) MoCDC14 is important for septation during conidiation and appressorium formation in Magnaporthe oryzae. *Mol Plant Pathol* **19**(2):328-340.

Li, C., Melesse, M., Zhang, S., Hao, C., Wang, C., Zhang, H., Hall, M. C., Xu, J. R. (2015) FgCDC14 regulates cytokinesis, morphogenesis, and pathogenesis in Fusarium graminearum. *Mol Microbiol* **98**(4):770-86.

Li, L., Ljungman, M., Dixon, J. E. (2000). The Human Cdc14 Phosphatases Interact with and Dephosphorylate the Tumor Suppressor Protein p53. *Journal of Biological Chemistry* **275**:2410-2414.

Liem, Y. S., Bode, L., Freeze, H. H., Leebeek, F. W., Zandbergen, A. A., Paul Wilson, J. (2008) Using heparin therapy to reverse protein-losing enteropathy in a patient with CDG-Ib. *Nat Clin Pract Gastroenterol Hepatol* **5**:220-224.

Lilly, M., Carlson, J. (1990). smellblind: A Gene Required for Drosophila Olfaction *Genetic Society of America* 293-302.

Lin, H., Ha, K., Lu, G., Fang, X., Cheng, R., Zuo, Q., Zhang, P. Cdc14A and Cdc14B Redundantly Regulate DNA Double-Strand Break Repair. *Mol Cell Biol* **35**(21):3657-68.

Lippincott, J., Shannon, K. B., Shou, W., Deshaies, R. J., Li, R. (2001). The Tem1 small GTPase controls actomyosin and septin dynamics during cytokinesis. *J. Cell Sci* **114**:1379-1386.

Liu, D., Vleugel, M., Backer, C. B., Hori, T., Fukagawa, T., Cheeseman, I. M., Lampson, M. A. (2010). Regulated targeting of protein phosphatase 1 to the outer kinetochore by KNL1 opposes Aurora B kinase. *J. Cell Biol* **188**:809-820.

Liu, X., Jiang, F., Kalidas, S., Smith, D., Liu, Q. (2006). Dicer-2 and R2D2 coordinately bind siRNA to promote assembly of the siRISC complexes. *RNA* **12**:1514-20.

Lu, Y., Cross, F. R. (2010) This observation together with its mechanism suggests that the intrinsically autonomous Cdc14 release cycles are locked. *Cell* **141**(2):268–279.

Lübbehusen, J., Thiel, C., Rind, N., Ungar, D., Prinsen, B. H., de Koning, T. J., van Hasselt, P. M., Körner, C. (2010) Fatal outcome due to deficiency of subunit 6 of the conserved oligomeric Golgi complex leading to a new type of congenital disorders of glycosylation. *Hum Mol Genet* **19**:3632–3633.

Ma, L., Jarman, A. P. (2011). Dilatory is a Drosophila protein related to AZI1 (CEP131) that is located at the ciliary base and required for cilium formation. *J Cell Sci* **124**:2622-30.

MacDonald, B.T., Tamai, K., He, X. (2009) Wnt/beta-catenin signaling: components, mechanisms, and diseases. *Dev Cell* **17**(1):9-26.

Machin, F., Quevedo, O., Ramos-Perez, C., Garcia-Luis, J. (2016). Cdc14 phosphatase: warning, no delay allowed for chromosome segregation! *Curr Genet* **62**:7-13.

Maggert, K. A., Gong, W. J., Golic, K. G. (2008). Methods for homologous recombination in Drosophila. *Methods Mol Biol* **420**:155-74.

Mahalingam, B., Cuesta-Munoz, A., Davis, E. A., Matschinsky, F. M., Harrison, R. W., Weber, I. T. (1999) Structural model of human glucokinase in complex with glucose and ATP: implications for the mutants that cause hypo- and hyperglycemia. *Diabetes* **48**:1698-1705.

Mailand, N., Lukas, C., Kaiser, B. K., Jackson, P. K., Bartek, J., Lukas, J. (2002). Deregulated human Cdc14A phosphatase disrupts centrosome separation and chromosome segregation. *Nat. Cell Biol*. **4**:317-322.

Malhotra, D., Yang, Y. (2014). Wnts' fashion statement: from body stature to dysplasia. *Bonekey Rep* **3**:541.

Maltese, C. E., Conigliaro, G., Shaw, D. S. (1995) The development of sporangia of Phytophthora infestans. *Mycol Res* **99**:1175–1181.

Manning, G., Whyte, D. B., Martinez, R., Hunter, T., Sudarsanam, S. (2002). The protein kinase complement of the human genome. *Science* **298**:1912-1934.

Manzoni, R., Montani, F., Visintin, C., Caudron, F., Ciliberto, A., Visintin, R. (2010) Oscillations in Cdc14 release and sequestration reveal a circuit underlying mitotic exit. *J Cell Biol* **190**(2):209.

Mao, J., Wang, J., Liu, B., Pan, W., Farr, G. H. 3rd, Flynn, C., Yuan, H., Takada, S., Kimelman, D., Li, L., Wu, D. (2001) Low-density lipoprotein receptor-related protein-5 binds to Axin and regulates the canonical Wnt signaling pathway. *Mol Cell* **7**(4):801-9.

Marks, G. E. (1965) The cytology of *Phytophthora infestans*. *Chromosoma* **16**:681–692.

Marquardt, T., Luhn, K., Srikrishna, G., Freeze, H.H., Harms, E., Vestweber, D. (1999) Correction of leukocyte adhesion deficiency type II with oral fucose. *Blood* **94**:3976-3985.

Mason, J. O., Kitajewski, J., Varmus, H. E. (1992) Mutational analysis of mouse Wnt-1 identifies two temperature-sensitive alleles and attributes of Wnt-1 protein essential for transformation of a mammary cell line. *Mol Biol Cell* **3**:521–33.

Matos-Perdomo, E., Machín, F. (2018) The ribosomal DNA metaphase loop of Saccharomyces cerevisiae gets condensed upon heat stress in a Cdc14-independent TORC1-dependent manner. *Cell Cycle* **17**(2):200-215.

Matsui, T., Raya, A., Kawakami, Y., Callol-Massot, C., Capdevila, J., Rodriguez-Esteban, C., Izpisua Belmonte, J. C. (2005) Noncanonical Wnt signaling regulates midline convergence of organ primordia during zebrafish development. *Genes Dev* **19**:164-175.

Matthijs, G., Schollen, E., Pardon, E., Veiga-Da-Cunha, M., Jaeken, J., Cassiman, J. J., Van Schaftingen, E. (1997) Mutations in PMM2, a phosphomannomutase gene on chromosome 16p13, in carbohydrate-deficient glycoprotein type I syndrome (Jaeken syndrome). *Nat Genet* **16**(1):88-92.

McMahon, A. P., Moon, R. T. (1989) Ectopic expression of the proto-oncogene int-1 in Xenopus embryos leads to duplication of the embryonic axis. *Cell* **58**:1075-1084.

Meitinger, F., Petrova, B., Lombardi, I. M., Bertazzi, D. T., Hub, B., Zentgraf, H., Pereira, G. (2010). Targeted localization of Inn1, Cyk3 and Chs2 by the mitotic-exit network regulates cytokinesis in budding yeast. *J. Cell Sci*. **123**:1851-1861.

Menssen, R., Neutzner, A., Seufert, W. (2001). Asymmetric spindle pole localization of yeast Cdc15 kinase links mitotic exit and cytokinesis. *Curr. Biol* **11**:345-350.

Miller, D. P., Hall, H., Chaparian, R., Mara, M., Mueller, A., Hall, M. C., Shannon, K. B. (2015) Dephosphorylation of Iqg1 by Cdc14 regulates cytokinesis in budding yeast. *Mol Biol Cell* **26**(16):2913-26

Mir, A., Kofron, M., Heasman, J., Mogle, M., Lang, S., Birsoy, B., Wylie, C. (2008) Long- and short-range signals control the dynamic expression of an animal hemisphere-specific gene in Xenopus. *Dev Biol* **315**:161-172.

Miwa, I., Mita, Y., Murata, T., Okuda, J., Sugiura, M., Hamada, Y., Chiba, T. (1994) Utility of 3-O-methyl-N-acetyl-D-glucosamine, an N-acetylglucosamine kinase inhibitor, for accurate assay of glucokinase in pancreatic islets and liver. *Enzyme Protein* **48**:135-142.

Miyamoto, T., Wright, G., Amrein, H. (2013) Nutrient sensors. *Current Biology* **9**(23):R369–R373

Miyazaki, A., Ishii, K., Yamashita, S., Nejigane, S., Matsukawa, S., Ito, Y., Onuma, Y., Asashima, M., Michiue, T. (2012) mNanog possesses dorsal mesoderm-inducing ability by modulating both BMP and Activin/nodal signaling in Xenopus ectodermal cells. *PLoS One* **7**:e46630.

Mocciaro, A., Berdougo, E., Zeng, K., Black, E., Vagnarelli, P., Earnshaw, W., Gillespie, D., Jallepalli, P., Schiebel, E. (2010). Vertebrate cells genetically deficient for Cdc14A or Cdc14B retain DNA damage checkpoint proficiency but are impaired in DNA repair. *J Cell Biol* **189**:631-9.

Mocciaro, A., Schiebel, E. (2010) Cdc14: a highly conserved family of phosphatases with non-conserved functions? *J Cell Sci*. **123**(Pt 17): p. 2867-76.

Molenaar, M., van de Wetering, M., Oosterwegel, M., Peterson-Maduro, J., Godsave, S., Korinek, V., Roose, J., Destree, O., Clevers, H. (1996) XTcf-3 transcription factor mediates beta-catenin-induced axis formation in *Xenopus* embryos. *Cell* **86**:391–399.

Moloney, D. J., Panin, V. M., Johnston, S. H., Chen, J., Shao, L., Wilson, R., Wang, Y., Stanley, P., Irvine, K. D., Haltiwanger, R. S., Vogt, T. F. (2000). Fringe is a glycosyltransferase that modifies Notch. *Nature* **406**:369-375.

Momoi, A., Yoda, H., Steinbeisser, H., Fagotto, F., Kondoh, H., Kudo, A., Driever, W., Furutani-Seiki, M. (2003) Analysis of Wnt8 for neural posteriorizing factor by identifying Frizzled 8c and Frizzled 9 as functional receptors for Wnt8. *Mech Dev* **120**:477-489.

Morava, E. (2014) Galactose supplementation in phosphoglucomutase-1 deficiency: review and outlook for a novel treatable CDG. *Mol Genet Metab* **112**:275–279.

Morava, E., Lefeber, D. J., Urban, Z., de Meirleir, L., Meinecke, P., Gillessen Kaesbach, G., Sykut-Cegielska, J., Adamowicz, M., Salafsky, I., Ranells, J., Lemyre, E., van Reeuwijk, J., Brunner, H. G., Wevers, R. A. (2008) Defining the phenotype in an autosomal recessive cutis laxa syndrome with a combined congenital defect of glycosylation. *Eur J Hum Genet* **16**:28–35.

Morava, E., Tiemes, V., Thiel, C., Seta, N., de Lonlay, P., de Klerk, H., Mulder, M., Rubio-Gozalbo, E., Visser, G., van Hasselt, P., Horovitz, D. D. G., de Souza, C. F. M., Schwartz, I. V. D., Green, A., Al-Owain, M., Uziel, G., Sigaudy, S., Chabrol, B., van Spronsen, F. J., Steinert, M., Komini, E., Wurm, D., Bevot, A., Ayadi, A., Huijben, K., Dercksen, M., Witters, P., Tham, E., Eklund, E. A., Hammarsjö, A., Bengtson, P., Geiberger, S., Lagerstedt-Robinson, K., Malmgren, H., Nilsson, D., Grigelionis, G., Conner, P., Lindgren, P., Lindstrand, A., Wedell, A., Albåge, M., Zielinska, K., Nordgren, A., Papadogiannakis, N., Nishimura, G., Grigelioniene, G. (2016) A novel phenotype in N-glycosylation disorders: Gillessen-Kaesbach-Nishimura skeletal dysplasia due to pathogenic variants in ALG9. *Eur J Hum Genet* **24**(2):198-207.

Morava, E., Wopereis, S., Coucke, P., Gillessen-Kaesbach, G., Voit, T., Smeitink, J., Wevers, R., Grünewald, S. (2005) Defective protein glycosylation in patients with cutis laxa syndrome. *Eur J Hum Genet* **13**:414–421.

Morava, E., Zeevaert, R., Korsch, E., Huijben, K., Wopereis, S., Matthijs, G., Keymolen, K., Lefeber, D. J., De Meirleir, L., Wevers, R. A. (2007) A common mutation in the COG7 gene with a consistent phenotype including microcephaly, adducted thumbs, growth retardation, VSD and episodes of hyperthermia. *Eur J Hum Genet* **15**:638–645.

Moriishi, T., Shibata, Y., Tsukazaki, T., Yamaguchi, A. (2005) Expression profile of Xenopus banded hedgehog, a homolog of mouse Indian hedgehog, is related to the late development of endochondral ossification in Xenopus laevis. *Biochem Biophys Res Commun* **328**:867-873.

Munkley, J., Vodak, D., Livermore, K.E., James, K., Wilson, B. T., Knight, B., McCullagh, P., McGrath, J., Crundwell, M., Harries, L. W., Leung, H. Y., Robson, C. N., Mills, I. G., Rajan, P., Elliott, D. J. (2016) Glycosylation is an Androgen-Regulated Process Essential for Prostate Cancer Cell Viability. *EBioMedicine* **8**:103-116.

Musselman, L. P., Fink, J. L., Ramachandran, P. V., Patterson, B. W., Okunade, A. L., Maier, E., Brent, M. R., Turk, J., Baranski, T. J. (2013) Role of Fat Body Lipogenesis in Protection against the Effects of Caloric Overload in Drosophila. *jour biol chem* **288:**8028-8042.

Nalepa, G., Harper, J. W. (2004). Visualization of a highly organized intranuclear network of filaments in living mammalian cells. *Cell Motil. Cytoskeleton* **59**:94-108.

Ng, B. G., Freeze, H. H. (2018) Perspectives on Glycosylation and Its Congenital Disorders. *Trends Genet* **34**(6);466-476.

Ng, B. G., Kranz, C., Hagebeuk, E. E., Duran, M., Abeling, N. G., Wuyts, B., Ungar, D., Lupashin, V., Hartdorff, C. M., Poll-The, B. T., Freeze, H. H. (2007) Molecular and clinical characterization of a Moroccan Cog7-deficient patient. *Mol Genet Metab* **91**:201–204.

Nichols, C. D. (2015). Life Extension Lessons from Drosophila. Switzerland: Springer.

Nichols, C. D., Becnel, J., Pandey, U. B. (2012). Methods to assay Drosophila behavior. *J Vis Exp*.

Niehues, R., Hasilik, M., Alton, G., Korner, C., Schiebe-Sukumar, M., Koch, H.G., Zimmer, K.P., Wu, R., Harms, E., Reiter, K., von Figura, K., Freeze, H. H., Harms, H. K., Marquardt, T. (1998) Carbohydrate-deficient glycoprotein syndrome type Ib. Phosphomannose isomerase deficiency and mannose therapy. *J Clin Invest* **101**:1414-1420.

Nishimoto, S., Nishida, E. (2007) Fibroblast growth factor 13 is essential for neural differentiation in xenopus early embryonic development. *Journal of Biological Chemistry* **282**:24255-24261.

Nita-Lazar, M., Noonan, V., Rebustini, I., Walker, J., Menko, A. S., Kukuruzinska, M. A. (2009) Overexpression of DPAGT1 leads to aberrant N-glycosylation of E-cadherin and cellular discohesion in oral cancer. *Cancer Res* **69**:5673-5680.

Ohtsubo, K., Marth, J. D. (2006). Glycosylation in cellular mechanisms of health and disease. *Cell* **126**(5):855-67.

Pacheco-Cuellar, G., Gauthier, J., Desilets, V., Lachance, C., Lemire-Girard, M., Rypens, F., Le Deist, F., Decaluwe, H., Duval, M., Bouron-Dal Soglio, D., Kokta, V., Haddad, E., Campeau, P. M. (2017) A Novel PGM3 Mutation Is Associated With a Severe Phenotype of Bone Marrow Failure, Severe Combined Immunodeficiency, Skeletal Dysplasia, and Congenital Malformations. *J Bone Miner Res* **32**:1853-1859.

Paesald-Burda, P., Maag, C., Troxler, H., Foulquier, F., Kleinert, P., Schnabel, S., Baumgartner, M., Hennet, T. (2009) Deficiency in COG5 causes a moderate form of congenital disorders of glycosylation. *Hum Mol Genet* **18**:4350–4356.

Palani, S., Meitinger, F., Boehm, M. E., Lehmann, W. D., Pereira, G. (2012) Cdc14-dependent dephosphorylation of Inn1 contributes to Inn1-Cyk3 complex formation. *J Cell Sci* **125**(Pt 13):3091-6.

Pan, W., Choi, S. C., Wang, H., Qin, Y., Volpicelli-Daley, L., Swan, L., Lucast, L., Khoo, C., Zhang, X., Li, L., Abrams, C. S., Sokol, S. Y., Wu, D. (2008) Wnt3a-mediated formation of phosphatidylinositol 4,5-bisphosphate regulates LRP6 phosphorylation. *Science* **321**(5894):1350-3.

Panneerselvam, K., Freeze, H. H. (1996) Mannose enters mammalian cells using a specific transporter that is insensitive to glucose. *J Biol Chem* **271**(16):9417-21.

Panneerselvam, K., Freeze, H. H. (1996) Mannose corrects altered N-glycosylation in carbohydrate-deficient glycoprotein syndrome fibroblasts. *J Clin Invest*. **97**(6):1478-87.

Papadopoulou, K., Chen, J. S., Mead, E., Feoktistova, A., Petit, C., Agarwal, M., Jamal, M., Malik, A., Spanos, A., Sedgwick, S. G., Karagiannis, J., Balasubramanian, M. K., Gould, K. L., McInerny, C. J. (2010). Regulation of cell cycle-specific gene expression in fission yeast by the Cdc14p-like phosphatase Clp1p. *J Cell Sci* **123**:4374-81.

Park, J. H., Hogrebe, M., Grüneberg, M., DuChesne, I., von der Heiden, A. L., Reunert, J., Schlingmann, K. P., Boycott, K. M., Beaulieu, C. L., Mhanni, A. A., Innes, A. M., Hörtnagel, K., Biskup, S., Gleixner, E. M., Kurlemann, G., Fiedler, B., Omran, H., Rutsch, F., Wada, Y., Tsiakas, K., Santer, R., Nebert, D. W., Rust, S., Marquardt, T. (2015) SLC39A8 deficiency: a disorder of manganese transport and glycosylation. *Am J Hum Genet* **97**:894–903.

Peng, J., Chen, S., Busser, S., Liu, H., Honegger, T., Kubli, E. (2005). Gradual release of sperm bound sex-peptide controls female postmating behavior in Drosophila. *Curr Biol* **15**:207-13.

Pereira, G., Schiebel, E. (2003). Separase regulates INCENP-Aurora B anaphase spindle function through Cdc14. *Science* **302**:2120-2124.

Peters, J. M., McKay, R. M., McKay, J. P., Graff, J. M. (1999) Casein kinase I transduces Wnt signals. *Nature* **401**:345-350.

Pinson, K. I., Brennan, J., Monkley, S., Avery, B. J., Skarnes, W. C. (2000) An LDL-receptor-related protein mediates Wnt signalling in mice. *Nature* **407**(6803):535-8.

Port, F., Basler, K. (2010) Wnt trafficking: new insights into Wnt maturation, secretion and spreading. *Traffic* **11**(10):1265-71.

Port, F., Hausmann, G., Basler, K. (2011) A genome-wide RNA interference screen uncovers two p24 proteins as regulators of Wingless secretion. *EMBO Rep* **12**(11):1144-52.

Pospisilik, J. A., Schramek, D., Schnidar, H., Cronin, S. J., Nehme, N. T., Zhang, X., Knauf, C., Cani, P. D., Aumayr, K., Todoric, J. Bayer, M., Haschemi, A., Puviindran, V., Tar, K., Orthofer, M., Neely, G. G., Dietzl, G., Manoukian, A., Funovics, M., Prager, G., Wagner, O., Ferrandon, D., Aberger, F., Hui, C. C., Esterbauer, H., Penninger, J. M. (2010). Drosophila genome-wide obesity screen reveals hedgehog as a determinant of brown versus white adipose cell fate. *Cell* **140:**148-60.

Powers, B. L., Hall, M. C. (2017) Re-examining the role of Cdc14 phosphatase in reversal of Cdk phosphorylation during mitotic exit. *J Cell Sci* **130**(16):2673-2681.

Price, C. S., Dyer, K. A., Coyne, J. A. (1999). Sperm competition between Drosophila males involves both displacement and incapacitation. *Nature* **400**:449-52.

Purves, D. C., Brachmann, C. (2007). Dissection of imaginal discs from 3rd instar Drosophila larvae. *J Vis Exp*, 140.

Qian, D., Jones, C., Rzadzinska, A., Mark, S., Zhang, X., Steel, K. P., Dai, X., Chen, P. (2007) Wnt5a functions in planar cell polarity regulation in mice. *Dev Biol* **306**:121–133.

Queralt, E., Uhlmann, F. (2008). Separase cooperates with Zds1 and Zds2 to activate Cdc14 phosphatase in early anaphase. *J Cell Biol* **182**:873-83.

Quevedo, O., Ramos-Pérez, C., Petes, T. D., Machín, F. (2015) The Transient Inactivation of the Master Cell Cycle Phosphatase Cdc14 Causes Genomic Instability in Diploid Cells of Saccharomyces cerevisiae. *Genetics* **200**(3):755-69.

Ranheim, E. A., Kwan, H. C., Reya, T., Wang, Y. K., Weissman, I. L., Francke, U. (2005). Frizzled 9 knock-out mice have abnormal B-cell development. *Blood* **105**(6):2487-2494.

Rao, X., Huang, X., Zhou, Z., Lin, X. (2013) An improvement of the 2^(-delta delta CT) method for quantitative real-time polymerase chain reaction data analysis. *Biostat Bioinforma Biomath* **3**:71-85.

Raspelli E, Cassani C, Chiroli E, Fraschini R. (2015) Budding yeast Swe1 is involved in the control of mitotic spindle elongation and is regulated by Cdc14 phosphatase during mitosis. *J Biol Chem* **290**(10):6006.

Rauch, G. J., Hammerschmidt, M., Blader, P., Schauerte, K. E., Strahle, U., Ingham, P. W., McMahon, A. P., Haffter, P. (1997) WNT5 is required for tail formation in the zebrafish embryo. *Cold Spring Harbor Symposia on Quantitative Biology* **62**:227-234.

Regal, L., van Hasselt, P. M., Foulquier, F., Cuppen, I., Prinsen, H., Jansen, K., Keldermans, L., De Meirleir, L., Matthijs, G., Jaeken, J. (2014) ALG11-CDG: Three novel mutations and further characterization of the phenotype. *Mol Genet Metab Rep* **25**:2:16-19.

Reynders, E., Foulquier, F., Leao Teles, E., Quelhas, D., Morelle, W., Rabouille, C., Annaert, W., Matthijs, G. (2009) Golgi function and dysfunction in the first COG4-deficient CDG type II patient. *Hum Mol Genet* **18**:3244–3256.

Ricciardiello, F., Votta, G., Palorini, R., Raccagni, I., Brunelli, L., Paiotta, A., Tinelli, F., D'Orazio, G., Valtorta, S., De Gioia, L., Pastorelli, R., Moresco, R. M., La Ferla, B., Chiaradonna, F. (2018) Inhibition of the Hexosamine Biosynthetic Pathway by targeting PGM3 causes breast cancer growth arrest and apoptosis. *Cell Death Dis* **9**:377.

Rind, N., Schmeiser, V., Thiel, C., Absmanner, B., Lübbehusen, J., Hocks, J., Apeshiotis, N., Wilichowski, E., Lehle, L., Körner, C. (2010) A severe human metabolic disease caused by deficiency of the endoplasmatic mannosyltransferase hALG11 leads to congenital disorder of glycosylation-Ip. *Hum Mol Genet* **19**:1413–1424.

Riparbelli, M. G., Callaini, G., Megraw, T. L. (2012). Assembly and persistence of primary cilia in dividing Drosophila spermatocytes. *Dev Cell* **23**:425-32.

Ro, H., Dawid, I. B. (2011) Modulation of Tcf3 repressor complex composition regulates cdx4 expression in zebrafish. *The EMBO Journal* **30**:2894-2907.

Roccuzzo, M., Visintin, C., Tili, F., Visintin, R. (2015) FEAR-mediated activation of Cdc14 is the limiting step for spindle elongation and anaphase progression. *Nat Cell Bio*l **17**(3):251-61

Rochard, L., Monica, S. D., Ling, I., T., C., Kong, Y., Roberson, S., Harland, R., Halpern, M., Liao, E. C. (2016) Roles of Wnt pathway genes *wls*, *wnt9a*, *wnt5b*, *frzb* and *gpc4* in regulating convergent-extension during zebrafish palate morphogenesis. *Development* **143**(14):2541–2547.

Rodier, G., Coulombe, P., Tanguay, P. L., Boutonnet, C., Meloche, S. (2008). Phosphorylation of Skp2 regulated by CDK2 and Cdc14B protects it from degradation by APC (Cdh1) in G1 phase. *EMBO J* **27**:679-91.

Rogers, D. W., Baldini, F., Battaglia, F., Panico, M., Dell, A., Morris, H. R., Catteruccia, F. (2009). Transglutaminase-mediated semen coagulation controls sperm storage in the malaria mosquito. *PLoS Biol* **7**:e1000272.

Rorth, P. (1998). Gal4 in the Drosophila female germline. *Mech Dev* **78**:113-8.

Rosso, L., Marques, A. C., Weier, M., Lambert, N., Lambot, M. A., Vanderhaeghen, P., Kaessmann, H. (2008). Birth and rapid subcellular adaptation of a hominoid-specific CDC14 protein. *PLoS Biol* **6**:e140.

Rothbächer, U., Laurent, M. N., Deardorff, M. A., Klein, P. S., Cho, K. W., Fraser, S. E. (2000) Dishevelled phosphorylation, subcellular localization and multimerization regulate its role in early embryogenesis. *EMBO J* **19**(5):1010-22.

Roy, S. H., Clayton, J. E., Holmen, J., Beltz, E., Saito, R. M. (2011) Control of Cdc14 activity coordinates cell cycle and development in Caenorhabditis elegans. *Mech Dev* **128**(7-10):317-26.

Rubin, G. M., Spradling, A. C. (1982). Genetic transformation of Drosophila with transposable element vectors. *Science* **218**:348-53.

Ruthnick, D., Schiebel, E. (2016). Duplication of the Yeast Spindle Pole Body Once per Cell Cycle. *Mol Cell Biol* **36**:1324-31.

Saal, H. M., C. A. Prows, I. Guerreiro, M. Donlin, L. Knudson, K. L. Sund, C. F. Chang, S. A. Brugmann and R. W. Stottmann (2015) A mutation in FRIZZLED2 impairs Wnt signaling and causes autosomal dominant omodysplasia. *Hum Mol Genet* **24**(12):3399-3409.

Saito, R. M., Perreault, A., Peach, B., Satterlee, J. S., van den Heuvel, S. (2004). The CDC-14 phosphatase controls developmental cell-cycle arrest in C. elegans. *Nat Cell Biol* **6**:777-83.

Saito-Diaz, K., Benchabane, H., Tiwari, A., Tian, A., Li, B., Thompson, J. J., Hyde, A. S., Sawyer, L. M., Jodoin, J. N., Santos, E., Lee, L. A., Coffey, R. J., Beauchamp, R. D., Williams, C. S., Kenworthy, A. K., Robbins, D. J., Ahmed, Y., Lee, E. (2018) APC Inhibits Ligand-Independent Wnt Signaling by the Clathrin Endocytic Pathway. *Dev Cell* **44**:566-581 e568.

Saito-Diaz, K., Chen, T. W., Wang, X., Thorne, C. A., Wallace, H. A., Page-Mccaw, A., Lee, E. (2013) The way Wnt works: Components and mechanism. *Growth Factors* **31**(1): 1–31.

Sakanaka, C., Leong, P., Xu, L., Harrison, S. D., Williams, L. T. (1999) Casein kinase Iε in the Wnt pathway: Regulation of β-catenin function. *Proceedings of the National Academy of Sciences of the United States of America* **99**:12548-12552.

Salic, A., Lee, E., Mayer, L., Kirschner, M. W. (2000) Control of beta-catenin stability: reconstitution of the cytoplasmic steps of the wnt pathway in Xenopus egg extracts. *Mol Cell* **5**(3):523-32.

Sanchez-Diaz A., Nkosi P. J., Murray S., Labib K. (2012) The Mitotic Exit Network and Cdc14 phosphatase initiate cytokinesis by counteracting CDK phosphorylations and blocking polarised growth. *EMBO J* **31**(17):3620-34.

Sarkissian, T., Timmons, A., Arya, R., Abdelwahid, E., White, K. (2014). Detecting apoptosis in Drosophila tissues and cells. *Methods* **68**:89-96.

Schachter, H. (2000) The joys of HexNAc. The synthesis and function of N- and O-glycan branches. *Glycoconjugate Journal* **17**:465-483.

Schwarz, K., Iolasco, A., Verissimo, F., Trede, N. S., Horsley, W., Chen, W., Paw, B. H., Hopfner, K. P., Holzmann, K., Russo, R., Esposito, M. R., Spano, D., De Falco, L., Heinrich, K., Joggerst, B., Rojewski, M. T., Perrotta, S., Denecke, J., Pannicke, U., Delaunay, J., Pepperkok, R., Heimpel, H. (2009) Mutations affecting the secretory COPII coat component SEC23B cause congenital dyserythropoietic anemia type II. *Nat Genet* **41**:936–940.

Semenov, M. V., Habas, R., Macdonald, B. T., He, X. (2007) SnapShot: Noncanonical Wnt signaling pathways. *Cell* **131**:1378.e1–1378.e2.

Semënov, M. V., Snyder, M. (1997) Human dishevelled genes constitute a DHR-containing multigene family. *Genomics* **42**(2):302-10.

Senderek, J., Müller, J. S., Dusl, M., Strom, T. M., Guergueltcheva, V., Diepolder, I., Laval, S. H., Maxwell, S., Cossins, J., Krause, S., Muelas, N., Vilchez, J. J., Colomer, J., Mallebrera, C. J., Nascimento, A., Nafissi, S., Kariminejad, A., Nilipour, Y., Bozorgmehr, B., Najmabadi, H., Rodolico, C., Sieb, J. P., Steinlein, O. K., Schlotter, B., Schoser, B., Kirschner, J., Herrmann, R., Voit, T., Oldfors, A., Lindbergh, C., Urtizberea, A.,-von der Hagen, M., Hübner, A., Palace, J., Bushby, K., Straub, V., Beeson, D., Abicht, A., Lochmüller, H. (2011) Hexosamine biosynthetic pathway mutations cause neuromuscular transmission defect. *Am J Hum Genet* **88**(2):162-72.

Sengupta, P.K., Bouchie, M.P., Nita-Lazar, M., Yang, H.Y., Kukuruzinska, M.A. (2013) Coordinate regulation of N-glycosylation gene DPAGT1, canonical Wnt signaling and E-cadherin adhesion. *J Cell Sci* **126**:484-496.

Sharif, S.R., Islam, A., Moon, I.S. (2016) N-Acetyl-D-Glucosamine Kinase Interacts with Dynein-Lis1-NudE1 Complex and Regulates Cell Division. *Mol Cells* **39**:669-679.

Shim, J., Lee, Y., Jeong, Y. T., Kim, Y., Lee, M. G., Montell, C., Moon, S. J. (2015). The full repertoire of Drosophila gustatory receptors for detecting an aversive compound. *Nat Commun* **6**:8867.

Simanis, V. (2003) The mitotic exit and septation initiation networks. *J. Cell Sci* **116**:4261-4262.

Simons, M., Mlodzik, M. (2008) Planar cell polarity signaling: From fly development to human disease. *Annu Rev Genet* **42**:517–540.

Sitaram, P., Hainline, S. G., Lee, L. A. (2014). Cytological analysis of spermatogenesis: live and fixed preparations of Drosophila testes. *J Vis Exp* e51058.

Snijders Blok, L., E. Madsen, J. Juusola, C. Gilissen, D. Baralle, M. R. Reijnders, H. Venselaar, C. Helsmoortel, M. T. Cho, A. Hoischen, L. E. Vissers, T. S. Koemans, W. Wissink-Lindhout, E. E. Eichler, C. Romano, H. Van Esch, C. Stumpel, M. Vreeburg, E. Smeets, K. Oberndorff, B. W. van Bon, M. Shaw, J. Gecz, E. Haan, M. Bienek, C. Jensen, B. L. Loeys, A. Van Dijck, A. M. Innes, H. Racher, S. Vermeer, N. Di Donato, A. Rump, K. Tatton-Brown, M. J. Parker, A. Henderson, S. A. Lynch, A. Fryer, A. Ross, P. Vasudevan, U. Kini, R. Newbury-Ecob, K. Chandler, A. Male, D. D. D. Study, S. Dijkstra, J. Schieving, J. Giltay, K. L. van Gassen, J. Schuurs-Hoeijmakers, P. L. Tan, I. Pediaditakis, S. A. Haas, K. Retterer, P. Reed, K. G. Monaghan, E. Haverfield, M. Natowicz, A. Myers, M. C. Kruer, Q. Stein, K. A. Strauss, K. W. Brigatti, K. Keating, B. K. Burton, K. H. Kim, J. Charrow, J. Norman, A. Foster-Barber, A. D. Kline, A. Kimball, E. Zackai, M. Harr, J. Fox, J. McLaughlin, K. Lindstrom, K. M. Haude, K. van Roozendaal, H. Brunner, W. K. Chung, R. F. Kooy, R. Pfundt, V. Kalscheuer, S. G. Mehta, N. Katsanis and T. Kleefstra (2015) Mutations in DDX3X Are a Common Cause of Unexplained Intellectual Disability with Gender-Specific Effects on Wnt Signaling. *Am J Hum Genet* **97**(2):343-352.

Song, W., Veenstra, J. A., Perrimon, N. (2014) Control of lipid metabolism by Tachykinin in Drosophila Cell Rep **9**(1):40–47.

Stapleton, M., Liao, G., Brokstein, P., Hong, L., Carninci, P., Shiraki, T., Hayashizaki, Y., Champe, M., Pacleb, J., Wan, K., Yu, C., Carlson, J., George, R., Celniker, S., Rubin, G. M. (2002). The Drosophila gene collection: identification of putative full-length cDNAs for 70% of D. melanogaster genes. *Genome Res* **12**:1294-300.

Stegmeier, F., Amon, A. (2004). Closing mitosis: the functions of the Cdc14 phosphatase and its regulation. *Annu Rev Genet* **38**:203-32.

Stegmeier, F., Visintin, R., Amon, A. (2002). Separase, polo kinase, the kinetochore protein Slk19, and Spo12 function in a network that controls Cdc14 localization during early anaphase. *Cell* **108**:207-220.

Stewart, S., Koh, T. W., Ghosh, A. C., Carlson, J. R. (2015). Candidate ionotropic taste receptors in the Drosophila larva. *Proc Natl Acad Sci U S A* **112**:4195-201.

Stichelen, S. O., Dehennaut, V., Buzy, A., Zachayus, J., Guinez, C., Mir, A., El Yazidi-Belkoura, A., Copin, M., Boureme, D., Loyaux, D., Ferrara, P., Lefebvre T. (2014) O-GlcNAcylation stabilizes β-catenin through direct competition with phosphorylation at threonine 41. *FASEB* **28**(8):3325–3338.

Stoick-Cooper, C. L., Weidinger, G., Riehle, K. J., Hubbert, C., Major, M. B., Fausto, N., Moon, R. T. (2007) Distinct Wnt signaling pathways have opposing roles in appendage regeneration. *Development* **134**:479-489.

Stray-Pedersen, A., Backe, P. H., Sorte, H. S., Morkrid, L., Chokshi, N. Y., Erichsen, H. C., Gambin, T., Elgstoen, K. B., Bjoras, M., Wlodarski, M. W., Kruger, M., Jhangiani, S. N., Muzny, D. M., Patel, A., Raymond, K. M., Sasa, G. S., Krance, R. A., Martinez, C. A., Abraham, S. M., Speckmann, C., Ehl, S., Hall, P., Forbes, L. R., Merckoll, E., Westvik, J., Nishimura, G., Rustad, C. F., Abrahamsen, T. G., Ronnestad, A., Osnes, L. T., Egeland, T., Rodningen, O. K., Beck, C. R., Baylor-Johns Hopkins Center for Mendelian, G., Boerwinkle, E. A., Gibbs, R. A., Lupski, J. R., Orange, J. S., Lausch, E., Hanson, I. C. (2014) PGM3 mutations cause a congenital disorder of glycosylation with severe immunodeficiency and skeletal dysplasia. *Am J Hum Genet* **95**:96-107.

Sullivan, M., Higuchi, T., Katis, V. L., Uhlmann, F. (2004). Cdc14 phosphatase induces rDNA condensation and resolves cohesin-independent cohesion during budding yeast anaphase. *Cell* **117**:471-482.

Sun, G., Hu, Z., Min, Z., Yan, X., Guan, Z., Su, H., Fu, Y., Ma, X., Chen, Y.G., Zhang, M.Q., Tao, Q., Wu, W. (2015) Small C-terminal Domain Phosphatase 3 Dephosphorylates the Linker Sites of Receptor-regulated Smads (R-Smads) to Ensure Transforming Growth Factor beta (TGFbeta)-mediated Germ Layer Induction in Xenopus Embryos. *J Biol Chem* **290**:17239-17249.

Swain, R. K., Katoh, M., Medina, A., Steinbeisser, H. (2005) Xenopus frizzled-4S, a splicing variant of Xfz4 is a context-dependent activator and inhibitor of Wnt/beta-catenin signaling. *Cell Commun Signal* **3**:12.

Swiatek, W., Tsai, I. C., Klimowski, L., Pepler, A., Barnette, J., Yost, H. J., Virshup, D. M. (2004) Regulation of casein kinase I epsilon activity by Wnt signaling. *J Biol Chem* **279**:13011-13017.

Swinnen, M. Phan, F. Conte, N. Ishorst, C. Gilissen, L. RoaFuentes, M. van de Vorst, A. Henkes, M. Steehouwer, E. van Beusekom, M. Bloemen, B. Vankeirsbilck, S. Berge, G. Hens, J. Schoenaers, V. V. Poorten, J. Roosenboom, A. Verdonck, K. Devriendt, N. Roeleveldt, S. N. Jhangiani, L. Vissers, J. R. Lupski, J. de Ligt, J. W. Von den Hoff, R. Pfundt, H. G. Brunner, H. Zhou, J. Dixon, E. Mangold, H. van Bokhoven, M. J. Dixon, T. Kleefstra, A. Hoischen and C. E. L. Carels (2016). "Novel mutations in LRP6 highlight the role of WNT signaling in tooth agenesis." *Genet Med* **18**(11):1158-1162.

Tahinci, E., Thorne, C. A., Franklin, J. L., Salic, A., Christian, K. M., Lee, L. A., Coffey, R. J., Lee, E. (2007) Lrp6 is required for convergent extension during Xenopus gastrulation. *Development* **134**:4095-4106.

Takada, R., Satomi, Y., Kurata, T., Ueno, N., Norioka, S., Kondoh, H., Takao, T., Takada, S. (2006) Monounsaturated fatty acid modification of Wnt protein: its role in Wnt secretion. *Dev Cell* **11**(6):791-801.

Takizawa, C. G., Morgan, D. O. (2000). Control of mitosis by changes in the subcellular location of cyclin-B1-Cdk1 and Cdc25C. *Curr. Opin. Cell Biol* **12**:658-665.

Tamai, K., Semenov, M., Kato, Y., Spokony, R., Liu, C., Katsuyama, Y., Hess, F., Saint-Jeannet, J. P., He, X. (2000) LDL-receptor-related proteins in Wnt signal transduction. *Nature* **407**(6803):530-5.

Tanaka, K., Kitagawa, Y., Kadowaki, T. (2002) Drosophila segment polarity gene product porcupine stimulates the posttranslational N-glycosylation of wingless in the endoplasmic reticulum. *Biol Chem* **277**(15):12816-23.

Tang, X., Wu, Y., Belenkaya, T. Y., Huang, Q., Ray, L., Qu, J., Lina, X. (2012) Roles of N-glycosylation and lipidation in Wg secretion and signaling. *Dev Biol* **364**(1):32–41.

Tanguay, P., Rodier, G., Meloche, S. (2010) C-terminal domain phosphorylation of ERK3 controlled by Cdk1 and Cdc14 regulates its stability in mitosis. *Biochemical Journal* **428**(1):103-111.

Tauriello, D. V., Jordens, I., Kirchner, K., Slootstra, J. W., Kruitwagen, T., Bouwman, B. A., Noutsou, M., Rüdiger, S. G., Schwamborn, K., Schambony, A., Maurice, M. M. (2012) Wnt/β-catenin signaling requires interaction of the Dishevelled DEP domain and C terminus with a discontinuous motif in Frizzled. *Proc Natl Acad Sci U S A* **109**(14):E812-20.

Taylor, G.S., Liu, Y., Baskerville, C., Charbonneau, H. l. (1997) The activity of Cdc14p, an oligomeric dual specificity protein phosphatase from Saccharomyces cerevisiae, is required for cell cycle progression. *J Biol Chem* **272**(38):24054-63.

Taylor S. S., Kornev, A. P. (2011) Protein Kinases: Evolution of Dynamic Regulatory Proteins. *Trends Biochem Sci* **36**(2):65–77.

Thorpe, C.J., Moon, R.T. (2004) nemo-like kinase is an essential co-activator of Wnt signaling during early zebrafish development. *Development* **131**:2899-2909.

Thrasivoulou, C., Millar, M., Ahmed, A. (2013) Activation of Intracellular Calcium by Multiple Wnt Ligands and Translocation of β-Catenin into the Nucleus: a convergent model of Wnt/Ca^{2+} and Wnt/β-catenin pathways. *J Biol Chem* **288**(50):35651–35659.

Tonks, N. K. (2006). Protein tyrosine phosphatases: from genes, to function, to disease. *Nat. Rev. Mol. Cell Biol* **7**:833-846.

Trautmann, S., Wolfe, B. A., Jorgensen, P., Tyers, M., Gould, K. L., McCullum, D. (2001). Fission yeast Clp1p phosphatase regulates G2/M transition and coordination of cytokinesis with cell cycle progression. *Curr. Biol* **11**:931-940.

Trautmann, S., Rajagopalan, S., McCollum, D. (2004). The S. pombe Cdc14-like phosphatase Clp1p regulates chromosome biorientation and interacts with Aurora kinase. *Dev. Cell* **7**:755-762.

Trinkle-Mulcahy, L., Andrews, P. D., Wickramasinghe, S., Sleeman, J., Prescott, A., Lam, Y. W., Lyon, C., Swedlow, J. R., Lamond, A. I. (2003). Time-lapse imaging reveals dynamic relocalization of PP1gamma throughout the mammalian cell cycle. *Mol. Biol. Cell* **14**:107-117.

Turner, D. L., Weintraub, H. (1994) Expression of achaete-scute homolog 3 in Xenopus embryos converts ectodermal cells to a neural fate. *Genes & Development* **8**:1434-1447.

Tzeng, Y. W., Huang, J. N., Schuyler, S. C., Wu, C. H., Juang, Y. L. (2011) Functions of the mitotic B-type cyclins CLB1, CLB2, and CLB3 at mitotic exit antagonized by the CDC14 phosphatase. *Fungal Genet Biol* **48**(10):966-78.

Ubersax, J. A., Woodbury, E. L., Quang, P. N., Paraz, M., Blethrow, J. D., Shah, K., Shokat, K. M., Morgan, D. O. (2003). Targets of the cyclin-dependent kinase Cdk1. *Nature* **425**:859-864.

Ungar, A. R., Kelly, G. M., Moon, R. T. (1995) Wnt4 affects morphogenesis when misexpressed in the zebrafish embryo. *Mech Dev* **52**:153-164.

Van Amerongen, R. (2012) Alternative Wnt Pathways and Receptors. *Cold Spring Harb Perspect Biol* **4**(10):a007914.

Van de Water, S., van de Wetering, M., Joore, J., Esseling, J., Bink, R., Clevers, H., Zivkovic, D. (2001) Ectopic Wnt signal determines the eyeless phenotype of zebrafish masterblind mutant. *Development* **128**:3877-3888.

Van den Heuvel, M., Harryman-Samos, C., Klingensmith, J., Perrimon, N., Nusse, R. (1993) Mutations in the segment polarity genes wingless and porcupine impair secretion of the wingless protein. *EMBO J* **12**(13):5293-302.

Van den Steen, P., Rudd, P. M., Dwek, R. A., Opdenakker, G. (1998) Concepts and principles of O-linked glycosylation. *Crit Rev Biochem Mol Biol* **33**:151-208.

Van Maldergem, L., Yuksel-Apak, M., Kayserili, H., Seemanova, E., Giurgea, S., Basel-Vanagaite, L., Leao-Teles, E., Vigneron, J., Foulon, M., Greally, M., Jaeken, J., Mundlos, S., Dobyns, W. B. (2008) Cobblestone-like brain dysgenesis and altered glycosylation in congenital cutis laxa, Debré type. *Neurology* **71**:1602–1608.

Van Schaftingen, E., Jaeken, J. (1995) Phosphomannomutase deficiency is a cause of carbohydrate-deficient glycoprotein syndrome type I. *FEBS Lett* **377**(3):318-20.

Varela, E., Schlecht, U., Moina, A., Fackenthal, J. D., Washburn, B. K., Niederhauser-Wiederkehr, C., Tsai-Pflugfelder, M., Primig, M., Gasser, S. M., Esposito, R. E. (2010) Mitotic expression of Spo13 alters M-phase progression and nucleolar localization of Cdc14 in budding yeast. *Genetics* **185**(3):841-54

Varelas, X., Bouchie, M. P., Kukuruzinska, M. A. (2014) Protein N-glycosylation in oral cancer: dysregulated cellular networks among DPAGT1, E-cadherin adhesion and canonical Wnt signaling. *Glycobiology* **24**(7):579-91.

Vargas, D. A., Sun, M., Sadykov, K., Kukuruzinska, M. A., Zaman, M. H. (2016) The Integrated Role of Wnt/β-Catenin, N-Glycosylation, and E-Cadherin-Mediated Adhesion in Network Dynamics. *PLoS Comput Biol* **12**(7):e1005007.

Varki, A., Chrispeels, M. J. (1999). Essentials of glycobiology. *Cold Spring Harbor, N.Y.*

Vazquez-Novelle, M. D., Esteban, V., Bueno, A. and Sacristan, M. P. (2005). Functional homology among human and fission yeast CDC14 phosphatases. *J. Biol. Chem*. **280**:29144-29150.

Vieillard, J., Duteyrat, J. L., Cortier, E., Durand, B. (2015) Imaging cilia in Drosophila melanogaster. *Methods Cell Biol* **127**:279-302.

Vigetti, D., Karousou, E., Viola, M., Deleonibus, S., De Luca, G., Passi, A. (2014) Hyaluronan: biosynthesis and signaling. *Biochim Biophys Acta* **1840**(8):2452-9.

Villoria, M. T., Ramos, F., Dueñas, E., Faull, P., Cutillas, P. R., Clemente-Blanco, A. (2017) Stabilization of the metaphase spindle by Cdc14 is required for recombinational DNA repair. *EMBO J* **36**(1):79-101.

Virshup, D. M., Shenolikar, S. (2009) From promiscuity to precision: protein phosphatases get a makeover. *Mol. Cell* **33**:537-545.

Visintin, R., Craig, K., Hwang, E. S., Prinz, S., Tyers, M., Amon, A. (1998) The phosphatase Cdc14 triggers mitotic exit by reversal of Cdk-dependent phosphorylation. *Mol. Cell* **2**, 709-718.

Vleugels, W., Haeuptle, M. A., Ng, B. G., Michalski, J. C., Battini, R., Dionisi-Vici, C., Ludman, M. D., Jaeken, J., Foulquier, F., Freeze, H. H., Matthijs, G., Hennet, T. (2009) RFT1 deficiency in three novel CDG patients. *Hum Mutat* **30**:1428–1434.

Vogt, G., Chapgier, A., Yang, K., Chuzhanova, N., Feinberg, J., Fieschi, C., Boisson-Dupuis, S., Alcais, A., Filipe-Santos, O., Bustamante, J., de Beaucoudrey, L., Al-Mohsen, I., Al-Hajjar, S., Al-Ghonaium, A., Adimi, P., Mirsaeidi, M., Khalilzadeh, S., Rosenzweig, S., de la Calle Martin, O., Bauer, T. R., Puck, J. M., Ochs, H. D., Furthner, D., Engelhorn, C., Belohradsky, B., Mansouri, D., Holland, S. M., Schreiber, R. D., Abel, L., Cooper, D. N., Soudais, C., Casanova, J. L. (2005) Gains of glycosylation comprise an unexpectedly large group of pathogenic mutations. *Nat Genet* **37**:692-700.

Vogt, G., Bustamante, J., Chapgier, A., Feinberg, J., Boisson, Dupuis, Picard, C., Mahlaoui, N., Gineau, L., Alcaïs, A., Lamaze, C., Puck, J. M., de Saint Basile, G., Khayat, C. D., Mikhael, R., Casanova, J. L. (2008) Complementation of a pathogenic IFNGR2 misfolding mutation with modifiers of N-glycosylation. *J Exp Med* **205**(8):1729-37.

Wang C., Lehmann R. (1991) Nanos is the localized posterior determinant in drosophila. *Cell* **66**:637-47.

Wang, J., Liu, J., Hu, Y., Ying, S. H., Feng, M. G. (2013) Cytokinesis-required Cdc14 is a signaling hub of asexual development and multi-stress tolerance in Beauveria bassiana. *Sci Rep.* **30**:3:3086.

Wang, Y., Guo, N., Nathans, J. (2006) The role of Frizzled3 and Frizzled6 in neural tube closure and in the planar polarity of inner-ear sensory hair cells. *J Neurosci* **26**:2147–2156.

Warnakula, S., Hsieh, J., Adeli, K., Hussain, M. M., Tso, P., Proctor, S. D. (2011) New insights into how the intestine can regulate lipid homeostasis and impact vascular disease: frontiers for new pharmaceutical therapies to lower cardiovascular disease risk. *Can J Cardiol* **27**:183–191.

Wehrli, M., Dougan, S. T., Caldwell, K., O'Keefe, L., Schwartz, S., Vaizel-Ohayon, D., Schejter, E., Tomlinson, A., DiNardo, S. (2000) Arrow encodes an LDL-receptor-related protein essential for Wingless signalling. *Nature* **407**(6803):527-30.

Weihofen, W. A., Berger, M., Chen, H., Saenger, W., Hinderlich, S. (2006) Structures of human N-Acetylglucosamine kinase in two complexes with N-Acetylglucosamine and with ADP/glucose: insights into substrate specificity and regulation. *J Mol Biol* **364**:388-399.

White, J. J., Mazzeu, J. F., Coban-Akdemir, Z., Bayram, Y., Bahrambeigi, V., Hoischen, A., van Bon, B. W. M., Gezdirici, A., Gulec, E. Y., Ramond, F., Touraine, R., Thevenon, J., Shinawi, M., Beaver, E., Heeley, J., Hoover-Fong, J., Durmaz, C. D., Karabulut, H. G., Marzioglu-Ozdemir, E., Cayir, A., Duz, M. B., Seven, M., Price, S., Ferreira, B. M., Vianna-Morgante, A. M., Ellard, S., Parrish, A., Stals, K., Flores-Daboub, J., Jhangiani, S. N., Gibbs, R. A., Baylor-Hopkins Center for Mendelian Genetics, Brunner, H. G., Sutton, V. R., Lupski, J. R., Carvalho, C. M. B. (2018) WNT Signaling Perturbations Underlie the Genetic Heterogeneity of Robinow Syndrome. *Am J Hum Genet* **102**(1):27-43.

Whittaker, S. L., Shattock, R. C., Shaw, D. S. (1991) Variation in DNA content of nuclei of Phytophthora infestans as measured by a microfluorimetric method using the fluorochrome DAPI. *Mycol Res* **95**:602–610.

Willert, K., Brown, J. D., Danenberg, E., Duncan, A. W., Weissman, I. L., Reya, T., Yates, J. R. 3rd, Nusse, R. (2003) Wnt proteins are lipid-modified and can act as stem cell growth factors. *Nature* **423**(6938):448-52.

Wilson, P.A., Lagna, G., Suzuki, A., Hemmati-Brivanlou, A. (1997) Concentration-dependent patterning of the Xenopus ectoderm by BMP4 and its signal transducer Smad1. *Development* **124**:3177-3184.

Witters, P., Cassiman, D., Morava, E. (2017) Nutritional Therapies in Congenital Disorders of Glycosylation (CDG). *Nutrients* **9**.

Wodarz, A., Nusse, R. (1998) Mechanisms of Wnt signaling in development. *Annu Rev Cell Dev Biol* **14**:59-88.

Wolfe, B. A., Gould, K. L. (2004). Fission yeast Clp1p phosphatase affects G2/M transition and mitotic exit through Cdc25p inactivation. *EMBO J* **23**:919-929.

Wong, H. C., Bourdelas, A., Krauss, A., Lee, H. J., Shao, Y., Wu, D., Mlodzik, M., Shi, D. L., Zheng, J. (2003) Direct binding of the PDZ domain of Dishevelled to a conserved internal sequence in the C-terminal region of Frizzled. *Mol Cell* **12**(5):1251-60.

Wong, H. C., Mao, J., Nguyen, J. T., Srinivas, S., Zhang, W., Liu, B., Li, L., Wu, D., Zheng, J. (2000) Structural basis of the recognition of the dishevelled DEP domain in the Wnt signaling pathway. *Nat Struct Biol* **7**(12):1178-84.

Wu, J., Cho, H. P., Rhee, D. B., Johnson, D. K., Dunlap, J., Liu, Y., Wang, Y. (2008) Cdc14B depletion leads to centriole amplification, and its overexpression prevents unscheduled centriole duplication. *J Cell Biol* **181**:475-83.

Wu, Q., Zhao, Z. W., Shen, P. (2005) Regulation of aversion to noxious food by Drosophila neuropeptide Y- and insulin-like systems. *Nature Neuroscience* **8**:1350-1355.

Wu, X., Rush, J. S., Karaoglu, D., Krasnewich, D., Lubinsky, M. S., Waechter, C. J., Gilmore, R., Freeze, H. H. (2003) Deficiency of UDP-GlcNAc:dolichol phosphate N-acetylglucosamine-1 phosphate transferase (DPAGT1) causes a novel congenital disorder of glycosylation type Ij. *Hum Mutat* **22**:144–150.

Wu, X., Steet, R. A., Bohorov, O., Bakker, J., Newell, J., Krieger, M., Spaapen, L., Kornfeld, S., Freeze, H. H. (2004) Mutation of the COG complex subunit gene COG7 causes a lethal congenital disorder. *Nat Med* **10**:518–523.

Xing, Y. Y., Cheng, X. N., Li, Y. L., Zhang, C., Saquet, A., Liu, Y. Y., Shao, M., Shi, D. L. (2018) Mutational analysis of dishevelled genes in zebrafish reveals distinct functions in embryonic patterning and gastrulation cell movements. *PLoS Genet* **14**(8):e1007551.

Yamamoto, A., Nagano, T., Takehara, S., Hibi, M., Aizawa, S. (2005) Shisa promotes head formation through the inhibition of receptor protein maturation for the caudalizing factors, Wnt and FGF. *Cell* **120**:223–235.

Yanagawa, S., van Leeuwen, F., Wodarz, A., Klingensmith, J., Nusse, R. (1995) The dishevelled protein is modified by wingless signaling in Drosophila. *Genes Dev* **9**(9):1087-97.

Yang, G., Hu, Y., Fasoyin, O. E., Yue, Y., Chen, L., Qiu, Y., Wang, X., Zhuang, Z., Wang, S. (2018) The Aspergillus flavus Phosphatase CDC14 Regulates Development, Aflatoxin Biosynthesis and Pathogenicity*. Front Cell Infect Microbiol* **8**:141.

Yeh, S. D., Chan, C., Ranz, J. M. (2013). Assessing differences in sperm competitive ability in Drosophila. *J Vis Exp* e50547.

Young, T., Poobalan, Y., Tan, E. K., Tao, S., Ong, S., Wehner, P., Schwenty-Lara, J., Lim, C. Y., Sadasivam, A., Lovatt, M., Wang, S. T., Ali, Y., Borchers, A., Sampath, K., Dunn, N. R. (2014) The PDZ domain protein Mcc is a novel effector of non-canonical Wnt signaling during convergence and extension in zebrafish. *Development* **141**:3505-3516.

Zamore, P. D., Ma, S. (2011) Isolation of Drosophila melanogaster testes. *J Vis Exp*.

Zeevaert, R., Foulquier, F., Cheillan, D. et al. (2009) A new mutation in COG7 extends the spectrum of COG subunit deficiencies. *Eur J Med Genet* **52**:303–305.

Zeitler, R., Giannis, A., Danneschewski, S., Henk, E., Henk, T., Bauer, C., Reutter, W., Sandhoff, K. (1992) Inhibition of N-acetylglucosamine kinase and N-acetylmannosamine kinase by 3-O-methyl-N-acetyl-D-glucosamine in vitro. *Eur J Biochem* **204**:1165-1168.

Zeng, X., Huang, H., Tamai, K., Zhang, X., Harada, Y., Yokota, C., Almeida, K., Wang, J., Doble, B., Woodgett, J., Wynshaw-Boris, A., Hsieh, J. C., He, X. (2008) Initiation of Wnt signaling: control of Wnt coreceptor Lrp6 phosphorylation/activation via frizzled, dishevelled and axin functions. *Development* **135**(2):367-75.

Zeng, X., Tamai, K., Doble, B., Li, S., Huang, H., Habas, R., Okamura, H., Woodgett, J., He, X. (2005) A dual-kinase mechanism for Wnt co-receptor phosphorylation and activation. *Nature* **438**(7069):873-7.

Zheng, X., Narayanan, S., Zheng, X., Luecke-Johansson, S., Gradin, K., Catrina, S. B., Poellinger, L., Pereira, T. S. (2017) A Notch-independent mechanism contributes to the induction of Hes1 gene expression in response to hypoxia in P19 cells. *Exp Cell Res* **358**:129-139.

Appendix 1:

References for NAGK phenotypes

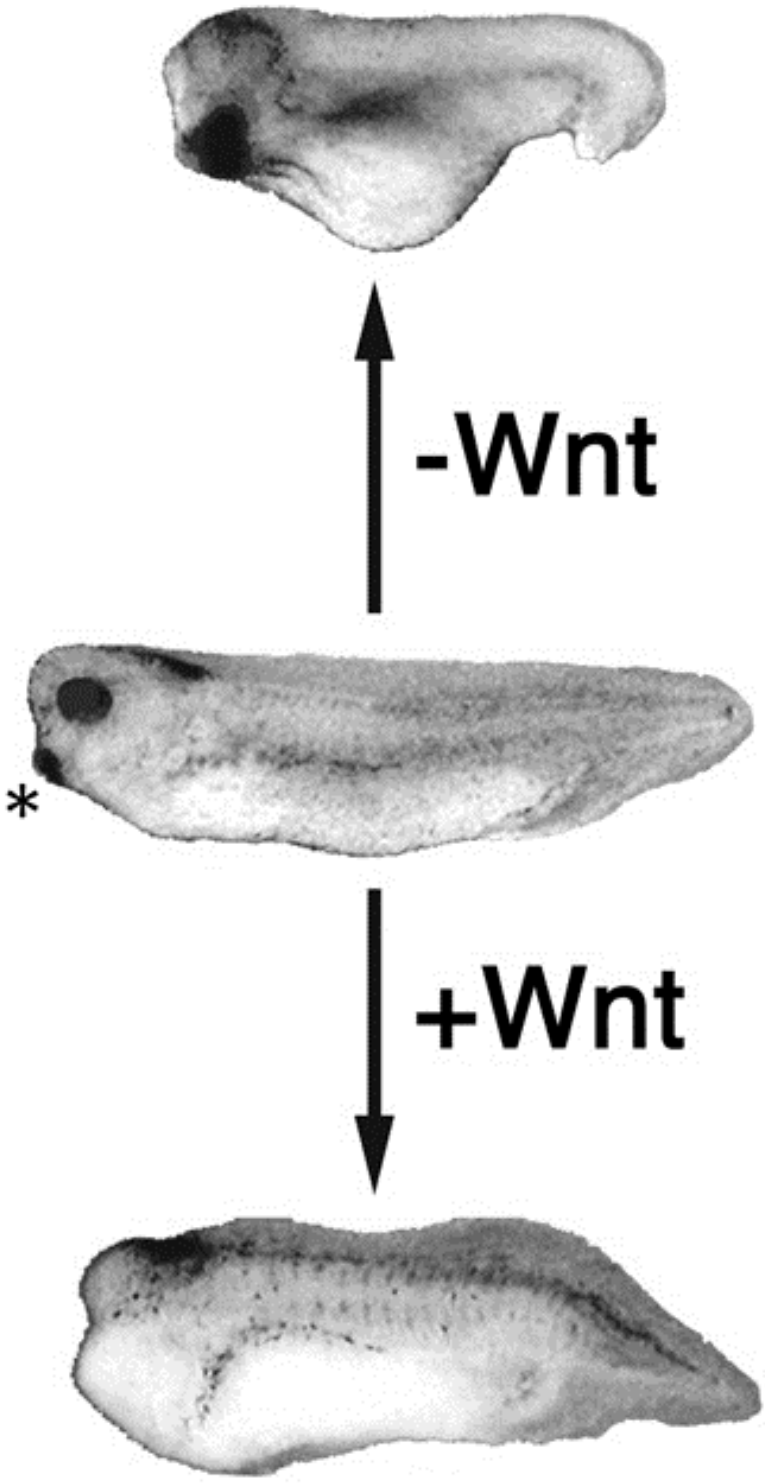
-Wnt
*
+Wnt

Figure appendix-1: Examples of post-midblastula transition Wnt signaling phenotypes in the early *Xenopus laevis* embryo (Edited from Kiecker and Niehrs 2013). (Middle) a wildtype embryo at approximately stage 34-35. (Top) Inhibition of the Wnt/β-catenin pathway (-Wnt) post the midblastula transition anteriorizes *Xenopus* embryos. (Bottom) Activation of the Wnt/β-catenin pathway (+Wnt) post the midblastula transition posteriorizes *Xenopus* embryos. Post the midblastula transition Wnt represses anterior structures, suppressing head formation. Wnt also promotes posterior development (tail and trunk) after the midblastula transition. Posteriorization results in the loss or reduction of the cement gland. Conversely, anteriorization results in an enlarged or expanded cement gland. * indicates the cement gland.

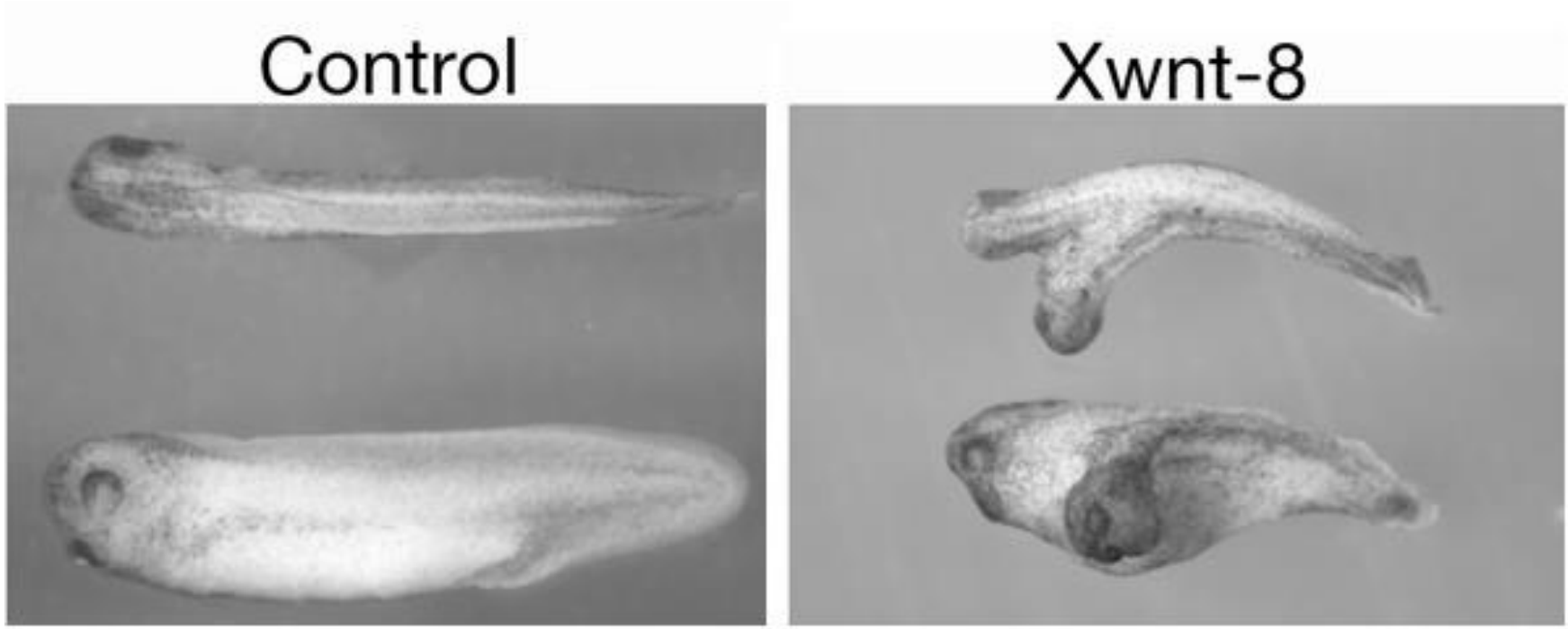
Control
Xwnt-8

Figure appendix-2: Examples of pre-midblastula transition Wnt signaling phenotypes in the early *Xenopus laevis* embryo (Edited from Peters et al. 1999). Pre-midblastula transition ectopic activation of Wnt in the Ventral blastomeres of a 2 or 4 cell embryo results in a full axis duplication**.** Embryos are approximately stage 34-35.

Small eyes and eyeless

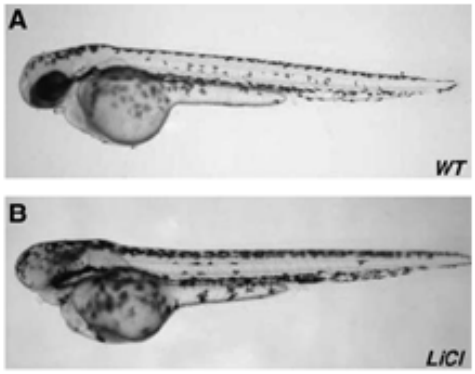

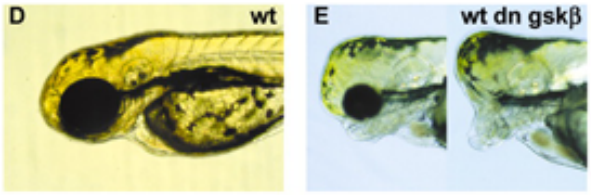

Cyclopia

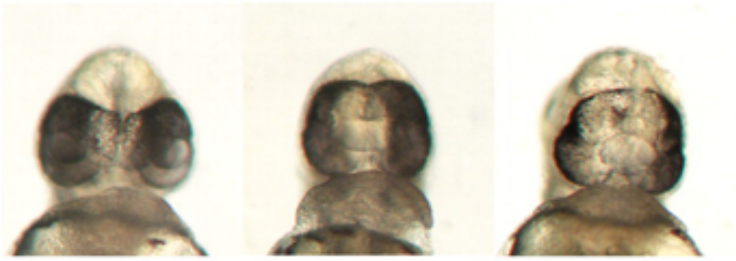

Figure appendix-3: Examples of Wnt signaling phenotypes in the early *Danio rerio* embryo. (Top) examples of Wnt overexpression inhibiting eye formation in the early *Danio rerio* embryo from the literature. (Top left) examples of LiCl treated embryos from D'Costalain and Shepherd (2009). LiCl activates Wnt signaling by inhibiting GSK3. Images are of 48 hours post fertilization embryos. (Top right) embryos injected with dominant negative GSK3β from Van de Water et al. (2001). Images are of 24 hours post fertilization embryos. (Bottom) examples of non-canonical Wnts resulting in cyclopia in the early *Danio rerio* embryo from the literature. Embryos were injected with Morpholinos to knockdown Wnt11 expression and imaged at 48 hours post fertilization. Images are from Thorpe and Moon (2004).

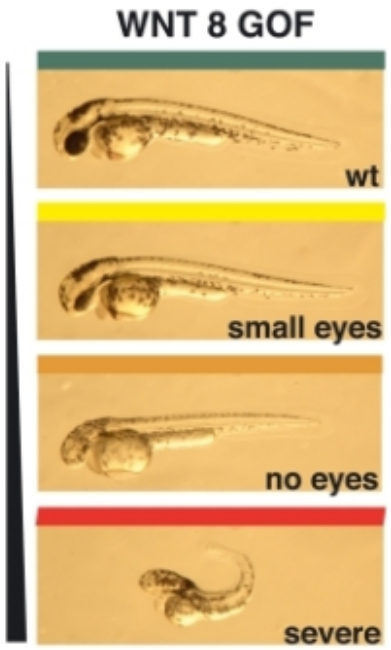
WNT 8 GOF
wt
small eyes
no eyes
severe

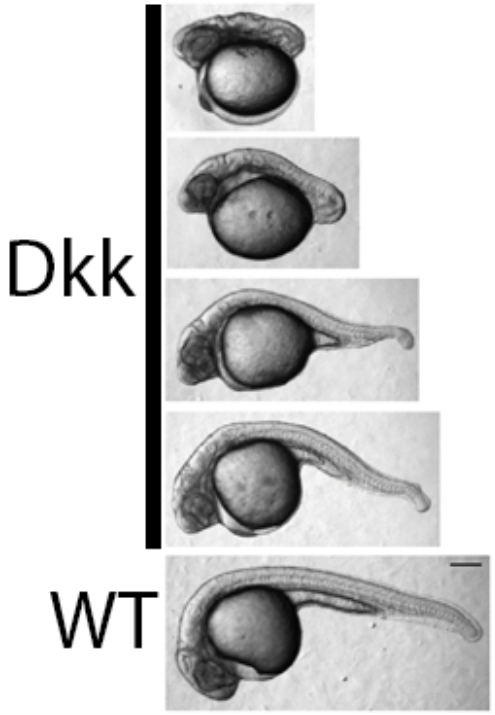
Dkk
WT

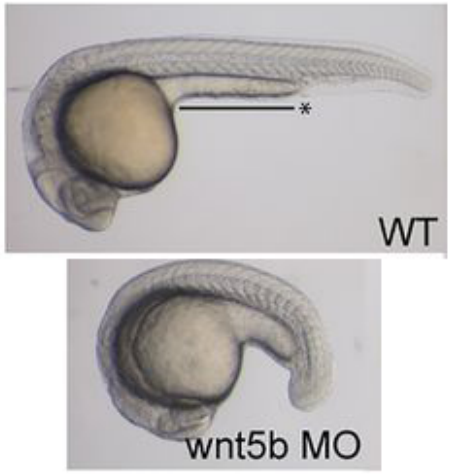
WT
wnt5b MO

Figure appendix-4: Examples of Wnt mediated posteriorization of *Danio rerio* embryos. (Left) Overexpression of Wnt in the early *Danio rerio* embryo can result in convergent extension defects. Embryos are injected with Wnt8 and imaged at 36 hours post fertilization. Images are from Kategaya, et al. (2009). (Middle) inhibition of Wnt in the early *Danio rerio* embryo can also result in convergent extension defects. Images are of 26 hours post fertilization embryos. Images are from dkk injected embryos from Ro and Dawid (2011). (Right) Inhibition of non-canonical Wnt can result in convergent extension defects. Images are 1 day post fertilization embryos. Images are from Young et al. (2014).

Appendix 2:

The following are all published works by Leif Richard Neitzel, completed during graduate school that are not discussed in the main text.

The Drosophila MCPH1-B isoform is a substrate of the APCCdh1 E3 ubiquitin ligase complex

Hainline SG, Rickmyre JL, **Neitzel LR**, Lee LA, Lee E.

***Biol Open*. 2014 3(7):669-76**

doi: 10.1242/bio.20148318

© 2014. Published by The Company of Biologists Ltd | Biology Open (2014) 3, 669–676 doi:10.1242/bio.20148318

RESEARCH ARTICLE

The *Drosophila* MCPH1-B isoform is a substrate of the APC^{Cdh1} E3 ubiquitin ligase complex

Sarah G. Hainline[‡], Jamie L. Rickmyre[‡,*], Leif R. Neitzel, Laura A. Lee[§] and Ethan Lee[§]

ABSTRACT

The Anaphase-Promoting Complex (APC) is a multi-subunit E3 ubiquitin ligase that coordinates progression through the cell cycle by temporally and spatially promoting the degradation of key proteins. Many of these targeted proteins have been shown to play important roles in regulating orderly progression through the cell cycle. Using a previously described *Drosophila* in vitro expression cloning approach, we screened for new substrates of the APC in *Xenopus* egg extract and identified *Drosophila* MCPH1 (dMCPH1), a protein encoded by the homolog of a causative gene for autosomal recessive primary microcephaly in humans. The dMCPH1-B splice form, but not the dMCPH1-C splice form, undergoes robust degradation in *Xenopus* interphase egg extract in a Cdh1-dependent manner. Degradation of dMCPH1-B is controlled by an N-terminal destruction box (D-box) motif as its deletion or mutation blocks dMCPH1-B degradation. dMCPH1 levels are increased in *Drosophila morula* (*APC2*) mutant embryos, consistent with dMCPH1 being an APC substrate in vivo. Using a purified, reconstituted system, we show that dMCPH1-B is ubiquitinated by APC^{Cdh1}, indicating that the effect of APC on dMCPH1-B ubiquitination and degradation is direct. Full-length human MCPH1 (hMCPH1) has been predicted to be an APC substrate based on its interaction with the APC subunit Cdc27. We were not able to detect changes in hMCPH1 levels during the cell cycle in cultured human cells. Overexpression of hMCPH1 (or dMCPH1-B) in developing *Xenopus* embryos, however, disrupts cell division, suggesting that proper regulation of hMCPH1 and dMCPH1-B activity plays a critical role in proper cell-cycle progression.

KEY WORDS: Anaphase-Promoting Complex, *Drosophila*, MCPH1, Ubiquitination, *Xenopus* egg extract

INTRODUCTION

The Anaphase-Promoting Complex (APC) is a multi-subunit E3 ubiquitin ligase that catalyzes ubiquitin-mediated proteasomal degradation of target proteins. A major function of the APC is to promote degradation of key cell-cycle proteins so as to coordinate orderly progression through the cell cycle (Peters, 2006). Human and yeast APC are each composed of 14–15 identified subunits and two primary co-activators, Cdc20 and Cdh1 (Kulkarni et al., 2013). Destruction of APC substrates is required in eukaryotes for the initiation of anaphase and exit from mitosis. Cdc20 associates with the APC in early mitosis, leading to the destruction of proteins that control the onset of anaphase, whereas Cdh1 promotes degradation of APC substrates that control late mitosis and the following G1 phase. These co-activators provide APC substrate specificity by facilitating the recognition of specific destruction motifs (e.g. degrons) such as the D-box (RxxLxxxxN) or KEN box (Lys–Glu–Asn) (King et al., 1996; Min and Lindon, 2012; Pfleger and Kirschner, 2000). Mutations of these motifs block the recognition of the protein by the APC, preventing their APC-mediated destruction.

Xenopus egg extract contains many of the components necessary for ubiquitin-mediated degradation such as E1, E2, and E3 enzymes, ubiquitin, and the proteasome. Moreover, biochemical regulation of APC^{Cdc20}- and APC^{Cdh1}-mediated degradation has been well studied and characterized in this system. *Xenopus* egg extract lacks Cdh1, and Cdc20 is the primary activator of APC (Lorca et al., 1998). Addition of exogenous human Cyclin B lacking its N-terminal D-box (CycBΔ90) to interphase *Xenopus* egg extract drives the extract into mitosis and promotes the degradation of APC^{Cdc20} substrates (Glotzer et al., 1991). Addition of exogenous Cdh1 to interphase *Xenopus* egg extract similarly promotes the degradation of APC^{Cdh1} substrates (Pfleger and Kirschner, 2000).

The in vitro expression cloning (IVEC) strategy involves generating [^{35}S]methionine-labeled proteins by in vitro-coupled transcription and translation of small, random pools of cDNAs; these radiolabeled proteins can then be used for biochemical screening in a powerful approach that allows for rapid isolation of relevant cDNAs corresponding to "hits" in the screen (King et al., 1997). IVEC has been successfully used in *Xenopus* egg extract to identify important APC substrates such as Geminin, Securin, Xkid, Tome-1, and Sororin (Ayad et al., 2003; Funabiki and Murray, 2000; McGarry and Kirschner, 1998; Rankin et al., 2005; Zou et al., 1999). A weakness of the original IVEC strategy, however, is that, depending on the cDNA library being used, certain genes are over-represented whereas other genes are under-represented in the library. Thus, the same substrate is often identified over and over again, and substantial screening is necessary to identify relevant rare clones. Furthermore, the pools of cDNAs used for IVEC screening must be deconvoluted in order to isolate single hits as the identities of the clones in the pools are unknown.

To overcome these limitations, we previously modified the IVEC methodology to generate radiolabeled protein pools from Release 1 of the *Drosophila* Gene Collection (DGC), an annotated unigene set of 5,849 full-length cDNA clones representing 43% of the fly genome (Lee et al., 2005; Stapleton et al., 2002). Clones were individually arrayed in 17 × 384-well

Department of Cell and Developmental Biology, Vanderbilt University Medical Center, Nashville, TN 37232-8240, USA.
*Present address: Sarah Cannon Research Institute, Nashville, TN 37203, USA.
‡These authors contributed equally to this work.

§Authors for correspondence (ethan.lee@vanderbilt.edu; laura.a.lee@vanderbilt.edu)

Received 14 March 2014; Accepted 3 June 2014

Biology Open (2014) 3, 669–676 doi:10.1242/bio.20148318

plates, and in vitro transcription and translation was performed on small pools containing equivalent amounts of cDNA (or mRNA) for each gene. This *Drosophila* IVEC (DIVEC) approach has allowed for efficient genome-scale screening to identify substrates of the Pan Gu kinase and binding partners of p53 (Lee et al., 2005; Lunardi et al., 2010).

Given the conservation across phyla between cell cycle proteins, we herein applied the DIVEC approach to perform a biochemical screen for APC substrates in *Xenopus* interphase egg extract and identified *Drosophila* Microcephalin (dMCPH1) as a candidate. Human MCPH1 (hMCPH1) is a causative gene of autosomal recessive primary microcephaly (MCPH), a neurodevelopment disorder characterized by reduced brain size (Jackson et al., 2002; Woods et al., 2005). In humans, MCPH1 has been shown to prevent premature mitotic entry by regulating centrosomal recruitment of Chk1 at the G2/M transition as well as premature chromosome condensation by negatively regulating the activity of condensin II (Gruber et al., 2011; Tibelius et al., 2009; Trimborn et al., 2006; Yamashita et al., 2011). hMCPH1 has also been reported to have several functions in the DNA damage response (Gavvovidis et al., 2012; Lin et al., 2005; Peng et al., 2009; Rai et al., 2006; Tibelius et al., 2009; Trimborn et al., 2006; Yamashita et al., 2011; Yang et al., 2008). We previously reported that *Drosophila* syncytial embryos derived from *mcph1*-null females exhibit Chk2-mediated mitotic arrest in response to damaged or incompletely replicated DNA (Rickmyre et al., 2007). Because *mcph1* mutants contain an intact DNA checkpoint, and MCPH1 has been shown to regulate premature chromosome condensation in other systems, we previously proposed that dMCPH1 prevents accumulation of DNA damage by delaying chromosome condensation until DNA replication is completed. Although MCPH1 is reported to function in multiple cellular processes, its regulation is not well understood. In this report, we demonstrate that dMCPH1 is a substrate of the critical cell cycle regulator, APC^{Cdh1}.

MATERIALS AND METHODS

cDNA clones and mutagenesis

cDNA clones encoding dMCPH1-B (clone LD42241), dMCPH1-C (clone LP15451), or p78 (GH13229) were obtained from the *Drosophila* Gene Collection Release 1 or the *Drosophila* Genomics Resource Center (Indiana University, Bloomington, IN), respectively. cDNA clones encoding hMCPH1, Cyclin B, NT-Cyclin B, Mos, Luciferase, and GFP were gifts from Marc Kirschner's lab (Harvard Medical School, Boston, MA). dMCPH1-B and dMCPH1-C were subcloned into vector pCS2 for in vitro transcription and translation reactions. dMCPH1-$B^{\Delta N}$, dMCPH1-$B^{DboxMut}$, and dMCPH1-B^{1-64} were generated from CS2-dMCPH1-B by mutagenesis to remove the first 40 amino acids, replace amino acids 36–40 with alanines, or remove the last 762 amino acids, respectively. dMCPH1-B, dMCPH1-$B^{DboxMut}$, and hMCPH1 were also subcloned into pCS2 derivatives encoding six N- or C-terminal Myc tags.

DIVEC screen and APC degradation assay

Xenopus interphase egg extract was prepared as previously described (Pfleger and Kirschner, 2000). Baculoviruses encoding human His6-tagged CDH1 and His6-tagged Cyclin BΔ90 (gifts from Marc Kirschner's lab) were expressed in *Sf9* cells by baculovirus infection and purified over nickel beads. For the DIVEC screen, radiolabeled protein pools were generated from pools of cDNAs from the *Drosophila* Gene Collection Release 1 by transcription and translation in reticulocyte lysates using a Gold TNT T7 kit according to the manufacturer's protocol (Promega, Madison, WI) as previously described (Lee et al., 2005). The identity of positive clones was confirmed by DNA sequencing.

For testing individual proteins in the APC degradation assay, 1 µl of radiolabeled protein was added to 10 µl of *Xenopus* egg extract supplemented with energy mix (1 mM HEPES, pH 7.7, 1 mM ATP, 10 mM creatine phosphate, and 1 mM $MgCl_2$) and 10 µg/ml ubiquitin. Egg extract was incubated with *Xenopus* Buffer control (100 mM KCl, 1 mM $MgCl_2$, 0.1 mM $CaCl_2$, 10 mM HEPES, 50 mM sucrose, 5 mM EGTA), His6-Cyclin BΔ90 (60 µg/ml), or His6-CDH1 (0.4 nM) prior to starting the reaction with addition of radiolabeled proteins, and reactions were allowed to proceed at room temperature as previously described (Ayad et al., 2003). All radiolabeled, in vitro-translated protein migrated at the expected size as assessed by SDS-PAGE/autoradiography. For radiolabeled degradation assays, loading controls were not necessary as equivalent volumes (0.5 µl) were removed at the indicated times for processing by SDS-PAGE/autoradiography. NT-Cyclin B peptide 100 µM was prepared as previously described (Pfleger and Kirschner, 2000). Pixel intensity measurements of autoradiograms were performed using ImageJ and statistical analysis was performed using the paired equal variance two-tailed t-test.

Drosophila stocks, embryo lysates, and immunoblotting

Flies were maintained at 25℃ using standard techniques (Greenspan, 2004). *morula* stocks (mr^1 and mr^2) were gifts from T. Orr-Weaver (Whitehead Institute, Cambridge, MA) (Reed and Orr-Weaver, 1997). y^1 w^{1118} flies were used as the "wild-type" stock. Embryo lysates were made by homogenizing embryos (0–1 hour) in urea sample buffer (100 mM Tris, pH 7.6, 8 M urea, 2% SDS, 5% β-mercaptoethanol, and 5% Ficoll). Lysates were analyzed by SDS-PAGE and immunoblotting using standard techniques. Primary antibodies used included guinea pig anti-MCPH1 (1:200) (Rickmyre et al., 2007); mouse anti-Cyclin B (1:200, F2F4, Developmental Studies Hybridoma Bank, Iowa City, IA); and mouse anti-α-tubulin (1:5000, DM1α, Sigma–Aldrich, St Louis, MO). HRP-conjugated secondary antibodies were used to detect primary antibodies by chemiluminescence.

In vitro ubiquitination assay

APC was purified by immunoprecipitation of Cdc27 from *Xenopus* interphase egg extract using Protein G Sepharose beads (GE Healthcare Life Sciences, Pittsburgh, PA) and anti-Cdc27 antibodies (AF3.1; Santa Cruz Biotechnology, Dallas, TX) as previously described (Wei et al., 2004). For each ubiquitination reaction, 5 µl of APC-bound beads was incubated with 0.75 µM purified E1 (Boston Biochem, Cambridge, MA), 2 µM His-UbcH10 (Boston Biochem), 7.5 mg/ml ubiquitin (Boston Biochem), 0.5 µl 20× Energy Regeneration Mix (2 mg/ml creatine phosphokinase, 20 mM ATP, 200 mM Creatine Phosphate, 20 mM HEPES, 20 mM $MgCl_2$, 0.1% BSA), 5 µM ubiquitin aldehyde (Boston Biochem), and 10 mM DTT. 1 µl of in vitro transcription/translation reaction product and 0.4 nM His-Cdh1 or equal volume of Cdh1 dialysis buffer was incubated in each reaction for 90 minutes. Reaction products were separated by SDS-PAGE and visualized by autoradiography.

Xenopus embryo injection, immunostaining, and immunoblotting

Capped mRNA encoding Mos, GFP, hMCPH1, dMCPH1-B, or dMCPH1-$B^{DboxMut}$ was generated by in vitro transcription reactions using the mMessage mMachine kit per manufacturer's instructions (Life Technologies, Carlsbad, CA). Embryos were injected at the 2- or 4-cell stage with 2 ng of RNA and fixed in MEMFA (100 µM MOPS pH 7.4, 2 mM EGTA, 1 mM $MgSO_4$, and 3.7% formaldehyde) after 4 hours. After fixation, embryos were washed 2× in PBS and dehydrated stepwise (1 hour/step) in 75% PBS/25% methanol, 50% PBS/50% methanol, and 100% methanol and stored at 4℃. The percentage of injected embryos exhibiting cell-cycle defects was quantified and statistical analysis was performed using the Fisher exact test.

For tubulin staining, MEMFA-fixed embryos (in 100% methanol) were bleached in 10% H_2O_2/67% methanol for 8 hours at room temperature. Bleached embryos were rehydrated (1 hour/step) in 50% methanol/50% TBS (155 mM NaCl, 10 mM Tris-HCl pH 7.5), 25% methanol/75% TBS, and finally 100% TBST (TBS plus 0.1% Triton X-100). Embryos were then blocked in WMBS (TBS plus 10% fetal bovine serum and 5% DMSO) for 1 hour. Mouse anti-α-tubulin (DM1α, 1:500, Sigma), RNAse A (1 mg/ml), and propidium iodide (2 µg/ml) were then added and

Biology Open (2014) 3, 669–676 doi:10.1242/bio.20148318

embryos were incubated overnight at 4℃. Embryos were washed 5× (1 hour each) with TBST and incubated in WMBS with RNAse A, propidium iodide, and Cy2-conjugated secondary antibodies (1:500, Sigma). Embryos were washed 5× (1 hour each) with TBST, placed in MatTek dishes (Ashland, MA), and imaged using a Leica TCS SP5 inverted confocal microscope (Buffalo Grove, IL).

For immunoblotting, capped mRNA encoding C-terminally Myc-tagged hMCPH1, dMCPH1-B, or dMCPH1-B^{DboxMut} was generated, and 1 ng of RNA was injected into each cell of a two-cell staged *Xenopus* embryo. At 4 hours post-injection, the embryos were lysed in 6× Sample Buffer (300 mM Tris pH 6.8, 12% w/v SDS, 30% w/v glycerol, 600 mM DTT, and 0.01% w/v bromophenol blue). One quarter of each lysate was analyzed by SDS-PAGE and immunoblotting using standard techniques. Primary antibodies used included mouse anti-Myc-tag (1:500, 9E10) and mouse anti-α-tubulin (1:2000, DM1α, Sigma–Aldrich, St Louis, MO). HRP-conjugated secondary antibodies were used to detect primary antibodies by chemiluminescence.

All *Xenopus* experiments conform to institutional and national animal welfare policies.

Cell synchronization

24 hours after plating HeLa cells on 150 mm dishes at 20% confluency, cells were treated with nocodazole (25 ng/ml) for 13 hours. Plates were firmly tapped to loosen the rounded, mitotic cells from the dish. Cells were then collected by centrifugation for 5 minutes, and washed 3 times in fresh serum-free medium. After the final wash, cells were resuspended in medium containing 10% FBS and plated at 50% confluency in 6-well dishes. Cells were collected every 2 hours by removing medium, washing in PBS, treating with 100 µl 0.25% trypsin-EDTA, and collecting in 1 ml medium. Collected cells were washed once in PBS and lysed in non-denaturing lysis buffer (50 mM Tris-HCl, pH 7.4, 300 mM NaCl, 5 mM EDTA, 1% Triton X-100). Lysates were analyzed by SDS-PAGE and immunoblotting using standard techniques. Antibodies used were rabbit anti-hMCPH1 (D38G5, 1:100, Cell Signaling Technology, Danvers, MA), rabbit anti-Cdk1 (1:4000, Millipore, Billerica, MA), rabbit anti-Cyclin A (H-432, 1:500, Santa Cruz), rabbit anti-Cyclin B1 (H-20, 1:500, Santa Cruz), and rabbit anti-p27 (C-19, 1:100, Santa Cruz). HRP-conjugated secondary antibodies and chemiluminescence were used to detect primary antibodies.

RESULTS

DIVEC screen for APC substrates

In order to identify APC^{Cdc20} or APC^{Cdh1} substrates using DIVEC, bacterial stocks containing cDNA clones from the *Drosophila* Gene Collection Release 1 were individually grown and their plasmids purified and pooled (Fig. 1A). Pooled clones (24 clones/pool) were used to generate radiolabeled proteins in rabbit reticulocyte lysate as previously described (Lee et al., 2005). To test proteins for their capacity to undergo APC^{CDC20}- or APC^{Cdh1}-mediated degradation, protein pools were incubated in *Xenopus* interphase egg extract supplemented with *Xenopus* buffer (XB), human CycBΔ90, or Cdh1. Candidate APC substrates were identified by their decreased band intensity after incubation in CycBΔ90 or Cdh1-supplemented extract relative to the buffer control as revealed by SDS-PAGE and autoradiography.

We identified two candidate substrates of APC in *Xenopus* egg extract using the DIVEC approach (Fig. 1B). We initially named these candidates "p78" and "p91" based on their apparent SDS-PAGE mobility. In the primary screen that involved the use of radiolabeled protein pools, both candidates were stable in the presence of XB and CycBΔ90 (mitotic extract containing activated APC^{Cdc20}), but they degraded in *Xenopus* egg extract supplemented with Cdh1, suggesting that they are substrates of APC^{Cdh1} and not APC^{Cdc20}. In addition, both candidates exhibited decreased mobility on SDS-PAGE when incubated in Cyclin BΔ90-supplemented (mitotic) extract, suggesting that they may be phosphorylated during mitosis.

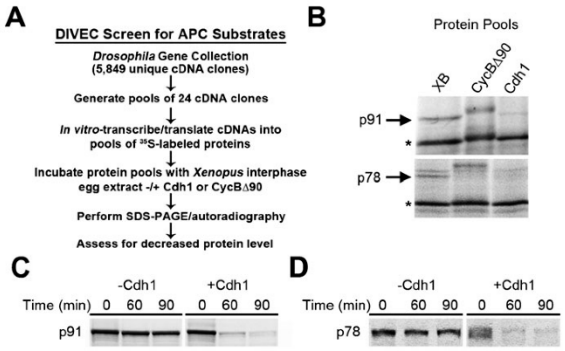

Fig. 1. A *Drosophila* In Vitro Expression Cloning (DIVEC) screen identifies two novel APC substrates. (A) Schematic of the DIVEC screen strategy to identify APC substrates. ^{35}S-radiolabeled proteins were produced from pools of cDNA clones from the *Drosophila* Gene Collection Release 1 as previously described (Lee et al., 2005). Radiolabeled protein pools were incubated in *Xenopus* interphase egg extract supplemented with *Xenopus* buffer (XB), non-degradable Cyclin B (CycBΔ90), or Cdh1. Reaction products were analyzed by SDS-PAGE and autoradiography to identify proteins degraded via APC-Cdc20 or APC-Cdh1. (B) p91 and p78 are candidate APC substrates. Autoradiogram of two protein pools containing p91 and p78. Both p91 and p78 exhibited an upward electrophoretic mobility shift in CycBΔ90-supplemented (mitotic) extract and decreased band intensity in Cdh1-supplemented extract. Asterisks mark proteins in the pools that did not exhibit decreased intensity in the supplemented extract and therefore served as negative controls. (C,D) Retesting of radiolabeled p91 and p78 (prepared from individual cDNA clones) by incubation in *Xenopus* interphase egg extract in the presence of Cdh1 confirmed that the clones encode putative APC substrates.

The corresponding cDNA clones for the two candidate substrates were identified based on the predicted molecular weights of their encoded proteins and retesting in the degradation assay. We confirmed that the protein products generated by in vitro transcription and translation of these individual cDNA clones were degraded in Cdh1-supplemented *Xenopus* egg extract (Fig. 1C,D). p91 is encoded by clone LD43341 and corresponds to the *Drosophila mcph1* gene (Brunk et al., 2007; Rickmyre et al., 2007). p78 is encoded by clone GH13229 and corresponds to *CG32982*, an uncharacterized *Drosophila* gene. Cyclin B, a well-characterized APC substrate, was not identified in our screen because it is not present in the *Drosophila* Gene Collection Release 1. Radiolabeled Cyclin B, however, was used as a positive control in our screen and was shown to degrade in both mitotic (activated APC^{Cdc20}) and Cdh1-supplemented interphase *Xenopus* egg extract (data not shown).

Drosophila MCPH1-B stability is regulated by APC

We previously identified a requirement for dMCPH1 during early embryogenesis in *Drosophila* (Rickmyre et al., 2007). Two distinct isoforms of *Drosophila* MCPH1 (referred to as MCPH1-B and MCPH1-C) are produced by alternative splicing (Rickmyre et al., 2007). Both isoforms are present in larval brains and imaginal discs. *Drosophila* MCPH1-B (dMCPH1-B) is predominantly expressed in the ovaries and syncytial embryos, whereas MCPH1-C (dMCPH1-C) is expressed primarily in the testes. The two isoforms differ primarily at their N- and C-termini. dMCPH1-B contains an additional 47 amino acids at its N-terminal end and lacks 200 amino acids at its C-terminal end when compared to the dMCPH1-C isoform (supplementary

Biology Open (2014) 3, 669–676 doi:10.1242/bio.20148318

material Fig. S1A). Both isoforms contain an N-terminal BRCT domain. Only dMCPH1-C, however, contains an additional pair of BRCT domains at its C-terminal end.

We identified the B isoform of dMCPH1 as a hit in our DIVEC screen for APC substrates. To demonstrate that the degradation of dMCPH1-B in *Xenopus* egg extract was specific to APC^{Cdh1} activity, we tested whether Cdh1-mediated degradation of dMCPH1-B in *Xenopus* interphase egg extract could be inhibited by addition of an N-terminal peptide of Cyclin B (NT-Cyclin B) containing a functional D-box (Fig. 2A). NT-Cyclin B is degraded in Cdh1-supplemented egg extract and competitively blocks APC^{Cdh1}-mediated degradation of Cdc20 (Pfleger and Kirschner, 2000). Similarly, if dMCPH1-B degradation in Cdh1-supplemented *Xenopus* interphase egg extract were mediated by APC^{Cdh1}, addition of excess NT-Cyclin B should inhibit its degradation. Consistent with this model, we found that addition of NT-Cyclin B potently blocked dMCPH1-B degradation in Cdh1-supplemented extract (Fig. 2A).

We next asked if the MCPH1-C isoform is also a substrate of APC^{Cdh1}. We incubated radiolabeled dMCPH1-C in *Xenopus* interphase egg extract in the absence or presence of Cdh1 and assessed its levels after 30 and 60 minutes by performing SDS-PAGE/autoradiography (Fig. 2B; supplementary material Fig. S1B). For dMCPH1-B and Cyclin B (positive control), we detected robust turnover in Cdh1-supplemented *Xenopus* interphase egg extract. Although we detected statistically significant Cdh1-mediated degradation for dMCPH1-C, it was not nearly as robust as that of dMCPH1-B or Cyclin B.

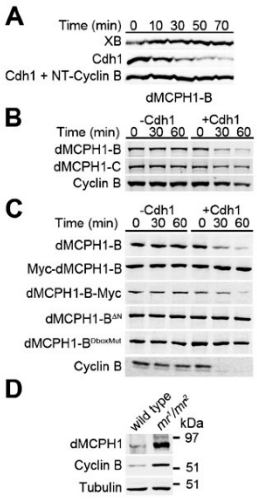

Fig. 2. dMCPH1-B stability is regulated by APC. (A) dMCPH1 degradation in *Xenopus* egg extract is stimulated by Cdh1. Radiolabeled dMCPH1-B was incubated in *Xenopus* interphase egg extract supplemented with XB (buffer control), Cdh1, or Cdh1 plus an N-terminal Cyclin B peptide (NT-Cyclin B). (B) Degradation of dMCPH1-C in *Xenopus* egg extract. Radiolabeled dMCPH1-B, dMCPH1-C, or Cyclin B was incubated in *Xenopus* interphase egg extract in the absence or presence of Cdh1. See supplementary material Fig. S1B for quantification of gel band intensities. (C) A free N-terminal end of dMCPH1-B, which contains a putative D-box, is required for its Cdh1-stimulated degradation in *Xenopus* egg extract. Wild-type dMCPH1-B and a C-terminally Myc-tagged version (dMCPH1-B-Myc) degraded in *Xenopus* egg extract in the presence of Cdh1. In contrast, an N-terminally Myc-tagged version (Myc-dMCPH1-B), an N-terminal deletion mutant ($dMCPH1\text{-}B^{\Delta N}$), or an N-terminal D-box mutant ($dMCPH1\text{-}B^{DboxMut}$) failed to degrade in Cdh1-stimulated *Xenopus* egg extract. (D) Immunoblot analysis of dMCPH1, Cyclin B, and alpha-Tubulin levels in lysates derived from embryos (0–1 hour) of *APC2* mutant (mr^1/mr^2) females indicate that dMCPH1 levels are increased in the mutant embryos compared to wild-type embryos.

During our characterization of dMCPH1-B degradation, we found that an N-terminally Myc-tagged, but not a C-terminally Myc-tagged, version of dMCPH1-B degraded in *Xenopus* interphase egg extract (Fig. 2C), suggesting that the N-terminal Myc-tag might mask a nearby degron. These findings were consistent with a model in which the first 47 amino acids of dMCPH1-B that is not shared with dMCPH1-C contains the relevant degron that mediates degradation by APC^{Cdh1}. To test this possibility, we generated an N-terminal truncation mutant of dMCPH1-B ($dMCPH1\text{-}B^{\Delta N}$) in which the first 40 amino acids was deleted. We found that this mutant was stable in Cdh1-supplemented extract, indicating that the N-terminal end of dMCPH1-B contains a degron necessary for APC^{Cdh1}-mediated degradation (Fig. 2C).

We identified a putative D-box motif (RRPLHDSN) within the first 40 amino acids of dMCPH1-B and generated a mutant in which the first four amino acids of this sequence were replaced with alanines ($dMCPH1\text{-}B^{DboxMut}$). We found that, in contrast to the wild-type protein, $dMCPH1\text{-}B^{DboxMut}$ was stable in Cdh1-supplemented extract (Fig. 2C). These data indicate the D-box sequence found within the N-terminal 40 amino acids of dMCPH1-B mediates its APC^{Cdh1}-dependent degradation.

Mutants of the *Drosophila morula* (*mr*) gene, which encodes the homolog of the vertebrate APC2 subunit of APC, have increased levels of Cyclin B due to reduced APC activity (Reed and Orr-Weaver, 1997). Syncytial embryos laid by females transhetersozygous for mr^1 and mr^2 alleles (mr^1/mr^2) arrest in mitosis shortly after a few cell cycles. dMCPH1-B is primarily expressed in syncytial embryos (Brunk et al., 2007; Rickmyre et al., 2007). If dMCPH1-B were an APC substrate, we reasoned that its levels should be increased in *morula* mutant flies. To test this possibility, we prepared lysates from 0–1 hour syncytial embryos derived from wild-type or mr^1/mr^2 females and assessed endogenous dMCPH1, Cyclin B (positive control), and alpha-tubulin (loading control) levels by immunoblotting (Fig. 2D). Embryos derived from mr^1/mr^2 females had increased levels of both dMCPH1-B and Cyclin B compared to wild type, suggesting that dMCPH1-B is an APC substrate in vivo. mr^1/mr^2-derived embryos also contain dMCPH1, which exhibits slower mobility on SDS-PAGE (Fig. 2D). Because mr^1/mr^2-derived embryos are reported to arrest in mitosis, it is possible that this form of dMCPH1 is the result of mitotic phosphorylation.

dMCPH1-B is ubiquitinated by APC

We next sought to determine whether dMCPH1-B is a direct substrate of APC^{Cdh1} using a purified system as previously described (King et al., 1995; Pfleger and Kirschner, 2000). The APC was purified from *Xenopus* interphase egg extract by immunoprecipitation using an antibody against the Cdc27 subunit. Purified APC was then used for in vitro ubiquitination reactions containing recombinant human E1, E2 (UbcH10), Cdh1, and ubiquitin. The radiolabeled NT-Cyclin B peptide (positive control) was polyubiquinated as evidenced by the presence of higher molecular weight laddering on SDS-PAGE (Fig. 3A). In contrast, no laddering was detected for firefly luciferase (negative control).

Biology Open (2014) 3, 669–676 doi:10.1242/bio.20148318

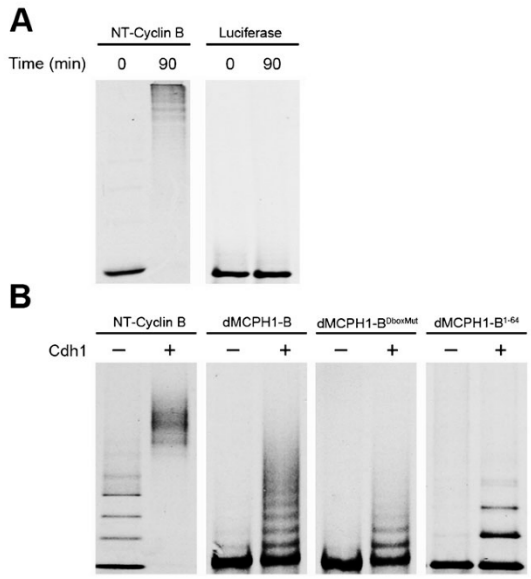

Fig. 3. dMCPH1-B is ubiquitinated by APC in vitro. (A) Establishment of an in vitro APC ubiquitination assay. Radiolabeled N-terminal peptide of Cyclin B (NT-Cyclin B) and Luciferase protein were incubated in a reaction containing APC purified from *Xenopus* interphase egg extract, purified human E1, His-UbcH10, His-Cdh1, ubiquitin, and an energy regeneration system. Reactions were terminated by addition of sample buffer followed by SDS-PAGE/autoradiography. (B) dMCPH1-B is an in vitro substrate of APC^{Cdh1}, and its ubiquitination is mediated in large part by its N-terminal D-box. Radiolabeled NT-Cyclin B, dMCPH1-B, dMCPH1-$B^{Dboxmut}$, and the N-terminal 64 amino acid fragment of dMCPH1-B (dMCPH1-$B^{1–64}$) were incubated in the APC ubiquitination assay and reaction products assessed by SDS-PAGE/autoradiography.

We next tested whether dMCPH1-B was ubiquitinated in our purified system and whether addition of Cdh1 would enhance ubiquitination. We found that ubiquitination of dMCPH1-B and NT-Cyclin B (positive control) was dramatically enhanced in the presence of Cdh1 in our reconstituted ubiquitination system, consistent with dMCPH1-B being an APC^{Cdh1} substrate (Fig. 3B). Ubiquitination of the D-box mutant, dMCPH1-$B^{DboxMut}$, was observed in the presence of Cdh1, albeit at a much reduced level (Fig. 3B). This phenomenon has been observed with other APC substrates in the purified system (Araki et al., 2005; Fang et al., 1998b; Pfleger and Kirschner, 2000), and the low level of ubiquitination observed likely reflects the fact that the purified system lacks many regulatory proteins present in an extract or cell. To further confirm that the N-terminal end of dMCPH1-B contains a functional D-box, we showed that the first 64 amino acids of dMCPH1-B (dMCPH1-$B^{1–64}$) was ubiquitinated in the purified system and that ubiquitination was enhanced in the presence of Cdh1 (Fig. 3B). These results indicate that dMCPH1-B is a direct substrate of APC^{Cdh1} in vitro and that the N-terminal D-box of dMCPH1-B plays a major role in mediating its ubiquitination by APC.

Steady state-levels of hMCPH1 do not change in a cell cycle-dependent manner in cultured human cells

Human MCPH1 (hMCPH1) contains one N-terminal and two C-terminal BRCT domains and is more similar to dMCPH1-C in organization than dMCPH1-B (supplementary material Fig. S1A). Although hMCPH1 lacks an N-terminal degron similar to dMCPH1-B, it contains several putative D-boxes and a candidate KEN box. To determine if hMCPH1 is also degraded via APC^{Cdh1}, radiolabeled hMCPH1 was incubated in *Xenopus* interphase egg extract in the absence or presence of Cdh1. In contrast to dMCPH1-B, hMCPH1 did not degrade in Cdh1-supplemented extract (supplementary material Fig. S2A). The observed doublet is consistent with an alternative translation initiation downstream (35 amino acids) of the canonical start site using the rabbit reticulocyte translation system. It is possible that the incapacity of *Xenopus* interphase egg extract to support hMCPH1 degradation by APC^{Cdh1} is due to differences between the amphibian and human systems.

We next assessed the steady-state levels of hMCPH1 throughout the cell cycle in cultured human cells. HeLa cells were synchronized by nocodazole block and release, and aliquots were taken at two-hour time points in order to assess endogenous levels of hMCPH1, Cyclin B, Cyclin A, p27, and Cdk1 by immunoblotting (supplementary material Fig. S2B). From 2–10 hours after nocodazole release, p27 levels were elevated, and Cyclin A and Cyclin B levels were decreased, consistent with cell-cycle progression into G1. By 10 hours after nocodazole release, p27 levels were decreased, whereas Cyclin A and Cyclin B levels were increased, indicating cell-cycle progression through S, G2, and M-phase. Throughout the time course, hMCPH1 levels remained constant. Taken together, these data suggest that the overall cellular levels of hMCPH1 do not fluctuate in an APC-dependent manner.

Overexpression of hMCPH1 or dMCPH1-B results in cell-cycle defects

Because APC-mediated degradation of substrates is required for cell-cycle progression, we sought to determine if increasing MCPH1 levels would lead to disruption of cell division. The *Xenopus* embryo system has been previously used as an in vivo readout of cell cycle progression (Fang et al., 1998a; Ivanovska et al., 2004; McGarry and Kirschner, 1998; Pfleger et al., 2001a; Pfleger et al., 2001b; Rankin et al., 2005). An advantage of the *Xenopus* embryo system is that the non-injected cells act as a negative control within the same embryo.

We tested whether injecting mRNAs encoding hMCPH1 or dMCPH1-B into developing *Xenopus* embryos at the 2–4 cell stage would lead to disruption of cell division. Because Cdh1 is absent in the early embryo, levels of injected MCPH1 should not be regulated by APC, leading to inappropriate activity during these early embryonic cell cycles (Lorca et al., 1998). Injected embryos were allowed to develop, fixed, and assessed for cell division defects (Fig. 4A,B). Mos (a component of cytostatic factor; positive control) is required to maintain metaphase arrest during meiosis II by inhibiting APC activity (Tunquist and Maller, 2003). Injection of Mos mRNA resulted in a block in cell division in the injected half of the embryo. Injection of GFP (negative control) had no observable cell cycle effect on the injected cells. In contrast, 92% of embryos injected with hMCPH1 and 67% of those injected with dMCPH1-B exhibited reduced cell number and increased cell size, likely due to cell-cycle arrest. The levels of the human and *Drosophila* MCPH1 proteins expressed in embryos are nearly equivalent as assessed by immunoblotting (supplementary material Fig. S3). Thus, we attribute the difference in potency between hMCPH1 and dMCPH1-B to be due to differences in sequence identity

Biology Open (2014) 3, 669–676 doi:10.1242/bio.20148318

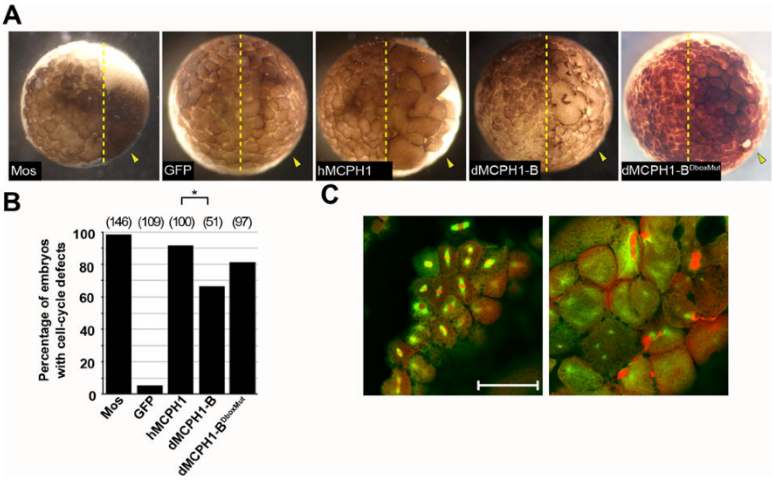

Fig. 4. Overexpression of dMCPH1-B or hMCPH1 results in cell-cycle defects. (A) Representative images of whole *Xenopus* embryos fixed four hours after injection of Mos, GFP, full-length human MCPH1 (hMCPH1), dMCPH1-B, or dMCPH1-B^{DboxMut} RNA at the 2–4-cell stage. Arrows indicate injected halves of embryos. (B) Quantification of *Xenopus* embryos displaying cell division defects 4 hours post-injection. Total number of embryos injected is indicated in parentheses. *$p<0.005$ (C) Confocal sections of the uninjected (left) and injected (right) areas of a representative whole embryo following injection with hMCPH1 mRNA. Microtubules, green; DNA, red. Scale bar: 100 µm.

between the insect and vertebrate proteins. Finally, injections of the D-box mutant of dMCPH1-B also result in embryos with cell cycle arrest (Fig. 4A,B). As expected, levels of the mutant are comparable to that of the wild-type dMCPH1-B protein (not degraded due to the absence of Cdh1 in the early embryo) (supplementary material Fig. S3).

Embryos injected with hMCPH1 were fixed and stained for tubulin and DNA to further examine the cell-cycle defects associated with hMCPH1 overexpression (Fig. 4C). In contrast to the uninjected cells, hMCPH1-injected cells contained abnormal spindle arrangements, free centrosomes, lack of DNA, and/or DNA trapped between daughter blastomeres. These findings are consistent with a previous study in which Sororin, another substrate of APC^{Cdh1}, was overexpressed in *Xenopus* embryos (Rankin et al., 2005).

DISCUSSION

In our DIVEC screen for APC substrates in *Xenopus* egg extract, we identified two candidates: the protein encoded by *CG32982*, a previously uncharacterized *Drosophila* gene, and dMCPH1-B, a splice variant of *Drosophila mcph1*, the homologue of a human microcephaly gene. We show that dMCPH1-B undergoes Cdh1-dependent degradation in *Xenopus* egg extract and not Cdc20-dependent degradation. We show that APC-mediated degradation of dMCPH1 is restricted primarily to the splice variant dMCPH1-B, which contains an N-terminal D-box sequence required for Cdh1-mediated degradation. This restriction may allow for tissue- or developmental-specific regulation of dMCPH1 levels during the cell cycle. Consistent with this idea, we show that dMCPH1 levels are up-regulated in syncytial embryos with reduced APC activity (mr^1/mr^2), a developmental stage in which dMCPH1-B is preferentially expressed. The low level of dMCPH1-C degradation may reflect cryptic APC^{Cdh1} site(s) that is recognized in our optimized system. Alternatively, our system may be missing a co-factor required for efficient turnover of dMCPH1-C by APC^{Cdh1} in *Drosophila* embryos that allows for differential regulation of dMCPH1-B and dMCPH1-C by the APC.

Because dMCPH1-B is preferentially expressed during *Drosophila* syncytial embryogenesis and is down-regulated by the APC, one would predict that dMCPH1-B levels would oscillate throughout the cell cycle during this developmental stage. However, oscillations in total levels of APC substrates, such as mitotic cyclins, are not observed until the later cycles of syncytial embryogenesis (Raff et al., 2002). In fact, localized degradation of Cyclin B by the APC is proposed to control cell-cycle progression during these syncytial cycles (Raff et al., 2002). Thus, it is not surprising that Brunk et al. observed no change in total levels of dMCPH1 during the cell cycles of syncytial embryogenesis (Brunk et al., 2007). It is possible that dMCPH1-B, like Cyclin B, is targeted for degradation in a localized manner.

In vitro ubiquitination assays also revealed that the N-terminal D-box of dMCPH1-B is sufficient for APC^{Cdh1}-mediated ubiquitination. The finding that the N-terminal D-box is also not required for APC^{Cdh1}-mediated ubiquitination suggests that dMCPH1-B contains additional degrons. This finding is not surprising because many APC substrates have been shown to contain multiple APC-targeting motifs (Min and Lindon, 2012). Although dMCPH1-B contains multiple predicted D-box motifs, we show that deletion of the N-terminal D-box is sufficient to significantly block its Cdh1-dependent degradation in *Xenopus* interphase egg extract. dMCPH1-C also contains many of these putative D-boxes motifs, as well two motifs in the C-terminal region that are not shared with dMCPH1-B. These motifs potentially mediate the low level of degradation in APC^{Cdh1}-activated *Xenopus* egg extract.

Two isoforms of human MCPH1 produced by alternative splicing have been previously described and are structurally similar to *Drosophila* dMCPH1-B and C (Gavvovidis et al., 2012). The full-length form of hMCPH1 (used in the current study) contains an N-terminal and two C-terminal BRCT domains, whereas the short form lacks the C-terminal paired BRCT domain region. A previous report has shown that the C-terminal paired BRCT domains of full-length hMCPH1 interact with Cdc27, a subunit of the APC, and the authors hypothesized that hMCPH1 is a substrate of the APC or may regulate APC activity (Singh et al., 2012). In our current study, however, we were not able to observed changes in bulk steady-state hMCPH1 levels in cultured human cells during the cell cycle.

MCPH1 has been shown to be a rapidly evolving gene that exhibits low sequence similarity between homologs (Ponting and

Jackson, 2005). Therefore, it is perhaps not surprising that several functions of MCPH1 appear to be species-specific. For example, only hMCPH1 has been shown to regulate condensin II-dependent chromosome condensation (Yamashita et al., 2011). Thus, it is possible that APC-dependent regulation of *Drosophila* MCPH1 is not a conserved feature in humans. Alternatively, similar to the situation with Cyclin B in early embryos of *Drosophila*, levels of hMCPH1 may be regulated locally. Alternatively, the activity of hMCPH1 could be regulated via its binding partners/effectors. Indeed, binding partners, SET/Phosphatase Inhibitor 2 and E2F1, are potential or known APC substrates, respectively (Brautigan et al., 1990; Budhavarapu et al., 2012; Leung et al., 2011; Peart et al., 2010; Yang et al., 2008). Thus, the regulation of these two MCPH1 binding partners by the APC could serve as a mechanism to regulate MCPH1 activity in a cell cycle-dependent manner in vertebrates.

We show herein that overexpression of either hMCPH1 or dMCPH1-B in *Xenopus* embryos, an assay that has been previously used to characterize important cell-cycle regulators, leads to cell-cycle defects (Fang et al., 1998a; Ivanovska et al., 2004; McGarry and Kirschner, 1998; Pfleger et al., 2001a; Pfleger et al., 2001b; Rankin et al., 2005). This finding suggests that tight regulation of the levels of MCPH1 may be required for proper cell-cycle progression. Because hMCPH1 is known to negatively regulate mitotic entry and chromosome condensation, the cell-cycle defects we observe in *Xenopus* embryos overexpressing MCPH1 may be due to misregulation of these processes (Alderton et al., 2006; Tibelius et al., 2009; Trimborn et al., 2006; Yamashita et al., 2011). Although MCPH1 has been implicated in many cellular processes, regulation of its activity is not well understood. Future studies to elucidate how the activities and/or levels of MCPH1 are controlled will be important to fully understand how this evolutionarily conserved, highly evolving protein functions in regulating critical processes within the developing organism.

Acknowledgements
We thank Matthew Broadus and Andrea Page-McCaw for critical reading of the manuscript; Matt Benasutti and Terry Orr-Weaver for assistance with preparation of DNA pools for DIVEC screening; Danny Ooi and Marc Kirschner for primary screening of the DIVEC pools in *Xenopus* egg extract. *Drosophila morula* mutants were a gift from Terry Orr-Weaver.

Competing interests
The authors have no competing interests to declare.

Author contributions
All authors contributed to the conception and design of experiments, analysis of data, and manuscript preparation. Experiments were performed by S.G.H., J.L.R. and L.R.N.

Funding
The following grants from the National Institutes of Health supported this work: GM081635 and GM103926 (to E.L.), GM074044 (to L.A.L.) and GM008554 (to S.G.H.).

References
Alderton, G. K., Galbiati, L., Griffith, E., Surinya, K. H., Neitzel, H., Jackson, A. P., Jeggo, P. A. and O'Driscoll, M. (2006). Regulation of mitotic entry by microcephalin and its overlap with ATR signalling. *Nat. Cell Biol.* **8**, 725-733.

Araki, M., Yu, H. and Asano, M. (2005). A novel motif governs APC-dependent degradation of Drosophila ORC1 in vivo. *Genes Dev.* **19**, 2458-2465.

Ayad, N. G., Rankin, S., Murakami, M., Jebanathirajah, J., Gygi, S. and Kirschner, M. W. (2003). Tome-1, a trigger of mitotic entry, is degraded during G1 via the APC. *Cell* **113**, 101-113.

Brautigan, D. L., Sunwoo, J., Labbé, J. C., Fernandez, A. and Lamb, N. J. (1990). Cell cycle oscillation of phosphatase inhibitor-2 in rat fibroblasts coincident with p34cdc2 restriction. *Nature* **344**, 74-78.

Brunk, K., Vernay, B., Griffith, E., Reynolds, N. L., Strutt, D., Ingham, P. W. and Jackson, A. P. (2007). Microcephalin coordinates mitosis in the syncytial Drosophila embryo. *J. Cell Sci.* **120**, 3578-3588.

Budhavarapu, V. N., White, E. D., Mahanic, C. S., Chen, L., Lin, F. T. and Lin, W. C. (2012). Regulation of E2F1 by APC/C Cdh1 via K11 linkage-specific ubiquitin chain formation. *Cell Cycle* **11**, 2030-2038.

Fang, G., Yu, H. and Kirschner, M. W. (1998a). The checkpoint protein MAD2 and the mitotic regulator CDC20 form a ternary complex with the anaphase-promoting complex to control anaphase initiation. *Genes Dev.* **12**, 1871-1883.

Fang, G., Yu, H. and Kirschner, M. W. (1998b). Direct binding of CDC20 protein family members activates the anaphase-promoting complex in mitosis and G1. *Mol. Cell* **2**, 163-171.

Funabiki, H. and Murray, A. W. (2000). The Xenopus chromokinesin Xkid is essential for metaphase chromosome alignment and must be degraded to allow anaphase chromosome movement. *Cell* **102**, 411-424.

Gavvovidis, I., Rost, I., Trimborn, M., Kaiser, F. J., Purps, J., Wiek, C., Hanenberg, H., Neitzel, H. and Schindler, D. (2012). A novel MCPH1 isoform complements the defective chromosome condensation of human MCPH1-deficient cells. *PLoS ONE* **7**, e40387.

Glotzer, M., Murray, A. W. and Kirschner, M. W. (1991). Cyclin is degraded by the ubiquitin pathway. *Nature* **349**, 132-138.

Greenspan, R. J. (2004). *Fly Pushing: The Theory and Practice of Drosophila Genetics*. Cold Spring Harbor, NY: Cold Spring Harbor Laboratory Press.

Gruber, R., Zhou, Z., Sukchev, M., Joerss, T., Frappart, P. O. and Wang, Z. Q. (2011). MCPH1 regulates the neuroprogenitor division mode by coupling the centrosomal cycle with mitotic entry through the Chk1-Cdc25 pathway. *Nat. Cell Biol.* **13**, 1325-1334.

Ivanovska, I., Lee, E., Kwan, K. M., Fenger, D. D. and Orr-Weaver, T. L. (2004). The Drosophila MOS ortholog is not essential for meiosis. *Curr. Biol.* **14**, 75-80.

Jackson, A. P., Eastwood, H., Bell, S. M., Adu, J., Toomes, C., Carr, I. M., Roberts, E., Hampshire, D. J., Crow, Y. J., Mighell, A. J. et al. (2002). Identification of microcephalin, a protein implicated in determining the size of the human brain. *Am. J. Hum. Genet.* **71**, 136-142.

King, R. W., Peters, J. M., Tugendreich, S., Rolfe, M., Hieter, P. and Kirschner, M. W. (1995). A 20S complex containing CDC27 and CDC16 catalyzes the mitosis-specific conjugation of ubiquitin to cyclin B. *Cell* **81**, 279-288.

King, R. W., Glotzer, M. and Kirschner, M. W. (1996). Mutagenic analysis of the destruction signal of mitotic cyclins and structural characterization of ubiquitinated intermediates. *Mol. Biol. Cell* **7**, 1343-1357.

King, R. W., Lustig, K. D., Stukenberg, P. T., McGarry, T. J. and Kirschner, M. W. (1997). Expression cloning in the test tube. *Science* **277**, 973-974.

Kulkarni, K., Zhang, Z., Chang, L., Yang, J., da Fonseca, P. C. and Barford, D. (2013). Building a pseudo-atomic model of the anaphase-promoting complex. *Acta Crystallogr. D Biol. Crystallogr.* **69**, 2236-2243.

Lee, L. A., Lee, E., Anderson, M. A., Vardy, L., Tahinci, E., Ali, S. M., Kashevsky, H., Benasutti, M., Kirschner, M. W. and Orr-Weaver, T. L. (2005). Drosophila genome-scale screen for PAN GU kinase substrates identifies Mat89Bb as a cell cycle regulator. *Dev. Cell* **8**, 435-442.

Leung, J. W., Leitch, A., Wood, J. L., Shaw-Smith, C., Metcalfe, K., Bicknell, L. S., Jackson, A. P. and Chen, J. (2011). SET nuclear oncogene associates with microcephalin/MCPH1 and regulates chromosome condensation. *J. Biol. Chem.* **286**, 21393-21400.

Lin, S. Y., Rai, R., Li, K., Xu, Z. X. and Elledge, S. J. (2005). BRIT1/MCPH1 is a DNA damage responsive protein that regulates the Brca1-Chk1 pathway, implicating checkpoint dysfunction in microcephaly. *Proc. Natl. Acad. Sci. USA* **102**, 15105-15109.

Lorca, T., Castro, A., Martinez, A. M., Vigneron, S., Morin, N., Sigrist, S., Lehner, C., Dorée, M. and Labbé, J. C. (1998). Fizzy is required for activation of the APC/cyclosome in Xenopus egg extracts. *EMBO J.* **17**, 3565-3575.

Lunardi, A., Di Minin, G., Provero, P., Dal Ferro, M., Carotti, M., Del Sal, G. and Collavin, L. (2010). A genome-scale protein interaction profile of Drosophila p53 uncovers additional nodes of the human p53 network. *Proc. Natl. Acad. Sci. USA* **107**, 6322-6327.

McGarry, T. J. and Kirschner, M. W. (1998). Geminin, an inhibitor of DNA replication, is degraded during mitosis. *Cell* **93**, 1043-1053.

Min, M. and Lindon, C. (2012). Substrate targeting by the ubiquitin–proteasome system in mitosis. *Semin. Cell Dev. Biol.* **23**, 482-491.

Peart, M. J., Poyurovsky, M. V., Kass, E. M., Urist, M., Verschuren, E. W., Summers, M. K., Jackson, P. K. and Prives, C. (2010). APC/C(Cdc20) targets E2F1 for degradation in prometaphase. *Cell Cycle* **9**, 3956-3964.

Peng, G., Yim, E. K., Dai, H., Jackson, A. P., Burgt, I., Pan, M. R., Hu, R., Li, K. and Lin, S. Y. (2009). BRIT1/MCPH1 links chromatin remodelling to DNA damage response. *Nat. Cell Biol.* **11**, 865-872.

Peters, J. M. (2006). The anaphase promoting complex/cyclosome: a machine designed to destroy. *Nat. Rev. Mol. Cell Biol.* **7**, 644-656.

Pfleger, C. M. and Kirschner, M. W. (2000). The KEN box: an APC recognition signal distinct from the D box targeted by Cdh1. *Genes Dev.* **14**, 655-665.

Pfleger, C. M., Lee, E. and Kirschner, M. W. (2001a). Substrate recognition by the Cdc20 and Cdh1 components of the anaphase-promoting complex. *Genes Dev.* **15**, 2396-2407.

Pfleger, C. M., Salic, A., Lee, E. and Kirschner, M. W. (2001b). Inhibition of Cdh1-APC by the MAD2-related protein MAD2L2: a novel mechanism for regulating Cdh1. *Genes Dev.* **15**, 1759-1764.

Ponting, C. and Jackson, A. P. (2005). Evolution of primary microcephaly genes and the enlargement of primate brains. *Curr. Opin. Genet. Dev.* **15**, 241-248.

Raff, J. W., Jeffers, K. and Huang, J. Y. (2002). The roles of Fzy/Cdc20 and Fzr/Cdh1 in regulating the destruction of cyclin B in space and time. *J. Cell Biol.* **157**, 1139-1149.
Rai, R., Dai, H., Multani, A. S., Li, K., Chin, K., Gray, J., Lahad, J. P., Liang, J., Mills, G. B., Meric-Bernstam, F. et al. (2006). BRIT1 regulates early DNA damage response, chromosomal integrity, and cancer. *Cancer Cell* **10**, 145-157.
Rankin, S., Ayad, N. G. and Kirschner, M. W. (2005). Sororin, a substrate of the anaphase-promoting complex, is required for sister chromatid cohesion in vertebrates. *Mol. Cell* **18**, 185-200.
Reed, B. H. and Orr-Weaver, T. L. (1997). The Drosophila gene morula inhibits mitotic functions in the endo cell cycle and the mitotic cell cycle. *Development* **124**, 3543-3553.
Rickmyre, J. L., Dasgupta, S., Ooi, D. L., Keel, J., Lee, E., Kirschner, M. W., Waddell, S. and Lee, L. A. (2007). The Drosophila homolog of MCPH1, a human microcephaly gene, is required for genomic stability in the early embryo. *J. Cell Sci.* **120**, 3565-3577.
Singh, N., Wiltshire, T. D., Thompson, J. R., Mer, G. and Couch, F. J. (2012). Molecular basis for the association of microcephalin (MCPH1) protein with the cell division cycle protein 27 (Cdc27) subunit of the anaphase-promoting complex. *J. Biol. Chem.* **287**, 2854-2862.
Stapleton, M., Liao, G., Brokstein, P., Hong, L., Carninci, P., Shiraki, T., Hayashizaki, Y., Champe, M., Pacleb, J., Wan, K. et al. (2002). The Drosophila gene collection: identification of putative full-length cDNAs for 70% of D. melanogaster genes. *Genome Res.* **12**, 1294-1300.
Tibelius, A., Marhold, J., Zentgraf, H., Heilig, C. E., Neitzel, H., Ducommun, B., Rauch, A., Ho, A. D., Bartek, J. and Krämer, A. (2009). Microcephalin and pericentrin regulate mitotic entry via centrosome-associated Chk1. *J. Cell Biol.* **185**, 1149-1157.
Trimborn, M., Schindler, D., Neitzel, H. and Hirano, T. (2006). Misregulated chromosome condensation in MCPH1 primary microcephaly is mediated by condensin II. *Cell Cycle* **5**, 322-326.
Tunquist, B. J. and Maller, J. L. (2003). Under arrest: cytostatic factor (CSF)-mediated metaphase arrest in vertebrate eggs. *Genes Dev.* **17**, 683-710.
Wei, W., Ayad, N. G., Wan, Y., Zhang, G. J., Kirschner, M. W. and Kaelin, W. G., Jr. (2004). Degradation of the SCF component Skp2 in cell-cycle phase G1 by the anaphase-promoting complex. *Nature* **428**, 194-198.
Woods, C. G., Bond, J. and Enard, W. (2005). Autosomal recessive primary microcephaly (MCPH): a review of clinical, molecular, and evolutionary findings. *Am. J. Hum. Genet.* **76**, 717-728.
Yamashita, D., Shintomi, K., Ono, T., Gavvovidis, I., Schindler, D., Neitzel, H., Trimborn, M. and Hirano, T. (2011). MCPH1 regulates chromosome condensation and shaping as a composite modulator of condensin II. *J. Cell Biol.* **194**, 841-854.
Yang, S. Z., Lin, F. T. and Lin, W. C. (2008). MCPH1/BRIT1 cooperates with E2F1 in the activation of checkpoint, DNA repair and apoptosis. *EMBO Rep.* **9**, 907-915.
Zou, H., McGarry, T. J., Bernal, T. and Kirschner, M. W. (1999). Identification of a vertebrate sister-chromatid separation inhibitor involved in transformation and tumorigenesis. *Science* **285**, 418-422.

Biology Open (2014) 000, 1–8 doi:10.1242/bio.20148318

Supplementary Material
Sarah G. Hainline et al. doi: 10.1242/bio.20148318

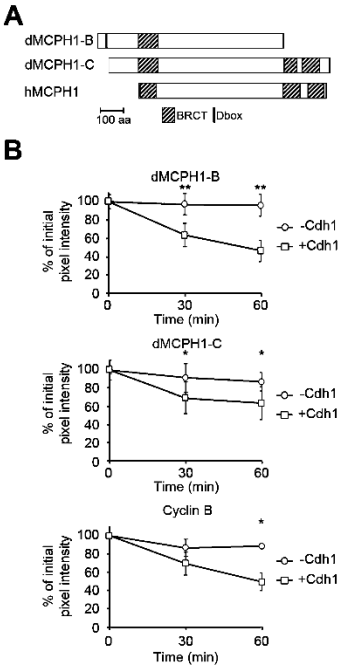

Fig. S1. APC regulates stability of dMCPH1-B and dMCPH1-C. (A) Schematic representation of dMCPH1-B, dMCPH1-C, and hMCPH1. (B) Quantitation of pixel intensity of autoradiogram in Fig. 2B. Percent of initial pixel intensity was plotted over time for radiolabeled dMCPH1-B, dMCPH1-C, or Cyclin B incubated in *Xenopus* interphase egg extract in the absence or presence of Cdh1. $^{**}p<0.005$, $^{*}p<0.05$.

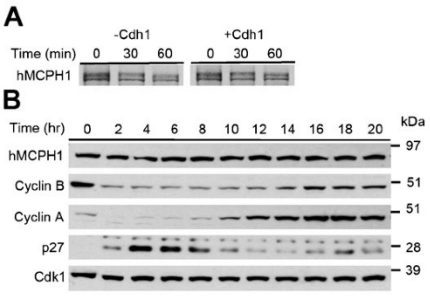

Fig. S2. APC does not regulate the stability of hMCPH1. (A) Autoradiogram of radiolabeled hMCPH1 incubated in *Xenopus* interphase egg extract in the absence or presence of Cdh1. (B) Levels of hMCPH1 do not notably fluctuate in a cell cycle-dependent manner. Immunoblot analysis of hMCPH1, Cyclin B, Cyclin A, p27, and Cdk1 in lysates derived from synchronized HeLa cells 0–20 hours after nocodazole release. Degradation of Cyclin A and B occurs in prophase and metaphase, respectively, whereas degradation of p27 marks late G1/S.

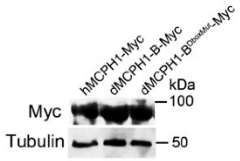

Fig. S3. *Xenopus* embryos express hMCPH1-Myc, dMCPH1-B-Myc, and dMCPH1-B^{DboxMut}-Myc at similar levels. Immunoblot for Myc and tubulin (loading control) of lysates derived from *Xenopus* embryos after injection with mRNA encoding hMCPH1-Myc, dMCPH1-B-Myc, or dMCPH1-B^{DboxMut}-Myc.

The Small Molecule IMR-1 Inhibits the Notch Transcriptional Activation Complex to Suppress Tumorigenesis

Astudillo L, Da Silva TG, Wang Z, Han X, Jin K, VanWye J, Zhu X, Weaver K, Oashi T, Lopes PE, Orton D, **Neitzel LR**, Lee E, Landgraf R, Robbins DJ, MacKerell AD Jr, Capobianco AJ.

Cancer Res **2016 76(12):3593-603**

doi: 10.1158/0008-5472.CAN-16-0061

HHS Public Access

Author manuscript

Cancer Res. Author manuscript; available in PMC 2017 June 15.

Published in final edited form as:

Cancer Res. 2016 June 15; 76(12): 3593–3603. doi:10.1158/0008-5472.CAN-16-0061.

The small molecule IMR-1 inhibits the Notch transcriptional activation complex to suppress tumorigenesis

Luisana Astudillo[1,@], **Thiago G. Da Silva**[1,@], **Zhiqiang Wang**[1,#], **Xiaoqing Han**[1,#], **Ke Jin**[1,#], **Jeffrey VanWye**[1,#], **Xiaoxia Zhu**[1], **Kelly Weaver**[1], **Taiji Oashi**[2], **Pedro E.M. Lopes**[2], **Darren Orton**[3], **Leif R. Neitzel**[4], **Ethan Lee**[4], **Ralf Landgraf**[5], **David J Robbins**[1], **Alexander D. MacKerell Jr.**[2], and **Anthony J. Capobianco**[1,*]

[1]Molecular Oncology Program, Division of Surgical Oncology, Dewitt Daughtry Family Department of Surgery, and Sylvester Comprehensive Cancer Center, Miller School of Medicine, University of Miami, 1600 NW 10th Ave. Miami, FL 33136 USA

[2]Department of Pharmaceutical Sciences, University of Maryland, School of Pharmacy, 20 Penn Street, Baltimore, MD 21201, USA

[3]StemSynergy Therapeutics, Inc., 1951 NW 7th Ave, Suite 300, Miami, Florida, 33136, USA

[4]Department of Cell and Developmental Biology and Ingram Cancer Center, Vanderbilt University Medical Center, Nashville, TN 37232, USA

[5]Department of Biochemistry and Molecular Biology and Sylvester Comprehensive Cancer Center, Miller School of Medicine, University of Miami, 1600 NW 10th Ave. Miami, FL 33136 USA

Abstract

In many cancers, aberrant Notch activity has been demonstrated to play a role in the initiation and maintenance of the neoplastic phenotype and in cancer stem cells, which may allude to its additional involvement in metastasis and resistance to therapy. Therefore, Notch is an exceedingly attractive therapeutic target in cancer, but the full range of potential targets within the pathway have been under-explored. To date, there are no small molecule inhibitors that directly target the intracellular Notch pathway or the assembly of the transcriptional activation complex. Here, we describe an *in vitro* assay that quantitatively measures the assembly of the Notch transcriptional complex on DNA. Integrating this approach with computer-aided drug design, we explored potential ligand binding sites and screened for compounds that could disrupt the assembly of the Notch transcriptional activation complex. We identified a small molecule inhibitor, termed Inhibitor of Mastermind Recruitment-1 (IMR-1), that disrupted the recruitment of Mastermind-like 1 (Maml1) to the Notch transcriptional activation complex on chromatin, thereby attenuating Notch target gene transcription. Furthermore, IMR-1 inhibited the growth of Notch-dependent cell lines and significantly abrogated the growth of patient-derived tumor xenografts. Taken together, our findings suggest that a novel class of Notch inhibitors targeting the transcriptional activation

*Corresponding author: Anthony J. Capobianco, University of Miami, 1600 NW 10th Avenue RMSB 1040 (R-104), Miami, FL 33136 USA, Phone: 305-243-6308 Fax: 305-243-8039, tcapobianco@med.miami.edu.

@Authors contributed equally.

#Authors contributed equally.

EL, DJR and AJC disclose that they are cofounders in Stemsynergy Therapeutics, Inc.

complex may represent a new paradigm for Notch-based anticancer therapeutics, warranting further preclinical characterization.

Keywords

Notch; Mastermind; transcription; Computer-aided drug design; cancer

INTRODUCTION

The promise of precision treatment for cancer is predicated on the assumption that a comprehensive array of targeted therapeutics will be available in the future. Therefore, there is a substantial unmet need to identify and successfully drug not only the drivers but also the signaling pathways that are critical for the maintenance of the neoplastic phenotype. Furthermore, there is a need for therapeutic depth in these critical pathways to overcome acquired resistance. However, the number of "druggable" targets is finite which represents a potential hurdle to personalized medicine. As most proteins function in higher order complexes mediated by protein-protein interactions, targeting these interactions represents a broad range of potential targets and therapeutics to be explored.

The Notch pathway is widely utilized in development to govern cell fate specification and to balance proliferative capacity and differentiation state(1,2). In the adult, the Notch pathway is restricted to small populations of progenitor and stem cells of regenerating tissues such as the colon and brain(3,4). However, in many human cancers, the Notch pathway becomes reactivated (for review(5)). The deregulation of the Notch pathway underlies many aspects of cancer physiology in a cell type- and context-dependent manner(5–7). Aberrant Notch activity has been demonstrated to play a role in the initiation and maintenance of the neoplastic phenotype as well as playing a central role in cancer stem cells, thereby underlying a role in metastasis and resistance to therapy(8,9).

Notch drives a context dependent cellular response by initiating and maintaining a transcriptional cascade(10,11). This transcriptional response is mediated by Notch by directing the formation of a core transcriptional activation complex, termed the Notch Ternary Complex (NTC). The NTC comprises the DNA binding protein CSL (CBF-1/RBP-J, Su(H), Lag-1), the intracellular domain of Notch (NICD) and the co-activator protein Mastermind-like 1 (Maml1)(12–14). Current approaches to inhibit the Notch pathway include monoclonal antibodies that target and disrupt Notch-ligand interactions or small molecule inhibition of the presenilin-dependent γ-secretase (γ-secretase inhibitors, GSI)(15–21). Both of these approaches serve to block ligand-dependent production of NICD, acting at the top of the Notch signaling cascade. Alternatively, truncated forms of Maml1 have been demonstrated to act in a dominant negative manner in the Notch pathway(13,22–26). Along these lines, Moellering *et al.* designed and synthesized a peptide derived from Maml1, termed SAHM, which competes with Maml1 and inhibits the formation of the NTC(27). Therefore, SAHM functions as a dominant negative inhibitor(27). Although this approach worked at a scale feasible for mouse studies, the use of peptides as therapeutics still face significant challenges, whereas small molecule inhibitors represent a more desirable

approach for cancer therapeutics. However, to date there are no small molecule inhibitors of the transcriptional activation complex or that are specific to the Notch pathway itself.

Herein, we present *proof of concept* for a first in class inhibitor of the Notch transcriptional activation complex. We describe the identification and validation of a small molecule inhibitor of Mastermind recruitment-1 (IMR-1) to the Notch transcriptional activation complex. We demonstrate that IMR-1 prevents the recruitment of Maml1 to the NTC on chromatin, inhibits Notch target gene transcription and dramatically inhibits tumor growth in a patient-derived tumor xenograft model.

MATERIALS AND METHODS

Compounds

Compounds were purchased from ChemDiv (USA), ChemBridge (USA) or SPECS (The Netherlands). Catalogue numbers and chemical details are available upon request.

Cell lines

OE19 and OE33 human esophageal adenocarcinoma cell lines were obtained from the European Collection of Cell Culture (Salisbury, UK). SUM-149 and SUM-159 (human ER- basal breast cancer) were obtained from Dr. Joyce Slingerland at the University of Miami, Miller School of Medicine. Cell lines 786-0 (human renal adenocarcinoma), HT-1080 (human fibrosarcoma), MCF-7 and T47D (ER+ luminal breast cancer), and H-23 (non-small cell lung adenocarcinoma) were obtained from ATCC (USA). All cell lines were tested for mycoplasma contamination and propagated in growth media as specified by the provider. Cell lines were obtained between 2008 and 2015 and authenticated by ATCC (cell line authentication profiling utilizing short tandem repeat profiling).

Notch complex assembly assay

Recombinant proteins were expressed using baculovirus expression vectors in SF21 cells and purified as previously described(13,28). Unless otherwise stated, all assays contained 125 fmol of double-stranded (DS) oligonucleotide, CSL, Notch, and Maml1 proteins in TBS-T buffer containing 0.2% BSA (bovine serum albumin) and 100 μg/mL salmon sperm DNA. Briefly, the Notch complex was assembled on a biotinylated DS oligonucleotide harboring one CSL binding site (5′-AAACACGCCGTGGGAAAAAATTTATG-3′). Complex assembly was quantitated using AlphaScreen technology on an Envision plate reader (Perkin Elmer, USA), following manufacturer's instructions. Proteins in the complex were detected using specific antibodies to either Maml1 (Cell Signaling; D3K7B), Notch1 (Abcam, 52627), or CSL (anti-His, Abcam, 18184). Streptavidin-conjugated donor beads (Perkin Elmer) were used to bind the DS oligonucleotide and Protein-A conjugated acceptor beads (Perkin Elmer) to detect antibody-coated proteins. NTC components were added to wells containing the small molecules to be assayed and incubated for 30 minutes. Acceptor beads and the antibody specific for Maml1, Notch1 or CSL were then added to the reaction mixture and incubated in the dark for 30 minutes, followed by addition of the donor beads and incubated for in the dark for 1 h. Assays were performed in 384-well plates in triplicate

(AlphaScreen plate, Perkin Elmer). Data analysis was performed using GraphPad Prism software (Version 5).

Western analysis

Protein analysis was performed as previously described (28) using anti-Notch1 (Abcam, ab52627), anti-Notch1^{val1744} (Cell Signaling, 4147S) and anti-GAPDH (Abcam, ab9483) antibodies.

Real-time qPCR analysis

Reverse transcription and qPCR analysis were performed as previously described(28). Gene expression was normalized to *TBP* and *HPRT*. TaqMan primer sequences are available upon request.

DNA pulldown

DNA pulldown was performed as previously described (28). 293T cells were transfected with Maml1, NICD and NICD single mutants (R2096, R2105, R2061 and R2071) using LipoJet *in vitro* transfection kit (SignaGen Laboratories). Proteins bound to the beads were analyzed by Western blotting.

Surface Plasmon Resonance

Notch1 was covalently immobilized to the sensor chip surface (CM5 chip, GE) by standard amine coupling(29). Experiments were performed on a Biacore T200 instrument (GE Healthcare) at 25 °C using PBS (10 mM, pH 7.5) containing 5% DMSO as running buffer. The sample SPR signal was corrected with its respective control containing DMSO. Data visualization and analysis were performed using Biacore T200 software (GE Healthcare) and Origin 8.0 (OriginLab).

Statistics

P value was calculated using chi-square in contingency table. The sample size was chosen to be greater than the minimal sample size from power assessment as described previously(30). Data are presented as mean ± SEM and were analyzed by 2-tailed Student's t test. A *P* value of less than 0.05 was considered significant.

RESULTS

Computer-aided drug design (CADD) of CSL-Notch1 interface inhibitors

Assembly of the Notch transcriptional activation complex is thought to occur in a stepwise fashion(13,28,31,32). The crystal structure of the NTC (PDB ID: 2F8X) shows a protein-protein interface between the ANK repeat domain of Notch1 and CSL that could act as a binding site for small molecules. Notch1 and CSL create a cleft required for stable Maml1 association to the complex. Once bound, Maml1 locks the core scaffold together and serves to recruit the higher order transcription regulatory machinery, thereby initiating the expression of Notch target genes(12,28,33). We reasoned that CSL-Notch1 interactions could be disrupted upon small molecule binding, thus preventing Maml1 recruitment and

leading to inhibition of NTC assembly. Since Maml1 is critical to Notch activity(27), compounds that prevent Maml1 recruitment would potentially inhibit Notch transcriptional activation. Therefore, to identify compounds that could inhibit the NTC assembly we performed *in silico* analysis of the NTC structure to obtain structural variability for the initial screening of a large database of small molecules. We utilized 8 representative structures of the NTC core complex that were generated using Molecular Dynamics (MD) simulations and the X-ray crystallographic structure. Sites on the NTC were evaluated by docking 1000 chemically distinct probe molecules and calculating the binding response (BR) score, which is based on energetic and geometric criteria(34). A common site on the ANK repeat domain of Notch1 was identified on 7 of the MD conformations and the crystal conformation, yielding a total of 8 conformations for screening. This site is composed of residues that span the 4^{th} through 7^{th} ankyrin repeats of Notch1. Primary *in silico* screening of this pocket was performed on an in-house database (>1.5 million commercially available drug-like small molecules). Each ligand was docked into the putative binding site for each protein conformation using the program DOCK(35) and a score was assigned based on the most favorable normalized van der Waals (vdW) attractive energy among all the protein conformations. A secondary screening of the top 50,000 molecules selected from the primary screens involved more rigorous optimization during docking. Each compound was docked individually against each of the 8 protein conformations with the most favorable normalized total interaction energy over all the conformations taken as the score for each compound. The top scoring 1000 compounds were selected. The final compounds for experimental evaluation were chosen based on their chemical diversity to maximize the possibility of identifying unique leads for further optimization and development and on their physicochemical properties to maximize their potential bioavailability(36). We selected 150 compounds that were obtained from commercial vendors for testing.

Development of a Notch ternary complex assembly assay

We developed an *in vitro* assay that quantitatively measures the assembly of the NTC on DNA to screen for compounds that could inhibit NTC formation. Briefly, baculovirus-produced CSL, Notch1, and Maml1 are used to build the NTC on a biotinylated oligonucleotide scaffold that harbors a CSL binding site. A Maml1 specific antibody is used to detect recruitment of Maml1 to the complex on DNA and complex formation is then detected with the proximity-based AlphaScreen technology (Perkin Elmer) using streptavidin donor and protein A acceptor beads (Fig. 1A). Therefore, a signal should only be generated when Maml1 is recruited to CSL on DNA. To demonstrate that the signal observed resulted from the recruitment of Maml1 to the complex, Maml1 was titrated against a fixed amount of the remaining reaction components. A dose-dependent increase in signal was observed upon Maml1 addition up to the stoichiometric equivalence point (250 fmol, Fig. 1B, left panel). Similar results were observed upon titration of Notch1 (Fig. 1B, right panel), indicating that recruitment of Maml1 depends on Notch1 binding to CSL. Furthermore, complex assembly is dependent on CSL binding to DNA, since an oligonucleotide that harbors a mutant CSL binding site does not generate an appreciable signal (Fig. 1C, shaded area).

To further authenticate the *in vitro* NTC assembly assay, we probed different components and conditions to determine if the assay recapitulates established parameters of the NTC on DNA. As previously described for Maml1 (Fig. 1B, left panel), a signal is only observed when all components of the NTC are present in the reaction (Fig. 1D, lanes 1-5). No signal is observed when either CSL or Notch1 is absent from the reaction (Fig. 1D, lanes 6 and 7), indicating that binding of Maml1 to the complex requires both CSL and Notch1. Furthermore, CSL binds to DNA in the absence of the other NTC components (Fig. 1D, lanes 16–19), whereas Notch1 requires CSL, but not Maml1, to bind to DNA (Fig. 1D, lanes 11–13). We also tested the requirement of specific protein domains(37). Deletion of the Notch RAM domain caused a loss in the binding of both Notch1 and Maml1 to the complex (Fig. 1D, lanes 9 and 15), whereas deletion of the Notch PEST domain did not alter the assembly of the NTC (Fig. 1D, lanes 8 and 14). The results described here demonstrate that the assay measures the assembly of a *bona fide* NTC, as the recruitment of Maml1 to the NTC is dependent on the high affinity binding of Notch1 to CSL through its RAM domain.

Screening of small molecule inhibitors of the NTC led to the identification of IMR-1

The *in vitro* NTC assay was utilized to screen small molecules derived from computer-aided drug design (CADD). From the 150 compounds tested, 30 compounds showed a decrease in Maml1 recruitment of at least 50% compared to the positive control (all components of the NTC) (supplementary Fig. 1A). In particular, three compounds showed remarkable inhibitory activity (> 90%), and compound 1–134 inhibited assembly by 97% (supplementary Fig. 1A, shaded area). To obtain structural variability and validate these results, the scaffold of 1–134 was subjected to *in silico* similarity search(38) using a virtual 2D database. Fifty-four of the 1–134 derivative compounds were commercially available and tested at 30 μM. Only 16 compounds inhibited complex assembly by more than 50% (supplementary Fig. 1B). These compounds were counter-screened against Notch1 and CSL antibodies using the *in vitro* NTC assembly assay to demonstrate their specificity at displacing Maml1 from the complex. The data indicates that the 1–134 derivatives did not displace CSL or Notch1 from the complex (supplementary Fig. 1C, white bars and striped bars, respectively). Therefore, the 1–134 derivatives specifically disrupt the binding of Maml1 to the NTC *in vitro*. To better evaluate the potency of these compounds, the *in vitro* NTC assay was used to generate dose-response curves and determine their IC_{50}.

The core molecular scaffold of 1–134 and its derivatives is a thiazolidinone consisting of a phenyl ring and a rhodanine moiety connected by a double bond. Dose-response curves of 1–134 and its sixteen prioritized analogs indicated that the parent compound 1–134 showed promising *in vitro* potency (IC_{50} = 6 μM) in the NTC assay. The rhodanine ester compound (1-134-83, termed IMR-1) exhibited an IC_{50} of 26 μM (Fig. 1E), whereas the other compounds exhibited IC_{50} greater than 26 μM (data not shown). Since ester containing compounds may undergo hydrolysis *in vivo* by the action of several esterases(39), we also tested the acid metabolite of IMR-1 (compound IMR-1A) and observed a 50-fold increase in potency for IMR-1A (IC_{50} = 0.5 μM) with respect to IMR-1. Interestingly, removal of the methoxy group of 1-134-2, corresponding to compound 1-134-22 (Fig. 1E), leads to no inhibition of NTC formation as evident by the large concentration of 1-134-22 required to

observe a small decrease in signal in the *in vitro* NTC assay (Fig. 1E). These results also suggest a role of the methoxy group at this position in binding to the target protein(s).

IMR-1 demonstrates non-covalent binding to Notch1 with micromolar affinity

To determine the affinity of small molecule inhibitors of the NTC for Notch1 and characterize their molecular interactions, we used surface plasmon resonance (SPR). Representative sensorgrams determined for the association of 1–134, IMR-1 and IMR-1A to NICD are presented in Fig. 2A–C. The dissociation constants associated with binding of the compounds to NICD was determined using the equilibrium approach by plotting the equilibrium response (R_{eq}) as a function of the compound concentration and fitting the data to a 1:1 binding model (Fig. 2D). Compound 1–134 binds with moderate affinity to NICD ($K_D = 17 \pm 5$ μM). A slightly higher affinity was observed for IMR-1 ($K_D = 11 \pm 3$ μM), whereas a significantly higher affinity to NICD was observed for IMR-1A ($K_D = 2.9 \pm 0.6$ μM). Noteworthy, the SPR sensorgrams measured for association of 1–134, IMR-1 and IMR-1A indicate non-covalent, reversible binding to Notch1 as evident by the dissociation curves reaching baseline upon introduction of buffer solution with a rate constant within the range of small molecule dissociation from proteins (Fig. 2A–C).

To obtain insight into the molecular interactions between IMR-1 and the NTC and assessment of the binding site, we performed molecular docking simulations of the inhibitors to the NTC (PDB file: 2F8X). The data suggested that residues from ANK (R2096, R2105, R2061 and R2071) were located within the binding pocket. To determine the effect of each residue on the binding of IMR-1 to Notch1, the affinity of NTC inhibitors to wild type NICD and single point mutated NICD (R2096A, R2105A, R2061A and R2071A) was determined by SPR. Replacement of R2061 and R2071 with alanine decreases the affinity of IMR-1 to NICD by approximately 5-fold (K_D of 35.6 μM and 38.7 μM, respectively) (Fig. 2E). No effect was observed upon substitution of R2096 and R2105 by alanine. These results suggest that R2061 and R2071 play an intimate role in the binding of IMR-1 to NICD. Docking of IMR-1 to the NTC suggests that IMR-1 interacts with Notch1 and CSL residues (Fig. 2F). CSL residues interacting with IMR-1 include Q362, N363, G384 and M126. In addition, the carbonyl group from the ester moiety of IMR-1 interacts with one of the –NH groups from the side chain of R2061 from Notch1 through hydrogen bonding, consistent with the lower affinity of IMR-1 to R2061A (Fig. 2E). The docking model also suggests that R2071 (Notch1) is located in close proximity to IMR-1 (Fig. 2F) and may be involved in long-range interactions with IMR-1, which would explain the decrease in affinity of IMR-1 to R2071A. To determine if these mutations effect the ability of Notch1 to form the NTC, we analyzed complex formation by DNA pulldown and the *in vitro* NTC assay. DNA pulldown on CSL oligonucleotide beads (Fig. 2G) as well as the NTC assay (Fig. 2H) demonstrates mutated NICD proteins retain the ability to form the ternary complex, as evident by the similar signal observed between the wild type (WT) and mutated NICD proteins.

IMR-1 inhibits Notch target gene transcription by disrupting Maml1 recruitment to chromatin

Once we established that the CADD-derived compounds specifically disrupts the recruitment of Maml1 to the activation complex *in vitro*, we sought to determine if 1-134 and its sixteen prioritized derivatives exhibit biological activity using a cell-based assay. A colony formation assay was used a secondary screening to test biological activity. To this end, cell lines selected for screening were classified into two groups based on their sensitivity to DAPT (a GSI) to establish a criterion for Notch dependence. We reasoned that inhibition of cell growth and gene transcription by DAPT indicates specific inhibition of Notch activity. Therefore, cell lines exhibiting inhibition of growth and transcription of Notch target genes upon treatment with DAPT were classified as Notch-dependent, whereas those in which transcription and growth did not significantly change upon DAPT treatment were classified as Notch-independent cell lines. A decrease in colony formation of Notch dependent cell lines is observed upon treatment with IMR-1 when compared to the control (DMSO). However, no effect was observed for 1-134 and its other derivatives up to concentrations of 30–45 μM (data not shown), likely due to low cell permeability. Therefore, IMR-1 was prioritized for further testing.

To determine the effect of IMR-1 treatment on the assembly of the NTC in cells, Notch-dependent cell lines OE33 and 786-0 were treated with DAPT or IMR-1. Treatment with DAPT decreased the occupancy of Notch and Maml1 on the *HES1* promoter using a chromatin immunoprecipitation (ChIP) assay (Fig. 3A). This effect is caused by a decrease in the NICD pool due to the inhibition of presenilin-dependent γ-secretase. Treatment of OE33 and 786-0 with IMR-1 also decreased the occupancy of Maml1 on the *HES1* promoter but, in contrast to DAPT treatment, IMR-1 treatment did not affect the occupancy of Notch1 on the *HES1* promoter (Fig 3A). Western analysis of the lysates demonstrates that IMR-1 treatment does not change the levels of NICD in cells (Fig. 3A, right panel). Therefore, these data indicate that IMR-1 specifically disrupts the recruitment of Maml1 to chromatin while the binding of NICD to CSL is unaffected. As IMR-1 treatment leads to disruption of the NTC on chromatin, we sought to determine whether IMR-1 also abrogates Notch target gene transcription (Fig. 3B). IMR-1 treated cells displayed a dose-dependent decrease in Notch target gene transcription similar to the control cells treated with DAPT. As proof of specificity, transcription of the housekeeping gene *HPRT* was unaltered in treated cells. In order to test the effects of Notch inhibition on proliferation, we performed a colony formation assay. Treatment of cells with IMR-1 displayed a dose-dependent reduction in colony formation in both 786-0 and OE33 cell lines (Fig. 3C). To extend the analysis of tumor cell growth inhibition, we selected several commonly used cancer cell lines to test for sensitivity to IMR-1 (Fig. 4A). The sensitivity profile for cells treated with either IMR-1 or DAPT was comparable indicating that IMR-1 is specifically inhibiting Notch activity (Fig. 4A). Colony formation displayed a similar stratification: i.e., cells with transcriptional sensitivity to IMR-1 and DAPT treatment exhibited impaired colony forming ability (Fig. 4B). Cells that are refractory to DAPT were equally resistant to IMR-1. Taken together, these data indicate that IMR-1 selectively affect Notch-dependent cell lines via the inhibition of Notch-directed transcriptional activation by blocking the recruitment of Mam1 to the Notch transcriptional complex on chromatin.

IMR-1 inhibits xenograft tumor growth

To determine the effect of IMR-1 on tumor formation in an animal model of cancer, we utilized an established xenograft model(40). When introduced into the flank of a nude mouse, 5×10^6 OE19 human esophageal adenocarcinoma cells readily form tumors over the course of 4 weeks. Treatment of these mice with 15 mg/kg IMR-1 readily blocks tumor establishment. In contrast, treatment with DMSO (control) had no effect on tumor growth (supplementary Fig. 2). IMR-1 treatment at 15 mg/kg caused no observable adverse effects on the animal and body weight remained constant throughout the treatment course (supplementary Fig. 2). To further examine the effect of IMR-1 on established tumors, we utilized two independent patient-derived esophageal adenocarcinoma xenograft (PDX) models. Tumors were established in NSG mice to the size of 200 mm^3 prior to the initiation of treatment. Mice were then dosed daily via i.p. injection with either IMR-1 (15 mg/kg) or DAPT (20 mg/kg) and compared to DMSO (control). Treatment of both PDX tumors with IMR-1 significantly abrogated growth to a similar level achieved with DAPT treatment (Fig. 5A and 5B), without any significant weight loss or other visible signs of adverse effects in the treated animals (Supplementary Fig. 3). Following 24 days of treatment, tumors were harvested and Notch target gene transcription was evaluated. These data demonstrate that treatment with IMR-1 dramatically reduced the expression level of the tested Notch target genes (Hes1, HeyL, and Notch3; Fig. 5C) in both PDX models. Similar reductions in Notch transcription were observed in DAPT treated tumors (Fig. 5C, right panel). Therefore, these data demonstrate that the small molecule IMR-1 is an inhibitor of the Notch transcriptional activation complex with demonstrated efficacy in xenograft tumor models.

IMR-1 is metabolized *in vivo* to its acid metabolite IMR-1A

In vitro studies indicate that compound IMR-1 is as a potential lead candidate for a specific Notch pathway inhibitor. Therefore, we determined the plasma pharmacokinetic profile associated with IMR-1 treatment following single intravenous (i.v.) and intraperitoneal (i.p.) dose administration in male C57 BL/6 mice (Fig. 5D). Treatment with IMR-1 did not induce any clinical signs in mice through last sample withdrawal, as evidenced by their normal appearance (data not shown). Following single i.v and i.p. administration of IMR-1 to the mice at 2 mg/kg and 100 mg/kg, respectively, no signal was detected in plasma corresponding to the m/z ratio of IMR-1 at any time point. However, a signal corresponding to the m/z ratio of IMR-1A was present in the spectra, thereby the PK parameters of IMR-1A were determined based on the parent dose (Fig. 5D) and are listed in Table 1. Following a single i.v. administration of IMR-1 at 2 mg/kg, IMR-1A exhibited low systematic plasma clearance (CL = 7 mL/min/kg) with terminal elimination half-life ($T_{1/2}$) of 2.22 h. The normal liver blood flow in mice is 90 mL/min/kg. In addition, the V_{ss} (volume of distribution) was ~ 4-fold higher than the normal volume of total body water (0.7 L/kg). After i.p. administration of IMR-1 at 100 mg/kg dose, plasma concentrations were quantifiable up to 24 h with T_{max} of 0.50 h. These results indicate that IMR-1 metabolizes in plasma and its acid metabolite exhibits drug-like properties, suggesting that IMR-1 (containing an ester moiety) acts as a pro-drug for IMR-1A, most likely by increasing the solubility and cell permeability of IMR-1A.

IMR-1 inhibits Notch-dependent somite development in zebrafish

The effects of IMR-1 *in vivo* were also investigated using *D. rerio* (zebrafish). Notch signaling plays a critical role in somite formation in developing vertebrate embryos, and changes in levels of Notch signaling during development result in disruption of the symmetric, bilaterally formed somites that can be readily observed in the zebrafish embryo(37,41–43) (Fig. 5E and 5F). Thus, disruption of somitogenesis in zebrafish represents a convenient dose-sensitive readout for Notch pathway stimulation or inhibition. The data indicates that injecting 100 pg *hNotch1* mRNA results in defects in somitogenesis in 90% of the embryos (compared to 0% disrupted embryos in control injected animals) (Fig. 5E). Disruption of somite formation was observed in 69.7% of embryos soaked in 40 μM IMR-1 (Fig. 5E), consistent with alteration in Notch signaling. However, no effect was observed in embryos soaked in DMSO vehicle (control) (Fig 5E–F). These results support the role of IMR-1 as a small molecule inhibitor of Notch signaling *in vivo*.

DISCUSSION

Precision medicine will likely be combinatorial, as is the case for the HIV paradigm of HAART, where "class action" combinations (targeting distinct viral proteins (classes) in combination), serve to keep viral loads at a minimal level while therapeutic depth with respect to the targets improves durability(44–46). Similarly, in cancer it is well accepted that there are distinct "hallmarks" of cancer physiology and that a "class action" approach may provide the best way forward for improved efficacy and durability in cancer treatment(47,48). Therefore, there exists an urgency to identify and develop novel therapeutics to provide a comprehensive array of target-specific drugs.

There are several features of the Notch pathway mechanism that make it an attractive target for cancer therapeutics. Therefore, inhibition of complex assembly represents an attractive node for therapeutic intervention. However, to date there are no small molecule inhibitors directly targeting the Notch intracellular pathway, which could provide greater specificity for Notch pathway inhibition. To identify inhibitors of the Notch intracellular pathway that directly target the NTC, we used CADD in combination with a novel *in vitro* assay that quantitatively measures the formation of the NTC. Cell-based assays were used to screen inhibitors with promising NTC inhibition effects and prioritize compounds for further studies, which led to the identification of IMR-1 as a potential small molecule inhibitor of the Notch transcriptional activation complex. Herein, we demonstrate that IMR-1 prevents the recruitment of Maml1, therefore uncoupling the Notch-mediated transcriptional cascade in response to activation.

A range of experimental data indicates that IMR-1 is a *bona fide* candidate for consideration as an anti-neoplastic agent that targets Notch. The compound specifically inhibits the binding of Maml1 to the DNA-bound complex, selectively inhibits cell growth in cell lines that are dependent on Notch signaling for viability and affects transcription in Notch target genes, indicating IMR-1 acts on the Notch pathway through on-target effects. Furthermore, ChIP data suggest that IMR-1 functions with a mode of action distinct from the GSI DAPT to block Maml1 recruitment to the NTC. Specific inhibition of Notch-dependent activity also occurs *in vivo*. The plasma pharmacokinetic profile upon treatment with IMR-1 (ester)

and the 50-fold higher potency observed for IMR-1A (acid metabolite of IMR-1) with respect to IMR-1 suggest that IMR-1 acts as a prodrug of IMR-1A. The ester moiety is commonly used in medicinal chemistry for the design of prodrugs to increase lipophilicity of polar or ionizable functionalities, such as carboxyl groups, resulting in increased cell permeability of the drug(49,50). Furthermore, SPR data demonstrate that two arginine residues (R2061 and R2071) found in the ANK domain of Notch1 mediate binding between IMR-1 and Notch1, which confirms binding to the target and the critical importance of these two arginine residues.

The core molecular scaffold of compound IMR-1 is a thiazolidinone. Thiazolidinones are heterocyclic compounds that contain a rhodanine moiety. Many Thiazolidinones have had success in the clinic. However there are perceived liabilities related to the rhodanine moiety in drug discovery and development since rhodanines may lead to non-specific interactions due to its potential reactivity, thus rhodanines have been referred as PAIN (pan-assay interference) molecules(51,52). Although there is a general concern about the potential promiscuity and reactivity of this moiety, many studies have suggested that these concerns are more relevant at screening concentrations and that a comprehensive characterization of their interaction with the target should be performed, including biophysical characterization before prioritizing such compounds(53). Given the specificity of IMR-1 observed experimentally, we conclude that issues related with reactivity and non-specific effects are not occurring since: (1) The data indicate that not all IMR-1 analogs (containing a rhodanine moiety), inhibit assembly of the NTC as exemplified by inactive compounds exhibiting no effect in the *in vitro* NTC assay (i.e., compound 1-134-22). (2) SPR data demonstrate reversible (non-covalent) binding of IMR-1 to Notch1, and a similar profile was observed for its analogs. (3) IMR-1 show specificity for Notch target genes and (4) no general toxicity was observed upon *in vivo* treatment with IMR-1.

In summary, this study provides *proof of principle* for targeting the Notch transcriptional activation complex to inhibit Notch activity and presents a novel class of Notch inhibitors with the potential to be developed into therapeutic agents for the treatment of cancer. This class of inhibitors may fulfill an unmet need in terms of therapeutic agents targeting the Notch signaling pathway, providing specific inhibition of the Notch transcriptional activation complex, which could complement and/or offer an alternative to current therapeutic approaches and therefore fulfill a basic tenet of the precision medicine strategy.

Supplementary Material

Refer to Web version on PubMed Central for supplementary material.

Acknowledgments

Financial support: This work was supported by the National Cancer Institute (NCI R01CA083736-12A1, NCI R01CA125044-02 to A.J. Capobianco), the National Institutes of Health (R01GM081635 and R01GM103926 to E. Lee; the Training Program in Stem Cell and Regenerative Developmental Biology T32HD007502 to L.R. Neitzel), the Waxman Foundation to A.J. Capobianco and A.D. MacKerell, the UM/Sylvester Braman Family Breast Cancer Institute's Women's Cancer League Developmental Grant to A.J. Capobianco. This project was also generously supported by funding from the Dewitt Daughtry Family Department of Surgery and the Sylvester Comprehensive Center to A.J. Capobianco.

We thank members of the Capobianco and Robbins laboratory and the University of Maryland Computer-Aided Drug Design Center for support and technical assistance.

References

1. Hoppe PE, Greenspan RJ. Local function of the NOTCH gene for embryonic ectodermal pathway choice in Drosophila. Cell. 1986; 46:773–83. [PubMed: 3091259]
2. Artavanis-Tsakonas S, Rand MD, Lake RJ. Notch signaling: Cell fate control and signal integration in development. Science. 1999; 284:770–6. [PubMed: 10221902]
3. Sander GR, Powell BC. Expression of notch receptors and ligands in the adult gut. J Histochem Cytochem. 2004; 52:509–16. [PubMed: 15034002]
4. Stump G, Durrer A, Klein A-L, Lütolf S, Suter U, Taylor V. Notch1 and its ligands Delta-like and Jagged are expressed and active in distinct cell populations in the postnatal mouse brain. Mech Dev. 2002; 114:153–9. [PubMed: 12175503]
5. Ranganathan P, Weaver KL, Capobianco AJ. Notch signalling in solid tumours: a little bit of everything but not all the time. Nat Rev Cancer. 2011; 11:338–51. [PubMed: 21508972]
6. Koch U, Radtke F. Notch and cancer: a double-edged sword. Cell Mol Life Sci. 2007; 64:2746–62. [PubMed: 17687513]
7. Radtke F, Raj K. The role of Notch in tumorigenesis: oncogene or tumour suppressor? Nat Rev Cancer. 2003; 3:756–67. [PubMed: 14570040]
8. Wang J, Sullenger BA, Rich JN. Notch signaling in cancer stem cells. Adv Exp Med Biol. 2012; 727:174–85. [PubMed: 22399347]
9. Espinoza I, Pochampally R, Xing F, Watabe K, Miele L. Notch signaling: targeting cancer stem cells and epithelial-to-mesenchymal transition. Onco Targets Ther. 2013; 6:1249–59. [PubMed: 24043949]
10. Tamura K, Taniguchi Y, Minoguchi S, Sakai T, Tun T, Furukawa T, et al. Physical interaction between a novel domain of the receptor Notch and the transcription factor RBP-J kappa/Su(H). Curr Biol. 1995; 5:1416–23. [PubMed: 8749394]
11. Aster JC, Robertson ES, Hasserjian RP, Turner JR, Kieff E, Sklar J. Oncogenic forms of NOTCH1 lacking either the primary binding site for RBP-J kappa or nuclear localization sequences retain the ability to associate with RBP-J kappa and activate transcription. J Biol Chem. 1997; 272:11336–43. [PubMed: 9111040]
12. Nam Y, Sliz P, Song LY, Aster JC, Blacklow SC. Structural basis for cooperativity in recruitment of MAML coactivators to Notch transcription complexes. Cell. 2006; 124:973–83. [PubMed: 16530044]
13. Jeffries S, Robbins DJ, Capobianco AJ. Characterization of a high-molecular-weight Notch complex in the nucleus of Notch(ic)-transformed RKE cells and in a human T-cell leukemia cell line. Mol Cell Biol. 2002; 22:3927–41. [PubMed: 11997524]
14. Wilson JJ, Kovall RA. Crystal structure of the CSL-Notch-Mastermind ternary complex bound to DNA. Cell. 2006; 124:985–96. [PubMed: 16530045]
15. Tiyanont K, Wales TE, Siebel CW, Engen JR, Blacklow SC. Insights into Notch3 activation and inhibition mediated by antibodies directed against its negative regulatory region. J Mol Biol. 2013; 425:3192–204. [PubMed: 23747483]
16. Takebe N, Nguyen D, Yang SX. Targeting notch signaling pathway in cancer: clinical development advances and challenges. Pharmacol Ther. 2014; 141:140–9. [PubMed: 24076266]
17. Sharma A, Paranjape AN, Rangarajan A, Dighe RR. A monoclonal antibody against human Notch1 ligand-binding domain depletes subpopulation of putative breast cancer stem-like cells. Mol Cancer Ther. 2012; 11:77–86. [PubMed: 22075160]
18. Fischer M, Yen W-C, Kapoun AM, Wang M, O'Young G, Lewicki J, et al. Anti-DLL4 inhibits growth and reduces tumor-initiating cell frequency in colorectal tumors with oncogenic KRAS mutations. Cancer Res. 2011; 71:1520–5. [PubMed: 21193546]
19. Berezovska O, Jack C, McLean P, Aster JC, Hicks C, Xia W, et al. Aspartate mutations in presenilin and gamma-secretase inhibitors both impair notch1 proteolysis and nuclear translocation

with relative preservation of notch1 signaling. J Neurochem. 2000; 75:583–93. [PubMed: 10899933]

20. Shih I-M, Wang T-L. Notch signaling, gamma-secretase inhibitors, and cancer therapy. Cancer Res. 2007; 67:1879–82. [PubMed: 17332312]
21. De Kloe GE, De Strooper B. Small molecules that inhibit Notch signaling. Methods Mol Biol. 2014; 1187:311–22. [PubMed: 25053499]
22. Alves-Guerra M-C, Ronchini C, Capobianco AJ. Mastermind-like 1 Is a specific coactivator of beta-catenin transcription activation and is essential for colon carcinoma cell survival. Cancer Res. 2007; 67:8690–8. [PubMed: 17875709]
23. Maillard I, Weng AP, Carpenter AC, Rodriguez CG, Sai H, Xu L, et al. Mastermind critically regulates Notch-mediated lymphoid cell fate decisions. Blood. 2004; 104:1696–702. [PubMed: 15187027]
24. Helms W, Lee H, Ammerman M, Parks AL, Muskavitch MA, Yedvobnick B. Engineered truncations in the Drosophila mastermind protein disrupt Notch pathway function. Dev Biol. 1999; 215:358–74. [PubMed: 10545243]
25. Wu L, Aster JC, Blacklow SC, Lake R, Artavanis-Tsakonas S, Griffin JD. MAML1, a human homologue of Drosophila mastermind, is a transcriptional co-activator for NOTCH receptors. Nat Genet. 2000; 26:484–9. [PubMed: 11101851]
26. Kankel MW, Hurlbut GD, Upadhyay G, Yajnik V, Yedvobnick B, Artavanis-Tsakonas S. Investigating the genetic circuitry of mastermind in Drosophila, a notch signal effector. Genetics. 2007; 177:2493–505. [PubMed: 18073442]
27. Moellering RE, Cornejo M, Davis TN, Del Bianco C, Aster JC, Blacklow SC, et al. Direct inhibition of the NOTCH transcription factor complex. Nature. 2009; 462:182–8. [PubMed: 19907488]
28. Weaver KL, Alves-Guerra M-C, Jin K, Wang Z, Han X, Ranganathan P, et al. NACK is an integral component of the Notch transcriptional activation complex and is critical for development and tumorigenesis. Cancer Res. 2014; 74:4741–51. [PubMed: 25038227]
29. Drescher DG, Ramakrishnan NA, Drescher MJ. Surface plasmon resonance (SPR) analysis of binding interactions of proteins in inner-ear sensory epithelia. Methods Mol Biol. 2009; 493:323–43. [PubMed: 18839357]
30. Heitjan DF, Manni A, Santen RJ. Statistical Analysis of in Vivo Tumor Growth Experiments. Cancer Res. 1993; 53:6042–50. [PubMed: 8261420]
31. Kovall RA. More complicated than it looks: assembly of Notch pathway transcription complexes. Oncogene. 2008; 27:5099–109. [PubMed: 18758478]
32. Vasquez-Del Carpio R, Kaplan FM, Weaver KL, VanWye JD, Alves-Guerra M-C, Robbins DJ, et al. Assembly of a Notch Transcriptional Activation Complex Requires Multimerization. Mol Cell Biol. 2011; 31:1396–408. [PubMed: 21245387]
33. Choi SH, Wales TE, Nam Y, O'Donovan DJ, Sliz P, Engen JR, et al. Conformational Locking upon Cooperative Assembly of Notch Transcription Complexes. Structure. 2012; 20:340–9. [PubMed: 22325781]
34. Zhong S, MacKerell AD Jr. Binding response: A descriptor for selecting ligand binding site on protein surfaces. J Chem Inf Model. 2007; 47:2303–15. [PubMed: 17900106]
35. Kuntz ID, Blaney JM, Oatley SJ, Langridge R, Ferrin TE. A geometric approach to macromolecule-ligand interactions. J Mol Biol. 1982; 161:269–88. [PubMed: 7154081]
36. Oashi T, Ringer AL, Raman EP, MacKerell AD Jr. Automated Selection of Compounds with Physicochemical Properties To Maximize Bioavailability and Druglikeness. J Chem Inf Model. 2011; 51:148–58. [PubMed: 21142079]
37. Kageyama R, Niwa Y, Isomura A, González A, Harima Y. Oscillatory gene expression and somitogenesis. Wiley Interdiscip Rev Dev Biol. 2012; 1:629–41. [PubMed: 23799565]
38. Macias AT, Mia MY, Xia GJ, Hayashi J, MacKerell AD. Lead validation and SAR development via chemical similarity searching; Application to compounds targeting the pY+3 site of the SH2 domain of p56(lck). J Chem Inf Model. 2005; 45:1759–66. [PubMed: 16309282]
39. Williams FM. Clinical significance of esterases in man. Clin Pharmacokinet. 1985; 10:392–403. [PubMed: 3899454]

40. Wang Z, Da Silva TG, Jin K, Han X, Ranganathan P, Zhu X, et al. Notch signaling drives stemness and tumorigenicity of esophageal adenocarcinoma. Cancer Res. 2014; 74:6364–74. [PubMed: 25164006]
41. Soza-Ried C, Öztürk E, Ish-Horowicz D, Lewis J. Pulses of Notch activation synchronise oscillating somite cells and entrain the zebrafish segmentation clock. Development. 2014; 141:1780–8. [PubMed: 24715465]
42. Lewis J, Hanisch A, Holder M. Notch signaling, the segmentation clock, and the patterning of vertebrate somites. J Biol. 2009; 8:44. [PubMed: 19486506]
43. Fongang B, Kudlicki A. The precise timeline of transcriptional regulation reveals causation in mouse somitogenesis network. BMC Dev Biol. 2013; 13:42. [PubMed: 24304493]
44. DeVita VT, Eggermont AMM, Hellman S, Kerr DJ. Clinical cancer research: the past, present and the future. Nat Rev Clin Oncol. 2014; 11:663–9. [PubMed: 25245981]
45. Srinivasa S, Grinspoon SK. Metabolic and body composition effects of newer antiretrovirals in HIV-infected patients. Eur J Endocrinol. 2014; 170:R185–202. [PubMed: 24523497]
46. Du W, Elemento O. Cancer systems biology: embracing complexity to develop better anti-cancer therapeutic strategies. Oncogene. 2014; 34:3215–25. [PubMed: 25220419]
47. Hanahan D, Weinberg RA. The hallmarks of cancer. Cell. 2000; 100:57–70. [PubMed: 10647931]
48. Lazebnik Y. What are the hallmarks of cancer? Nat Rev Cancer. 2010; 10:232–3. [PubMed: 20355252]
49. Rautio J, Kumpulainen H, Heimbach T, Oliyai R, Oh D, Järvinen T, et al. Prodrugs: design and clinical applications. Nat Rev Drug Discov. 2008; 7:255–70. [PubMed: 18219308]
50. Huttunen KM, Raunio H, Rautio J. Prodrugs--from serendipity to rational design. Pharmacol Rev. 2011; 63:750–71. [PubMed: 21737530]
51. Baell JB. Observations on screening-based research and some concerning trends in the literature. Future Med Chem. 2010; 2:1529–46. [PubMed: 21426147]
52. Tomašić T, Peterlin Mašič L. Rhodanine as a scaffold in drug discovery: a critical review of its biological activities and mechanisms of target modulation. Expert Opin Drug Discov. 2012; 7:549–60. [PubMed: 22607309]
53. Mendgen T, Steuer C, Klein CD. Privileged scaffolds or promiscuous binders: a comparative study on rhodanines and related heterocycles in medicinal chemistry. J Med Chem. 2012; 55:743–53. [PubMed: 22077389]

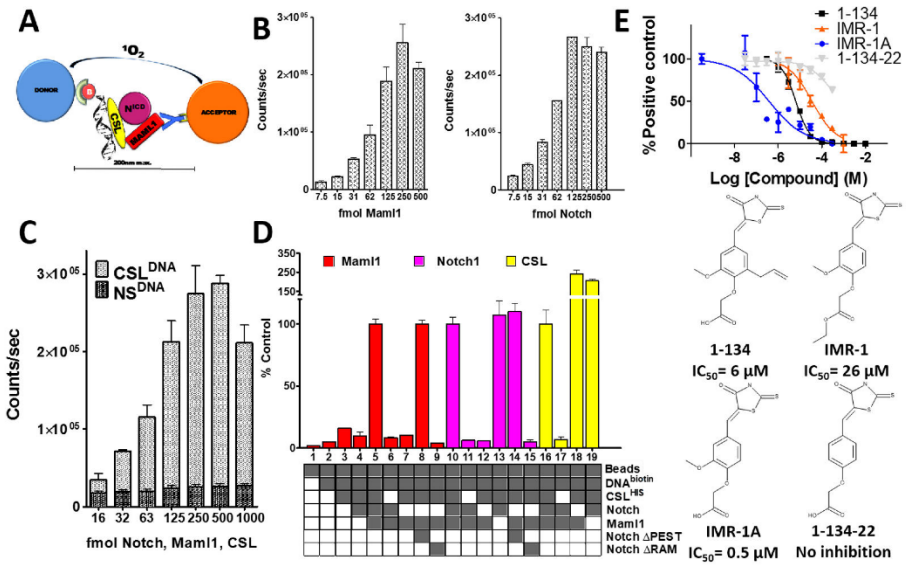

Figure 1. The Notch ternary complex (NTC) assembly assay

A. Schematic representation of the *in vitro* NTC assay. B. Titration of Maml1 (left panel) and NICD (right panel) in NTC assay. C. NTC assay requires intact CSL consensus site. CSL^{DNA} represents an oligonucleotide harboring the CSL consensus sequence, whereas NS^{DNA} represents an oligonucleotide that harbors a mutant CSL binding site. D. NTC assay represents a *bona fide* Notch ternary complex. Colors denote probes for specific components: anti-Maml1 specific Ab (red), anti-Notch1 specific Ab (purple), anti-His Tag Ab specific for His-tagged CSL (yellow). Box grid indicates components present (shaded) in the reactions. E. IC_{50} determination for compounds 1-134, IMR-1, IMR-1A and 1-134-22 and corresponding structures (bottom panel).

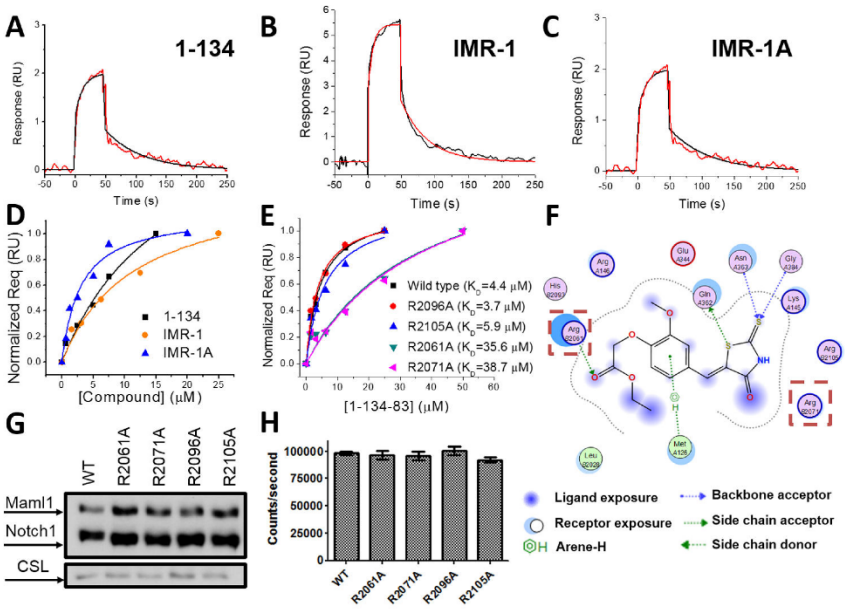

Figure 2. Affinity of NTC inhibitors to Notch1

A–C. Sensorgrams determined for 1-134 (A), IMR-1 (B) and IMR-1A (C) binding to NICD. D. Dose-response curves of 1-134, IMR-1 and IMR-1A to NICD determined by SPR. E. Affinity of IMR-1 to NICD and mutants determined by SPR. F. Docking model of IMR-1 binding to the NTC. Arginine residues located in the binding pocket of IMR-1 are enclosed in red boxes. DNA pull-down (G) in 293T cells and NTC assay (H) with NICD and single arginine mutated NICD demonstrate no effect of single mutations on NTC assembly.

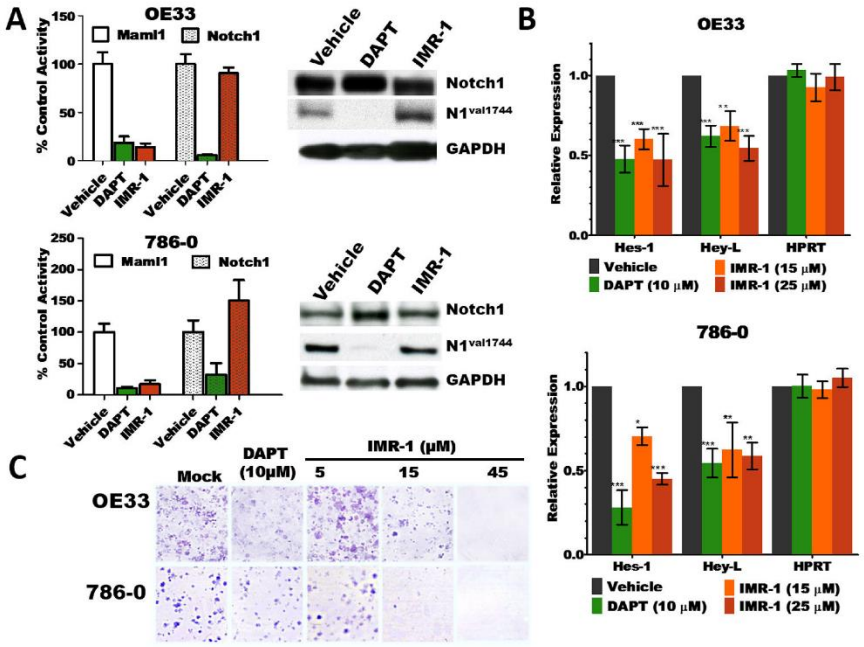

Figure 3. IMR-1 is an inhibitor of the Notch transcriptional activation complex

A. ChIP assay on the *HES1* promoter using the indicated antibodies (left panel) following treatment of OE33 (top panel) and 786-0 cells (bottom panel) with DAPT (15 μM), IMR-1 (25 μM), or vehicle (DMSO) using GAPDH as loading control. Western blot analysis of Notch1 and cleaved Notch1 ($N1^{Val1744}$) from cells used in ChIP assay (right panel). B. RT-qPCR analysis of Notch target genes (Hes-1, Hey-L) in treated OE33 and 786-0 cells (control gene: HPRT). Data are expressed as relative expression to vehicle control (set to 1). C. Colony formation assay in Notch-dependent cell lines (OE33 and 786-0).

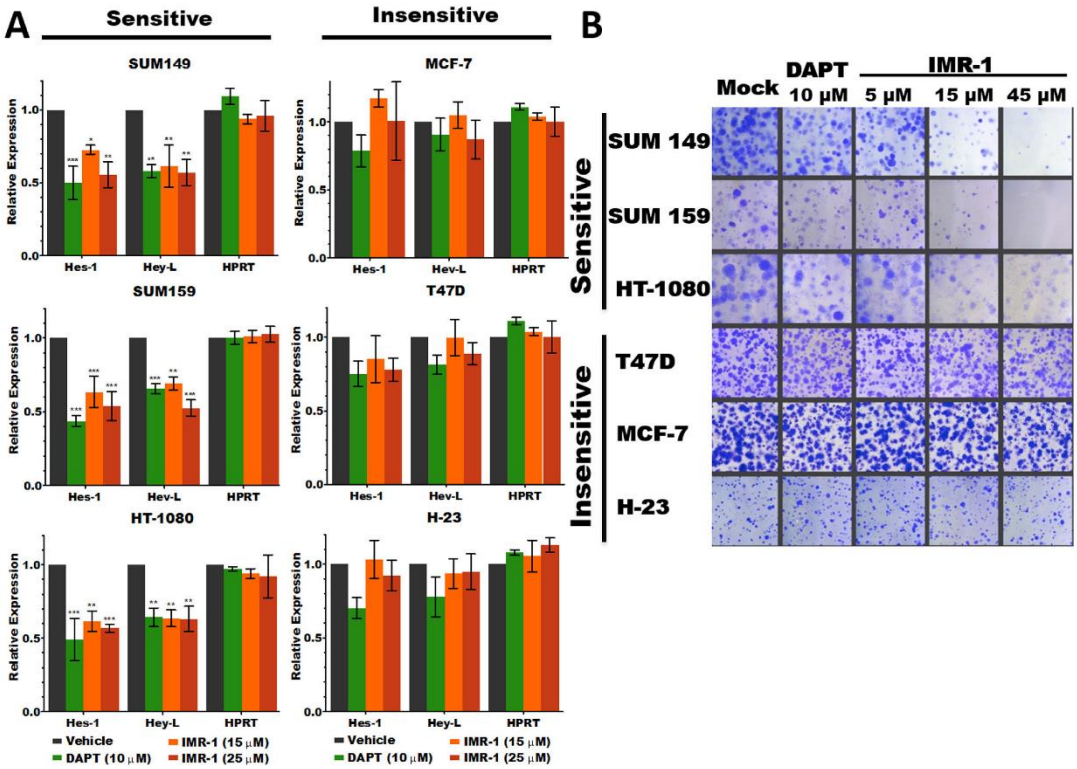

Figure 4. IMR-1 is a specific inhibitor of the Notch pathway

A. RT-qPCR analysis on Notch-dependent (left) and Notch-independent (right) cell lines. Notch-dependence is based on sensitivity to DAPT (a GSI). Relative expression of Notch target genes (*Hes-1* and *Hey-L*) compared to control (*HPRT*) is shown. B. Colony formation assay on corresponding cell lines under indicated conditions compared to DMSO control.

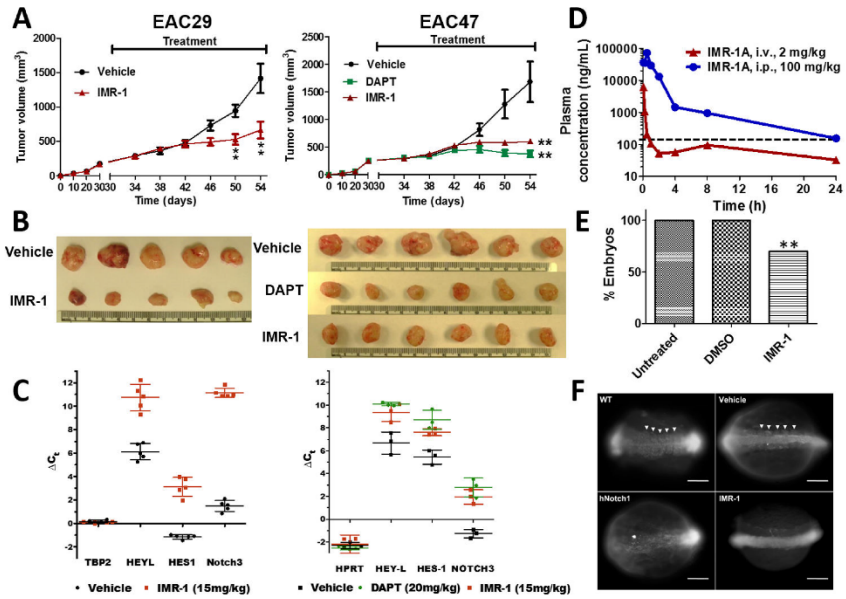

Figure 5. IMR-1 inhibits Notch-dependent tumor growth in patient-derived xenograft models, somite development in zebrafish and is metabolized *in vivo* to yield IMR-1A

A. Tumor volume over time upon treatment (treatment for 24 days) of two independently-derived esophageal adenocarcinoma PDX models (EAC29 and EAC47) with DMSO (vehicle), IMR-1(15 mg/kg) (EAC29, left panel), or DAPT (20 mg/kg) (EAC47, right panel). Treatment was initiated on day 2 following transplantation of cells. Data is displayed as averages (EAC29, $n = 5$, EAC47 $n = 6$) and standard error of the mean. Unpaired two-tailed t-test was used to determine significance (**, p=0.01). B. Size of excised tumors. C. RT-qPCR analysis of Notch target genes (*HeyL*, *Hes1*, and *Notch3*) from excised tumors. *TBP* (left panel) and *HPRT* (right panel) are used as internal controls and display no change in expression upon treatment. D. Plasma pharmacokinetic profile determined for the acid metabolite of IMR-1, IMR-1A, upon intravenous (2 mg/kg) and intraperitoneal (100 mg/kg) treatment of mice with IMR-1. The dashed line represents efficacy line considering an IC_{50} of 500 nM. E. Percentage of embryos with somites. ** indicates a $p<0.0001$ by fisher's exact test between both untreated and drug treated embryos and DMSO and drug treated embryos. F. Somite formation in zebrafish is sensitive to perturbations in Notch signaling. Coronal view of 13 hpf zebrafish exposed to IMR-1 at 8 hpf. Anterior to the left. Arrowheads denote somites. Negative controls are WT (untreated) and Vehicle (DMSO). Positive control is hNotch1 (human Notch1 intracellular domain) mRNA (100 pg) injected embryos. Scale bar represents 0.1 mm.

Table 1

Plasma pharmacokinetic profile determined for IMR-1A in mice upon treatment with IMR-1.

Compound	Route	Dose (mg/kg)	T_{max} (h)	$T_{1/2}$ (h)	CL (mL/min/kg)
IMR-1	i.v.	2	-	NC	NC
	i.p.	100	NC	NC	-
IMR-1A	i.v.	2	-	2.22	10.33
	i.p.	100	0.50	6.16	-

IMR-1 was administered in C57BL/6 mice via intraperitoneal (i.p.) or intravenous (i.v.) route.

Supplementary Figure 1

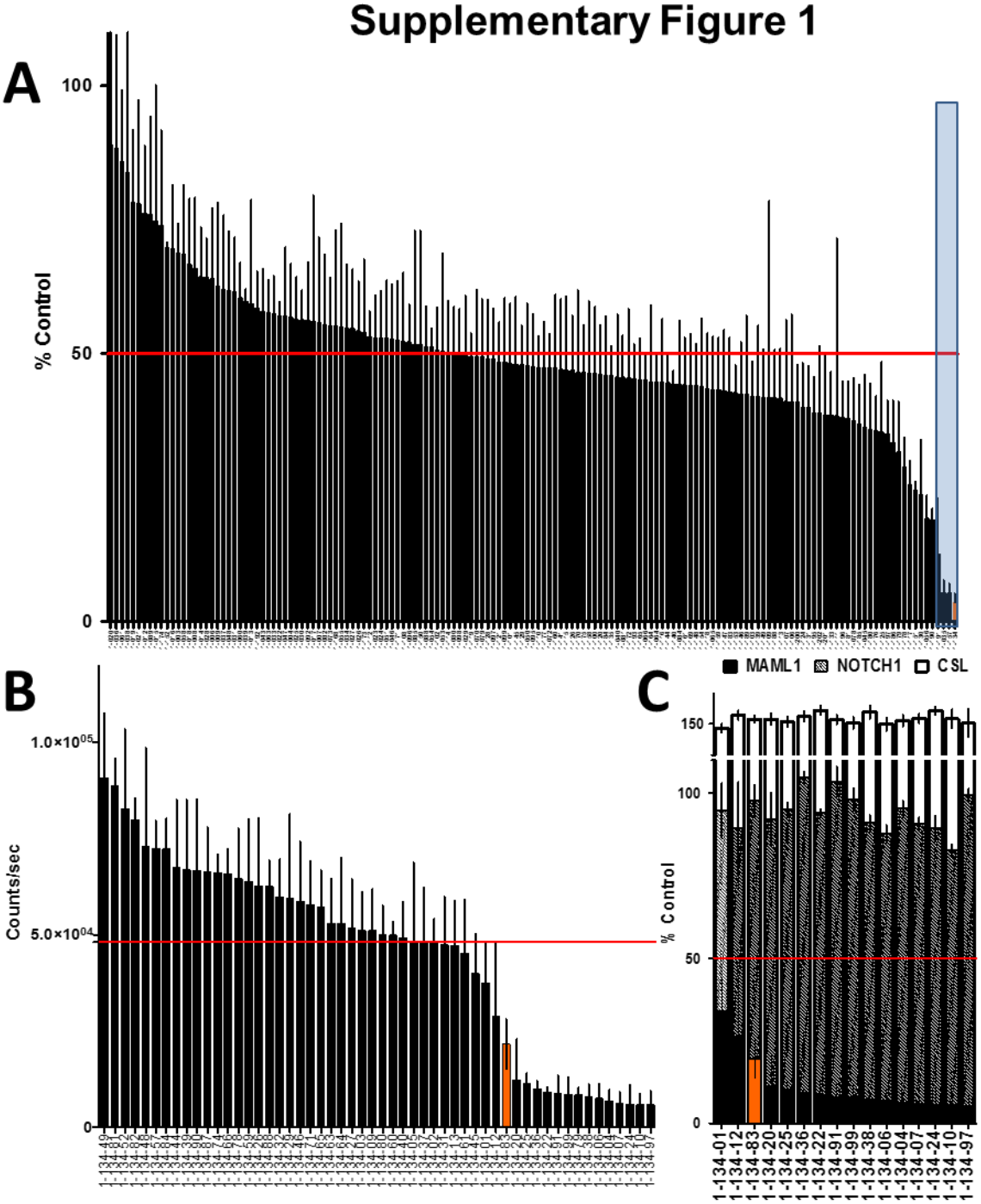

Supplementary Figure 2

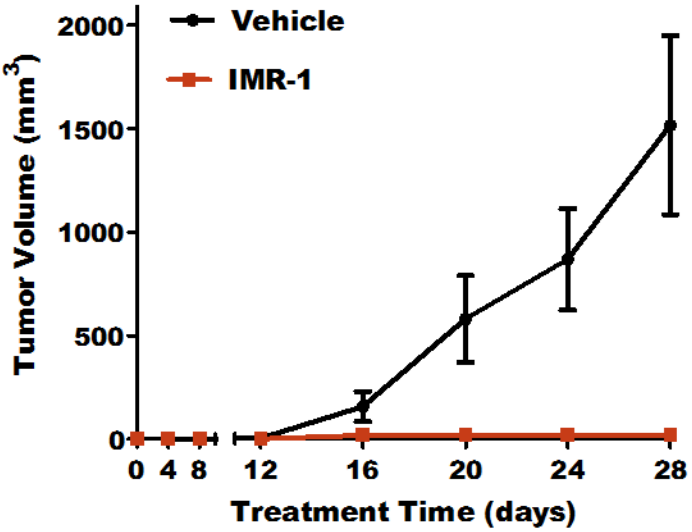

Supplementary Figure 3

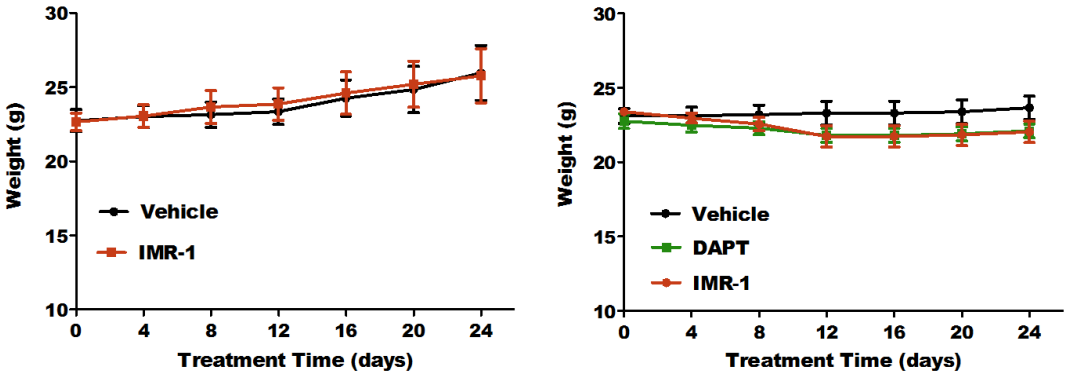

Supplementary Figure Legends

Supplementary Figure 1. Primary screen of CADD-derived compounds. A. Histogram displaying values of selected compounds expressed as % Positive Control. The red line indicates the 50% activity mark. The shaded area highlights compounds exhibiting more than 97% inhibition and the orange highlighted bar indicates 1-134. B. NTC assay on compounds derived from the 1-134 similarity searching. Data are expressed in raw values as counts/sec. The orange highlighted bar indicates IMR-1 (1-134-83). C. NTC counter-screen to demonstrate specificity. Black shaded bars indicate probe for Maml1, grey shaded bars indicate probe for Notch1, and white bars indicate probe for CSL using specific antibodies for Maml1, Notch1 and CSL, respectively. Orange shaded bar indicates IMR-1 probed for Maml1.

Supplemetary Figure 2. IMR-1 inhibits tumor growth. Graph of OE19 xenograft tumor volumes (in mm^3) over time (days) in mice treated with vehicle (DMSO) or IMR-1 (15 mg/kg) administered daily via i.p. injection. Treatment was initiated on day 2 following transplantation of cells and continued until day 28. Data is displayed as average tumor volume (*n* = 5) per group and standard error of the mean.

Supplementary Figure 3. IMR-1 treatment does not induce weight loss in treated mice. Graph of mice weight determined during treatment with vehicle (DMSO), IMR-1 (15 mg/kg) or DAPT (15 mg/kg), administered daily via i.p. injection over the course of 24 days, in two patient-derived xenograft tumors: EAC29 (left panel) and EAC47 (right panel). Data is displayed as averages (EAC29, *n* = 5, EAC47 *n* = 6) and standard error of the mean.

Supplementary methods

Compound IMR-1 (1-134-83, ethyl{2-methoxy-4[(Z)-(4-oxo-2-thioxo-1,3-thiazolidin-5-ylidene)methyl]phenoxy}acetate, CID:1246061) was synthesized and characterized by Xcess Biosciences (San Diego, CA, USA). The purity of IMR-1 is > 95% and its NMR spectra is identical to previously published data (see PubChem CID:1246061).

Colony formation assay. Cells were plated into a 6-well plate at a density of 2000 cells/cm^2. Drug treatment commenced 24 h post-seeding. Media and compounds were changed every 48 h thereafter. After 168 h cells were fixed with ice cold methanol, stained with crystal violet, de-stained with water, and allowed to dry at room temperature.

Chromatin immunoprecipitation (ChIP) analysis. ChIP analysis was performed as previously described (1). Cells (8×10^6 OE33 cells or 10×10^6 786-0 cells) were plated onto a 15 cm tissue culture dish a day prior to treatment. Cells were then treated for 24 h with DAPT (5 μM), IMR-1 (25 μM), or DMSO vehicle (control). Following treatment, cells were cross-linked for 10 mins with 1% formaldehyde. The reaction was then stopped by adding 0.125 M glycine. Cells were collected in SDS lysis buffer (50 mM Tris-HCl (pH 8.0), 1% SDS, 10 mM EDTA) and sonicated to yield chromatin fragments of approximately 300 to 800 bp (8 mins at high level for OE33 cells; 5 mins at medium level for 786-0 cells in Bioruptor™ UCD-200 sonicator). Lysates were divided into equal parts and immunoprecipitated with either α-Notch1 (Bethyl Laboratories, Montgomery, TX; A301-894A) or α-Maml1 (Cell Signaling, 12166s) antibody. Protein:DNA immunoprecipitates were then reverse cross-linked at 65 °C in 200 mM NaCl for 4 h, followed by incubation with RNase A and proteinase K. DNA was then purified using a PCR purification kit

(Qiagen, Gaithersburg, MD, USA). Immunoprecipitated DNA was then detected by Syber green qPCR using *HES1* specific oligonucleotide primers (forward: 5'CGTGTCTCCTCCTCCCATT3'; reverse: 5'GGGGGATTCCGCTGTTAT3').

Mouse xenograft studies. Six-week-old male and female NOD-SCID gamma (NSG) mice were purchased from Jackson Laboratories (USA) and CD-1 Nude mice were purchased from Charles River Laboratories (USA). Animal experiments were approved by the University of Miami Institutional Animal Care and Use Committee (protocol 13-128, approval date 10 July 2015). For the cell line-based xenograft assay, 5×10^6 OE19 cells in 200 µL serum-free culture medium were injected subcutaneously per mouse(2). The mice in the treatment group were injected (i.p.) with 15 mg/kg IMR-1 daily and the mice in control group were injected with the same volume of vehicle (DMSO). Body weight and tumor growth were measured every 4 days for 28 days. Tumor volume = (S×S×L)/2, where S and L are the short and long dimensions, respectively. PDX cancer models were established as previously described in NSG mice(2). When the tumors reached 200 mm^3, the mice were randomly split into two uniform groups for treatment. IMR-1 (15 mg/kg) and vehicle were administered daily by i.p. injection for 24 days. Tumor growth was monitored every 4 days. The xenograft tumors were harvested and weighed and samples were analyzed.

Pharmacokinetics. A group of 18 male C57BL/6 mice (8-12 weeks old) were divided into two groups as group 1 (i.v.: 2 mg/kg) and group 2 (i.p.: 100 mg/kg). Animals in group 1 were administered through intravenous (i.v.) route with IMR-1 solution formulation in 5% NMP, 5% Solutol-HS 15 and 90% Normal saline at 2 mg/kg dose. Animals in group 2 were administered

through intraperitoneal (i.p.) route with IMR-1 solution formulation in 7.5% NMP, 5% Solutol, 40% PEG-400, and 47.5% Normal Saline at 100 mg/kg dose. Blood samples (approximately 60 µL) were collected from retro orbital plexus under light isoflurane anesthesia such that the samples were obtained at pre-dose (0.08, 0.25, 0.5, 1, 2, 4, 8 and 24 h) for both i.v. and i.p. treatments. The blood samples were collected from set of three mice at each time point in labeled microcentrifuge tube containing K_2EDTA as anticoagulant. Plasma was separated from blood immediately by centrifugation at 4000 rpm for 10 min at 4 ºC and stored below -70 ºC until bioanalysis. All samples were processed for analysis by protein precipitation using acetonitrile and analyzed for IMR-1 and its acid metabolite IMR-1A with fit for purpose LC-MS/MS method. Pharmacokinetic parameters were calculated using the non-compartmental analysis module of Phoenix WinNonlin (Version 6.3). Maximum concentrations (C_{max}) and time to reach the maximum concentration (T_{max}) were the observed values. The areas under the concentration time curve (AUC_{last} and AUC_{inf}) were calculated by linear trapezoidal rule. The terminal elimination rate constant, k_e, was determined by regression analysis of the linear terminal portion of the Log plasma concentration-time curve. The terminal half-life ($T_{1/2}$) was estimated as $0.693/k_e$; $CL_{i.v.}$ = Dose/AUC_{inf}; V_{ss}=MRT $CL_{i.v,}$ where MRT represents the mean residence time.

Zebrafish methodology. Zebrafish embryos were cultured as previously described(3). Briefly, on three separate days, multiple clutches of embryos from two or more breeding pairs of the AB wild type line were combined and incubated at 28.5 ºC for 8 h in E3 medium with 0.1% (w/v) methylene blue. The embryos were then placed into fresh E3 medium with 0.1% (w/v) methylene blue containing DMSO, 40 µM IMR-1, or no treatment. As a positive control, zygotes

were injected with 100 pg of human *Notch1* intracellular domain mRNA mixed with 0.05% phenol red using the MPPI-2 injection system from ASI. At 13 h post-fertilization, samples were collected and scored for the presence of discrete somite boarders on a Zeiss stemi 2000-CS scope. Data were analyzed using fisher's exact test in R3.1.0. Immunofluoresence was used to visualize the phenotype. Embryos were permeabilized with 10 µg/ml Proteinase K for 1 min and stained with EphA4 (Tyr-602) phospho-specific rabbit polyclonal antibody (1:100) from ECM Biosciences for two days at 4 ºC as previously described(4). Embryos were then stained with alexa-488 anti-rabbit antibody at 1:200 overnight. Samples were visualized on a Nikon eclipse 80I and imaged with a Photometrics Cool Snap ES.

Computational methods. Simulation was initiated with the 3D structures of human Notch1 taken from the transcription complex consisting of the ANK domain of human Notch1, transcription factor CSL, cognate DNA, and coactivator MAML1 (PDB ID 2F8X) retrieved from the Protein Data Bank(5,6). Missing residues were restored by the program MODELLER(7). The program Reduce(8) was used to add hydrogen atoms and optimize the orientations of the sidechain OH, SH, NH_3^+, -S-CH_3, and amide moieties, as well as the imidazole rings of the histidines. To obtain multiple conformations of the putative binding sites in the NOTCH1 interface with CSL suitable for database screening, MD simulation was performed with the programs CHARMM(9) and NAMD(10). Calculations used the CHARMM 22 all-atom protein force field(11) including the CMAP backbone energy correction(12). Preparation for the MD simulation involved overlaying the structure of human NOTCH1 with 96 Å pre-equilibrated cubic box of TIP3P water containing 150 mM NaCl(13). Solvent molecules with non-hydrogen atoms within 2.8 Å of protein non-hydrogen atoms were deleted. The solvent was initially

minimized with the protein restrained followed by minimization of the entire system. The MD simulation initially involved heating to 298K at a rate of 10K/ps and equilibration in the NPT ensemble (1 atm, 298K) for 100ps(14). The production MD simulation was performed in the NPT (1 atm, 298K) ensemble for 25ns with time frames from trajectory saved every 5 ps for analysis. Simulations were performed with a 2 fs integration time step using the SHAKE algorithm(15) to constrain covalent bonds to hydrogens. Electrostatic forces were calculated with the particle mesh Ewald method(16) using a real space cutoff of 12 Å with a kappa value of 0.4 Å-1 and a 4th order spline interpolation. Van der Waals (vdW) forces were truncated with a cutoff distance of 12 Å with smoothing performed using a force switching function(17) starting at 10 Å.

Preparation of conformationally diverse structures to identify putative binding pockets used for docking. To identify unique conformations for the identification of putative binding pockets used for docking, conformations from the 25ns MD simulation of human Notch1 were subjected to Cartesian clustering based on the root-mean-square differences (RMSD)(18). RMSDs were based on all non-hydrogen atoms in the interfacial residues that are located within 3.5 Å from CSL in CSL-Notch-MAML-DNA transcription complex crystal structure. RMSD based clustering using the neural network-based ART-2 algorithm(19,20) showed the presence of 9 distinct clusters for human Notch1 MD simulation with RMSD radii of 2.1 Å. Representative conformations were selected from each cluster. These conformations as well as the X-ray crystallographic structures of human Notch1 taken from the transcription complex were used to identify putative binding pockets used for subsequent database screening. Of these, the four conformations with the highest binding response scores were used for the primary screens with

all the conformations in which the putative binding pocket was present used for the secondary screen.

Identification of putative binding sites. Putative binding sites were identified using the binding response method(21). To prepare the structures for binding pocket identification and docking, atomic partial charges based on the AMBER 99 force field were assigned using the program Molecular Operating Environment (MOE) (Chemical Computing Group Inc.). All database screens were performed with an in-house modified MPI version of DOCK4(22) using flexible ligand docking based on the anchored search method(23). The solvent accessible surface(24) was calculated with the program DMS(25) using surface density of 2.76 vertex points per $Å^2$ and a probe radius of 1.4 Å. Sphere sets, required for initial placement of ligands for targeting binding sites, were obtained with the program SPHGEN within the DOCK package.

In silico **database screening**. A virtual database of more than 1.5 million low-molecular weight commercially available compounds was used for the virtual screening. The database has been created in the MacKerell laboratory by converting files obtained from the vendors in the 2D SDF format to the 3D MOL2 format through a procedure that included addition of hydrogen, assignment of protonation state, geometry optimization with MMFF94 force field(26,27) using the programs MOE, and assignment of atomic partial charges based on CM2 charge model at the semi-empirical quantum chemical AM1 level using the program AMSOL(28,29). The compounds that were screened had 10 or fewer rotatable bonds and between 10 and 40 heavy atoms. The four most structurally diverse conformations from the MD simulations and clustering analysis were used for the primary docking. During docking the protein structures

were fixed with ligand flexibility treated using the anchored search method(23). In this approach each compound was divided into a collection of non-overlapping rigid segments connected though rotatable bonds. Segments with more than five heavy atoms were considered as anchors, each of which was individually docked into the binding site in 200 orientations and then minimized. The remainder of the each molecule was constructed around the anchors in a stepwise fashion by connecting other segments through rotatable bonds. At each step, the dihedral of the rotatable bond connecting previously constructed to new segments was sampled in increments of 10° and then the lowest energy conformation was chosen. During primary docking, each rotatable bond was minimized as it was created without re-minimizing the other bonds. Selected conformations were eliminated based on energetic criteria, ensuring conformational diversity and energetically favorable conformations(30,31). Energy minimization was performed after building the entire molecule, with the ligand orientation with the most favorable interaction energy for all the protein conformations selected for each molecule. The GRID method(32) implemented in the DOCK package was used to approximate the ligand-protein interaction energies during ligand placement as a sum of electrostatics and vdW attractive components. The GRID box dimensions were 37.3 Å ×39.4Å ×38.4 Å, centered on the sphere set to ensure that docked molecules were within the grid.

Scoring of compounds from the primary docking was performed using the vdW attractive interaction energy (IE) to evaluate the shape complementarity between ligands and the protein binding site. Due to the contribution of the molecular size to the energy score, compound selection favors higher molecular weight compounds(33). To avoid this size bias, the vdW

attractive IE was normalized based on the number of non-hydrogen atoms N raised to a power x, as shown in equation 1 (33).

$$IE_{norm} = \frac{IE}{N^x} \quad \text{(Eq. 1)}$$

Normalization based on vdW attractive IE was performed with x = m/12, where m ranges from 0 to 12. The selected value of x for each screen was that corresponding to a median MW of the selected compounds closest to 300 Daltons to correct for molecular weight (MW) bias in docking(33).Compound ranking was performed using the most favorable IE for each compound from the four protein conformations used in the database screening.

The top 50,000 compounds obtained from the primary database screen were subjected to a more rigorous and computationally demanding docking procedure, referred to as secondary docking. The procedure described for primary docking was followed with the additional step of simultaneous energy minimization of all rotatable bonds that connect anchor fragments during the stepwise building of the molecule. More receptor flexibility was taken into account by using 7 of the 9 representative conformations of human Notch1 obtained from the MD simulations along with the crystal structure. Each compound was docked individually to each conformation, from which one with the most favorable total interaction energy was chosen as the energy score of the compound. The total ligand-receptor IE was then normalized as described above. The top 1000 compounds were selected from the secondary searches.

Final selection of compounds for experimental assay involved maximizing chemical and structural diversity of the compounds as well as considering their physicochemical properties with respect to bioavailability. Top 1,000 compounds identified in secondary database screening were subjected to chemical and structural clustering. The Jarvis-Patrick algorithm(34) implemented in MOE was used to identify the dissimilar clusters of compounds using BIT-packed version of MACCS structural key (BIT-MACCS) fingerprints with the Tanimoto coefficient (TC) as similarity index(35). First, the BIT-MACCS fingerprint was calculated and assigned to each of the top 1,000 compounds. Then the pairwise similarity matrix A(i,j) was constructed between compounds i and j for all top 1,000 compounds using binary TC scores $TC_b(i,j)$ that are metrics to evaluate similarity score between two compounds as described in equation 2, where a is the number of features in compound i, b is the number of features in compounds j, and c is the number of common features in compounds i and j(36).

$$TC_b(i,j) = \frac{c}{a + b - c} \quad \text{(Eq. 2)}$$

Pairwise similarity matrix A(i,j) was converted into binary matrix B(i,j), where each $TC_b(i,j)$ was replaced by either 0 or 1 that represents similarity score below or above the user selected similarity threshold value (S). Each of two compounds i and j in top 1,000 molecules were compared as two row vectors B(i) and B(j), from which molecules above the predefined overlap threshold (T) were grouped into the same clusters. The values of S and T were adjusted to generate a reasonable number (~300 clusters) and size (3-10 compounds per cluster) of the clusters as done in our previous studies(37,38), with clusters containing more than 20

compounds subjected to an additional step of clustering using higher similarity and overlap thresholds. Compounds for experimental assay were then manually selected from the clusters, with priority given to those compounds with drug-like properties with respect to bioavailability criteria. Bioavailability was based on Lipinski's rule of 5 (39), as defined as compounds with MW ≤ 500, logP(o/w) ≤ 5 , the number of hydrogen bond donors ≤ 5, and the number of hydrogen bond acceptors ≤ 10. It should be noted that a significant number of clusters only contained a single compound and only a small number of those compounds were selected for biological assays. A search resulted in 202 compounds selected for experimental testing in this study. A selected number of compounds were then purchased from ChemBridge (San Diego, CA) and dissolved in dimethyl sulfoxide (DMSO) at a stock concentration of 25 mM. The purity of compounds shown to have biological activity was verified by mass spectrometry.

Lead validation and SAR development via chemical similarity searching(40). The 2D structural fingerprint (BIT-MACCS) was calculated for active parent compound by the program MOE, and was used to quantify chemical similarity to other molecules using TC as similarity metrics. A virtual 2D database containing over 5.5 million low-molecular weight commercially available compounds was used for the chemical similarity search. The TC was adjusted to limit the search to 100 compounds.

References

1. Weaver KL, Alves-Guerra M-C, Jin K, Wang Z, Han X, Ranganathan P, et al. NACK is an integral component of the Notch transcriptional activation complex and is critical for development and tumorigenesis. Cancer Res 2014;74:4741–51.

2. Wang Z, Da Silva TG, Jin K, Han X, Ranganathan P, Zhu X, et al. Notch signaling drives stemness and tumorigenicity of esophageal adenocarcinoma. Cancer Res 2014;74:6364–74.

3. Bill BR, Petzold AM, Clark KJ, Schimmenti LA, Ekker SC. A primer for morpholino use in zebrafish. Zebrafish 2009;6:69–77.

4. Henry CA, Poage CT, McCarthy MB, Campos-Ortega J, Cooper MS. Regionally autonomous segmentation within zebrafish presomitic mesoderm. Zebrafish 2005;2:7–18.

5. Nam Y, Sliz P, Song LY, Aster JC, Blacklow SC. Structural basis for cooperativity in recruitment of MAML coactivators to Notch transcription complexes. Cell 2006;124:973–83.

6. Bernstein FC, Koetzle TF, Williams GJ, Meyer EF, Brice MD, Rodgers JR, et al. The Protein Data Bank: a computer-based archival file for macromolecular structures. J Mol Biol 1977;112:535–42.

7. Martí-Renom MA, Stuart AC, Fiser A, Sánchez R, Melo F, Sali A. Comparative protein structure modeling of genes and genomes. Annu Rev Biophys Biomol Struct 2000;29:291–325.

8. Word JM, Lovell SC, Richardson JS, Richardson DC. Asparagine and glutamine: using hydrogen atom contacts in the choice of side-chain amide orientation. J Mol Biol 1999;285:1735–47.

9. Brooks BR, Brooks CL, Mackerell AD, Nilsson L, Petrella RJ, Roux B, et al. CHARMM: the biomolecular simulation program. J Comput Chem 2009;30:1545–614.

10. Phillips JC, Braun R, Wang W, Gumbart J, Tajkhorshid E, Villa E, et al. Scalable molecular dynamics with NAMD. J Comput Chem 2005;26:1781–802.

11. MacKerell AD, Bashford D, Bellott M, Dunbrack RL, Evanseck JD, Field MJ, et al. All-atom empirical potential for molecular modeling and dynamics studies of proteins. J Phys Chem B 1998;102:3586–616.

12. Mackerell AD, Feig M, Brooks CL. Extending the treatment of backbone energetics in protein force fields: limitations of gas-phase quantum mechanics in reproducing protein conformational distributions in molecular dynamics simulations. J Comput Chem 2004;25:1400–15.

13. Jorgensen WL, Chandrasekhar J, Madura JD, Impey RW, Klein ML. Comparison of simple potential functions for simulating liquid water. J Chem Phys 1983;79:926.

14. Feller SE, Zhang Y, Pastor RW, Brooks BR. Constant pressure molecular dynamics simulation: The Langevin piston method. J Chem Phys 1995;103:4613.

15. Ryckaert J-P, Ciccotti G, Berendsen HJ. Numerical integration of the cartesian equations of motion of a system with constraints: molecular dynamics of n-alkanes. J Comput Phys 1977;23:327–41.

16. Darden T, York D, Pedersen L. Particle mesh Ewald: An N·log(N) method for Ewald sums in large systems. J Chem Phys 1993;98:10089.

17. Steinbach PJ, Brooks BR. New spherical-cutoff methods for long-range forces in macromolecular simulation. J Comput Chem 1994;15:667–83.

18. Karpen ME, Tobias DJ, Brooks CL. Statistical clustering techniques for the analysis of long molecular dynamics trajectories: analysis of 2.2-ns trajectories of YPGDV. Biochemistry 1993;32:412–20.

19. Carpenter GA, Grossberg S. ART 2: self-organization of stable category recognition codes for analog input patterns. Appl Opt 1987;26:4919–30.

20. Pao Y-H. Adaptive pattern recognition and neural networks. Addison-Wesley Longman Publishing Co. Inc.; 1989.

21. Zhong S, MacKerell Jr. AD. Binding response: A descriptor for selecting ligand binding site on protein surfaces. J Chem Inf Model 2007;47:2303–15.

22. Kuntz ID, Blaney JM, Oatley SJ, Langridge R, Ferrin TE. A geometric approach to macromolecule-ligand interactions. J Mol Biol 1982;161:269–88.

23. Kuntz ID. Structure-based strategies for drug design and discovery. Science 1992;257:1078–82.

24. Connolly ML. Solvent-accessible surfaces of proteins and nucleic acids. Science 1983;221:709–13.

25. Ferrin TE, Huang CC, Jarvis LE, Langridge R. The MIDAS database system. J Mol Graph 1988;6:2–12.

26. Halgren TA. MMFF VI. MMFF94s option for energy minimization studies. J Comput Chem 1999;20:720–9.

27. Halgren TA. MMFF VII. Characterization of MMFF94, MMFF94s, and other widely available force fields for conformational energies and for intermolecular-interaction energies and geometries. J Comput Chem 1999;20:730–48.

28. Li J, Zhu T, Cramer CJ, Truhlar DG. New Class IV Charge Model for Extracting Accurate Partial Charges from Wave Functions. J Phys Chem A 1998;102:1820–31.

29. Chambers CC, Hawkins GD, Cramer CJ, Truhlar DG. Model for Aqueous Solvation Based on Class IV Atomic Charges and First Solvation Shell Effects. J Phys Chem 1996;100:16385–98.

30. Ewing TJA, Kuntz ID. Critical evaluation of search algorithms for automated molecular docking and database screening. J Comput Chem 1997;18:1175–89.

31. Leach AR, Kuntz ID. Conformational analysis of flexible ligands in macromolecular receptor sites. J Comput Chem 1992;13:730–48.

32. Goodford PJ. A computational procedure for determining energetically favorable binding sites on biologically important macromolecules. J Med Chem 1985;28:849–57.

33. Pan YP, Huang N, Cho S, MacKerell AD. Consideration of molecular weight during compound selection in virtual target-based database screening. J Chem Inf Comput Sci 2003;43:267–72.

34. Jarvis RA, Patrick EA. Clustering Using a Similarity Measure Based on Shared Near Neighbors. IEEE Trans Comput 1973;C-22:1025–34.

35. Tanimoto TT. An elementary mathematical theory of classification and prediction. IBM Intern Rep. New York; 1957.

36. Butina D. Unsupervised Data Base Clustering Based on Daylight's Fingerprint and Tanimoto Similarity: A Fast and Automated Way To Cluster Small and Large Data Sets. J Chem Inf Model 1999;39:747–50.

37. Furci LM, Lopes P, Eakanunkul S, Zhong S, MacKerell Jr. AD, Wilks A. Inhibition of the bacterial heme oxygenases from Pseudomonas aeruginosa and Neisseria meningitidis: Novel antimicrobial targets. J Med Chem 2007;50:3804–13.

38. Yu WM, Guvench O, MacKerell AD, Qu CK. Identification of Small Molecular Weight Inhibitors of Src Homology 2 Domain-Containing Tyrosine Phosphatase 2 (SHP-2) via in Silico Database Screening Combined with Experimental Assay. J Med Chem 2008;51:7396–404.

39. Lipinski CA, Lombardo F, Dominy BW, Feeney PJ. Experimental and computational approaches to estimate solubility and permeability in drug discovery and development settings. Adv Drug Deliv Rev 2001;46:3–26.

40. Macias AT, Mia MY, Xia GJ, Hayashi J, MacKerell AD. Lead validation and SAR development via chemical similarity searching; Application to compounds targeting the pY+3 site of the SH2 domain of p56(lck). J Chem Inf Model 2005;45:1759–66.

Identification of a Paralog-Specific Notch1 Intracellular Domain Degron

Broadus MR, Chen TW, **Neitzel LR**, Ng VH, Jodoin JN, Lee LA, Salic A, Robbins DJ, Capobianco AJ, Patton JG, Huppert SS, Lee E.

Cell Rep **2016 15(9):1920-9**

doi: 10.1016/j.celrep.2016.04.070

Report

Cell Reports

Identification of a Paralog-Specific Notch1 Intracellular Domain Degron

Graphical Abstract

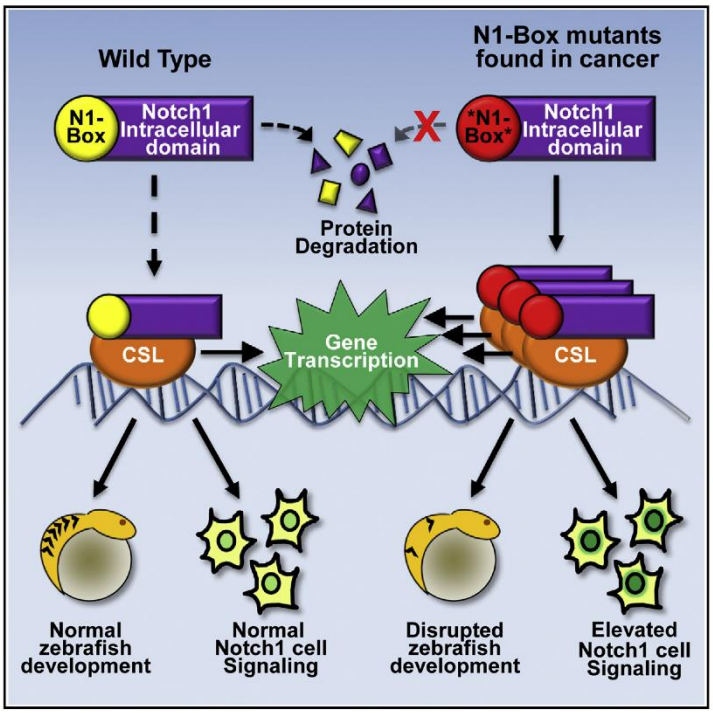

Highlights

- A biochemical assay identifies the N1-Box degron of the Notch1 intracellular domain
- Mutations in the Notch1 N1-Box promote signaling in human cells and zebrafish
- The N1-Box functions independently of other known Notch1 degrons
- Human cancer mutations within the N1-Box exhibit elevated Notch1 activity in vivo

Authors

Matthew R. Broadus, Tony W. Chen, Leif R. Neitzel, ..., James G. Patton, Stacey S. Huppert, Ethan Lee

Correspondence

stacey.huppert@cchmc.org (S.S.H.), ethan.lee@vanderbilt.edu (E.L.)

In Brief

Notch is essential for metazoan development and is mutated in human cancers. Broadus et al. identify a paralog-specific degron (N1-Box) that promotes degradation of the Notch1 intracellular domain, thereby limiting Notch1 pathway activity. Cancer mutations within the N1-Box exhibit enhanced Notch1 signaling in zebrafish, highlighting the importance of N1-Box in proper Notch1 signaling.

Broadus et al., 2016, Cell Reports *15*, 1920–1929
May 31, 2016
http://dx.doi.org/10.1016/j.celrep.2016.04.070

CellPress

OPEN ACCESS
CellPress

Cell Reports
Report

Identification of a Paralog-Specific Notch1 Intracellular Domain Degron

Matthew R. Broadus,[1,2,9] Tony W. Chen,[1,9] Leif R. Neitzel,[1] Victoria H. Ng,[1] Jeanne N. Jodoin,[1,7] Laura A. Lee,[1] Adrian Salic,[2] David J. Robbins,[3,4] Anthony J. Capobianco,[3,4] James G. Patton,[5] Stacey S. Huppert,[6,10,*] and Ethan Lee[1,8,10,*]

[1]Department of Cell and Developmental Biology, Vanderbilt University Medical Center, Nashville, TN 37232, USA
[2]Department of Cell Biology, Harvard Medical School, Boston, MA 02115, USA
[3]Molecular Oncology Program, Division of Surgical Oncology, Dewitt Daughtry Family Department of Surgery
[4]Sylvester Comprehensive Cancer Center, Miller School of Medicine
University of Miami, Miami, FL 33136, USA
[5]Department of Biological Sciences, Vanderbilt University, Nashville, TN 37232, USA
[6]Division of Gastroenterology, Hepatology, and Nutrition, Cincinnati Children's Hospital Medical Center, Cincinnati, OH 45229, USA
[7]Department of Biology, Massachusetts Institute of Technology, Cambridge, MA 02142, USA
[8]Vanderbilt Ingram Cancer Center, Vanderbilt Medical Center, Nashville, TN 37232, USA
[9]Co-first author
[10]Co-senior author
*Correspondence: stacey.huppert@cchmc.org (S.S.H.), ethan.lee@vanderbilt.edu (E.L.)
http://dx.doi.org/10.1016/j.celrep.2016.04.070

SUMMARY

Upon Notch pathway activation, the receptor is cleaved to release the Notch intracellular domain (NICD), which translocates to the nucleus to activate gene transcription. Using *Xenopus* egg extracts, we have identified a Notch1-specific destruction signal (N1-Box). We show that mutations in the N1-Box inhibit NICD1 degradation and that the N1-Box is transferable for the promotion of degradation of heterologous proteins in *Xenopus* egg extracts and in cultured human cells. Mutation of the N1-Box enhances Notch1 activity in cultured human cells and zebrafish embryos. Human cancer mutations within the N1-Box enhance Notch1 signaling in transgenic zebrafish, highlighting the physiological relevance of this destruction signal. We find that binding of the Notch nuclear factor, CSL, to the N1-Box blocks NICD1 turnover. Our studies reveal a mechanism by which degradation of NICD1 is regulated by the N1-Box to minimize stochastic flux and to establish a threshold for Notch1 pathway activation.

INTRODUCTION

The Notch pathway is a highly conserved, metazoan signaling pathway critical for organismal development (Kopan and Ilagan, 2009). The Notch pathway communicates transcriptional decisions between adjacent cells through direct interaction of a Delta/Serrate/Lag-2 (DSL) type 1 transmembrane ligand on the signaling cell and a Notch type 1 transmembrane receptor on a receiving cell. This interaction promotes a series of proteolytic events resulting in liberation of the Notch intracellular domain (NICD) from its membrane tether. Liberated NICD enters the nucleus, where it forms a complex with CSL (CBF1/RBPjk/Su(H)/Lag-1), MAML (Mastermind-like), and CoA (coactivators) (Kovall and Blacklow, 2010). Formation of this complex drives transcription of Notch target genes. In the prevailing model, transcriptional termination is mediated, in part, by the E3 ubiquitin ligase complex, SCF^{Fbxw7}, which promotes ubiquitin-mediated degradation of NICD in a PEST domain-dependent manner (Moretti and Brou, 2013). Herein, we identify a hNICD1-specific degron within the N-terminal region distinct from its C-terminal PEST domain.

RESULTS

NICD1 Is Degraded in *Xenopus* Extract

To recapitulate cytoplasmic NICD turnover, we used the *Xenopus* extract system previously shown to support β-catenin degradation via Wnt pathway components (Chen et al., 2014). In our *Xenopus* extract system, no ongoing transcription or translation confounds our results. We found that radiolabeled in-vitro-translated (IVT) hNICD1 degraded robustly when added to *Xenopus* extract (Figure 1A). Addition of MG132, a proteasome inhibitor, inhibited degradation of both radiolabeled hNICD1 and β-catenin (Figure 1A). Excess recombinant β-catenin inhibited turnover of radiolabeled β-catenin but had no effect on hNICD1 turnover (Figure 1B). Thus, hNICD1 degradation in *Xenopus* extract occurs in a proteasome-dependent manner distinct from that of β-catenin.

NICD Degradation within *Xenopus* Extract Is Restricted to the NICD1 Paralog

In contrast to hNICD1, we found that its paralogs (hNICD2, hNICD3, and hNICD4) were stable throughout the time course

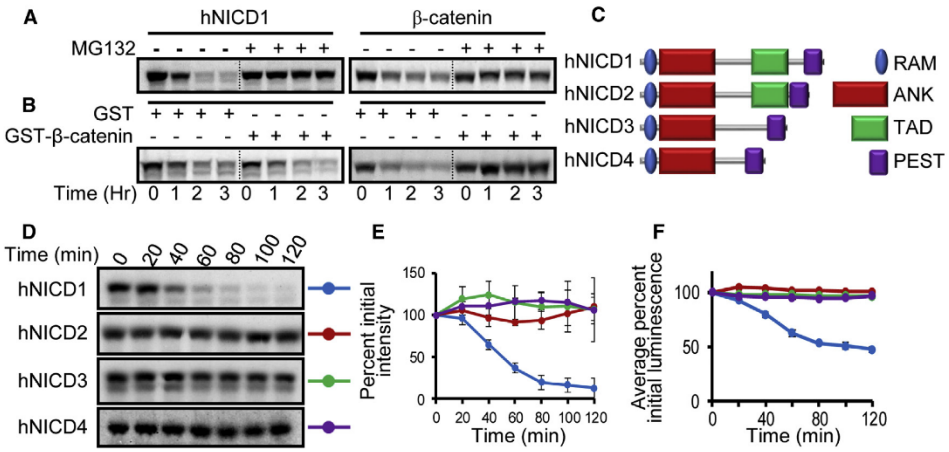

Figure 1. hNICD1 Is Degraded in *Xenopus* Egg Extract

(A) In-vitro-translated (IVT) [^{35}S]hNICD1 and [^{35}S]β-catenin were incubated in extract with DMSO (–) or MG132 (+). Samples were analyzed by SDS-PAGE/autoradiography.

(B) Same as for (A), except extract was supplemented with GST or GST-β-catenin.

(C) Schematic of human NICD paralogs. RAM, RBP-Jκ-associated module domain; ANK, ankyrin repeats domain; TAD, transcriptional activation domain; PEST is proline-, glutamic-acid-, serine-, and threonine-rich region.

(D) Radiolabeled hNICD paralogs were incubated in extract, and samples were removed at the indicated times for SDS-PAGE/autoradiography.

(E) Graph of mean ± SD densitometry measurements for autoradiography experiments.

(F) Degradation of IVT hNICD luciferase fusions incubated in extract parallels degradation of radiolabeled, untagged versions. Graph is mean luciferase signal for two independent experiments (performed in triplicate) and normalized to initial time point (100%).

See also Figure S1.

of our experiment (Figure 1C–1E). To quantify the degradation of NICD proteins in *Xenopus* extract, hNICD paralogs were fused at their C-terminal ends to firefly luciferase (Chen et al., 2014). Although a high background signal is caused by use of internal translational start sites (Chen et al., 2014), the hNICD1 luciferase fusion had a similar half-life as radiolabeled hNICD1 (Figures 1F and S1A). hNICD2, 3, and 4 luciferase fusions were stable, similar to their radiolabeled non-fusion proteins (Figure 1F). This differential degradation was conserved for mouse NICD1 and NICD4 (Figure S1B). We found that the single *Drosophila* NICD ortholog was stable in *Xenopus* extract (Figure S1B).

The N-terminal End of hNICD1 Contains a Degron Required for Degradation in *Xenopus* Extract

Next, we assessed the turnover rates of NICD proteins in *Xenopus* extract versus cultured human cells. We found that NICD-MYC fusions had turnover rates essentially identical to those of their non-tagged versions in extract (Figure S1C). In contrast, all NICD paralogs degraded at similar rates in cultured human cells (Figure S1D), consistent with previous reports (Fryer et al., 2004; Malyukova et al., 2007; Mo et al., 2007; Palermo et al., 2012; Tsunematsu et al., 2004).

The degradation differences between *Xenopus* extract and cultured cells suggest that an uncharacterized degron exists in mammalian NICD1 mechanistically uncoupled in *Xenopus* extract. To identify the NICD1-specific degron, we generated chimeric proteins in which N-terminal or C-terminal portions of hNICD1 were swapped with corresponding portions of other hNICD paralogs (Figures S1E–S1L). These results identified the N terminus of hNICD1 as necessary for its instability within *Xenopus* extract. To narrow the N-terminal portion of hNICD1 responsible for degradation, smaller corresponding swaps of hNICD2 were made with hNICD1 (Figure 2A). We found that the N-terminal 35-amino-acid fragment of hNICD1 was sufficient to confer degradation of hNICD2 (Figures 2B and S1E–S1L). These results show that the amino terminus of hNICD1 contains a Notch1-specific degron (N1-Box) necessary and sufficient to degrade hNICD1 in *Xenopus* extract.

The N-terminal ends of the human NICD paralogs (Figure 2C) contain non-conserved residues within the first 35 amino acids of hNICD1 (residues 1754–1788 of Notch1) that may mediate its degradation. To test this possibility, we mutated these residues to the corresponding hNICD2 residues. In contrast to wild-type hNICD1, the L1755Δ, S1757M, and Q1763K single mutants and triple-mutant hNICD1^{LSQ} were stable in extract (Figures 2D, 2E, and S2A). hNICD1$^{NT\Delta10}$, which lacks the N-terminal ten residues of hNICD1, was also stable in extract, confirming the importance of this region in mediating hNICD1 stability (Figure S2A). All five mutant proteins tested could activate a HES1-luciferase reporter, indicating that they were not grossly misfolded (Figures 2F and 2H). Furthermore, the stabilized mutants demonstrated enhanced reporter activity. The Q1766S mutant demonstrated a slight increased stability in *Xenopus* extract, although Hes1-Luc activation was similar to wild-type. This may reflect subtle differences between *Xenopus* extracts and mammalian cultured cells.

To assess whether the N-terminal region of hNICD1 could promote protein turnover in an autonomous fashion, we fused the N-terminal 50 residues of hNICD1 to luciferase. In contrast to luciferase, hNICD1(1-50)-Luc degraded in extract (Figure S2B). The analogous N1-Box mutants (L1755, S1757, and Q1763) in the hNICD1(1-50)-Luc fusion were stable in *Xenopus* extract (Figure S2B). Next, we altered the first ten residues of NICD2 to those corresponding to NICD1. We found that the chimera, NICD1/2^{NT10}, did not have an increased rate of degradation when compared to wild-type NICD2 (Figure S2C). Enhanced degradation of NICD2, however, was observed on addition of the N-terminal 35 amino acids of NICD1 (Figure S2C). Thus, the N-terminal 35 amino acids of NICD1 constitute the minimal transferable element capable of promoting degradation of the Notch intracellular domain in *Xenopus* extract.

Next, we tested whether N1-Box-regulated degradation of hNICD1 functioned in cultured cells. The N1-Box mutants hNICD1$^{NT\Delta10}$ and hNICD1^{LSQ} were expressed in HEK293 cells, and protein levels assessed by immunoblotting (Figure 2G). Both mutant proteins had higher steady-state levels than did wild-type hNICD1 (Figures 2G and S3A). Consistent with their increased stability, both hNICD1$^{NT\Delta10}$ and hNICD1^{LSQ} had enhanced transcriptional activity (Figure 2H). To test autonomous function of the hNICD1 N1-Box in human cells, we fused the N1-Box to GFP and monitoring turnover by live-cell imaging. In contrast to GFP, hNICD1(1-50)-GFP showed loss of fluorescence at a rate similar to that of full-length hNICD1-GFP (Figures S2D and S2E). A N1-Box double mutant (hNICD1(1-50)^{LS}-GFP) and GFP fusions of the first 50 residues of hNICD2 and 3 did not exhibit substantial turnover (Figure S2E). These results suggest the degradation machinery for the N1-Box of hNICD1 is evolutionarily conserved. We observed turnover of the N1-Box GFP fusion in both the nucleus and cytoplasm, suggesting that N1-Box-mediated degradation could occur in both compartments.

The N1-Box Controls hNICD1 Stability and Activity In Vivo

To ensure that the N1-Box functioned in the complete Notch1 receptor, and to further demonstrate evolutionary conservation, we generated the analogous N1-Box mutant in full-length mouse Notch1 (mNotch1^{LSQ}). Consistent with our hNICD1 studies, mNotch1^{LSQ} exhibited elevated Notch transcriptional activity compared to wild-type mNotch1 (Figure S3B).

To demonstrate that the N1-Box regulates Notch1 function in vivo, we assessed its effects on somite formation in zebrafish embryos. Notch1 plays a role in vertebrate somitogenesis (Harima and Kageyama, 2013; Lewis et al., 2009), and misregulation of Notch signaling during development results in disruption of the symmetric, bilateral somites (Figure 3A). This biological readout was dose sensitive (Figure 3B). Consistent with a role for N1-Box in vivo, injecting mRNA of the N1-Box mutant, *mNotch1*^{LSQ}, caused defective somite formation in nearly double that of *mNotch1* mRNA injected emybros (Figure 3B). It is possible that the enhanced activity of the NICD1 N1-Box mutant is due to its more efficient processing. A mutation in the HD domain of human Notch1 (L1601P) resulted in a constitutively activated "leaky" Notch1 receptor due to its constitutive cleavage from the plasma membrane (Chiang et al., 2006; Thompson et al., 2007; Weng et al., 2004). When combined, the mNotch1$^{L1601P;LSQ}$ mutant had an additive defect in somitogenesis (Figure 3B). These results suggest that the greater activity of the Notch1^{LSQ} is due to increased stability and not more efficient processing.

Inhibition of neural differentiation is a major role of Notch signaling during development. Using the transgenic zebrafish line, Tg(NGN1:GFP), which expresses GFP controlled by the *neurogenin1* (*ngn1*) promoter (marks primary neurons) (Blader et al., 2003), we found that injection of *mNotch1* mRNA decreases the normal *ngn1* expression along the rostral-caudal axis (particularly in the hindbrain) (Figures 3C and S3C). mNotch1^{LSQ} led to a severe decrease in expression of GFP, consistent with its more potent activity. In contrast, injection of *mNotch1* mRNA into Tg(Her4:dRFP), a zebrafish line that expresses RFP under control of the promoter for *her4*, a Notch target gene (Yeo et al., 2007), enhanced RFP expression throughout the central nervous system (Figures 3C and S3C). The expression of RFP was further enhanced (extended caudally) when *mNotch1*^{LSQ} mRNA was injected.

Mutations within the N1-Box Found in Human Tumors Inhibit hNICD1 Degradation

Using the NIH Catalog of Somatic Mutations in Cancer database, we identified two mutations (R1758S and S1776C) in patient tumors located within the first N-terminal 35 residues of hNICD1 (Figure 3D). We found that both mutants exhibit elevated Notch transcriptional activity and steady-state protein levels (Figures 3E and 3F). These mutants also have enhanced activity in vivo as indicated by significantly greater somitogenesis defects on injection of their mRNAs into zebrafish embryos (Figure 3G).

To demonstrate physiologically relevance, we generated transgenic zebrafish encoding the human mutations in the corresponding positions of endogenous zebrafish Notch1 by CRISPR/Cas9-mediated knockin. For all embryos, we performed PCR followed by sequencing to confirm the absence or presence of mutations. We found that all embryos harboring R1758S or S1776C exhibited disrupted somitogenesis (Figure 3H). In contrast, embryos with the wild-type phenotype did not harbor mutant sequences. As control, transgenic animals harboring silent mutations within the N1-Box were generated. We found that none of silent N1-Box mutants exhibited defects in somitogenesis. Transgenic R1758S and S1776C animals demonstrated decreased GFP expression from the *ngn1* promoter and enhanced RFP expression from the *her4* promoter (Figures 3I–3L), consistent with enhanced Notch1 signaling. These changes are not due to gross disruption in embryonic structures (Figures S3D and S3E). No changes in GFP or RFP expression were observed for the control silent mutant embryos. These studies provide strong evidence for an in vivo role of the N1-Box in regulating Notch1 signaling.

The N1-Box Facilitates hNICD1 Degradation Independent of Other *cis* Stability Elements

Two *cis* elements have been identified within the NICD PEST domain that facilitate turnover: the LTPSPE sequence recognized by the SCF^{Fbxw7} complex (Fryer et al., 2002, 2004; O'Neil et al., 2007; Thompson et al., 2007) and the WSSSSP sequence (Chiang et al., 2006). We tested the relative contributions of these

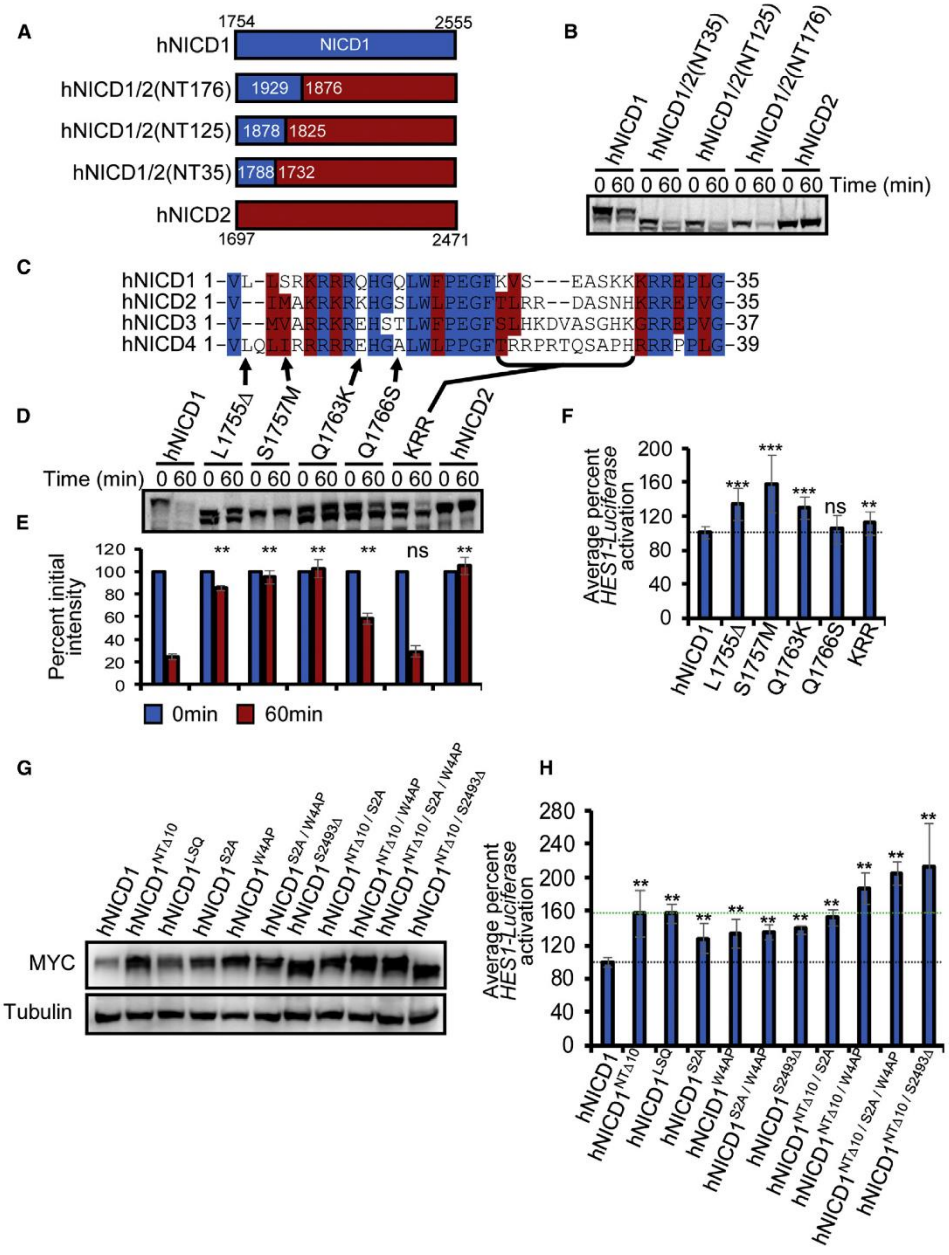

Figure 2. Mutation of N1-Box Inhibits hNICD1 Degradation in *Xenopus* Egg Extract and Elevates Steady-State Levels and Transcriptional Activity in Cultured Human Cells

(A) Schematic of hNICD1 and hNICD2 chimeras. Parentheses indicate the number of N-terminal residues of hNICD1 in each chimera.

(B) Radiolabeled hNICD1/2 chimeras containing at least the N-terminal 35 residues of hNICD1 degraded robustly in *Xenopus* egg extract.

(C) Alignment of N-terminal regions of human NICD paralogs.

(legend continued on next page)

two elements and the N1-Box to NICD1 stability. Consistent with previous studies, mutation of LTPSPE (S2514A/S2517A; hNICD1^{S2A}), WSSSSP (hNICD1^{W4AP}), both LTPSPE and WSSSSP (hNICD1$^{S2A/W4AP}$), or truncation of the PEST region (hNICD1$^{S2493\Delta}$) resulted in increased protein levels in cultured cells (Figure 2G) (Chiang et al., 2006; Fryer et al., 2004; O'Neil et al., 2007; Thompson et al., 2007; Weng et al., 2004). Increased steady-state levels of hNICD1^{S2A} and hNICD1^{W4AP} were also observed in combination with NTΔ10. Interestingly, combining hNICD1$^{NT\Delta10}$ with W4AP and/or S2493Δ, but not with S2A, enhanced protein levels. All stabilizing mutants demonstrated enhanced HES1 reporter activation, and protein levels of each hNICD1 mutant roughly correlated with the degree of activation of Notch transcription (Figure 2H). We observed a similar effect in zebrafish embyros in which injected Notch1$^{LSQ/S2647\Delta}$ (S2647Δ is the mouse PEST deletion) was more potent in disrupting somitogenesis (Figure 3B). These results suggest that WSSSSP and the N1-Box act independent of each other. The absence of further activation by hNICD1$^{NT\Delta10}$ or hNICD1^{W4AP} on mutation of the Fbxw7 binding site may indicate that stabilization by NTΔ10 or WSSSSP fully saturates the SCF^{Fbxw7} complex, which may be limiting.

The N1-Box Is Not Regulated by Fbxw7 or Itch

In addition to known *cis* factors, we also assessed whether two known NICD E3 ubiquitin ligases contributed to N1-Box-mediated degradation. We overexpressed Fbxw7 and a dominant-negative form (Fbxw7DN) (Skaar et al., 2013; Wu et al., 2001). As previously reported, overexpression of Fbxw7 decreased, and Fbxw7DN increased, steady-state levels of hNICD1 (Figure S4A) (Gupta-Rossi et al., 2001; Wu et al., 2001). In contrast, overexpressing Fbxw7 or Fbxw7DN did not affect levels of the Fbxw7 binding site mutant, hNICD1^{S2A} (Figure S4A). The effects of overexpressing Fbxw7 and Fbxw7DN on wild-type hNICD1 were similarly observed for hNICD1^{W4AP} (Figure S4A), consistent with our results and a previous study suggesting that WSSSSP acts independent of the SCF^{Fbxw7} complex (Chiang et al., 2006). A similar effect was observed for NICD1$^{NT\Delta10}$, indicating that the N1-Box mediates degradation of NICD1 independent of the SCF^{Fbxw7} complex.

All NICD paralogs contain a C-terminal PEST domain recognized by the SCF^{Fbxw7} ubiquitin ligase (Gupta-Rossi et al., 2001; Moretti and Brou, 2013; Oberg et al., 2001; Wu et al., 2001). The Fbxw7 isoform shown to ubiquitinate NICD proteins is localized to the nucleus (O'Neil et al., 2007). In support of this, we could not detect Fbxw7 by immunoblotting *Xenopus* extract, which does not contain nuclei (Figure S4B). In addition, two Fbxw7 binding mutants hNICD1^{S3A} and hNICD$^{S2493\Delta}$ degraded at rates indistinguishable from that of wild-type hNICD1 (Figures S4C–S4F). Thus, the incapacity of extract to degrade NICD2-4 is likely due to the absence of Fbxw7, and NICD1 degradation in *Xenopus* extract does not require its PEST domain or Fbxw7.

The E3 ligase, Itch, promotes PEST domain-independent NICD1 degradation (Qiu et al., 2000). As previously shown, overexpression of Itch decreased, whereas overexpression of a dominant-negative form, Itch^{C380A}, increased, hNICD1 steady-state levels in HEK293 cells (Figure S4G). We obtained similar results for all of our mutants, indicating that Itch does not mediate NICD1 degradation through the N1-Box.

hNICD1 Turnover Is Inhibited by CSL

Based on sequence overlap between the N1-Box and RAM domain (the major *cis* factor involved in CSL binding (Nam et al., 2003; Tamura et al., 1995) (Figure 4A), we tested whether binding of CSL to hNICD1 could influence hNICD1 stability. Given the cytoplasmic nature of *Xenopus* egg extract (lacks nuclei), it likely contains low levels of CSL. Incubation of recombinant CSL with *Xenopus* extract inhibited hNICD1 degradation in a dose-dependent manner (Figures 4B and 4C). Inhibition of hNICD1 degradation by CSL requires direct binding because degradation of hNICD1$^{1771\text{-}74A}$, which cannot bind CSL (Chu and Bresnick, 2004; Vasquez-Del Carpio et al., 2011), is not inhibited by recombinant CSL (Figures 4B and 4C). In cultured human cells, where CSL is present, we predicted that hNICD1$^{1771\text{-}74A}$ would be less stable than wild-type hNICD1. In support of this idea, we observed lower steady-state levels of hNICD1$^{1771\text{-}74A}$ than for wild-type hNICD1 when expressed in HEK293 cells (Figures 4D and 4E).

Degradation of NICD via the SCF^{Fbxw7}/PEST domain depends on assembly of a CSL transcriptional complex (Fryer et al., 2002, 2004). We predicted that hNICD1$^{1771\text{-}74A}$ instability is primarily mediated by the N1-Box. Thus, an N1-Box/CSL-binding double mutant should be more stable than the N1-Box mutant, and a hNICD1 PEST/CSL binding double mutant should be less stable than a PEST domain mutant due to enhanced N1-Box-mediated degradation. Consistent with this idea, we found that hNICD1$^{NT\Delta10/1771\text{-}74A}$ steady-state levels are statistically higher than those of hNICD1$^{NT\Delta10}$ and that hNICD1$^{1771\text{-}74A\ /\ S2493\Delta}$ steady-state levels are lower than those of hNICD1$^{S2493\Delta}$

(D) Mutation of hNICD1 non-conserved residues at position L1755, S1757, or Q1763 inhibits degradation in extract. Δ, amino acid deletion; KRR, lysine-rich region. Intervening lanes were removed. The lower bands observed in (B) and (D) represent an internal translational initiation product (thus are missing an N-terminal fragment) resistant to degradation (Chen et al., 2014).

(E) Mean ± SD quantification of densitometry for experiments represented in (D). Data are from three independent experiments. $^{**}p < 0.05$; ns, not significant.

(F) N-terminal mutants of hNICD1 are transcriptionally active as assessed by HES1-luciferase Notch reporter activity in HEK293 cells. Luciferase activity was measured after 24 hr. Graph represents ± SD of luciferase signal normalized to *Renilla* luciferase of at least three independent experiments (performed in triplicate). $^{***}p < 0.0001$, $^{**}p < 0.05$ relative to hNCID1. ns, not significant.

(G) N1-Box mutants (hNICD$^{NT\Delta10}$ and hNICD^{LSQ}), Fbxw7 binding mutant (hNICD1^{S2A}), WSSSSP mutant (hNICD1^{W4AP}), or combinations were expressed in HEK293 cells, and immunoblotting of lysates was performed. Tubulin was used as a control.

(H) Stabilizing hNICD1 N1-Box mutants, Fbxw7, and WSSSP exhibit higher transcriptional activity than does hNICD1 as assessed by HES1-luciferase reporter activity in HEK293 cells. Luciferase activity was measured after 24 hr. Graphs show mean ± SD of the luciferase signal normalized to *Renilla* luciferase of at least two independent experiments (performed in triplicate). $^{**}p < 0.002$ relative to hNICD1.

See also Figures S2, S3, and S4.

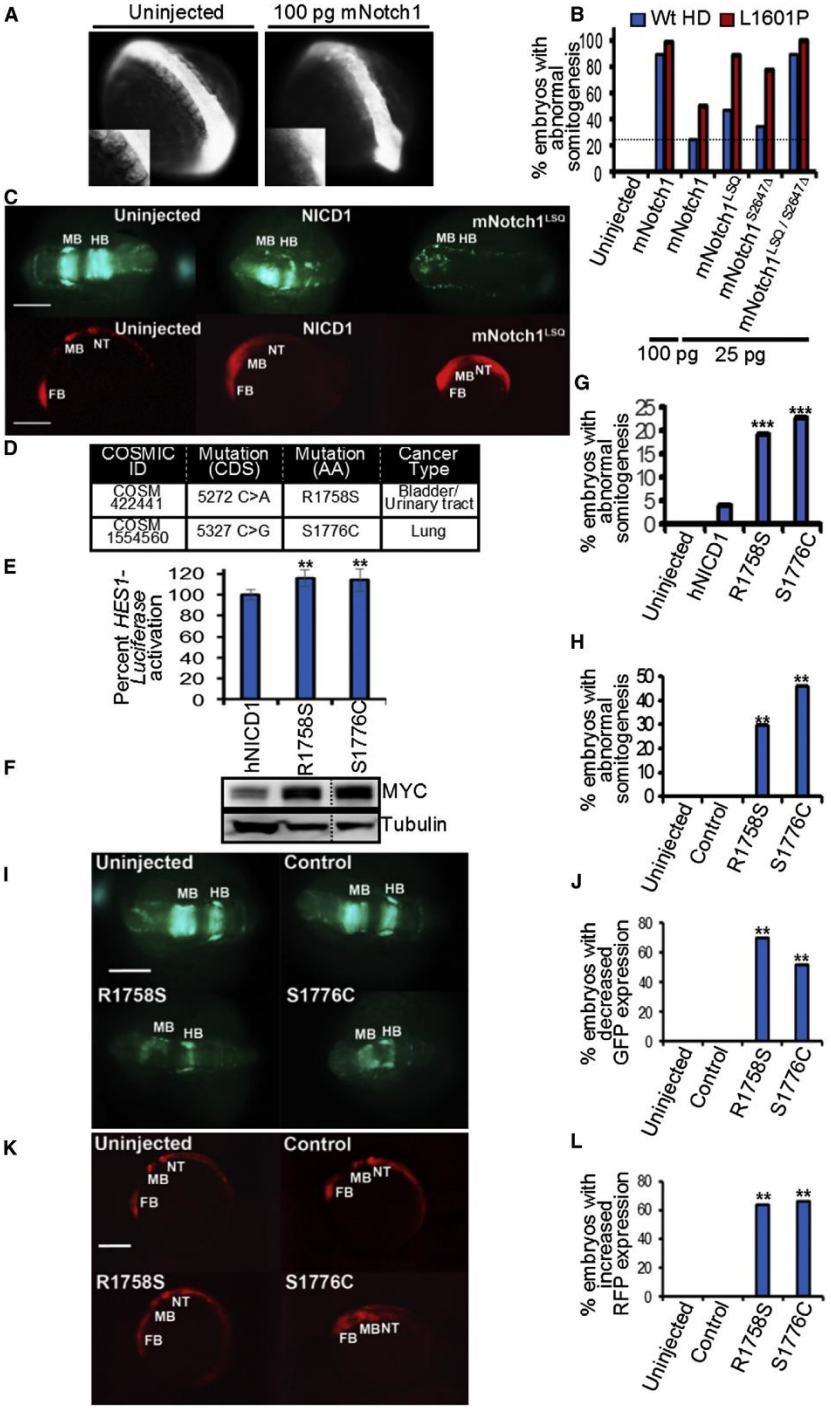

(legend on next page)

(Figures 4D and 4E). These results suggest that CSL binding to NICD1 inhibits its turnover by blocking N1-Box-mediated degradation.

DISCUSSION

Evidence for an in vivo role of the N1-Box comes from a previous report showing that a chimeric receptor containing the Notch2 extracellular domain and Notch1 intracellular domain (Notch21) is 2-fold more active than is a wild-type Notch1 when expressed at similar levels in mice (Liu et al., 2013). Interestingly, the Notch21 chimeric fusion deleted the N1-Box of NICD1. Our data suggest that increased activity of this chimera is due to increased stability of its intracellular domain. We propose a model (Figure 4F) in which liberated NICD1 (on cleavage from the Notch1 receptor) has two possible fates: (1) rapid degradation and inactivation via its N1-Box or (2) binding to CSL and Notch transcriptional complex components to drive Notch target gene transcription. Termination of Notch1 signaling occurs on ubiquitin-mediated degradation by the SCF^{Fbxw7}/proteasome.

It is not as clear why a cell needs to regulate cytoplasmic NICD1 degradation. One possibility is that this system dampens stochastic flux in the system, thereby minimizing noise: a threshold level of Notch receptor activation must occur for activation of transcription. Indeed, recent models of juxtacrine signaling indicate that such systems are inherently noisy (Yaron et al., 2014). This may explain why *Drosophila* NICD does not have an N1-Box, as stochastic flux in Notch signaling plays an important role during neuroblast differentiation via lateral inhibition (Artavanis-Tsakonas et al., 1999). Conversely, once the transcriptional complex is fully saturated (i.e., all CSL is occupied by NICD1), unbound NICD1 could be degraded to limit the activation window. This model is consistent with the digital response model proposed for Notch1 pathway activation (Ilagan et al., 2011).

We favor a model in which N1-Box mutants stabilize NICD1 protein by directly disrupting the interaction of NICD1 with an as yet unknown E3 ligase. Because the N1-Box and the RAM domains overlap, however, it is possible that certain cancer mutations may enhance NICD1-CSL interaction and indirectly block the action of the E3 ligase. Activating mutations in Notch have been found in a large percentage of T-ALL cases. To date, we have not found N1-Box mutations in T-ALL. It is possible that T cells have other mechanisms to control cytoplasmic levels of NICD1. Alternatively, turnover by other E3 ligases (e.g., Fbxw7 and/or Itch) may be the predominant mechanism by which cytoplasmic NICD1 levels are regulated.

EXPERIMENTAL PROCEDURES

Animals

All *Xenopus laevis* and zebrafish studies were approved by the Vanderbilt University Institutional Animal Care and Use Committee and were performed in accordance with institutional and federal guidelines. See Supplemental Information for more details.

Cell Culture

HEK293 cells were maintained in DMEM (Corning) supplemented with 1% L-glutamine, 10% (v/v) fetal bovine serum, 100 μg/ml streptomycin, and 100 U/ml penicillin at 37°C with 5% CO_2. Transient transfections were performed using Fugene HD (Promega) in accordance with the manufacturer's

Figure 3. Notch1 N1-Box Mutants Found in Human Cancers Have Increased Activity in Cultured Human Cell and Zebrafish Embryos

(A) The N1-Box Notch1 mutant exhibits enhanced capacity to disrupt somitogenesis in embryos. Representative images of 10–13 somite stage zebrafish embryos, uninjected and injected (100 pg of *mNotch1* mRNA). Inset is higher magnification.

(B) Quantification of zebrafish embryos (10–13 somite stage) with defective somites. Data are from three clutches collected from three different breeding pairs per clutch. n = 78–200 embryos per injection. **$p < 0.05$ relative to 25 pg *Notch1* mRNA injection. ***$p < 0.005$ relative to 25 pg $hNICD1^{LSQ; S2467\Delta}$ mRNA injection, except for comparison to *Notch1* 100 pg injection (not significant).

(C) (Top) Injection into the zebrafish line, Tg[NGN1:GFP], that expresses GFP in primary neurons under control of the *ngn1* promoter. Coronal views of embryos at 8× magnification. Embryos with reduced GFP expression: uninjected = 0/44, mNotch1 = 24/32, and $mNotch1^{LSQ}$ = 17/40. Injection of 25 pg. (Bottom) Injection into the zebrafish line, Tg[Her4:dRFP], that expresses RFP under the control of the *her4* Notch target gene promoter. Sagittal view of embryos (14 hpf) at 5× magnification. Data are from at least three clutches collected from three different breeding pairs. Embryos with increased RFP expression: uninjected = 0/75, mNotch1 = 60/68, and $mNotch1^{LSQ}$ = 45/53. Injection of 25 pg. Hpf is14 hr post-fertilization. Scale bar, 0.3 mm.

(D) Table of somatic mutations found within residues 1754–1788 of hNotch1 (residues 1–35 of hNICD1) from the COSMIC database.

(E) Human cancer mutants in the N1-Box expressed in HEK293 cells show elevated HES1-luciferase reporter activity. Graph shows mean ± SD of the luciferase signal normalized to *Renilla* luciferase of at least three independent experiments performed in triplicate. **$p \leq 0.007$ relative to hNICD1.

(F) hNotch1 R1758S and S1776C mutants expressed in cultured cells have elevated steady-state levels. Tubulin was used as a loading control. Intervening lanes were removed.

(G) Quantification of 10–13 somite stage zebrafish embryos with defective somites (injected with 50 pg of indicated mRNA). Data are from at least three clutches collected from three different breeding pairs. n = 30–320 embryos per injection. ***$p < 0.0005$ relative to hNICD1.

(H) Zebrafish embryos were injected with Cas9 nuclease mRNA, short guide RNA, and donor single-strand oligonucleotides encoding R1758S, S1776C, or Notch1 silent mutation (control). Transgenics expressing the R1758S or S1776C mutation in zebrafish Notch1 exhibit defects in somite formation. In contrast, no somitogenesis defects are observed in transgenics harboring silent mutations of zebrafish Notch1. Graph shows quantification of zebrafish embryos (10–13 somite stage) with defective somites. Number of embryos: uninjected = 210, control = 70, S1776C = 165, and R1758S = 189.

(I–L) R1758S and S1776C transgenic mutants exhibit decreased GFP (I) and increased RFP (K) expression in the Tg[NGN1:GFP] and Tg[Her4:dRFP] lines, respectively, when compared to uninjected and Notch1 silent mutant embryos. For Tg[NGN1:GFP] transgenics, coronal views are shown at 8× magnification. Embryos with reduced GFP expression: uninjected = 0/75, control = 0/44, R1758S = 28/40, and S1776C = 16/31. For Tg[Her4:dRFP] transgenics, sagittal views are shown at 5× magnification. Embryos with enhanced RFP expression: uninjected = 0/75, control = 0/30, R1758S = 36/57, and S1776C = 49/74. **$p < 0.005$ relative to control injected embryos. Scale bar, 0.3 mm. For (J) and (L), graphs show quantification of zebrafish embryos with reduced GFP (J) or enhanced RFP expression (L). Sequencing confirms the presence of the mutations for all affected embryos and the absence of amino acid changes for all non-affected animals. Embryos are 14 hr post-fertilization. FB, forebrain; MB, midbrain; HB, hindbrain; NT, neural tube.

See also Figure S3.

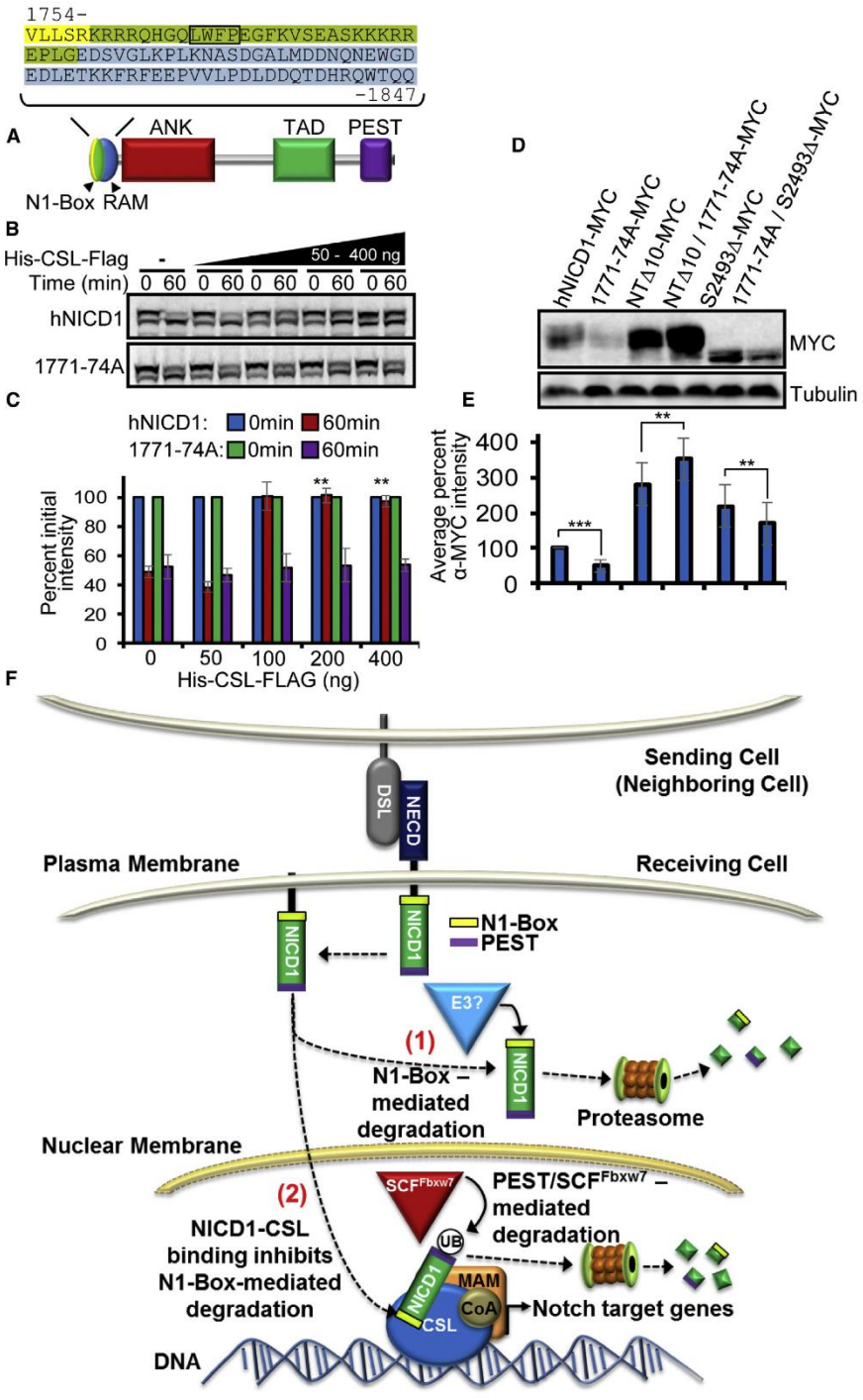

(legend on next page)

suggestions. For cyclohexamide (Sigma-Alderich) chase experiments, media supplemented with 100 μg/ml cyclohexamide was added to cells at the 0 min time point. Cells were then incubated in the presence of cyclohexamide for the duration of the experiment.

Transcriptional Activity Assays

HEK293 cells were transiently transfected with 1 μg Hes1-luciferase, 0.5 μg Renilla luciferase, and 1 μg of the indicated Notch construct. Luciferase and Renilla activities were assessed after 24 hr using the Dual-Glo Luciferase Assay System (Promega) in accordance with the manufacturer's instructions. Experiments were performed in triplicate and replicated at least two times. Significance was determined using a two-tailed Student's t test.

Xenopus Egg Extract Degradation Assays

Detailed methodology for preparing *Xenopus* egg extract and performing degradation assays with radiolabeled and luciferase fusion proteins can be found in Chen et al. (2014). His-CSL-Flag was purified from SF21 cells as previously described (Vasquez-Del Carpio et al., 2011). Glutathione S-transferase (GST)-β-catenin (gift from Wenqing Xu) was expressed and purified from bacterial cell lysates with glutathione beads (Merck Millipore) in accordance with the manufacturer's suggestions.

Immunoblot Analysis

To assess changes in steady-state protein levels, 1 μg of each DNA construct was transfected into an equivalent number of HEK293 cells. 48 hr post-transfection, cells were lysed by incubation in non-denaturing lysis buffer (50 mM Tris-HCl [pH 7.4], 300 mM NaCl, 5 mM EDTA, 1% (w/v) Trition X-100, and 1 mM PMSF) for 30 min on ice. Lysates were rigorously vortexed once at 15 min during the incubation. Lysates were cleared by centrifugation. 50 μg of total protein, assessed using the Bio-Rad protein assay dye reagent (Bio-Rad), was processed for SDS-PAGE/immunoblotting using standard techniques. The following antibodies were used: α-Fbxw7 (Bethyl Laboratories, Cat# A301-720A), α-MYC (9E10), α-Flag (Sigma-Aldrich), and α-β-tubulin (Clone E7, Developmental Studies Hybridoma Bank, University of Iowa). Secondary antibodies conjugated to horseradish peroxidase were purchased from Bethyl Laboratories. Blots were analyzed using ImageJ software.

Statistical Methods

Luciferase fusion degradation experiments were repeated at least twice and in triplicate. Significance was calculated using a two-tailed Student's t test in Excel. Transcriptional assays were performed in triplicate and replicated at least two times. Significance was determined using a two-tailed Student's t test. Autoradiography, immunoblots, and fluoresence microscopy experiments were analyzed using ImageJ software and significance (two-tailed Student's t test) was calculated in Excel. Somite formation assays were assessed using Fisher's exact test calculated in Excel.

Additional experimental methods are provided within the Supplemental Experimental Procedures.

SUPPLEMENTAL INFORMATION

Supplemental Information includes Supplemental Experimental Procedures and four figures and can be found with this article online at http://dx.doi.org/10.1016/j.celrep.2016.04.070.

AUTHOR CONTRIBUTIONS

M.R.B. conceived of, designed, executed, and interpreted the experiments. T.W.C. designed and executed experiments and provided intellectual input. J.N.J. performed microscopy-based turnover studies. L.R.N. performed zebrafish experiments. J.G.P. provided expertise on zebrafish. L.A.L. provided intellectual input and final manuscript editing. A.S. provided reagents and intellectual input. D.J.R. and A.J.C. provided Flag-CSL-His protein and intellectual input. E.L. and S.S.H. provided intellectual guidance and reagents. M.R.B., S.S.H., and E.L. wrote the manuscript.

ACKNOWLEDGMENTS

The authors thank A. Marchese, R. Deshaies, R. Kopan, and DNASU for reagents and members of the E.L. lab for helpful discussions. The authors also thank Q. Guan for help with zebrafish husbandry. M.R.B. was supported by a National Cancer Institute training grant (T32 CA119925). T.W.C. was supported by an American Heart Association predoctoral fellowship (12PRE6590007). L.R.N. was supported by the Training Program in Stem Cell and Regenerative Developmental Biology (T32 HD007502). V.H.N. was supported by the Microenvironment Influences in Cancer Training Grant (T32 CA00959228). J.G.P. and S.S.H. were supported by the NIH (RO1 EY024354 and R01DK078640, respectively). A.S. was supported by the NIH (RO1GM092924 and RO1GM110041). A.J.C. was supported by the National Cancer Institute (NCI R01CA083736-12A1 and NCI R01CA125044-02). E.L. was supported by the NIH (R01GM081635, R01GM103926, and P30 CA068485).

Received: October 27, 2014
Revised: March 14, 2016
Accepted: April 19, 2016
Published: May 19, 2016

REFERENCES

Artavanis-Tsakonas, S., Rand, M.D., and Lake, R.J. (1999). Notch signaling: cell fate control and signal integration in development. Science *284*, 770–776.

Blader, P., Plessy, C., and Strähle, U. (2003). Multiple regulatory elements with spatially and temporally distinct activities control neurogenin1 expression in primary neurons of the zebrafish embryo. Mech. Dev. *120*, 211–218.

Chen, T.W., Broadus, M.R., Huppert, S.S., and Lee, E. (2014). Reconstitution of β-catenin degradation in Xenopus egg extract. J. Vis. Exp. *(88)*

Chiang, M.Y., Xu, M.L., Histen, G., Shestova, O., Roy, M., Nam, Y., Blacklow, S.C., Sacks, D.B., Pear, W.S., and Aster, J.C. (2006). Identification of a conserved negative regulatory sequence that influences the leukemogenic activity of NOTCH1. Mol. Cell. Biol. *26*, 6261–6271.

Chu, J., and Bresnick, E.H. (2004). Evidence that C promoter-binding factor 1 binding is required for Notch-1-mediated repression of activator protein-1. J. Biol. Chem. *279*, 12337–12345.

Fryer, C.J., Lamar, E., Turbachova, I., Kintner, C., and Jones, K.A. (2002). Mastermind mediates chromatin-specific transcription and turnover of the Notch enhancer complex. Genes Dev. *16*, 1397–1411.

Figure 4. N1-Box-Mediated hNICD1 Degradation in *Xenopus* Egg Extract and Cultured Human Cells Is Inhibited by Its Binding to CSL

(A) Schematic showing overlap of N1-Box (yellow) and RAM domains (blue). Overlapping sequence is displayed in green. A black box outlines the ΦWΦP motif.
(B) CSL inhibits degradation of hNICD1 (but not a CSL binding mutant) in a dose-dependent manner. Radiolabeled hNICD1 or $hNICD^{11771-74A}$ was incubated in *Xenopus* egg extract with increasing amounts of recombinant CSL. Samples were removed after 1 hr and subjected to SDS-PAGE/autoradiography.
(C) Graph shows the mean ± SD of densitometry measurements for two independent experiments represented in (B). $^{**}p < 0.05$.
(D) Steady-state levels of the CSL binding mutant, $hNICD1^{11771-74A}$, are lower than hNICD1 in cultured cells. Plasmids encoding indicated N1-Box and CSL binding mutants were transfected into HEK293 cells and immunoblotting performed. Tubulin was used as a loading control.
(E) Graph of densitometry measurements in (D). Graph shows mean ± SD of MYC intensities normalized to tubulin for six independent experiments. $^{**}p < 0.05$, $^{***}p \leq 0.001$.
(F) Model of N1-Box-mediated regulation of hNotch1 signaling. See text for details.
See also Figure S4.

Fryer, C.J., White, J.B., and Jones, K.A. (2004). Mastermind recruits CycC:CDK8 to phosphorylate the Notch ICD and coordinate activation with turnover. Mol. Cell *16*, 509–520.

Gupta-Rossi, N., Le Bail, O., Gonen, H., Brou, C., Logeat, F., Six, E., Ciechanover, A., and Israël, A. (2001). Functional interaction between SEL-10, an F-box protein, and the nuclear form of activated Notch1 receptor. J. Biol. Chem. *276*, 34371–34378.

Harima, Y., and Kageyama, R. (2013). Oscillatory links of Fgf signaling and Hes7 in the segmentation clock. Curr. Opin. Genet. Dev. *23*, 484–490.

Ilagan, M.X., Lim, S., Fulbright, M., Piwnica-Worms, D., and Kopan, R. (2011). Real-time imaging of notch activation with a luciferase complementation-based reporter. Sci. Signal. *4*, rs7.

Kopan, R., and Ilagan, M.X. (2009). The canonical Notch signaling pathway: unfolding the activation mechanism. Cell *137*, 216–233.

Kovall, R.A., and Blacklow, S.C. (2010). Mechanistic insights into Notch receptor signaling from structural and biochemical studies. Curr. Top. Dev. Biol. *92*, 31–71.

Lewis, J., Hanisch, A., and Holder, M. (2009). Notch signaling, the segmentation clock, and the patterning of vertebrate somites. J. Biol. *8*, 44.

Liu, Z., Chen, S., Boyle, S., Zhu, Y., Zhang, A., Piwnica-Worms, D.R., Ilagan, M.X., and Kopan, R. (2013). The extracellular domain of Notch2 increases its cell-surface abundance and ligand responsiveness during kidney development. Dev. Cell *25*, 585–598.

Malyukova, A., Dohda, T., von der Lehr, N., Akhoondi, S., Corcoran, M., Heyman, M., Spruck, C., Grandér, D., Lendahl, U., and Sangfelt, O. (2007). The tumor suppressor gene hCDC4 is frequently mutated in human T-cell acute lymphoblastic leukemia with functional consequences for Notch signaling. Cancer Res. *67*, 5611–5616.

Mo, J.S., Kim, M.Y., Han, S.O., Kim, I.S., Ann, E.J., Lee, K.S., Seo, M.S., Kim, J.Y., Lee, S.C., Park, J.W., et al. (2007). Integrin-linked kinase controls Notch1 signaling by down-regulation of protein stability through Fbw7 ubiquitin ligase. Mol. Cell. Biol. *27*, 5565–5574.

Moretti, J., and Brou, C. (2013). Ubiquitinations in the notch signaling pathway. Int. J. Mol. Sci. *14*, 6359–6381.

Nam, Y., Weng, A.P., Aster, J.C., and Blacklow, S.C. (2003). Structural requirements for assembly of the CSL.intracellular Notch1.Mastermind-like 1 transcriptional activation complex. J. Biol. Chem. *278*, 21232–21239.

O'Neil, J., Grim, J., Strack, P., Rao, S., Tibbitts, D., Winter, C., Hardwick, J., Welcker, M., Meijerink, J.P., Pieters, R., et al. (2007). FBW7 mutations in leukemic cells mediate NOTCH pathway activation and resistance to gamma-secretase inhibitors. J. Exp. Med. *204*, 1813–1824.

Oberg, C., Li, J., Pauley, A., Wolf, E., Gurney, M., and Lendahl, U. (2001). The Notch intracellular domain is ubiquitinated and negatively regulated by the mammalian Sel-10 homolog. J. Biol. Chem. *276*, 35847–35853.

Palermo, R., Checquolo, S., Giovenco, A., Grazioli, P., Kumar, V., Campese, A.F., Giorgi, A., Napolitano, M., Canettieri, G., Ferrara, G., et al. (2012). Acetylation controls Notch3 stability and function in T-cell leukemia. Oncogene *31*, 3807–3817.

Qiu, L., Joazeiro, C., Fang, N., Wang, H.Y., Elly, C., Altman, Y., Fang, D., Hunter, T., and Liu, Y.C. (2000). Recognition and ubiquitination of Notch by Itch, a hect-type E3 ubiquitin ligase. J. Biol. Chem. *275*, 35734–35737.

Skaar, J.R., Pagan, J.K., and Pagano, M. (2013). Mechanisms and function of substrate recruitment by F-box proteins. Nat. Rev. Mol. Cell Biol. *14*, 369–381.

Tamura, K., Taniguchi, Y., Minoguchi, S., Sakai, T., Tun, T., Furukawa, T., and Honjo, T. (1995). Physical interaction between a novel domain of the receptor Notch and the transcription factor RBP-J kappa/Su(H). Curr. Biol. *5*, 1416–1423.

Thompson, B.J., Buonamici, S., Sulis, M.L., Palomero, T., Vilimas, T., Basso, G., Ferrando, A., and Aifantis, I. (2007). The SCFFBW7 ubiquitin ligase complex as a tumor suppressor in T cell leukemia. J. Exp. Med. *204*, 1825–1835.

Tsunematsu, R., Nakayama, K., Oike, Y., Nishiyama, M., Ishida, N., Hatakeyama, S., Bessho, Y., Kageyama, R., Suda, T., and Nakayama, K.I. (2004). Mouse Fbw7/Sel-10/Cdc4 is required for notch degradation during vascular development. J. Biol. Chem. *279*, 9417–9423.

Vasquez-Del Carpio, R., Kaplan, F.M., Weaver, K.L., VanWye, J.D., Alves-Guerra, M.C., Robbins, D.J., and Capobianco, A.J. (2011). Assembly of a Notch transcriptional activation complex requires multimerization. Mol. Cell. Biol. *31*, 1396–1408.

Weng, A.P., Ferrando, A.A., Lee, W., Morris, J.P., 4th, Silverman, L.B., Sanchez-Irizarry, C., Blacklow, S.C., Look, A.T., and Aster, J.C. (2004). Activating mutations of NOTCH1 in human T cell acute lymphoblastic leukemia. Science *306*, 269–271.

Wu, G., Lyapina, S., Das, I., Li, J., Gurney, M., Pauley, A., Chui, I., Deshaies, R.J., and Kitajewski, J. (2001). SEL-10 is an inhibitor of notch signaling that targets notch for ubiquitin-mediated protein degradation. Mol. Cell. Biol. *21*, 7403–7415.

Yaron, T., Cordova, Y., and Sprinzak, D. (2014). Juxtacrine signaling is inherently noisy. Biophys. J. *107*, 2417–2424.

Yeo, S.Y., Kim, M., Kim, H.S., Huh, T.L., and Chitnis, A.B. (2007). Fluorescent protein expression driven by her4 regulatory elements reveals the spatiotemporal pattern of Notch signaling in the nervous system of zebrafish embryos. Dev. Biol. *301*, 555–567.

Cell Reports, Volume *15*

Supplemental Information

Identification of a Paralog-Specific Notch1 Intracellular Domain Degron

Matthew R. Broadus, Tony W. Chen, Leif R. Neitzel, Victoria H. Ng, Jeanne N. Jodoin, Laura A. Lee, Adrian Salic, David J. Robbins, Anthony J. Capobianco, James G. Patton, Stacey S. Huppert, and Ethan Lee

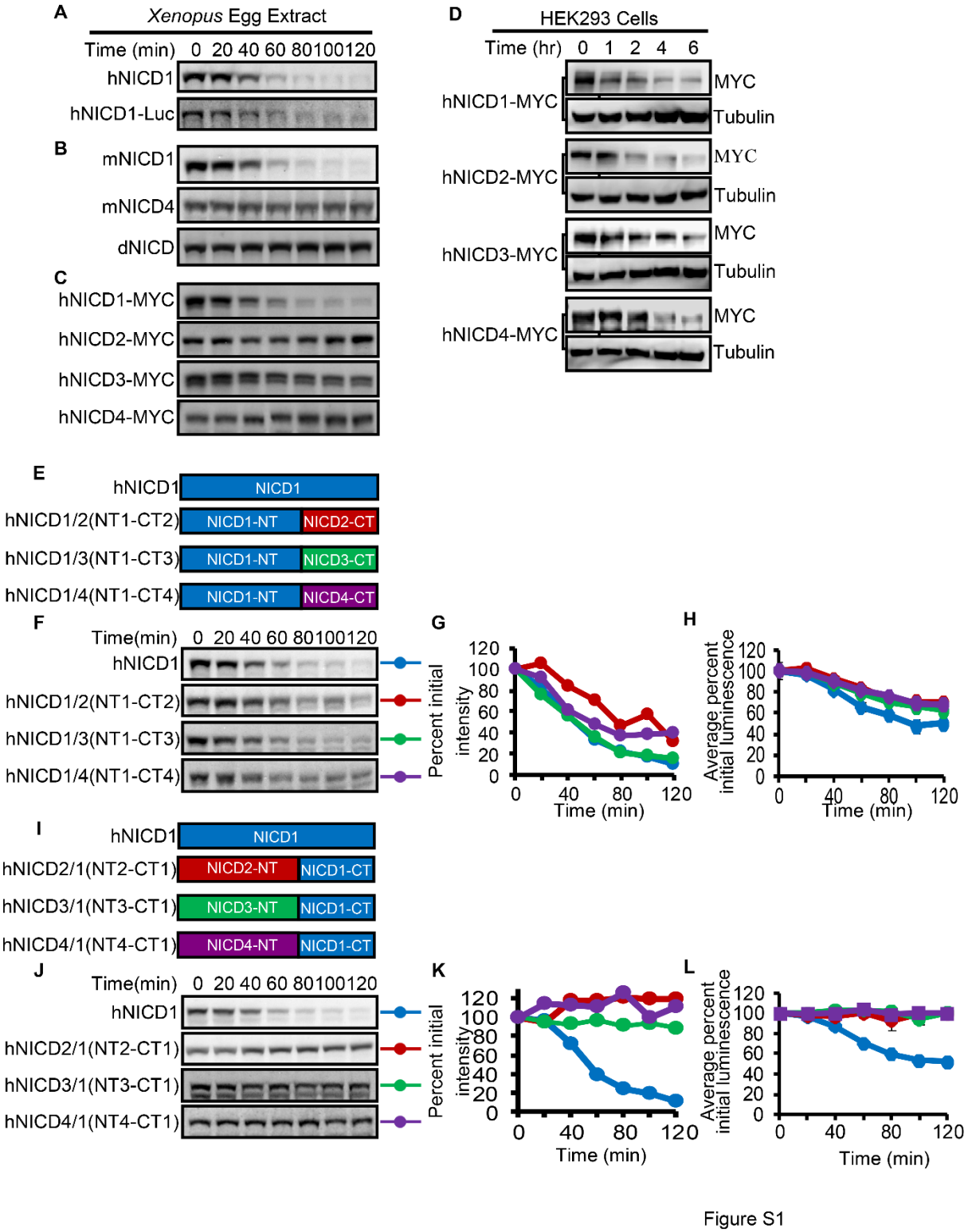
A
Xenopus Egg Extract
Time (min) 0 20 40 60 80100120
hNICD1
hNICD1-Luc
B
mNICD1
mNICD4
dNICD
C
hNICD1-MYC
hNICD2-MYC
hNICD3-MYC
hNICD4-MYC
D
HEK293 Cells
Time (hr) 0 1 2 4 6
hNICD1-MYC
hNICD2-MYC
hNICD3-MYC
hNICD4-MYC
MYC
Tubulin
E
hNICD1
NICD1
hNICD1/2(NT1-CT2)
NICD1-NT
NICD2-CT
hNICD1/3(NT1-CT3)
NICD3-CT
hNICD1/4(NT1-CT4)
NICD4-CT
F
Time(min) 0 20 40 60 80100120
G
Percent initial intensity
Time (min)
H
Average percent initial luminescence
I
hNICD2/1(NT2-CT1)
NICD2-NT
NICD1-CT
hNICD3/1(NT3-CT1)
NICD3-NT
hNICD4/1(NT4-CT1)
NICD4-NT
J
K
L

Figure S1

Figure S1. NICD1 is degraded in *Xenopus* egg extract, in contrast to other NICD paralogs, and degradation is not affected by C-terminal fusions; related to Figure 1. (A) [^{35}S]Met-labeled hNICD1 and hNICD1-Luc (Luciferase) were incubated in *Xenopus* egg extract, and sample were removed at the indicated times for analysis by SDS-PAGE/autoradiography. (B) Mouse NICD1 and NICD4 paralogs (mNICD1 and mNICD4) degrade similarly to their human counterparts in *Xenopus* egg extract. *Drosophila* dNICD does not degrade in extract. Mouse NICD1 (mNICD1), mouse NICD4 (mNICD4), and *Drosophila* NICD (dNICD1) were incubated in *Xenopus* egg extract and analyzed as in (A). (C) Degradation rates of radiolabeled hNICD paralogs fused at the C-terminal end to a MYC epitope are indistinguishable from their non-tagged versions. Radiolabeled hNICD paralogs fused at their C-terminal ends with the MYC epitope were incubated in *Xenopus* egg extract and analyzed by SDS-PAGE/autoradiography. (D) In contrast to *Xenopus* egg extract, C-terminal MYC fusions of all hNICD paralogs degrade when expressed in HEK293 cells. Cells expressing hNICD-MYC paralogs were collected at the indicated times after addition of cyclohexamide (100 μg/ml) and immunoblotting was performed. Tubulin is loading control. (E) Schematic of hNICD chimeras containing N-terminal hNICD1 fusions. (F) Chimeric mutants of NICD paralogs containing the N-terminal half of hNICD1 all degrade in *Xenopus* egg extract. Radiolabeled chimeric mutants were incubated in extract, and samples removed at the indicated time points for analysis by SDS-PAGE/autoradiography. (G) Graph of densitometry measurements in (F). (H) N-terminal hNICD1 chimeras fused to Luciferase degrade at a similar rate as the non-tagged proteins. *In vitro*-translated proteins were incubated in *Xenopus* egg extract, samples were removed at the indicated times, and Luciferase activity determined. Experiments were performed in triplicate. Graphs show mean $\pm$ S.D. of Luciferase signal normalized to the value of the initial time point. (I) Schematic of hNICD chimeras encoding C-terminal hNICD1 fusions. (J) Chimeric mutants of NICD paralogs containing the C-terminal half of hNICD1 are stable in *Xenopus* egg extract. (K) Graph of densitometry measurements in (J). (L) Similar to their radiolabeled, untagged versions, C-terminal hNICD1 chimeras fused to Luciferase are stable in *Xenopus* egg extract.

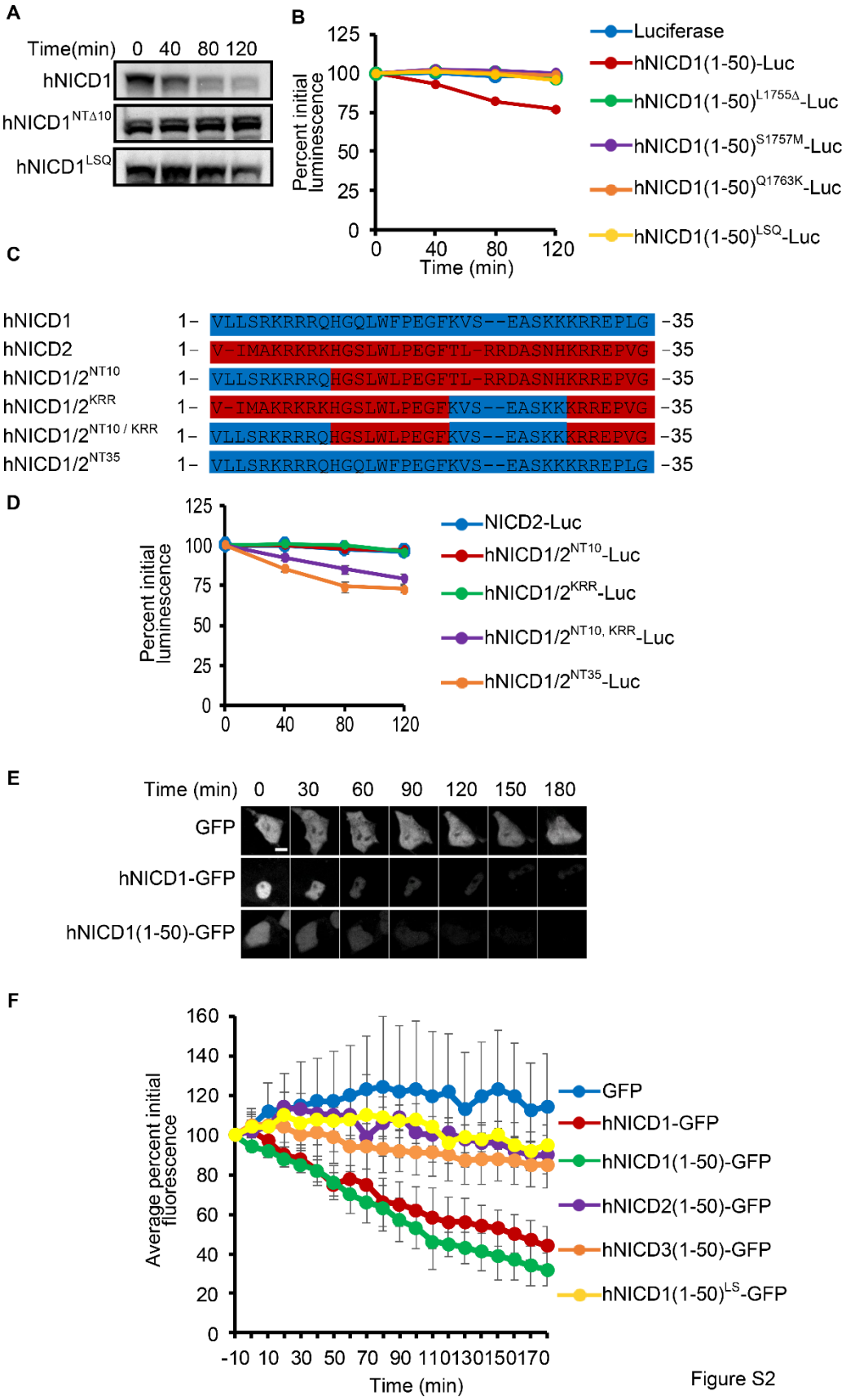
A
Time(min) 0 40 80 120
hNICD1
hNICD1NTΔ10
hNICD1LSQ
B
Percent initial luminescence
125
100
75
50
25
0
0 40 80 120
Time (min)
Luciferase
hNICD1(1-50)-Luc
hNICD1(1-50)L1755Δ-Luc
hNICD1(1-50)S1757M-Luc
hNICD1(1-50)Q1763K-Luc
hNICD1(1-50)LSQ-Luc
C
hNICD1 1- VLLSRKRRRQHGQLWFPEGFKVS--EASKKKRREPLG -35
hNICD2 1- V-IMAKRKRKHGSLWLPEGFTL-RRDASNHKRREPVG -35
hNICD1/2NT10 1- VLLSRKRRRQHGSLWLPEGFTL-RRDASNHKRREPVG -35
hNICD1/2KRR 1- V-IMAKRKRKHGSLWLPEGFKVS--EASKKKRREPVG -35
hNICD1/2NT10 / KRR 1- VLLSRKRRRQHGSLWLPEGFKVS--EASKKKRREPVG -35
hNICD1/2NT35 1- VLLSRKRRRQHGQLWFPEGFKVS--EASKKKRREPLG -35
D
Percent initial luminescence
125
100
75
50
25
0
0 40 80 120
NICD2-Luc
hNICD1/2NT10-Luc
hNICD1/2KRR-Luc
hNICD1/2NT10, KRR-Luc
hNICD1/2NT35-Luc
E
Time (min) 0 30 60 90 120 150 180
GFP
hNICD1-GFP
hNICD1(1-50)-GFP
F
Average percent initial fluorescence
160
140
120
100
80
60
40
20
0
-10 10 30 50 70 90 110130150170
Time (min)
GFP
hNICD1-GFP
hNICD1(1-50)-GFP
hNICD2(1-50)-GFP
hNICD3(1-50)-GFP
hNICD1(1-50)LS-GFP

Figure S2

Figure S2. The first 10 amino acids of hNICD1 are critical for N1-Box-mediated degradation, whereas the first 50 amino acids of hNICD1 are required to promote degradation of heterologous proteins; related to Figure 2. (A) The N-terminal ten amino acids of hNICD1 contain amino acids critical for its degradation. Radiolabeled hNICD1$^{NT\Delta 10}$ and hNICD1^{LSQ} were incubated in *Xenopus* egg extract and samples removed at the indicated times for analysis by SDS-PAGE/autoradiography. (B) The N-terminal 50 amino acids of hNICD1 and their mutants were fused to Luciferase and incubated in *Xenopus* egg extract. Samples were removed at the indicated times, and Luciferase activity measured. Graph represents mean ± S.D.. of two independent experiments (preformed in triplicate) and normalized to the value of the initial time point. (C) Schematic for the first 35 residues of NICD1/2 chimeric proteins used in (D). Blue represents residues found in hNICD1 while red residues represent those found in hNICD2. (D) The N-terminal 35 amino acids of hNICD1 contain the minimal components sufficient to promote degradation. hNICD2-Luc was mutated to the corresponding hNICD1 residues. The graph represents the mean ± S.D. of at least two independent experiments (preformed in triplicate) and normalized to the initial time point. (E) Fusion of the N-terminal 50 amino acids of hNICD1 to GFP promotes its degradation in human cultured cells. GFP, hNICD1-GFP and hNICD1(1-50)-GFP were expressed in HEK293 cells. At time 0 min, cycloheximide (100 μg/ml) was added and live cell imaging performed. Representative images are shown. (F) In contrast to hNICD1, a double N1-box mutant and the N-terminal 50 amino acids of hNICD2 and 3 fused to GFP were stable in HEK293 cells. Graph represents mean ± S.D. of GFP fluorescence normalized to value of the initial time point. Experiments were performed at least twice with 10>cells quantified for each construct.

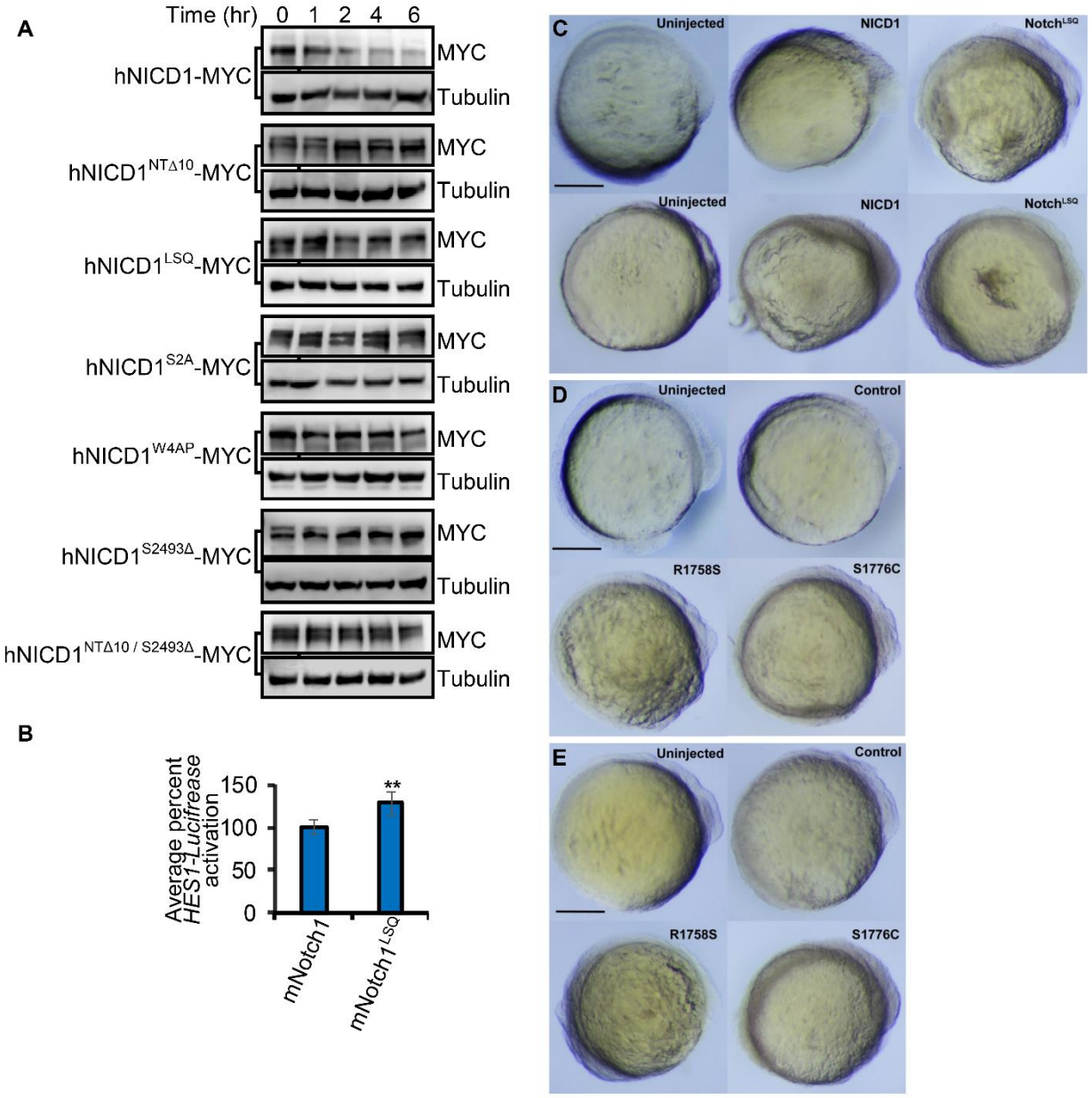
A
Time (hr) 0 1 2 4 6
hNICD1-MYC
hNICD1NTΔ10-MYC
hNICD1LSQ-MYC
hNICD1S2A-MYC
hNICD1W4AP-MYC
hNICD1S2493Δ-MYC
hNICD1NTΔ10 / S2493Δ-MYC
MYC
Tubulin
B
Average percent HES1-Luciferase activation
150
100
50
0
**
mNotch1
mNotch1LSQ
C
Uninjected
NICD1
NotchLSQ
D
Uninjected
Control
R1758S
S1776C
E
Uninjected
Control
R1758S
S1776C

Figure S3

Figure S3. hNICD1 degron mutants have decreased rates of degradation in cultured human cells; related to Figures 2 and 3. (A) MYC-tagged hNICD1, N1-Box mutants (hNICD$^{NT\Delta10}$ and hNICD^{LSQ}), PEST mutants (hNotch1^{S2A}, hNotch1^{W4AP}, and hNICD1$^{S2493\Delta}$) and a combination mutant (hNICD1$^{NT\Delta10/S2493\Delta}$) were expressed in HEK293 cells. Cycloheximide (100 μg/ml) was added at 0 min and samples collected at the indicated times for immunoblotting. Tubulin is loading control. (B) Full length mNotch1 or mNotch1 mutants were assessed by HES1-Luciferase Notch reporter activity in HEK293 cells. Luciferase activity was measured after 24 hr. Graph represents the mean ± S.D. of Luciferase signal normalized to *Renilla* Luciferase of at least 3 independent experiments (performed in triplicate). **$p<0.05$. (C) Bright field images of zebrafish lines Tg[NGN1:GFP] (top) and Tg[Her4:dRFP] (bottom) injected with indicated mRNAs. Small reduction of posterior structures was observed for both NICD1 and NICD1^{LSQ} injected embryos. Sagittal views of 14 hr post fertilization embryos at 5x magnification are shown. Head is on the right. Scale bar is 0.3 mm. (D-E) Bright field images of transgenic zebrafish lines Tg[NGN1:GFP] (D) and Tg[Her4:dRFP] (E) harboring the R1758S and S1776C mutations that exhibited normal anterior development and minor reduction in posterior structures. Control represents transgenic animals harboring silent mutations of Notch1. Sagittal views of 14 hr post fertilization embryos at 5x magnification are shown. Head is on the right. Scale bar is 0.3 mm.

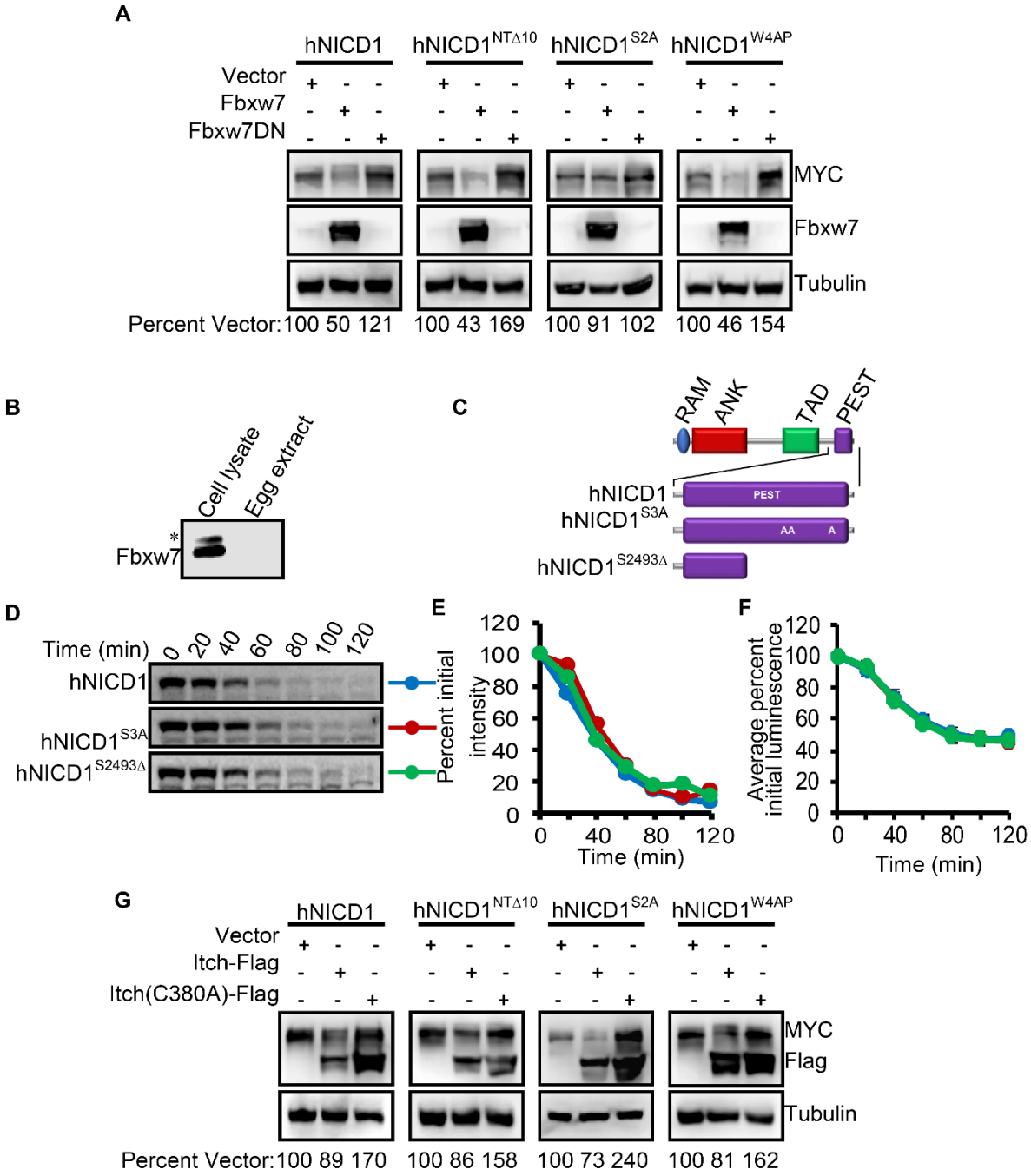
A
hNICD1
hNICD1NTΔ10
hNICD1S2A
hNICD1W4AP
Vector
Fbxw7
Fbxw7DN
MYC
Fbxw7
Tubulin
Percent Vector: 100 50 121 100 43 169 100 91 102 100 46 154
B
Cell lysate
Egg extract
Fbxw7*
C
RAM
ANK
TAD
PEST
hNICD1
hNICD1S3A
hNICD1S2493Δ
D
Time (min) 0 20 40 60 80 100 120
hNICD1
hNICD1S3A
hNICD1S2493Δ
Percent initial intensity
E
Time (min)
F
Average percent initial luminescence
Time (min)
G
hNICD1
hNICD1NTΔ10
hNICD1S2A
hNICD1W4AP
Vector
Itch-Flag
Itch(C380A)-Flag
MYC
Flag
Tubulin
Percent Vector: 100 89 170 100 86 158 100 73 240 100 81 162

Figure S4

Figure S4. N1-Box mutants do not affect the capacities of the E3 ligases, Fbxw7 and Itch, to regulate hNICD1 levels in cultured human cells; related to Figure 2 and 4. (A) Overexpression of Fbxw7 and Fbxw7DN decreases and increases, respectively, steady-state levels of hNICD1, hNICD$^{NT\Delta 10}$, and hNotch1^{W4AP}. In contrast, overexpression of Fbxw7 and Fbxw7DN had no effect on levels of the Fbxw7 binding mutant, hNICD^{S2A}. (B) Fbxw7 is not detectable in *Xenopus* egg extract. HEK293 cell lysates and extract (30 ug each) were processed for immunoblotting using an antibody against a conserved region of *Xenopus* and human Fbxw7. Asterisk marks non-specific band. (C) Schematic of hNICD1 PEST domain mutants. (D) Fbwx7 binding (hNICD^{S3A}) and PEST domain truncation (hNICD$^{S2493\Delta}$) mutants degrade at similar rates as hNICD1. (E) Graph of densitometry measurements in (I). (F) Turnover rates of IVT hNICD1^{S3A} and hNICD1$^{S2493\Delta}$ Luciferase fusions in *Xenopus* extract are similar to untagged, radiolabeled forms. Graph is mean of 2 independent experiments (performed in triplicate) normalized to initial time point (100%). (G) Overexpression of Itch and its dominant-negative mutant, Itch^{C380A}, decreases and increases, respectively, steady-state levels of all hNICD1 constructs. Expression studies were performed in HEK293 cells. hNICD1 constructs were tagged at their C-terminal ends with MYC, and Itch and Itch^{C380A} were tagged at their C-terminal ends with FLAG to facilitate their detection by immunoblotting. Tubulin is loading control.

EXPERIMENTAL PROCEDUES

Plasmids

All constructs used were constructed via standard PCR-based molecular biology approaches.

Gene	Vector	Collection #
hNICD1	CS2	EL1868
hNICD1-Luciferase	CS2	EL1869
hNICD1-MYC	CS2	EL1870
hNICD1-GFP	CS2	EL1871
hNICD2	CS2	EL1872
hNICD2-Luciferase	CS2	EL1873
hNICD2-MYC	CS2	EL1874
hNICD3	CS2	EL1875
hNICD3-Luciferase	CS2	EL1876
hNICD3-MYC	CS2	EL1877
hNICD4	CS2	EL1878
hNICD4-Luciferase	CS2	EL1879
hNICD4-MYC	CS2	EL1880
$hNICD1^{S3A}$	CS2	EL1881
$hNICD1^{S3A}$-Luciferase	CS2	EL1882
$hNICD1^{S3A}$-MYC	CS2	EL1883
$hNICD1^{S2493\Delta}$	CS2	EL1891
$hNICD1^{S2493\Delta}$ -Luciferase	CS2	EL1892
$hNICD1^{S2493\Delta}$ -MYC	CS2	EL1893
hNICD1/2(NT1-CT2)	CS2	EL1896
hNICD1/2(NT1-CT2)-Luciferase	CS2	EL1897
hNICD1/3(NT1-CT3)	CS2	EL1898
hNICD1/3(NT1-CT3)-Luciferase	CS2	EL1899
hNICD1/4(NT1-CT4)	CS2	EL1900
hNICD1/4(NT1-CT4)-Luciferase	CS2	EL1901
hNICD2/1(NT2-CT1)	CS2	EL1902
hNICD2/1(NT2-CT1)-Luciferase	CS2	EL1903
hNICD3/1(NT3-CT1)	CS2	EL1904
hNICD3/1(NT3-CT1)-Luciferase	CS2	EL1905
hNICD4/1(NT4-CT1)	CS2	EL1906
hNICD4/1(NT4-CT1)-Luciferase	CS2	EL1907
hNICD1/2(NT35)	CS2	EL1908
hNICD1/2(NT35)-Luciferase	CS2	EL1909
hNICD1/2(NT125)	CS2	EL1910
hNICD1/2(NT125)-Luciferase	CS2	EL1911
hNICD1/2(NT176)	CS2	EL1912
hNICD1/2(NT176)-Luciferase	CS2	EL1913

hNICD1$^{L1755\Delta}$	CS2	EL1914
hNICD1$^{L1755\Delta}$-Luciferase	CS2	EL1915
hNICD1$^{L1755\Delta}$-MYC	CS2	EL1916
hNICD1^{S1757M}	CS2	EL1917
hNICD1^{S1757M}-MYC	CS2	EL1918
hNICD1^{Q1763K}	CS2	EL1920
hNICD1^{Q1763S}	CS2	EL1921
hNICD1^{KRR}	CS2	EL1922
hNICD1$^{NT\Delta10}$	CS2	EL1851
hNICD1$^{NT\Delta10}$-Luciferase	CS2	EL1852
hNICD1$^{NT\Delta10}$-MYC	CS2	EL1923
hNICD1$^{L1755\Delta}$-GFP	CS2	EL1925
hNICD1^{S1757M}-GFP	CS2	EL1926
hNICD1$^{L1755\Delta\ /\ S1757M}$-GFP	CS2	EL1927
hNICD1^{LSQ}	CS2	EL1931
hNICD1^{LSQ}-MYC	CS2	EL1932
hNICD1(1-50)-Luciferase	CS2	EL1933
hNICD1(1-50)-GFP	CS2	EL1934
hNICD1(1-50)$^{L1755\Delta}$-Luciferase	CS2	EL1935
hNICD1(1-50)^{S1757M}-Luciferase	CS2	EL1937
hNICD1(1-50)^{S1757M}-GFP	CS2	EL1938
hNICD1(1-50)$^{L1755\Delta\ /\ S1757M}$-Luciferase	CS2	EL1947
hNICD1(1-50)$^{L1755\Delta\ /\ S1757M}$-GFP	CS2	EL1948
hNICD1(1-50)^{LS}-Luciferase	CS2	EL1950
hNICD1(1-50)^{LS}-GFP	CS2	EL1951
hNICD2(1-50)-GFP	CS2	EL1952
hNICD2(1-50)-Luciferase	CS2	EL1953
hNICD3(1-50)-GFP	CS2	EL1954
hNICD3(1-50)-Luciferase	CS2	EL1955
hNICD4(1-50)-GFP	CS2	EL1956
hNICD4(1-50)-Luciferase	CS2	EL1957
hNICD1$^{NT\Delta10\ /\ S2493\Delta}$-MYC	CS2	EL1958
hNICD1$^{NT\Delta10\ /\ S2493\Delta}$	CS2	EL1959
hNICD1$^{LSQ\ /\ S2493\Delta}$	CS2	EL1962
hNICD1$^{LSQ\ /\ S2493\Delta}$-MYC	CS2	EL1963
hNICD1^{R1758S}	CS2	EL1964
hNICD1^{R1758S}-MYC	CS2	EL1965
hNICD1^{R1761W}	CS2	EL1966
hNICD1^{R1761W}-MYC	CS2	EL1967
hNICD1^{S1776C}	CS2	EL1968
hNICD1^{S1776C}-MYC	CS2	EL1969

hNICD1^{R1783W}	CS2	EL1970
hNICD1^{R1783W}-MYC	CS2	EL1971
hNICD1^{R1784L}	CS2	EL1972
hNICD1^{R1784L}-MYC	CS2	EL1973
hNICD1$^{LSQ / S2A}$	CS2	EL1976
hNICD1$^{LSQ / S2A}$	CS2	EL1977
hNICD1$^{NTΔ10 / S2A}$	CS2	EL1978
hNICD1$^{NTΔ10 / S2A}$-MYC	CS2	EL1979
hNICD1^{W4AP}	CS2	EL1980
hNICD1^{W4AP}-MYC	CS2	EL1981
hNICD1$^{S2A / W4AP}$	CS2	EL1982
hNICD1$^{S2A / W4AP}$-MYC	CS2	EL1983
hNICD1$^{NTΔ10 / W4AP}$	CS2	EL1984
hNICD1$^{NTΔ10 / W4AP}$-MYC	CS2	EL1985
hNICD1$^{NTΔ10 / S2A / W4AP}$	CS2	EL1986
hNICD1$^{NTΔ10 / S2A / W4AP}$-MYC	CS2	EL1987
hNICD1$^{1771-74A}$	CS2	EL1988
hNICD1$^{1771-74A}$-MYC	CS2	EL1989
hNICD1/2^{KRR}-Luciferase	CS2	EL1994
hNICD1/2$^{NT10 / KRR}$-Luciferase	CS2	EL1996
hNICD1$^{NTΔ10 / 1771-74A}$-MYC	CS2	EL1997
hNICD1$^{1771-74A / S2493Δ}$-MYC	CS2	EL1998
hNICD$^{NTΔ10 / 1771-74A / S2493Δ}$-MYC	CS2	EL1999
mNotch1^{S2467Δ}	pcDNA3.1	EL2001
mNotch1^{LSQ}	pcDNA3.1	EL2003
mNotch1$^{LSQ / S2467Δ}$	pcDNA3.1	EL2004
mNICD1	CS2	EL2007
mNICD4	CS2	EL2008
dNICD1	CS2	EL2009
Fbxw7DN	CS2	EL2013
Fbxw7	CS2	EL2014
mNotch1	pcDNA3.1	Gift from Stacey Huppert
FLAG-Itch	pCMV-10	Gift from Adriano Marchese
FLAG-Itch^{C380A}	pCMV-10	Gift from Adriano Marchese
Renilla luciferase	CS2	EL986
Hes1-Luciferase	pGL2-Basic	Gift from Stacey Huppert
GST-β-catenin	pGEX	Gift from Wenqing Xu
GST	pGEX	GE Healthcare Life Sciences

Somite formation assay

mRNAs were synthesized using the T7 MAXIscript Kit (Ambion). Zygotes were either injected with 25 pg/nl, 50 pg/nl, or 100 pg/nl mRNA mixed with phenol red using the MPPI-2 injection system (Applied Scientific Instruments). Injected embryos were incubated at 28°C until the 10-13 somite stage and scored for proper somitogenesis using a Zeiss stemi 2000-CS scope. Live embryos were embedded in 0.8% agarose and images taken with an Olympus DP72 camera at 4X magnification. For immunostaining, embryos were permeabilized with 10 µg/ml Proteinase K and stained with α-EphA4 (Tyr-602) (ECM Biosciences) overnight at 4°C. Primary antibodies were then detected with Alexa-488 secondary antibodies (Life Technologies) and imaged on a Nikon Eclipse 80I equipped with a photometrics CoolSNAP ES camera. Significance was assessed using Fisher's exact test.

CRISPR/Cas9-mediated knock-in

Human Notch1 (NM_017617.3) and zNotch1 (NM_131302.2) were aligned in LALIGN and the region of interest assessed for mutagenesis. The mMessage mMachine T7/T3 Kit (Ambion) was used to generate Cas9-nickase mRNA from the pT3Ts-nCas9n plasmid (from Wenbiao Chen, Vanderbilt University). A short guide RNA and three single stranded DNAs (IDT) were generated with 75 nt upstream and 68 nt downstream of the region of interest.

Donor Oligonucleotides (5' to 3')

Silent mutant Notch1 control:
GAGATGTACCCCATGTTCCTGGTCCTGCTGGCTCTGGCTGTTCTGGCTCTGGCCGCTATCGGTGTGGTcG
TaTCgAGGAAGAGaAAGCGcGAACATGGCCAGCTcTGGTTtCCaGAaGGcTTcAAgGTCAACGAACCCAAA
AAGAAGAGGAGAGAACCAGTGGGAGAGGACTCTGTCGGACTCAAGTCAGTTTCCACACA

R1758S mutant:
GAGATGTACCCCATGTTCCTGGTCCTGCTGGCTCTGGCTGTTCTGGCTCTGGCCGCTATCGGTGTGGTcG
TaTCg**AGt**AAGAGaAAGCGcGAACATGGCCAGCTcTGGTTtCCaGAaGGcTTcAAgGTCAACGAACCCAAAA
AGAAGAGGAGAGAACCAGTGGGAGAGGACTCTGTCGGACTCAAGTCAGTTTCCACACA

S1776C mutation:
GAGATGTACCCCATGTTCCTGGTCCTGCTGGCTCTGGCTGTTCTGGCTCTGGCCGCTATCGGTGTGGTcG
TaTCgAGGAAGAGaAAGCGcGAACATGGCCAGCTcTGGTTtCCaGAaGGcTTcAAgGTC**tgc**GAACCCAAAA
AGAAGAGGAGAGAACCAGTGGGAGAGGACTCTGTCGGACTCAAGTCAGTTTCCACACA

Short guide RNA:
TCGTCTCCAGGAAGAGGAAG NGG
Lower case indicates change from the Wildtype sequence. Bold indicates mutated amino acid.

A one nl mixture containing 150 ng Cas9 mRNA, 7 ng sgRNA, and 7 ng ssDNA were injected into Tg(NGN1:GFP) and Tg[Her4:dRFP] zygotes[3]. Embryos were then incubated at 28.5°C in E3 medium with 0.1% (w/v) methylene blue until the 10-13 somite stage and then scored for defects in somitogenesis. Samples were either fixed overnight in 4% paraformaldehyde or lysed for genomic DNA. Fixed embryos were assessed for fluorescence and imaged using a Zeiss SteREO Discovery.V8 and AxioCam ICc3. For Tg[Her4:dRFP], twenty images were averaged in Fiji and noise outliers remove (Radius 2.0 pixels, Threshold 50). Tg[NGN1:GFP] are single images and were not processed in Fiji.

Genomic DNA were as described previously by Meeker et al[4]. The mutant N1-box regions were amplified using the following primers:
Uninjected Fwd: GCCGAGTACAGTATACAATTTCAA
Uninjected Rev: GAGCTCTCATGCAAGTGTGTG
Silent Control Fwd: GTGGTCGTATCGAGGAAGAGAAAG
Silent Control Rev: GAGCTCTCATGCAAGTGTGTG

R1758S Fwd: GTGGTCGTATCGAGTAAGAG
R1758S Rev: GAGCTCTCATGCAAGTGTGTG
S1776C Fwd: GCCGAGTACAGTATACAATTTCAA
S1776C Rev: TTCGCAGACCTTGAAGCCTTC

The following sequencing primers were used to confirm presence of mutations.
Silent Control Seq: GAGCTCTCATGCAAGTGTGTG
R1758S Seq: GAGCTCTCATGCAAGTGTGTG
S1776C Seq: GATGTACCCCATGTTCCTGGT

Live-Cell Imaging

MatTek dishes were maintained at 37°C by heated stage (Warner Instruments). Single-plane confocal videos were taken using a Yokogawa QLC-100/CSU-10 spinning disk head (Visitec assembled by Vashaw) attached to a Nikon TE2000E microscope using a CFI PLAN APO VC 100× oil lens, NA 1.4, with or without 1.5× intermediate magnification, and a back-illuminated EM-CCD camera Cascade 512B (Photometrics) driven by IPLab software (Scanalytics). A krypton-argon laser (75 mW 488; Melles Griot) with AOTF was used for color excitation. Custom double dichroic mirror and filters (Chroma) in a filter wheel (Ludl) were used in the emission light path. Intensity in live-cells expressing various GFP constructs was measured using ImageJ software. Cells of interest were outlined with a selection tool, and measurements were set (area, integrated density, and mean gray value). Data points are plotted as the percent of initial intensity.

REFERENCES

Auer, T.O., Duroure, K., De Cian, A., Concordet, J. and Del Bene, F. (2015) Highly efficient CRISPR/Cas9-mediated knock-in in zebrafish by homology-independent DNA repair. Genome Research *24*, 142-153.
Bill, B.R., Petzold, A.M., Clark, K.J., Schimmenti, L.A. and Ekker, S.C. (2009) A Primer for Morpholino Use in Zebrafish. Zebrafish *6*, 69–77.
Chen, T.W., Broadus, M.R., Huppert, S.S., and Lee, E. (2014). Reconstitution Of beta-catenin Degradation In Xenopus Egg Extract. Journal of visualized experiments : JoVE.
Henry, C.A., McNulty, I.M., Durst, W.A., Munchel, S.E., Amacher, S.L. (2005). Interactions between muscle fibers and segment boundaries in Zebrafish. Dev Biol *15*, 346-360.

Nathan D. Meeker, Sarah A. Hutchinson, Linh Ho, Nikolaus S. Trede (2007) Method for isolation of PCR-ready genomic DNA from zebrafish tissues. BioTechniques *43*, 610–614.
Vasquez-Del Carpio, R., Kaplan, F.M., Weaver, K.L., VanWye, J.D., Alves-Guerra, M.C., Robbins, D.J., and Capobianco, A.J. (2011). Assembly of a Notch transcriptional activation complex requires multimerization. Mol Cell Biol *31*, 1396-1408.

The MAPK Pathway Regulates Intrinsic Resistance to BET Inhibitors in Colorectal Cancer

Ma Y, Wang L, **Neitzel LR**, Loganathan SN, Tang N, Qin L, Crispi EE, Guo Y, Knapp S, Beauchamp RD, Lee E, Wang J.

Clin Cancer Res **2017 23(8):2027-2037**

doi: 10.1158/1078-0432.CCR-16-0453

HHS Public Access

Author manuscript

Clin Cancer Res. Author manuscript; available in PMC 2018 April 15.

Published in final edited form as:

Clin Cancer Res. 2017 April 15; 23(8): 2027–2037. doi:10.1158/1078-0432.CCR-16-0453.

The MAPK pathway regulates intrinsic resistance to BET inhibitors in colorectal cancer

Yufang Ma[†,1], **Lihong Wang**[†,2], **Leif R. Neitzel**[3], **Sudan N. Loganathan**[4], **Nan Tang**[5], **Lili Qin**[1], **Emily E Crispi**[3], **Yan Guo**[6], **Stefan Knapp**[7], **R. Daniel Beauchamp**[2], **Ethan Lee**[3], and **Jialiang Wang**[*,1,6,9]

[1]Department of Neurological Surgery, Vanderbilt University, Nashville, TN, USA

[2]Department of Surgery, Vanderbilt University, Nashville, TN, USA

[3]Department of Cell and Developmental Biology, Vanderbilt University, Nashville, TN, USA

[4]Department of Neuroscience and Pharmacology, Meharry Medical College, Nashville, TN, USA

[5]Union Hospital, Tongji Medical College, Huazhong University of Science and Technology, Wuhan, P.R. China

[6]Department of Cancer Biology, Vanderbilt University, Nashville, TN, USA

[7]Nuffield Department of Clinical Medicine, Structural Genomics Consortium, University of Oxford, Oxford, OX3 7DQ, United Kingdom

[9]Department of Pharmacology, Vanderbilt University, Nashville, TN, USA

Abstract

Purpose—The bromodomain and extra-terminal domain (BET) family proteins are epigenetic readers for acetylated histone marks. Emerging BET bromodomain inhibitors have exhibited antineoplastic activities in a wide range of human cancers through suppression of oncogenic transcription factors, including MYC. However, the preclinical activities of BET inhibitors in advanced solid cancers are moderate at best. To improve BET-targeted therapy, we interrogated mechanisms mediating resistance to BET inhibitors in colorectal cancer (CRC).

Experimental Design—Using a panel of molecularly defined CRC cell lines, we examined the impact of BET inhibition on cellular proliferation and survival as well as MYC activity. We further tested the ability of inhibitors targeting the RAF/MEK/ERK (MAPK) pathway to enhance MYC suppression and circumvent intrinsic resistance to BET inhibitors. Key findings were validated using genetic approaches.

Results—BET inhibitors as monotherapy moderately reduced CRC cell proliferation and MYC expression. Blockade of the MAPK pathway synergistically sensitized CRC cells to BET inhibitors, leading to potent apoptosis and MYC downregulation *in vitro* and *in vivo*. A

[*]**Corresponding authors**: Jialiang Wang, T4224 Medical Center North, Vanderbilt University Medical Center, Nashville, TN 37232, Tel: (615) 936-6421, Fax: (615) 343-8104, jialiang.wang@vanderbilt.edu.

[†]Both authors contributed to the manuscript equally.

Conflict of interest: The authors have declared that no conflict of interest exists.

combination of JQ1 and trametinib, but neither agent alone, induced significant regression of subcutaneous CRC xenografts.

Conclusions—Our findings suggest that the MAPK pathway confers intrinsic resistance to BET inhibitors in CRC and propose an effective combination strategy for the treatment of CRC.

Keywords

BET bromodomain protein; colorectal cancer; RAF; MEK; ERK; MAPK

Introduction

Aberrant activation of WNT signaling through loss-of-function of *adenomatous polyposis coli* (*APC*) or mutation of β-catenin (*CTNNB1*) is the key oncogenic event in colorectal cancer (CRC) (1). The pluripotent transcription factor MYC is arguably the most important target gene of the WNT/β-catenin pathway in CRC (2). Data from the Cancer Genome Atlas suggest that MYC-dependent transcription program is activated in nearly all CRC (1). Depletion or reduction of MYC impairs tumorigenesis in *APC* loss-driven mouse models of colorectal cancer (3, 4). Therefore, targeting MYC has the potential to disrupt key oncogenic functions in CRC. While direct pharmacological intervention for transcription factors like MYC remains difficult, small molecule compounds targeting the bromodomain and extra-terminal domain (BET) family epigenetic readers recently emerged as alternative approaches to suppress oncogenic transcription factors, including MYC (5).

The BET family includes ubiquitously expressed BRD2, BRD3, BRD4, and a testis-specific BRDT. These proteins contain two evolutionarily conserved bromodomains that recognize acetylated lysine residues on histone tails (5). Through this interaction, BET proteins direct assembly of nuclear macromolecular complexes, such as the mediator complex and the transcription elongation complex, to acetylated chromatin (6). Hence, BET proteins have important roles in transcription initiation and elongation. Small molecule BET bromodomain inhibitors, such as JQ1, PFI-1, MS417 and i-BET762, exhibit promising antineoplastic activities in a range of preclinical models of human cancers (7–13). The antineoplastic activities of BET bromodomain inhibitors are associated with suppression of prominent oncogenic transcription programs frequently activated in human cancers, such as MYC (9–11), MYCN (12, 14), GLI1/2 (15), and NF-κB (16). As such, BET bromodomain inhibitors represent an appealing therapeutic option for cancers dependent on oncogenic transcription factors. Oncogenic transcription programs driven by β-catenin and MYC are key players in the molecular pathogenesis of CRC. Hu and colleagues recently reported that BET inhibition by MS417 attenuated CRC liver metastasis, although the impact on xenograft tumor growth was limited (17). In addition, McCleland et al. showed that knockdown of BRD4 induced MYC downregulation, differentiation and growth inhibition in CRC xenograft models (18). This study also suggested that CRC with the CpG island methylator phenotype (CIMP) were preferentially sensitive to BET inhibitors (18), although this link was not confirmed by a more recent study (19). Nevertheless, response to BET inhibitors in CRC is modest in general, suggesting that CRC tumors are intrinsically resistant to BET inhibition. In this study, we assessed the therapeutic potential of BET inhibitors in CRC and interrogated mechanisms conferring resistance to BET inhibitors. Our results demonstrated that blockade

of the RAS/RAF/MAPK pathway rendered CRC cells significantly more sensitive to BET inhibitors. Concurrent inhibition of BET proteins and the MAPK pathway was necessary and sufficient to effectively downregulate MYC and to induce significant tumor regression in xenograft models. Collectively, our findings suggest that the combination of BET inhibitors and MEK inhibitors is a promising therapeutic strategy for CRC.

MATERIALS AND METHODS

Cell culture

CRC cell lines were purchased from ATCC. MC38 mouse colon adenocarcinoma cells and DLD1 derivative lines, DKO1 and DKS8, were provided by Dr. Robert Coffey, Vanderbilt University. RKO derivative lines were provided by Dr. Daniel Liebeler, Vanderbilt University, which were originally purchased from Horizon Discovery (Cambridge, MA). All cells used were amplified from early passages and maintained in cultures for no more than 2 months. These lines were not further authenticated. Mycoplasma test were performed regularly using PCR detection kit from American Type Culture Collection (ATCC #30-1012K). All cell lines were maintained in RPMI-1640 medium supplemented with 10% fetal bovine serum and 100 U/mL penicillin-streptomycin (Life Technologies) at 37°C in 5% CO_2. The immortalized non-tumorigenic immortalized young adult mouse colon (YAMC) cells were obtained from Dr. Robert Whitehead, Vanderbilt University. YAMC cells were maintained and analyzed at 33°C to activate a temperature-sensitive mutant of SV40 large T antigen (20). Additional supplements were added in the growth medium for YAMC cells as previously described (20). The integrity of cell lines used in this study is described in our recent publications (21). The patient-derived xenograft line, CR-IGR-0034P, was purchased from Oncodesign, France. This line is serially passaged in immunocompromised mice without *in vitro* culture.

Plasmids, antibodies and lentivirus production

The pLKO.1 lentiviral vectors directing expression of shRNA sequences specific to BRD2 (2a: TRCN000006309, 2b: TRCN000006310), BRD3 (3a: TRCN0000021374; 3b: TRCN0000021376), and BRD4 (4a: TRCN0000196576; 4b: TRCN0000199427) have been described in our previous publications (13). KRAS knockdown constructs (sh-KRAS-1: TRCN000003260 and sh-KRAS-2L: TRCN000003262) were purchased from Sigma. Lentivirus was produced by co-transfection of the lentiviral vectors with the packaging vectors psPAX2 and pCI-VSVG (Addgene) into 293FT cells. Viral supernatants were collected 2 days after transfection and applied to cells at an approximate MOI of 5. Cells were selected with 1 μg/ml puromycin for at least 48 hours prior to experiments. Most antibodies used in this study are described in our recent publications, except that KRAS-specific antibody was purchased from Santa Cruz Biotechnology (#sc-30) (13). Immunohistochemical staining of xenograft tumor sections were performed with primary antibody against MYC (#sc-40, Santa Cruz Biotechnology) at a 1:500 dilution, Ki67 (#VP-K451, Vector Laboratories) at a 1:2000 dilution or cleaved Caspase-3 (# 9664, Cell Signaling) at a 1:300 dilution. Staining was visualized by the Bond Polymer Refine detection system.

Quantitative real-time PCR (qRT-PCR)

Total RNA was isolated using the Illustra RNAspin kit (GE Healthcare) and reverse transcribed using the iScript cDNA synthesis kit (Bio-Rad). Gene expression was measured by real-time PCR using universal SYBR-Green Mastermix (Bio-Rad). The reaction comprises 40 cycles of 95°C for 20 seconds and 60°C for 45 seconds. Primers are listed in Supplementary Table 1. Beta-actin was used as the loading control.

RNA seq and Gene Set Enrichment Analysis (GSEA)

CRC Cells were treated with DMSO or 1 μmol/L JQ1 for 24 hours. Total RNA was extracted using the Illustra RNAspin kit with on-column DNA digestion according to the manufacturer's instructions. RNAseq were performed by Vanderbilt Technologies for Advanced Genomics. All RNA samples were quantified using the QuBit RNA assay kit. RNA quality was checked using Agilent Bioanalyzer. The Illumina TruSeq RNA Sample Preparation kit (Illumina) was used for library preparation. Samples were sequenced on HiSeq 2500 to obtain at least 30 million paired end (2 × 50 bp) reads per sample. The RNAseq data went through multiple stages of thorough quality control as recommended (22). Raw data and alignment quality control were performed using QC3, gene quantification quality control was conducted using MultiRankSeq. Raw data were aligned with TopHat2 against human transcript genome HG19. Gene expression were quantified using Cufflinks(23). Differentially expression analysis is performed using Cuffdiff command from Cufflinks package. False discovery rate < 0.05 was used as the significant threshold.

We employed the GSEA method (http://www.broadinstitute.org/gsea) for statistical analysis of changes in gene expression patterns (24). GSEA determines whether a defined set of genes shows statistically significant differences between two phenotypes. The complete list of genes and their scores were used in GSEA with a focus on the C6 MSigDB collection (oncogenic signatures). According to the developer's instructions, the false discovery rate (FDR) q value represents 'the estimated probability that a gene set with a given normalized enrichment score represents a false positive finding' and the nominal p value estimates 'the statistical significance of the enrichment score for a single gene set.

Cell cycle distribution

Cells were treated for 24 hours, fixed in 75% ethanol, treated with RNase A, and stained with 10 μg/ml propidium iodide. Cell cycle distribution was measured by flow cytometry on a BD LSRFortessa cell Analyzer. The percentage of cells in each cell cycle phase was assessed by the ModFit LT software.

Caspase activation assays

To measure caspase activity, 2500 cells were plated in 96-well plates and treated for 72 hours prior to analysis. Activities of caspase-3/7 were measured using a Caspase-Glo 3/7 assay kit (Promega) following the manufacturer's instructions. Relative caspase 3/7 activities were calculated by normalizing the values of caspase-3/7 activities to the values of cell titers measured by a CellTiter-Glo assay kit (Promega) in replicated wells.

Colony formation assay

CRC cells were plated at 200 cells per well in 6-well plates in triplicates and treated the next day with 500 nmol/L JQ1 ± 25 nmol/L trametinib. However, RKO was treated with 100 nmol/L JQ1 and 25 nmol/L trametinib, because this line appeared to be highly sensitive to BET inhibitors alone in vitro. Drugs were withdrawn after 5-day incubation. Cells were allowed to grow for 7 additional days prior to be fixed and stained with 0.5% crystal violet. Colonies were counted using the Image J software.

Cell viability assay

CRC cells were plated 2500/well in 96-well plates and treated with BET inhibitors with or without the MAPK pathway inhibitors following a 2-fold serial dilution. Five days later, cell viability was measured using a Sensolyte Cell Viability and Proliferation Assay kit (Anaspec). The dose-response curves were fitted and IC_{50} values were calculated using GraphPad Prism following a nonlinear regression (least squares fit) method.

Subcutaneous xenograft tumor assays

All animal experiments were performed under protocols approved by the Vanderbilt University Institutional Animal Care and Use Committee. The xenograft assays used female athymic nude mice 6–8 weeks old. CRC cells were trypsinized, suspended in PBS and mixed with equal volume of growth factor reduced Matrigel (BD Biosciences). Both flank sites of mice received injection of two million tumor cells. Tumor size were measured by a digital caliper and calculated following a formula of Size = Length × Width × Width/2. Treatment began when the median tumor size reached approximately 100 mm^3. Prior to treatment, tumor-bearing mice were randomized into 4 arms that the median tumor sizes of each arm were roughly the same. JQ1 was first dissolved in DMSO and diluted to 9 volumes of 10% β-cyclodextrin in sterile saline and administrated through intraperitoneal injection. Trametinib was prepared in 1% β-cyclodextrin and administrated through oral gavage. Gefitinib was prepared in 1% Tween-80 and administrated through oral gavage. Tumor-bearing mice were treated daily with vehicle, 50 mg/kg/day JQ1, trametinib (0.5 mg/kg for SW480 and Difi, or 1 mg/kg for RKO), or both. Mice bearing the patient-derived xenograft tumors were treated with 100 mg/kg/day JQ1 and 1 mg/kg trametinib, of which JQ1 was given twice a day and trametinib was given once a day. In addition, a group of mice bearing Difi xenograft tumor were treated with 50 mg/kg gefitinib daily. Tumors were measured two to three times a week. Animals were monitored for significant adverse effects. Mice accidentally died of injury caused by oral gavage or intraperitoneal injection was excluded from analyses.

Other statistical analyses

GraphPad Prism 5.0 was used to determine statistical significance. P-values of less than 0.05 were considered significant. The combination index values were calculated using the Chou-Talalay method with the Compusyn software following the developer's instructions.

Results

BET inhibition leads to moderate MYC downregulation in CRC

It has been increasingly documented that inhibition of BET proteins results in potent downregulation of MYC in hematologic cancers, such as multiple myeloma, Burkitt's lymphoma, and acute myeloid leukemia (9–11). However, regulation of MYC by BET proteins in solid cancers appears to be heterogeneous and context-dependent (13, 14, 25). MYC is commonly activated in CRC and plays a critical role in disease initiation and progression. Therefore, we asked whether MYC expression in CRC was sensitive to BET inhibition. Our results showed that BET inhibition by JQ1 commonly downregulated MYC at both protein and mRNA levels in CRC cell lines (Fig. 1A and 1B). However, the reductions of MYC at protein levels were moderate and less significant compared with changes at mRNA levels, suggesting implications of post-transcriptional regulations. Following BET inhibition, expression of MYC targets, such as Bcl-2, Bcl-xL and hTERT, was decreased; while the MYC-repressed tumor suppressor, p21 (a.k.a. *CDKN1A*), was increased, albeit to various extents in different lines (Fig. 1C and Supplementary Fig. S1A–S1C). Selective depletion of individual BET family members by RNA interference suggested that BRD4 was the primary MYC regulator within the family, but BRD2 and BRD3 might also contribute to MYC regulation (Supplementary Fig. S1D–1G). We further assessed the impact of JQ1 on gene expression profiles in CRC cells using RNA seq and employed GSEA to analyze the changes in MYC-dependent gene signatures. In DLD1, KM12C and RKO cells, JQ1 significantly suppressed MYC-dependent transcription modules (Fig. 1D and Supplementary Fig. S1H). However, JQ1-induced repression of MYC signature was not statistically significant in SW480 cells (FDR q = 0.127, NES = −1.27). These results collectively suggest that BET proteins are commonly implicated in regulation of MYC expression and activity in CRC. However, in heterogeneous solid caners like CRC, MYC regulation by BET proteins can be context-dependent.

BET inhibition impair proliferation and survival of CRC cells

We next assessed activities of BET inhibitors in a subset of CRC cell lines harboring genetic alterations commonly found in CRC (26, 27). JQ1 dose-dependently decreased cell growth in all of the tested CRC cells (Fig. 2A and Supplementary Table 2). Similar response was observed using distinct BET bromodomain inhibitors, such as PFI-1 (Supplementary Fig. S2A). The anti-growth effects of BET inhibitors were partially phenocopied by knockdown of BRD4, while knockdown of BRD2 and BRD3 had less significant impact (Fig. 2B, Supplementary Fig. S2B, S2C). Inhibition of BET proteins was associated with cell cycle arrest in G1/G2 phases and moderate caspase activation (Fig. 2C, 2D, and Supplementary Fig. S2D–S2F). While these findings are consistent with recently published studies and underscore the potential of BET proteins as drug targets in CRC (17–19), BET inhibitors alone were largely cytostatic in CRC cultures, raising the concern whether they may be clinically effective as monotherapy.

Blockade of the RAS/RAF/MAPK pathway sensitizes CRC cells to BET inhibitors

The modest response to BET inhibitors and the lack of significant cell death suggest that intrinsic resistance to BET inhibitors is common in CRC, which can be a critical obstacle for

successful translation. The RAS/RAF/MAPK pathway is activated in most CRC tumors via activating mutations of KRAS, NRAS, BRAF, amplification of EGFR, in addition to other mechanisms (1). Among the CRC cell lines used in our study, phosphorylation levels of ERK were the highest in $BRAF^{V600E}$–expressing RKO and HT29, whereas KRAS mutations did not always result in hyperactivation of the MAPK pathway (Supplementary Fig. S3). Activation of RAS/RAF and the downstream MAPK pathway through mutations or other mechanisms is a common key oncogenic event in CRC. Introduction of an oncogenic KRAS mutant drastically promotes tumor formation and progression in *APC* deficient mouse model of intestinal tumors (28). RAS activation augments WNT signaling (29) and also promotes MYC protein stability, through mechanisms such as ERK-mediated MYC phosphorylation (30). Hence, we asked whether blockade of the MAPK pathway might affect CRC response to BET inhibitors. We treated CRC cells using a FDA-approved MEK inhibitor, trametinib, with or without JQ1 at a fixed molar ratio of 1:100 following a 2-fold serial dilution. This combination treatment induced significantly more potent reduction of cell growth than either agent alone in all tested lines across a wide range of concentrations (Fig. 3A–3C, Supplementary Fig. S4A and Table 2). Among the 14 CRC cell lines that we have tested, the median IC_{50} value of JQ1 was approximately 330 nmol/L. The median IC_{50} value of JQ1 was reduced to 130 nmol/L when combined with trametinib (Fig. 3C and Supplementary Table 2). The median IC_{50} value of trametinib was approximately 11 nmol/L as monotherapy, while it was reduced to merely 1 nmol/L in the presence of JQ1 (Fig. 3C and Supplementary Table 2). The interaction between JQ1 and trametinib was further assessed by the Chou-Talalay statistical method (31). In KM12C, RKO and SW480, the combination index (CI) values of JQ1 and trametinib were substantially less than 1 at concentrations across multiple orders of magnitude, indicating strong drug synergism (Fig. 3A, 3B, and Supplementary Fig. S4A, green cross, right Y axis). Similar synergistic interactions between JQ1 and the BRAF inhibitor vemurafenib were shown in $BRAF^{V600E}$ HT29 cells (Supplementary Fig. S4B). In addition, combinations of JQ1 with an ERK inhibitor SCH772984, or i-BET762 with an MEK inhibitor selumetinib also produced synergistic response (Supplementary Fig. S4C and S4D). In contrast, non-tumorigenic YAMC cells were refractory to JQ1 and trametinib, either alone or in combination (Supplementary Fig. S4E), whereas MC38, a cell line derived from genetic mouse models of colon cancer, was highly sensitive to the combination (Supplementary Fig. S4F). Clonogenic assays showed that transient exposure to JQ1 and trametinib almost completely abolished the ability of CRC cells to form colonies at concentrations that single-agent had limited impact (Fig. 3D and Supplementary Fig. S5), suggesting that this combination therapy induced prolonged damage to the tumorigenic potential of CRC cells. To further validate the specificity of actions of chemical probes, we showed that selective depletion of BRD4 sensitized KM12C and RKO cells to trametinib (Supplementary Fig. S6). Conversely, knockdown of BRD2 or BRD3 did not significantly altered response to MEK inhibition, suggesting that BRD4 plays a major role in regulation the crosstalk with the MAPK pathway. In addition, knockdown of KRAS decreased phosphorylation levels of ERK in both KRAS-mutant SW480 cells and KRAS-wild type KM12C cells and rendered cells more sensitive to JQ1 (Supplementary Fig. S7). These results collectively suggest that the synergism between of BET inhibitors and MAPK pathway inhibitors are primarily mediated via their respective on-target effects.

Our results showed that the combination of BET inhibitors and MEK inhibitors induced synergistic response in all tested CRC cell lines, irrespective of KRAS and BRAF mutations. These findings suggest an intrinsic role of MAPK signaling in mediating resistance to BET inhibitors that is not dependent on the mechanisms by which the MAPK pathway is activated. To further test this hypothesis, we investigated two sets of isogenic CRC lines that were genetically modified to deplete either the mutant allele of KRAS/BRAF or the wild type one. DLD1 cells has one copy of wild type KRAS and one copy of $KRAS^{G13D}$. This line had low MAPK activity compared with other KRAS-mutant CRC lines (Supplementary Fig. S3). The derivative line DKS8 lost the mutant $KRAS^{G13D}$ allele. Interestingly, phosphorylation of ERK in DKS8 was moderately higher than the parental line, despite loss of the mutant KRAS (Supplementary Fig. S8A). The response to JQ1, trametinib or the combination was similar between DKS8 and the parental DLD1 (Supplementary Fig. S8B and S8C). In contrast, the other derivative line depleted of the wild type KRAS allele, DKO1, showed much more potent activation of ERK (Supplementary Fig. S8A). DKO1 appeared to be more resistant to JQ1 than two other isogenic lines, but the resistance was essentially abolished by trametinib (Supplementary Fig. S8D and Table 2). In BRAF-mutant RKO cells, loss of the V600E allele significantly reduced phosphorylation of ERK (Supplementary Fig. S9A), but did not affect the synergistic interaction between JQ1 and trametinib (Supplementary Fig. S9B–9D). However, RKO-$BRAF^{wt}$ cells had lower cell viability in the presence of JQ1 at micromolar concentrations (Supplementary Fig. S9E). Taken together, these results suggest that modulations of MAPK activity may affect CRC cell sensitivity to BET inhibitors. However, at least in CRC, the synergistic interaction between BET inhibitors and MEK inhibitors is not genotype-dependent.

Concurrent inhibition of MEK and BET results in potent MYC downregulation

We next assessed changes in MYC expression when BET proteins, MAPK, or both were targeted. Our results showed that MYC protein was more effectively decreased following exposure to the combination of JQ1 and trametinib compared with either agent alone (Fig. 4A). However, the combination did not result in a more effective reduction of MYC mRNA (Fig. 4B and Supplementary Fig. S10A). Hence, the ability of trametinib to augment JQ1-induced downregulation of MYC protein appeared to be primarily mediated through post-transcriptional mechanisms. Expression of a constitutively active MEK1 mutant, $MEK1^{C121S}$, resulted in accumulation of MYC protein and counteracted JQ1-induced MYC repression (Fig. 4C). $MEK1^{C121S}$ also attenuated the effects of JQ1 and trametinib in Difi and SW480 cells, either alone or in combination (Fig. 4D and Supplementary Fig. S10B).

The combination of BET inhibitors and MEK inhibitors shift the balance among apoptosis regulators

While either JQ1 or trametinib alone was largely cytostatic in CRC cells, we noticed that targeting both BET and the MAPK pathway induced massive cell death and potent caspase activation (Fig. 5A and 5B). Several anti-apoptosis genes, Bcl-2 in particular, have been found to be targets of BET inhibitors in various cancers (9–11). Bcl-2 may play a primary role in neutralizing apoptotic stresses in some hematologic cancers, as the selective Bcl-2 inhibitors navitoclax and venetoclax generate significant response in patients with chronic lymphocytic leukemia (32, 33). However, the apoptosis regulatory network in solid cancers

is more complex and heterogeneous. Our results showed that BET inhibition induced downregulation of multiple anti-apoptotic Bcl-2 family members, Bcl-2 and Bcl-xL, as well as the inhibitor of apoptosis (IAP) family member, survivin (Fig. 5C and Supplementary Fig. S11A). In SW480 cells, BET inhibition also increased expression of BIM, a pro-apoptotic member of the Bcl-2 family (Fig. 5D). However, BET inhibition resulted in downregulation of certain pro-apoptotic genes, such as BIK in SW480 cells and BIK and PUMA in KM12C cells, which are expected to mitigate the impact of loss of anti-apoptotic genes (Fig. 5D and Supplementary Fig. S11B). Trametinib exhibited context-dependent effects on expression of these apoptosis regulators. Combining trametinib with JQ1 resulted in more effective suppression of anti-apoptotic genes, as exemplified by survivin in SW480 cells (Fig. 5C), and further increased BIM expression (Fig. 5D and Supplementary Fig. S11B). Interestingly, JQ1-induced suppression of BIK and PUMA was neutralized by trametinib (Fig. 5D and Supplementary Fig. S11B). Although changes of individual apoptosis regulators following treatments of JQ1 and/or trametinib were not identical across CRC lines with different genetic backgrounds, our results showed a pattern that BET inhibitors and MEK inhibitors in combination induced a more effective downregulation of anti-apoptosis genes and upregulation of pro-apoptosis genes compared with monotherapies, leading to strong apoptotic cell death.

A combination of JQ1 and trametinib induces CRC xenograft tumor regression

We next sought to assess the *in vivo* efficacy of the combination of JQ1 and trametinib using subcutaneous xenograft models. A few recent studies showed that BET inhibitors, JQ1 or MS417, had limited impact on CRC xenograft tumor growth (17, 19). Our data demonstrated that either JQ1 or trametinib alone moderately reduced the rate of tumor growth. In contrast, the combination of these two agents decreased median tumor size by 45% in $KRAS^{G12V}$ SW480 xenografts and 60% in $BRAF^{V600E}$ RKO xenografts following 2 weeks of treatment (Fig. 6A, 6B). Tumor regression was associated with decreased proliferation and increased apoptosis as shown by Ki67 and cleaved caspase 3 staining (Supplementary Fig. S12A). Animals treated with the combination experienced approximately 15% loss of body weight in the RKO experiment, while changes in the SW480 experiment were minor (Supplementary Fig. S12B and S12C). Using a patient-derived $BRAF^{V600E}$-expressing CRC xenograft model (34), we further showed that JQ1 or trametinib alone decreased tumor growth, whereas the combination induced a 75% reduction in median tumor size (Fig. 6C). Anti-EGFR therapy has been approved for the management of KRAS- and BRAF-wild type CRC. We asked whether the efficacy of the combination of BET inhibitors and MEK inhibitors was comparable to anti-EGFR agents in EGFR-dependent CRCs, such as Difi. Daily administration of 50 mg/kg gefitinib over 15 days decreased growth of Difi xenografts from 176% to 20%. In comparison, the combination of JQ1 and trametinib reduced median tumor volume by approximately 40% (Fig. 6D). Immunohistochemical staining of MYC in tumors treated for 5 days showed that JQ1 or trametinib alone only moderately decreased MYC-expressing cells in RKO tumors and marginally affected MYC expression in SW480 cells. However, MYC-expressing cells were drastically decreased in tumors treated with both compounds (Figure 6E and Supplementary Fig. S12D and S12E). Taken together, our results strongly suggest that a combination of BET bromodomain inhibitors and MEK inhibitors have broad therapeutic potential for

treating CRC, including those therapeutically refractory tumors that harbor BRAF and KRAS mutations.

Discussion

BET bromodomain inhibitors are a class of emerging drug candidates with attractive anti-cancer and anti-inflammatory activities through modulation of aberrantly activated transcription factors. Favorable clinical response was recently reported in hematologic cancers (35). However, the efficacy of BET inhibitors in preclinical models of advanced solid cancers is generally moderate. Mechanisms mediating acquired resistance to BET inhibitors just began to emerge. Acute myeloid leukemia may reactivate MYC expression through WNT signaling that confers resistance to BET inhibitors (36, 37). Alternatively, triple negative breast cancer may gain resistance through increasing phosphorylation of BRD4 that renders BRD4 maintain its transcription regulatory activities independent of bromodomains (38). Mechanisms mediating intrinsic resistance to BET inhibitors remain elusive. Identification of these mechanisms may direct development of more effective combination therapy and expedite translation of BET inhibitors as viable therapeutic options for advanced solid cancers. In the present study, we showed that activation of the MAPK pathway conferred intrinsic resistance to BET inhibitors. Thus, a combination of BET inhibitors and the MAPK pathway inhibitors generated synergistic response in CRC cell cultures and xenograft models. This approach is particularly appealing for CRC tumors carrying mutations in the RAS/RAF/MAPK pathway, which is highly resistant to currently available therapeutics.

A hallmark of CRC is prevalent co-activation of β-catenin/MYC-driven transcription and the RAS/RAF/MAPK pathway that act synergistically to promote CRC pathogenesis (1, 28, 39). The RAS/RAF/MAPK pathway may augment β-catenin and MYC activity through a multitude of mechanisms (30, 40, 41). Alternatively, activation of the WNT/β-catenin/MYC pathway is implicated in resistance to BRAF and MEK inhibitors (42–45). As such, accumulating evidence support the rationale to co-target both pathways for the treatment of CRC and a range of other cancers. However, the master regulators of these two pathways, KRAS and β-catenin, are both difficult drug targets. Our findings suggest that BET bromodomain proteins represent a druggable signaling hub in the oncogenic network driven by the WNT pathway and the RAS/RAF/MAPK pathway. As a result, the combination comprising a BET inhibitor and an inhibitor blocking the MAPK pathway holds great promise to treat cancers affected by aberrations of these two pathways, such as CRC.

In our study, we observed synergistic interaction between BET inhibitors and MAPK inhibitors in all tested CRC cell lines, irrespective of mutational status of KRAS and BRAF. In addition, our data did not suggest a linear correlation between sensitivity to JQ1 and activation of the MAPK pathway. Although the broad response in CRC may raise concerns over off-target effects, it is in concordance with prevalent activation of the MAPK pathway in this disease, which can be induced through not only mutations of KRAS/BRAF but also many other mechanisms. Using two sets of isogenic CRC cell lines, we showed that depletion of the mutant KRAS or BRAF alleles might alter JQ1 sensitivity according to the changes in MAPK activation. However, the synergistic interaction between JQ1 and

trametinib was not compromised. Thus, the crosstalk between MAPK signaling and BET proteins appears to be an intrinsic phenotype of CRC that is independent of the mechanisms through which the MAPK pathway is activated or the degree of MAPK activation. On the contrary, non-tumorigenic YAMC cells was spared by this combination therapy. Several genetic approaches, such as selective depletion of individual BET genes or KRAS and expression of a constitutively active MEK1 mutant, also underscored the on-target actions of BET inhibitors and MEK inhibitors. It is an interesting question if this paradigm can be applied to additional cancers transformed by MYC and oncogenic KRAS.

The mechanisms mediating the synergistic effects of the combination of BET inhibitors and MEK inhibitors remain to be fully elucidated in different CRC subtypes. While many downstream signaling molecules are affected by the combination therapy, MYC is a particularly important target. Overexpression of MYC is extensively documented in CRC and associated with poor survival (46). The Cancer Genome Atlas (TCGA) data indicate that MYC-dependent transcription is activated in nearly all CRC samples (1). We found that trametinib did not augment JQ1-induced downregulation of MYC mRNA, but further decreased MYC protein levels in the presence of JQ1, suggesting that trametinib modulated MYC levels through posttranslational mechanisms. The detailed mechanisms through which the MAPK pathway regulates MYC protein levels remain an open question and can be context-dependent. Nonetheless, our findings suggest that targeting both BET proteins and the MAPK pathway is necessary to effectively downregulate MYC proteins in CRC, in contrast to observations in MYC-amplified hematopoietic cancers. The resistance of MYC to BET inhibition is even more obvious *in vivo*, as most cells in CRC xenografts remained positively stained for MYC following administration of JQ1. In contrast, the combination of JQ1 and trametinib drastically reduced the percentage of MYC-positive cells. Hence, this combination strategy has important indications to pharmacologically target oncogenic MYC in solid cancers.

Another phenotype consistently shown in CRC cells treated with both BET inhibitors and MEK inhibitors was the shift of the balance between anti-apoptotic genes and pro-apoptotic genes. BET inhibition unexpectedly reduced expression of certain pro-apoptotic genes, such as BIK and PUMA. As such, despite reduced expression of anti-apoptotic genes, the overall impact of BET inhibitors on apoptosis regulatory network might not be sufficient to induce significant cell death. Addition of trametinib neutralized JQ1-induced downregulation of BIK and PUMA, augmented induction of BIM, and further decreased survivin. Hence, blockade of both pathways appears to be necessary and sufficient to effectively shift the balance between pro-apoptotic genes and anti-apoptotic genes to activate apoptosis. A recent study shows that concurrent upregulation of NOXA/BIK and inactivation of Bcl-2/Bcl-xL is necessary to induce apoptosis in KRAS-mutant colon cancer cells, underscoring the importance of coordinated changes in the apoptotic regulatory network (47). In addition, Conery and colleagues recently reported that activity of BET inhibitors in preclinical cancer models largely correlated with apoptotic response (48). Collectively, the coordinated actions of BET inhibitors and MEK inhibitors on expression of apoptosis regulators may have an important role in mediating the synergistic response.

To date, BET inhibitors alone exhibit generally moderate preclinical activities in solid tumor models. To realize the therapeutic potential of BET inhibitors, it is crucial to identify the mechanisms of resistance and to develop rational combinations that can produce meaningful response in a preclinical setting. In the current study, we identified a role of the MAPK pathway in mediating intrinsic resistance to BET inhibitors in CRC. As a result, combinations of BET inhibitors with inhibitors targeting the MAPK pathway induced synergistic response *in vitro* and *in vivo*. These findings propose a combination strategy that may substantially promote the uses of BET inhibitors and FDA-approved BRAF and MEK inhibitors. Crosstalks between signal transduction pathways and epigenetic regulation have recently emerged as a key factor to determine therapeutic response to BET inhibitors (38, 49–51). As such, combining with additional targeted agents is likely essential to optimize BET-targeted therapy.

Supplementary Material

Refer to Web version on PubMed Central for supplementary material.

Acknowledgments

We want to thank Drs. Robert Coffey, Daniel Liebler, and Robert Whitehead for providing important cell lines.

Grant Supports

J.W. is supported by the National Institutes of Health grant (R01CA166492) and the Voice Against Brain Cancer Foundation. E. L. is supported by NIH grants R01GM103926 and R01GM081635, and R. D. B. is supported by R01CA069457. S.K. is grateful for support by the Structural Genomics Consortium, a registered charity (No. 1097737) that receives funds from AbbVie, Bayer, Boehringer Ingelheim, Genome Canada through Ontario Genomics Institute Grant OGI-055, GlaxoSmithKline, Janssen, Lilly Canada, the Novartis Research Foundation, the Ontario Ministry of Economic Development and Innovation, Pfizer, Takeda, and Welcome Trust Grant 092809/Z/10/Z. L.N. is a recipient of NIH training grant 5T32HD007502.

References

1. Comprehensive molecular characterization of human colon and rectal cancer. Nature. 2012; 487:330–7. [PubMed: 22810696]
2. He TC, Sparks AB, Rago C, Hermeking H, Zawel L, da Costa LT, et al. Identification of c-MYC as a target of the APC pathway. Science. 1998; 281:1509–12. [PubMed: 9727977]
3. Sansom OJ, Meniel VS, Muncan V, Phesse TJ, Wilkins JA, Reed KR, et al. Myc deletion rescues Apc deficiency in the small intestine. Nature. 2007; 446:676–9. [PubMed: 17377531]
4. Athineos D, Sansom OJ. Myc heterozygosity attenuates the phenotypes of APC deficiency in the small intestine. Oncogene. 2010; 29:2585–90. [PubMed: 20140021]
5. Filippakopoulos P, Knapp S. Targeting bromodomains: epigenetic readers of lysine acetylation. Nat Rev Drug Discov. 2014; 13:337–56. [PubMed: 24751816]
6. Dawson MA, Kouzarides T, Huntly BJ. Targeting epigenetic readers in cancer. N Engl J Med. 2012; 367:647–57. [PubMed: 22894577]
7. Shi J, Wang Y, Zeng L, Wu Y, Deng J, Zhang Q, et al. Disrupting the interaction of BRD4 with diacetylated Twist suppresses tumorigenesis in basal-like breast cancer. Cancer Cell. 2014; 25:210–25. [PubMed: 24525235]
8. Filippakopoulos P, Qi J, Picaud S, Shen Y, Smith WB, Fedorov O, et al. Selective inhibition of BET bromodomains. Nature. 2010; 468:1067–73. [PubMed: 20871596]
9. Delmore JE, Issa GC, Lemieux ME, Rahl PB, Shi J, Jacobs HM, et al. BET bromodomain inhibition as a therapeutic strategy to target c-Myc. Cell. 2011; 146:904–17. [PubMed: 21889194]

10. Mertz JA, Conery AR, Bryant BM, Sandy P, Balasubramanian S, Mele DA, et al. Targeting MYC dependence in cancer by inhibiting BET bromodomains. Proc Natl Acad Sci U S A. 2011; 108:16669–74. [PubMed: 21949397]
11. Zuber J, Shi J, Wang E, Rappaport AR, Herrmann H, Sison EA, et al. RNAi screen identifies Brd4 as a therapeutic target in acute myeloid leukaemia. Nature. 2011; 478:524–8. [PubMed: 21814200]
12. Puissant A, Frumm SM, Alexe G, Bassil CF, Qi J, Chanthery YH, et al. Targeting MYCN in Neuroblastoma by BET Bromodomain Inhibition. Cancer Discov. 2013; 3:308–23. [PubMed: 23430699]
13. Cheng Z, Gong Y, Ma Y, Lu K, Lu X, Pierce LA, et al. Inhibition of BET Bromodomain Targets Genetically Diverse Glioblastoma. Clin Cancer Res. 2013; 19:1748–59. [PubMed: 23403638]
14. Baratta MG, Schinzel AC, Zwang Y, Bandopadhayay P, Bowman-Colin C, Kutt J, et al. An in-tumor genetic screen reveals that the BET bromodomain protein, BRD4, is a potential therapeutic target in ovarian carcinoma. Proc Natl Acad Sci U S A. 2015; 112:232–7. [PubMed: 25535366]
15. Tang Y, Gholamin S, Schubert S, Willardson MI, Lee A, Bandopadhayay P, et al. Epigenetic targeting of Hedgehog pathway transcriptional output through BET bromodomain inhibition. Nat Med. 2014; 20:732–40. [PubMed: 24973920]
16. Huang B, Yang XD, Zhou MM, Ozato K, Chen LF. Brd4 coactivates transcriptional activation of NF-kappaB via specific binding to acetylated RelA. Mol Cell Biol. 2009; 29:1375–87. [PubMed: 19103749]
17. Hu Y, Zhou J, Ye F, Xiong H, Peng L, Zheng Z, et al. BRD4 Inhibitor Inhibits Colorectal Cancer Growth and Metastasis. Int J Mol Sci. 2015; 16:1928–48. [PubMed: 25603177]
18. McCleland ML, Mesh K, Lorenzana E, Chopra VS, Segal E, Watanabe C, et al. CCAT1 is an enhancer-templated RNA that predicts BET sensitivity in colorectal cancer. J Clin Invest. 2016; 126:639–52. [PubMed: 26752646]
19. Togel L, Nightingale R, Chueh AC, Jayachandran A, Tran H, Phesse T, et al. Dual Targeting of Bromodomain and Extraterminal Domain Proteins, and WNT or MAPK Signaling, Inhibits c-MYC Expression and Proliferation of Colorectal Cancer Cells. Mol Cancer Ther. 2016
20. Whitehead RH, Robinson PS. Establishment of conditionally immortalized epithelial cell lines from the intestinal tissue of adult normal and transgenic mice. Am J Physiol Gastrointest Liver Physiol. 2009; 296:G455–60. [PubMed: 19109407]
21. Tripathi MK, Deane NG, Zhu J, An H, Mima S, Wang X, et al. Nuclear factor of activated T-cell activity is associated with metastatic capacity in colon cancer. Cancer Res. 2014; 74:6947–57. [PubMed: 25320007]
22. Guo Y, Ye F, Sheng Q, Clark T, Samuels DC. Three-stage quality control strategies for DNA re-sequencing data. Brief Bioinform. 2013
23. Trapnell C, Roberts A, Goff L, Pertea G, Kim D, Kelley DR, et al. Differential gene and transcript expression analysis of RNA-seq experiments with TopHat and Cufflinks. Nat Protoc. 2012; 7:562–78. [PubMed: 22383036]
24. Subramanian A, Tamayo P, Mootha VK, Mukherjee S, Ebert BL, Gillette MA, et al. Gene set enrichment analysis: a knowledge-based approach for interpreting genome-wide expression profiles. Proceedings of the National Academy of Sciences of the United States of America. 2005; 102:15545–50. [PubMed: 16199517]
25. Shimamura T, Chen Z, Soucheray M, Carretero J, Kikuchi E, Tchaicha JH, et al. Efficacy of BET bromodomain inhibition in Kras-mutant non-small cell lung cancer. Clin Cancer Res. 2013; 19:6183–92. [PubMed: 24045185]
26. Ahmad I, Patel R, Liu Y, Singh LB, Taketo MM, Wu XR, et al. Ras mutation cooperates with beta-catenin activation to drive bladder tumourigenesis. Cell Death Dis. 2011; 2:e124. [PubMed: 21368895]
27. Barretina J, Caponigro G, Stransky N, Venkatesan K, Margolin AA, Kim S, et al. The Cancer Cell Line Encyclopedia enables predictive modelling of anticancer drug sensitivity. Nature. 2012; 483:603–7. [PubMed: 22460905]
28. Janssen KP, Alberici P, Fsihi H, Gaspar C, Breukel C, Franken P, et al. APC and oncogenic KRAS are synergistic in enhancing Wnt signaling in intestinal tumor formation and progression. Gastroenterology. 2006; 131:1096–109. [PubMed: 17030180]

29. Horst D, Chen J, Morikawa T, Ogino S, Kirchner T, Shivdasani RA. Differential WNT activity in colorectal cancer confers limited tumorigenic potential and is regulated by MAPK signaling. Cancer Res. 2012; 72:1547–56. [PubMed: 22318865]
30. Sears R, Nuckolls F, Haura E, Taya Y, Tamai K, Nevins JR. Multiple Ras-dependent phosphorylation pathways regulate Myc protein stability. Genes Dev. 2000; 14:2501–14. [PubMed: 11018017]
31. Chou TC. Drug combination studies and their synergy quantification using the Chou-Talalay method. Cancer Res. 2010; 70:440–6. [PubMed: 20068163]
32. Roberts AW, Seymour JF, Brown JR, Wierda WG, Kipps TJ, Khaw SL, et al. Substantial susceptibility of chronic lymphocytic leukemia to BCL2 inhibition: results of a phase I study of navitoclax in patients with relapsed or refractory disease. J Clin Oncol. 2012; 30:488–96. [PubMed: 22184378]
33. Roberts AW, Davids MS, Pagel JM, Kahl BS, Puvvada SD, Gerecitano JF, et al. Targeting BCL2 with Venetoclax in Relapsed Chronic Lymphocytic Leukemia. N Engl J Med. 2016; 374:311–22. [PubMed: 26639348]
34. Julien S, Merino-Trigo A, Lacroix L, Pocard M, Goere D, Mariani P, et al. Characterization of a large panel of patient-derived tumor xenografts representing the clinical heterogeneity of human colorectal cancer. Clin Cancer Res. 2012; 18:5314–28. [PubMed: 22825584]
35. Herait PDH, Thieblemont C, Facon T, Stathis A, Cunningham D, Palumbo A, Vey N, Michallet M, Recher C, Rezai K, Preudhomme C. BET-bromodomain (BRD) inhibitor OTX015: Final results of the dose-finding part of a phase I study in hematologic malignancies. Annals of Oncology. 2015; 26(suppl 2):ii10–1.
36. Fong CY, Gilan O, Lam EY, Rubin AF, Ftouni S, Tyler D, et al. BET inhibitor resistance emerges from leukaemia stem cells. Nature. 2015; 525:538–42. [PubMed: 26367796]
37. Rathert P, Roth M, Neumann T, Muerdter F, Roe JS, Muhar M, et al. Transcriptional plasticity promotes primary and acquired resistance to BET inhibition. Nature. 2015; 525:543–7. [PubMed: 26367798]
38. Shu S, Lin CY, He HH, Witwicki RM, Tabassum DP, Roberts JM, et al. Response and resistance to BET bromodomain inhibitors in triple-negative breast cancer. Nature. 2016; 529:413–7. [PubMed: 26735014]
39. Hung KE, Maricevich MA, Richard LG, Chen WY, Richardson MP, Kunin A, et al. Development of a mouse model for sporadic and metastatic colon tumors and its use in assessing drug treatment. Proc Natl Acad Sci U S A. 2010; 107:1565–70. [PubMed: 20080688]
40. Lemieux E, Cagnol S, Beaudry K, Carrier J, Rivard N. Oncogenic KRAS signalling promotes the Wnt/beta-catenin pathway through LRP6 in colorectal cancer. Oncogene. 2014
41. Singh A, Sweeney MF, Yu M, Burger A, Greninger P, Benes C, et al. TAK1 inhibition promotes apoptosis in KRAS-dependent colon cancers. Cell. 2012; 148:639–50. [PubMed: 22341439]
42. Mologni L, Brussolo S, Ceccon M, Gambacorti-Passerini C. Synergistic effects of combined Wnt/KRAS inhibition in colorectal cancer cells. PLoS One. 2012; 7:e51449. [PubMed: 23227266]
43. Sprenfico A, Tentler JJ, Pitts TM, Tan AC, Gregory MA, Arcaroli JJ, et al. Rational combination of a MEK inhibitor, selumetinib, and the Wnt/calcium pathway modulator, cyclosporin A, in preclinical models of colorectal cancer. Clin Cancer Res. 2013; 19:4149–62. [PubMed: 23757356]
44. Sun C, Hobor S, Bertotti A, Zecchin D, Huang S, Galimi F, et al. Intrinsic resistance to MEK inhibition in KRAS mutant lung and colon cancer through transcriptional induction of ERBB3. Cell Rep. 2014; 7:86–93. [PubMed: 24685132]
45. Anastas JN, Kulikauskas RM, Tamir T, Rizos H, Long GV, von Euw EM, et al. WNT5A enhances resistance of melanoma cells to targeted BRAF inhibitors. J Clin Invest. 2014; 124:2877–90. [PubMed: 24865425]
46. Toon CW, Chou A, Clarkson A, DeSilva K, Houang M, Chan JC, et al. Immunohistochemistry for myc predicts survival in colorectal cancer. PLoS One. 2014; 9:e87456. [PubMed: 24503701]
47. Okamoto K, Zaanan A, Kawakami H, Huang S, Sinicrope FA. Reversal of Mutant KRAS-Mediated Apoptosis Resistance by Concurrent Noxa/Bik Induction and Bcl-2/Bcl-xL Antagonism in Colon Cancer Cells. Mol Cancer Res. 2015; 13:659–69. [PubMed: 25548100]

48. Conery AR, Centore RC, Spillane KL, Follmer NE, Bommi-Reddy A, Hatton C, et al. Preclinical anticancer efficacy of BET bromodomain inhibitors is determined by the apoptotic response. Cancer Res. 2016

49. De Raedt T, Beert E, Pasmant E, Luscan A, Brems H, Ortonne N, et al. PRC2 loss amplifies Ras-driven transcription and confers sensitivity to BRD4-based therapies. Nature. 2014; 514:247–51. [PubMed: 25119042]

50. Knoechel B, Roderick JE, Williamson KE, Zhu J, Lohr JG, Cotton MJ, et al. An epigenetic mechanism of resistance to targeted therapy in T cell acute lymphoblastic leukemia. Nat Genet. 2014; 46:364–70. [PubMed: 24584072]

51. Stratikopoulos EE, Dendy M, Szabolcs M, Khaykin AJ, Lefebvre C, Zhou MM, et al. Kinase and BET Inhibitors Together Clamp Inhibition of PI3K Signaling and Overcome Resistance to Therapy. Cancer Cell. 2015; 27:837–51. [PubMed: 26058079]

52. Ahmed D, Eide PW, Eilertsen IA, Danielsen SA, Eknaes M, Hektoen M, et al. Epigenetic and genetic features of 24 colon cancer cell lines. Oncogenesis. 2013; 2:e71. [PubMed: 24042735]

53. Kim IJ, Kang HC, Park JH, Shin Y, Ku JL, Lim SB, et al. Development and applications of a beta-catenin oligonucleotide microarray: beta-catenin mutations are dominantly found in the proximal colon cancers with microsatellite instability. Clin Cancer Res. 2003; 9:2920–5. [PubMed: 12912937]

Translational Relevance

BET bromodomain inhibitors are promising drug candidates, particularly for cancers driven by aberrantly activated oncogenic transcription programs. However, the moderate preclinical efficacy of BET inhibitors in advance solid cancer models raises concerns over their clinical potential as monotherapy. Hence, identifying mechanisms of resistance and developing rational combination approaches are critical for successful clinical translation. In CRC, BET inhibitors alone was inadequate to induce significant cell death and depletion of MYC protein. Our findings showed that the MAPK pathway mediated intrinsic resistance to BET inhibitors. Consequently, a combination of BET inhibitors and MEK inhibitors effectively reduced MYC protein levels and induced significant tumor regression in xenograft models, including those bearing KRAS or BRAF mutations. These findings suggest that rationally designed drug combinations hold promise to optimize BET bromodomain-targeted therapy.

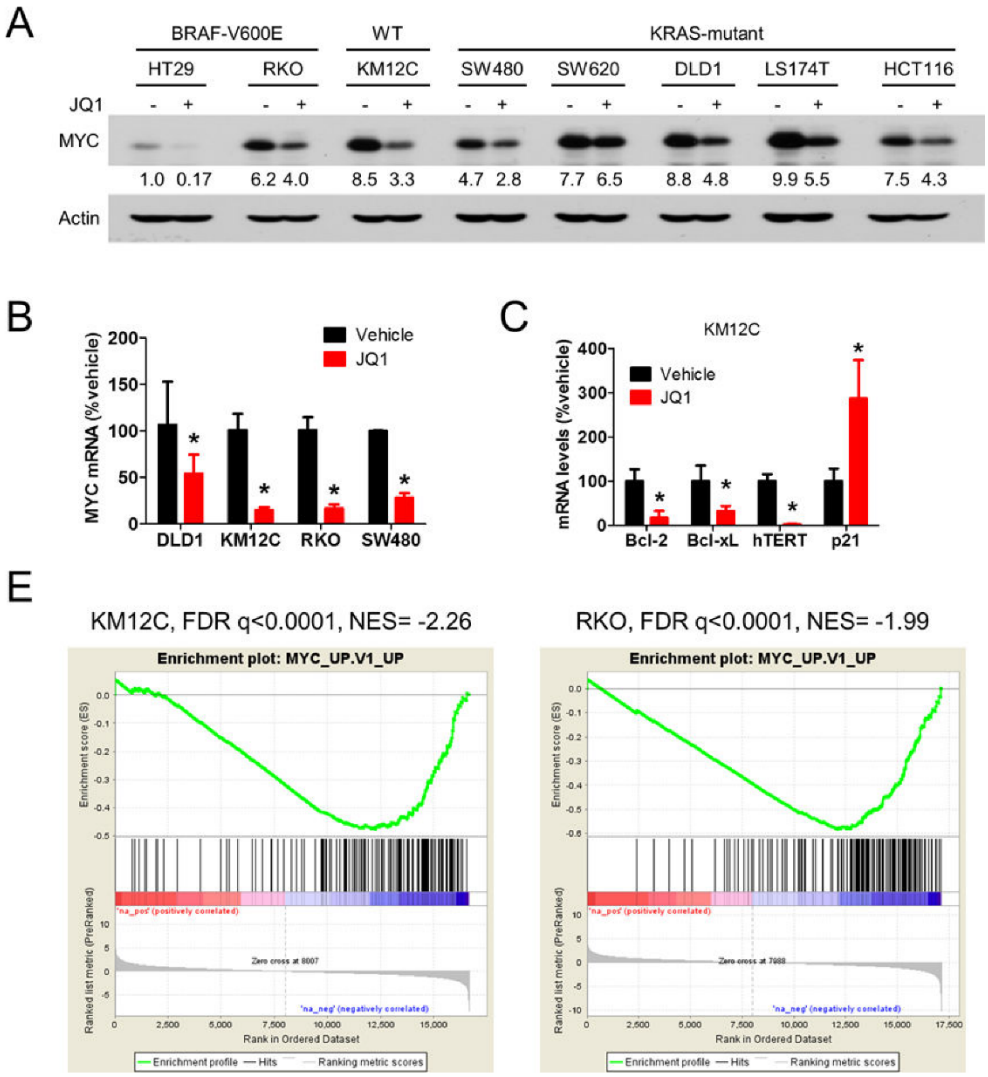

Figure 1. BET inhibition suppresses MYC in CRC

(A) CRC cells were treated with 2.5 μmol/L JQ1 for 24 hours and subject to immunoblotting. Similar experiments have been performed for at least three times unless otherwise indicated. Density of MYC bands were determined by Image J and normalized to the corresponding actin bands. The relative density of MYC in vehicle-treated RKO cells was assigned as 1. (B) CRC cells were treated with 1 μmol/L JQ1 for 24 hours. RNA was extracted and subject to qRT- PCR using beta-actin as the loading control. Error bars represent standard deviations in all figures unless otherwise indicated. Standard deviations were calculated from at least three technical replicates. *: $p < 0.05$ by Student's *t*-test. (C) Expression of MYC target genes in KM12C cells treated as described above. (E) KM12C and RKO cells were treated with 1 μmol/L JQ1 for 24 hours and subject to RNA seq. GSEA

enrichment plots show suppression of a MYC-dependent gene signature (MYC_UP.V1_UP, 200 genes). FDR: false discovery rate. NES: Normalized enrichment score.

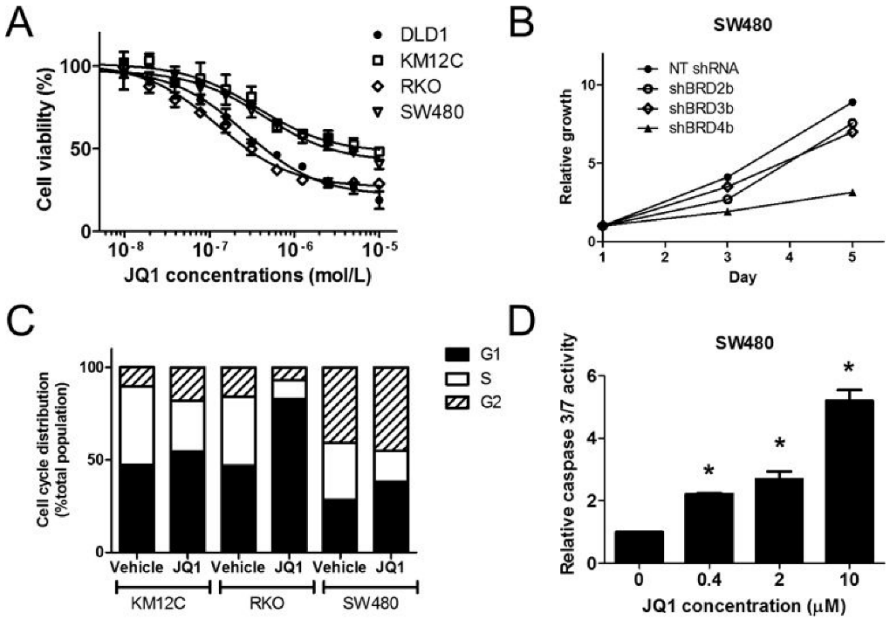

Figure 2. Inhibition of BET proteins impairs proliferation and survival of CRC cells

(A) CRC cells in 96-well plates were treated with JQ1 following a 12-point 2-fold serial dilution. Dose-response curves were determined following a three-parameter non-linear regression method. (B) Following lentiviral infection and puromycin selection, SW480 cell growth was measured every two days and normalized to the corresponding values of day 1. (C) CRC cells were treated with 1 μmol/L JQ1 for 24 hours. Cell cycle distribution was measured by flow cytometry and analyzed using the ModFit software. Representative plots are shown. (D) SW480 cells were treated with JQ1 for 72 hours at indicated concentrations. Caspase activities were determined using Caspase-Glo 3/7 assay kit (Promega) and normalized to cell titers determined using the CellTiter-Glo assay kit. *: $p < 0.05$ by Student's *t*-test compared with the corresponding control groups.

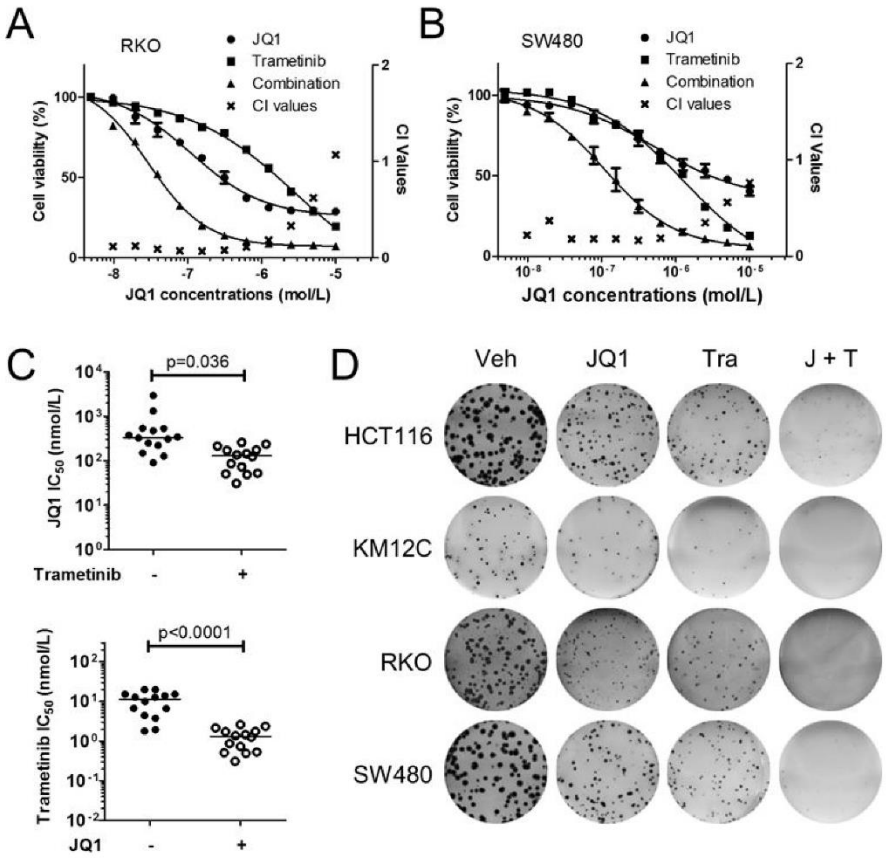

Figure 3. MEK inhibition synergistically improves the efficacy of BET inhibitors

(A) RKO and (B) SW480 cells were treated with JQ1 ± trametinib at a fixed ratio (100:1). Dose-response curves were determined as described in Fig. 2A. Combination index (CI) values were determined following the Chou-Talalay method. (C) IC_{50} values of JQ1 or trametinib either alone or in combination. Each dot represents mean of IC_{50} values of one CRC line generated from at least three independent experiments. (D) Colony formation by CRC cells treated for 5 days and cultured for additional 7 days after drug withdrawal. Veh: vehicle, Tra: trametinib, J + T: the combination of JQ1 and trametinib.

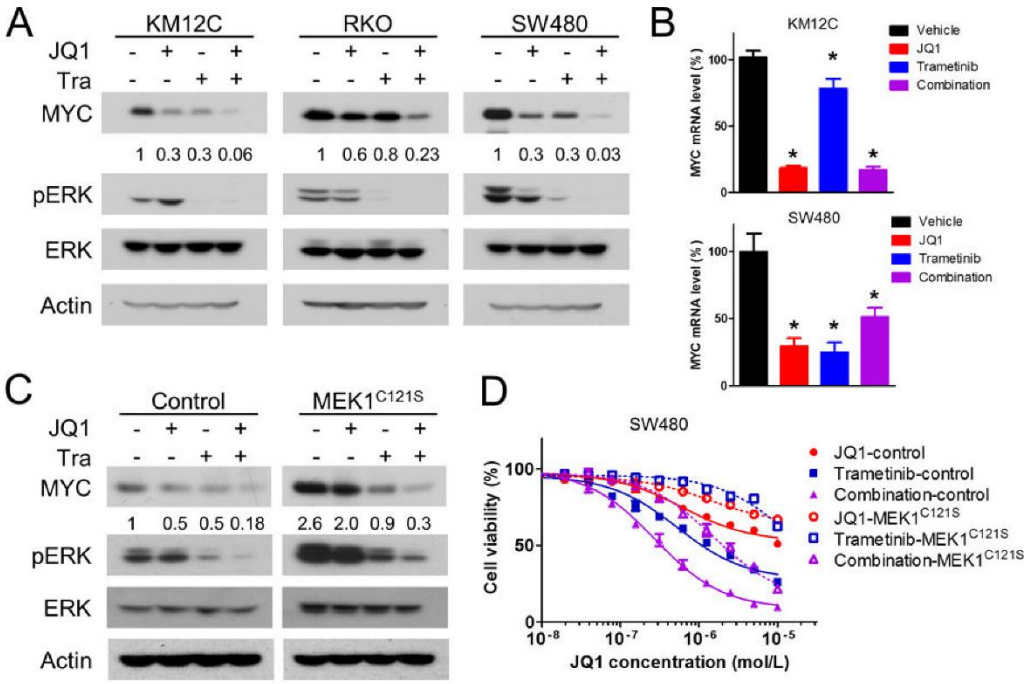

Figure 4. Co-targeting BET proteins and MEK induces potent downregulation of MYC

(A) CRC cells were treated with 500 nmol/L JQ1 ± 50 nmol/L trametinib for 2 days prior to lysis for immunoblotting. The relative density of MYC bands are calculated as described in Figure 1A. (B) KM12C and SW480 cells were treated as described above. MYC mRNA levels were determined by qRT-PCR using beta-actin as loading control. *: treated vs. control, $p < 0.05$ by Student's *t*-test. (C) SW480 cells were infected with control lentivirus or lentivirus directing expression of $MEK1^{C121S}$. After puromycin selection, cells were treated as described above and MYC protein levels were shown. (D) Dose response to JQ1 ± trametinib in SW480 cells infected with control lentivirus or lentivirus directing expression of $MEK1^{C121S}$.

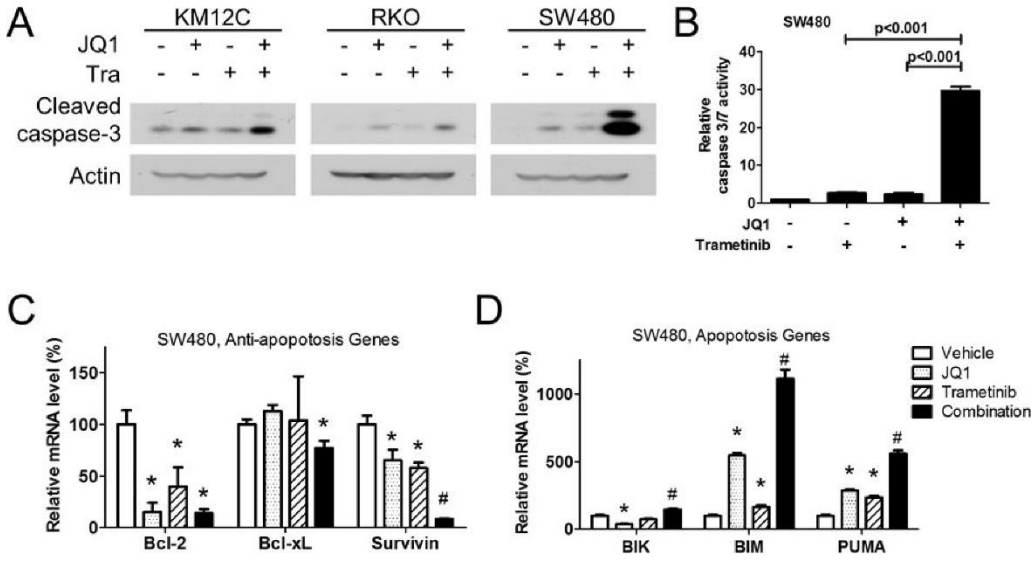

Figure 5. Combining BET inhibitors and MEK inhibitors induces potent apoptosis

(A) CRC cells were treated with 500 nmol/L JQ1 ± 50 nmol/L trametinib for 2 days. Immunoblotting of cleaved caspase 3 was presented. (B) Activation of caspase was assessed using the Promega Caspase-Glo 3/7 kit in SW480 cells. P values were determined by student's *t*-test. (C) SW480 cells were treated as described above. Expression of indicated target genes was determined by qRT-PCR using beta-actin as loading control. *: treated vs. vehicle, $p < 0.05$ by Student's *t*-test. #: combination vs. JQ1, $p < 0.05$ by Student's *t*-test.

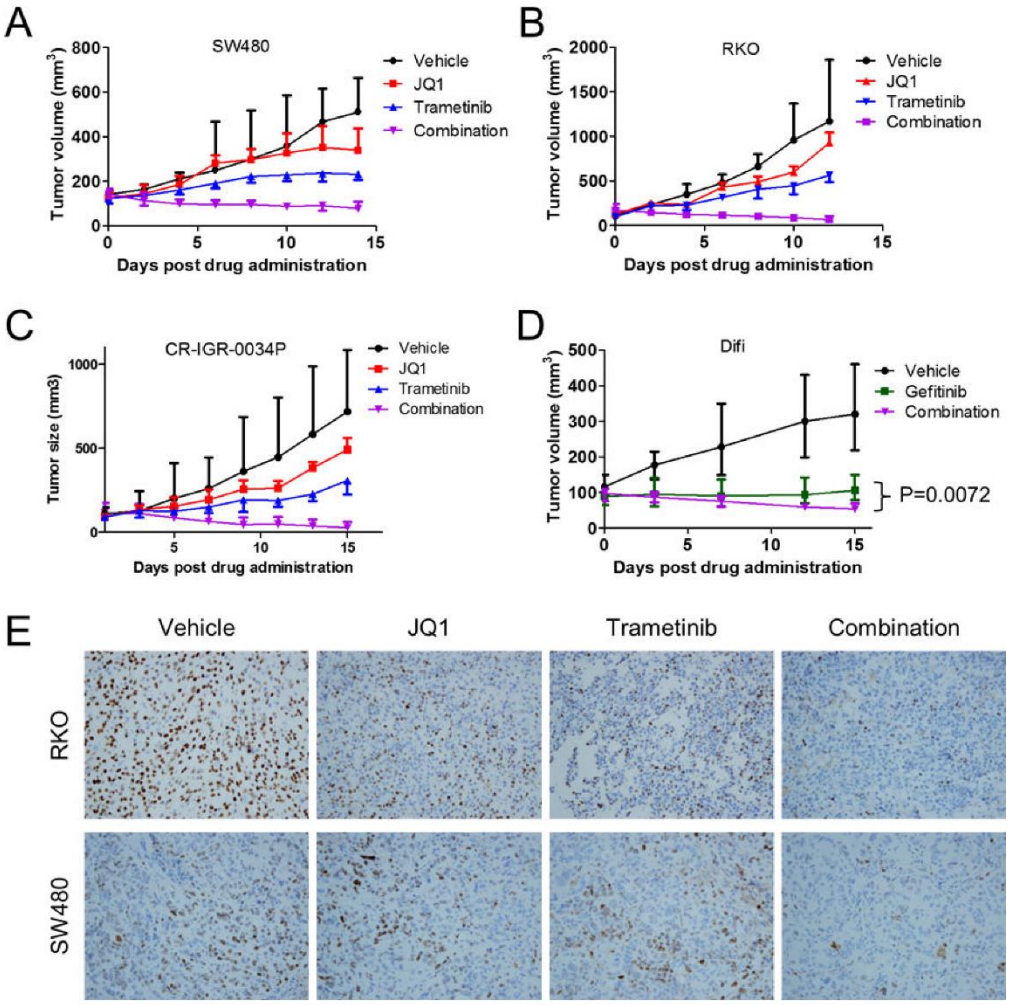

Figure 6. The combination of JQ1 and trametinib induces CRC xenograft tumor regression

(A) SW480 subcutaneous xenograft tumors (n=7, 14 tumors) were treated with 50 mg/kg/day JQ1 (i.p., once per day) ± 0.5 mg/kg/day trametinib (p.o., once per day) for 14 days. (B) RKO subcutaneous xenograft tumors (n=6, 12 tumors) were treated with 50 mg/kg/day JQ1 ± 1 mg/kg/day trametinib for 12 days. (C) CR-IGR-0034P subcutaneous tumors (n=7, 14 tumors) were treated with 100 mg/kg/day JQ1 (twice per day) ± 1 mg/kg/day trametinib (once per day) for 15 days. (D) Difi subcutaneous xenograft tumors (n=5, 10 tumors) were treated with 50 mg/kg/day gefitinib (p.o.) or 50 mg/kg/day JQ1 + 0.5 mg/kg/day trametinib as described above for 15 days. All tumor size data presented are median tumor size ± interquartile range. (E) After 5 days of treatment, selected tumors were resected for immunohistochemical staining of MYC. Representative images are presented (200×).

The MAPK pathway regulates intrinsic resistance to BET inhibitors in colorectal cancer

Supplementary Figures and Tables

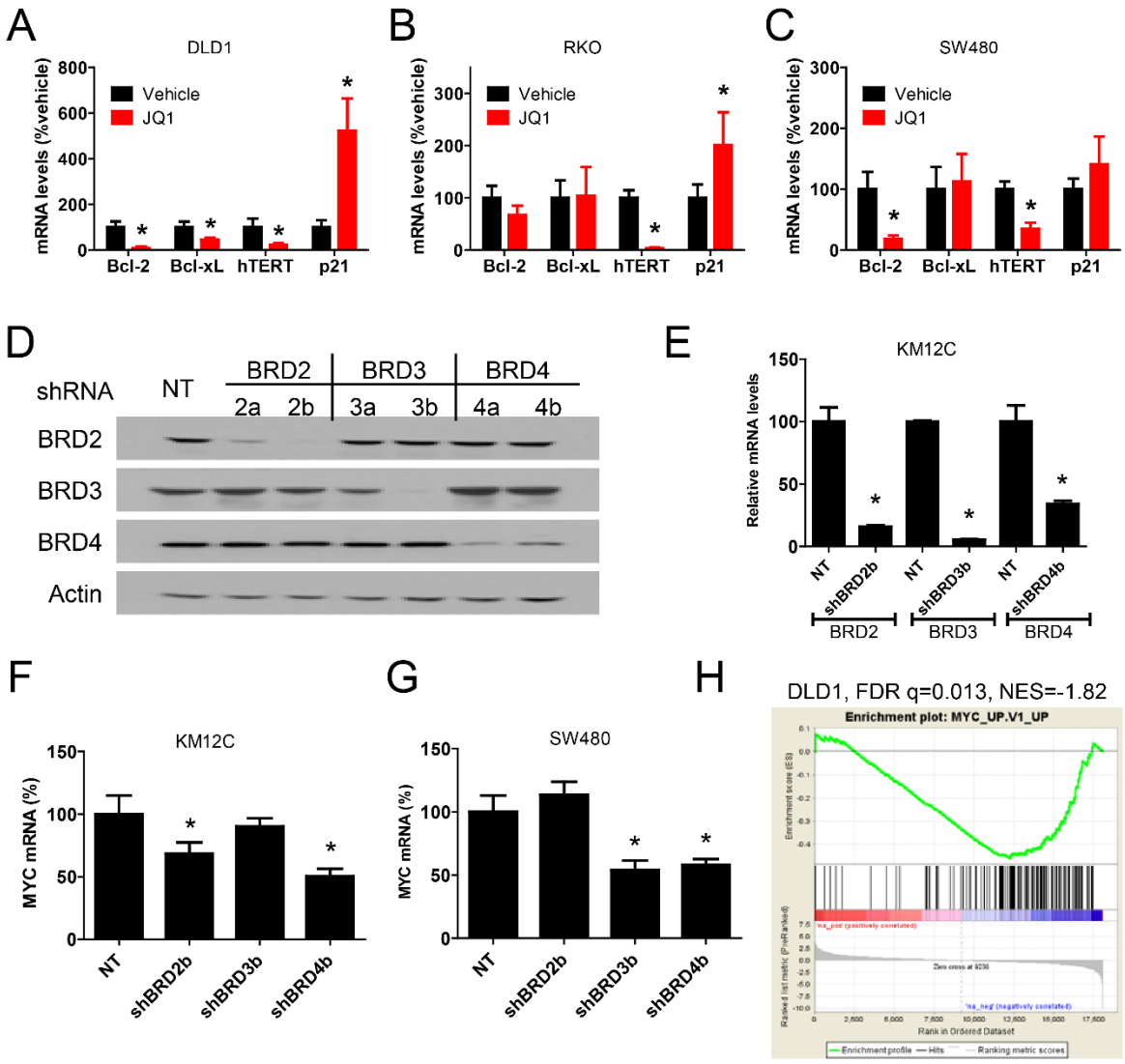

Supplementary Figure 1. BET inhibition reduces MYC expression and MYC-dependent transcription. (A-C) qRT-PCR of indicated target genes in DLD1, RKO and SW480 cells assessed after 24-hours treatment with 1 μmol/L JQ1. Beta-actin was used as the loading control. *: $p < 0.05$ by Student's *t*-test. (D) Immunoblotting or (E) qRT-PCR of BET family members following lentivirus-mediated expression of shRNA specific to BET genes in KM12C. (F) Expression of MYC in KM12C cells or (G) SW480 cells expressing non-targeting shRNA (NT) or shRNA sequences specific to BET genes. (H) GSEA plots of a MYC-dependent gene signature (MYC_UP.V1_UP) in DLD1 cells treated with 1 μmol/L JQ1 for 24 hours.

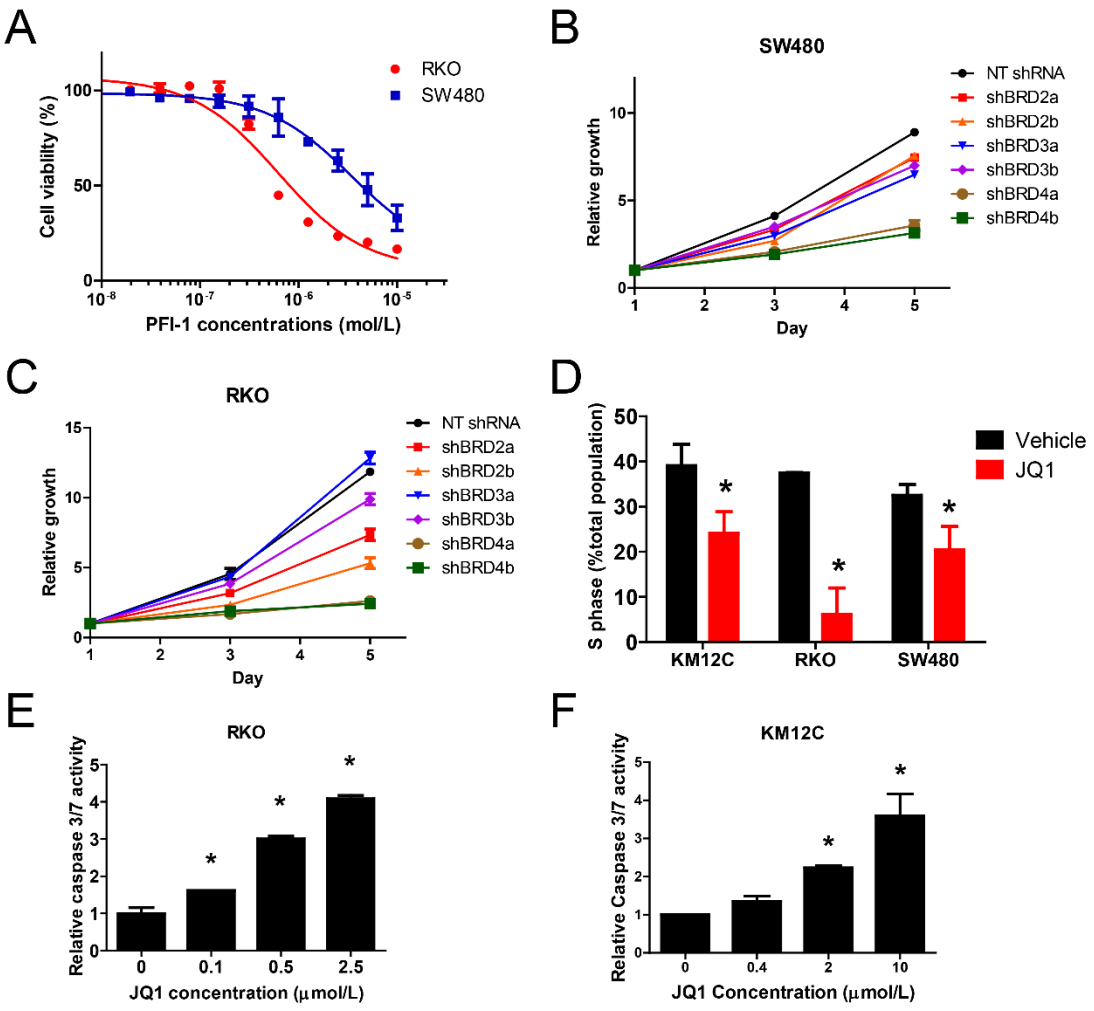

Supplementary Figure 2. BET inhibition impairs proliferation and survival of CRC cells. (A) Representative dose-response curves of PFI-1 in RKO and SW480 cells. (B) Growth curves of SW480 cells or (C) RKO cells following knockdown of BRD2, BRD3 or BRD4. (D) The percentage of S phase cells in total population of KM12C, RKO and SW480 cells 24 hours after 1 μmol/L JQ1 treatment. Data were generated from at least two independent experiments. (E, F) Relative caspase 3/7 activity in JQ1-treated RKO and KM12C cells. *: $p < 0.05$ by Student's *t*-test.

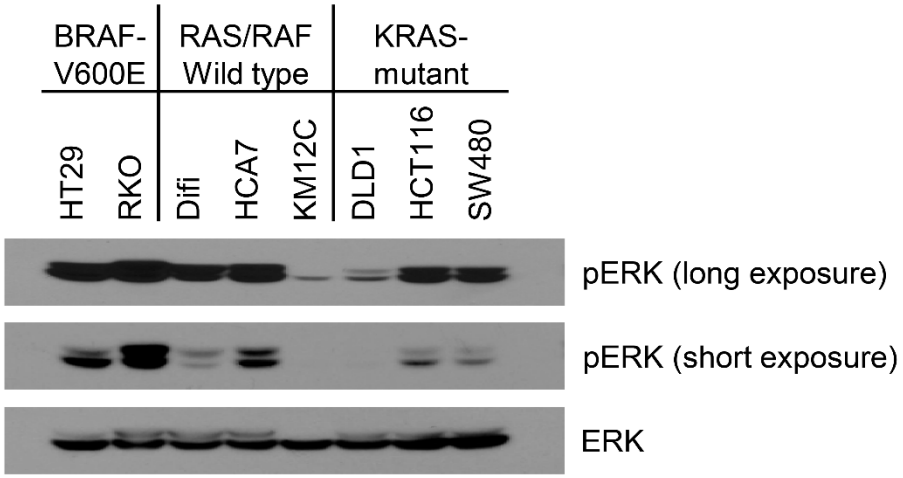

Supplementary Figure 3. Phosphorylation status of ERK in CRC cell lines.

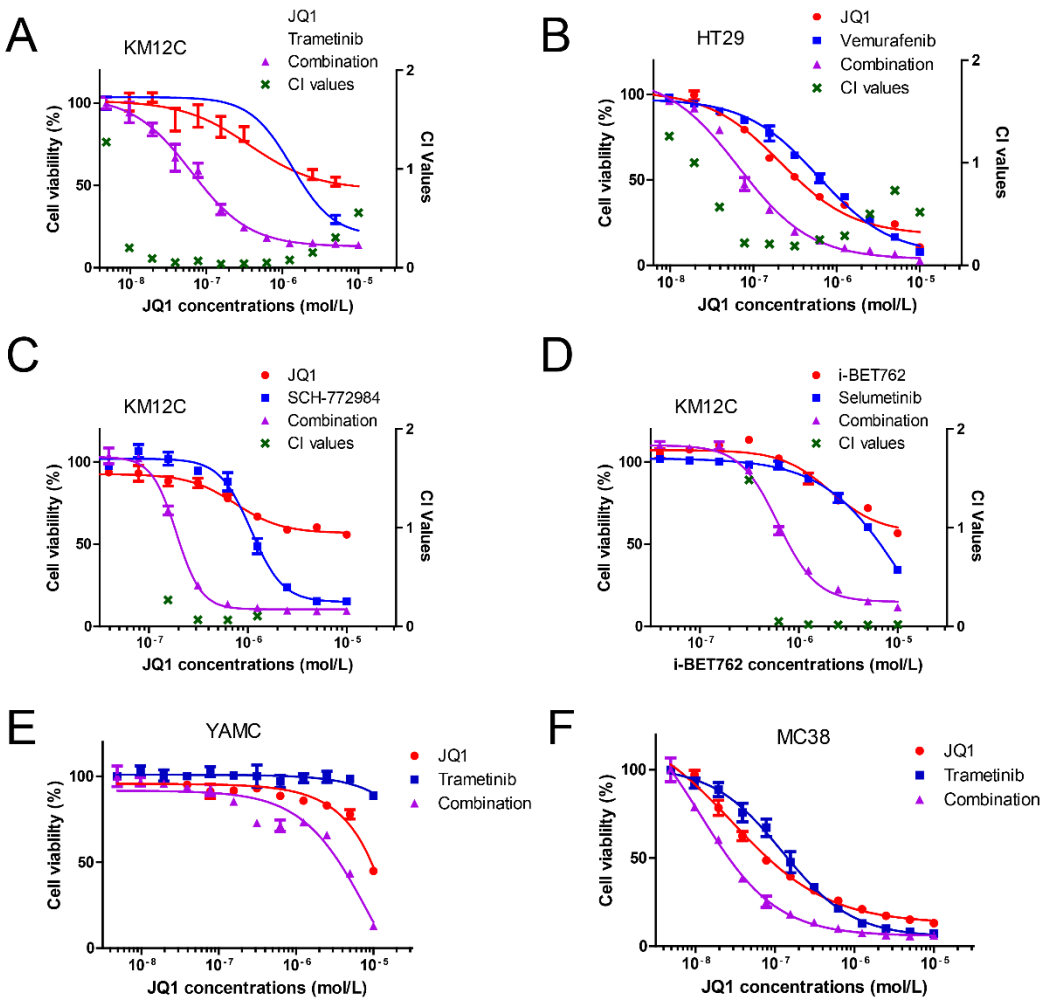

Supplementary Figure 4. BET inhibition sensitizes CRC cells to inhibitors of the MAPK pathway. Different compounds are mixed at fixed ratios according to approximately the ratio of their corresponding IC_{50} values. (A) Dose-response curves of JQ1 ± trametinib (100:1 ratio) in KM12C cells. (B) Dose-response curves of JQ1 ± vemurafenib (1:1 ratio) in HT29 cells. (C) Dose-response curves of JQ1 ± SCH-772984 (10:1 ratio) in KM12C cells. (D) Dose-response curves of i-BET762 ± selumetinib (5:1 ratio) in KM12C cells. (E) Dose-response curves of JQ1 ± trametinib (100:1 ratio) in YAMC cells or (F) MC38 cells. X axis indicates the respective concentrations of JQ1 or i-BET762.

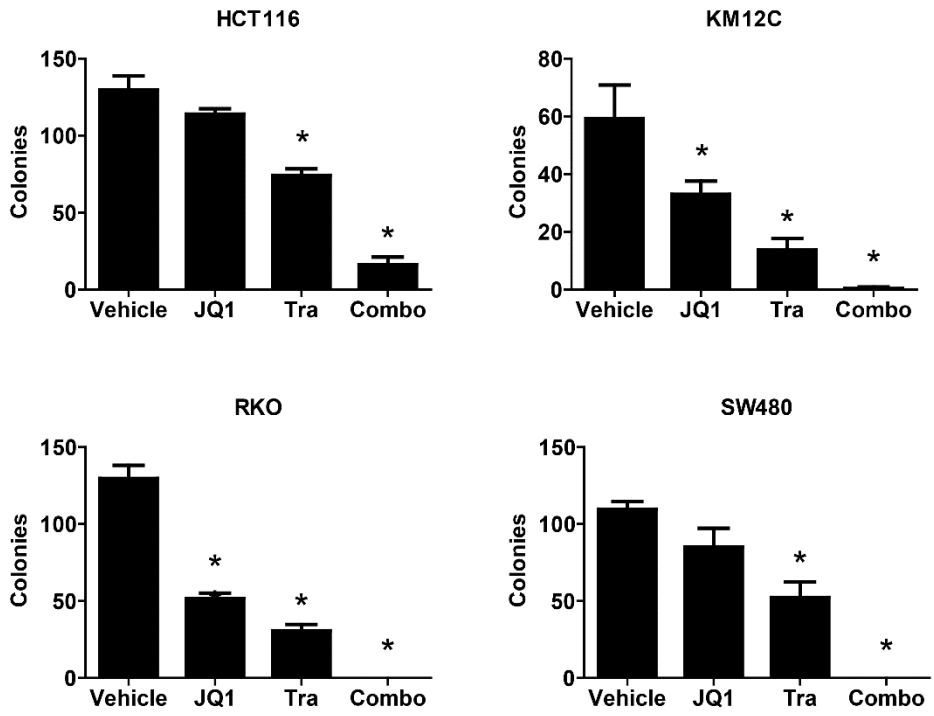

Supplementary Figure 5. The combination of JQ1 and trametinib impairs colony formation in CRC cells. Cells were plated at 200 cells per well in 6-well plates in triplicates, treated with 500 nmol/L JQ1 ± 25 nmol/L trametinib for 5 days, grew for 7 additional day, stained and counted using Image J. Note: RKO cells were treated with 100 nmol/L JQ1.

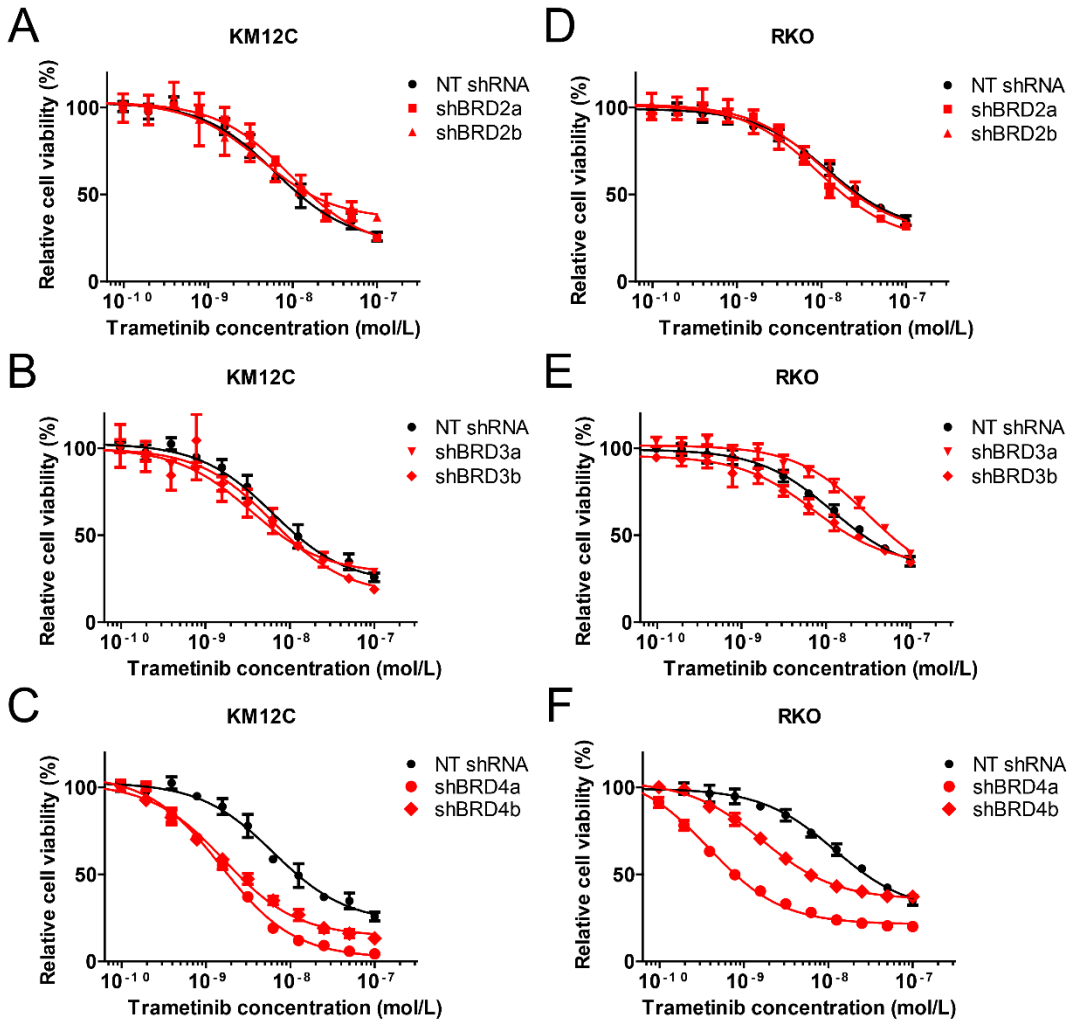

Supplementary Figure 6. Depletion of BRD4 sensitizes CRC cells to trametinib. (A-C) KM12C or (D-F) RKO cells were infected with lentivirus directing expression of NT shRNA or shRNA specific to individual BET genes, selected with 1 μg/ml puromycin. Dose-response curves of trametinib (from 100 nmol/L) were determined as described in Figure 2A.

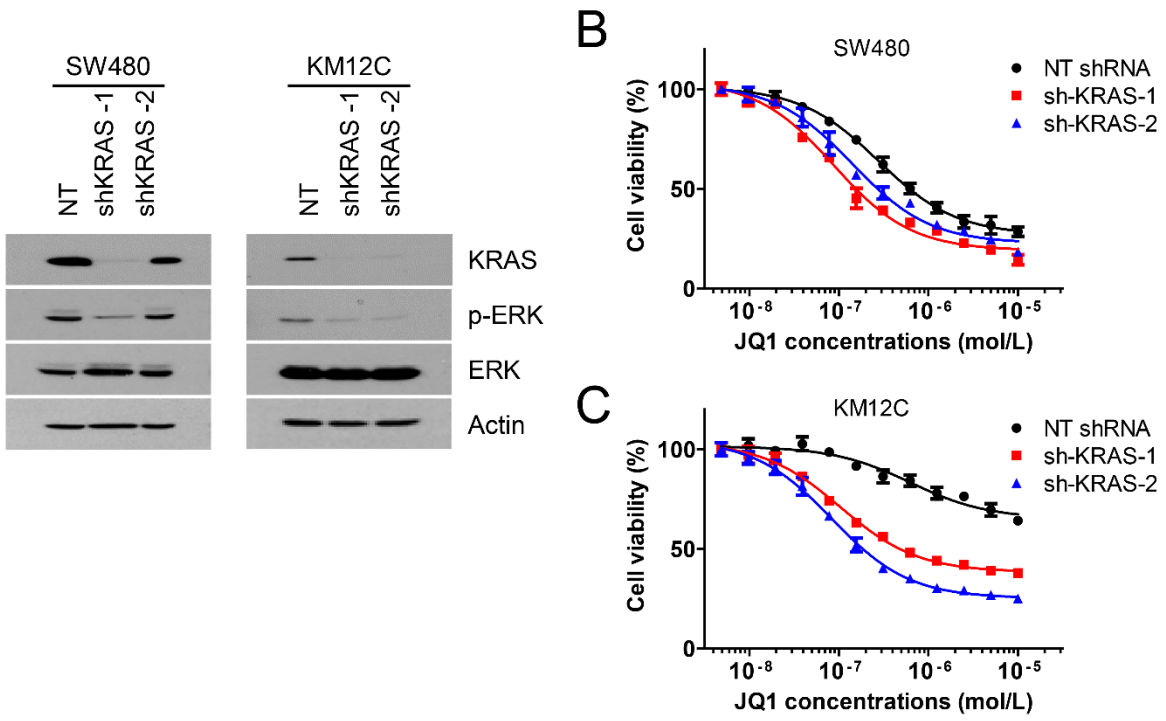

Supplementary Figure 7. Knockdown of KRAS recapitulates the ability of MAPK pathway inhibitors to sensitize CRC cells to JQ1. (A) SW480 and KM12C cells were infected with lentivirus directing expression of KRAS-specific shRNA sequences. Immunoblotting was performed following puromycin selection. (B) Response to JQ1 was determined in cells expressing NT shRNA or KRAS-specific shRNA as described in Fig. 2A.

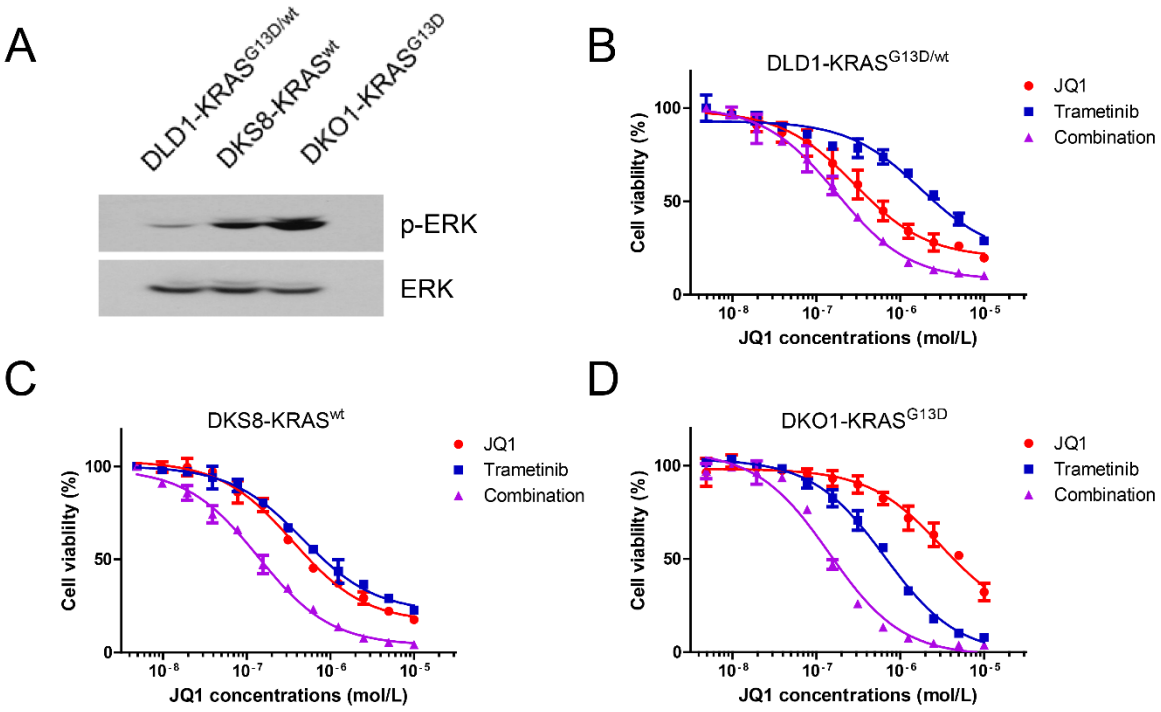

Supplementary Figure 8. Response to JQ1 ± trametinib in DLD1 and derivative lines. (A) Immunoblotting of phosphorylated ERK and total ERK in exponentially growing DLD1, DKS8 and DKO1 cells. (B-D) Dose response to JQ1 ± trametinib determined as described in Fig. 3A.

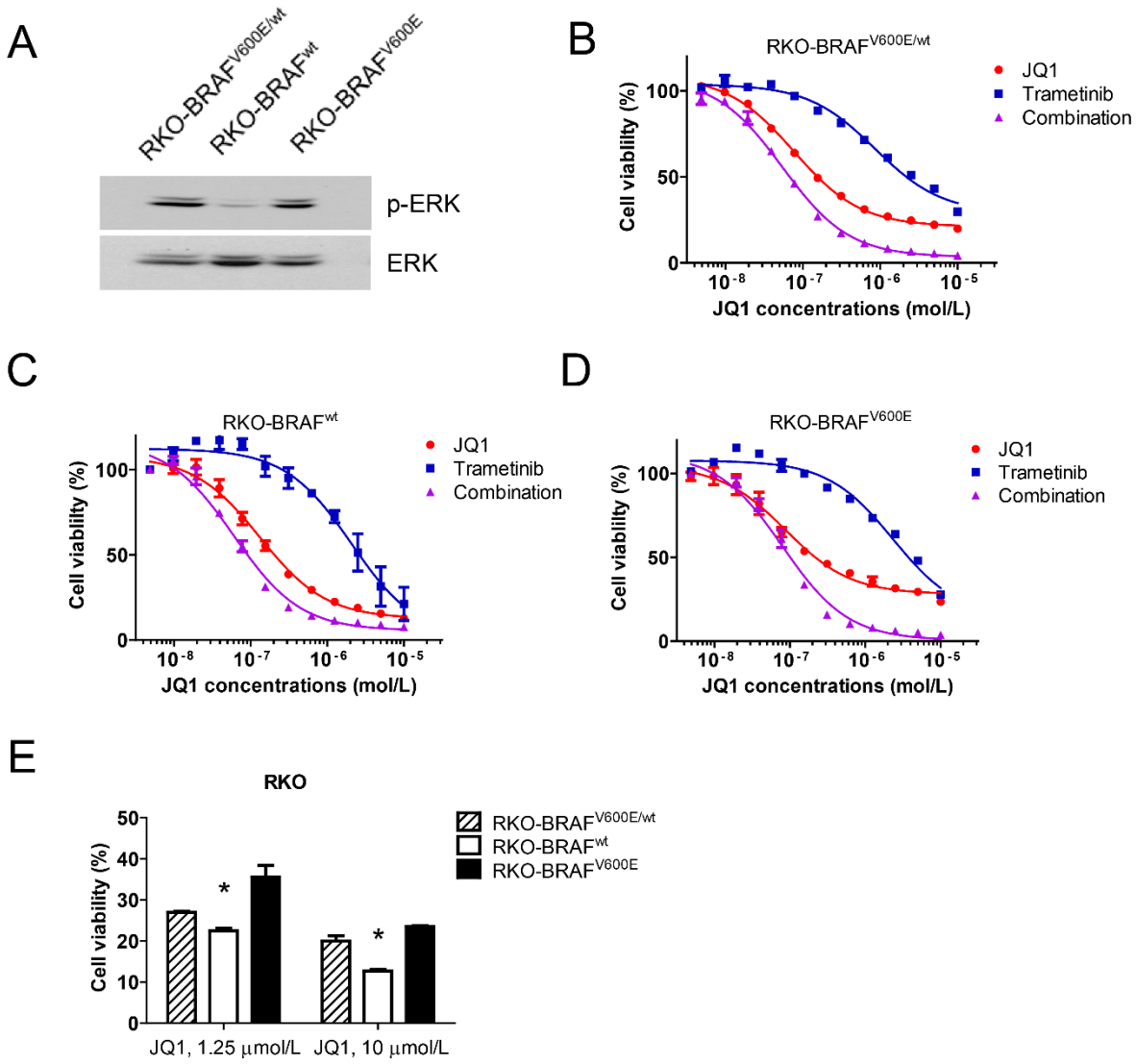

Supplementary Figure 9. Response to JQ1 ± trametinib in RKO and derivative lines. (A) Immunoblotting of phosphorylated ERK and total ERK in exponentially growing RKO and the derivative cells. (B-D) Dose response to JQ1 ± trametinib determined as described in Fig. 3A. E) Relative cell viability of RKO and derivative cells in the presence of JQ1 at 1.25 µmol/L or 10 µmol/L. *: $p < 0.05$ by Student's *t*-test, RKO-BRAF^{wt} vs. parental or BRAF^{V600E} cells.

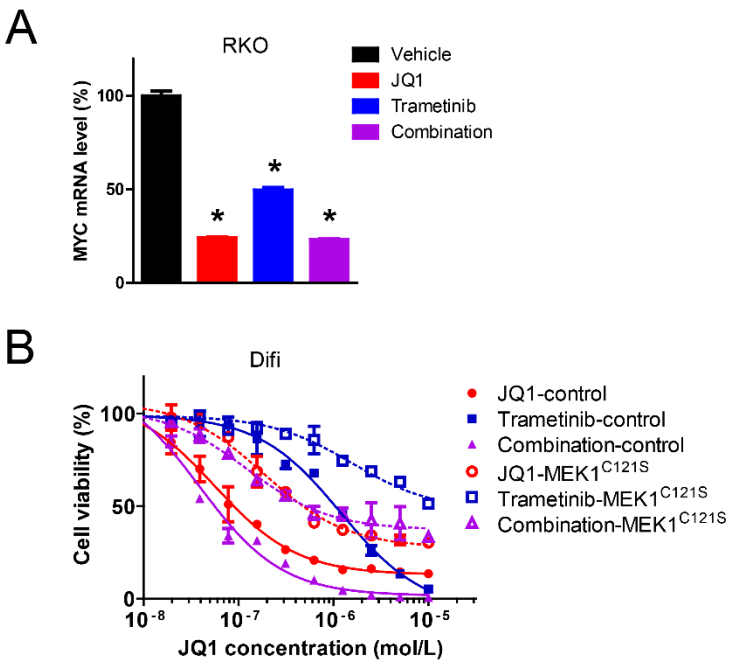

Supplementary Figure 10. (A) MYC mRNA levels in RKO cells treated with 500 nmol/L JQ1 ± 50 nmol/L trametinib for 2 days. (B) Difi cells were infected with control lentivirus or lentivirus directing expression of MEK1^{C121S}. After puromycin selection, dose response to JQ1 ± trametinib was determined as described in Figure 2A.

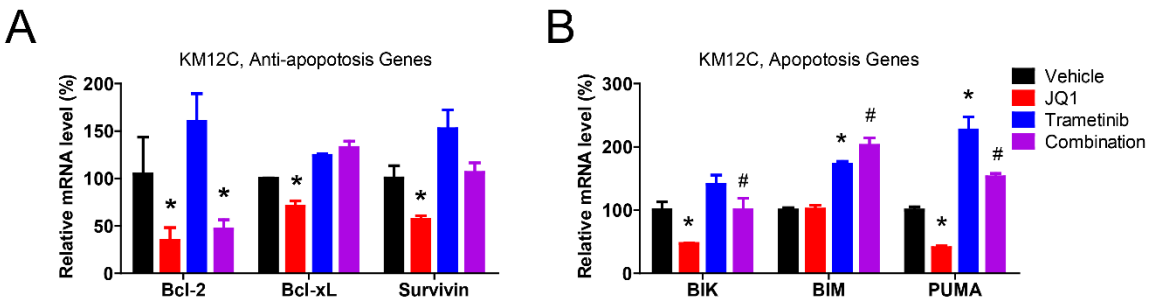

Supplementary Figure 11. Co-targeting of BET proteins and MEK effectively shifts expression of apoptotic regulators to promote apoptosis. (A, B) KM12C cells were treated with 500 nmol/L JQ1 ± 50 nmol/L trametinib for 2 days. Expression of indicated apoptosis regulators was determined by qRT-PCR using beta-actin as loading control. *: treated vs. vehicle, $p < 0.05$ by Student's *t*-test. #: combination vs. JQ1, $p < 0.05$ by Student's *t*-test.

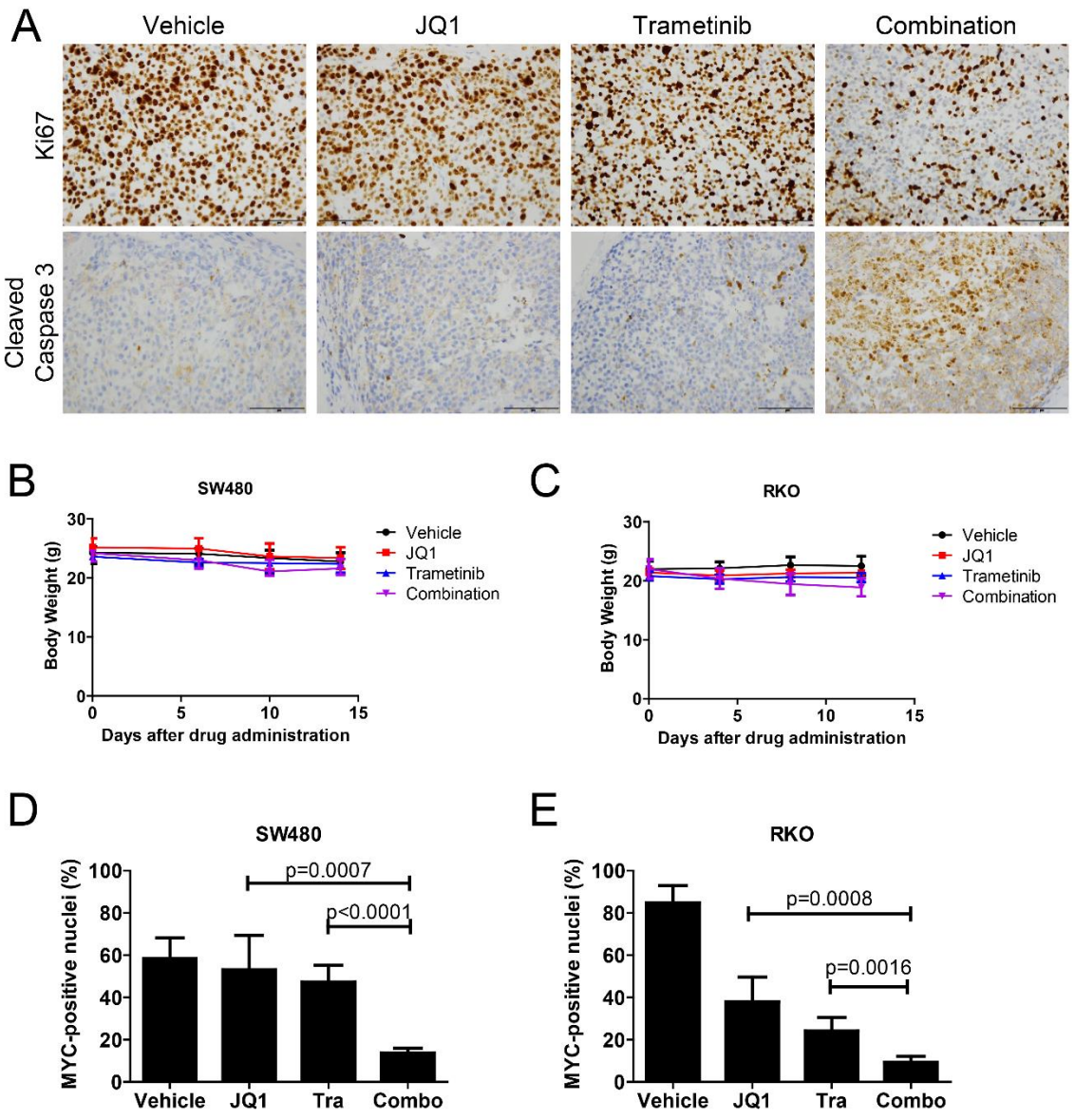

Supplementary Figure 12. The combination of JQ1 and trametinib induced CRC xenograft tumor regression. (A, B) Immunohistochemical staining of Ki67 and cleaved caspase 3 in RKO tumors. (B and C) Body weight of animals in the corresponding xenograft assays. Data presented are mean ± standard deviation. (D and E) MYC-positive nuclei were counted from at least 5 randomly selected areas (200 ×) and normalized to total nuclei using the ImageJ-Fiji software.

Gene name	Forward primer	Reserve primer
beta-actin	5'-TCGTGCGTGACATTAAGGA	5'-AGGAAGGAAGGCTGGAAGAG
Bcl-2	5'-CTGGTGGGAGCTTGCATCAC	5'-ACAGCCTGCAGCTTTGTTTC
Bcl-xL	5'-CATGGCAGCAGTAAAGCAAGCG	5'-AGGCTCTAGGTGGTCATTCAGG
BIK	5'-TCCTATGGCTCTGCAATTGTCA	5'-GGCAGGAGTGAATGGCTCTTC
BIM	5'-CACAAACCCCAAGTCCTCCTT	5'-TTCAGCCTGCCTCATGGAA
BRD2	5'-GTGGTTCTCGGCGGTAAG	5'-ACACCCCGGATTACATACCC
BRD3	5'-GAAGGCCAACAGCACGAC	5'-CCCTCCTCCTCTTCCTCTGA
BRD4	5'-TCCTGACCATGAGGTGGTG	5'-CAAAGCGCATTTCGAACAC
MYC	5'-TCAAGAGGCGAACACACAAC	5'-GGCCTTTTCATTGTTTTCCA
$p21^{CIP1/WAF1}$	5'-GGCAGACCAGCATGACAGATT	5'-GCGGATTAGGGCTTCCTCTT
PUMA	5'-GGGCCCAGACTGTGAATCC	5'-CGTCGCTCTCTCTAAACCTATGC
Survivin	5'-TCCGGTTGCGCTTTCCTTTC	5'-TCTTCTTATTGTTGGTTTCCTTTGC
hTERT	5'-TCCACTCCCCACATAGGAATAGTC	5'-TCCTTCTCAGGGTCTCCACCT

Supplementary Table 1. Real-time PCR primers used in this study.

Cell line	MSI status	APC	CTNNB1	KRAS	BRAF	IC_{50} (nmol/L)			
						JQ1	Tra	JQ1 (+ Tra)	Tra (+ JQ1)
HT29	MSS	E853*, E1554fs	WT	WT	V600E	311.33	3.78	260.73	2.61
HT55	MSS	Q1131*, Q1303*	L275F	WT	N581Y	149.65	1.94	52.64	0.53
RKO1	MSI	WT	WT	WT	V600E	90.69	12.68	31.09	0.31
HCT116	MSI	WT	S45del	G13D	WT	1337.43	15.22	237.24	2.37
LS174T	MSI	WT	S45F	G12D	WT	327.43	12.77	145.33	1.45
SW480#	MSS	Q1338*	WT	G12V	WT	345.03	4.43	124.93	1.25
SW620#	MSS	Q1338*	WT	G12V	WT	222.87	1.78	50.57	0.51
DLD1##	MSI	G1416fs, R2166*	WT	WT/G13D	WT	475.53	15.13	171.63	1.72
DKO1##	MSI	G1416fs, R2166*	WT	G13D	WT	2960.93	19.70	215.20	2.15
DKS8##	MSI	G1416fs, R2166*	WT	WT	WT	380.13	6.59	136.54	1.37
DiFi	MSS	ND	ND	WT	WT	252.70	19.86	175.38	1.75
KM12C#	MSI	L1816fs	WT	WT	A712T	542.43	13.86	73.10	0.73
KM12SM#	MSI	L1816fs	WT	WT	A712T	539.23	6.73	86.66	0.87
HCA7	MSI	WT	WT	WT	WT	128.80	9.98	49.27	0.49
Median						336.23	11.33	130.74	1.31

Supplementary Table 2. Genotypes and IC_{50} values for JQ1 and trametinib in CRC cell lines. IC_{50} presented in the table were mean values derived from at least three independent experiments. **#:** SW480/SW620 and KM12C/KM12SM are syngeneic pairs, with the latter lines being metastatic derivatives. ##: DKO1 and DKS8 are derived from DLD1, as the wild type KRAS allele is deleted in DKO1 and the mutant allele is deleted in DKS8. MSI, microsatellite instability; MSS, microsatellite stable; WT, wild type; fs, frame shift; *: truncation, ND, not determined. Mutations are annotated as changes of indicated amino acid residues. Data are collected from published studies and the Cancer Cell Line Encyclopedia database (27, 52, 53).

Comparative genetic screens in human cells reveal new regulatory mechanisms in WNT signaling

Lebensohn AM, Dubey R, **Neitzel LR**, Tacchelly-Benites O, Yang E, Marceau CD, Davis EM, Patel BB, Bahrami-Nejad Z, Travaglini KJ, Ahmed Y, Lee E, Carette JE, Rohatgi R.

Elife **2016 5. pii: e21459**

doi: 10.7554/eLife.21459

eLIFE elifesciences.org

RESEARCH ARTICLE

Comparative genetic screens in human cells reveal new regulatory mechanisms in WNT signaling

Andres M Lebensohn[1,2], Ramin Dubey[1,2], Leif R Neitzel[3], Ofelia Tacchelly-Benites[4], Eungi Yang[4], Caleb D Marceau[5], Eric M Davis[6], Bhaven B Patel[1,2], Zahra Bahrami-Nejad[7], Kyle J Travaglini[1], Yashi Ahmed[4], Ethan Lee[3], Jan E Carette[5]*, Rajat Rohatgi[1,2]*

[1]Department of Biochemistry, Stanford University School of Medicine, Stanford, United States; [2]Department of Medicine, Stanford University School of Medicine, Stanford, United States; [3]Department of Cell and Developmental Biology, Vanderbilt University Medical Center, Nashville, United States; [4]Department of Molecular and Systems Biology and the Norris Cotton Cancer Center, Geisel School of Medicine at Dartmouth College, Hanover, United States; [5]Department of Microbiology and Immunology, Stanford University School of Medicine, Stanford, United States; [6]Department of Molecular Cellular, and Developmental Biology, University of Colorado, Boulder, Boulder, United States; [7]Department of Chemical and Systems Biology, Stanford University School of Medicine, Stanford, United States

Abstract The comprehensive understanding of cellular signaling pathways remains a challenge due to multiple layers of regulation that may become evident only when the pathway is probed at different levels or critical nodes are eliminated. To discover regulatory mechanisms in canonical WNT signaling, we conducted a systematic forward genetic analysis through reporter-based screens in haploid human cells. Comparison of screens for negative, attenuating and positive regulators of WNT signaling, mediators of R-spondin-dependent signaling and suppressors of constitutive signaling induced by loss of the tumor suppressor adenomatous polyposis coli or casein kinase 1α uncovered new regulatory features at most levels of the pathway. These include a requirement for the transcription factor AP-4, a role for the DAX domain of AXIN2 in controlling β-catenin transcriptional activity, a contribution of glycophosphatidylinositol anchor biosynthesis and glypicans to R-spondin-potentiated WNT signaling, and two different mechanisms that regulate signaling when distinct components of the β-catenin destruction complex are lost. The conceptual and methodological framework we describe should enable the comprehensive understanding of other signaling systems.
DOI: 10.7554/eLife.21459.001

***For correspondence:** carette@stanford.edu (JEC); rrohatgi@stanford.edu (RR)

Competing interests: The authors declare that no competing interests exist.

Funding: See page 35

Received: 13 September 2016
Accepted: 07 December 2016
Published: 20 December 2016

Reviewing editor: Utpal Banerjee, University of California, Los Angeles, United States

Introduction

Cellular signaling systems have evolved complex circuitry involving multiple layers of regulation, making their comprehensive characterization a major challenge. Forward genetics in model organisms has been a general and unbiased way to identify new components in signaling pathways and to map their connectivity. However, since signaling pathways have often diverged between humans and these simpler model systems, their analysis in human cells becomes an important goal. Indeed, our ability to identify the best therapeutic strategy or to predict the effectiveness of drugs targeting

eLife digest When an embryo is developing, its cells must communicate with one another to coordinate the processes that shape the body's tissues and organs. Cells often communicate by releasing signaling molecules that engage with proteins called receptors on the surface of other cells. This triggers a series of events that sends the signal along a "pathway" of biochemical reactions inside the receiving cell and leads to the activation of genes. One such signaling pathway is triggered by the WNT proteins and is used extensively in all animals. The WNT pathway instructs cells to grow and divide, establishes the identity of specific cell types and maintains populations of stem cells that can regenerate tissues in adulthood as well. The WNT pathway must be carefully regulated because various types of cancer can develop if the pathway becomes too active.

Some signaling pathways are well conserved between different animals. Many genetic studies into the WNT pathway have focused on animals that are easier to work with in the laboratory, like worms or flies. However, there may be differences in the way these pathways are regulated between these model animals and humans. Therefore, to understand how the WNT pathway operates in humans, it was important to study it in human cells too.

Lebensohn et al. have now carried out a series of genetic screens in human cells that contain only one copy of each gene instead of the usual two. These cells – referred to as haploid cells – are ideal for genetic studies because only a single copy of a gene has to be disrupted in order to analyze the consequences of that gene's loss. The screens searched for genes that regulate WNT signaling: those that keep the pathway "off" in the absence of WNT and those that turn the pathway "on" in response to WNT.

By comparing the outcomes of these screens, Lebensohn et al. identified previously unknown regulators and uncovered new roles for known regulators of the WNT pathway. For instance, a regulator called TFAP4, which had not previously been linked to the pathway, was shown to activate WNT signaling. In another case, enzymes that make molecules called glycophosphatidylinositol anchors, and cell-surface proteins that are modified with those anchors, were found to amplify WNT signaling.

Lebensohn et al. also identified genes that were needed to sustain the uncontrolled WNT signaling in cells that carried cancer-causing mutations in this pathway. Further studies could now explore if drugs can target these genes, or the molecules encoded by them, to treat cancers in which the WNT pathway is excessively activated. Other studies could also use the same methods to explore more signaling pathways and gain new insights into important biological processes in human cells.

DOI: 10.7554/eLife.21459.002

specific proteins is often hampered by an incomplete understanding of signaling circuitry in human cells (***Lito et al., 2013***). Recent methodological advances have enabled the interrogation of biological processes in human cells through powerful genome-wide screens that overcome many of the limitations associated with previous platforms (***Carette et al., 2009***; ***Gilbert et al., 2014***; ***Shalem et al., 2014***; ***Wang et al., 2014***). Yet, inferring functional relationships in complex pathways from such screens remains a major obstacle that has only recently began to be addressed (***Bassik et al., 2013***; ***Blomen et al., 2015***; ***Parnas et al., 2015***; ***Wang et al., 2015***).

Genetics has long relied on the use of sensitized backgrounds, modifier screens and synthetic effects to uncover the myriad layers of regulation in signaling pathways. We reasoned that one way to discover both epistatic relationships on a genome scale and unique context-specific requirements would be through the quantitative comparison of genome-wide screens in which the pathway is activated by different ligands, and of suppressor screens following targeted disruption of critical nodes. We took advantage of two methodologies to conduct a systematic genetic analysis of WNT signaling in human cells: forward genetics in haploid cells using gene trap (GT)-based insertional mutagenesis (***Carette et al., 2009***), and targeted genome engineering by clustered regularly-interspaced short palindromic repeats (CRISPR)/CRISPR-associated protein 9 (Cas9) (***Cong et al., 2013***; ***Mali et al., 2013***).

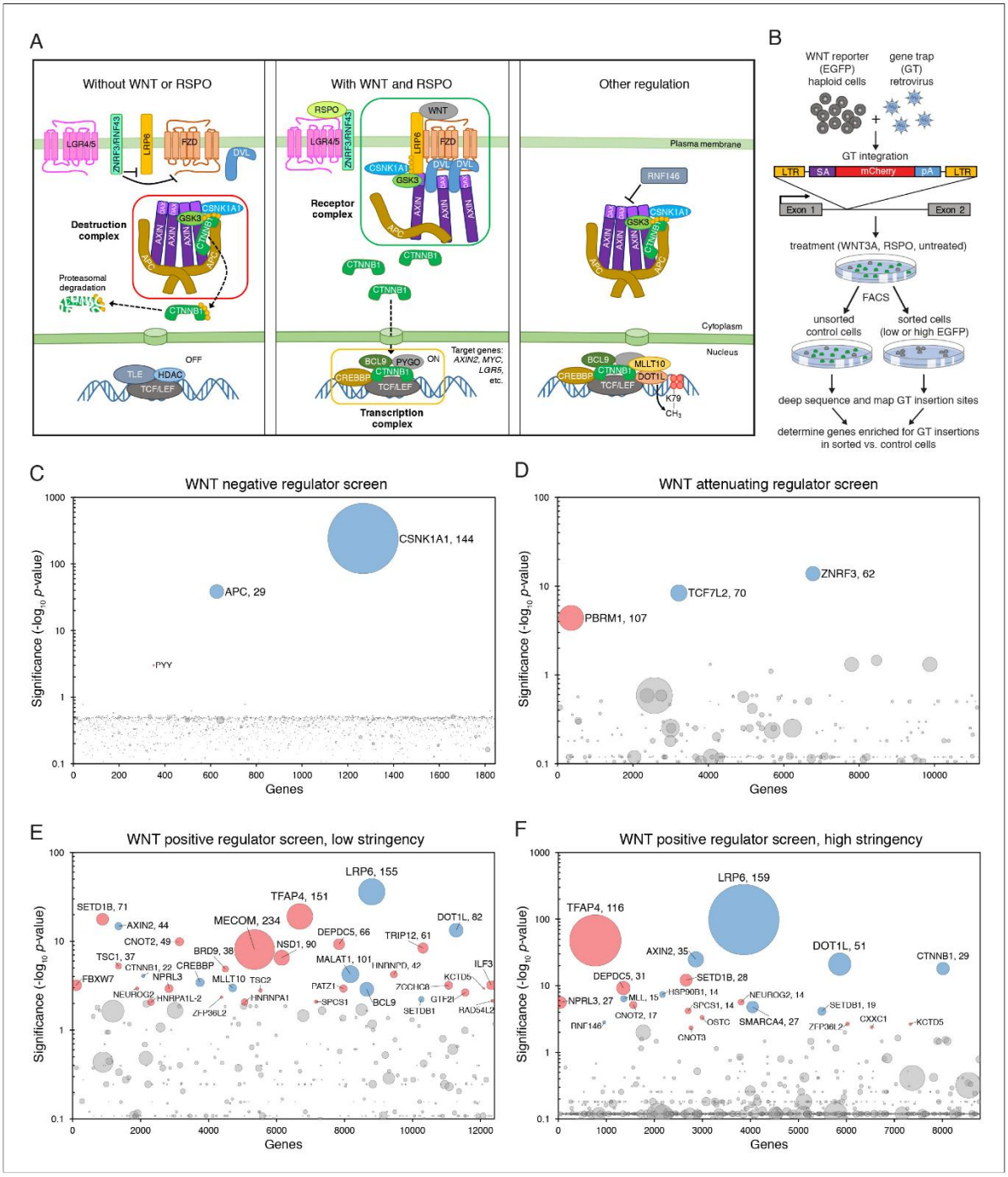

Figure 1. Reporter-based, forward genetic screens in haploid human cells identify negative, attenuating and positive regulators of WNT signaling. (**A**) Schematic model of canonical WNT signaling, highlighting the main pathway components and regulatory events in the absence (left panel) and presence (center panel) of ligands, and other known regulators relevant to this work (right panel). When the pathway is off, the transcriptional co-activator β-catenin (CTNNB1) is constitutively targeted for proteasomal degradation by the destruction complex, composed of the scaffold proteins

Figure 1 continued on next page

Figure 1 continued

adenomatous polyposis coli (APC) and AXIN, and the kinases glycogen synthase kinase 3 (GSK3) and casein kinase 1α (CSNK1A1). The T-cell-specific transcription factor (TCF)/lymphoid enhancer-binding factor (LEF) family of transcription factors, together with transducin like enhancer of split (TLE) and histone deacetylases (HDAC), repress WNT target genes. Binding of WNT to its co-receptors frizzled (FZD) and low-density lipoprotein receptor-related protein 6 (LRP6) leads to the assembly of a receptor complex that inactivates the destruction complex through a mechanism involving recruitment of AXIN by LRP6 and the adapter protein dishevelled (DVL). Consequently, CTNNB1 accumulates in the cytoplasm, translocates to the nucleus and promotes WNT target gene transcription in cooperation with TCF/LEF and other co-activators such as CREB-binding protein (CREBBP) and B-cell CLL/lymphoma 9 protein (BCL9). R-spondins (RSPOs) are secreted proteins that potentiate the response of stem cells to WNT ligands by blocking the degradation of FZD and LRP6 receptors. RSPO binds to leucine-rich repeat-containing G-protein-coupled receptors (LGRs) and neutralizes two transmembrane E3 ubiquitin ligases, ZNRF3 and RNF43, that clear WNT receptors from the cell surface. Other regulatory mechanisms include modulation of AXIN levels by the poly ADP-ribosylation-dependent E3 ubiquitin ligase RNF146, and recruitment of DOT1L and MLLT10, two proteins involved in histone H3 K79 methylation, to WNT target genes. (**B**) Schematic of WNT reporter-based forward genetic screens in haploid human cells using a GT-bearing retrovirus for mutagenesis, followed by phenotypic enrichment by FACS. LTR, long terminal repeats; SA, splice acceptor; pA, polyadenylation signal. (**C–F**) Circle plots depicting genes enriched for GT insertions in screens for negative (**C**), attenuating (**D**) and positive (**E and F**) regulators of WNT signaling. Two independent screens for positive regulators were performed at low (**E**) and high (**F**) selection stringencies by sorting for cells with the lowest 10% and 2% WNT reporter fluorescence, respectively. The y-axis indicates the significance of GT insertion enrichment in the sorted vs. the control cells (expressed in units of $-\log_{10}$FDR-corrected *p*-value) and the x-axis indicates genes (in random order) for which GT insertions were mapped in the sorted cells. Genes with FDR-corrected *p*-value<0.01 are labeled and colored in light blue if they encode a known pathway component, or in pink if their product has not been previously implicated as a regulator of canonical WNT signaling. The diameter of each circle is proportional to the number of unique inactivating GT insertions mapped in the sorted cells, which is also indicated next to the gene name for the most significant hits with FDR-corrected *p*-values<10^{-4}.

DOI: 10.7554/eLife.21459.003

The following figure supplement is available for figure 1:

Figure supplement 1. Characterization of HAP1-7TGP, a haploid human cell line harboring a WNT-responsive fluorescent reporter (**A–D**), and depiction of FACS gates and phenotypic enrichment during various reporter-based forward genetic screens (**E–H**).

DOI: 10.7554/eLife.21459.004

The WNT pathway is a fundamental signaling system that plays central roles in embryonic development, regeneration and cancer (reviewed in ***Hoppler and Moon, 2014***). During development, WNT signaling orchestrates transcriptional programs that regulate cell proliferation and survival, cell fate determination, and tissue patterning. In adults, WNT signaling is instrumental in defining stem cell niches in multiple organs, which maintain tissue homeostasis during routine turnover or following injury. Overactive WNT signaling can be oncogenic, driving both the initiation and maintenance of various types of cancer, most notably colorectal cancer (CRC).

While the pathway has been studied intensively (we provide a snapshot in ***Figure 1A*** and refer readers to the legend for details), critical steps remain poorly understood even 34 years after the discovery of '*int1*', as mammalian WNT was initially called (***Nusse and Varmus, 1982***). The complex circuitry of the pathway may mask unknown regulatory mechanisms overlaid on the core module, making it an ideal system for an in-depth, methodical genetic dissection, extending a rich tradition of genetic studies (***Nüsslein-Volhard and Wieschaus, 1980***). Known pathway components would serve to benchmark any new discoveries, and new discoveries would likely have important therapeutic implications due to the pathway's direct relevance to stem cell biology and cancer.

We initially probed the intact pathway through genome-wide, forward genetic screens for negative, attenuating and positive regulators to define the basic set of genes required for signaling in haploid human cells. We identified many of the known core pathway components and found a new requirement for the transcription factor AP-4 (TFAP4). Unexpectedly, these screens uncovered a dominant allele of *AXIN2* that dissociated β-catenin (CTNNB1) protein stabilization, considered the decisive event in WNT signaling, from its transcriptional activity. To find factors required for amplification of WNT responses by R-spondins (RSPOs, ***Figure 1A***), we devised a sensitized screen for RSPO-enhanced WNT signaling and uncovered a requirement for the glycophosphatidylinositol (GPI) anchor biosynthetic machinery and glypicans. Finally, we searched for mutations that could suppress constitutive signaling in cells with compromised function of the CTNNB1 destruction complex, recapitulating the most common defect in oncogenic WNT signaling. Suppressor screens in cells lacking adenomatous polyposis coli (APC) or casein kinase 1α (CSNK1A1), the two rate-limiting negative regulators of the pathway in haploid cells, revealed two distinct mechanisms that regulate CTNNB1 abundance and transcriptional activity, respectively. One mechanism was specific to cells

lacking CSNK1A1, but not APC, suggesting that different components of the destruction complex have different functions in WNT signaling beyond their common function controlling CTNNB1 protein abundance.

Through a quantitative comparative analysis across seven screens, we confirmed epistatic relationships for known regulators and predicted them for new ones. The combined results of these screens provide a comprehensive resource for understanding the regulation of canonical WNT signaling.

Results

Forward genetic screens in haploid human cells identify negative, attenuating, and positive regulators of WNT signaling

A central goal of this project was to search for quantitative and context-specific regulators of WNT signaling in an unbiased and comprehensive manner. We adopted two design principles that exploited the flexibility of forward genetics in cultured human cells. First, as a means of phenotypic enrichment, we chose a fluorescence-based, quantitative transcriptional reporter of WNT signaling. Since WNT reporter fluorescence is a continuous readout, in contrast to digital readouts such as cell viability or the presence or absence of a phenotype, it enabled us to enrich for cells with enhanced or reduced signaling phenotypes by fluorescence activated cell sorting (FACS) with complete flexibility on the stringency of selection. Second, all screens were performed in a pooled format following genome-scale insertional mutagenesis using a GT-bearing retrovirus, which contains a strong splice acceptor site and can therefore disrupt genes when it integrates in either exons or introns. This mutagenesis method is untargeted, distinguishing it from approaches in which short hairpin RNAs or single guide RNAs (sgRNAs) are designed to perturb a pre-defined set of cistrons.

We constructed and thoroughly characterized a clonal haploid human cell line, hereafter called HAP1-7TGP, in which expression of enhanced green fluorescent protein (EGFP) is driven by an established WNT-responsive element containing the seven TCF/LEF-binding sites, minimal promoter and 5'UTR of the SuperTOPflash reporter (***Fuerer and Nusse, 2010***; ***Figure 1—figure supplement 1A–1D***). While this construct has been used extensively to report on WNT responses, it may not mimic all endogenous regulatory sequences driving WNT target gene expression. In particular, the effects of proteins involved in modifying chromatin structure could differ between the reporter and endogenous target genes. Given these limitations, whenever possible we confirmed new regulatory mechanisms by measuring endogenous WNT target gene activity or assessing WNT-dependent phenotypes in model organisms.

To obtain saturating mutational coverage of the genome, we started our screens with 120 million HAP1-7TGP cells (or engineered derivatives thereof) mutagenized with the GT retrovirus, ensuring that the mutant cell population as a whole contained multiple (up to a few hundred) independent lesions in every gene (***Figure 1B***). The screens should therefore capture most genes involved in the phenotype being enriched for, except for genes required for the viability of haploid cells and genes with redundant function, since the probability of independent GT integrations disrupting redundant genes in the same haploid cell is vanishingly small. This limitation is inherent to all forward genetic screens that use random or untargeted mutagenesis.

After sequential rounds of FACS-based phenotypic enrichment and growth (HAP1-7TGP cells do not require WNT signaling for growth, enabling the propagation of cells with decreased or increased WNT signaling activity following phenotypic enrichment), we mapped retroviral integration sites at nucleotide resolution by deep sequencing an amplified library containing junctions between GTs and flanking genomic DNA (***Figure 1B***; see Materials and methods). Sequence reads from the sorted cells were compared to those from control, unsorted cells to identify genes enriched for GT insertions in the sorted cell population. Disruption of these genes would be expected to cause the phenotype used as the basis for selection.

We devised a genome-wide screen to identify the rate-limiting negative regulators of WNT signaling (i.e. genes whose disruption leads to constitutive pathway activity) in haploid human cells. We used FACS to sort mutagenized HAP1-7TGP cells with high WNT reporter activity in the absence of WNT ligand ('$EGFP^{+}$' gate in ***Figure 1—figure supplement 1E***). Following two rounds of sorting (see Materials and methods), GT insertions in only three genes showed statistically significant (false

Table 1. Relative gene expression level of selected WNT pathway regulators in HAP1 cells. RPKM values from duplicate RNAseq datasets generated as described in Materials and methods from two different passages of WT HAP1 cells are shown. Groups of paralogues and genes with similar functions are shaded in alternating colors to facilitate comparisons.

	RPKM		
Gene	Replicate 1	Replicate 2	Average
LGR4	160.61	174.69	167.65
LGR5	0.02	0.00	0.01
LGR6	0.02	0.00	0.01
ZNRF3	30.90	33.30	32.10
RNF43	0.12	0.08	0.10
LRP5	55.92	64.38	60.15
LRP6	109.51	121.08	115.30
FZD1	19.57	18.85	19.21
FZD2	19.56	21.09	20.33
FZD3	48.02	55.82	51.92
FZD4	19.60	22.10	20.85
FZD5	31.85	34.52	33.19
FZD6	33.53	31.95	32.74
FZD7	13.89	14.89	14.39
FZD8	4.02	4.48	4.25
FZD9	3.66	2.80	3.23
FZD10	10.40	9.86	10.13
DVL1	73.91	69.61	71.76
DVL2	51.74	48.80	50.27
DVL3	88.84	90.25	89.54
APC	80.47	85.22	82.84
APC2	2.94	3.69	3.32
AXIN1	55.97	54.07	55.02
AXIN2	10.04	12.51	11.27
CSNK1A1	111.18	109.57	110.37
GSK3A	75.97	69.21	72.59
GSK3B	62.79	69.98	66.39
TCF7L2	23.89	27.69	25.79
LEF1	12.34	14.80	13.57
CTNNB1	324.05	308.53	316.29
CREBBP	141.92	165.58	153.75
PIGL	4.07	4.51	4.29
GPC4	209.39	229.86	219.63
GPC6	13.88	14.90	14.39
TFAP4	36.99	41.94	39.46
SERBP1	721.65	698.99	710.32
HUWE1	631.58	777.06	704.32

DOI: 10.7554/eLife.21459.005

discovery rate (FDR)-corrected *p*-value<0.01) enrichment in the sorted cells: *CSNK1A1*, *APC* and *PYY* (***Figure 1C*** and ***Supplementary file 1***). We mapped 144 independent GT insertions in *CSNK1A1* and 29 in *APC*, showing that our mutagenesis had indeed targeted each gene multiple times. CSNK1A1 and APC are core components of the destruction complex that suppresses WNT signaling by promoting CTNNB1 degradation (***Figure 1A***); their identification as top hits reassured us that our screening strategy could identify important regulators of canonical WNT signaling. Genes encoding other known negative regulators of the pathway, such as *GSK3A* and *GSK3B* or *AXIN1* and *AXIN2*, presumably did not score as hits in this screen due to redundancy, as suggested by their expression profile in HAP1 cells (***Table 1***). We demonstrate later that AXIN1 and AXIN2 are indeed functionally redundant in HAP1 cells (***Figure 3—figure supplement 1B***). The fact that *APC*, but not *APC2*, was identified as a hit indicates that these two genes are not redundant in HAP1 cells, a conclusion that is supported by the relatively low expression level of *APC2* (***Table 1***).

To identify attenuating regulators of WNT signaling (i.e. genes whose disruption amplifies cellular responses to WNT ligands), we stimulated mutagenized HAP1-7TGP cells with a sub-saturating dose of WNT3A (12.5% WNT3A conditioned medium (CM), ***Figure 1—figure supplement 1B***) and sorted for cells with the highest 2% EGFP fluorescence ('highest 2%' gate in ***Figure 1—figure supplement 1F***). Following two rounds of FACS sorting, three genes were significantly enriched for GT insertions (***Figure 1D*** and ***Supplementary file 1***). *ZNRF3* was the top hit. Eliminating ZNRF3 or RNF43, two transmembrane E3 ubiquitin ligases, has been shown to amplify WNT signaling by increasing FZD and LRP6 levels on the cell surface (***Hao et al., 2012***; ***Koo et al., 2012***; ***Figure 1A***). Only *ZNRF3* is expressed at significant levels in HAP1 cells (***Table 1***), explaining why it was a hit in this screen. The second most significant hit of this screen was *TCF7L2*, encoding a TCF/LEF family transcription factor that can also function as an attenuating regulator of WNT target genes (***Tang et al., 2008***). Loss of either ZNRF3 or TCF7L2 is predicted to potentiate signaling responses rather than making them WNT-independent, explaining why these genes did not score in the negative regulator screen (***Figure 1C*** and ***Supplementary file 1***). These findings highlight one of the advantages of using a reporter with a graded output: different regulatory layers

in the pathway can be revealed by subtle alterations in selection conditions.

In a screen for positive regulators of canonical WNT signaling (i.e. genes whose disruption reduces signaling output), we stimulated mutagenized HAP1-7TGP cells with a near-saturating dose of WNT3A (50% WNT3A CM, ***Figure 1—figure supplement 1B***) and enriched for cells with the lowest 10% reporter fluorescence ('lowest 10%' gate in ***Figure 1—figure supplement 1G***) during two sequential rounds of FACS sorting and amplification. Thirty-three genes were significantly enriched for GT insertions in the sorted cells (***Figure 1E*** and ***Supplementary file 1***). These included genes encoding several known positive regulators of the pathway, such as the WNT co-receptor LRP6, components of the WNT transcription complex including CTNNB1, CREBBP and BCL9, and components of a histone H3 K79 methyltransferase complex including DOT1L and MLLT10 (***Figure 1A***). As expected, regulators with redundant expression profiles in HAP1 cells, such as FZDs or DVLs (***Table 1***), were not recovered in this screen. Increasing the stringency of selection by sorting for cells with the lowest 2% reporter fluorescence ('lowest 2%' gate in ***Figure 1—figure supplement 1H***) did not change the results of the screen significantly (***Figure 1F*** and ***Supplementary file 1***); despite differences in the significance of GT insertion enrichment compared to the less stringent screen, the order of the top hits was generally maintained. Considering the multiple experimental steps involved, the results are remarkably reproducible. Henceforth, we refer to each of these two screens for positive regulators as the 'low stringency' (***Figure 1E***) and the 'high stringency' (***Figure 1F***) screen, respectively, and to both of them jointly as the 'WNT screens'.

The second most significant hit in both WNT screens for positive regulators, following *LRP6*, was *TFAP4* (***Figure 1E and F***, and ***Supplementary file 1***), a gene encoding a transcription factor not previously implicated in regulation of canonical WNT signaling. The fourth and third most significant hit in the low (***Figure 1E***) and high (***Figure 1F***) stringency WNT screens, respectively, was *AXIN2*, encoding the CTNNB1 destruction complex scaffold AXIN2. It was perplexing to find *AXIN2* in a screen for *positive* regulators, since components of the destruction complex are *negative* regulators of the pathway, as illustrated by the presence of *APC* and *CSNK1A1* in our initial screen (***Figure 1C***). Experimental validation and analysis of both *TFAP4* and *AXIN2* follows in the two sections below.

These results establish that reporter-based, genome-wide forward genetic screens in haploid human cells are an effective way to identify many non-redundant components of signaling pathways. The versatility afforded by the combination of a reporter with a continuous fluorescence readout and FACS as a means of enrichment enables identification of functionally distinct classes of genes including negative, attenuating and positive regulators.

TFAP4 regulates WNT signaling downstream of the CTNNB1 destruction complex

The second most significant hit in both screens for positive regulators of WNT signaling (***Figure 1E and F***, and ***Supplementary file 1***), was the gene encoding the transcription factor TFAP4, outranked only by the gene encoding the WNT co-receptor LRP6. TFAP4 is a helix-loop-helix leucine zipper transcription factor and a target of MYC (***Jung and Hermeking, 2009***) that has been implicated in epithelial-to-mesenchymal transformation and metastasis in CRC (***Jackstadt et al., 2013***; ***Shi et al., 2014***). Despite multiple reports correlating *TFAP4* expression and malignancy in gastrointestinal tumors (***Cao et al., 2009***; ***Liu et al., 2012***; ***Xinghua et al., 2012***), TFAP4 has not been previously implicated as a regulator of canonical WNT signaling.

We used CRISPR/Cas9 to generate two HAP1-7TGP cell lines, designated TFAP4^{CR-1} and TFAP4^{CR-2}, the first of which lacks TFAP4 and the second of which produces a truncated protein product that retains the leucine zipper motif (see Materials and methods, ***Figure 2C*** and ***Supplementary file 2***). We note that these and all the other cell lines generated using CRISPR/Cas9 and used in this work were isolated without any phenotypic selection and were genotyped by sequencing the single allele of the disrupted gene (see Materials and methods and ***Supplementary file 2***). TFAP4^{CR-1} and TFAP4^{CR-2} cells showed a substantial reduction in WNT3A-induced expression of endogenous *AXIN2*, a target gene commonly used as a metric for pathway activity (***Figure 2A***). The defect in target gene induction correlated with the severity of the two mutant alleles of *TFAP4*. WNT3A-induced reporter activation in TFAP4^{CR-1} cells could be rescued by re-expression of TFAP4 (***Figure 2B***). TFAP4 overexpression in WT HAP1-7TGP cells increased WNT3A-induced reporter signal by 2.6-fold but did not induce reporter activity in unstimulated cells (***Figure 2B***), suggesting TFAP4 is a limiting factor for WNT signaling in these cells. The gain- and

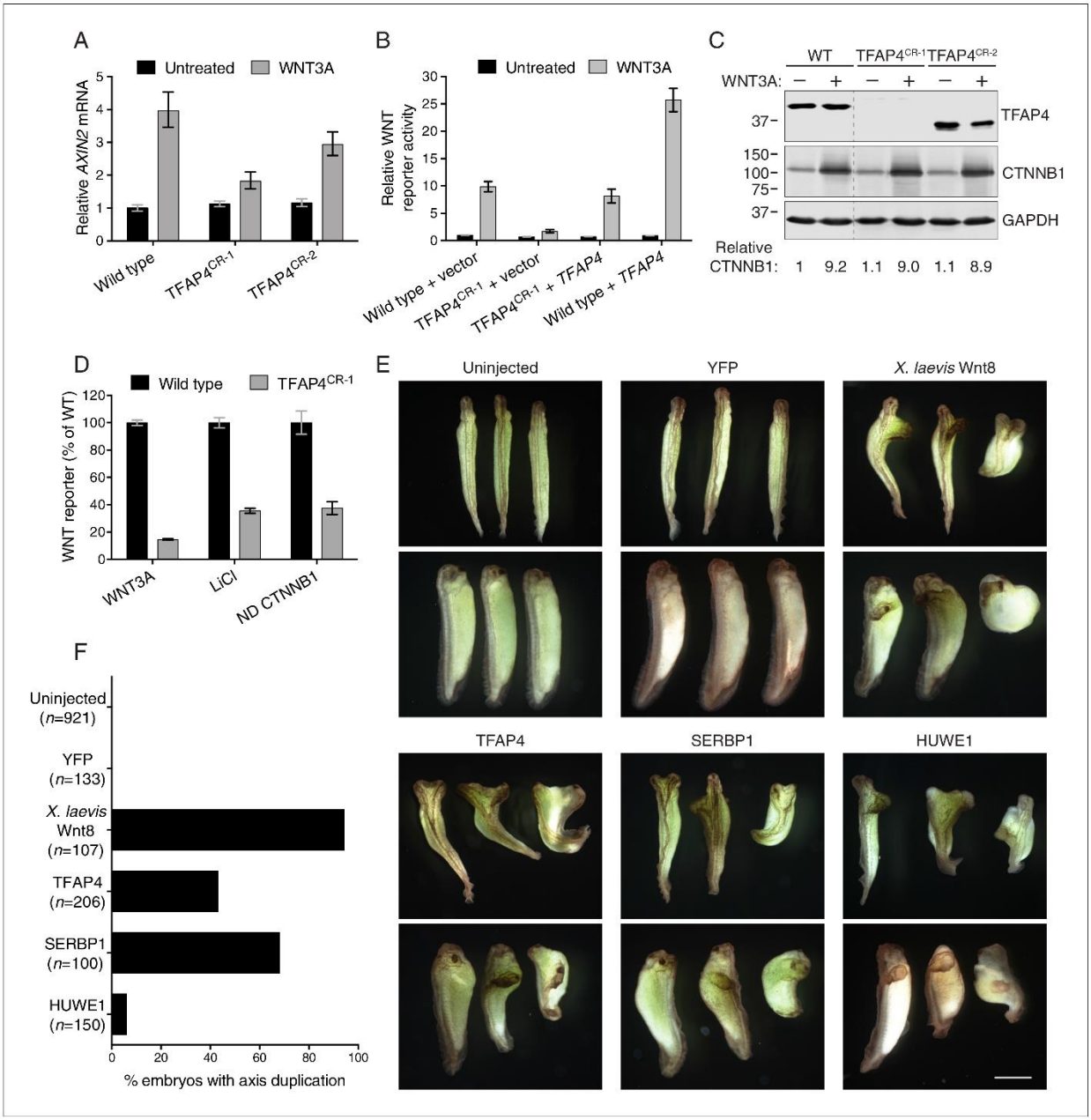

Figure 2. The transcription factor TFAP4 regulates WNT signaling downstream of the CTNNB1 destruction complex (**A–D**), and ectopic expression of TFAP4, SERBP1 and HUWE1 in *X. laevis* embryos induces secondary body axis formation (**E–F**). (**A**) *AXIN2* mRNA (average ± standard deviation (SD) *AXIN2* mRNA normalized to *HPRT1* mRNA, each measured in triplicate reactions), relative to untreated WT cells, for single WT HAP1-7TGP and TFAP4^{CR} clonal cell lines (see Materials and methods and ***Supplementary file 2*** for descriptions of all CRISPR/Cas9-engineered and GT-containing clonal cell lines). Cells were treated with 50% WNT3A CM where indicated. (**B**) WNT reporter activity (median ± standard error of the median (SEM) EGFP fluorescence from 1000 transfected cells), relative to untreated WT cells transfected with empty vector, for WT and TFAP4^{CR-1} cells transfected with pCS2^{+} empty vector or pCSDest-TFAP4 (together with pmCherry as a co-transfection marker). Cells were treated with 50% WNT3A CM where indicated. (**C**) Immunoblot analysis of WT and TFAP4^{CR} clonal cell lines treated with 50% WNT3A CM where indicated. CTNNB1 protein levels (CTNNB1 intensity normalized to GAPDH intensity), relative to untreated WT cells, are shown below the blots. Molecular weight standards (in

Figure 2 continued on next page

Figure 2 continued

kilodaltons (kDa)) are indicated on the left and the identity of the protein measured in each blot is indicated on the right. (**D**) WNT reporter activity (median ± SEM EGFP fluorescence from 10,000 WNT3A- or LiCl-treated cells, or from 2800 cells transfected with non-degradable (ND, S33Y mutant) CTNNB1) for WT and TFAP4^{CR-1} cells, depicted as percentage of WT. Cells were treated with 50% WNT3A CM or with 40 mM of the GSK3 inhibitor LiCl, or they were transfected with ND CTNNB1 and pmCherry as a co-transfection marker. (**E**) Four-cell stage *X. laevis* embryos were injected ventrally with 5 ng of mRNA encoding yellow fluorescent protein (YFP), *X. laevis* Wnt8, TFAP4, SERBP1 or HUWE1 and grown to stage 34. Dorsal (top panel of each pair) and lateral (bottom panel of each pair) views for groups of three embryos are shown. Scale bar = 1 mm. (**F**) Percentage of embryos with a secondary body axis. The total number of injected embryos is indicated below the group name.

DOI: 10.7554/eLife.21459.006

loss-of-function effects of TFAP4 demonstrate an important regulatory role in WNT signaling in human cells, consistent with its prominent position among the hits of the WNT screens—and indeed of several other screens described later in this work.

Because it is a transcription factor, TFAP4 is likely to function downstream of the destruction complex (***Figure 1A***). Depletion and truncation of TFAP4 in TFAP4^{CR-1} and TFAP4^{CR-2} cells, respectively, did not affect WNT-dependent accumulation of CTNNB1 protein, a measure of destruction complex activity (***Figure 2C***). We confirmed this conclusion by epistasis analysis, in which we activated signaling in WT HAP1-7TGP and TFAP4^{CR-1} cells at various levels of the pathway by 1) addition of WNT3A, which acts at the cell surface, 2) addition of the GSK3 inhibitor LiCl, which inactivates the destruction complex, or 3) transfection with a non-degradable (ND), constitutively active CTNNB1 mutant (S33Y), which activates the transcription complex directly (***Figure 2D***). The response of TFAP4^{CR-1} cells was reduced in all cases when compared to WT HAP1-7TGP cells. Thus, TFAP4 must act together with or downstream of CTNNB1.

To test if TFAP4 can influence WNT signaling during development, we employed an established body axis duplication assay in *Xenopus laevis* embryos. Activation of WNT signaling in the dorsal side of the early *X. laevis* embryo is a critical event in the formation of the Spemann organizer, an important tissue-organizing center found in vertebrates (***Spemann, 1938***), and ectopic activation of WNT signaling in the ventral side leads to formation of a second body axis. Microinjection of mRNA encoding TFAP4 into *X. laevis* embryos caused the formation of a secondary body axis (***Figure 2E and F***), demonstrating that TFAP4 can promote ectopic activation of WNT signaling during development.

Future work will focus on defining the contexts in which TFAP4 regulates WNT transcriptional responses under physiological and pathological conditions, given that its site of action downstream of the CTNNB1 destruction complex could be favorable for therapeutic intervention in cancers where WNT signaling is activated by loss of APC or by mutations that stabilize CTNNB1.

The C-terminal DAX domain of AXIN2 controls CTNNB1 transcriptional activity

AXIN genes encode the principal scaffold (reviewed in ***Tacchelly-Benites et al., 2013***; ***Song et al., 2014***) and limiting component (***Lee et al., 2003***) of the CTNNB1 destruction complex. The two paralogues in mammals, *AXIN1* and *AXIN2*, are functionally redundant (***Chia and Costantini, 2005***), although their expression patterns are quite distinct: *AXIN1* is expressed ubiquitously, while *AXIN2* is expressed at low levels in the absence of WNT signals (***Jho et al., 2002***). *AXIN2* is also the key component of a negative feedback loop in the WNT pathway (***Lustig et al., 2002***). As a universal and direct target gene of the pathway, its increased expression following stimulation with WNT can lead to elevated levels of the destruction complex and, consequently, reduced levels of CTNNB1. Given this well-established negative regulatory role, the enrichment of GT insertions mapping to *AXIN2* in HAP1-7TGP cells with *reduced* WNT reporter activity recovered during the WNT screens (***Figure 1E and F***, and ***Supplementary file 1***) presented us with a paradox.

An important clue emerged from a careful inspection of the distribution of GT insertions mapping to *AXIN2* in the sorted cells. In most hits from haploid genetic screens, exemplified by *LRP6* (***Figure 3A***), GT insertions cluster at the 5' end of the gene because of the propensity of retroviral integration near transcriptional start sites and because such insertions are likely to generate null alleles (***Carette et al., 2011a***). Contrary to this general case, nearly all GT insertions in *AXIN2* mapped to the opposite end of the gene in the last intron (***Figure 3A***). These insertions are

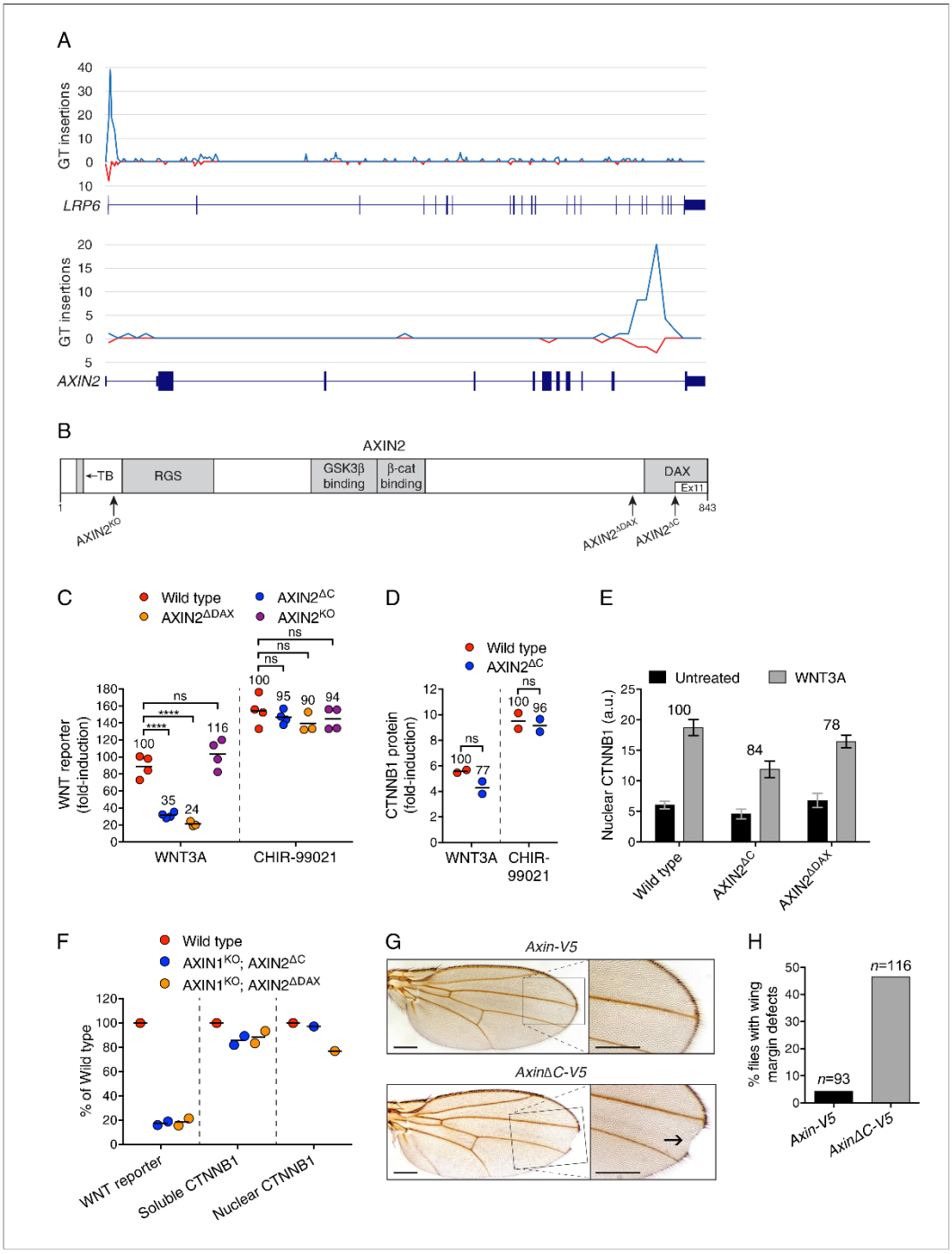

Figure 3. The C-terminal DAX domain of AXIN2 controls CTNNB1 transcriptional activity. (**A**) GT insertions in *LRP6* (top histogram) and *AXIN2* (bottom histogram) mapped for the sorted cells from the WNT positive regulator, low stringency screen (***Figure 1E***). The histograms depict the number of GT integrations in the sense (blue) or antisense (red) orientation, relative to the coding sequence of the gene, within consecutive 500 base pair (bp) intervals along the length of each gene. Due to the directionality of the splice acceptor in the GT, typically only sense GT insertions in introns disrupt

Figure 3 continued on next page

Figure 3 continued

the gene, whereas GT insertions in exons generally disrupt the gene regardless of orientation. RefSeq gene tracks for *LRP6* and *AXIN2* are shown beneath each histogram following the University of California, Santa Cruz (UCSC) genome browser display conventions: coding exons are represented by thick blocks, UTRs by thin blocks, and introns by horizontal lines connecting the blocks. Both genes are displayed with their 5' ends to the left, and encompass chromosome 12, bps 12267499–12116000 for *LRP6*, and chromosome 17, bps 65561999–65528500 for *AXIN2* (hg18). (**B**) Schematic representation of the human AXIN2 protein drawn to scale in the horizontal dimension. Amino acid numbers are indicated below, and arrows show the sites at which truncations were made by CRISPR/Cas9-mediated genome editing in the indicated cell lines. Known domains, regions and motifs (based on UniProt annotation) are depicted in gray (TB, tankyrase-binding motif). Exon 11, eliminated by GT insertions found in cells sorted during the WNT screens for positive regulators, is delineated by a thinner white block. (**C**) Fold-induction in WNT reporter (median EGFP fluorescence from 20,000 cells) following treatment with 50% WNT3A CM or 10 μM of the GSK3 inhibitor CHIR-99021. Each circle represents a unique clonal cell line (determined by genotyping, ***Supplementary file 2***), and the average of three to four independent clones for each genotype is indicated by a horizontal line. For each treatment, percentage reporter activation relative to WT cells is also indicated above each group of circles to facilitate comparisons. Significance was determined by one-way ANOVA, and is indicated as ****($p<0.0001$) or ns (not significant). (**D**) Fold-induction in soluble CTNNB1 protein (average CTNNB1 intensity normalized to ACTIN intensity from duplicate immunoblots) following treatment with 50% WNT3A CM or 10 μM CHIR-99021. Each circle represents a unique clonal cell line, and the average of two independent clones for each genotype is indicated by a horizontal line. Significance was determined by unpaired t-test with Welch's correction. Representative immunoblots used for quantification of CTNNB1 and ACTIN are shown in ***Figure 3—figure supplement 1C***. (**E**) Nuclear CTNNB1 (average nuclear fluorescence per unit area from three fields of view) in single clonal cell lines of the indicated genotypes was quantified as described in Materials and methods. Cells were treated with 50% WNT3A CM where indicated. For each cell line, the fold-increase in CTNNB1 nuclear accumulation following treatment with WNT3A, expressed as percentage of WT, is also indicated above the bars to facilitate comparisons. For WNT3A-treated cells, differences in nuclear CTNNB1 between WT and mutant cells were not statistically significant as determined by one-way ANOVA. Examples of confocal sections used for quantification of nuclear CTNNB1 are shown in ***Figure 3—figure supplement 2B–2D***. (**F**) WNT reporter activity (median EGFP fluorescence from 10,000 cells), soluble CTNNB1 protein (average CTNNB1 intensity normalized to ACTIN intensity from duplicate immunoblots), and nuclear CTNNB1 protein (average nuclear fluorescence per unit area from 2 to 3 fields of view), depicted as percentage of WT, for cells treated with 50% WNT3A CM. Each circle represents a unique clonal cell line, and where applicable the average of two independent clones is indicated by a horizontal line. (**G**) Adult *D. melanogaster* wings expressing *Axin-V5* (top images) or *AxinΔC-V5* (bottom images) under the control of the c765-Gal4 driver. Loss of sensory bristles and tissue at the wing margin, indicative of impaired Wg signaling, is shown (arrow) in the higher magnification view of the delineated area. While loss of Notch signaling can also result in wing margin defects due to a requirement of Notch signaling for Wg expression at the dorso-ventral boundary in the wing imaginal disc (***Diaz-Benjumea and Cohen, 1995***), we ruled out that possibility by confirming intact Wg expression in the wing imaginal disc of flies expressing *AxinΔC-V5* (***Figure 3—figure supplement 3B***). Scale bars = 20 μm. (**H**) Percentage of flies with wing margin defects. 4.3% of flies expressing *Axin-V5* exhibited loss of bristles at the wing margin, but no loss of wing tissue; 46.6% of flies expressing *AxinΔC-V5* exhibited loss of bristles at the wing margin as well as loss of wing tissue.

DOI: 10.7554/eLife.21459.007

The following figure supplements are available for figure 3:

Figure supplement 1. AXIN1 and AXIN2 are redundant in haploid human cells (**A–B**), and CTNNB1 protein is stabilized normally in $AXIN2^{\Delta C}$ cells (**C**).

DOI: 10.7554/eLife.21459.008

Figure supplement 2. Cells lacking the C-terminal DAX domain of AXIN2 exhibit normal CTNNB1 nuclear accumulation following WNT treatment.

DOI: 10.7554/eLife.21459.009

Figure supplement 3. Expression of an *Axin* transgene encoding C-terminally truncated protein compromises Wg signaling in *D. melanogaster*.

DOI: 10.7554/eLife.21459.010

predicted to produce a truncated AXIN2 protein product lacking exon 11 (***Figure 3B***), comprising half of the DAX domain, which has been implicated both in CTNNB1 destruction complex function and in interactions with the receptor complex at the plasma membrane (reviewed in ***Tacchelly-Benites et al., 2013***; ***Song et al., 2014***).

The results of the WNT screens (***Figure 1E and F***, and ***Supplementary file 1***) suggested that deletion of half of the DAX domain of AXIN2 reduces responsiveness to WNT. The ease of genome editing in haploid cells enabled us to precisely assess the magnitude of signaling defects by comparing multiple independent WT and mutant HAP1-7TGP clonal cell lines containing specific mutations in the single endogenous *AXIN2* allele, which minimized the likelihood of non-specific effects and accounted for interclonal variability. We used CRISPR/Cas9 to generate HAP1-7TGP cell lines lacking exon 11 of *AXIN2* (designated $AXIN2^{\Delta C}$, ***Figure 3B*** and ***Supplementary file 2***). Since incomplete protein domains can remain unfolded, we also generated multiple cell lines lacking the complete DAX domain ($AXIN2^{\Delta DAX}$) and, as a control, cell lines lacking *AXIN2* entirely ($AXIN2^{KO}$) (***Figure 3B*** and ***Supplementary file 2***). $AXIN2^{KO}$ clones exhibited no defect in WNT3A-dependent reporter induction (***Figure 3C***) due to redundancy with AXIN1 (***Figure 3—figure supplement 1A and B***, and ***Table 1***). However, $AXIN2^{\Delta C}$ and $AXIN2^{\Delta DAX}$ clones exhibited, on average, a 65% and a 76% reduction in WNT3A-induced signaling, respectively, compared to WT HAP1-7TGP cells (***Figure 3C***). All

AXIN2 mutant cell lines responded normally to the GSK3 inhibitor CHIR-99021 (**Figure 3C**), demonstrating that the reduction in WNT3A-induced signaling was not due to defects in downstream steps or to irrelevant factors affecting reporter fluorescence. The fact that C-terminally truncated AXIN2 reduced signaling induced by WNT3A explained why GT insertions generating this unusual *AXIN2* allele were enriched in the WNT screens for positive regulators. Since HAP1-7TGP cells also express AXIN1 (**Figure 3—figure supplement 1A** and **Table 1**), the effect of C-terminally truncated AXIN2 must be dominant.

We asked whether the reduction in WNT signaling caused by truncated AXIN2 was due to a defect in WNT3A-induced CTNNB1 stabilization. Surprisingly, WNT3A robustly promoted the stabilization of soluble CTNNB1 protein in AXIN2$^{\Delta C}$ cells (**Figure 3D** and **Figure 3—figure supplement 1C**), revealing a disconnect between CTNNB1 protein abundance and transcriptional activity. CTNNB1 accumulation in response to CHIR-99021 was also normal in AXIN2$^{\Delta C}$ cells (**Figure 3D**, and **Figure 3—figure supplement 1C**). The discrepancy between CTNNB1 stability and transcriptional activity was not caused by defective nuclear accumulation; in both AXIN2$^{\Delta C}$ and AXIN2$^{\Delta DAX}$ cells, accumulation of nuclear CTNNB1 following WNT treatment was largely normal (**Figure 3E** and **Figure 3—figure supplement 2**). We conclude from these experiments that deleting the DAX domain of AXIN2 dissociates CTNNB1 protein abundance from its transcriptional activity.

These effects could reflect an autonomous property of the AXIN2 protein lacking the DAX domain, or a more complex interaction with the remaining WT AXIN1. To rule out confounding effects due to AXIN1, we disrupted the single allele of *AXIN1* in individual AXIN2$^{\Delta C}$ and AXIN2$^{\Delta DAX}$ clonal cell lines to generate double-mutant cell lines (AXIN1^{KO}; AXIN2$^{\Delta C}$ and AXIN1^{KO}; AXIN2$^{\Delta DAX}$, respectively, **Supplementary file 2** and **Figure 3—figure supplement 1A**). The only AXIN protein present in these cells is truncated AXIN2 lacking either half or the entire DAX domain. Truncated AXIN2 caused the same effects upon elimination of AXIN1—decreased WNT3A-induced reporter activity despite normal accumulation of soluble and nuclear CTNNB1 (**Figure 3F** and **Figure 3—figure supplement 2**). These findings provide further evidence that AXIN2 truncations disrupt CTNNB1-mediated transcription through a novel mechanism intrinsic to this allele.

We tested the generality of our findings by introducing *Axin* transgenes into the fly *Drosophila melanogaster*, a model organism that has been used extensively for genetic studies of WNT signaling. We generated a transgene encoding an epitope-tagged (V5) fusion of the single *D. melanogaster* Axin protein lacking the last 41 amino acids (AxinΔC-V5, **Figure 3—figure supplement 3A**). These amino acids correspond to those encoded by exon 11 of human *AXIN2*, the exon disrupted by GT insertions in the WNT screens (**Figure 3A and B**). Expression of *AxinΔC-V5* impaired Wingless (Wg, fly WNT) signaling based on target gene expression and phenotypic readouts during both embryonic and larval development (**Figure 3G and H**, and **Figure 3—figure supplement 3B–H**). The observed defects in Wg signaling were not due to decreased expression of Wg itself (**Figure 3—figure supplement 3B and C**) or to increased expression of AxinΔC-V5 protein (**Figure 3—figure supplement 3E and F**). In control experiments, expression of WT *Axin-V5* (**Figure 3—figure supplement 3A**) at physiological levels (**Wang et al., 2016**) using the same promoter as for *AxinΔC-V5* did not disrupt Wg signaling (**Figure 3G and H**, and **Figure 3—figure supplement 3B–H**). The fact that in flies, like in haploid human cells, expression of an *Axin* transgene lacking the C-terminal domain reduces Wg signaling even in the presence of endogenous *Axin* is consistent with a dominant effect that restrains CTNNB1 transcriptional activity.

In summary, unbiased genome-wide screens for positive regulators of WNT signaling uncovered an unsuspected role for the C-terminal DAX domain of AXIN2 in controlling CTNNB1 transcriptional activity, since deletion of this domain led to a severely compromised transcriptional response despite normal accumulation of CTNNB1 protein. While the mechanistic basis of this process remains to be elucidated, our results cannot be explained by previously described functions of the AXIN DAX domain. The DAX domain has been implicated in AXIN polymerization, in interactions with DVL, and in mediating an intramolecular, auto-inhibitory interaction that allows the receptor complex to inactivate the destruction complex in a catalytic manner (**Fiedler et al., 2011**; **Kim et al., 2013**). These models predict that loss of the DAX domain would impair communication between the receptor complex and the destruction complex, leading to defective WNT-induced CTNNB1 stabilization, in contrast to our results (**Figure 3D and F**). Thus, the disconnect between CTNNB1 abundance and transcriptional activity caused by deletion of the DAX domain demonstrates a new biochemical function for this domain.

The discovery of this dominant allele of *AXIN2* was made possible by the untargeted nature of GT-based insertional mutagenesis and thus would not have emerged from strict loss-of-function screens such as those mediated by RNA interference or CRISPR/Cas9. Given that rare dominant alleles can provide mechanistic insights distinct from those afforded by null alleles, our findings justify the design of comprehensive 'exome-wide' sgRNA libraries for CRISPR/Cas9-based screens.

A comparative analysis of screens uncovers requirements for RSPO-potentiated signaling in response to low levels of WNT

RSPOs are stem cell growth factors that potentiate responses to WNT ligands by binding to LGR-family receptors and neutralizing the ZNRF3 and RNF43 E3 ubiquitin ligases to increase levels of WNT receptors on the cell surface (reviewed in ***de Lau et al., 2014***; ***Figure 1A***). Recurrent translocations in genes encoding RSPOs are found in some colorectal tumors and targeting the resulting fusion proteins blocks tumorigenesis (***Seshagiri et al., 2012***; ***Storm et al., 2016***). Mutations in RNF43 that mimic the effect of stimulation with RSPO have also been reported in multiple cancers (***Giannakis et al., 2014***). Regulators of RSPO-enhanced WNT signaling could therefore be important both in normal physiological and in pathological contexts.

HAP1-7TGP cells were responsive to RSPO-mediated effects on WNT signaling. RSPO1 markedly amplified the reporter response to low concentrations of WNT3A CM but was completely inactive in the absence of WNT (***Figure 4—figure supplement 1A***). We determined the concentration of WNT3A CM at which responsiveness to RSPO1 was maximal (***Figure 4—figure supplement 1B***) and used these conditions in a sensitized genome-wide screen for mediators of RSPO-enhanced WNT signaling. Notably, the concentration of WNT used in this screen, henceforth referred to as the 'low WNT + RSPO screen,' was 49-fold lower than that used in the WNT screens for positive regulators (***Figure 1E and F***).

Following treatment with WNT3A CM plus RSPO1, we isolated cells with the lowest 7% EGFP fluorescence ('lowest 7%' gate in ***Figure 4—figure supplement 1C***). After four consecutive sorts, which resulted in a marked enrichment of cells with diminished responsiveness to WNT3A CM plus RSPO1 (***Figure 4—figure supplement 1C***), we sequenced and mapped GT integrations (***Figure 4A*** and ***Supplementary file 1***). Reassuringly, the top hit was *LGR4*, the gene encoding the RSPO1 receptor, confirming that the screen was sensitive to requirements for RSPO1-dependent signaling. Top hits of this screen included many genes encoding known WNT regulators also uncovered in the WNT screens for positive regulators (***Figure 1E and F***, and ***Supplementary file 1***): *LRP6, AXIN2, DOT1L, MLL, CTNNB1, CREBBP, BCL9* and *RNF146*. *TFAP4*, encoding the required transcription factor we described earlier in this study, was also among the top hits (***Figure 4A*** and ***Supplementary file 1***).

We distinguished genes selectively required for RSPO-enhanced WNT signaling through a comparative analysis of the low WNT + RSPO screen (***Figure 4A*** and ***Supplementary file 1***) and both WNT screens for positive regulators conducted at a near-saturating dose of WNT (***Figure 1E and F***, and ***Supplementary file 1***). For this analysis, we used two different measures of gene disruption caused by GT integrations (see Materials and methods, ***Figure 4B*** and ***Supplementary file 3***). First, the FDR-corrected *p*-value, reflecting enrichment of GT integrations in the sorted vs. the unsorted cells from each screen, was used to set a stringent cutoff for inclusion of hits in the analysis. Second, an Intronic GT Insertion Orientation Bias (IGTIOB) score, reflecting enrichment of sense vs. antisense GT integrations (relative to the coding sequence of the gene) in introns only for the sorted cells from each screen, was used to compare hits between screens. The IGTIOB score relies on the fact that generally only sense GT insertions in introns should inactivate genes due to the directionality of the splice acceptor. Genes selectively required for RSPO-enhanced WNT signaling should show a pattern of GT enrichment similar to that of the gene encoding the RSPO receptor, *LGR4*. Conversely, regulators required for WNT signaling under all treatment conditions should be equally enriched for GT integrations in all screens (***Figure 4B*** and ***Supplementary file 3***).

The most striking outcome of this analysis was the identification of multiple genes encoding components of the GPI-anchor biosynthetic pathway that were enriched for GT insertions in the low WNT + RSPO screen but not the WNT screens (***Figure 4B*** and ***Supplementary file 3***). Fourteen genes in the GPI biosynthesis pathway had an FDR-corrected *p*-value<0.05 (***Supplementary file 1*** and ***Figure 4—figure supplement 1D***). Therefore, a GPI-anchored protein may be particularly important in mediating signaling triggered by a combination of RSPO and a low dose of WNT. The

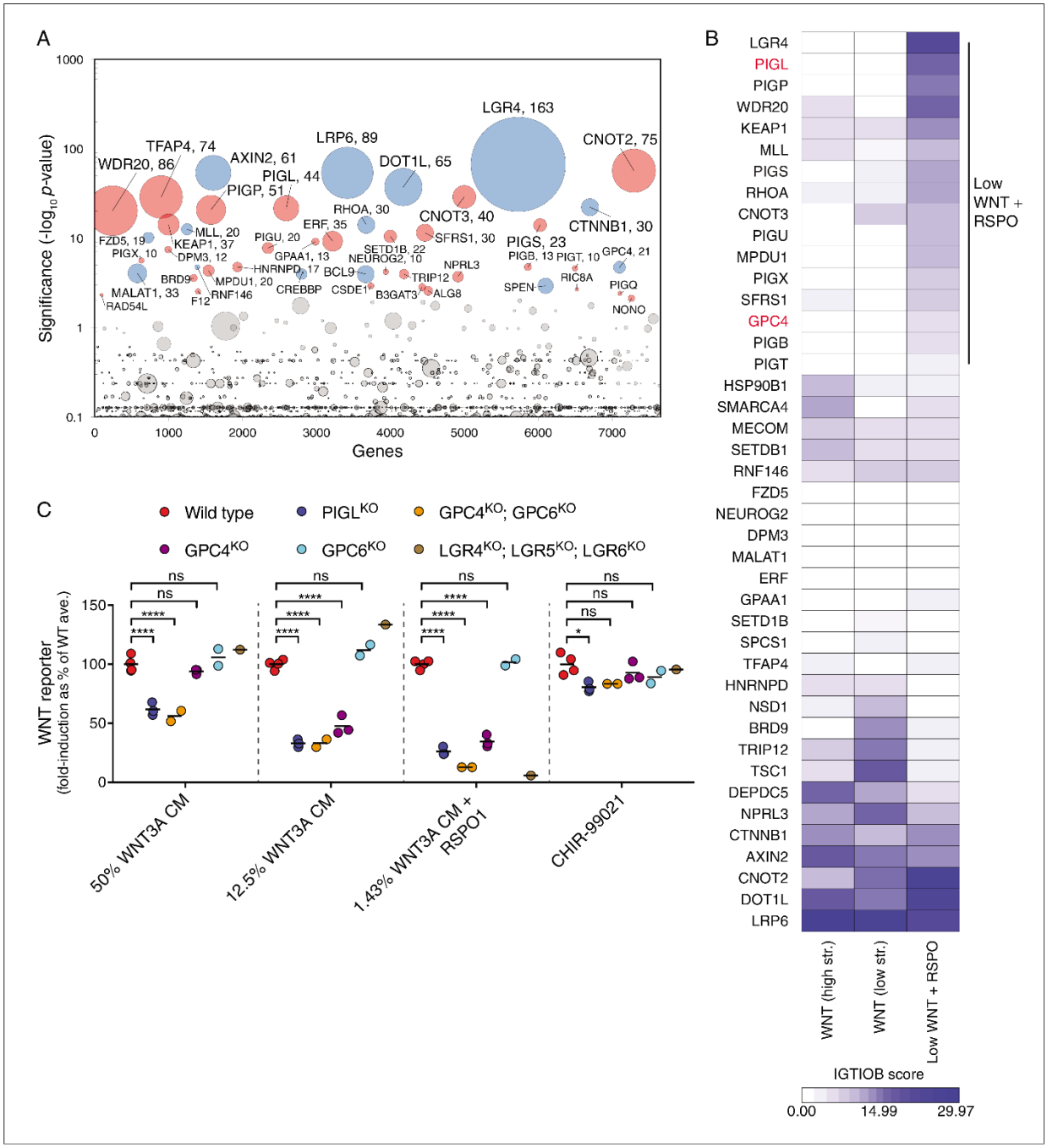

Figure 4. A comparative analysis of screens uncovers requirements for RSPO-potentiated signaling in response to low levels of WNT. (**A**) Circle plot depicting genes enriched for GT insertions in the low WNT + RSPO screen for regulators of RSPO-enhanced WNT signaling. See legend to ***Figure 1C–F*** for details. (**B**) Heat map comparing the two WNT positive regulator screens (***Figure 1E and F***) and the low WNT + RSPO screen (***Figure 4A***). Genes enriched for GT insertions (FDR-corrected *p*-value<10^{-4}) in at least one of the three screens were clustered based on their IGTIOB score in each screen (see Materials and methods and ***Supplementary file 3***). A group of genes preferentially enriched for GT insertions in the low WNT + RSPO screen is

Figure 4 continued on next page

Figure 4 continued

indicated, headlined by the RSPO receptor LGR4. Genes selected for a detailed analysis are labeled in red. (**C**) Fold-induction in WNT reporter (average EGFP fluorescence from 10,000 cells) following treatment with 50% WNT3A CM, 12.5% WNT3A CM, 1.43% WNT3A CM + 20 ng/ml RSPO1 or 10 μM of the GSK3 inhibitor CHIR-99021, expressed as percentage of the average for WT cells to facilitate comparisons. Each circle represents the fold-induction for a unique clonal cell line (determined by genotyping, ***Supplementary file 2***), and where applicable, the average of two to four independent clones for each genotype is indicated by a horizontal line. Significance was determined by one-way ANOVA, and is indicated as **** (p<0.0001), *(p<0.05) or ns (not significant).

DOI: 10.7554/eLife.21459.011

The following figure supplement is available for figure 4:

Figure supplement 1. Comparative genetic screens uncover requirements for RSPO-potentiated signaling in response to low levels of WNT.

DOI: 10.7554/eLife.21459.012

gene encoding the glypican GPC4, a GPI-linked heparan sulfate proteoglycan (HSPG), was also preferentially enriched for GT insertions in the low WNT + RSPO screen (***Figure 4B*** and ***Supplementary file 3***), with an FDR-corrected *p*-value=1.92x10^{-5}, more significant than those of established WNT signaling components such as *CREBBP* and *BCL9* (***Figure 4A*** and ***Supplementary file 1***). Glypicans are important for concentrating extracellular ligands at the cell surface, and GPC4 has been proposed to bind and concentrate WNT3A and WNT5A in the vicinity of their receptors (***Sakane et al., 2012***). However, since neither GPI biosynthesis nor glypican genes were significant hits in the WNT screens for positive regulators (***Figure 1E and F***, and ***Supplementary file 1***), we hypothesized that these genes must play a crucial role under the conditions of the low WNT + RSPO screen, either by mediating RSPO responsiveness like *LGR4*, or by selectively affecting reception of WNT3A at the very low concentration used in this screen.

To distinguish between these two possibilities, we analyzed the signaling response to WNT3A alone or to a low concentration of WNT3A plus RSPO1 in clonal HAP1-7TGP cell lines in which we disrupted *PIGL*, a gene in the GPI biosynthesis pathway (***Figure 4—figure supplement 1D***), or *GPC4* (designated PIGL^{KO} and GPC4^{KO}, respectively, ***Supplementary file 2***). The glypican GPC6 is redundant with GPC4 in certain contexts (***Allen et al., 2012***), so we also generated HAP1-7TGP cell lines in which we disrupted *GPC6* alone or in combination with *GPC4* (designated GPC6^{KO} and GPC4^{KO}; GPC6^{KO}, respectively, ***Supplementary file 2***). As a control we generated a HAP1-7TGP cell line lacking all three RSPO receptors (designated LGR4^{KO}; LGR5^{KO}; LGR6^{KO}, ***Supplementary file 2***).

As expected from the role of LGRs as exclusive mediators of responsiveness to RSPO but not to WNT, LGR4^{KO}; LGR5^{KO}; LGR6^{KO} cells did not respond to RSPO1 in the presence of a low dose of WNT3A, but exhibited no signaling defects when stimulated with higher doses of WNT3A alone (***Figure 4C*** and ***Figure 4—figure supplement 1E***). In contrast, PIGL^{KO} and GPC4^{KO}; GPC6^{KO} cells manifested some reduction in signaling when stimulated with a near-saturating dose of WNT3A alone, but this reduction was more pronounced following treatment with lower doses of WNT3A alone or a low dose of WNT3A combined with RSPO1 (***Figure 4C*** and ***Figure 4—figure supplement 1E***). GPC4^{KO} cells were stimulated normally by a near-saturating dose of WNT3A and exhibited a smaller defect than GPC4^{KO}; GPC6^{KO} when stimulated with a lower dose of WNT3A alone or in combination with RSPO1, while GPC6^{KO} cells had no signaling defect at all (***Figure 4C***). These results suggest that GPC4 and GPC6 are partially redundant in HAP1 cells, since they are both expressed albeit at very different levels (***Table 1***). In a control experiment, WNT signaling induced by the GSK3 inhibitor CHIR-99021 was largely unaffected in all mutant cell lines (***Figure 4C***), demonstrating that there were no signaling defects downstream of the receptor complex (***Figure 1A***).

Taken together these results indicate that genes in the GPI biosynthesis pathway and *GPC4/6* are required for signaling in response to low levels of WNT, and explain why they may have been more prominent hits in the low WNT + RSPO than in the WNT screens (***Figures 1E,F*** and ***4A*** and ***Supplementary file 1***). Presently, we cannot confirm or discount an additional, direct contribution of GPC4/6 or another GPI-anchored protein to RSPO reception, as we have been unable to directly measure responses to RSPO alone in HAP1 cells. Yet, the presence in all RSPOs of a thrombospondin domain capable of binding heparin sulfate and mediating interactions with HSPGs such as glypicans (***Nam et al., 2006***; ***Ohkawara et al., 2011***) makes this an intriguing possibility.

In summary, our comparative analysis shows that forward genetic screens in haploid human cells are exquisitely sensitive to both the identity and concentration of ligands used to initiate signaling. They can uncover ligand-specific receptors, such as LGR4, or accessory factors that are rate-limiting for signaling only under specific regimes of ligand concentrations, such as GPI biosynthetic enzymes and glypicans. Of note, the low WNT + RSPO screen (***Figure 4A*** and ***Supplementary file 1***) was sensitive enough to reveal redundant regulators, such as *FZD5* and *DVL3* (***Table 1***), that were not significant hits under the near-saturating WNT3A dose used in the WNT screens (***Figure 1E and F***, and ***Supplementary file 1***).

Suppressor screens reveal genotype-specific signaling requirements

Given the potential of comparative screens to identify context-specific regulators, we searched for genes whose inactivation would suppress the pathological signaling that ensues when key negative regulators of the WNT pathway are lost. Since negative regulators such as APC are frequently mutated in cancer, suppressor mutations and the mechanisms through which the affected genes regulate signaling may reveal therapeutic targets.

Our initial screen for rate-limiting negative regulators of WNT signaling (***Figure 1C*** and ***Supplementary file 1***) suggested that disruption of the single allele of *APC* or *CSNK1A1* in HAP1-7TGP cells should lead to constitutive activation of the pathway. We designed two screens to uncover suppressors of ligand-independent signaling induced by loss of *APC* or *CSNK1A1* (***Figure 5A***). We disrupted *APC* or *CSNK1A1* in HAP1-7TGP cells using CRISPR/Cas9 and isolated two clonal cell lines designated $APC^{KO\text{-}1}$ and $CSNK1A1^{KO\text{-}1}$, respectively (***Supplementary file 2***). Sequencing revealed frameshift mutations in the single allele of each gene. We confirmed by immunoblotting that the APC signal was reduced by >96.5% in $APC^{KO\text{-}1}$ cells, and CSNK1A1 was undetectable in $CSNK1A1^{KO\text{-}1}$ cells (***Figure 5—figure supplement 1A***). The level of constitutive WNT reporter fluorescence in both the $APC^{KO\text{-}1}$ and $CSNK1A1^{KO\text{-}1}$ clones was higher than that induced by near-saturating WNT3A or by the GSK3 inhibitor CHIR-99021 in WT HAP1-7TGP cells (***Figure 5—figure supplement 1B***).

In two independent screens, henceforth referred to as the 'APC suppressor screen' and the 'CSNK1A1 suppressor screen,' respectively, we mutagenized $APC^{KO\text{-}1}$ and $CSNK1A1^{KO\text{-}1}$ cells with GT retrovirus and enriched for cells with the lowest 10% WNT reporter fluorescence ('lowest 10%' gate in ***Figure 5—figure supplement 1C and D***). Following two sequential rounds of sorting and amplification, 43% of $APC^{KO\text{-}1}$ and 42% of $CSNK1A1^{KO\text{-}1}$ cells were within this gate (***Figure 5—figure supplement 1C and D***). We analyzed the cells sorted during each screen and their respective unsorted control populations for enrichment of GT insertions (***Figure 5B and C***, and ***Supplementary file 1***).

A three-way comparative analysis of the WNT positive regulator, low stingency screen in WT HAP1-7TGP cells (***Figure 1E***), the APC suppressor screen and the CSNK1A1 suppressor screen (all done at similar selection stringencies) revealed expected similarities and differences based on established epistatic relationships, as well as a number of unexpected findings (***Figure 5D*** and ***Supplementary file 3***). The isogenic background of the cells in these three screens and the very high statistical significance of the top hits (only genes with an FDR-corrected *p*-value<10^{-4} in at least one screen were included in this analysis) enabled us to make meaningful predictions, some of which we confirmed experimentally.

Several groups of genes were clearly discernible based on their GT insertion enrichment patterns across the three screens (***Figure 5D*** and ***Supplementary file 3***). As expected, genes encoding components of the pathway that function downstream of the destruction complex, including *CTNNB1* and *CREBBP*, were enriched for GT insertions in all three screens (***Figure 5D*** and ***Supplementary file 3***). *TFAP4* was also significantly enriched for GT insertions in all three screens (***Supplementary file 3***), and it acts downstream of the destruction complex, as we confirmed experimentally (***Figure 2***). However, *TFAP4* had a low IGTIOB score in all screens (***Figure 5D*** and ***Supplementary file 3***) because it represents a rare case of a gene that can be disrupted by both sense and antisense GT insertions in an intron (***Supplementary file 1***), a finding that will be described in detail elsewhere.

Also as expected, genes encoding components of the pathway upstream of the destruction complex, such as *LRP6*, were predominantly enriched for GT insertions in the WNT, but not the APC or CSNK1A1 suppressor screens (***Figure 5D*** and ***Supplementary file 3***). *AXIN2* was also enriched for

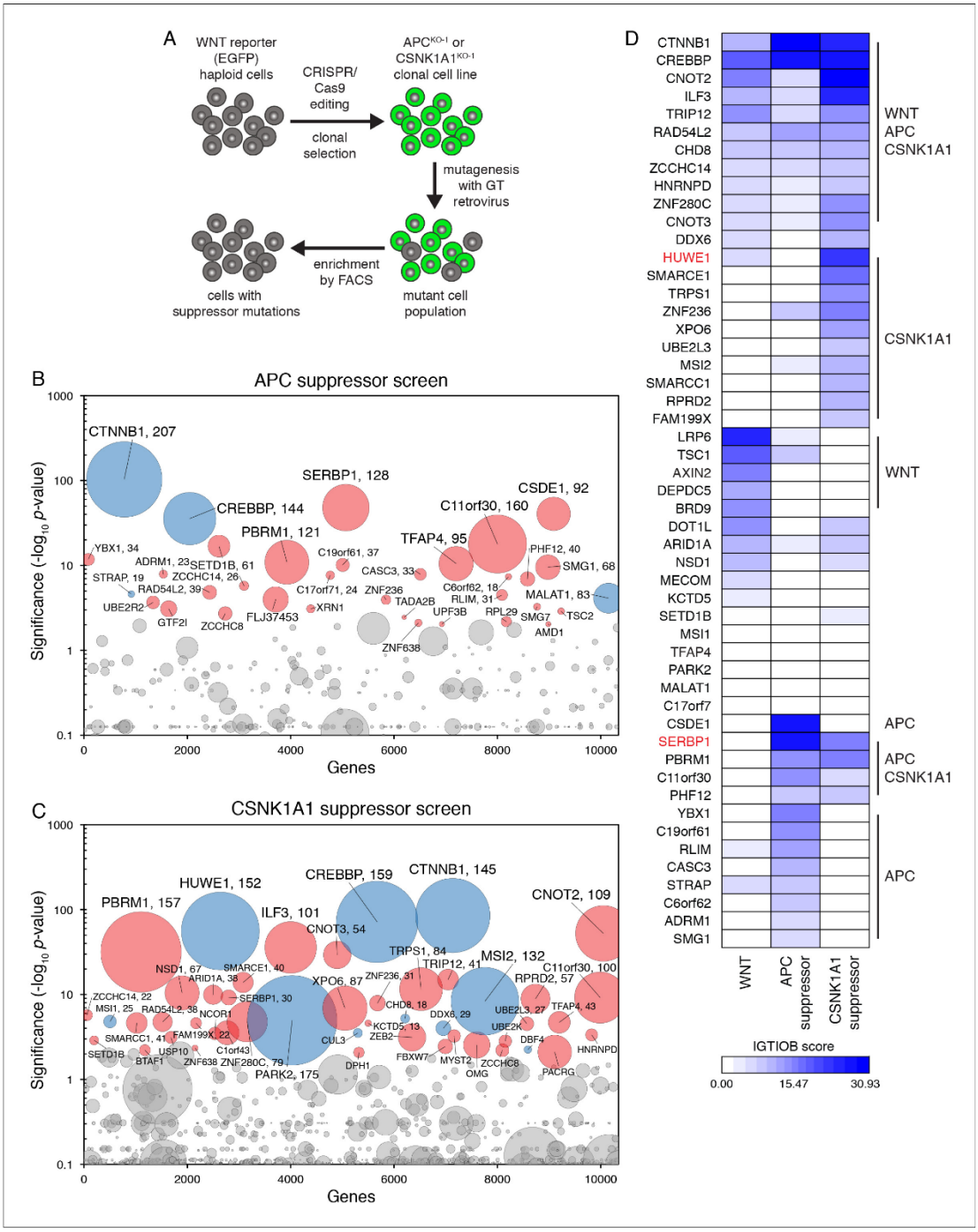

Figure 5. Suppressor screens in cells lacking APC or CSNK1A1 reveal genotype-specific signaling requirements. (**A**) Schematic of WNT reporter-based suppressor screens. *APC* or *CSNK1A1* was disrupted by CRISPR/Cas9-mediated genome editing of the WNT reporter haploid cell line HAP1-7TGP. Individual clonal cell lines were isolated (APC^{KO-1} and $CSNK1A1^{KO-1}$, ***Supplementary file 2***) and mutagenized using GT retrovirus. Cells with reduced reporter activity were enriched by FACS to identify suppressor mutations. (**B–C**) Circle plots depicting genes enriched for GT insertions in suppressor

Figure 5 continued on next page

Figure 5 continued

screens in which constitutive WNT signaling was induced by loss of APC (**B**) or CSNK1A1 (**C**). See legend to ***Figure 1C–1F*** for details. (**D**) Heat map comparing the WNT positive regulator, low stringency screen (***Figure 1E***), and the APC and CSNK1A1 suppressor screens (***Figure 5B and C***). Genes enriched for GT insertions (FDR-corrected *p*-value<10^{-4}) in at least one of the three screens were clustered based on their IGTIOB score in each screen (see Materials and methods and ***Supplementary file 3***). Classes of genes preferentially enriched for GT insertions in various screens are indicated. Genes selected for a detailed analysis are labeled in red.

DOI: 10.7554/eLife.21459.013

The following figure supplement is available for figure 5:

Figure supplement 1. Suppressor screens in cells lacking APC or CSNK1A1 reveal genotype-specific signaling requirements.

DOI: 10.7554/eLife.21459.014

GT insertions in the WNT screen exclusively, suggesting that the mechanism responsible for reducing WNT responsiveness in cells containing AXIN2 truncations depends on other components of the CTNNB1 destruction complex.

Hits enriched for GT insertions in both the APC and CSNK1A1 supprssor screens, but not the WNT screen, likely represent a class of genes capable of modulating WNT signaling in the absence of destruction complex activity. The most prominent hit in this category was *SERBP1* (***Figure 5D*** and ***Supplementary file 3***), encoding an RNA binding protein that has not been previously implicated in WNT signaling. In the section that follows we explored how SERBP1 regulates WNT signaling in cells lacking destruction complex activity.

Genes enriched for GT insertions predominantly in the APC suppressor screen included those encoding various RNA binding proteins, components of the mRNA nonsense-mediated decay pathway, and negative regulators of RNA polymerase (***Figure 5D*** and ***Supplementary file 3***), suggesting a connection between RNA metabolism and signaling in APC^{KO-1} cells.

Surprisingly, there were a number of genes predominantly enriched for GT insertions in the CSNK1A1 suppressor screen (***Figure 5D*** and ***Supplementary file 3***). Given that the principal role of CSNK1A1 in WNT signaling is thought to be phosphorylation of CTNNB1 through the destruction complex, it was not obvious why these same genes were not enriched for GT insertions in the APC suppressor screen, where destruction complex activity was also disabled. The existence of this class of genes, apparently required for WNT signaling only in cells lacking CSNK1A1, suggested a role for CSNK1A1 in WNT signaling independent of the destruction complex. The most prominent gene in this class encodes HUWE1, an E3 ubiquitin ligase that has been proposed to downregulate WNT signaling by ubiquitinating DVL and preventing its multimerization (***de Groot et al., 2014***). In contrast, the fact that mutations of HUWE1 caused a reduction in WNT reporter fluorescence during the CSNK1A1 suppressor screen suggests a positive regulatory role. Below, we describe the peculiar role of HUWE1 in mediating WNT signaling specifically in the context of CSNK1A1 loss.

APC is a prototypical human tumor suppressor gene frequently lost in both sporadic and familial CRC. Importantly, reduction of WNT signaling through restoration of APC in a mouse model of CRC can reverse tumorigenesis even in the presence of mutations in other potent cancer genes such as *TP53* and *KRAS* (***Dow et al., 2015***). Hence, genes selectively required to sustain the high-level WNT signaling that ensues when *APC* or *CSNK1A1* are lost, such as those suggested by our comparative analysis, may represent potential therapeutic targets.

SERBP1 controls CTNNB1 abundance in cells lacking APC

The second top hit of the APC suppressor screen, after *CTNNB1*, was the gene encoding the mRNA binding protein SERBP1 (***Figure 5B*** and ***Supplementary file 1***), also known as PAI-RBP1. *SERBP1* was also a significant hit in the CSNK1A1 suppressor screen (***Figure 5C*** and ***Supplementary file 1***). SERBP1 was initially identified as an mRNA binding protein that interacts with the cyclic nucleotide-responsive sequence of the Type-1 plasminogen activator inhibitor mRNA and may play a role in regulation of mRNA stability (***Heaton et al., 2001***). Yet, its cellular function remains largely unknown, and it has never been implicated in regulation of WNT signaling.

To explore the consequences of disrupting SERBP1 in cells lacking APC we used an independently isolated HAP1-7TGP clonal cell line with a lesion in the *APC* locus introduced by a GT insertion (APC^{KO-2}, see Materials and methods, ***Supplementary file 2*** and ***Figure 6D***). This ensured that any effects on WNT signaling were not specific to the CRISPR/Cas9-induced lesion in the APC^{KO-1}

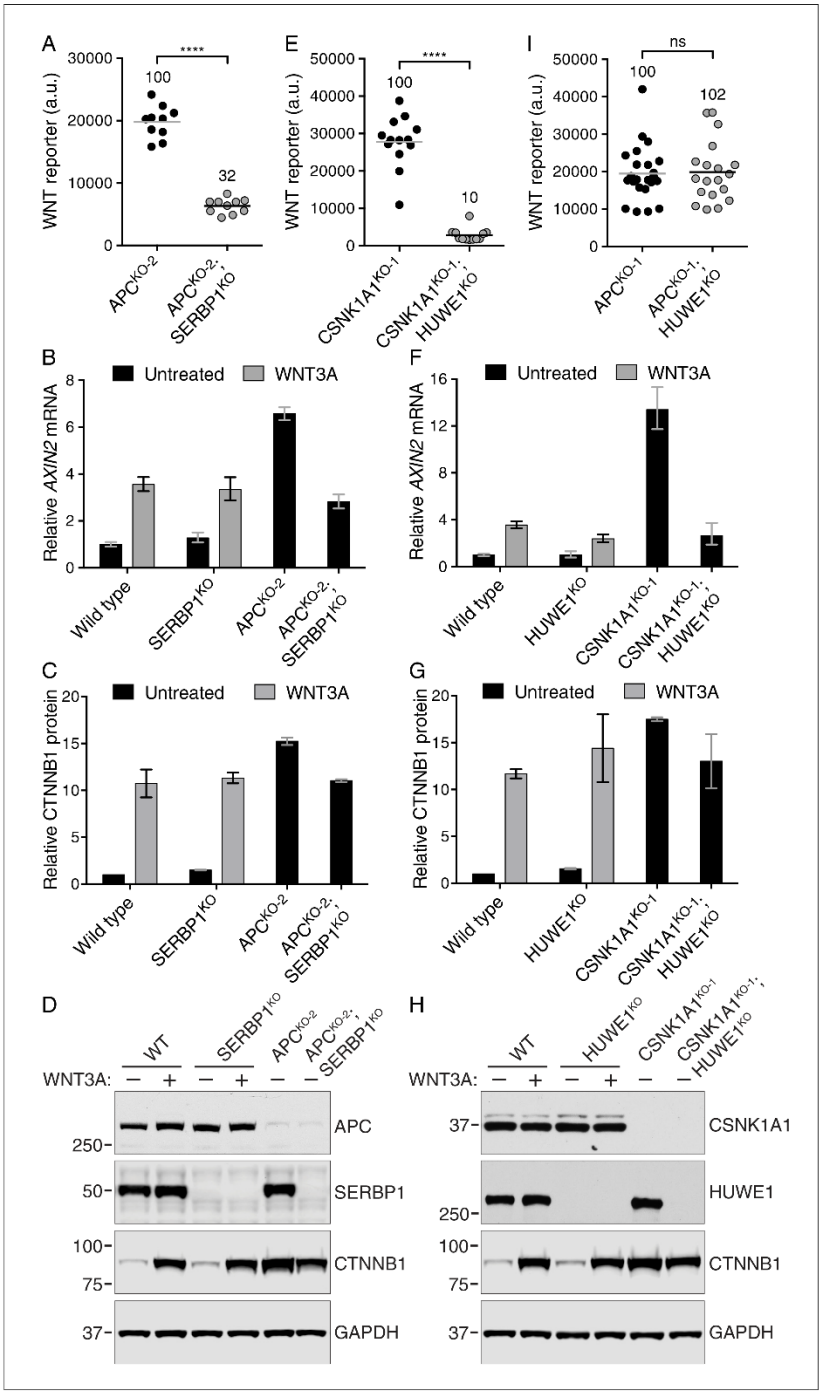

Figure 6. The mRNA binding protein SERBP1 controls CTNNB1 abundance in cells lacking APC (**A–D**), and the E3 ubiquitin ligase HUWE1 regulates WNT signaling in the absence of CSNK1A1 (**E–I**). (**A**, **E**, **I**) WNT reporter activity (median EGFP fluorescence from 5000 (**A**), 20,000 (**E**) or 2000 (**I**) cells) for the indicated single- and double-mutant cell lines. Each circle represents a unique clonal cell line and the average of 10 (**A**), ≥12 (**E**) or ≥19 (**I**) independent clones for each genotype is indicated by a horizontal line. The average percentage reporter activity relative to single-mutant cell lines is

Figure 6 continued on next page

Figure 6 continued

also indicated above each group of circles. Significance was determined by unpaired t-test with Welch's correction and is indicated as ****($p<0.0001$) or ns (not significant). (**B**,**F**) *AXIN2* mRNA (average ± SD of *AXIN2* mRNA normalized to *HPRT1* mRNA, each measured in triplicate reactions), relative to untreated WT cells, for a single clonal cell line of each indicated genotype. Cells were treated with 50% WNT3A CM where indicated. The same cell lines analyzed in B were also analyzed in C and D; the same cell lines analyzed in F were also analyzed in G and H. Analysis of additional independent clonal cell lines is presented in ***Figure 6—figure supplement 1***. (**C**,**G**) Soluble CTNNB1 protein (average ± SD of CTNNB1 intensity normalized to GAPDH intensity from duplicate immunoblots), relative to untreated WT cells. Cells were treated with 50% WNT3A CM where indicated.(**D**,**H**) Representative immunoblots of the indicated clonal cell lines. The CTNNB1 and corresponding GAPDH blots depicted in D and H were used for quantification in C and G, respectively. Genotypes and treatments are indicated above the blots.

DOI: 10.7554/eLife.21459.015

The following figure supplement is available for figure 6:

Figure supplement 1. The mRNA binding protein SERBP1 controls CTNNB1 abundance in cells lacking APC (**A–C**), and the E3 ubiquitin ligase HUWE1 regulates WNT signaling in the absence of CSNK1A1 (**D–G**).

DOI: 10.7554/eLife.21459.016

cells used for the APC suppressor screen. As expected, APC^{KO-2} cells had constitutive WNT reporter expression (***Figure 5—figure supplement 1B***). We used CRISPR/Cas9 to generate multiple independent clonal cell lines derived from APC^{KO-2} cells that harbored additional inactivating mutations in *SERBP1*, hereafter called APC^{KO-2}; $SERBP1^{KO}$ cells (***Supplementary file 2*** and ***Figure 6D***). Disrupting *SERBP1* in cells lacking APC caused a substantial reduction in constitutive WNT reporter fluorescence, endogenous *AXIN2* mRNA and soluble CTNNB1 protein abundance (***Figure 6A–D***, and ***Figure 6—figure supplement 1A and B***). Disrupting *SERBP1* in WT HAP1-7TGP cells ($SERBP1^{KO}$, ***Supplementary file 2*** and ***Figure 6D***) did not affect basal or WNT3A-induced levels of *AXIN2* mRNA or soluble CTNNB1 (***Figure 6B–D***, and ***Figure 6—figure supplement 1A and B***), explaining why *SERBP1* was not enriched for GT insertions in the WNT screen for positive regulators of ligand-induced signaling (***Figure 5D*** and ***Supplementary file 3***). Microinjection of *SERBP1* mRNA into *X. laevis* embryos resulted in duplication of the body axis, establishing SERBP1 as a *bona fide* positive regulator of WNT signaling in vertebrates (***Figure 2E and F***).

In the absence of destruction complex activity, SERBP1 could conceivably reduce CTNNB1 abundance by decreasing transcript or protein levels. No significant changes in *CTNNB1* mRNA levels were detected when *SERBP1* was disrupted in either WT or mutant *APC* genetic backgrounds (***Figure 6—figure supplement 1C***), suggesting instead a reduction in CTNNB1 protein. Thus, SERBP1 can regulate CTNNB1 abundance in cells lacking APC. This mechanism, independent of destruction complex activity, could be particularly well suited for therapeutic interference in tumors where APC function is lost.

HUWE1 regulates WNT signaling in the absence of CSNK1A1

The third most significant hit of the CSNK1A1 suppressor screen, following *CTNNB1* and *CREBBP*, was *HUWE1* (***Figure 5C*** and ***Supplementary file 1***). *HUWE1* (also known as *MULE*, *LASU1* and *UREB1*) encodes a 480–482 kDa E3 ubiquitin ligase containing a C-terminal HECT domain with diverse cellular functions (***Bernassola et al., 2008***). Previous work has implicated HUWE1 as a negative regulator of WNT signaling (***de Groot et al., 2014***). However, the results of our screens suggested that in the absence of CSNK1A1, HUWE1 is a positive regulator of WNT signaling. To test the role of HUWE1 in this context, we further engineered the $CSNK1A1^{KO-1}$ cells used for the CSNK1A1 suppressor screen, as well as an independently derived cell line with a different lesion in *CSNK1A1* ($CSNK1A1^{KO-2}$, ***Supplementary file 2***). In each parental cell line, we used two different sgRNAs to disrupt *HUWE1* and isolated multiple double-mutant clonal cell lines (designated $CSNK1A1^{KO-1}$; $HUWE1^{KO}$ and $CSNK1A1^{KO-2}$; $HUWE1^{KO}$, ***Supplementary file 2*** and ***Figure 6H***). Disruption of HUWE1 resulted in a consistent 82–90% reduction of constitutive WNT reporter fluorescence and an 80–85% reduction of endogenous *AXIN2* mRNA (***Figure 6E and F***, and ***Figure 6—figure supplement 1D and E***). In addition, microinjection of *HUWE1* mRNA into *X. laevis* embryos resulted in duplication of the body axis at low frequency (***Figure 2E and F***), supporting a more general role as a positive regulator.

In contrast to the 80–90% reduction in both WNT reporter fluorescence and target gene expression (***Figure 6E and F***, and ***Figure 6—figure supplement 1D and E***), depleting HUWE1 in

CSNK1A1^{KO-1}; HUWE1^{KO} cells reduced soluble CTNNB1 levels by only 20–32% (***Figure 6G and H***, and ***Figure 6—figure supplement 1F***). These results show that in cells lacking CSNK1A1, HUWE1 has a minor influence on CTNNB1 abundance, but that its predominant role in WNT signaling is distinct from the regulation of CTNNB1 protein levels.

Additionally, *HUWE1* was not a significant hit in the WNT screens or the APC suppressor screen (***Figure 5D*** and ***Supplementary file 3***), suggesting that its role is specific to cells lacking CSNK1A1. Indeed, disruption of *HUWE1* in WT HAP1-7TGP cells (HUWE1^{KO}, ***Supplementary file 2*** and ***Figure 6H***) did not cause significant changes in WNT3A-induced *AXIN2* mRNA or CTNNB1 protein abundance (***Figure 6F–H***, and ***Figure 6—figure supplement 1E and F***). To directly test whether HUWE1 disruption reduces WNT signaling in cells lacking CSNK1A1 but not other destruction complex components, we disrupted *HUWE1* in APC^{KO-1} cells (APC^{KO-1}; HUWE1^{KO}, ***Supplementary file 2***), and found no measurable defect in WNT reporter florescence (***Figure 6I***). Signaling driven by inhibition of GSK3 was also unaffected by the loss of HUWE1 in HUWE1^{KO} cells (***Figure 6—figure supplement 1G***).

In summary, the drastic defect in signaling caused by loss of HUWE1 in cells lacking CSNK1A1 and its ability to promote formation of a secondary body axis when expressed ectopically in *X. laevis* embryos demonstrate a positive role for HUWE1 in WNT signaling. These effects are largely independent of changes is CTNNB1 protein abundance and are not observed when other components of the destruction complex are inactivated. From these results we conclude that CSNK1A1 regulates WNT signaling by an additional mechanism distinct from its established role in CTNNB1 turnover, and that this mechanism is mediated by HUWE1.

Discussion

A systematic genetic analysis in human cells revealed new regulatory features at most levels of the WNT pathway, from signal reception to transcriptional activation (***Figure 7***). Based on a comparative analysis of seven genome-wide screens, we confirmed known epistatic connections and assigned new ones (***Figure 7A***). Even for some of the known WNT components, our analysis suggested unexpected regulatory mechanisms.

First, as predicted by their enrichment in the WNT screens for positive regulators (***Figure 7A***), atypical GT insertions in *AXIN2* caused an unexpected decrease in WNT signaling (***Figure 3***). These results are explained by the observation that in cells lacking the DAX domain of AXIN2, CTNNB1 is appropriately stabilized and localized to the nucleus following WNT stimulation, but remains inactive (***Figure 3***). Second, genes encoding components of the GPI anchor biosynthetic machinery, such as PIGL, and the glypican GPC4 were predominantly enriched for GT insertions in the low WNT + RSPO screen (***Figure 7A***), and we demonstrated that they indeed play a critical role in mediating signaling especially under the low WNT conditions in which RSPOs exert their strongest effect (***Figure 4***). Third, the enrichment of GT insertions in *HUWE1* only in the CSNK1A1 suppressor screen (***Figure 7A***) revealed a unique signaling condition created by disruption of CSNK1A1, but not other destruction complex components such as APC or GSK3. Only in this very specific context WNT signaling was dependent on HUWE1 (***Figure 6***). This positive regulatory function of HUWE1 is evidently different from the negative feedback regulation described previously (***de Groot et al., 2014***).

The presence of mutations in known regulators in the expected screens demonstrates the predictive power of our approach, which enabled us to infer the site of action of newly identified pathway components. The transcription factor TFAP4 would be predicted to act downstream of the CTNNB1 destruction complex based on its disruption in all screens for positive regulators of signaling (***Figure 7A***), as our experimental results confirmed (***Figure 2***). The selective disruption of *SERBP1* in only the APC and CSNK1A1 suppressor screens (***Figure 7A***) suggests a regulatory role on signaling independent of destruction complex activity, which we demonstrated experimentally (***Figure 6***).

An important conclusion from our studies is that WNT signaling can be regulated by processes other than control of CTNNB1 protein abundance by the destruction complex. We demonstrate two distinct instances in which CTNNB1 transcriptional activity can be dissociated from protein levels, one caused by truncation of the AXIN2 DAX domain and the other caused by depletion of HUWE1 in cells lacking CSNK1A1. It will be interesting to explore if these phenomena can be exploited for therapeutic purposes in tumors driven by inappropriate stabilization of CTNNB1. We also provide evidence that the destruction complex does not have a unitary function in controlling CTNNB1

A

	Screen	WNT negative regulator	WNT attenuating regulator	Low WNT + RSPO	WNT positive regulator	APC suppressor	CSNK1A1 suppressor
Known regulators	**Gene**						
RSPO receptor/signaling	*ZNRF3*		X				
	LGR4			X			
WNT receptor complex	*FZD5*			X			
	DVL3			X			
	LRP6			X	X		
CTNNB1 destruction complex	*APC*	X					
	CSNK1A1	X					
Histone methyltransferase	*MLL*			X	X		
	DOT1L			X	X		
	MLLT10				X		
Transcription complex	*TCF7L2*		X				
	CTNNB1			X	X	X	X
	CREBBP			X	X	X	X
	BCL9			X	X	X	X
Other	*RNF146*			X	X		X
New mechanisms	**Gene**						
WNT receptor complex	*PIGL*			X			
	GPC4			X			
CTNNB1 destruction complex	*AXIN2*			X*	X*		
Transcription complex	*TFAP4*			X	X	X	X
Other	*SERBP1*					X	X
	HUWE1						X

* Truncation

B

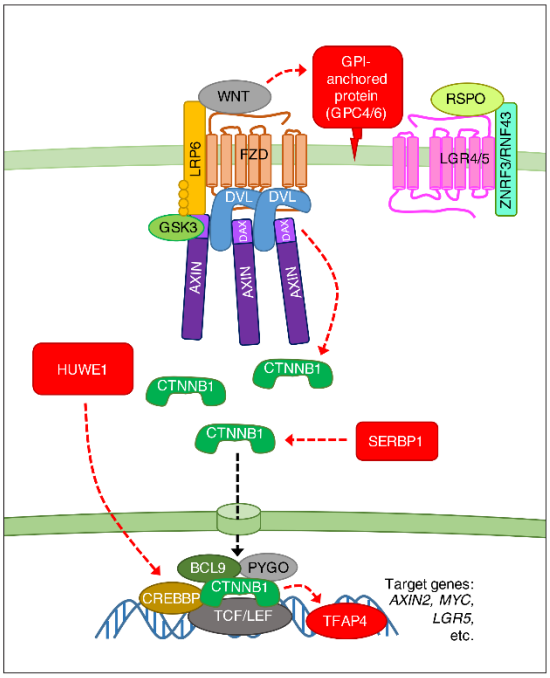

Figure 7. A comparative analysis of seven genome-wide screens revealed epistatic connections and regulatory mechanisms in WNT signaling. (**A**) Summary of known regulators, and new regulators or regulators mediating new mechanisms in WNT signaling validated in this study. An 'X' denotes that the gene was enriched for GT insertions in the sorted cells from the indicated genetic screen (FDR-corrected *p*-value<0.05). Known regulators are grouped into functional modules and arranged according to previously described epistatic relationships. Epistatic relationships for new regulators or regulators mediating new mechanisms are inferred based on their patterns across screens. The screens in which cells were sorted for increased WNT reporter fluorescence are labeled in red, and those in which cells were sorted for reduced WNT reporter fluorescence are labeled in green. For the 'WNT positive regulator' column, hits from the WNT screens done at both low and high stringency (***Figure 1E and F***) were considered together. For *AXIN2*, the asterisk indicates that GT insertions mapped in the sorted cells generate a dominant allele that encodes a truncated protein product. (**B**) Model of WNT/CTNNB1 signaling, highlighting in red new regulatory mechanisms uncovered and validated in this study. Red arrows represent genetic (rather than biochemical) interactions. The various proposed mechanisms are discussed throughout the Results and Discussion sections.
DOI: 10.7554/eLife.21459.017

protein abundance, since disrupting distinct components produces different outcomes. Supressor screens in cells lacking APC or CSNK1A1 revealed mutations in substantially different sets of genes (***Figure 5***), and while SERBP1 controls CTNNB1 abundance in cells lacking APC, the effects of HUWE1 in cells lacking CSNK1A1 are largely independent of changes in CTNNB1 levels (***Figure 6***).

From these studies a more elaborate picture of the core WNT signaling cascade emerges, with additional regulation superimposed on the core module (***Figure 7B***). Further studies will be required to elucidate the mechanisms that mediate each of these new layers of regulation and to identify the

physiological or pathological contexts in which they act. Yet, the comparative analysis of seven unbiased genome-wide screens and the characterization of hits through a quantitative assessment of CRISPR/Cas9-engineered clonal cell lines provided many insights into this complex developmental signaling pathway. The conceptual and methodological framework described in this work should enable the comprehensive understanding of other signaling systems.

Materials and methods

Reagent providers

Reagents were obtained from the following companies: Thermo Fisher Scientific, Waltham, MA; Sigma-Aldrich, St. Louis, MO; Bio-Rad, Hercules, CA; Cell Biolabs, San Diego, CA; Clontech, Mountain View, CA; Promega, Madison, WI; GE Healthcare Life Sciences, Logan, UT; GE Dharmacon, Lafayette, CO; Addgene, Cambridge, MA; BD Biosciences, San Jose, CA; Abcam, Cambridge, MA; EMD Millipore, Billerica, MA; Bethyl Laboratories, Montgomery, TX; Santa Cruz Biotechnology, Dallas, TX; R and D Systems, Minneapolis, MN; Cell Signaling Technology, Danvers, MA; Li-Cor, Lincoln, NE; Jackson ImmunoResearch Laboratories, West Grove, PA; Developmental Studies Hybridoma Bank at the University of Iowa (DSHB), Iowa City, IA; American Type Culture Collection (ATCC), Manassas, VA; Atlanta Biologicals, Flowery Branch, GA; Pall Corporation, Fribourg, Switzerland; Selleckchem, Houston, TX; Roche, Mannheim, Germany; QIAGEN Sciences, Hilden, Germany; New England Biolabs (NEB), Ipswich, MA; Epicentre, Madison, WI; Corning, Corning, NY; Bloomington Drosophila Stock Center at Indiana University (BDSC), Bloomington, IN.

Plasmids

7TGP was a gift from Roel Nusse (Addgene plasmid # 24305). pX330-U6-Chimeric_BB-CBh-hSpCas9 (pX330) was a gift from Feng Zhang (Addgene plasmid # 42230). pCSDest was a gift from Nathan Lawson (Addgene plasmid # 22423). pCS2^{+}, pCS2-YFP, pCS2-β-cat-S33Y, pCS2-xWnt8, VSV-G and Δ8.9 were a gift from Henry Ho.

The following plasmids were purchased: pAdVAntage (Promega Cat. # E1711), pCMV-VSV-G (Cell Biolabs Cat. # RV-110), pCMV-Gag-Pol (Cell Biolabs Cat. # RV-111), pENTR-D-TOPO (Thermo Fisher Scientific Cat. # K240020), pENTR2B (Thermo Fisher Scientific Cat. # A10463).

To generate pCSDest-TFAP4, human *TFAP4* was amplified by PCR from MGC Human Sequence-verified cDNA (Clone ID 4181538, GE Dharmacon Cat. # MHS6278-202757542) using primers hTFAP4-FOR (5'-CACCATGGAGTATTTCATGGTGCCCA-3') and hTFAP4-REV (5'- TCAGGGAAGC TCCCCGT-3'), designed to add a directional TOPO cloning sequence at the 5' end. The resulting PCR product was cloned directionally into pENTR-D-TOPO. Individual clones were screened by digestion with NotI and PstI for the presence of the insert in the correct orientation, and one clone was sequenced completely and subcloned into pCSDest using the Gateway LR Clonase II Enzyme mix (Thermo Fisher Scientific Cat. # 11791100).

To generate pCSDest-1D4-SERBP1, human *SERBP1* was amplified by PCR from MGC Human Sequence-verified cDNA (Clone ID 4477452, GE Dharmacon Cat. # MHS6278-202758125) using primers FNNterminal (5'-TTTTGAATTCGCCACCATGACCGAGACCAGCCAGGTGGCCCC TGCAGGCGGCCGGCCACCTGGGCACTTACAGGAAGG-3'), designed to add an N-terminal Kozak sequence, a 1D4 tag and a single glycine linker flanked by EcoR1 and FseI restriction sites, and RNNterminal (5'-TTTTCTCGAGGGCGCGCCTTAAGCCAGAGCTGGGAATG-3'), designed to add tandem AscI and XhoI restriction sites after the stop codon. The product was digested with EcoRI and XhoI, and subcloned into pENTR2B digested at the same sites. One clone was sequenced completely and subcloned into pCSDest using the Gateway LR Clonase II Enzyme mix.

To generate pCSDest-HUWE1, codon optimized *HUWE1* in pDONR221, a gift from Sarah J. Luchansky (Developmental and Molecular Pathways, Novartis Institutes for Biomedical Research, Cambridge, MA), was subcloned into pCSDest using the Gateway LR Clonase II Enzyme mix.

pCherry-C1 was created by replacing DsRed with mCherry RFP (***Shaner et al., 2004***) in pDsRed-monomer-C1 (Clontech Cat. # 632466). An mCherry RFP PCR fragment was obtained using primers 5'-GATCGCTAGCACCATGGTGAGCAAGGGCGAGGAGGATAAC-3' and 5'-GATCCTCGAGATCTC TTGTACAGCTCGTCCATGCCGCC-3'. The PCR product was digested with NheI and XhoI and ligated into pDsRed-monomer-C1 digested with the same enzymes.

pGT-mCherry and pGT+1mCherry retroviral gene trap (GT) vectors (diagrammed schematically in ***Figure 1B***), containing an inactivated 3'LTR, a strong adenoviral (Ad40) splice acceptor site, mCherry RFP in two different reading frames following the splice acceptor site, and the SV40 polyadenylation signal, were created by replacing GFP with mCherry RFP in pGT-GFP (***Carette et al., 2009***). To create pGT-mCherry, the following primers were used to generate a PCR product containing the splice acceptor site followed by mCherry: 5'-GATCATCGATGCGCAGGCGCAATCTTCGCATTTC TTTTTTCCAGATGGTGAGCAAGGGCGAGG-3' and 5'-GATCGGATCCTTACTTGTACAGCTCGTCCA TG-3'. To create pGT+1mCherry, the following primers were used: 5'-GATCATCGATGCGCAGGCG-CAATCTTCGCATTTCTTTTTTCCAGGATGGTGAGCAAGGGCGAGG-3' and 5'-GATCGGATCCTTAC TTGTACAGCTCGTCCATG-3'. The PCR products were digested with ClaI and BamHI and cloned into pGT-GFP digested with the same enzymes.

All constructs were confirmed by sequencing.

Antibodies

For immunoblotting

Primary antibodies: mouse anti-β-catenin (Clone 14/Beta-Catenin) (1:1000, BD Biosciences Cat. # 610154), mouse anti-GAPDH [6 C5] (1:5000, Abcam Cat. # ab8245), mouse anti-ACTIN (clone C4) (1:500, EMD Millipore Cat. # MAB1501), rabbit anti-AP4 (TFAP4) serum (1:2000, a gift from Takeshi Egawa; ***Egawa and Littman, 2011***), rabbit anti-SERBP1 (1:5000, Bethyl Laboratories Cat. # A303-938A), goat anti-casein kinase Iα (C-19) (1:200, Santa Cruz Biotechnology Cat. # sc-6477), rabbit anti-APC (C-20) (1:500, Santa Cruz Biotechnology Cat. # sc-896), rabbit anti-Lasu1/Ureb1 (HUWE1) (Bethyl Laboratories Cat. # A300-486A), goat anti-AXIN1 (1:1250, R and D Systems Cat. # AF3287), rabbit anti-AXIN2 (76 G6) (1:500, Cell Signaling Technology Cat. # 2151), mouse anti-V5 (1:5000, Thermo Fisher Scientific Cat. # R960CUS (formerly 46–1157)), mouse anti-α-Tubulin (clone DM1A) (1:10,000, Sigma-Aldrich Cat. # T6199).

Secondary antibodies: IRDye 800CW donkey anti-mouse IgG (H+L) (1:10,000, Li-Cor Cat. # 926–32212), IRDye 680RD donkey anti-rabbit IgG (H+L) (1:10,000, Li-Cor Cat. # 925–68073), peroxidase AffiniPure donkey anti-goat IgG (H+L) (1:5000, Jackson ImmunoResearch Laboratories Cat. # 705-035-003), peroxidase AffiniPure goat anti-rabbit IgG (H+L) (1:7500, Jackson ImmunoResearch Laboratories Cat. # 111-035-003), peroxidase AffiniPure donkey anti-mouse IgG (H+L) (1:5000, Jackson ImmunoResearch Laboratories Cat. # 715-035-150), goat anti-mouse IgG (H+L) HRP conjugate (1:10,000, Bio-Rad Cat. # 1706516).

Primary and secondary antibodies used for detection with the Li-Cor Odyssey imaging system were diluted in a 1 to 1 mixture of Odyssey Blocking Buffer (Li-Cor Cat. # 927–40000) and TBST (Tris buffered saline (TBS) + 0.1% Tween-20), and those used for detection by chemiluminescence were diluted in TBST + 5% skim milk. All primary antibody incubations were done overnight at 4°C, and secondary antibody incubations were done for 1 hr at room temperature (RT).

For immunostaining

Primary antibodies: mouse anti-β-catenin (Clone 14/Beta-Catenin) (1:500, BD Biosciences Cat. # 610154), mouse anti-Wingless (1:25, DSHB Cat. # 4D4 (supernatant) for *D. melanogaster* wing imaginal discs and 1:200, DSHB Cat. # 4D4 (concentrate) for embryos), guinea pig anti-Senseless (1:1000; ***Nolo et al., 2000***), mouse anti-Engrailed/Invected (1:100, DSHB Cat. # 4D9 (concentrate)).

Secondary antibodies: donkey anti-mouse IgG (H+L) Alexa Fluor 647 conjugate (1:250, Thermo Fisher Scientific Cat. # A-31571), donkey anti-mouse IgG (H+L) Alexa Fluor 555 conjugate (1:400, Thermo Fisher Scientific Cat. # A-31570), goat anti-guinea pig IgG (H+L) highly cross-adsorbed, Alexa Fluor 488 conjugate (1:400, Thermo Fisher Scientific Cat. # A-11073).

Cell lines and growth conditions

L Wnt-3A (ATCC Cat. # CRL-2647), L cells (ATCC Cat. # CRL-2648), 293T (ATCC Cat. # CRL-3216) and 293FT cells (Thermo Fisher Scientific Cat. # R70007) were grown at 37°C and 5% CO_2 in complete growth medium (CGM) 1: Dulbecco's Modified Eagles Medium (DMEM) with High Glucose, without L-Glutamine and Sodium Pyruvate (GE Healthcare Life Sicences Cat. # SH30081.01); 1X GlutaMAX-I (Thermo Fisher Scientific Cat. # 35050079); 1X MEM Non-Essential Amino Acids (Thermo Fisher Scientific Cat. # 11140050); 1 mM Sodium Pyruvate (Thermo Fisher Scientific Cat. #

11360070); 40 Units/ml Penicillin, 40 µg/ml Streptomycin (Thermo Fisher Scientific Cat. # 15140122); 10% Fetal Bovine Serum (FBS) (Atlanta Biologicals Cat. # S11150). HAP1 haploid human cells (kindly provided by Thijn Brummelkamp, now available from Horizon Discovery, Cambridge, United Kingdom) were derived and characterized as described previously (***Carette et al., 2011b***). Throughout the course of experiments, the ploidy of HAP1 cells and derivatives thereof was routinely tested by DNA content analysis of propidium iodide (PI)-stained nuclei, as described below. Genetically modified clonal derivatives were confirmed by sequencing of target loci and in some cases immunoblotting, as described below (see also ***Supplementary file 2***). HAP1 cells and derivatives thereof were grown at 37°C and 5% CO_2 in CGM 2: Iscove's Modified Dulbecco's Medium (IMDM) with L-glutamine, with HEPES, without Alpha-Thioglycerol (GE Healthcare Life Sciences Cat. # SH30228.01); 1X GlutaMAX-I; 40 Units/ml Penicillin, 40 µg/ml Streptomycin; 10% FBS.

Preparation of WNT3A and L cell conditioned media

L Wnt-3A cells or L cells were seeded in 15 cm tissue culture-treated dishes at a density of 1.5×10^6 cells per dish and grown in 25 ml of CGM 1. After 3 days, the medium was refreshed, and after an additional 3 days, WNT3A or L cell conditioned medium (used as a control) was collected, filtered through a 0.2 µm polyethersulfone (PES) membrane filter, aliquoted, flash-frozen in liquid nitrogen and stored at −80°C. The medium was thawed immediately before use, and leftover medium was used only after one additional freeze-thaw cycle.

Construction of HAP1-7TGP WNT reporter haploid cell line

Lentivirus containing the 7TGP WNT reporter construct (***Fuerer and Nusse 2010***) was produced in 293T cells. ~24 hr before transfection, 293T cells were seeded in a 10 cm dish at a density of 4×10^6 per dish and grown in 10 ml of CGM 1. When the cells were nearly confluent, the medium was replaced with CGM 1 without antibiotics. To prepare a calcium phosphate transfection mix, 8 µg of 7TGP plasmid, 4 µg of VSV-G, 4 µg of Δ8.9 and 0.5 µg of pCS2-YFP (used as a co-transfection marker) in 450 µl of sterile water were mixed with 50 µl of 2.5 M $CaCl_2$. The DNA/$CaCl_2$ solution was added to 500 µl of 2X HBS (42 mM HEPES pH 7.04, 274 mM NaCl, 10 mM KCl, 15 mM dextrose, 1.4 mM $Na_2HPO_4.7H_2O$) and mixed by bubbling air through the solution. Following a 20 min incubation at RT, the transfection mix was added drop-wise to the dish of cells and mixed by gentle agitation. The medium was refreshed 16 hr post-transfection, at which time the efficiency of transfection was assessed by microscopic inspection of YFP fluorescence. Lentivirus-containing medium was collected 36, 48 and 60 hr post-transfection (30 ml total), filtered through 0.45 µm filters (Acrodisc syringe filters with Supor membrane, Pall Corporation) and concentrated by ultracentrifugation for 1.5 hr at 23,000 rpm in a Sorvall Surespin 630 rotor. The supernatants were discarded, and the pellets overlaid by a total of 200 µl of sterile phosphate buffered saline (PBS) supplemented with 1 mg/ml bovine serum albumin (BSA). Following 12 hr of incubation at 4°C, the pellets were resuspended, aliquoted, flash-frozen in liquid nitrogen, and stored at −80°.

Approximately 48 hr before transduction, HAP1 cells were seeded in 10 cm dishes at a density of 1.5×10^6 per dish and grown in 10 ml of CGM 2. Cells were transduced with 145 µl of freshly thawed lentivirus diluted in 10 ml of CGM 2 supplemented with 4 µg/ml polybrene. ~48 hr post-transduction cells were treated with 1 µg/ml puromycin to select for those with a stably integrated 7TGP cassette. After selection was complete (assessed by death of >99% of control, untransduced HAP1 cells), surviving cells were treated for 16–24 hr with 50% WNT3A CM in CGM 2, and single WNT3A-responsive cells exhibiting the highest ~50% EGFP fluorescence were sorted by FACS into 96-well plates containing 200 µl of CGM 2 per well. After 14 days of undisturbed growth, individual clones were amplified and haploid HAP1-7TGP clonal cell lines were identified by DNA content analysis of PI-stained nuclei (***Nicoletti et al., 1991***): 1.5×10^6 cells were incubated with 300 µl of hypotonic fluorochrome solution (50 µg/ml PI, 0.1% sodium citrate, 0.1% Triton X-100) for >15 min at RT and PI fluorescence was measured by FACS in a BD LSRFortessa cell analyzer (BD Biosciences) using a 561 laser and 600 LP, 610/20 BP filters. A haploid cell line with low basal reporter activity and a high dynamic range of EGFP fluorescence in response to WNT3A (***Figure 1—figure supplement 1A***) was expanded and used in all subsequent studies.

Analysis of WNT reporter fluorescence

To measure WNT reporter activity in HAP1-7TGP cells or derivatives thereof, ~24 hr before treatment cells were seeded in 24-well plates at a density of 8×10^4 per well and grown in 0.5 ml of CGM 2. Cells were treated for 16–24 hr with the indicated concentrations of WNT3A CM, L cell CM, recombinant mouse WNT3A (R and D Systems Cat. # 1324-WN) recombinant human RSPO1 (R and D Systems Cat. # 4645-RS), LiCl, CHIR-99021 (CT99021) (Selleckchem Cat. # S2924) or XAV-939 (Selleckchem Cat. # S1180) diluted in CGM 2. Cells were washed with 0.5 ml PBS, harvested in 150 µl of 0.05% Trypsin-EDTA (0.05%) (Thermo Fisher Scientific Cat. # 25300054), resuspended in 450 µl of CGM 2, and EGFP fluorescence was measured immediately by FACS on a BD LSRFortessa cell analyzer (BD Biosciences) using a 488 laser and 505 LP, 530/30 BP filters, or on a BD Accuri RUO Special Order System (BD Biosciences). Typically, fluorescence data for 5000–20,000 singlet-gated cells was collected and, unless indicated otherwise, the median EGFP fluorescence ± standard error of the median (SEM = 1.253 $\sigma/\sqrt{n}$, where σ = standard deviation and n = sample size) was used to represent the data.

Reporter-based forward genetic screens

Mutagenesis of haploid cells with GT retrovirus

HAP1-7TGP cells or derivatives thereof were mutagenized as described previously (***Carette et al., 2011a***), with some modifications. GT-containing retrovirus was produced in 293FT cells. ~24 hr before transfection, a total of 9×10^7 cells were seeded in 6 T-175 flasks (1.5×10^7 per flask), each containing 30 ml of CGM 1 without antibiotics. The medium in each T-175 flask was refreshed immediately before transfection, and cells were transfected with a transfection mix prepared as follows: 3.3 µg each of pGT-mCherry and pGT+1mCherry, 1.7 µg pAdVAntage, 2.6 µg pCMV-VSV-G and 4 µg pCMV-Gag-Pol were prepared in 450 µl serum-free DMEM (GE Healthcare Life Sicences Cat. # SH30081.01), and 45 µl of the X-tremeGENE HP DNA transfection reagent (Roche Cat. # 06366546001) were added and incubated for 20 min at RT. The medium was refreshed ~24 hr post-transfection, and retrovirus-containing supernatant was collected ~48 and ~56 hr post-transfection. The virus-containing supernatant was immediately filtered through 0.45 µm filters and concentrated by ultracentrifugation for 1.5 hr at 23,000 rpm in a Beckman SW 32 Ti or a Sorvall Surespin 630 rotor. Most of the supernatant was removed, leaving behind a small volume to cover the pellet. The virus was incubated at 4°C for ~12 hr, resuspended in CGM 2, pooled and supplemented with 4 µg/ml polybrene.

Approximately 1.2×10^8 HAP1-7TGP, APC^{KO-1} or $CSNK1A1^{KO-1}$ cells were mutagenized by transduction with retroviral supernatant. ~24 hr before transduction, 6×10^7 cells sere seeded in 3 T-175 flasks (2×10^7 per flask), each containing 30 ml of CGM 2. All the freshly prepared retrovirus was divided into three equal parts, and added to each of the three flasks of cells in two doses ~8 hr apart. Cells were amplified by passaging every ~48 hr, and during each passage cells from all flasks were pooled and 1.2×10^8 were re-seeded in order to retain the complexity of the mutagenized library. 3×10^7 mutagenized cells were used to generate a control dataset of GT insertions (see below).

FACS-based phenotypic enrichment

Screens were started at least 6 days following mutagenesis; for some screens, mutagenized cells were frozen 3 days following transduction with GT-containing retrovirus, and allowed to recover for at least 3 days after thawing and before starting treatments for the screens. ~24 hr before treatment, a total of 1.25×10^8 cells were seeded in 5 T-175 flasks (2.5×10^7 per flask), and grown in 30 ml of CGM 2. Cells were treated for 16–24 hr as follows: for the WNT negative regulator screen (***Figure 1C***), and for the APC (***Figure 5B***) and CSNK1A1 (***Figure 5C***) suppressor screens, cells were left untreated; for the WNT attenuating regulator screen (***Figure 1D***) cells were treated with 12.5% WNT3A CM; for the WNT positive regulators screens at low (***Figure 1E***) and high (***Figure 1F***) stringencies, cells were treated with 50% WNT3A CM; for the low WNT + RSPO screen (***Figure 4A***), cells were treated with 1.04% WNT3A CM and 10 ng/ml recombinant human RSPO1. Cells were harvested, concentrated to ~2×10^7 per ml, strained through a 70 µm cell strainer and a minimum of 2.5×10^7 singlet-gated cells from each flask were sorted in a BD FACSAria Special Order Research Product (BD Biosciences) cell sorter through a 70 µm nozzle, using gates encompassing the

indicated levels of WNT reporter (EGFP) fluorescence. In this way, a total of 1.25×10^8 cells from five flasks were sorted, retaining the diversity of the initial mutant library. A population of singlet-gated cells (not gated based on WNT reporter fluorescence) was also sorted and carried along as a control to set FACS gates during subsequent sorts.

Cells were expanded for 6–8 days to allow recovery and resetting of the WNT reporter, and a portion of the cells (three to four times the number of cells enriched for during the prior sort, in order to maintain an over-representation of the library diversity) was used in the subsequent round of sorting, following the same treatments and FACS gating criteria described above for each screen. For the WNT negative (***Figure 1C***), attenuating (***Figure 1D***), and positive regulator screens at low (***Figure 1E***) and high (***Figure 1F***) stringencies, as well as for the APC (***Figure 5B***) and CSNK1A1 (***Figure 5C***) suppressor screens, cells underwent a total of two consecutive rounds of FACS sorting. For the low WNT + RSPO screen (***Figure 4A***), cells underwent a total of four consecutive rounds of FACS sorting. 3×10^7 cells expanded following the final sort for each screen were used to generate a dataset of GT insertions in the sorted cell populations (see below).

Preparation of genomic GT insertion libraries for deep sequencing

To map GT insertions in control and sorted cells, sequencing libraries were prepared using a linear amplification (LAM) PCR-mediated method described previously (***Carette et al., 2011a***), with modifications. Steps prior to and following each of the two PCR amplifications were carried out in separate dedicated lab spaces to avoid cross-contamination. Genomic DNA was extracted using the QIAamp DNA Mini Kit (QIAGEN Cat. # 51304) according to the manufacturer's 'Spin Protocol: DNA Purification from Blood or Body Fluids'. Each 3×10^7 cell pellet was resuspended in 600 µl PBS, split into three columns, and eluted in 100 µl ultrapure water per column. Typically, 100–130 µg of total genomic DNA were recovered.

A total of 40 µg of DNA were used for the subsequent step, in which 20 µg of DNA were separately digested with 100 units of MseI (NEB Cat. # R0525L) or SpeI (NEB Cat. # R0133L) in a 100 µl reaction containing 1X CutSmart buffer, with overnight incubation at 37°C. DNA from each digest was purified with the QIAquick PCR Purification Kit (QIAGEN Cat. # 28104) according to the manufacturer's protocol, using two separate columns and eluting from each column in 50 µl ultrapure water. DNA recovered from both digests was pooled to obtain approximately 20–30 µg.

A total of 14 µg of DNA were used as template in the subsequent LAM-PCR reaction, initiated from a 5' biotinylated primer specific to a unique viral packaging signal in the GT sequence, and elongating through the adjacent proviral LTR into the flanking sequence in the genome. Seven replicate reactions were set up, each containing 2 µg of DNA, 0.5 pmol of the primer 3LTRflanking-biot1 (5'-GGTCTCCAAATCTCGGTGGAAC-3'), 1X AccuPrime PCR Buffer II and 0.4 µl AccuPrime *Taq* DNA Polymerase, High Fidelity (Thermo Fisher Scientific Cat. # 12346) in a total volume of 50 µl. The following PCR program was run: (5 min at 95°C) x 1 cycle; (30 s at 95°C, 30 s at 58°C, 60 s at 68°C) x 100 cycles. After the first 51 cycles, the reaction was paused and another 0.4 µl of AccuPrime *Taq* DNA Polymerase were added to each reaction. A control reaction containing 2 µg of digested DNA from unmutagenized cells lacking the provirus was run in parallel.

The resulting PCR product from each replicate LAM-PCR reaction was purified on 8 µl of magnetic Dynabeads M280 (Dynabeads kilobaseBINDER Kit, Thermo Fisher Scientific Cat. # 60101). The beads were prewashed three times with 100 µl PBS and once with 20 µl of the Binding Solution included in the kit, using a multi-well magnet. The beads were resuspended in 50 µl Binding Solution, and each 50 µl LAM-PCR reaction was added and mixed thoroughly to resuspend the beads. Reactions were incubated overnight at RT with gentle rotation to capture the biotinylated PCR product on the streptavidin-coated beads.

A 5' phospho, 3' dideoxy DNA linker (5'-TCGTATGCCGTCTTCTGCTTGACTCAGTAGTTG TGCGATGGATTGATG-3') complementary to a Solexa adaptor sequence (see below) was appended to the 3' end of each amplicon using the CircLigase II ssDNA ligase (Epicentre, Cat. # CL9025K). The 3' dideoxy modification on the linker prevents self-ligation, while the biotinylated 5' end of the LAM-PCR product prevents amplicon multimerization. The beads were washed three times with 100 µl PBS (excess buffer was carefully removed), resuspended thoroughly in 20 µl of a reaction containing 25 pmol of DNA linker, 1X CircLigase II reaction buffer, 2.5 mM $MnCl_2$, 1 M Betaine and 0.75 µl CircLigase II ssDNA Ligase, and incubated at 60°C for 1 hr.

The LAM-PCR product comprising genomic sequence flanked by the LTR junction on the 5' end and by the linker on the 3' end was amplified exponentially using complementary primers containing Solexa adaptor sequences, LTRSolexal (5'-AATGATACGGCGACCACCGAGATCTGATGGTTCTC TAGCTTGCC-3') and Solexa adaptor II (5'-CAAGCAGAAGACGGCATACGA-3'). The beads were washed three times with 100 µl PBS (excess buffer was carefully removed) and resuspended thoroughly in 50 µl of a reaction containing 25 pmol of each primer, 1X AccuPrime PCR Buffer II and 0.6 µl of AccuPrime *Taq* DNA Polymerase, High Fidelity. The following PCR program was run: (2 min at 95˚C) x 1 cycle; (30 s at 95˚C, 30 s at 55˚C, 90 s at 68˚C) x 35 cycles; (7 min at 68˚C) x 1 cycle. Tubes were centrifuged briefly to recover the solution and pellet the beads, and the supernatant was removed for analysis and final PCR product purification.

8 µl of the PCR product was analyzed on a 2% agarose diagnostic gel, along with the control reaction prepared from unmutagenized cells. A smear between 100 and 500 base pairs (bp) is typically visible for reactions from GT-mutagenized DNA, indicative of a successful library preparation, but not for the control reaction from unmutagenized DNA. Successful reactions were pooled, and the final PCR product from 100 µl of solution was purified using the QIAquick PCR Purification Kit and eluted in 50 µl of ultrapure water. A 10 nM solution of the product (the concentration was calculated using an estimated average PCR product size of 360 bp) was sequenced on one lane of an Illumina Genome Analyzer IIx using a custom sequencing primer specific to the outer extreme end of the LTR (SolexaseqFlank: 5'-CTAGCTTGCCAAACCTACAGGTGGGGTCTTTCA-3'), resulting in 36 bp reads of the sequence directly flanking GT insertion sites. FASTQ files containing the sequencing data for unsorted (control) and sorted cells from each screen have been deposited in the National Center for Biotechnology Information (NCBI) Sequence Read Archive (SRA) with Study accession number SRP094861.

Mapping of sequencing reads and statistical analysis of GT insertion enrichment

GT insertions were mapped as described previously (***Carette et al., 2011a***). Briefly, the 36 bp sequences in the FASTQ sequencing data files were aligned to the human genome version 18 (hg18) using Bowtie alignment software (***Langmead et al., 2009***). To generate a dataset of unique GT insertion sites, we excluded ambiguous alignments (no mismatches in the full 36 bp sequence were allowed) and sequences that aligned non-uniquely to the human genome. Furthermore, the sequence was required to align uniquely to the human genome even when 1 or 2 mismatches were allowed, and if two sequences aligned 1 or 2 base pairs apart, only one was retained.

For each screen, insertions mapped to genes in the sorted cells were compared to those in the unsorted control population. The number of insertions per gene was determined by intersecting each dataset of unique insertion sites with a list of the chromosomal coordinates of RefSeq-annotated genes. If an insertion was located in a genomic region shared by multiple transcripts of the same gene, it was only counted once. GT insertions in annotated genes were classified as being in the sense or antisense orientation relative to the coding sequence of the gene, and as being in exons or introns. For the unsorted (control) cells, the number of GT insertions in each gene (regardless of orientation), and the total number of insertions for all genes was determined. For the sorted cells, the number of inactivating GT insertions in each gene, defined as sense and antisense insertions in exons and sense insertions in introns, and the total number of inactivating insertions for all genes was determined. Enrichment of GT insertions for a given gene was calculated by comparing the relative frequency at which that gene harbored *inactivating* GT insertions in the sorted cells compared to the relative frequency at which the gene carried *any* GT insertion in the control dataset. For each gene, a *p*-value was calculated using the one-sided Fisher exact test and was corrected for false discovery rate (FDR) (see ***Supplementary file 1***).

Comparative analysis of significant hits across screens

The FDR-corrected *p*-value for enrichment of GT insertions in the sorted compared to the control cells depends on many experimental variables affecting both datasets, making it an equivocal metric to directly compare hits between screens. We therefore developed an additional scoring metric that depends only on the dataset for the sorted cells. It relies on the fact that generally only sense GT insertions in introns should inactivate genes due to the directionality of the splice acceptor in the

GT, and it captures the relative abundance of intronic GT insertions in the sense and antisense orientations, as well as the overall number of intronic insertions. We defined the Intronic GT Insertion Orientation Bias (IGTIOB) score as $\log_2(S/A) \times \ln(S \times A)$, where 'S' and 'A' equal one plus the number of unique sense or antisense intronic GT insertions, respectively, in a given gene. High, positive IGTIOB scores generally indicate genes whose disruption promotes the phenotype enriched for during the screen.

To compare hits between screens, we first generated a list of genes including only those with a stringent GT enrichment FDR-corrected *p*-value<10^{-4} in at least one of the screens being considered ***Supplementary file 3.*** We then used the IGTIOB scores of those genes in all the relevant screens to build a heat map (***Figures 4B*** and ***5D***). Genes were clustered using the absolute value/city block setting and complete linkage method (without normalization) in the hierarchical clustering tool of the Partek Genomics Suite software, and the data range was adjusted to encompass only non-negative IGTIOB scores (i.e. negative values were displayed as 0). Groups of genes preferentially enriched for GT insertions in one or more screens (as determined by visual inspection) are indicated next to the heat maps.

Construction of mutant HAP1-7TGP cell lines by CRISPR/Cas9-mediated genome editing

Oligonucleotides encoding single guide RNAs (sgRNAs) (***Supplementary file 4***) were selected from a published library (***Shalem et al., 2014***), or designed using either of two online CRISPR design tools (***Hsu et al., 2013***; ***Doench et al., 2014***) and cloned into pX330 according to a published protocol (original version of 'Target Sequence Cloning Protocol' from http://www.genome-engineering.org/crispr/wp-content/uploads/2014/05/CRISPR-Reagent-Description-Rev20140509.pdf; ***Cong et al., 2013***).

Clonal HAP1-7TGP cell lines were established by transient transfection with pX330 containing the sgRNA followed by single cell sorting as follows. A transfection mix was prepared by diluting 450 ng of pX330 and 50 ng of pmCherry (used as a co-transfection marker for FACS sorting) in 48 µl Opti-MEM I, adding 2 µl of X-tremeGENE HP and incubating for 20 min at RT. HAP1-7TGP cells or derivatives thereof were reverse-transfected in a well of a 24-well plate by overlaying 0.5 ml of CGM 2 (without antibiotics) containing 6×10^5 cells over the 50 µl of transfection mix. Cells were passaged to a 10 cm dish ~24 hr post-transfection, using 150 µl of Trypsin-EDTA (0.25%) (Thermo Fisher Scientific Cat. # 25200056) to detach them (reverse-transfection of HAP1 cells caused unusually high adherence, hence the higher trypsin concentration). Four to five days post-transfection, single transfected (mCherry-positive) cells were sorted into 96-well plates containing 200 µl of CGM 2 per well and grown undisturbed for 16 to 17 days. Single colonies were passaged to 24-well plates, and a small number of cells was reserved for genotyping.

For genotyping, genomic DNA was extracted by adding 4 volumes of QuickExtract DNA Extraction Solution (Epicentre Cat. # QE09050) to the cells. Extracts were incubated 10 min at 65°C, 3 min at 98°C, and 5 µl were used as input for PCR amplification of the sgRNA target site in 15 µl reactions containing 1X LongAmp *Taq* reaction buffer, 300 µM of each dNTP, 400 nM of each of the flanking primers indicated in ***Supplementary file 4*** (most of them designed using the Primer-BLAST online tool from the NCBI) and 0.1 units/µl of LongAmp *Taq* DNA polymerase (NEB Cat. # M0323L). The presence of desired mutations was initially assessed by analysis of the PCR products on a 1% agarose gel (i.e. the absence of an amplicon or a shift in its size was deemed indicative of a lesion) and was confirmed by sequencing the amplicons using the primers indicated in ***Supplementary file 4***. Given that most engineered cell lines remained haploid, sequencing results were usually unequivocal. A summary of the sequencing results for all clonal cell lines used in the study is presented in ***Supplementary file 2***, and for selected clonal cell lines immunoblot analysis of the protein products is presented in ***Figures 2C***, ***6D and H***, ***Figure 3—figure supplement 1A*** and ***Figure 5—figure supplement 1A***.

Whenever possible, multiple independent mutant cells lines, often generated using two different sgRNAs (see ***Supplementary file 2***), were expanded and used for further characterization. For some of the comparisons between WT and mutant cells, multiple individual cell lines confirmed by sequencing to be WT at the sgRNA target site were also expanded and used as controls. To generate double and triple mutant cell lines, a single clonal cell line with the first desired mutation was used in a subsequent round of transfection with pX330 containing the second and, if applicable,

third sgRNAs. Alternatively, WT HAP1-7TGP cells were directly transfected with a combination of pX330 constructs targeting two genes simultaneously. To facilitate screening of mutant clones by PCR when targeting two genes simultaneously, we sometimes targeted one of them at two different sites within the same exon or on adjacent exons and amplified genomic sequence encompassing both target sites. Mutant clones were readily identified by the reduced size of the resulting amplicon, and the precise lesion was confirmed by sequencing.

Isolation of APC^{KO-2} mutant cell line containing a GT insertion

As an alternative to CRISPR/Cas9-mediated genome editing, a mutant cell line containing a GT insertion in APC was isolated as follows. Mutagenized HAP1-7TGP cells enriched during the WNT-negative regulator screen (***Figure 1C***) were used to isolate the APC^{KO-2} clone. Following the screen, the same FACS gate used during the screen was used to sort single cells into 96-well plates.

Colonies were harvested after 16 days, 1/10th of each clone was passaged for continued growth, and the remainder of the cells from adjacent pairs of rows in each plate were pooled. A portion of all the cells from pairs of plates were further pooled so as to obtain 'plate-pair' pools, and 'row-pair' sub-pools. Cells from plate-pair pools were harvested by centrifugation, genomic DNA was prepared using the QIAamp DNA mini kit and each pool was probed for clones containing GTs in *APC* using a nested PCR strategy. A genomic region of *APC* enriched for GT insertions was amplified by PCR using a forward primer complementary to a unique sequence in the GT (pGT-Puro4: 5'-TCTCCAAATCTCGGTGGAAC-3') and a reverse primer complementary to a unique genomic sequence adjacent to the GT-enriched region in *APC* (APC_GT: 5'-TGCTACAATGAGCTGTTAAAATGG-3'). 400 ng of genomic DNA was used as input for PCR amplification in 25 µl reactions containing 1X LongAmp *Taq* reaction buffer, 300 µM of each dNTP, 400 nM of each primer and 0.1 units/µl of LongAmp *Taq* DNA polymerase. For each plate-pair pool, the presence of clones containing a GT insertion was evident as discrete bands when the PCR products were analyzed on a 1% agarose gel.

Once positive plate-pair pools were identified, genomic DNA from the corresponding row-pair sub-pools was prepared using QuickExtract DNA Extraction Solution and the PCR procedure was repeated to identify row pairs containing clones with GT insertions. Finally, the individual clonal cell lines that had been passaged were harvested from the 96-well plates containing GT-positive row pairs, and GT-containing clones were identified using the same procedure. To map the precise genomic location of the GT insertion in APC^{KO-2} (see ***Supplementary file 2***), the final PCR product obtained from an individual GT-positive clone was sequenced.

Rescue of TFAP4^{CR-1} cells

Rescue of TFAP4^{CR-1} cells and overexpression of TFAP4 in WT HAP1-7TGP cells (***Figure 2B***) was done by transient transfection. TFAP4^{CR-1}and HAP1-7TGP were reverse-transfected in a well of a 24-well plate by overlaying 0.5 ml of CGM 2 (without antibiotics) containing 6 $\times$ 10^5 cells over 50 µl of a transfection mix containing 450 ng of pCSDest-TFAP4 or pCS2$^+$ (vector control) and 50 ng of pmCherry (as a co-transfection marker for FACS analysis) in Opti-MEM I, and 2 µl of X-tremeGENE HP. Cells were harvested using 150 µl of Trypsin-EDTA (0.25%) and passaged to a 6 cm dish ~24 hr post-transfection. ~48 hr post-transfection cells were treated for 16–24 hr with 50% WNT3A CM where indicated, and the WNT reporter (EGFP) fluorescence of mCherry-positive, singlet-gated cells was measured by FACS.

Epistasis analysis in TFAP4^{CR-1} cells

Epistasis analysis in WT HAP1-7TGP and TFAP4^{CR-1} cells (***Figure 2D***) was done following treatment with WNT3A, the GSK3 inhibitor LiCl, or following transient transfection with dominant negative CTNNB1 (S33Y mutant) as follows. WT HAP1-7TGP and TFAP4^{CR-1} cells were treated for 16–24 hr with 50% WNT3A CM or with 40 mM LiCl in CGM 2 where indicated, and the WNT reporter fluorescence of singlet-gated cells was measured by FACS. Alternatively, WT HAP1-7TGP and TFAP4^{CR-1} cells were reverse transfected with pCS2$^+$ (vector control) or pCS2-β-cat-S33Y and pmCherry (as a co-transfection marker for FACS analysis) as described in the previous section. Cells were passaged ~24 hr post-transfection, and ~48 hr post-transfection the WNT reporter (EGFP) fluorescence of mCherry-positive, singlet-gated cells was measured by FACS.

Quantitative RT-PCR analysis

Approximately 24 hr before treatment, cells were seeded in 24-well plates at a density of 2×10^5 per well and grown in 0.5 ml of CGM 2. Cells were treated for 12 hr with 50% WNT3A CM in CGM 2 where indicated. The medium was removed, and cells were harvested without washing in 800 µl of TRIzol Reagent (Thermo Fisher Scientific Cat. # 15596018). Extracts were processed according to the manufacturer's protocol taking the appropriate precautions to avoid contamination with nucleases, and total RNA was resuspended in 40 µl of DEPC-treated water (Thermo Fisher Scientific Cat. # AM9920). To synthesize cDNA, 250 ng of RNA were diluted in 8 µl DEPC-treated water, 2 µl of 5X iScript Reverse Transcrition Supermix for RT-qPCR (Bio-Rad Cat. # 170–8841) were added, and the reaction was incubated 5 min at 25°C, 30 min at 42°C and 5 min at 85°C. cDNA was diluted 1:100 in water, and 5 µl were mixed with 5 µl of iTaq Universal SYBR Green Supermix (Bio-Rad Cat. # 172–5121) containing 400 nM each of forward and reverse primer (hAXIN2-RT-PCR-1-FOR: 5'-GTCCAGCAAAACTCTGAGGG-3', hAXIN2-RT-PCR-1-REV: 5'-CTGGTGCAAAGACATAGCCA-3'; hCTNNB1-RT-PCR-1-FOR: 5'-AAAGCGGCTGTTAGTCACTGG-3', hCTNNB1-RT-PCR-1-REV: 5'-CGAGTCA TTGCATACTGTCCAT-3'; hHPRT1-RT-PCR-1-FOR: 5'-TGCTGAGGATTTGGAAAGGG-3', hHPRT1-RT-PCR-1-REV: 5'-ACAGAGGGCTACAATGTGATG-3'). Triplicate reactions for each cDNA and primer pair were prepared in a MicroAmp Optical 384-well Reaction Plate (Thermo Fisher Scientific Cat. # 4309849), sealed with MicroAmp Optical Adhesive Film (Thermo Fisher Scientific Cat. # 4311971) and run using standard parameters in an ABI 7900 Fast Real-Time PCR system (Applied Biosystems) controlled by the Sequence Detection Systems software version 2.4.1 provided by the manufacturer. The formula $2^{-\Delta Ct}$ was used to calculate the average relative abundance of *AXIN2* (***Figures 2A***, ***6B and F*** and ***Figure 6—figure supplement 1A and E***) or *CTNNB1* (***Figure 6—figure supplement 1C***) mRNA normalized to *HPRT1* mRNA, and fold-changes in mRNA abundance were calculated as the quotient between the experimental and reference samples, with appropriate error propagation of the respective standard deviations (SD).

Immunoblot analysis of HAP1-7TGP and mutant cell lines

Quantitative immunoblot analysis of soluble CTNNB1 from membrane-free supernatant (MFS) (***Figures 2C***, ***3D,F***, ***6C,D,G and H***, ***Figure 3—figure supplement 1C*** and ***Figure 6—figure supplement 1B and F***)

Approximately 24 hr before treatment cells were seeded in 6 cm dishes at a density of 4×10^6 per dish and grown in 6 ml of CGM 2. Cells were treated for 10 hr with 50% WNT3A CM or 10 µM of the GSK3 inhibitor CHIR-99021 in CGM 2 where indicated. Cells were harvested, lysed by hypotonic shock, and extracts were prepared as follows, with all handling done on ice or at 4°C. Cells were washed twice with ~5 ml cold PBS and twice with ~5 ml cold 10 mM HEPES pH 7.4. Residual buffer was removed, and 100 µl of ice cold SEAT buffer (10 mM triethanolamine/acetic acid pH 7.6, 250 mM sucrose, 1X SIGMA*FAST* Protease Inhibitor Cocktail Tablets EDTA-free (Sigma-Aldrich Cat. # S8830), 25 µM MG132 (Sigma-Aldrich Cat. # C2211), 1X PhosSTOP (Roche Cat. # 04906837001), 1 mM NaF, 1 mM Na_3VO_4, 1 mM dithiothreitol (DTT), 62.5 U/ml Benzonase Nuclease (EMD Millipore Cat. # 70664), 1 mM $MgCl_2$) were added to the cells. Cells were scraped using a cell lifter (Corning Cat. # 3008), transferred to 2-ml centrifuge tubes and disrupted mechanically by triturating 10 times. Crude extracts were centrifuged for 20 min at 20,000 x g to pellet membranes and nuclei, and the membrane-free supernatant (MFS) was carefully removed, avoiding contamination from the pellet. The MFS was flash-frozen in liquid nitrogen and stored at −80°C until further processing.

Extracts were thawed quickly at RT and transferred to ice. The protein concentration in the MFS was quantified with the Pierce BCA Protein Assay Kit (Thermo Fisher Scientific Cat. # 23225), using BSA as a standard, and samples were normalized by dilution with SEAT buffer. The MFS was diluted with 4X LDS sample buffer (Thermo Fisher Scientific Cat. # NP0007) supplemented with 50 mM *tris* (2-carboxyethyl)phosphine (TCEP), heated for 5 min at 95°C, and 30 µg of total protein were electrophoresed alongside Precision Plus Protein All Blue Prestained Protein Standards (Bio-Rad Cat. # 1610373) in NuPAGE 4–12% Bis-Tris gels (Thermo Fisher Scientific, various Cat. numbers) using 1X NuPAGE MOPS SDS running buffer (Thermo Fisher Scientific Cat. # NP0001), or on 8% Tris-polyacrylamide home-made gels using Tris-glycine SDS running buffer (25 mM Tris, 192 mM glycine, 0.1% SDS).

Proteins were transferred to nitrocellulose membranes in a Criterion Blotter apparatus (Bio-Rad Cat. # 1704071) using 1X NuPAGE transfer buffer (Thermo Fisher Scientific Cat. # NP0006) + 10% methanol for Bis-Tris gels, or Tris-glycine wet transfer buffer (12 mM Tris, 96 mM Glycine, 10% methanol) for Tris-polyacrylamide gels. Membranes were cut, blocked with Odyssey Blocking Buffer, incubated with mouse anti-β-catenin, mouse anti-GAPDH or mouse anti-ACTIN primary antibodies, washed with TBST, incubated with IRDye 800CW donkey anti-mouse IgG secondary antibody, washed with TBST followed by TBS, and imaged using the Li-Cor Odyssey imaging system. Acquisition parameters in the manufacturer's Li-Cor Odyssey Image Studio software were set so as to avoid saturated pixels in the bands of interest, and bands were quantified using manual background subtraction. The integrated intensity for CTNNB1 was normalized to that for GAPDH or ACTIN in the same blot, and the average ± SD from duplicate blots was used to represent the data, except for the TFAP4 experiment shown in ***Figure 2C***, for which only one blot was analyzed.

Other immunoblot analyses of MFS (***Figures 2C, 6D and H*** and ***Figure 5—figure supplement 1A***)

The same membrane probed for GAPDH in the experiment shown in ***Figure 2C*** was subsequently incubated with rabbit anti-AP4 (TFAP4). The same membranes or duplicates of the ones probed for GAPDH in the experiments shown in ***Figure 6D and H*** were subsequently incubated with rabbit anti-SERBP1 or goat anti-casein kinase 1α primary antibodies, respectively. The same membrane probed for CTNNB1 in the experiment shown in ***Figure 6D*** was subsequently incubated with rabbit anti-APC. Following washes, the blots were incubated with IRDye 680RD donkey anti-rabbit IgG, peroxidase AffiniPure donkey anti-goat IgG, or peroxidase AffiniPure goat anti-rabbit IgG secondary antibodies, as appropriate. The TFAP4 and SERBP1 blots were imaged using the Li-Cor Odyssey imaging system, and the CSNK1A1 and APC blots were developed using the SuperSignal West Femto Maximum Sensitivity Substrate (Thermo Fisher Scientific Cat. # 34095).

To probe for HUWE1 (~480 kDa, ***Figure 6H***) the same extracts used to quantify CTNNB1 in ***Figure 6H*** were electrophoresed in a 4% Tris-polyacrylamide gel strengthened with 0.5% agarose (based on the protocol of ***Kinoshita et al., 2009***) using Tris-glycine SDS running buffer. Proteins were transferred to nitrocellulose membranes using Tris-glycine wet transfer buffer, blocked with TBST + 5% skim milk, and incubated with rabbit anti-Lasu1/Ureb1 (HUWE1) primary antibody, followed by peroxidase AffiniPure goat anti-rabbit IgG secondary antibody. The membrane was developed using the SuperSignal West Femto Maximum Sensitivity Substrate.

Immunoblot analysis of total AXIN1 and AXIN2 (***Figure 3—figure supplement 1A***)

Approximately 24 hr before treatment, cells were seeded in 6 cm dishes at a density of 4×10^6 per dish, and grown in 6 ml of CGM 2. Cells were treated with 10 µM CHIR-99021 in CGM 2 for 14 hr to induce expression of *AXIN2*. Cells were harvested in 1 ml Trypsin-EDTA (0.05%), resuspended in 3 ml CGM 2, centrifuged at 400 x g for 5 min, washed in 1.9 ml PBS, transferred to 2-ml centrifuge tubes and centrifuged at 800 x g for 5 min. The supernatant was aspirated and the cell pellets were flash-frozen in liquid nitrogen and stored at −80°C. Pellets were thawed quickly at RT and transferred to ice. All subsequent steps were done on ice or at 4°C. The cell pellets were resuspended in 150 µl of ice-cold RIPA lysis buffer (50 mM Tris-HCl pH 8.0, 150 mM NaCl, 2% NP-40, 0.25% deoxycholate, 0.1% SDS, 1X SIGMA*FAST* protease inhibitors, 1 mM $MgCl_2$, 62.5 U/ml Benzonase Nuclease, 1 mM DTT, 10% glycerol), sonicated in a Bioruptor 300 (Diagenode) 4×30 s in the high setting, centrifuged 10 min at 20,000 x g and the supernatant was recovered.

The protein concentration in the supernatant was quantified using the Pierce BCA Protein Assay Kit. Samples were normalized by dilution with RIPA lysis buffer, further diluted with 4X LDS sample buffer supplemented with 50 mM TCEP, heated for 5 min at 95°C, and 100 µg of total protein were electrophoresed alongside Precision Plus Protein All Blue Prestained Protein Standards in NuPAGE 4–12% Bis-Tris gels using 1X NuPAGE MOPS SDS running buffer.

Proteins were transferred to nitrocellulose membranes using 1X NuPAGE transfer buffer + 10% methanol, and membranes were cut and blocked with TBST + 5% skim milk. Blots were incubated with goat anti-AXIN1, rabbit anti-AXIN2 or mouse anti-GAPDH primary antibodies, washed with

TBST, incubated with Peroxidase AffiniPure anti-goat, anti-rabbit or anti-mouse secondary antibodies, washed with TBST followed by TBS, and developed with SuperSignal West Femto.

Immunofluorescence of HAP1-7TGP and mutant cell lines

CTNNB1 immunostaining (*Figure 3—figure supplement 2B–2F*)

Approximately 24 hr before treatment, cells were seeded at a density of 4×10^4 per well on Poly-L-Lysine-coated #1 12 mm round coverslips placed in 24-well plates, and were grown in 0.5 ml of CGM 2. Cells were treated for 4 hr (or the periods indicated in the time-course experiment depicted in *Figure 3—figure supplement 2A*) with CGM 2 or with 50% WNT3A CM in CGM2 where indicated. Following treatment, the medium was removed, and cells were washed once with PBS and fixed with 4% paraformaldehyde in PBS for 10 min. Fixed cells were washed with PBS 3 × 5 min, blocked with blocking solution (PBS, 0.5% Triton X-100, 3% BSA) for 30 min and stained with mouse anti-β-catenin in blocking solution for 30 min at RT. Cells were washed with PBS 3 × 5 min and stained with donkey anti-mouse IgG (H+L) Alexa Fluor 647 conjugate in blocking solution for 30 min at RT. Cells were washed with PBS 3 × 5 min and mounted on slides using ProLong Diamond Antifade Mountant with DAPI (Thermo Fisher Scientific Cat. # P36962). Fluorescence micrographs were acquired on a Leica SP8 laser scanning confocal microscope equipped with a 63X oil immersion objective (NA 1.4) and an HyD hybrid detector, using Leica Application Suite X (LASX) software. During a given experiment, all Z-stacks were acquired with identical settings (laser power, gain, offset, frame format). Confocal sections were viewed and exported as TIF files using Volocity 6.3 (PerkinElmer), adjusted equally for contrast and brightness when necessary for clarity using Photoshop CS5 (Adobe), and arranged in Illustrator CS5 (Adobe).

Quantification of nuclear CTNNB1 (*Figure 3E and F* and *Figure 3—figure supplement 2A*)

Leica Image Files (LIF) were converted into MATLAB matrices (MAT) in Volocity 6.3 (PerkinElmer). Matrices were manually curated to remove out-of-focus optical planes and analyzed using MATLAB R2014b (MathWorks) to determine the mean fluorescence intensity of nuclear CTNNB1 staining. Briefly, the fluorescence values from the DAPI channel were smoothed using a low-pass Gaussian filter to remove fine noise, and a threshold was applied to generate a nuclear mask. The nuclear mask was eroded uniformly to prevent contamination with cytoplasmic signal and optical sections with poor nuclear masks were discarded. The fluorescence values from the irrelevant pool of CTNNB1 at tight junctions were removed from the CTNNB1 channel in each plane using a high-pass Gaussian filter. The sum of the corrected fluorescence intensity values from the CTNNB1 channel co-localizing with the nuclear mask were divided by the nuclear mask area to obtain the mean nuclear fluorescence per unit area for each optical plane. The final reported value for each field of view, referred to as 'nuclear CTNNB1', is the median of the mean nuclear fluorescence per unit area obtained from the three most central optical sections. The graphs presented in *Figure 3E* and *Figure 3—figure supplement 2A* display the average (± SD) nuclear CTNNB1 from two or three fields of view.

Xenopus laevis body axis duplication assay

mRNA was synthesized using the mMESSAGE mMACHINE SP6 Kit (Thermo Fisher Scientific Cat. # AM1340) from a pCSDest-based construct containing the CDS encoding the protein of interest. One microgram of plasmid DNA was linearized and mRNA was synthesized according to the protocol provided by the manufacturer. The mRNA was treated with TURBO DNase and purified using the RNeasy Mini Kit (QIAGEN Cat. # 74104), following the 'RNA cleanup' protocol. The purified product was analyzed on a 1% agarose gel. *X. laevis* eggs were fertilized, de-jellied with L-cysteine, and equilibrated in Marc's Modified Ringers (MMR: 0.1 M NaCl, 2 mM KCl, 1 mM $MgSO_4$, 2 mM $CaCl_2$, 5 mM HEPES pH 7.8, 0.1 mM EDTA) containing 2% Ficoll. One ventral blastomere of four-cell stage embryos was injected with 3 nl of a 1.67 ng/nl mRNA solution (5 ng total) using an MPPI-2 Pressure Injector (Applied Scientific Instrumentation). Embryos were incubated at RT in 1/3 MMR until stage 34 and scored for body axis duplication (*Figure 2F*) on a Zeiss Stemi 2000-C stereo microscope. Embryos were fixed overnight in MEMFA buffer (100 mM MOPS, 2 mM EGTA, 1 mM $MgSO_4$, 3.7% formaldehyde) transferred to 100% glycerol and images (*Figure 2E*) were taken with an Olympus DP72 camera at 2.5X magnification.

Drosophila melanogaster methods

Flies and transgenes

The driver *C765-Gal4* (BDSC) was used for all crosses. All experiments were performed at 25°C. *pUASTattB-Axin-V5* was generated as described previously (**Yang et al., 2016**). To generate the *pUASTattB-AxinΔC-V5* transgene, residues 705 through 745 were deleted by PCR-based mutagenesis of *pUASTattB-Axin-V5* using the oligonucleotide 5'-GGTCACTTTAGGAAGCTTGGTAAACC-3'. The resulting *AxinΔC-V5* fragment was digested with KpnI and HindIII, and cloned into the *pUAS-TattB* vector digested with the same enzymes. Transgenic flies were generated using site-specific integration at the *attP33* site using phiC31-based integration (**Bischof et al., 2007**).

Imaging of adult fly wings (**Figure 3G**)

Images of adult fly wings were acquired with a Nikon E800 Epifluorescence microscope using Olympus DP software.

Immunostaining of wing imaginal discs (**Figure 3—figure supplement 3B**)

Third instar larval wing imaginal discs were dissected in PBS, fixed with 4% paraformaldehyde in PBS for 20 min, washed with PBS + 0.1% Triton X-100, and incubated in blocking solution (PBS, 0.5% Triton X-100, 10% BSA) for 1 hr. Imaginal discs were incubated with anti-Senseless or anti-Wingless primary antibodies in PBS + 0.5% Triton X-100 overnight at 4°C, and with appropriate secondary antibodies for 2 hr at RT. Fluorescence images were acquired using a Nikon A1RSi confocal microscope and processed using Photoshop CS5 (Adobe).

Immunostaining of embryos (**Figure 3—figure supplement 3C**)

Embryos were fixed in 3.7% formaldehyde (**Vorwald-Denholtz and De Robertis, 2011**) and rehydrated in PBT (PBS, 1% BSA, 0.1% Tween-20). Following incubation for 1 hr in blocking solution (PBS, 10% BSA, 0.1% Tween-20), embryos were incubated with mouse anti-Engrailed/Invected or mouse anti-Wingless primary antibodies in PBT overnight at 4°C. After washing with PT (PBS, 0.1% Tween-20), embryos were incubated for 1 hr with donkey anti-mouse IgG (H+L) Alexa Fluor 555 secondary antibody for 1 hr at RT. Embryos were then washed with PT and mounted in ProLong Gold Antifade Mountant (Thermo Fisher Scientific Cat. # P10144). Fluorescence images were acquired on a Nikon NIS confocal microscope, processed using Photoshop CS5 (Adobe) and assembled using Illustrator CS5 (Adobe).

Immunoblotting of embryonic lysates (**Figure 3—figure supplement 3E**)

Embryos were lysed in lysis buffer (50 mM Tris-HCl pH 8.0, 100 mM NaCl, 1% NP-40, 10% glycerol, 1.5 mM EDTA pH 8.0, 1X Halt Protease and Phosphatase Inhibitor Cocktail (Thermo Fisher Scientific Cat. # 78440)). Lysates were fractionated on 8% SDS-PAGE, transferred to PVDF membranes and blocked in TBST + 5% skim milk. Membranes were incubated with mouse anti-V5 or mouse anti-α-Tubulin primary antibodies, washed with TBST, incubated with anti-mouse IgG HRP conjugated secondary antibody, washed, and developed using ECL reagent (250 mM luminol, 90 mM p-coumaric acid, 100 mM Tris-HCl pH 8.5, 30% hydrogen peroxide). Protein levels were quantified by densitometry of scanned film using Image J software (National Institutes of Health).

Cuticle preparations (**Figure 3—figure supplement 3G**)

Larval cuticles were prepared as described previously (**Wieschaus and Nüsslein-Volhard, 1986**).

Embryonic hatch rate determination (**Figure 3—figure supplement 3H**)

Fly eggs collected during a 1 hr period were incubated at 25°C for an additional 24 hr before the hatch rate was scored.

RNAseq analysis

Gene expression levels in WT HAP1 cells were determined from previously published data (**Dubey et al., 2016**). Briefly, the raw RNAseq data for WT HAP1 cells (NCBI Gene Expression Omnibus (GEO) Series accession number GSE75515) was aligned, quantified and analyzed using Partek

Flow software, version 4.0 (Partek Inc.). Reads were aligned to human reference genome build hg19 using the STAR Align and Quantify pipeline in Partek Flow. RPKM (Reads Per Kilobase of transcript per Million mapped reads) normalization was used to obtain the values reported in ***Table 1***. The normalized data was imported into Partek Genomics Suite 6.6 software (Partek Inc.) to visualize the quantification of normalized reads for selected genes, and ***Table 1*** was assembled in Excel (Microsoft).

Preparation of figures and statistical analysis

Illustrations were prepared using PowerPoint (Microsoft) and Illustrator CS6 (Adobe). Circle plots depicting the hits from each screen, GT insertion histograms, dose response graphs, tables and supplementary files were prepared using Excel (Microsoft). Bar and circle graphs were prepared using Prism 6 (GraphPad Software) and statistical analysis was performed using the same software (details of statistical tests used are given in the figure legends). Heat maps were generated using Partek Genomics Suite 6.6 software (Partek Inc.) and finished in Illustrator CS6. FACS histograms and dot plots were generated using FlowJo (FlowJo, LLC) and finished in Illustrator CS6. Pictures of immunoblots and model organisms were only adjusted for contrast and brightness when necessary for clarity using Photoshop CS6 (Adobe), and were arranged in Illustrator CS6.

Acknowledgements

We thank Marc Kirschner, Timothy Mitchison, Tom Rapoport, Henry Ho, Lingyin Li and Ganesh Pusapati for comments on the manuscript. We thank Marc Kirschner, Timothy Mitchison, Tom Rapoport, Roel Nusse and members of the Rohatgi and Carette labs for input on the project. We thank Yan Ma for help making constructs and cell lines. We thank Patty Lovelace and Jennifer Cheung for training and assistance with FACS, and the Stanford Institute for Stem Cell Biology and Regenerative Medicine FACS Core for use of instruments, purchased in part using an S10 Shared Instrumentation Grant (1S10RR029333801) from the National Institutes of Health (NIH). This work was funded in part by NIH grants DP2 GM105448 (RR), DP2 AI104557 (JEC), R01 GM081635 (EL), R01 GM103926 (EL) and RO1 CA105038 (YA), by the Norris Cotton Cancer Center (YA) and by start-up funds from the Stanford Cancer Institute (RR). JEC is a David and Lucile Packard Foundation fellow and RR is a Josephine Q. Berry Faculty Scholar in Cancer Research at Stanford. AML was supported by the Stanford Dean's Postdoctoral Fellowship, the Stanford Cancer Biology Program Training Grant and the Novartis sponsored Fellowship from the Helen Hay Whitney Foundation. The authors declare no conflicts of interest.

Additional information

Funding

Funder	Grant reference number	Author
Helen Hay Whitney Foundation	Novartis Fellowship	Andres M Lebensohn
National Institutes of Health	RO1 CA105038	Yashi Ahmed
National Institutes of Health	R01 GM081635	Ethan Lee
National Institutes of Health	R01 GM103926	Ethan Lee
National Institutes of Health	DP2 AI104557	Jan E Carette
David and Lucile Packard Foundation	Fellow Award	Jan E Carette
Stanford University School of Medicine	Josephine Q.Berry Fellowship	Rajat Rohatgi
National Institutes of Health	DP2 GM105448	Rajat Rohatgi

The funders had no role in study design, data collection and interpretation, or the decision to submit the work for publication.

Author contributions

AML, Conceived the study, Designed experiments, Analyzed the data, Conducted or oversaw all experiments except those in model organisms, Wrote the manuscript; RD, Executed the CSNK1A1 suppressor screen, Gave feedback on the manuscript; LRN, Conducted *X. laevis* experiments; OT-B, EY, Conducted *D. melanogaster* experiments; CDM, Prepared sequencing libraries; EMD, BBP, Developed computational tools for the comparative analysis of screens; ZB-N, Executed the APC suppressor screen; KJT, Imaged and quantified nuclear CTNNB1 in haploid human cells; YA, Oversaw *D. melanogaster* experiments, Gave feedback on the manuscript; EL, Oversaw *X. laevis* experiments, Gave feedback on the manuscript; JEC, Conceived the study, Designed experiments, Analyzed the data, Gave feedback on the manuscript; RR, Conceived the study, Designed experiments, Analyzed the data, Wrote the manuscript

Author ORCIDs

Andres M Lebensohn, http://orcid.org/0000-0002-4224-8819
Rajat Rohatgi, http://orcid.org/0000-0001-7609-8858

Additional files

Supplementary files

• Supplementary file 1. Ranked lists of hits from all screens. Genes containing at least one GT insertion in the population of sorted cells from each genetic screen described in this work are listed in separate spreadsheets (the screen name is indicated on the tab of each spreadsheet), and are ranked based on the significance of GT insertion enrichment (*p*-value) in the sorted vs. the unsorted (control) cells. For the unsorted cells, the number of GT insertions in genes (regardless of orientation) is indicated for the complete dataset and for each gene (column B). For the sorted cells, the number of inactivating GT insertions in genes (sense and antisense insertions in exons and sense insertions in introns), as well as the number of sense or antisense GT insertions in exons or in introns, is indicated for the complete dataset and for each gene (columns C-G). Three measures of GT insertion enrichment are shown: the *p*-value and the FDR-corrected *p*-value (both derived from columns B and C), and the Intronic GT Insertion Orientation Bias (IGTIOB) score (derived from columns F and G). See Materials and methods for details.
DOI: 10.7554/eLife.21459.018

• Supplementary file 2. List of clonal cell lines used in this study. Clones in which a single gene was targeted using CRISPR/Cas9 or disrupted by a GT insertion, and double- or triple-mutant clones in which multiple genes were disrupted using CRISPR/Cas9 or through a combination of CRISPR/Cas9 and a GT insertion are described in two separate spreadsheets labeled accordingly. For cell lines engineered using CRISPR/Cas9, when more than one clone was generated using the same CRISPR guide, the 'Clone Name' column indicates the generic name used throughout the manuscript to describe the genotype, and the 'Clone #' column identifies the specific allele in each individual clone. The 'CRISPR guide' column indicates the name of the guide used, which is the same as that of the oligos encoding sgRNAs (see Materials and methods and ***Supplementary file 4***). The 'Genomic Sequence' column shows 80 bases of genomic sequence (5' relative to the gene is to the left) surrounding the target site. For each group of clones made using the same CRISPR guide (separated by gray spacers), the 'Genomic Sequence' column is headlined by the reference WT genomic sequence (obtained from RefSeq), with the guide sequence colored blue. The site of the double strand cut made by Cas9 is between the two underlined bases. Sequencing results for individual clones are indicated below the reference sequence. Some WT clones are indicated as such and were used as controls. For mutant clones, mutated bases are colored red (dashes represent deleted bases, three dots are used to indicate that a deletion continues beyond the 80 bases of sequence shown, and large insertions are indicated in brackets), and the nature of the mutation, the resulting genotype (with the mutated amino acid number specified in parenthesis for selected clones) and any pertinent observations are also described. The figures in which each clone was used are also indicated. For the APC^{KO-2} clone containing a GT insertion, the 80 bases of genomic sequence (5' relative to the gene is to the left) flanking the GT are shown in the 'Genomic Sequence' column. For double- or triple- mutant clones, the CRISPR guide or pair of guides used (if two different guides

were used simultaneously to target adjacent sites in the same gene), the genomic sequence, the mutation, the genotype and any observations pertaining to each of the two or three targeted genes are designated '1', '2' and '3' in the column headings, and are shown under green, orange and purple spacers, respectively.
DOI: 10.7554/eLife.21459.019

• Supplementary file 3. Lists of the most significant hits included in comparative analyses across screens. Genes used to generate the heat map (***Figure 4B***) comparing the two WNT positive regulator screens (***Figure 1E and F***) and the low WNT + RSPO screen (***Figure 4A***) are shown in the first spreadsheet, and those used to generate the heat map (***Figure 5D***) comparing the WNT positive regulator, low stringency screen (***Figure 1E***) and the APC and CSNK1A1 suppressor screens (***Figure 5B and C***) are shown in the second spreadsheet. Genes with an FDR-corrected *p*-value<10^{-4} in at least one of the three screens included in each comparison are shown, and the FDR-corrected *p*-value and IGTIOB score for each gene in each screen is indicated. Genes are shown in the same order as in the heat maps, clustered based on their IGTIOB scores (see Materials and methods for details).
DOI: 10.7554/eLife.21459.020

• Supplementary file 4. List of oligonucleotides and primers used for generation and characterization of clonal cell lines engineered using CRISPR/Cas9. The names and sequences of pairs of oligonucleotides encoding sgRNAs (which were cloned into pX330) are shown in columns A and B, respectively. The names and sequences of pairs of primers used to amplify corresponding genomic regions flanking sgRNA target sites are shown in columns C and D, respectively. The names and sequences of single primers used to sequence the amplified target sites are shown in columns E and F, respectively.
DOI: 10.7554/eLife.21459.021

Major datasets

The following dataset was generated:

Author(s)	Year	Dataset title	Dataset URL	Database, license, and accessibility information
Lebensohn AM, Dubey R, Neitzel LR, Tacchelly-Benites O, Yang E, Marceau CD, Davis EM, Patel BB, Bahrami-Nejad Z, Travaglini KJ, Ahmed Y, Lee E, Carette JE, Rohatgi R	2016	Comparative genetic screens in human cells reveal new regulatory mechanisms in WNT signaling	https://trace.ncbi.nlm.nih.gov/Traces/sra/?study=SRP094861	Publicly available at the NCBI Sequence Read Archive website (accession no: SRP094861)

References

Allen NJ, Bennett ML, Foo LC, Wang GX, Chakraborty C, Smith SJ, Barres BA. 2012. Astrocyte glypicans 4 and 6 promote formation of excitatory synapses via GluA1 AMPA receptors. *Nature* **486**:410–414. doi: 10.1038/nature11059, PMID: 22722203

Bassik MC, Kampmann M, Lebbink RJ, Wang S, Hein MY, Poser I, Weibezahn J, Horlbeck MA, Chen S, Mann M, Hyman AA, Leproust EM, McManus MT, Weissman JS. 2013. A systematic mammalian genetic interaction map reveals pathways underlying ricin susceptibility. *Cell* **152**:909–922. doi: 10.1016/j.cell.2013.01.030, PMID: 23394947

Bernassola F, Karin M, Ciechanover A, Melino G. 2008. The HECT family of E3 ubiquitin ligases: multiple players in cancer development. *Cancer Cell* **14**:10–21. doi: 10.1016/j.ccr.2008.06.001, PMID: 18598940

Bischof J, Maeda RK, Hediger M, Karch F, Basler K. 2007. An optimized transgenesis system for Drosophila using germ-line-specific phiC31 integrases. *PNAS* **104**:3312–3317. doi: 10.1073/pnas.0611511104, PMID: 17360644

Blomen VA, Májek P, Jae LT, Bigenzahn JW, Nieuwenhuis J, Staring J, Sacco R, van Diemen FR, Olk N, Stukalov A, Marceau C, Janssen H, Carette JE, Bennett KL, Colinge J, Superti-Furga G, Brummelkamp TR. 2015. Gene essentiality and synthetic lethality in haploid human cells. *Science* **350**:1092–1096. doi: 10.1126/science.aac7557, PMID: 26472760

Cao J, Tang M, Li WL, Xie J, Du H, Tang WB, Wang H, Chen XW, Xiao H, Li Y. 2009. Upregulation of activator protein-4 in human colorectal cancer with metastasis. *International Journal of Surgical Pathology* **17**:16–21. doi: 10.1177/1066896908315813, PMID: 18480385

Carette JE, Guimaraes CP, Varadarajan M, Park AS, Wuethrich I, Godarova A, Kotecki M, Cochran BH, Spooner E, Ploegh HL, Brummelkamp TR. 2009. Haploid genetic screens in human cells identify host factors used by pathogens. *Science* **326**:1231–1235. doi: 10.1126/science.1178955, PMID: 19965467

Carette JE, Guimaraes CP, Wuethrich I, Blomen VA, Varadarajan M, Sun C, Bell G, Yuan B, Muellner MK, Nijman SM, Ploegh HL, Brummelkamp TR. 2011a. Global gene disruption in human cells to assign genes to phenotypes by deep sequencing. *Nature Biotechnology* **29**:542–546. doi: 10.1038/nbt.1857, PMID: 21623355

Carette JE, Raaben M, Wong AC, Herbert AS, Obernosterer G, Mulherkar N, Kuehne AI, Kranzusch PJ, Griffin AM, Ruthel G, Dal Cin P, Dye JM, Whelan SP, Chandran K, Brummelkamp TR. 2011b. Ebola virus entry requires the cholesterol transporter niemann-pick C1. *Nature* **477**:340–343. doi: 10.1038/nature10348, PMID: 21866103

Chia IV, Costantini F. 2005. Mouse axin and axin2/conductin proteins are functionally equivalent in vivo. *Molecular and Cellular Biology* **25**:4371–4376. doi: 10.1128/MCB.25.11.4371-4376.2005, PMID: 15899843

Cong L, Ran FA, Cox D, Lin S, Barretto R, Habib N, Hsu PD, Wu X, Jiang W, Marraffini LA, Zhang F. 2013. Multiplex genome engineering using CRISPR/Cas systems. *Science* **339**:819–823. doi: 10.1126/science.1231143, PMID: 23287718

de Groot RE, Ganji RS, Bernatik O, Lloyd-Lewis B, Seipel K, Šedová K, Zdráhal Z, Dhople VM, Dale TC, Korswagen HC, Bryja V. 2014. Huwe1-mediated ubiquitylation of dishevelled defines a negative feedback loop in the Wnt signaling pathway. *Science Signaling* **7**:ra26. doi: 10.1126/scisignal.2004985, PMID: 24643799

de Lau W, Peng WC, Gros P, Clevers H. 2014. The R-spondin/Lgr5/Rnf43 module: regulator of Wnt signal strength. *Genes & Development* **28**:305–316. doi: 10.1101/gad.235473.113, PMID: 24532711

Diaz-Benjumea FJ, Cohen SM. 1995. Serrate signals through notch to establish a wingless-dependent organizer at the dorsal/ventral compartment boundary of the Drosophila wing. *Development* **121**:4215–4225. PMID: 8575321

Doench JG, Hartenian E, Graham DB, Tothova Z, Hegde M, Smith I, Sullender M, Ebert BL, Xavier RJ, Root DE. 2014. Rational design of highly active sgRNAs for CRISPR-Cas9-mediated gene inactivation. *Nature Biotechnology* **32**:1262–1267. doi: 10.1038/nbt.3026, PMID: 25184501

Dow LE, O'Rourke KP, Simon J, Tschaharganeh DF, van Es JH, Clevers H, Lowe SW. 2015. Apc restoration promotes cellular differentiation and reestablishes crypt homeostasis in colorectal cancer. *Cell* **161**:1539–1552. doi: 10.1016/j.cell.2015.05.033, PMID: 26091037

Dubey R, Lebensohn AM, Bahrami-Nejad Z, Marceau C, Champion M, Gevaert O, Sikic BI, Carette JE, Rohatgi R. 2016. Chromatin-remodeling complex SWI/SNF controls multidrug resistance by transcriptionally regulating the drug efflux pump ABCB1. *Cancer Research* **76**:5810–5821. doi: 10.1158/0008-5472.CAN-16-0716, PMID: 27503929

Egawa T, Littman DR. 2011. Transcription factor AP4 modulates reversible and epigenetic silencing of the Cd4 gene. *PNAS* **108**:14873–14878. doi: 10.1073/pnas.1112293108, PMID: 21873191

Fiedler M, Mendoza-Topaz C, Rutherford TJ, Mieszczanek J, Bienz M. 2011. Dishevelled interacts with the DIX domain polymerization interface of axin to interfere with its function in down-regulating β-catenin. *PNAS* **108**:1937–1942. doi: 10.1073/pnas.1017063108, PMID: 21245303

Fuerer C, Nusse R. 2010. Lentiviral vectors to probe and manipulate the Wnt signaling pathway. *PLoS One* **5**:e9370. doi: 10.1371/journal.pone.0009370, PMID: 20186325

Giannakis M, Hodis E, Jasmine Mu X, Yamauchi M, Rosenbluh J, Cibulskis K, Saksena G, Lawrence MS, Qian ZR, Nishihara R, Van Allen EM, Hahn WC, Gabriel SB, Lander ES, Getz G, Ogino S, Fuchs CS, Garraway LA. 2014. RNF43 is frequently mutated in colorectal and endometrial cancers. *Nature Genetics* **46**:1264–1266. doi: 10.1038/ng.3127, PMID: 25344691

Gilbert LA, Horlbeck MA, Adamson B, Villalta JE, Chen Y, Whitehead EH, Guimaraes C, Panning B, Ploegh HL, Bassik MC, Qi LS, Kampmann M, Weissman JS. 2014. Genome-Scale CRISPR-Mediated control of gene repression and activation. *Cell* **159**:647–661. doi: 10.1016/j.cell.2014.09.029, PMID: 25307932

Hao HX, Xie Y, Zhang Y, Charlat O, Oster E, Avello M, Lei H, Mickanin C, Liu D, Ruffner H, Mao X, Ma Q, Zamponi R, Bouwmeester T, Finan PM, Kirschner MW, Porter JA, Serluca FC, Cong F. 2012. ZNRF3 promotes Wnt receptor turnover in an R-spondin-sensitive manner. *Nature* **485**:195–200. doi: 10.1038/nature11019, PMID: 22575959

Heaton JH, Dlakic WM, Dlakic M, Gelehrter TD. 2001. Identification and cDNA cloning of a novel RNA-binding protein that interacts with the cyclic nucleotide-responsive sequence in the Type-1 plasminogen activator inhibitor mRNA. *Journal of Biological Chemistry* **276**:3341–3347. doi: 10.1074/jbc.M006538200, PMID: 11001948

Hoppler S, Moon RT. 2014. *Wnt signaling in development and disease: molecular mechanisms and biological functions*. Hoboken, New Jersey: Wiley Blackwell. doi: 10.1002/9781118444122

Hsu PD, Scott DA, Weinstein JA, Ran FA, Konermann S, Agarwala V, Li Y, Fine EJ, Wu X, Shalem O, Cradick TJ, Marraffini LA, Bao G, Zhang F. 2013. DNA targeting specificity of RNA-guided Cas9 nucleases. *Nature Biotechnology* **31**:827–832. doi: 10.1038/nbt.2647, PMID: 23873081

Jackstadt R, Röh S, Neumann J, Jung P, Hoffmann R, Horst D, Berens C, Bornkamm GW, Kirchner T, Menssen A, Hermeking H. 2013. AP4 is a mediator of epithelial-mesenchymal transition and metastasis in colorectal cancer. *The Journal of Experimental Medicine* **210**:1331–1350. doi: 10.1084/jem.20120812, PMID: 23752226

Jho EH, Zhang T, Domon C, Joo CK, Freund JN, Costantini F. 2002. Wnt/beta-catenin/Tcf signaling induces the transcription of Axin2, a negative regulator of the signaling pathway. *Molecular and Cellular Biology* **22**:1172–1183. doi: 10.1128/MCB.22.4.1172-1183.2002, PMID: 11809808

Jung P, Hermeking H. 2009. The c-MYC-AP4-p21 cascade. *Cell Cycle* **8**:982–989. doi: 10.4161/cc.8.7.7949, PMID: 19270520

Kim SE, Huang H, Zhao M, Zhang X, Zhang A, Semonov MV, MacDonald BT, Zhang X, Garcia Abreu J, Peng L, He X. 2013. Wnt stabilization of β-catenin reveals principles for morphogen receptor-scaffold assemblies. *Science* **340**:867–870. doi: 10.1126/science.1232389, PMID: 23579495

Kinoshita E, Kinoshita-Kikuta E, Koike T. 2009. Separation and detection of large phosphoproteins using Phos-tag SDS-PAGE. *Nature Protocols* **4**:1513–1521. doi: 10.1038/nprot.2009.154, PMID: 19798084

Koo BK, Spit M, Jordens I, Low TY, Stange DE, van de Wetering M, van Es JH, Mohammed S, Heck AJ, Maurice MM, Clevers H. 2012. Tumour suppressor RNF43 is a stem-cell E3 ligase that induces endocytosis of Wnt receptors. *Nature* **488**:665–669. doi: 10.1038/nature11308, PMID: 22895187

Langmead B, Trapnell C, Pop M, Salzberg SL. 2009. Ultrafast and memory-efficient alignment of short DNA sequences to the human genome. *Genome Biology* **10**:R25. doi: 10.1186/gb-2009-10-3-r25, PMID: 19261174

Lee E, Salic A, Krüger R, Heinrich R, Kirschner MW. 2003. The roles of APC and Axin derived from experimental and theoretical analysis of the Wnt pathway. *PLoS Biology* **1**:E10. doi: 10.1371/journal.pbio.0000010, PMID: 14551908

Lito P, Rosen N, Solit DB. 2013. Tumor adaptation and resistance to RAF inhibitors. *Nature Medicine* **19**:1401–1409. doi: 10.1038/nm.3392, PMID: 24202393

Liu X, Zhang B, Guo Y, Liang Q, Wu C, Wu L, Tao K, Wang G, Chen J. 2012. Down-regulation of AP-4 inhibits proliferation, induces cell cycle arrest and promotes apoptosis in human gastric cancer cells. *PLoS One* **7**: e37096. doi: 10.1371/journal.pone.0037096, PMID: 22615908

Lustig B, Jerchow B, Sachs M, Weiler S, Pietsch T, Karsten U, van de Wetering M, Clevers H, Schlag PM, Birchmeier W, Behrens J. 2002. Negative feedback loop of Wnt signaling through upregulation of conductin/axin2 in colorectal and liver tumors. *Molecular and Cellular Biology* **22**:1184–1193. doi: 10.1128/MCB.22.4.1184-1193.2002, PMID: 11809809

Mali P, Yang L, Esvelt KM, Aach J, Guell M, DiCarlo JE, Norville JE, Church GM. 2013. RNA-guided human genome engineering via Cas9. *Science* **339**:823–826. doi: 10.1126/science.1232033, PMID: 23287722

Nam JS, Turcotte TJ, Smith PF, Choi S, Yoon JK. 2006. Mouse cristin/R-spondin family proteins are novel ligands for the frizzled 8 and LRP6 receptors and activate beta-catenin-dependent gene expression. *Journal of Biological Chemistry* **281**:13247–13257. doi: 10.1074/jbc.M508324200, PMID: 16543246

Nicoletti I, Migliorati G, Pagliacci MC, Grignani F, Riccardi C. 1991. A rapid and simple method for measuring thymocyte apoptosis by propidium iodide staining and flow cytometry. *Journal of Immunological Methods* **139**: 271–279. doi: 10.1016/0022-1759(91)90198-O, PMID: 1710634

Nolo R, Abbott LA, Bellen HJ. 2000. Senseless, a Zn finger transcription factor, is necessary and sufficient for sensory organ development in Drosophila. *Cell* **102**:349–362. doi: 10.1016/S0092-8674(00)00040-4, PMID: 10975525

Nusse R, Varmus HE. 1982. Many tumors induced by the mouse mammary tumor virus contain a provirus integrated in the same region of the host genome. *Cell* **31**:99–109. doi: 10.1016/0092-8674(82)90409-3, PMID: 6297757

Nüsslein-Volhard C, Wieschaus E. 1980. Mutations affecting segment number and polarity in Drosophila. *Nature* **287**:795–801. doi: 10.1038/287795a0, PMID: 6776413

Ohkawara B, Glinka A, Niehrs C. 2011. Rspo3 binds syndecan 4 and induces Wnt/PCP signaling via clathrin-mediated endocytosis to promote morphogenesis. *Developmental Cell* **20**:303–314. doi: 10.1016/j.devcel.2011.01.006, PMID: 21397842

Parnas O, Jovanovic M, Eisenhaure TM, Herbst RH, Dixit A, Ye CJ, Przybylski D, Platt RJ, Tirosh I, Sanjana NE, Shalem O, Satija R, Raychowdhury R, Mertins P, Carr SA, Zhang F, Hacohen N, Regev A. 2015. A Genome-wide CRISPR screen in primary immune cells to dissect regulatory networks. *Cell* **162**:675–686. doi: 10.1016/j.cell.2015.06.059, PMID: 26189680

Sakane H, Yamamoto H, Matsumoto S, Sato A, Kikuchi A. 2012. Localization of glypican-4 in different membrane microdomains is involved in the regulation of Wnt signaling. *Journal of Cell Science* **125**:449–460. doi: 10.1242/jcs.091876, PMID: 22302992

Seshagiri S, Stawiski EW, Durinck S, Modrusan Z, Storm EE, Conboy CB, Chaudhuri S, Guan Y, Janakiraman V, Jaiswal BS, Guillory J, Ha C, Dijkgraaf GJ, Stinson J, Gnad F, Huntley MA, Degenhardt JD, Haverty PM, Bourgon R, Wang W, et al. 2012. Recurrent R-spondin fusions in colon cancer. *Nature* **488**:660–664. doi: 10.1038/nature11282, PMID: 22895193

Shalem O, Sanjana NE, Hartenian E, Shi X, Scott DA, Mikkelsen TS, Heckl D, Ebert BL, Root DE, Doench JG, Zhang F. 2014. Genome-scale CRISPR-Cas9 knockout screening in human cells. *Science* **343**:84–87. doi: 10.1126/science.1247005, PMID: 24336571

Shaner NC, Campbell RE, Steinbach PA, Giepmans BN, Palmer AE, Tsien RY. 2004. Improved monomeric red, orange and yellow fluorescent proteins derived from Discosoma sp. red fluorescent protein. *Nature Biotechnology* **22**:1567–1572. doi: 10.1038/nbt1037, PMID: 15558047

Shi L, Jackstadt R, Siemens H, Li H, Kirchner T, Hermeking H. 2014. p53-induced miR-15a/16-1 and AP4 form a double-negative feedback loop to regulate epithelial-mesenchymal transition and metastasis in colorectal cancer. *Cancer Research* **74**:532–542. doi: 10.1158/0008-5472.CAN-13-2203, PMID: 24285725

Song X, Wang S, Li L. 2014. New insights into the regulation of Axin function in canonical Wnt signaling pathway. *Protein & Cell* **5**:186–193. doi: 10.1007/s13238-014-0019-2, PMID: 24474204

Spemann H. 1938. *Embryonic Development and Induction*. New Haven, London: Yale University Press.

Storm EE, Durinck S, de Sousa e Melo F, Tremayne J, Kljavin N, Tan C, Ye X, Chiu C, Pham T, Hongo JA, Bainbridge T, Firestein R, Blackwood E, Metcalfe C, Stawiski EW, Yauch RL, Wu Y, de Sauvage FJ. 2016.

Targeting PTPRK-RSPO3 colon tumours promotes differentiation and loss of stem-cell function. *Nature* **529**:97–100. doi: 10.1038/nature16466, PMID: 26700806

Tacchelly-Benites O, Wang Z, Yang E, Lee E, Ahmed Y. 2013. Toggling a conformational switch in Wnt/β-catenin signaling: regulation of Axin phosphorylation. The phosphorylation state of Axin controls its scaffold function in two Wnt pathway protein complexes. *BioEssays : news and reviews in molecular, cellular and developmental biology* **35**:1063–1070. doi: 10.1002/bies.201300101, PMID: 24105937

Tang W, Dodge M, Gundapaneni D, Michnoff C, Roth M, Lum L. 2008. A genome-wide RNAi screen for Wnt/beta-catenin pathway components identifies unexpected roles for TCF transcription factors in cancer. *PNAS* **105**:9697–9702. doi: 10.1073/pnas.0804709105, PMID: 18621708

Vorwald-Denholtz PP, De Robertis EM. 2011. Temporal pattern of the posterior expression of wingless in Drosophila blastoderm. *Gene Expression Patterns* **11**:456–463. doi: 10.1016/j.gep.2011.07.004, PMID: 21821151

Wang T, Birsoy K, Hughes NW, Krupczak KM, Post Y, Wei JJ, Lander ES, Sabatini DM. 2015. Identification and characterization of essential genes in the human genome. *Science* **350**:1096–1101. doi: 10.1126/science.aac7041, PMID: 26472758

Wang T, Wei JJ, Sabatini DM, Lander ES. 2014. Genetic screens in human cells using the CRISPR-Cas9 system. *Science* **343**:80–84. doi: 10.1126/science.1246981, PMID: 24336569

Wang Z, Tacchelly-Benites O, Yang E, Thorne CA, Nojima H, Lee E, Ahmed Y. 2016. Wnt/Wingless pathway activation Is promoted by a critical threshold of axin maintained by the tumor suppressor APC and the ADP-ribose polymerase tankyrase. *Genetics* **203**:269–281. doi: 10.1534/genetics.115.183244, PMID: 26975665

Wieschaus E, Nüsslein-Volhard C. 1986. *Drosophila: A practical approach*. Oxford: IRL Press.

Xinghua L, Bo Z, Yan G, Lei W, Changyao W, Qi L, Lin Y, Kaixiong T, Guobin W, Jianying C. 2012. The overexpression of AP-4 as a prognostic indicator for gastric carcinoma. *Medical Oncology* **29**:871–877. doi: 10.1007/s12032-011-9845-8, PMID: 21336989

Yang E, Tacchelly-Benites O, Wang Z, Randall MP, Tian A, Benchabane H, Freemantle S, Pikielny C, Tolwinski NS, Lee E, Ahmed Y. 2016. Wnt pathway activation by ADP-ribosylation. *Nature Communications* **7**:11430. doi: 10.1038/ncomms11430, PMID: 27138857

Differential abundance of CK1α provides selectivity for pharmacological CK1α activators to target WNT-dependent tumors

Li B, Orton D, **Neitzel LR**, Astudillo L, Shen C, Long J, Chen X, Kirkbride KC, Doundoulakis T, Guerra ML, Zaias J, Fei DL, Rodriguez-Blanco J, Thorne C, Wang Z, Jin K, Nguyen DM, Sands LR, Marchetti F, Abreu MT, Cobb MH, Capobianco AJ, Lee E, Robbins DJ.

Sci Signal 2017 10(485). pii: eaak9916

doi: 10.1126/scisignal.aak9916

HHS Public Access

Author manuscript

Sci Signal. Author manuscript; available in PMC 2017 August 14.

Published in final edited form as:

Sci Signal. ; 10(485): . doi:10.1126/scisignal.aak9916.

Differential abundance of CK1α provides selectivity for pharmacological CK1α activators to target WNT-dependent tumors

Bin Li[1], **Darren Orton**[2], **Leif R. Neitzel**[3], **Luisana Astudillo**[1], **Chen Shen**[1], **Jun Long**[1], **Xi Chen**[4,5], **Kellye C. Kirkbride**[2], **Thomas Doundoulakis**[2], **Marcy L. Guerra**[2], **Julia Zaias**[6], **Dennis Liang Fei**[1], **Jezabel Rodriguez-Blanco**[1], **Curtis Thorne**[7], **Zhiqiang Wang**[1], **Ke Jin**[1], **Dao M. Nguyen**[1], **Laurence R. Sands**[1], **Floriano Marchetti**[1], **Maria T. Abreu**[8], **Melanie H. Cobb**[7], **Anthony J. Capobianco**[1,5], **Ethan Lee**[3], and **David J. Robbins**[1,5,*]

[1]Molecular Oncology Program, Department of Surgery, Miller School of Medicine, University of Miami, Miami, FL 33136, USA

[2]StemSynergy Therapeutics Inc., Miami, FL 33136, USA

[3]Department of Cell and Developmental Biology, Vanderbilt University School of Medicine, Nashville, TN 37232, USA

[4]Department of Public Health Sciences, Miller School of Medicine, University of Miami, Miami, FL 33136, USA

[5]Sylvester Comprehensive Cancer Center, Miller School of Medicine, University of Miami, Miami, FL 33136, USA

[6]Department of Pathology and Laboratory Medicine, Miller School of Medicine, University of Miami, Miami, FL 33136, USA

[7]Department of Pharmacology, University of Texas Southwestern Medical Center, Dallas, TX 75390, USA

[8]Division of Gastroenterology, Department of Medicine, Miller School of Medicine, University of Miami, Miami, FL 33136, USA

Abstract

Constitutive WNT activity drives the growth of various human tumors, including nearly all colorectal cancers (CRCs). Despite this prominence in cancer, no WNT inhibitor is currently

*Corresponding author. drobbins@med.miami.edu.

SUPPLEMENTARY MATERIALS

www.sciencesignaling.org/cgi/content/full/10/485/eaak9916/DC1

Author contributions: B.L., D.O., and D.J.R. conceived and designed the study. B.L., D.O., L.R.N., C.S., L.A., J.L., X.C., K.C.K., J.Z., C.T., Z.W., K.J., D.M.N., L.R.S., and F.M. acquired the data and provided experimental support. B.L., D.O., L.R.N., L.A., X.C., J.Z., J.R.-B., M.T.A., A.J.C., and D.J.R. analyzed and interpreted the data. B.L. and D.J.R. drafted the manuscript. T.D., M.L.G., D.L.F., M.T.A., M.H.C., E.L., and D.J.R. critically revised the manuscript.

Competing interests: D.J.R., A.J.C., and E.L. are founders of StemSynergy Therapeutics Inc., a company commercializing small-molecule cell signaling inhibitors. D.O., K.C.K., M.L.G., and T.D. are employees of StemSynergy Therapeutics.

approved for use in the clinic largely due to the small number of druggable signaling components in the WNT pathway and the substantial toxicity to normal gastrointestinal tissue. We have shown that pyrvinium, which activates casein kinase 1α (CK1α), is a potent inhibitor of WNT signaling. However, its poor bioavailability limited the ability to test this first-in-class WNT inhibitor in vivo. We characterized a novel small-molecule CK1α activator called SSTC3, which has better pharmacokinetic properties than pyrvinium, and found that it inhibited the growth of CRC xenografts in mice. SSTC3 also attenuated the growth of a patient-derived metastatic CRC xenograft, for which few therapies exist. SSTC3 exhibited minimal gastrointestinal toxicity compared to other classes of WNT inhibitors. Consistent with this observation, we showed that the abundance of the SSTC3 target, CK1α, was decreased in WNT-driven tumors relative to normal gastrointestinal tissue, and knocking down CK1α increased cellular sensitivity to SSTC3. Thus, we propose that distinct CK1α abundance provides an enhanced therapeutic index for pharmacological CK1α activators to target WNT-driven tumors.

INTRODUCTION

Colorectal cancer (CRC) is the third most prevalent cancer in the United States (1), with ~50,000 CRC patients succumbing to their disease each year. The poor outcome of these patients underscores the urgent need for more effective CRC therapies. This need is especially great for patients harboring metastatic CRC, only 13% of whom survive beyond 5 years and for whom few targeted therapies exist (1). The mechanisms underlying the genesis and progression of CRC are now well established (2). Mutations in genes encoding components of the WNT signaling pathway (*APC*, which encodes adenomatous polyposis coli, and *CTNNB1*, which encodes β-catenin) were identified as early events in the vast majority of all CRCs, followed by mutations in additional oncogenic drivers such as *KRAS* and *P53* (2, 3). More advanced stages of CRC remain addicted to WNT signaling (4), including metastasis (5). Despite the well-established mechanistic paradigm implicating WNT signaling in the development and progression of CRC, no WNT inhibitors are currently approved for clinical use.

The critical event in WNT signaling is the posttranslational regulation of the transcriptional coactivator β-catenin. In the absence of a WNT ligand, cytoplasmic β-catenin is maintained at low levels because of its constitutive degradation. This degradation occurs primarily via its association with a "destruction complex," which consists of glycogen synthase kinase 3β (GSK3β), casein kinase 1α (CK1α), APC, and AXIN (6). The rate-limiting component in this complex is the scaffold protein AXIN, whose steady-state levels are tightly controlled by the adenosine diphosphate–ribose polymerase, tankyrase, targeting AXIN for ubiquitin-mediated proteolysis (7). All WNTs are palmitoylated in the endoplasmic reticulum by the membrane-bound O-acetyltransferase protein, Porcupine (8, 9). Post-translational modification of WNTs by palmitoylation is necessary for their exit from the endoplasmic reticulum and binding to Frizzled receptors (10–12). Upon Frizzled and co-receptor (LRP6) binding, β-catenin degradation is inhibited, and AXIN is ultimately degraded (13–16). In turn, β-catenin is translocated to the nucleus where it interacts with a variety of nuclear transcriptional regulators, such as BCL9 and PYGOPUS, to activate a T cell factor/lymphoid enhancer binding factor–mediated transcriptional program (17–20).

One emerging class of WNT inhibitors currently in clinical trials, Porcupine inhibitors, acts by blocking the palmitoylation of WNT ligands (21, 22). However, these inhibitors will likely not prove useful to target CRCs because the constitutive WNT activity driving CRC is ligand-independent. A second important class of WNT inhibitors is small-molecule Tankyrase inhibitors (TANKi) (7). Because tankyrase inhibition can attenuate the nonligand-driven WNT activity commonly found in CRC cells, such inhibitors represent a promising targeted therapeutic in CRC therapy (23). A significant hurdle to the clinical development of WNT inhibitors is overcoming the on-target toxicity that results from effects on the WNT-dependent intestinal stem cells that drive normal gastrointestinal (GI) homeostasis (24, 25). Such dose-limiting on-target toxicities have been observed using both Tankyrase and Porcupine inhibitors (23, 26, 27), with continuous dosing of both classes of small molecules disrupting normal GI structure and function. Thus, there appears to be only a limited therapeutic window for Porcupine and TANKi, which might ultimately limit their clinical utility.

We previously described a mechanistically distinct WNT inhibitor, pyrvinium, which was already Food and Drug Administration (FDA)–approved as an anthelmintic agent (28, 29). We showed that pyrvinium potently attenuated WNT activity by binding and activating CK1α. Pyrvinium also potently reduced the viability of CRC cell lines in culture, consistent with it attenuating WNT activity downstream of the common mutations that drive CRC growth. However, pyrvinium's limited bioavailability precluded testing its efficacy against CRC growth in vivo and thus reduced its potential clinical utility as a WNT inhibitor for CRC patients (30, 31). Here, we sought to identify and characterize a second-generation CK1α activator with improved bioavailability, which would allow us to determine its efficacy against WNT-driven cancers in vivo.

RESULTS

Activation of CK1α by SSTC3 inhibits WNT signaling

To identify a CK1α activator with the pharmacokinetic properties necessary to advance into the clinic, we used an in silico scaffold screening approach (32). These scaffolds were prioritized on the basis of their predicted physical and pharmacokinetic properties and subsequently tested for their ability to attenuate a WNT-driven reporter gene assay. Subsequent cycles of medicinal chemistry and assaying WNT reporter gene activity led to the identification of SSTC3 (fig. S1A). SSTC3 attenuated the activity of a WNT reporter gene in a potent, dose-dependent manner [median effective concentration (EC_{50}) = 30 nM; Fig. 1A] and bound directly to purified recombinant CK1α with a similar binding constant (K_d = 32 nM; Fig. 1B). SSTC3 treatment rapidly enhanced phosphorylation of CK1α substrates in vitro and in SW403 cells (Fig. 1, C and D). Further, SSTC3 coupled agarose beads associated with cellular CK1α (Fig. 1E and fig. S1B), and this association was reversible in the presence of uncoupled SSTC3 (fig. S1B) or pyrvinium (Fig. 1E). SSTC3 also attenuated WNT reporter activity (Fig. 1F) in a manner dependent on CK1α-dependent manner (fig. S1C). Injection of SSTC3 into *Xenopus laevis* embryos inhibited the ability of exogenous WNT to induce a secondary body axis (Fig. 1G), a classic WNT-driven phenotype (33), consistent with SSTC3 attenuating WNT signaling in vivo. Together, these

results suggest that SSTC3 inhibits WNT signaling via activation of CK1α in a manner similar to that of pyrvinium.

Activation of CK1α inhibits Apc mutation-driven tumor growth

Loss of the tumor suppressor *Apc* leads to sustained activation of WNT signaling and intestinal adenoma formation in various mouse models (34–36). Organoids derived from these adenomas can be isolated and grown in a minimal culture that requires endogenous WNT activity (37). SSTC3 attenuated the growth of such *Apc* mutant organoids in a dose-dependent manner (Fig. 2A and fig. S2A). Notably, we observed that the EC_{50} of SSTC3 in wild-type organoids (2.9 μM) was significantly higher than that in *Apc* mutant organoids (150 nM for $Apc^{-/-}$ and 70 nM for Apc^{min}) (Fig. 2A and fig. S2A). The expression of WNT target genes, *Axin2* and the crypt stem cell marker *Lgr5*, in the intestines of Apc^{min} mice were also reduced upon acute treatment with SSTC3 in vivo (Fig. 2B). Consistent with this reduced WNT activity in vivo, chronic exposure of Apc^{min} mice to SSTC3 reduced both the numbers and average size of their intestinal polyps (Fig. 2,C and D). The life span of Apc^{min} mice is reduced relative to wild-type mice because of bleeding complications secondary to polyp growth (38, 39). Given this reduction in polyp size and numbers, SSTC3 treatment provided an increased survival advantage to such mice (Fig. 2E). Thus, SSTC3 attenuates WNT signaling–driven polyp growth in vivo, and this decreased activity leads to prolonged survival of a commonly used mouse intestinal tumor model.

Activation of CK1α inhibits the growth of WNT activity–dependent CRC cell lines

To extend our findings to CRC, we treated CRC cell lines with different doses of SSTC3, two whose growth are driven by *APC* mutations (SW403 and HT29 cells), one whose growth is driven by a mutation in the β-catenin gene *CTNNB1* (HCT116 cells), and one that is not WNT-dependent (RKO cells). The viability of the WNT-dependent cell lines decreased in a dose-dependent manner (EC_{50} = 132, 63, and 123 nM for HT29, SW403, and HCT116 cells, respectively; Fig. 3A), as was their ability to form individual colonies (EC_{50} = 168, 61, and 80 nM for HT29, SW403, and HCT116 cells, respectively; Fig. 3B), whereas RKO cells were significantly less sensitive to SSTC3 (EC_{50} = 3.1 μM; fig. S2B). We noted that the EC_{50} doses of SSTC3 for attenuating WNT reporter activity, CRC cell viability, and the expression of two WNT target genes (EC_{50} = 100 nM for *AXIN2* and 106 nM for *LGR5*; Fig. 3C) were comparable to its binding affinity for CK1α (Fig. 1B). Further, SSTC3 exposure resulted in reduced expression of WNT target genes in all three sensitive CRC cell lines (Fig. 3D). The capacity of SSTC3 to decrease the viability of HCT116 cells was also significantly reduced when the mutant *CTNNB1* allele driving its carcinogenic properties was deleted (EC_{50} = 78 nM versus 1.5 μM; Fig. 3E). Furthermore, an inactive structural analog of SSTC3, SST111 (fig. S1A and Fig. 3F), had minimal effects on CRC cell viability (Fig. 3G) or WNT target gene expression (fig. S3, A and B). Finally, we determined the ability of a series of structurally distinct SSTC3 derivatives to reduce WNT activity in a reporter assay and to attenuate HCT116 cell viability, deriving a ratio of each compound's EC_{50} in both of these assays as an indicator of its on-target effects on viability (Fig. 3H). We found that, although the EC_{50} range for these SSTC3 derivatives varied about 100-fold, 90% of them exhibited an EC_{50} ratio within 1 SD of the idealized EC_{50} ratio of 1. Together, these

results suggest that SSTC's effect on CRC viability is primarily through an on-target mechanism, the attenuation of WNT activity.

Activation of CK1α inhibits growth of a patient-derived CRC xenograft

We injected SSTC3 into CD-1 mice and measured the plasma concentration by liquid chromatography–mass spectrometry (LC-MS) at five time points over 24 hours. On the basis of escalating doses in nude mice, a strong dose-dependent correlation of both maximal concentration (C_{max}) and area under the curve (AUC) for SSTC3 was obtained in the serum. Our data show that ~250 nM concentration of SSTC3 can be maintained for 24 hours after treatment (Fig. 4A). This result verifies that the pharmacokinetic properties of SSTC3 are significantly improved over that of pyrvinium (31). Taking advantage of the improved pharmacokinetic properties of SSTC3, we tested for the first time the capacity of a CK1α activator to attenuate the growth of CRC in vivo. SSTC3 significantly inhibited the growth of HCT116 xenografts, compared to the vehicle-treated mice (Fig. 4B). Hematoxylin and eosin (H&E) staining of the residual tumor samples showed substantial loss of cancer cells in the SSTC3-treated group (Fig. 4B and fig. S4A). The reduction of both WNT target gene expression (Fig. 4C) and the proliferation marker KI67 (Fig. 4D) was also observed in the tumors exposed to SSTC3. We obtained a panel of patient-derived CRC samples, two of which contained common *APC* mutations (CRC1 and CRC2), and established organoid cultures from them. SSTC3 treatment significantly reduced the growth of all three patient-derived CRC organoid cultures (Fig. 4E), relative to those treated with vehicle. One of these *APC* mutant CRCs, derived from a lung metastasis, was also used to establish patient-derived xenografts (PDXs) in mice. SSTC3 attenuated the growth of this metastatic CRC PDX (Fig. 4F) and markedly reduced the cell density of residual cancer (Fig. 4F and fig. S4B). SSTC3 also reduced the expression of WNT biomarkers in this CRC PDX (Fig. 4G), consistent with it acting in an on-target manner.

CK1α activation does not inhibit the proliferation of intestinal epithelium cells in vivo

One hurdle to the clinical development of WNT inhibitors is the on-target GI toxicity observed upon chronic dosing in animal models. Notably, mice exposed to either of two structurally distinct CK1α activators did not exhibit the weight loss typical of chronic effects on GI homeostasis [fig. S5, A and B, and (29)]. To explore this unexpected observation further, we directly compared the biological effects of SSTC3 to that of a TANKi (G007-LK) reported to disrupt normal GI physiology (23). We first compared their potency using a WNT reporter gene assay and noted that the TANKi was about 20 times more potent than SSTC3 in reducing ligand-induced WNT signaling (Fig. 5A). We next compared the activity of each of these WNT inhibitors on tumor growth and GI homeostasis within the same mice. For this experiment, we implanted an *APC* mutant CRC cell line (SW403), previously reported to be sensitive to TANKi (23), into the flanks of nude mice. Both WNT inhibitors significantly reduced the growth of the CRC xenograft (Fig. 5B), with SSTC3 exhibiting greater efficacy than the TANKi. Because the average body weight of TANKi-treated mice declined significantly and a number of the mice became moribund, we stopped this treatment after 12 days (Fig. 5C). However, the body weight of the SSTC3-treated mice remained similar to vehicle-treated mice. Sections of the mouse intestine were obtained from treated mice, H&E-stained, and examined by a pathologist. Although the crypt/villus axes of

TANKi-treated mice were severely disrupted, only minor differences in the intestinal tissue were observed between SSTC3- and vehicle-treated mice (Fig. 5D and fig. S5, C and D). Consistent with this finding, TANKi treatment disrupted the proliferation of WNT-dependent intestinal crypt base columnar cells, whereas SSTC3 did not (Fig. 5E). We next examined the ability of the two WNT inhibitors to attenuate the expression of WNT biomarkers in the intestines of nontumor-bearing mice, when acutely exposed to either inhibitor at doses capable of reducing CRC growth. The expression of *Axin2* and *Lgr5* were substantially reduced in the intestinal tissue of nontumor-bearing mice treated with TANKi, whereas SSTC3 exposure had no observable effects on their expression (Fig. 5F). Thus, the limited effects of SSTC3 on GI homeostasis were observed in both tumor- and nontumor-bearing mice. Comparing the two WNT inhibitors in vivo is likely complicated by differences in their pharmacodynamics and pharmacokinetics. Therefore, to more directly compare their effects on GI homeostasis, we took advantage of established procedures to grow and maintain mouse intestinal tissue as enteroids, which are composed of villi and primitive cryptlike intestinal stem cell compartments (40). Similar to what was observed in vivo, SSTC3 had little effect on intestinal crypt/villus structures ex vivo (Fig. 5G), whereas the TANKi severely attenuated their growth.

WNT activity regulates CK1α levels, modulating SSTC3 sensitivity

CK1α is an established negative regulator of the WNT signaling pathway, whose deficiency leads to hyperactivated WNT signaling, and contributes to metastatic CRC in mouse models (41). Thus, we hypothesized that the differential SSTC3 response we observe in tumor tissue, relative to normal intestinal tissue, results from distinct amounts of its cellular target, CK1α. To begin to test this hypothesis, we compared the abundance of CK1α in isolated intestinal crypts and tumors from Apc^{min} mice by immunoblotting and observed a 40% decrease in CK1α abundance in tumor tissue relative to normal intestinal crypts (Fig. 6A and fig. S6A). Similar differences were found in organoids derived from these tissues (Fig. 6B and fig. S6B). Knockdown of *APC* in 293T cells also resulted in decreased abundance of CK1α (Fig. 6C and fig. S6C), consistent with the notion that activation of WNT signaling negatively regulates steady-state amounts of CK1α. In line with a previous report (42), exogenous WNT and nicotinamide transform wild-type enteroid cultures, which exhibit increased proliferation and decreased differentiation reminiscent of organoids derived from tumors. CK1α abundance was significantly reduced in these hyperactivated enteroid cultures (Fig. 6, D and E, and fig. S6D). Unlike its effects on wild-type enteroids, SSTC3 potently suppressed the growth of these WNT-hyperactivated enteroids (Fig. 6E and fig. S6, E and F). To more directly address the role of CK1α expression on WNT activity and SSTC3 efficacy, we used different amounts of small interfering RNA (siRNA) to partially knock down CK1α abundance in 293T cells and examined the ability of SSTC3 to attenuate the increased WNT activity resulting from partial loss of CK1α. As expected, decreased CK1α abundance activated WNT signaling, and this increased activity was suppressed by the CK1α activator SSTC3 (Fig. 6F).

The expression of *CSNK1A1* (hereafter referred to as *CK1α*) is decreased in various human tumors relative to the tissue of origin, where it is thought to be tumor-suppressive. Taking advantage of a recent high-density transcriptome database of colorectal tumor samples

linked to patient outcome, we noted that the expression of *CK1α* was significantly lower in colorectal adenomas and carcinomas relative to normal colonic tissue (fig. S6G). Segregation of this cohort of CRC patients into two groups, based on *CK1α* expression, revealed that survival was significantly decreased in patients whose tumors expressed relatively lower amounts of CK1α (Fig. 6G). These data are consistent both with *CK1α* expression being modulated during CRC progression to hyperactivate WNT signaling and with lower expression of *CK1α* being predictive of a poorer patient outcome.

DISCUSSION

We found that a novel small-molecule activator of CK1α, SSTC3, attenuates the growth of CRC cells via a mechanism dependent on CK1α and in a manner that attenuates WNT signaling. Taking advantage of the significantly improved bioavailability of SSTC3, we show for the first time the ability of CK1α activators to attenuate the growth of WNT-driven CRC in vivo. We further show that CK1α levels are decreased by constitutive WNT signaling and that this modulation of CK1α levels likely determines the sensitivity of a tissue to CK1α activators (Fig. 6H). This result is consistent with the role CK1α plays as a negative regulator of WNT signaling and with increased CK1α activity acting to down-regulate WNT activity (6, 41). Thus, normal intestinal tissue has high amounts of CK1α and is relatively insensitive to SSTC3, whereas colorectal tumors have hyperactivated WNT signaling that effectively lowers the amount of CK1α and are sensitive to CK1α activators (Fig. 6H). We further show that, in a cohort of CRC patients, decreased tumor expression of *CK1α* is associated with a worse prognosis, similar to what has been reported for a number of other human cancers (43–46). These findings validate CK1α as a novel therapeutic target in CRC and identify a cohort of patients most likely to benefit from treatment with a CK1α activator such as SSTC3.

CK1α plays important roles in a number of distinct signaling pathways. Thus, it remains plausible that a subset of SSTC3's effects on CRC viability occur via a non-WNT–dependent mechanism. For example, CK1α has been implicated in the p53/MDM2 (47–49), FOXO1/autophagy (50–52), and sonic hedgehog–GLI (53–55) signaling pathways, all of which have also been implicated in aspects of CRC progression (56–59). Pyrvinium, the first-in-class CK1α activator, was reported to exert antitumor activity through suppression of GLI activity (60) or autophagy flux (61). Unlike its role in WNT signaling (62, 63), CK1α is able to function in multiple, and opposing, ways within these other signaling pathways (47, 48, 54, 55), complicating the ability to predict SSTC3 effects in different biological contexts. Because of this complexity, we cannot rule out that the simultaneous modulation of these other signaling pathways may affect the efficacy of SSTC3 in targeting WNT-dependent tumors, especially at high doses.

A number of WNT inhibitors are currently being evaluated in, or for, clinical trials (64). Given the importance of WNT signaling for stem cell function and homeostasis within numerous tissues (65), these trials are being scrutinized for both efficacy and on-target toxicities (64). On-target GI toxicity has been particularly problematic for both porcupine and TANKi (23, 26), with members of both classes of these drugs showing narrow concentration ranges between efficacy and GI toxicity in animal models (27). A number of

biological agents that target WNT signaling components are also being evaluated in the clinic, where on-target bone toxicities emerged as a dose-limiting factor (64). CK1α activators inhibit the growth of WNT-driven CRC without obvious on-target toxicities. These findings are consistent with the lack of GI toxicity observed in mice chronically dosed with pyrvinium or reported in pinworm patients treated with the FDA-approved anthelmintic doses of pyrvinium (66). We have suggested a model in which CK1α activators preferentially target the lower levels of CK1α found in colorectal tumors (67). Thus, CK1α activators represent the first class of WNT inhibitors that preferentially target the hyperactivated signaling typically found in WNT-driven tumors while minimizing the on-target toxicities resulting from attenuation of WNT signaling in various regenerative tissues.

MATERIALS AND METHODS

Synthesis of SSTC3 analogs

To synthesize 4-(*N*-methyl-*N*-(4-(trifluoromethyl)phenyl)sulfamoyl) benzoic acid, we mixed a solution of 4-(chlorosulfonyl)benzoic acid (0.5 g, 2.27 mmol) in methanol (10 ml) with *N*-methyl-4-(trifluoromethyl)aniline (1191 mg, 6.80 mmol). The reaction mixture was stirred at room temperature for 14 hours, concentrated, and then partitioned between ethyl acetate and 0.5 M HCl solution. The organics were separated and dried over magnesium sulfate. The resulting dark solid was partitioned between diethyl ether and 0.5 M sodium hydroxide solution. The aqueous layer was separated and acidified to pH 1 with concentrated HCl. The resulting suspension was extracted with ethyl acetate. The organic layers were combined, dried over magnesium sulfate, and concentrated. The resulting solid was triturated with diethyl ether to provide the desired benzoic acid as a white solid. The yield was 385mg (47%). ^{1}H–nuclear magnetic resonance (NMR): δ 8.11 (*J* = 8.5 Hz, 2H), 7.74 (d, *J* = 8.5 Hz, 2H), 7.66 (d, *J* = 8.5 Hz, 2H), 7.39 (d, *J* = 8.5 Hz, 2H), and 3.21 (s, 3H).

To synthesize 4-(*N*-methyl-*N*-(4-trifluoromethyl)phenyl)sulfamoyl)-*N*-(4-pyridin-2-yl)thiazol-2-yl)benzamide (SSTC3), we added diisopropylethylamine (0.12 ml, 0.69 mmol) and PyBOP (179 mg, 0.345 mmol) to a solution of 4-(*N*-methyl-*N*-(4-trifluoromethyl)phenyl) sulfamoyl)benzoic acid (100 mg, 0.28 mmol) in dimethylformamide (5 ml). The mixture was stirred for 10 min and was treated with 4-(pyridin-2-yl)thiazol-2-amine (41 mg, 0.23 mmol). The reaction mixture was stirred at room temperature for 48 hours, concentrated, and then partitioned between ethyl acetate and 5% lithium chloride solution. The organic layers were combined, dried over magnesium sulfate, and concentrated. The resulting dark oil was purified by column chromatography eluting with 50 to 100% ethyl acetate in hexanes. The resulting solid was triturated with diethyl ether to give the desired amide (SSTC3) as an off-white solid. The yield was 42 mg (35%). ^{1}H-NMR [400MHz, dimethyl sulfoxide (DMSO)–d6]: δ 8.60 (d, *J* = 4.0Hz, 1H), 8.28 (d, *J* = 8.5 Hz, 2H), 8.02 (d, *J* = 7.5 Hz, 1H), 7.89 (dt; *J* = 7.5, 7.5, and 1.5 Hz; 1H), 7.84 (s, 1H), 7.75 (d, *J* = 8.5 Hz, 2H), 7.68 (d, *J* =8.5Hz, 2H), 7.41 (d, *J* = 8.5 Hz, 2H), 7.33 (dd, *J* = 7.0, 5.0Hz, 1H), and 3.25 (s, 1H); ^{13}C-NMR (400 MHz, DMSO-d6): ^{1}H-NMR δ 129.3, 127.5, 127.1, 126.4, 126.1, 125.3, 122.9, 122.6, 120.1, and 112.5; high-resolution mass spectrometry (mass/charge ratio): [M]+ = calculated for C23H18F3N4O3S2, 519.0771; found, 519.0771; analysis (% calculated, %found for C23H17F3N4O3S2): C (53.28, 53.15),H(3.30, 3.43),

and N (10.81, 10.81). The synthesis of SSTC111 and SSTC3with an amine linker (SSTC3 linker) was performed using the same procedures used to synthesize SSTC3. SSTC111 synthesis incorporates a modified thiazol-2-amine in the last step. SSTC3 linker was produced via functionalization of the sulfonamide group using Boc-aminoethyl bromide followed by Boc group removal with trifluoroacetic acid to give the corresponding trifluoroacetic acid salt of the amine. For the SSTC3-conjugated beads, 1.2 mg of SSTC3 linker compound (solubilized in 30% DMSO) was covalently coupled to 2 ml of AminoLink Coupling Resin (Thermo Scientific) following the manufacturer's protocol.

Cell lines and assays

CRC cell lines were purchased from the American Type Culture Collection and maintained as recommended. An isogenic HCT116 cell line, in which the *CTNNB1* (β-*catenin*) mutant allele that drives its tumorigenic properties was deleted, was a gift of B. Vogelstein (Johns Hopkins University). The distinct shRNAs against *CK1*α used here were previously described (29). A luciferase-based TOPflash reporter system was used to assess WNT signaling activity and normalized to total protein. qRT-PCR using specific TaqMan probes (Invitrogen) was performed on total RNA. Expression of *GAPDH* (encoding glyceraldehyde-3-phosphate dehydrogenase) or 18*S* ribosomal RNA was used as reference genes for cells or tissues, respectively. Radioactive kinase reaction was performed as previously described (16). Briefly, a [γ^{32}P]-ATP kinase reaction buffer containing recombinant CK1α (25 nM; Invitrogen) and vehicle (DMSO) or SSTC3 (100 nM) was preincubated at 30°C for 5 min. The kinase reaction was initiated with the addition of recombinant β-catenin (final, 100 nM) and briefly vortexed. Samples were withdrawn at various times, and reactions were terminated with addition to protein sample buffer. The primary antibodies used for immunoblotting are CK1α (Santa Cruz Biotechnology), phosphorylated Ser^{45} β-catenin (Cell Signaling Technology), β-catenin (Cell Signaling Technology), GAPDH (Ambion), HSP90 (Santa Cruz Biotechnology), and APC (Santa Cruz Biotechnology). Immunohistochemistry was performed at the University of Miami Medical School Pathology Research core using the indicated antibodies. *APC* and *CK1*α siRNA SMARTpool and control siRNA were purchased from Dharmacon.

Surface plasmon resonance sensorgram analysis

Surface plasmon resonance (SPR) experiments were performed on a Biacore T200 instrument (GE Healthcare) at 25°C. SSTC3 linker molecule was covalently immobilized to the surface of a CM5 sensor chip by standard amine coupling. A reference flow cell was prepared by activation and deactivation of the surface. Different concentrations of CK1α (Thermo Fisher Scientific) in 50 mM tris buffer (pH 7.5), 150 mM NaCl, 1 mM EDTA, and 5% DMSO were injected for 60 s at 30 μl/ml. Regeneration of the surface was achieved with 30-s injections of Gly-HCl (pH 2.0) and 50% DMSO. Data were fitted to a 1:1 binding model using Biacore T200 evaluation software (GE Healthcare).

Three-dimensional organoid culture

Wild-type organoids (enteroids) were established from the isolated intestinal crypts of *BALB/c* mice as previously described (40). Briefly, jejunum from ~8-week-old mice was removed and gavage-washed with phosphate-buffered saline (PBS), followed by incubation

with cold PBS containing 1.5 mM dithiothreitol and 30 mM EDTA for 20 min. The intestinal tissue was then incubated with warm PBS containing 15 mM EDTA for 6 min, followed by extensive shaking to release the intestinal crypts. After centrifugation, the resulting crypt pellet was washed with 30× volume of organoid basal medium [Dulbecco's modified Eagle medium/F12 supplemented with 2 mM GlutaMAX, 10 mM Hepes, penicillin-streptomycin (100 U/ml), and 1× N2 and 1× B27 supplements]. The purified crypts were filtered through a 100-μm cell strainer and embedded in growth factor–reduced Matrigel (Corning). The resultant organoids were maintained in basal medium supplemented with niche factors [epidermal growth factor (50 ng/ml), R-spondin1 (250 ng/ml), Noggin (100 ng/ml), and 1 μM Jagged-1]. Organoids derived from Apc^{min} (35), $Apc^{-/-}$ mouse (36) adenomas, or clinical CRC-resected tissues were established using a similar protocol, with an additional collagenase and dispase digestion step after the EDTA-chelation step (68). Hyperactivation of WNT signaling in wild-type organoids was achieved by supplementing regular niche factor medium with 25% L-WRN conditioned medium (69) and 1mM nicotinamide for a week (42). Human tumor samples were obtained via an institutional review board–approved protocol.

X. laevis injections

Xenopus embryos were in vitro fertilized, dejellied, cultured, and injected as previously described (70). Capped *Xwnt8* was generated using mMESSAGE mMACHINE (Ambion) according to the manufacturer's instructions. All the work performed on *Xenopus* embryos was approved by the Institutional Animal Care and Use Committee (IACUC) at Vanderbilt University and was in accordance with their policies and guidelines.

Mouse experiments

All studies were carried out in accordance with recommendations in the *Guide for the Care and Use of Laboratory Animals* of the National Institutes of Health and with the policies of the University of Miami IACUC. Age-matched Apc^{min} mice (*C57BL/6J-ApcMin/J*) were obtained from The Jackson Laboratory. Cancer cell line xenografts were established using CD-1 nu/nu mice (Charles River Laboratories) and exposed to the indicated small molecules by intraperitoneal injection. Quantitation of intestinal tumor in Apc^{min} mice was performed as described (71). Briefly, whole intestine from vehicle- or SSTC3-treated Apc^{min} mice was isolated, flushed with PBS, opened, and mounted on a filter paper. Intestinal tissues were then fixed with formalin for 10 min and subject to methylene blue staining to visualize the polyps. For immunoblotting analysis of CK1α in *Apc* mutant tumors, small intestines from Apc^{min} mice were mounted on a filter paper via a similar procedure and isolated using a surgical scalpel. CRC PDXs were established using NOD scid gamma mice (The Jackson Laboratory). Resected CRCs were obtained from consented patients undergoing surgery at Sylvester Comprehensive Cancer Center of the University of Miami. Cancer-driving mutations in primary CRC samples were screened by TruSeq Amplicon technology (Illumina) using a designated cancer panel. To assess GI toxicity in vivo, the intestinal tract was removed from euthanized mice, opened and flushed with PBS, and subsequently fixed using 10% neutral buffered formalin. The fixed intestinal tissue was embedded in paraffin and cut into 4-μm-thick sections, and H&E staining was assessed via light microscopy. Tumor sections were similarly harvested and stained. We evaluated the pharmacokinetic

characteristics of SSTC3 by administering a single dose (25 mg/kg) to three mice via intraperitoneal injection. Blood samples were collected at about 1, 2, 4, 8, and 24 hours after dose. Plasma samples were assayed for SSTC3 using a validated bioanalytical LC-MS method performed by a contract research organization (Covance-Madison), and the results were used to determine various pharmacokinetic parameters, including C_{max} and AUC values. The C_{max} and $AUC_{0–24}$ values were 3910 ng/ml (7.5 μM) and 29,300 ng·hours/ml, respectively, with exposures above 250 nM in the plasma for >24 hours.

Bioinformatics analysis of CK1α expression

Gene expression data were downloaded from Gene Expression Omnibus (GSE17538) and normalized using Robust Multi-array Average in the Bioconductor package *Affy*. Box and whisker plots were used to show $\log_2$-transformed *CK1α* gene expression (probe 226920_at), where the box represents the first and third quartiles, the thick band is the median, and the bars extend to ±1.58 the interquartile range divided by the square root of the sample number.

Statistical analyses

Unless otherwise indicated, all error bars shown represent the SEM of at least three independent experiments. Statistical analysis was determined using Student's *t* test, Fisher's exact test, or a log-rank Mantel-Cox test to analyze the Kaplan-Meier survival curves. *P* values ≤0.05 were considered statistically significant and marked with an asterisk.

Supplementary Material

Refer to Web version on PubMed Central for supplementary material.

Acknowledgments

We would like to thank all members of the Robbins, Capobianco, and Lee laboratories, as well as F. de Sauvage (Genentech) and D. Hernandez (University of Miami) for providing helpful insights during discussions regarding this work. We are grateful to J. Shay (University of Texas Southwestern Medical Center) for providing colonic *Apc* mutant mice and B. Vogelstein (Johns Hopkins University) for providing isogenic HCT116 cells. **Funding:** This work was supported by NIH grants R37DK34128 (to M.H.C.), R01GM081635 (to E.L.), R01GM103926 (to E.L.), R35GM122516-01 (to E.L.), 1K99DK103126-01 (to C.T.), R01CA083736-12A1 (to A.J.C.), R01CA125044-02 (to A.J.C.), and R01CA082628 (to D.J.R.) and funds from the Sylvester Comprehensive Cancer Center.

References

1. Siegel RL, Miller KD, Jemal A. Cancer statistics, 2016. CA Cancer J. Clin. 2016; 66:7–30. [PubMed: 26742998]
2. Fearon ER. Molecular genetics of colorectal cancer. Annu. Rev. Pathol. 2011; 6:479–507. [PubMed: 21090969]
3. Fearon ER, Vogelstein B. A genetic model for colorectal tumorigenesis. Cell. 1990; 61:759–767. [PubMed: 2188735]
4. Dow LE, O'Rourke KP, Simon J, Tschaharganeh DF, van Es JH, Clevers H, Lowe SW. Apc restoration promotes cellular differentiation and reestablishes crypt homeostasis in colorectal cancer. Cell. 2015; 161:1539–1552. [PubMed: 26091037]
5. Cao H, Xu E, Liu H, Wan L, Lai M. Epithelial–mesenchymal transition in colorectal cancer metastasis: A system review. Pathol. Res. Pract. 2015; 211:557–569. [PubMed: 26092594]

6. Amit S, Hatzubai A, Birman Y, Andersen JS, Ben-Shushan E, Mann M, Ben-Neriah Y, Alkalay I. Axin-mediated CKI phosphorylation of β-catenin at Ser 45: A molecular switch for the Wnt pathway. Genes Dev. 2002; 16:1066–1076. [PubMed: 12000790]
7. Huang S-MA, Mishina YM, Liu S, Cheung A, Stegmeier F, Michaud GA, Charlat O, Wiellette E, Zhang Y, Wiessner S, Hild M, Shi X, Wilson CJ, Mickanin C, Myer V, Fazal A, Tomlinson R, Serluca F, Shao W, Cheng H, Shultz M, Rau C, Schirle M, Schlegl J, Ghidelli S, Fawell S, Lu C, Curtis D, Kirschner MW, Lengauer C, Finan PM, Tallarico JA, Bouwmeester T, Porter JA, Bauer A, Cong F. Tankyrase inhibition stabilizes axin and antagonizes Wnt signalling. Nature. 2009; 461:614–620. [PubMed: 19759537]
8. MacDonald BT, Tamai K, He X. Wnt/β-catenin signaling: Components, mechanisms, and diseases. Dev. Cell. 2009; 17:9–26. [PubMed: 19619488]
9. Port F, Basler K. Wnt trafficking: New insights into Wnt maturation, secretion and spreading. Traffic. 2010; 11:1265–1271. [PubMed: 20477987]
10. van den Heuvel M, Harryman-Samos C, Klingensmith J, Perrimon N, Nusse R. Mutations in the segment polarity genes wingless and porcupine impair secretion of the wingless protein. EMBO J. 1993; 12:5293–5302. [PubMed: 8262072]
11. Kadowaki T, Wilder E, Klingensmith J, Zachary K, Perrimon N. The segment polarity gene *porcupine* encodes a putative multitransmembrane protein involved in Wingless processing. Genes Dev. 1996; 10:3116–3128. [PubMed: 8985181]
12. Janda CY, Waghray D, Levin AM, Thomas C, Garcia KC. Structural basis of Wnt recognition by Frizzled. Science. 2012; 337:59–64. [PubMed: 22653731]
13. Yamamoto H, Kishida S, Kishida M, Ikeda S, Takada S, Kikuchi A. Phosphorylation of axin, a Wnt signal negative regulator, by glycogen synthase kinase-3β regulates its stability. J. Biol. Chem. 1999; 274:10681–10684. [PubMed: 10196136]
14. Tolwinski NS, Wehrli M, Rives A, Erdeniz N, DiNardo S, Wieschaus E. Wg/Wnt signal can be transmitted through arrow/LRP5,6 and Axin independently of Zw3/Gsk3β activity. Dev. Cell. 2003; 4:407–418. [PubMed: 12636921]
15. Kofron M, Birsoy B, Houston D, Tao Q, Wylie C, Heasman J. Wnt11/β-catenin signaling in both oocytes and early embryos acts through LRP6-mediated regulation of axin. Development. 2007; 134:503–513. [PubMed: 17202189]
16. Cselenyi CS, Jernigan KK, Tahinci E, Thorne CA, Lee LA, Lee E. LRP6 transduces a canonical Wnt signal independently of Axin degradation by inhibiting GSK3's phosphorylation of β-catenin. Proc. Natl. Acad. Sci. U.S.A. 2008; 105:8032–8037. [PubMed: 18509060]
17. Thompson B, Townsley F, Rosin-Arbesfeld R, Musisi H, Bienz M. A new nuclear component of the Wnt signalling pathway. Nat. Cell Biol. 2002; 4:367–373. [PubMed: 11988739]
18. Parker DS, Jemison J, Cadigan KM. Pygopus, a nuclear PHD-finger protein required for Wingless signaling in *Drosophila*. Development. 2002; 129:2565–2576. [PubMed: 12015286]
19. Kramps T, Peter O, Brunner E, Nellen D, Froesch B, Chatterjee S, Murone M, Zullig S, Basler K. Wnt/wingless signaling requires BCL9/legless-mediated recruitment of pygopus to the nuclear β-catenin-TCF complex. Cell. 2002; 109:47–60. [PubMed: 11955446]
20. Clevers H. Wnt/β-catenin signaling in development and disease. Cell. 2006; 127:469–480. [PubMed: 17081971]
21. Chen B, Dodge ME, Tang W, Lu J, Ma Z, Fan C-W, Wei S, Hao W, Kilgore J, Williams NS, Roth MG, Amatruda JF, Chen C, Lum L. Small molecule–mediated disruption of Wnt-dependent signaling in tissue regeneration and cancer. Nat. Chem. Biol. 2009; 5:100–107. [PubMed: 19125156]
22. Saito-Diaz K, Chen TW, Wang X, Thorne CA, Wallace HA, Page-McCaw A, Lee E. The way Wnt works: Components and mechanism. Growth Factors. 2013; 31:1–31. [PubMed: 23256519]
23. Lau T, Chan E, Callow M, Waaler J, Boggs J, Blake RA, Magnuson S, Sambrone A, Schutten M, Firestein R, Machon O, Korinek V, Choo E, Diaz D, Merchant M, Polakis P, Holsworth DD, Krauss S, Costa M. A novel tankyrase small-molecule inhibitor suppresses *APC* mutation–driven colorectal tumor growth. Cancer Res. 2013; 73:3132–3144. [PubMed: 23539443]
24. Pinto D, Gregorieff A, Begthel H, Clevers H. Canonical Wnt signals are essential for homeostasis of the intestinal epithelium. Genes Dev. 2003; 17:1709–1713. [PubMed: 12865297]

25. Fevr T, Robine S, Louvard D, Huelsken J. Wnt/β-catenin is essential for intestinal homeostasis and maintenance of intestinal stem cells. Mol. Cell. Biol. 2007; 27:7551–7559. [PubMed: 17785439]
26. Liu J, Pan S, Hsieh MH, Ng N, Sun F, Wang T, Kasibhatla S, Schuller AG, Li AG, Cheng D, Li J, Tompkins C, Pferdekamper A, Steffy A, Cheng J, Kowal C, Phung V, Guo G, Wang Y, Graham MP, Flynn S, Brenner JC, Li C, Villarroel MC, Schultz PG, Wu X, McNamara P, Sellers WR, Petruzzelli L, Boral AL, Seidel HM, McLaughlin ME, Che J, Carey TE, Vanasse G, Harris JL. Targeting Wnt-driven cancer through the inhibition of Porcupine by LGK974. Proc. Natl. Acad. Sci. U.S.A. 2013; 110:20224–20229. [PubMed: 24277854]
27. Zhong Y, Katavolos P, Nguyen T, Lau T, Boggs J, Sambrone A, Kan D, Merchant M, Harstad E, Diaz D, Costa M, Schutten M. Tankyrase inhibition causes reversible intestinal toxicity in mice with a therapeutic index < 1. Toxicol. Pathol. 2016; 44:267–278. [PubMed: 26692561]
28. Thorne CA, Hanson AJ, Schneider J, Tahinci E, Orton D, Cselenyi CS, Jernigan KK, Meyers KC, Hang BI, Waterson AG, Kim K, Melancon B, Ghidu VP, Sulikowski GA, LaFleur B, Salic A, Lee LA, Miller DM III, Lee E. Small-molecule inhibition of Wnt signaling through activation of casein kinase 1α. Nat. Chem. Biol. 2010; 6:829–836. [PubMed: 20890287]
29. Li B, Flaveny CA, Giambelli C, Fei DL, Han L, Hang BI, Bai F, Pei X-H, Nose V, Burlingame O, Capobianco AJ, Orton D, Lee E, Robbins DJ. Repurposing the FDA-approved pinworm drug pyrvinium as a novel chemotherapeutic agent for intestinal polyposis. PLOS ONE. 2014; 9:e101969. [PubMed: 25003333]
30. Lake RS, Kropko ML, de la Iglesia FA. Absence of in vitro genotoxicity of pyrvinium pamoate in sister-chromatid exchange, chromosome aberration, and HGPRT-locus mutation bioassays. J. Toxicol. Environ. Health. 1982; 10:255–266. [PubMed: 7143479]
31. Smith TC, Kinkel AW, Gryczko CM, Goulet JR. Absorption of pyrvinium pamoate. Clin. Pharmacol. Ther. 1976; 19:802–806. [PubMed: 1269218]
32. Astudillo L, Da Silva TG, Wang Z, Han X, Jin K, VanWye J, Zhu X, Weaver K, Oashi T, Lopes PEM, Orton D, Neitzel LR, Lee E, Landgraf R, Robbins DJ, MacKerell AD Jr, Capobianco AJ. The small molecule IMR-1 inhibits the Notch transcriptional activation complex to suppress tumorigenesis. Cancer Res. 2016; 76:3593–3603. [PubMed: 27197169]
33. Larabell CA, Torres M, Rowning BA, Yost C, Miller JR, Wu M, Kimelman D, Moon RT. Establishment of the dorso-ventral axis in *Xenopus* embryos is presaged by early asymmetries in β-catenin that are modulated by the Wnt signaling pathway. J. Cell Biol. 1997; 136:1123–1136. [PubMed: 9060476]
34. Su LK, Kinzler KW, Vogelstein B, Preisinger AC, Moser AR, Luongo C, Gould KA, Dove WF. Multiple intestinal neoplasia caused by a mutation in the murine homolog of the APC gene. Science. 1992; 256:668–670. [PubMed: 1350108]
35. Luongo C, Moser AR, Gledhill S, Dove WF. Loss of Apc^{+} in intestinal adenomas from Min mice. Cancer Res. 1994; 54:5947–5952. [PubMed: 7954427]
36. Hinoi T, Akyol A, Theisen BK, Ferguson DO, Greenson JK, Williams BO, Cho KR, Fearon ER. Mouse model of colonic adenoma-carcinoma progression based on somatic *Apc* inactivation. Cancer Res. 2007; 67:9721–9730. [PubMed: 17942902]
37. Sato T, Stange DE, Ferrante M, Vries RGJ, van Es JH, van den Brink S, van Houdt WJ, Pronk A, van Gorp J, Siersema PD, Clevers H. Long-term expansion of epithelial organoids from human colon, adenoma, adenocarcinoma, and Barrett's epithelium. Gastroenterology. 2011; 141:1762–1772. [PubMed: 21889923]
38. Moser AR, Pitot HC, Dove WF. A dominant mutation that predisposes to multiple intestinal neoplasia in the mouse. Science. 1990; 247:322–324. [PubMed: 2296722]
39. Shoemaker AR, Gould KA, Luongo C, Moser AR, Dove WF. Studies of neoplasia in the Min mouse. Biochim. Biophys. Acta. 1997; 1332:F25–F48. [PubMed: 9141462]
40. Sato T, Vries RG, Snippert HJ, van de Wetering M, Barker N, Stange DE, van Es JH, Abo A, Kujala P, Peters PJ, Clevers H. Single Lgr5 stem cells build crypt-villus structures in vitro without a mesenchymal niche. Nature. 2009; 459:262–265. [PubMed: 19329995]
41. Elyada E, Pribluda A, Goldstein RE, Morgenstern Y, Brachya G, Cojocaru G, Snir-Alkalay I, Burstain I, Haffner-Krausz R, Jung S, Wiener Z, Alitalo K, Oren M, Pikarsky E, Ben-Neriah Y.

CKIα ablation highlights a critical role for p53 in invasiveness control. Nature. 2011; 470:409–413. [PubMed: 21331045]

42. Andersson-Rolf A, Fink J, Mustata RC, Koo B-K. A video protocol of retroviral infection in primary intestinal organoid culture. J. Visualized Exp. 2014:e51765.
43. Sinnberg T, Menzel M, Kaesler S, Biedermann T, Sauer B, Nahnsen S, Schwarz M, Garbe C, Schittek B. Suppression of casein kinase 1α in melanoma cells induces a switch in β-catenin signaling to promote metastasis. Cancer Res. 2010; 70:6999–7009. [PubMed: 20699366]
44. Schittek B, Sinnberg T. Biological functions of casein kinase 1 isoforms and putative roles in tumorigenesis. Mol. Cancer. 2014; 13:231. [PubMed: 25306547]
45. Wang K, Ma L, Zhang L, Wang J. Clinicopathological significance and prognostic value of CK1α expression in esophageal squamous cell carcinoma. Int. J. Clin. Exp. Pathol. 2016; 9:1989–1995.
46. Lin T-C, Su C-Y, Wu P-Y, Lai T-C, Pan W-A, Jan Y-H, Chang Y-C, Yeh C-T, Chen C-L, Ger L-P, Chang H-T, Yang C-J, Huang M-S, Liu Y-P, Lin Y-F, Shyy JY-J, Tsai M-D, Hsiao M. The nucleolar protein NIFK promotes cancer progression via CK1α/β-catenin in metastasis and Ki-67-dependent cell proliferation. eLife. 2016; 5:e11288. [PubMed: 26984280]
47. Venerando A, Marin O, Cozza G, Bustos VH, Sarno S, Pinna LA. Isoform specific phosphorylation of p53 by protein kinase CK1. Cell. Mol. Life Sci. 2010; 67:1105–1118. [PubMed: 20041275]
48. Huart A-S, MacLaine NJ, Meek DW, Hupp TR. CK1α plays a central role in mediating MDM2 control of p53 and E2F-1 protein stability. J. Biol. Chem. 2009; 284:32384–32394. [PubMed: 19759023]
49. Wu S, Chen L, Becker A, Schonbrunn E, Chen J. Casein kinase 1α regulates an MDMX intramolecular interaction to stimulate p53 binding. Mol. Cell. Biol. 2012; 32:4821–4832. [PubMed: 23028042]
50. Szyniarowski P, Corcelle-Termeau E, Farkas T, Høyer-Hansen M, Nylandsted J, Kallunki T, Jäättelä M. A comprehensive siRNA screen for kinases that suppress macroautophagy in optimal growth conditions. Autophagy. 2011; 7:892–903. [PubMed: 21508686]
51. Hale CM, Cheng Q, Ortuno D, Huang M, Nojima D, Kassner PD, Wang S, Ollmann MM, Carlisle HJ. Identification of modulators of autophagic flux in an image-based high content siRNA screen. Autophagy. 2016; 12:713–726. [PubMed: 27050463]
52. Cheong JK, Zhang F, Chua PJ, Bay BH, Thorburn A, Virshup DM. Casein kinase 1α-dependent feedback loop controls autophagy in RAS-driven cancers. J. Clin. Invest. 2015; 125:1401–1418. [PubMed: 25798617]
53. Zhang Q, Shi Q, Chen Y, Yue T, Li S, Wang B, Jiang J. Multiple Ser/Thr-rich degrons mediate the degradation of Ci/Gli by the Cul3-HIB/SPOP E3 ubiquitin ligase. Proc. Natl. Acad. Sci. U.S.A. 2009; 106:21191–21196. [PubMed: 19955409]
54. Jia J, Zhang L, Zhang Q, Tong C, Wang B, Hou F, Amanai K, Jiang J. Phosphorylation by double-time/CKIε and CKIα targets cubitus interruptus for Slimb/β-TRCP-mediated proteolytic processing. Dev. Cell. 2005; 9:819–830. [PubMed: 16326393]
55. Chen Y, Sasai N, Ma G, Yue T, Jia J, Briscoe J, Jiang J. Sonic Hedgehog dependent phosphorylation by CK1α and GRK2 is required for ciliary accumulation and activation of smoothened. PLOS Biol. 2011; 9:e1001083. [PubMed: 21695114]
56. Naccarati A, Polakova V, Pardini B, Vodickova L, Hemminki K, Kumar R, Vodicka P. Mutations and polymorphisms in *TP53* gene—An overview on the role in colorectal cancer. Mutagenesis. 2012; 27:211–218. [PubMed: 22294769]
57. Varnat F, Duquet A, Malerba M, Zbinden M, Mas C, Gervaz P, Ruiz i Altaba A. Human colon cancer epithelial cells harbour active HEDGEHOG-GLI signalling that is essential for tumour growth, recurrence, metastasis and stem cell survival and expansion. EMBO Mol. Med. 2009; 1:338–351. [PubMed: 20049737]
58. Sato K, Tsuchihara K, Fujii S, Sugiyama M, Goya T, Atomi Y, Ueno T, Ochiai A, Esumi H. Autophagy is activated in colorectal cancer cells and contributes to the tolerance to nutrient deprivation. Cancer Res. 2007; 67:9677–9684. [PubMed: 17942897]
59. Akiyoshi T, Nakamura M, Koga K, Nakashima H, Yao T, Tsuneyoshi M, Tanaka M, Katano M. Gli1, downregulated in colorectal cancers, inhibits proliferation of colon cancer cells involving Wnt signalling activation. Gut. 2006; 55:991–999. [PubMed: 16299030]

60. Li B, Fei DL, Flaveny CA, Dahmane N, Baubet V, Wang Z, Bai F, Pei X-H, Rodriguez-Blanco J, Hang B, Orton D, Han L, Wang B, Capobianco AJ, Lee E, Robbins DJ. Pyrvinium attenuates Hedgehog signaling downstream of smoothened. Cancer Res. 2014; 74:4811–4821. [PubMed: 24994715]
61. Deng L, Lei Y, Liu R, Li J, Yuan K, Li Y, Chen Y, Liu Y, Lu Y, Edwards CK III, Huang C, Wei Y. Pyrvinium targets autophagy addiction to promote cancer cell death. Cell Death Dis. 2013; 4:e614. [PubMed: 23640456]
62. Hernández AR, Klein AM, Kirschner MW. Kinetic responses of β-catenin specify the sites of Wnt control. Science. 2012; 338:1337–1340. [PubMed: 23138978]
63. Sinnberg T, Wang J, Sauer B, Schittek B. Casein kinase 1α has a non-redundant and dominant role within the CK1 family in melanoma progression. BMC Cancer. 2016; 16:594. [PubMed: 27488834]
64. Kahn M. Can we safely target the WNT pathway? Nat. Rev. Drug Discov. 2014; 13:513–532. [PubMed: 24981364]
65. Nusse R. Wnt signaling and stem cell control. Cell Res. 2008; 18:523–527. [PubMed: 18392048]
66. Beck JW, Saavedra D, Antell GJ, Tejeiro B. The treatment of pinworm infections in humans (enterobiasis) with pyrvinium chloride and pyrvinium pamoate. Am. J. Trop. Med. Hyg. 1959; 8:349–352. [PubMed: 13661537]
67. Anastas JN, Moon RT. WNT signalling pathways as therapeutic targets in cancer. Nat. Rev. Cancer. 2013; 13:11–26. [PubMed: 23258168]
68. Xue X, Shah YM. In vitro organoid culture of primary mouse colon tumors. J. Visualized Exp. 2013:e50210.
69. Miyoshi H, Stappenbeck TS. In vitro expansion and genetic modification of gastrointestinal stem cells in spheroid culture. Nat. Protoc. 2013; 8:2471–2482. [PubMed: 24232249]
70. Peng HB. *Xenopus laevis*: Practical uses in cell and molecular biology. Solutions and protocols. Methods Cell Biol. 1991; 36:657–662. [PubMed: 1811156]
71. Yoneda M, Molinolo AA, Ward JM, Kimura S, Goodlad RA. A simple device to rapidly prepare whole mounts of the mouse intestine. J. Visualized Exp. 2015:e53042.

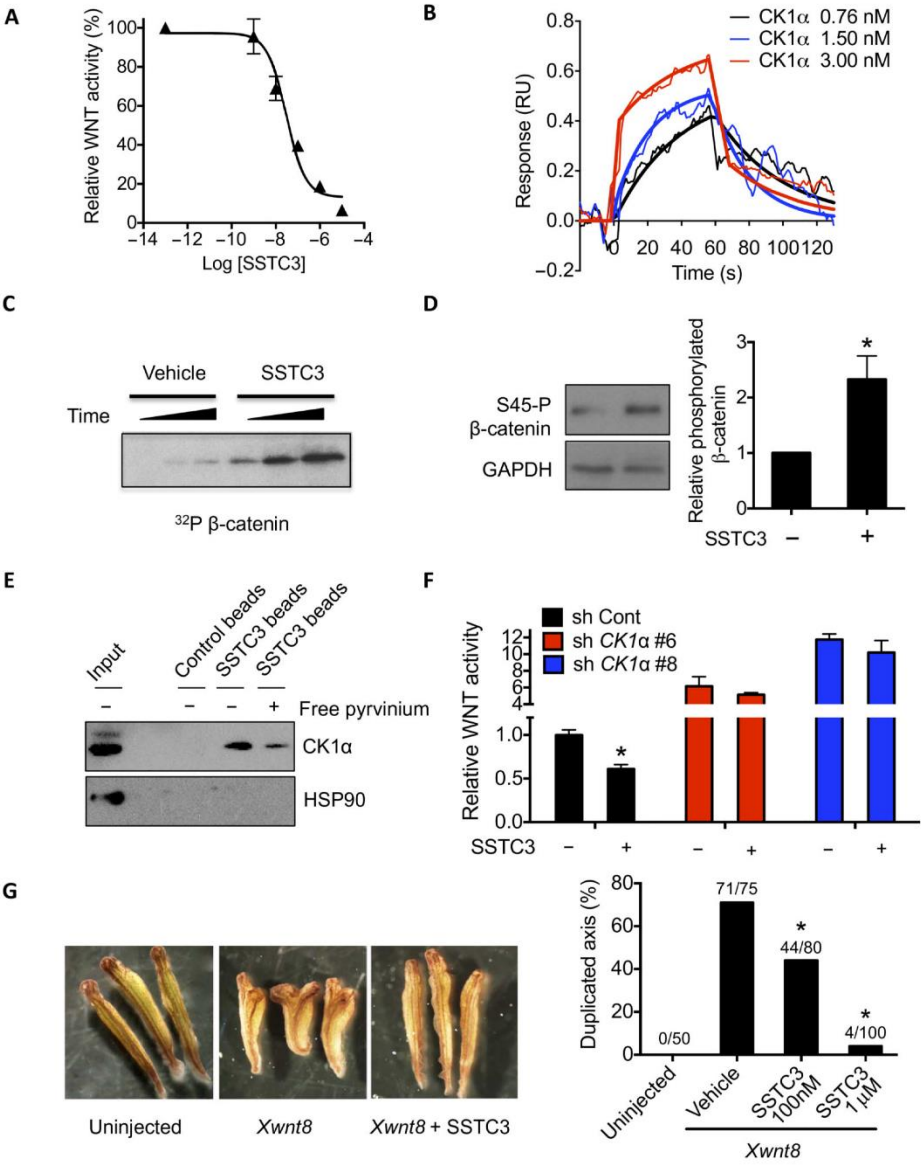

Fig. 1. A novel CK1α activator attenuates WNT signaling

(**A**) A TOPflash WNT reporter assay in 293T cells using the indicated doses of SSTC3 in the presence of WNT3A. A representative figure is shown (means ± SD, $n = 3$). (**B**) SSTC3 was covalently immobilized to the surface of a CM5 sensor chip, and SPR sensorgrams were generated by flowing the indicated concentrations of recombinant CK1α over it. Representative data are shown ($n = 3$). RU, resonance units. (**C**) CK1α was incubated with recombinant β-catenin plus vehicle or SSTC3 (100 nM) in a kinase reaction containing [γ^{32}P]–adenosine triphosphate (ATP) for 0.5, 1, or 3 min, followed by SDS–polyacrylamide gel electrophoresis and autoradiography. (**D**) SW403 cells were treated with 100 nM SSTC3

for 15 min, and the Ser^{45} phosphorylation status of β-catenin was determined by immunoblotting. A representative image (left) and quantification (means ± SEM; right) of three independent experiments is shown (Student's *t* test, $*P \leq 0.05$). (**E**) SSTC3-coupled agarose beads were used to isolate endogenous CK1α from 293T cell lysates in the presence or absence of free pyrvinium, followed by analysis of the indicated proteins by immunoblotting. (**F**) HCT116 cells expressing the indicated short hairpin RNA (shRNA) were transfected with the TOPflash reporter and treated with SSTC3 (100 nM) or vehicle. Luciferase activity was determined 48 hours later. Data are means ± SEM ($n = 3$; Student's *t* test, $*P \leq 0.05$). (**G**) Four- to eight-cell stage embryos were injected ventrally with *Xwnt8* mRNA (1 pg) plus vehicle or SSTC3 (100 nM or 1 μM), allowed to develop, and scored for secondary axis formation (Fisher's exact test, $*P \leq 0.05$).

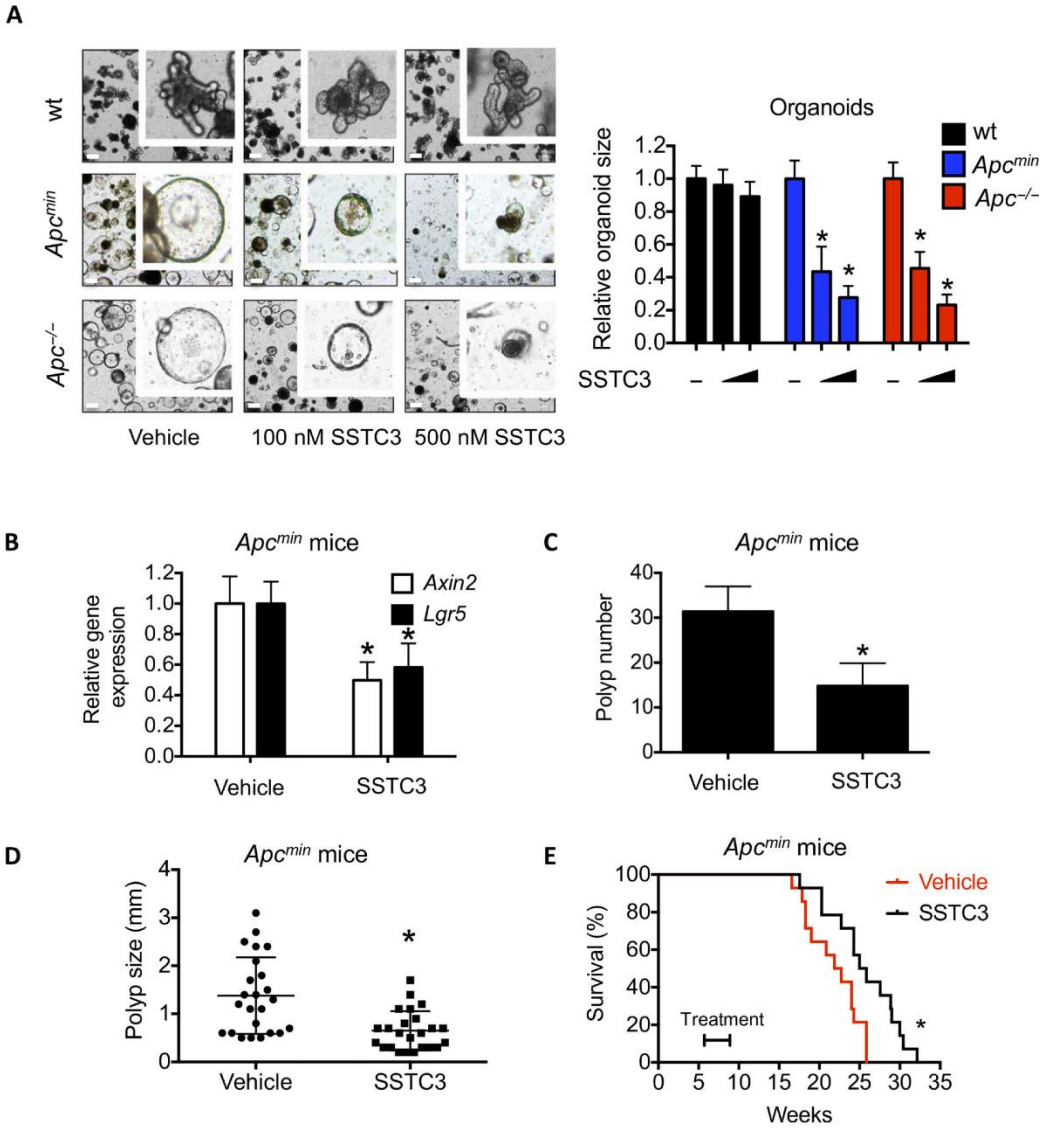

Fig. 2. SSTC3 inhibits the growth of *Apc* mutation-driven tumors

(**A**) Organoids derived from wild-type (wt) mouse intestine or *Apc* mutant tumors were treated with the indicated doses of SSTC3 for 4 days. Representative images (left) or quantification of organoid size (diameter) from four independent replicates (right) are shown. Data are means ± SEM (Student's *t* test, $*P \leq 0.05$). Scale bars, 200 μm. (**B**) Apc^{min} mice were dosed with SSTC3 [10 mg/kg intraperitoneally (ip)] or vehicle, and the small intestines were subsequently harvested and analyzed by quantitative reverse transcription polymerase chain reaction (qRT-PCR). Data are means ± SEM ($n = 4$ in control group and 5 in treatment group; Student's *t* test, $*P \leq 0.05$). (**C** and **D**) Apc^{min} mice were treated with

vehicle or SSTC3 (10 mg/kg ip) for 1 month, dosing every other day. Polyp number (C) and size (D) were quantitated. Data are means ± SEM ($n = 5$ mice in each group; Student's t test, $^*P \leq 0.05$). (**E**) Five-week-old Apc^{min} mice were treated with vehicle or SSTC3 (10 mg/kg ip) ($n = 14$ for each group) for 1 month as indicated, dosing every other day. Kaplan-Meier survival curves of these mice are shown, which was determined using a log-rank Mantel-Cox test ($^*P \leq 0.05$).

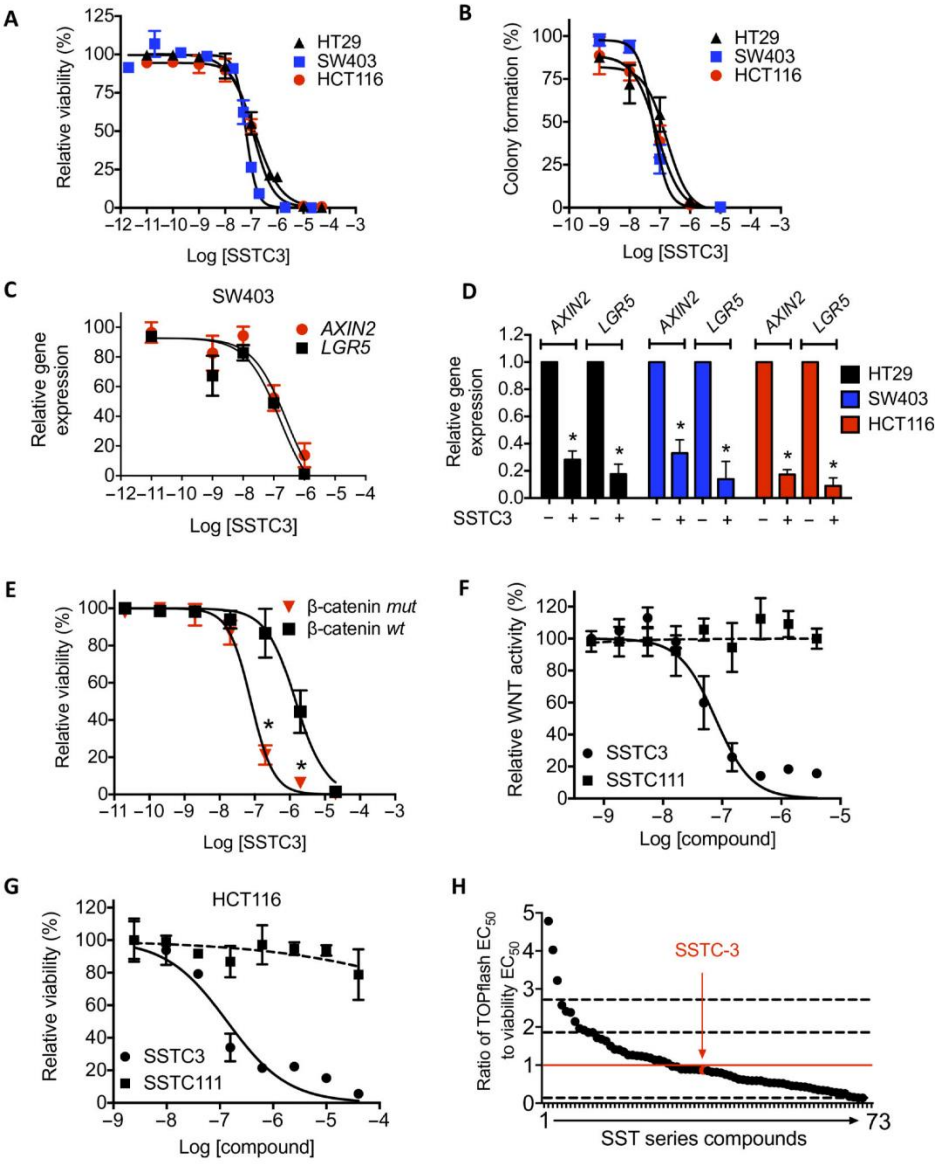

Fig. 3. SSTC3 reduces the viability of colorectal carcinoma cells in an on-target manner

(**A** and **B**) Viability (A) and colony formation (B) in CRC cells treated with SSTC3 for 5 days. (**C**) Expression of the indicated genes analyzed by qRT-PCR in SW403 cells treated with SSTC3 (as indicated) for 4 days analyzed by qRT-PCR. (**D**) Expression of the indicated genes analyzed by qRT-PCR in the indicated cells treated with vehicle or SSTC3 (2 μM) for 2 days. (**E**) Cell viability in β-catenin–mutant (*mut*) or *wt* HCT116 cells treated with a range of doses of SSTC3 for 5 days. (**F**) WNT reporter activity was determined in 293T cells using the indicated compounds and doses. (**G**) Cell viability in HCT116 cells treated with the indicated compounds for 72 hours. (**H**) Ratio of suppression of WNT reporter expression

(drug activity range, 18nM to 2.3 μM) in 293T cells to suppression of cell viability in HCT116 cells (drug activity range, 41 nM to 3.9 μM) by SSTC3 derivatives. Red line indicates an idealized ratio of 1. Dashed lines indicate 1 SD from the ratio of SSTC3. Data are means ± SEM from $n = 3$ experiments (A to E) and means ± SD from a representative of multiple independent experiments (F and G) ($*P \leq 0.05$).

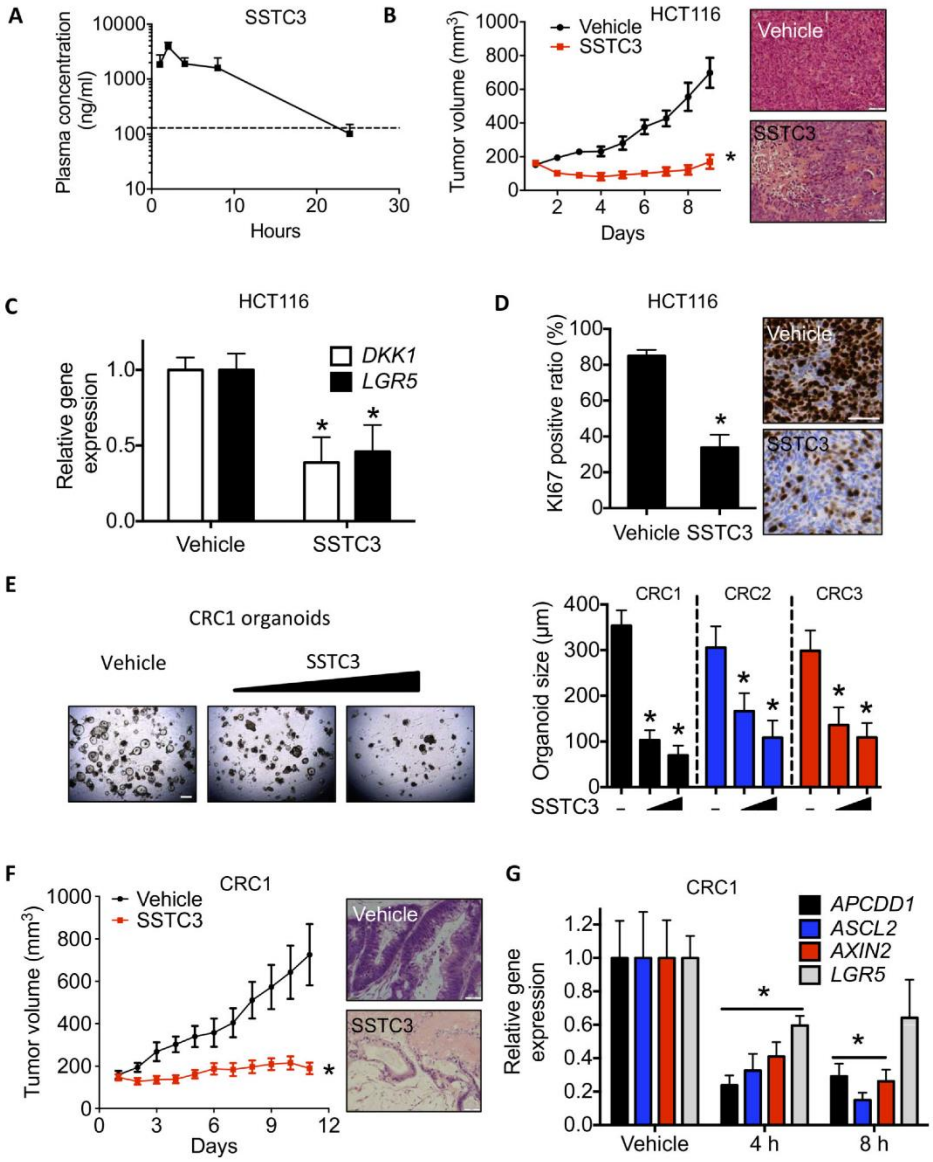

Fig. 4. SSTC3 suppresses the growth of colorectal carcinoma in vivo

(**A**) Plasma concentration of SSTC3 in CD-1 mice after intraperitoneal injection. Data are means ± SD ($n = 3$; dashed line, 250 nM). (**B**) Tumor volume (left) and H&E staining (right) of HCT116 xenografts in mice treated with vehicle or SSTC3 (25 mg/kg ip) for the indicated days ($n = 10$ in each group). Scale bars, 100 μm. (**C** and **D**) WNT-associated gene expression by qRT-PCR (C; $n = 7$ mice per group) and KI67 staining (D) in residual tumors from mice described in (B) ($n = 6$ mice per group). Scale bar, 50 μm. (**E**) Representative image showing organoids derived from a patient's CRC (CRC1) treated with vehicle or SSTC3 (200 nM and 2 μM, respectively) for 7 days is shown (left). Scale bar, 500 μm. The diameter

of organoid cultures ($n = 12$ separate cultures) derived from three distinct resected patient CRCs was quantitated (right). (**F**) Tumor growth in PDXs (CRC1) from mice treated with SSTC3 (15 mg/kg ip daily) or vehicle ($n = 10$ and 9 mice, respectively). Right: Representative H&E staining. Scale bar, 100 μm. (**G**) qRT-PCR analysis in CRC1 tumors from mice treated with SSTC3 (15 mg/kg) or vehicle ($n = 5$ each). Data are means ± SEM (Student's *t* test, $^*P \leq 0.05$).

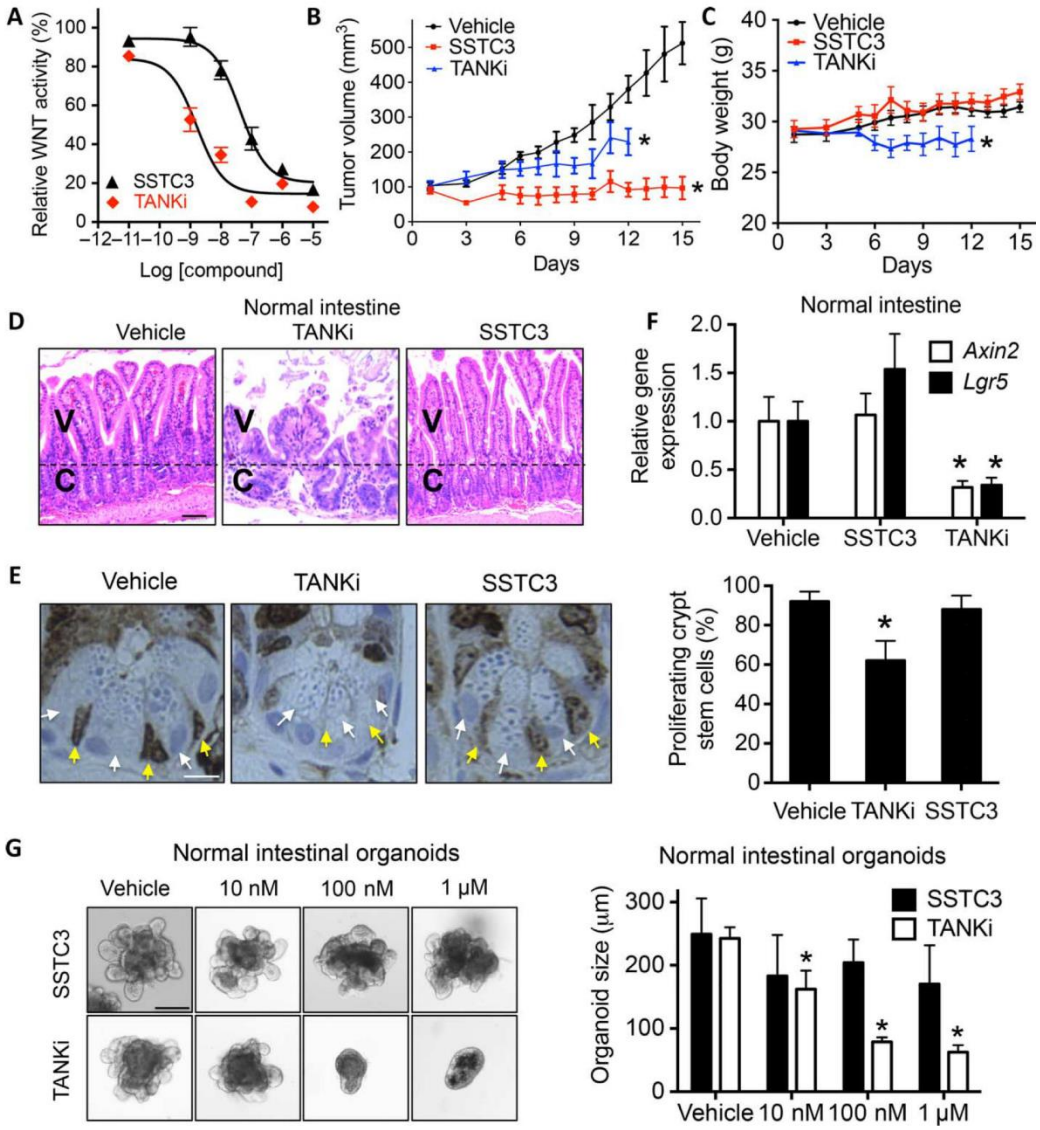

Fig. 5. SSTC3 exhibits efficacy with minimal GI toxicity

(**A**) TOPflash WNT reporter assay in 293T cells cultured with the indicated doses of SSTC3 and G007-LK (TANKi) in the presence of WNT3A. Representative data are shown (means ± SD, $n = 3$). (**B**) SW403 xenograft growth in mice treated with SSTC3 (15 mg/kg ip) or TANKi (40 mg/kg ip) for the indicated days ($n = 7$ in each group). (**C** to **E**) Body weight in mice (C) and representative H&E (D) and KI67 staining of mouse intestines (E) after treatment as described in (B). V, villi; C, crypt. Yellow and white arrows indicate crypt base columnar and paneth cells, respectively. Quantitative analysis of 120 crypts from four separate mice is shown (right) (E). Scale bars, 50 μm (D) and 10 μm (E). (**F**) qRT-PCR

analysis on intestines from nude mice treated with vehicle, TANKi (40 mg/kg), or SSTC3 (15 mg/kg) ($n = 4$ in each group). (**G**) Size of wt organoids after 5-day treatment with vehicle or the indicated doses of SSTC3 or TANKi. Left: Representative images. Right: Quantification of mean size from five independent cultures. Scale bar, 100 μm. Data are means ± SEM (Student's *t* test, $*P \leq 0.05$).

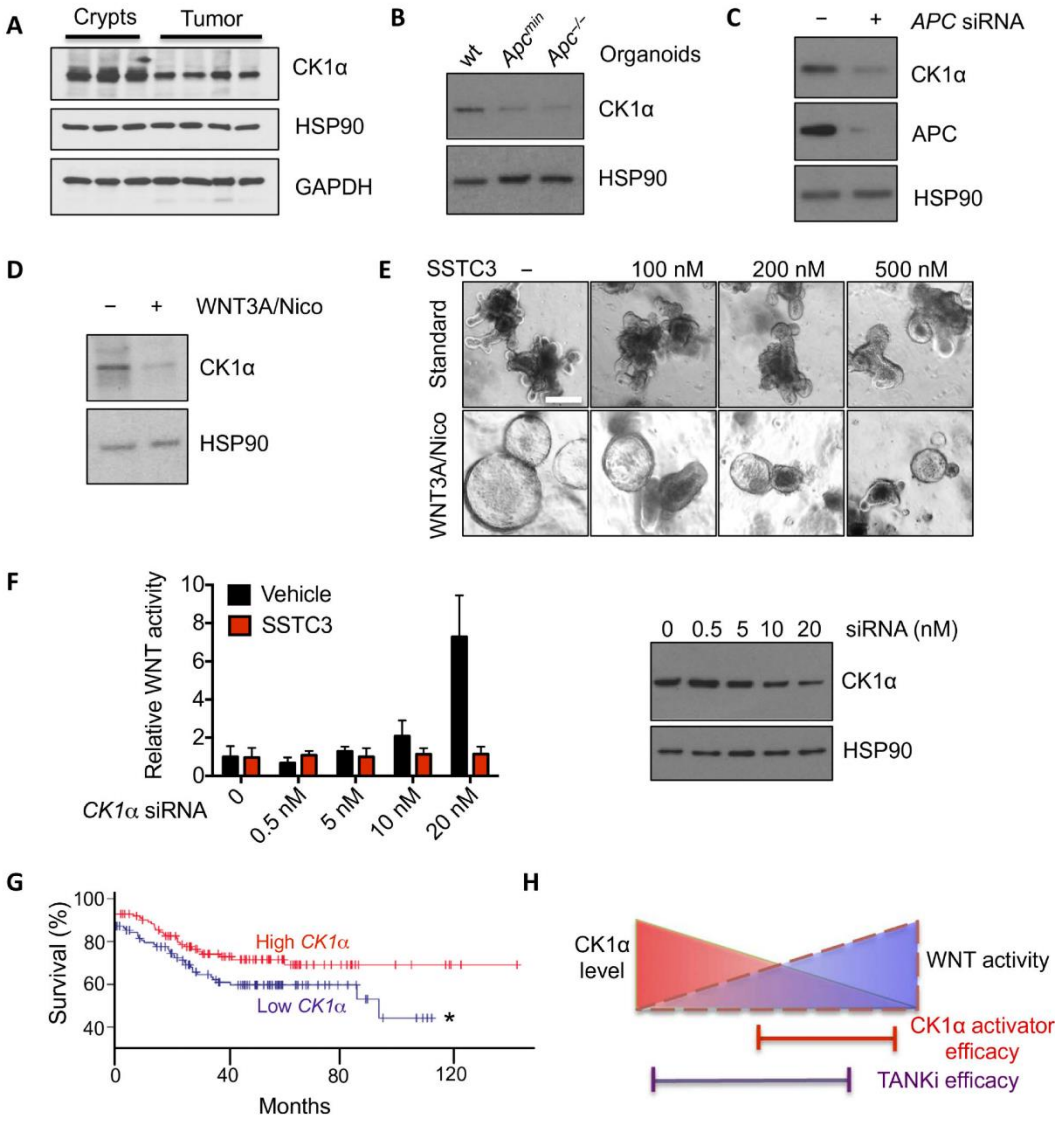

Fig. 6. CK1α abundance dictates SSTC3 sensitivity

(**A**) Representative immunoblot for CK1α abundance in intestinal crypts or tumors isolated from wt or *Apc*^{min} mice. GAPDH, glyceraldehyde-3-phosphate dehydrogenase. (**B**) Immunoblotting for CK1α abundance in organoids derived from wt mouse intestines or *Apc* mutant tumors. (**C**) Representative immunoblot for CK1α abundance in 293T cells transfected with control or *APC* siRNA. (**D**) Representative immunoblot for CK1α abundance in wt intestinal organoids maintained in regular niche factors alone (−) or supplemented with WNT3A and nicotinamide (Nico; 1 mM) to hyperactivate WNT signaling. (**E**) Morphology in intestinal organoids described in (D) treated with SSTC3 for 4

days. (**F**) TOPflash WNT reporter activity (left) in 293T cells after CK1α knockdown with SMARTpool siRNA (right) and treatment with vehicle or SSTC3 (100 nM for 24 hours). (**G**) Kaplan-Meier survival curves of patients with tumors that had relatively high or low *CK1α* expression (GSE17538; $n = 125$ patients per group; $^{*}P \leq 0.05$). (**H**) Schematic demonstrating the selectivity of CK1α activators for WNT-dependent tumors.

Science Signaling
AAAS

www.sciencesignaling.org/cgi/content/full/10/485/eaak9916/DC1

Supplementary Materials for

Differential abundance of CK1α provides selectivity for pharmacological CK1α activators to target WNT-dependent tumors

Bin Li, Darren Orton, Leif R. Neitzel, Luisana Astudillo, Chen Shen, Jun Long, Xi Chen, Kellye C. Kirkbride, Thomas Doundoulakis, Marcy L. Guerra, Julia Zaias, Dennis Liang Fei, Jezabel Rodriguez-Blanco, Curtis Thorne, Zhiqiang Wang, Ke Jin, Dao M. Nguyen, Laurence R. Sands, Floriano Marchetti, Maria T. Abreu, Melanie H. Cobb, Anthony J. Capobianco, Ethan Lee, David J. Robbins*

*Corresponding author. Email: drobbins@med.miami.edu

Published 27 June 2017, *Sci. Signal.* **10**, eaak9916 (2017)
DOI: 10.1126/scisignal.aak9916

This PDF file includes:

Fig. S1. SSTC3 inhibits WNT signaling via CK1α.
Fig. S2. SSTC3 attenuates the viability of cells dependent on WNT activity.
Fig. S3. A structural analog of SSTC3, SSTC111, does not inhibit WNT biomarkers in CRC cells.
Fig. S4. SSTC3 treatment decreases tumor cell density in CRC xenografts.
Fig. S5. SSTC3 has limited on-target GI toxicity in mice.
Fig. S6. Decreased abundance of CK1α sensitizes cells to SSTC3.

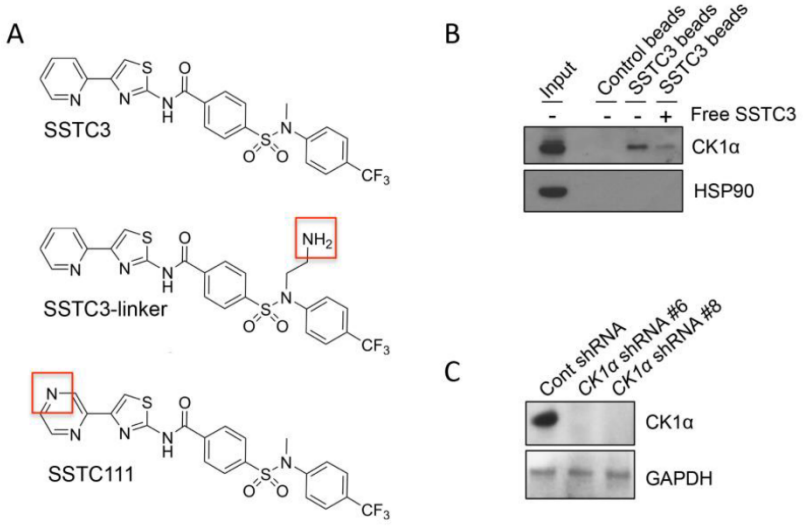

Fig. S1. SSTC3 inhibits WNT signaling via CK1α. (A) Structural formula of SSTC3, its derivative with a free amine (SSTC3 linker) and an inactive analog (SSTC111). **(B)** SSTC3 binds to CK1α in a competitive manner. SSTC3 coupled agarose beads were used to isolate endogenous CK1α from 293T cell lysates in the presence or absence of free SSTC3, followed by analysis of the indicated proteins by immunoblotting. **(C)** CK1α abundance was determined in HCT116 cells expressing control or *CK1α* specific shRNA by immunoblotting. Data are representative of 3 experiments.

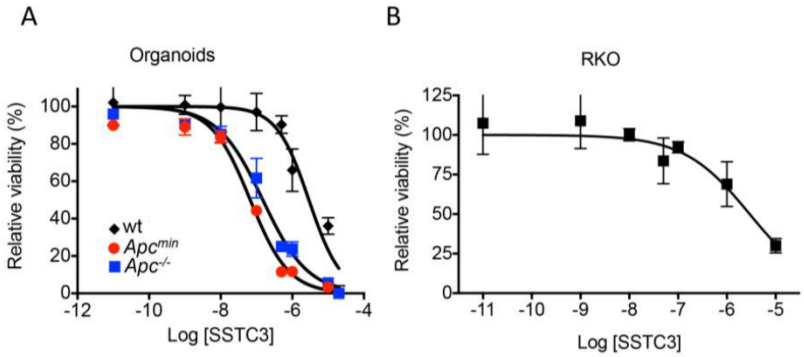

Fig. S2. SSTC3 attenuates the viability of cells dependent on WNT activity. (A) *Apc* mutant organoids are more sensitive to SSTC3 than wild-type (wt) intestinal organoids. The indicated organoids, derived from wt mouse intestines or *Apc* mutant tumors, were treated with the indicated doses of SSTC3 for 4 days and cell viability determined (n= 4 separate cultures). **(B)** The ability of SSTC3 to reduce the viability of non-WNT dependent CRC cells is significantly reduced. RKO cells were treated with the indicated concentrations of SSTC3 for 5 days and viability determined (n= 3 experiments).

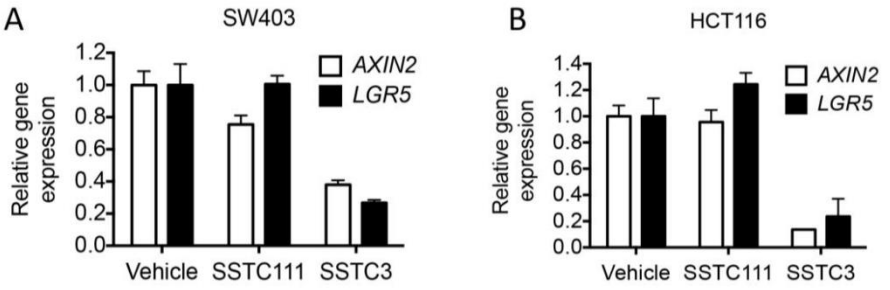

Fig. S3. A structural analog of SSTC3, SSTC111, does not inhibit WNT biomarkers in CRC cells. (A and B) Quantification of *AXIN2* or *LGR5* expression, determined by qRT-PCR, in SW403 (A) or HCT116 (B) cells treated with 2 μM of SSTC3 or SSTC111 for 48 hours. Representative data (mean ± S.D.) from at least two independent experiments are shown.

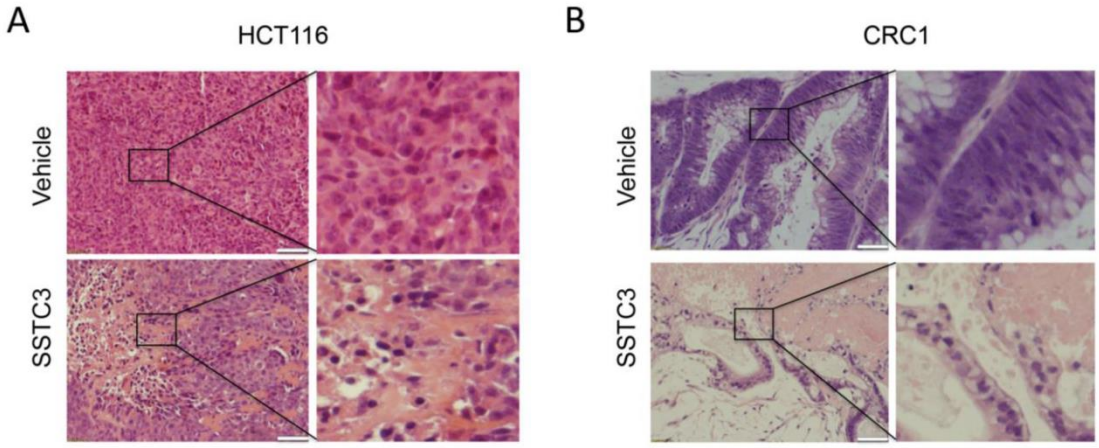

Fig. S4. SSTC3 treatment decreases tumor cell density in CRC xenografts. (A and B) Higher resolution H&E staining images for Fig. 4B and Fig. 4F, respectively.

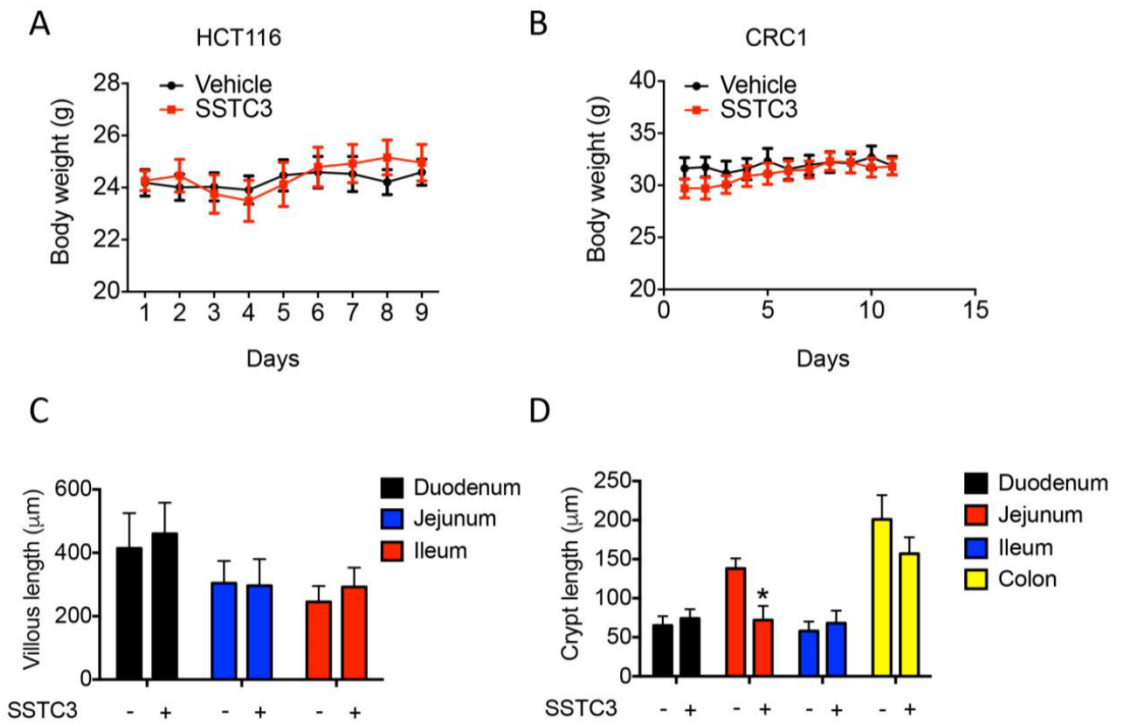

Fig. S5. SSTC3 has limited on-target GI toxicity in mice. (A and B) Body weight data for experiments in Fig. 4B and Fig. 4F respectively. **(C and D)** The intestines of the indicated drug treated mice (n= 4 in each group) were harvested, fixed and subjected to analysis for villous (C) and crypt (D) length. n= 10 random fields; * p≤ 0.05.

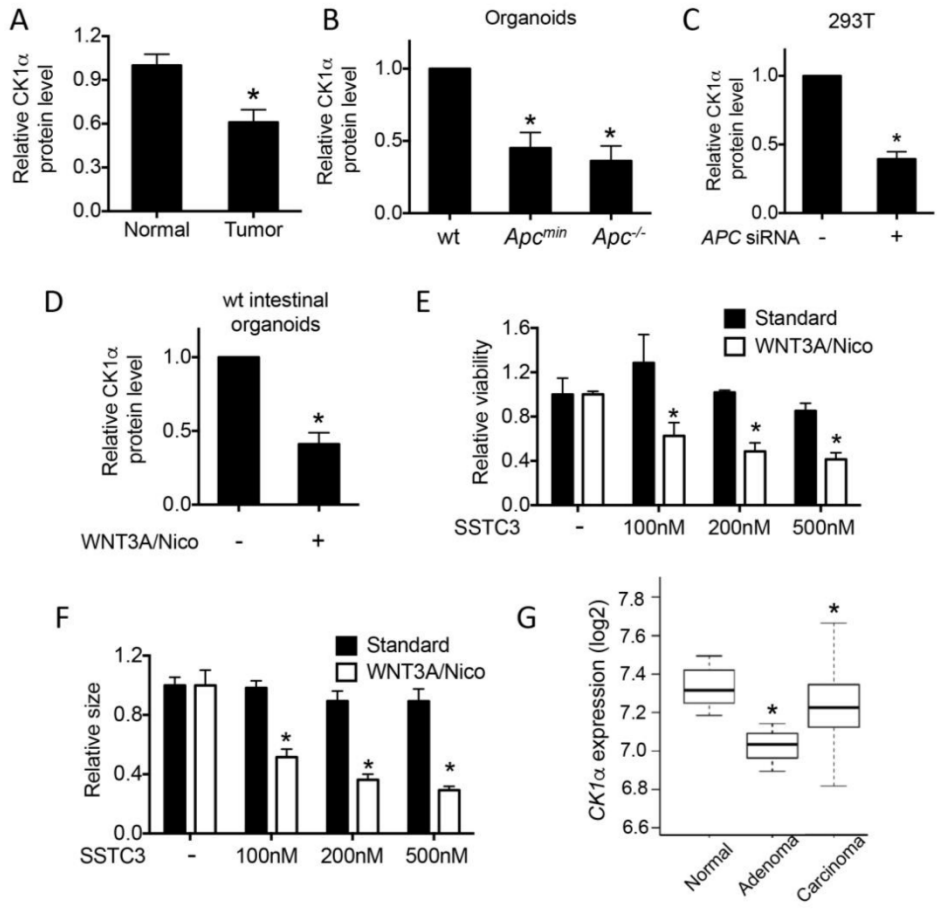

Fig. S6. Decreased abundance of CK1α sensitizes cells to SSTC3. (A and B) *Apc* mutant tumors have decreased amounts of CK1α. Quantitative data for Fig. 6A (n= 3 in normal and 4 in tumor) and Fig 6B (n= 3) are shown. **(C)** Loss of *APC* results in decreased levels of CK1α. Quantification from three independent experiments represented in Fig. 6C is shown. **(D)** Hyperactivated WNT activity decreases CK1α abundance in wild-type (wt) intestinal organoids. Organoids were treated with regular niche factors, or supplemented with WNT3A and 1 mM nicotinamide (Nico) for a week to activate WNT signaling. CK1α abundance was determined by immunoblotting and quantitated (represented in Fig. 6D; n= 3). **(E and F)** WNT hyperactivated intestinal organoids are sensitized to SSTC3. Size of intestinal organoids grown in the indicated medium and treated with increasing amounts of SSTC3 for 4 days (E; n= 4 independent replicates) or viability (F; n= 3 independent replicates). **(G)** *CK1α* expression is decreased in CRC samples. Gene expression data were downloaded from the Gene Expression Omnibus (GSE17538) and normalized using a Robust Multi-array Average (RMA). Shown is a box and whisker plot of log2 transformed *CK1α* expression values for normal colon tissue (n= 10), adenomas (n= 6) or carcinomas (n= 250). * p≤ 0.05, Wilcox rank sum test.

Phosphorylation of XIAP at threonine 180 controls its activity in Wnt signaling

Ng VH, Hang BI, Sawyer LM, **Neitzel LR**, Crispi EE, Rose KL, Popay TM, Zhong A, Lee LA, Tansey WP, Huppert S, Lee E.

J Cell Sci. **2018 131(10). pii: jcs210575**

doi: 10.1242/jcs.210575

© 2018. Published by The Company of Biologists Ltd | Journal of Cell Science (2018) 131, jcs210575. doi:10.1242/jcs.210575

SHORT REPORT

Phosphorylation of XIAP at threonine 180 controls its activity in Wnt signaling

Victoria H. Ng[1,*], Brian I. Hang[2,*], Leah M. Sawyer[2], Leif R. Neitzel[2], Emily E. Crispi[2], Kristie L. Rose[3], Tessa M. Popay[2], Alison Zhong[2], Laura A. Lee[4], William P. Tansey[2], Stacey Huppert[5] and Ethan Lee[1,2,6,‡]

ABSTRACT

X-linked inhibitor of apoptosis (XIAP) plays an important role in preventing apoptotic cell death. XIAP has been shown to participate in signaling pathways, including Wnt signaling. XIAP regulates Wnt signaling by promoting the monoubiquitylation of the co-repressor Groucho/TLE family proteins, decreasing its affinity for the TCF/Lef family of transcription factors and allowing assembly of transcriptionally active β-catenin–TCF/Lef complexes. We now demonstrate that XIAP is phosphorylated by GSK3 at threonine 180, and that an alanine mutant ($XIAP^{T180A}$) exhibits decreased Wnt activity compared to wild-type XIAP in cultured human cells and in *Xenopus* embryos. Although $XIAP^{T180A}$ ubiquitylates TLE3 at wild-type levels *in vitro*, it exhibits a reduced capacity to ubiquitylate and bind TLE3 in human cells. $XIAP^{T180A}$ binds Smac (also known as DIABLO) and inhibits Fas-induced apoptosis to a similar degree to wild-type XIAP. Our studies uncover a new mechanism by which XIAP is specifically directed towards a Wnt signaling function versus its anti-apoptotic function. These findings have implications for development of anti-XIAP therapeutics for human cancers.

KEY WORDS: GSK3, Wnt, XIAP, Apoptosis, Phosphorylation, Ubiquitylation

INTRODUCTION

Cellular inhibitor of apoptosis (cIAP) protein family members, which include XIAP, are well known for binding caspases and inhibiting their activities (Galbán and Duckett, 2010). XIAP has also been shown to have a critical role in Wnt signaling (Hanson et al., 2012). The Wnt signaling pathway plays an integral role in many developmental processes and in human cancer (Saito-Diaz et al., 2013). In the absence of a Wnt signal, cytoplasmic β-catenin is phosphorylated by casein kinase 1α (CK1α) and glycogen synthase kinase 3 (GSK3), and targeted for ubiquitin-mediated degradation by the proteasome. GSK3 is a serine/threonine kinase that has been shown to be involved in multiple signaling pathways, including insulin and Hedgehog signaling (Wu and Pan, 2010). Upon Wnt activation, β-catenin accumulates in the cytoplasm, translocates into the nucleus and displaces members of the co-repressor Groucho/TLE (Gro/TLE) family from members of the TCF/Lef transcription factor family to initiate a Wnt transcriptional program (Daniels and Weis, 2005). We previously demonstrated that XIAP associates with the co-repressor complex to promote monoubiquitylation of Gro/TLE proteins, thereby decreasing its affinity for TCF proteins and allowing β-catenin to bind these transcription factors (Hanson et al., 2012). How XIAP is recruited to Gro/TLE and how its activity is regulated during Wnt signaling versus during apoptosis is unknown. We now demonstrate that XIAP binds and is phosphorylated by GSK3 at threonine 180; this phosphorylation event is required for its activity in Wnt signaling, but is dispensable for its role in the apoptotic pathway.

RESULTS AND DISCUSSION

XIAP is a substrate of GSK3 *in vitro*

A previous study has demonstrated that XIAP interacts with GSK3 in mammalian cells (Sun et al., 2009). Consistent with this result, we also showed that endogenous GSK3 co-immunoprecipitates with endogenous XIAP in several cultured cell lines, including the colorectal cancer lines SW480 and HCT116 (Fig. 1A; Fig. S1A). We found, however, that this interaction was not altered upon active Wnt signaling. We previously demonstrated that Wnt signaling did not alter the overall level of XIAP or its intracellular localization and only a small, localized pool of XIAP associated with TCF proteins is affected (Hanson et al., 2012). Thus, the interaction between XIAP and GSK3 may be regulated similarly at a localized level. We found that XIAP was phosphorylated by GSK3 in an *in vitro* radioactive kinase assay (Fig. 1B; Fig. S1B). Certain GSK3 substrates require a previous (primed) phosphorylation on a serine or threonine residue (Beurel et al., 2015). We therefore tested whether previous phosphorylation by CK1 could enhance the phosphorylation of XIAP by GSK3. Prior incubation with CK1 (under *in vitro* kinase conditions) dramatically increased the phosphorylation of purified XIAP by GSK3 (Fig. 1C). This result suggests that CK1 (or possibly another kinase) may prime XIAP for GSK3 phosphorylation.

The online systems biology resource tool PhosphoSitePlus (Hornbeck et al., 2015) curates various data sources to provide information on protein phosphorylation sites. Using this resource, we searched for previously reported phosphorylation sites on XIAP (Fig. 1D). To determine whether any of these sites represent actual GSK3 phosphorylation sites on XIAP, we performed an *in vitro* kinase reaction with purified XIAP and GSK3 followed with liquid chromatography-mass spectrometry (LC-MS) analysis. One of the predicted sites, threonine 180 (T180), which is located within the BIR2 domain of XIAP, is phosphorylated by GSK3 *in vitro* (Fig. S1C). This result is consistent with previous studies demonstrating that XIAP is phosphorylated on T180 in human cells (Mertins et al., 2016; Sharma et al., 2014).

[1]Program in Cancer Biology, Vanderbilt University, Nashville, TN 37232, USA. [2]Department of Cell & Developmental Biology, Vanderbilt University, Nashville, TN 37232, USA. [3]Vanderbilt Mass Spectrometry Research Center Proteomics Core, Nashville, TN 37232, USA. [4]Department of Pathology, Microbiology, and Immunology, Vanderbilt University Medical Center, Nashville, TN, USA. [5]Division of Gastroenterology, Hepatology, and Nutrition, Cincinnati Children's Hospital Medical Center, Cincinnati, OH 45229, USA. [6]Vanderbilt Ingram Cancer Center, Vanderbilt Medical Center, Nashville, TN 37232, USA.
*These authors contributed equally to this work

‡Author for correspondence (ethan.lee@vanderbilt.edu)

V.H.N., 0000-0003-2344-8468; B.I.H., 0000-0003-4591-4466; A.Z., 0000-0003-4868-7406; E.L., 0000-0001-8405-6156

Received 4 September 2017; Accepted 16 April 2018

Journal of Cell Science (2018) 131, jcs210575. doi:10.1242/jcs.210575

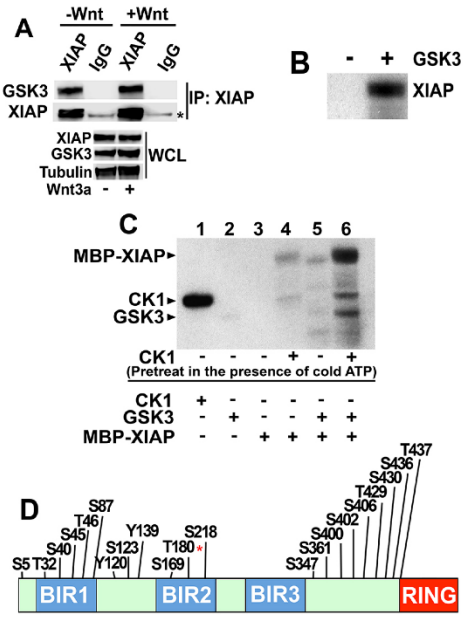

Fig. 1. XIAP is phosphorylated by GSK3 at T180. (A) Endogenous XIAP co-immunoprecipitates with endogenous GSK3. XIAP was immunoprecipitated (IP) from whole-cell lysates (WCL) of HEK293STF cells incubated in the absence or presence of recombinant Wnt3a followed by immunoblotting. The asterisk indicates the heavy chain of IgG. (B) Purified XIAP is phosphorylated by GSK3 *in vitro* in a [γ^{32}P]ATP kinase assay. Reactions were analyzed by SDS/PAGE followed by autoradiography. (C) CK1 enhances XIAP phosphorylation by GSK3. XIAP bound to beads was incubated with CK1 in a kinase reaction containing non-radioactive (cold) ATP (lanes 4 and 6). CK1 was washed away and XIAP-bound beads incubated with GSK3 in a kinase reaction containing [γ^{32}P]ATP. Reactions were analyzed by SDS/PAGE followed by autoradiography. Kinase only lanes show CK1 and GSK3 autophosphorylation (lanes 1 and 2). Results in A–C were replicated at least three times. (D) The predicted phosphorylation site at T180 of XIAP is an *in vitro* GSK3 phosphorylated site. Predicted phosphorylation sites on XIAP were curated by the PhosphoSitePlus online resource tool (Hornbeck et al., 2015). LC-MS analysis of XIAP identifies T180 (asterisk) as a prominent *in vitro* GSK3 phosphorylation site.

The XIAP^{T180A} phosphomutant exhibits decreased Wnt activity

We next tested whether an alanine mutant of XIAP at position T180 (XIAP^{T180A}) co-immunoprecipitated with GSK3 to a similar extent to wild-type XIAP (Fig. 2A), and found that the interaction was similar. The XIAP ligase mutant XIAP$^{H467A/F495A}$ (Gyrd-Hansen et al., 2008; Holley et al., 2002; Damgaard et al., 2012) also co-immunoprecipitated with GSK3 to a similar extent to wild-type XIAP (Fig. S2A), suggesting that the interaction between XIAP and GSK3 does not depend on the ligase activity of XIAP. We next performed immunolocalization of XIAP^{T180A} to determine whether it exhibited a different localization pattern compared to wild-type XIAP. We transfected MYC-tagged XIAP and XIAP^{T180A} into HEK293STF cells and performed immunostaining (Fig. 2B). We found no differences between the cellular localization of XIAP and XIAP^{T180A} as assessed by immunofluorescence. These results were confirmed by cytoplasmic and nuclear cellular fractionation studies of HEK293STF cells expressing XIAP or XIAP^{T180A} (Fig. 2B).

Consistent with our previous studies, we found that overexpression of XIAP is insufficient to promote Wnt activation

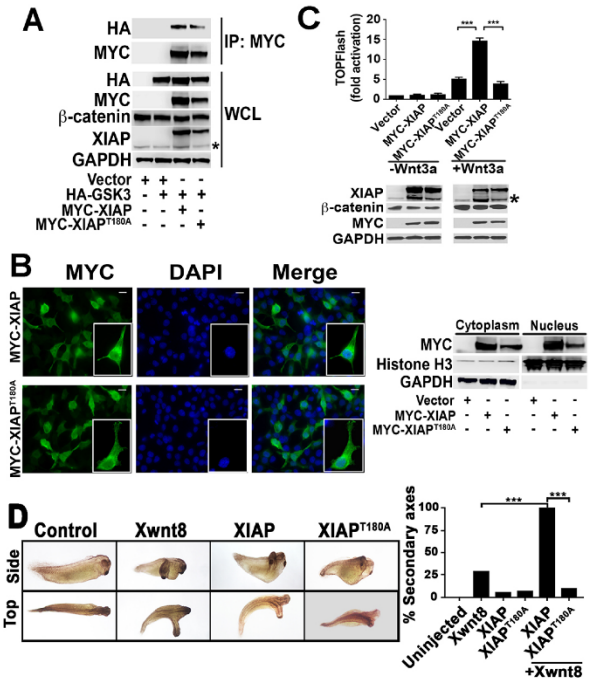

Fig. 2. The XIAP^{T180A} mutant exhibits decreased Wnt activity compared to wild-type XIAP in cultured human cells and in *Xenopus* embryos. (A) GSK3 associates with XIAP and the kinase mutant, XIAP^{T180A}, to a similar extent. HEK293STF cells were transfected with vector, HA–GSK3, MYC–XIAP and MYC-XIAP^{T180A} as indicated, whole cell lysates (WCL) were collected, and immunoprecipitation (IP) performed with anti-MYC antibody. The asterisk indicates endogenous XIAP. (B) The XIAP^{T180A} mutant does not exhibit a localization that is distinct from XIAP. Left, HEK293STF cells were transfected with MYC–XIAP or MYC–XIAP^{T180A}, fixed, and immunostained for MYC and DNA (DAPI). Scale bars: 12.5 µm. Right, cytoplasmic and nuclear fractionations were isolated from transfected cells and immunoblotted for MYC, Histone H3 (a nuclear marker) and GAPDH (a cytoplasmic marker). (C) In contrast to wild-type XIAP, XIAP^{T180A} does not potentiate Wnt3a signaling. HEK293STF cells were transfected with vector, MYC–XIAP or MYC–XIAP^{T180A} as indicated, for 24 h, and cells incubated in the absence or presence of recombinant Wnt3a for 24 h. The asterisk indicates endogenous XIAP. Graph shows mean±s.d. of TOPflash activation normalized to the cell titer. ***P<0.0001 (one-tailed Student's t-test). All experiments were repeated at least three times. (D) The XIAP^{T180A} mutant does not potentiate Wnt8 (Xwnt8)-induced axis formation in *Xenopus* embryos, in contrast to wild-type XIAP. Embryos (four-cell stage) were injected ventrally with control, *XIAP*^{T180A} or *XIAP* mRNA (2 ng each) with or without *Wnt8* mRNA (0.1 ng) and allowed to develop. Representative *Wnt8*-, *XIAP*- and *XIAP*^{T180A}-injected embryos are on the left. The percentage of embryos with secondary axis formation is shown on the right (n≥31 per group). ***P<0.0001 (Fisher's exact test, with Bonferroni correction). All results were replicated at least three times.

in cultured human cells (Fig. 2C). Thus, XIAP is unlikely to be a limiting component of the Wnt signal transduction pathway in mammalian cells (Hanson et al., 2012). Similarly, we did not detect Wnt activity when we overexpressed XIAP^{T180A} (Fig. 2C). We next tested whether XIAP could become limiting when the Wnt pathway is activated. Using HEK293STF cells, which contain a stably integrated luciferase-based Wnt reporter (Veeman et al., 2003), we found that overexpression of XIAP potentiates activation by Wnt3a (Fig. 2C). The lack of change in β-catenin levels in the XIAP (or XIAP^{T180A}) plus Wnt3a condition compared to that seen upon

Wnt3a treatment alone is consistent with the nuclear function of XIAP (which acts downstream of the β-catenin destruction complex and would not be expected to impact steady-state β-catenin levels) (Hanson et al., 2012). In contrast to what was seen with XIAP, we found no enhancement of Wnt reporter activity upon overexpression of XIAP^{T180A} (Fig. 2C; Fig. S2B), suggesting that phosphorylation at the T180 site is critical for the role of XIAP during Wnt signaling.

The XIAP^{T180A} phosphomutant exhibits reduced capacity to potentiate Wnt8 activity in *Xenopus* embryos

Dorsal-anterior structure formation in *Xenopus laevis* embryos is regulated by Wnt signaling (Heasman, 2006), and induction of secondary axis formation in *Xenopus* embryos represents a powerful readout for Wnt signaling *in vivo*. We previously demonstrated that morpholino knockdown of XIAP resulted in severely ventralized *Xenopus* embryos, while injection of XIAP mRNA induced secondary axis formation, consistent with a positive role for XIAP in Wnt signaling (Hanson et al., 2012). The latter result suggests that XIAP is a limiting factor in the developing *Xenopus* embryo. We found that *XIAP^{T180A}* induced secondary axis formation to a similar extent to *XIAP* (Fig. 2D,E). Immunoblotting confirmed that XIAP^{T180A} and XIAP were expressed at similar levels in the injected embryos (Fig. S2C). *XIAP* synergizes with *Wnt8* mRNA to induce axis formation in *Xenopus* embryos. In contrast, *XIAP^{T180A}* co-injection with *Wnt8* mRNA resulted in a lower percentage of embryos with duplicated axes versus what was seen upon *Wnt8* injection alone. Thus, the XIAP^{T180A} phosphomutant has impaired capacity to potentiate Wnt signaling.

The XIAP^{T180A} phosphomutant exhibits decreased capacity to bind and ubiquitylate TLE3

We previously demonstrated that XIAP monoubiquitylates TLE3 *in vitro* and in cultured mammalian cells. To test whether the decreased capacity of XIAP^{T180A} to potentiate Wnt signaling is due to its incapacity to ubiquitylate Gro/TLE proteins, we tested the capacity of XIAP^{T180A} to ubiquitylate TLE3 in an *in vitro* ubiquitylation assay. We found that XIAP^{T180A} ubiquitylates TLE3 to a similar degree to wild-type XIAP (Fig. 3A). This result suggests that XIAP^{T180A} does not have reduced intrinsic catalytic activity when compared to wild-type XIAP. In contrast, in cell-based ubiquitylation assays, the XIAP^{T180A} phosphomutant exhibited decreased capacity to ubiquitylate TLE3 when compared to wild-type XIAP (Fig. 3B). As a control, we could show that the ligase mutant XIAP$^{H467A/F495A}$ exhibited a reduced capacity (similar to control transfection) to ubiquitylate TLE3 compared to wild-type XIAP (Fig. S3A). Addition of the proteasome inhibitor, MG132, resulted in enhanced ubiquitylation of the XIAP$^{H467A/F495A}$ mutant itself (Fig. S3B), suggesting that the decreased activity of the XIAP$^{H467A/F495A}$ mutant may be, in part, due to its rapid turnover.

We found a reduced interaction between XIAP^{T180A} and TLE3 when compared to XIAP and TLE3, as assessed by co-immunoprecipitation assays. Wnt3a treatment did not significantly enhance the interaction between TLE3 and XIAP^{T180A} or XIAP (Fig. 3C). These results suggest that the decreased capacity of XIAP^{T180A} to ubiquitylate TLE3 in cultured cells is due, in part, to its decreased binding to TLE3.

The anti-apoptotic activity of XIAP^{T180A} is indistinguishable from that of wild-type XIAP

We next asked whether XIAP^{T180A} has reduced activity in the apoptotic pathway. One of the best-characterized substrates of XIAP is second mitochondria-derived activator of caspases (Smac; also known as DIABLO) (MacFarlane et al., 2002). We found that XIAP^{T180A} interacted with Smac to a similar extent to wild-type XIAP (Fig. 4A). Overexpression of XIAP inhibits apoptosis in cultured cells (Suzuki et al., 2001). We thus tested whether overexpressed XIAP^{T180A} inhibits Fas ligand-induced apoptosis in HeLa cells (Ashkenazi and Dixit, 1998). There was no observable difference in the capacity of MYC–XIAP or MYC–XIAP^{T180A} to inhibit Fas ligand-induced apoptosis in HeLa cells (Fig. 4B). Thus, phosphorylation of XIAP at the T180 site is required for the full activity of XIAP in the Wnt pathway, but not in the apoptotic pathway.

How the Wnt transcriptional complex is converted from a repressor complex into an activator complex is not well understood. Upon Wnt activation, XIAP is recruited onto Wnt target gene promoters to ubiquitylate Gro/TLE proteins bound to TCF/Lef proteins, decreasing their affinity for these proteins (Hanson et al., 2012). In the same study, we showed that XIAP interacts with Gro/TLE proteins in the absence or presence of Wnt stimulation, and we speculated that XIAP also decreases the pool of free Gro/TLE proteins that can interact with TCF/Lef proteins to inhibit transcription. Thus, Wnt signaling regulates XIAP activity by promoting its recruitment to the TCF/Lef transcriptional complex where it ubiquitylates TCF/Lef proteins bound to Gro/TLE proteins. We now demonstrate that XIAP is phosphorylated by GSK3, which could mediate this process. This result confirms data curated by PhosphoSitePlus from genome-scale proteomic studies indicating

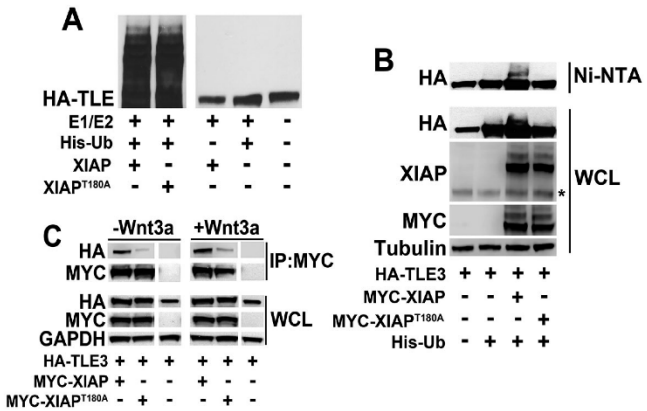

Fig. 3. The XIAP^{T180A} mutant shows decreased binding and ubiquitylation of TLE3. (A) XIAP^{T180A} ubiquitylates TLE3 to a similar extent to wild-type XIAP *in vitro*. *In vitro*-translated HA–TLE3 was incubated in an *in vitro* ubiquitylation reaction containing recombinant E1/E2, ubiquitin, and XIAP or XIAP^{T180A}. Ubiquitylated TLE3 was visualized by immunoblotting with anti-HA antibody. (B) XIAP^{T180A} exhibits reduced capacity to ubiquitylate TLE3 in cultured human cells compared to wild-type XIAP. HEK293STF cells were transfected as indicated, lysed under denaturing conditions, and His-Ub-modified proteins isolated by nickel affinity chromatography. XIAP and TLE3 were detected by immunoblotting with anti-MYC and anti-HA antibodies, respectively. The asterisk indicates endogenous XIAP. WCL, whole-cell lysates. (C) XIAP^{T180A} exhibits decreased affinity for HA–TLE3 compared to wild-type XIAP. HEK293STF cells were transfected for 24 h as indicated followed by incubation in the absence or presence of recombinant Wnt3a for 24 h. Lysates were collected and immunoprecipitated (IP) with anti-MYC antibody. Co-immunoprecipitated HA–TLE3 was detected by anti-HA antibody. All results were replicated at least three times.

Journal of Cell Science (2018) 131, jcs210575. doi:10.1242/jcs.210575

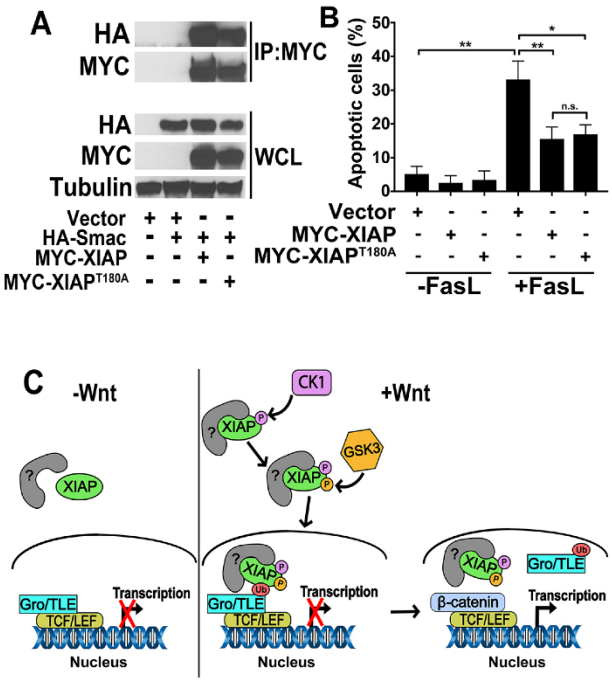

Fig. 4. In contrast to its activity in the Wnt pathway, XIAP^{T180A} has a similar activity to that of wild-type XIAP in the apoptotic pathway. (A) Smac co-immunoprecipitates (IP) with XIAP and XIAP^{T180A} to a similar extent. HEK293STF cells were transfected as indicated with vector or HA–Smac plus MYC–XIAP or MYC–XIAP^{T180A}. Lysates were collected and immunoprecipitation performed with anti-MYC antibody followed by immunoblotting with anti-HA antibody. WCL, whole cell lysates. Results were replicated at least three times. (B) Overexpression of XIAP and XIAP^{T180A} decreases the percentage of Fas ligand (FasL)-induced apoptosis to a similar extent. HeLa cells were transfected for 24 h as indicated and incubated in the absence or presence of recombinant Fas ligand (100 ng/ml) for 24 h. Cells were then stained with Annexin V and propidium iodide. Graph shows the mean±s.d. of percentage of apoptotic cells. Data was analyzed and processed using FlowJo. $^{**}P<0.001$, $^{*}P<0.01$; n.s., not significant (one-tailed Student's *t*-test). All experiments were repeated at least three times. (C) A model for the regulation of XIAP activity in the Wnt pathway by phosphorylation at position T180. See text for more information.

that XIAP is phosphorylated on T180 in human cells, although the significance of XIAP T180 phosphorylation was not clear (Mertins et al., 2016; Sharma et al., 2014). Our current data suggest that phosphorylation of T180 is required for full Wnt activation. Unfortunately, given the likely small pool of phosphorylated nuclear XIAP involved in Wnt signaling, we were unable to detect this form of XIAP in cell extracts by using conventional biochemical methods. The development of a phospho-T180 specific antibody would be a powerful tool to further assess the *in vivo* importance of this phosphorylated form of XIAP.

One possible model is that the interaction between XIAP and Gro/TLE proteins is facilitated by an as-yet-unidentified factor due to phosphorylation of XIAP at T180 by GSK3 (Fig. 4C). This model may explain why overexpression of XIAP^{T180A} does not potentiate Wnt signaling, as it would be incapable of binding Gro/TLE proteins and instead would act to sequester the unknown factor. It is not clear how phosphorylation of XIAP by GSK3 is regulated by Wnt signaling given that XIAP binds to GSK3 irrespective of Wnt activation (Sun et al., 2009 and our data). One possibility is that Wnt signaling either promotes phosphorylation of XIAP on the appropriate site(s) or primes the GSK3 site(s) on XIAP via regulation of another kinase (e.g. CK1). The latter possibility is particularly attractive given that CK1 has been shown to prime GSK3 sites on both β-catenin and LRP6 to inhibit and activate Wnt signaling, respectively (Liu et al., 2002; Zeng et al., 2005). One potential priming phosphorylation site for GSK3 is S186. Although the optimal distance between a primed site and a GSK3 target is four amino acids, greater distances have also been demonstrated (Cole et al., 2004).

Beyond its role in apoptosis, there is increasing evidence that XIAP can participate in a variety of signaling pathways. For example, in addition to our previous studies demonstrating the role of XIAP in the Wnt pathway, a number of studies have shown that XIAP overexpression is also capable of activating the nuclear factor (NF)-κB pathway (Barkett et al., 1997). How XIAP is recruited differentially to regulate NF-κB and/or Wnt signaling, as opposed to its apoptotic function has remained a mystery. Future studies would need to include CRISPR/Cas9-mediated editing of the T180 site in the endogenous XIAP gene to answer this question. Finally, it would be interesting to determine the role of additional post-translational modifications (e.g. ubiquitylation and sumoylation) on the activity of XIAP in other signaling pathways and apoptosis.

MATERIALS AND METHODS

Plasmids

pCS2-MYC-XIAP, pMAL-XIAP and pGEX-TEV-GST were constructed as previously described (Hanson et al., 2012). The following plasmids were gifts: pMT107-His-Ub (William Tansey, Vanderbilt University, Nashville, TN) and pCDNA.3-HA-TLE3 (Andreas Kispert, Hannover Medical School, Hanover, Germany). pCS2-MYC-XIAP^{T180A}, pMAL-XIAP^{T180A} and pCS2-MYC-XIAP$^{H467A/F495A}$ were generated using PCR-based mutagenesis techniques as previously described (Laible and Boonrod, 2009) using the following primers: forward, 5′-GGCCAGACTATGCTCACCTAGCCCCAAGAGAG-3′ and reverse 5′-CTCTCTTGGGGCTAGGTGAGCATAGTCTGGCC-3′ for XIAP^{T180A}; forward 5′-CATTGTTTACAAGTGACTAGAGCTCCACAAGGAACAAAAACGATAGC-3′ and reverse 5′-GCTATCGTTTTTGTTCCTTGTGGAGCTCTAGTCACTTGTAAACAATG-5′, then forward 5′-GGCGCGCCTTAAGACATAGCAATTTTTTGCTTGAAAGTAATGACTGTGTAGC-3′ and reverse 5′-GCTACACAGTCATTACTTTCAAGCAAAAAATTGCTATGTCTTAAGGCGCGCC-3′ for XIAP$^{H467A/F495A}$.

Cell lines

HEK293STF was a gift from the laboratory of Jeremy Nathans (Department of Molecular Biology and Genetics, Johns Hopkins University, MD). HCT116 was a gift from the laboratory of Bert Vogelstein (Sidney Kimmel Comprehensive Cancer Center, Johns Hopkins University, MD). SW480 and HeLa were purchased from ATCC (CCL-228, CCL-2). The cells lines used were fresh stocks from liquid nitrogen, and were, thus, not contaminated.

Antibodies

The following antibodies were used: rabbit anti-XIAP (3:200 for immunoprecipitation, cat. no. NB100-56185, Novus Biologicals, Littleton, CO), mouse anti-XIAP (1:1000, cat. no. 610716, BD Transduction, San Jose, CA), rat anti-HA (1:1000, cat. no. 11867423001, Roche, Basel, Switzerland), mouse anti-MYC (1:1000, Vanderbilt Antibody and Protein Resource, Nashville, TN), mouse anti-GAPDH (1:5000, cat. no. sc-47724, Santa Cruz Biotechnology, Dallas, TX), mouse anti-GAPDH (1:500, cat. no. DSHB-hGAPDH-2G7, DSHB, Iowa City, IA), rabbit anti-Histone H3 (1:2500, cat. no. sc-10809, Santa Cruz Biotechnology), mouse anti-β-catenin (1:5000, cat. no. 610153, BD Transduction), mouse anti-GSK3β (1:1000, cat. no. 610202, BD Transduction), rabbit IgG (Santa Cruz Biotechnology), goat anti-mouse-IgG conjugated to horseradish peroxidase (HRP; 1:5000, Promega, Madison, WI) and goat anti-rabbit-IgG conjugated to HRP (1:5000, Promega).

Expression and purification of XIAP

BL21 bacterial cells transformed with MBP–XIAP or MBP–XIAP^{T180A} plasmids were grown in a 37°C shaking incubator until cell density reached an optical density at 600 nm (OD_{600})=0.5. IPTG (300 µM) was then added and the cultures incubated at 18°C overnight. Cells were then spun down, and cell pellets lysed by sonication in Tris-NaCl-phenylmethylsulfonyl fluoride (TNP) buffer (50 mM Tris-HCl, 150 mM NaCl, 2 mM EDTA, 1 mM PMSF and 0.1% Triton X-100). Lysates were centrifuged at 16,000 ***g*** at 4°C for 10 min, and supernatants incubated with amylose beads on a shaking platform for 2 h at 4°C. Beads were then washed three times with 10× column volumes of TNP, and MBP-bound proteins were eluted with TNP buffer containing 1% maltose. Eluted proteins were further purified on a Mono Q anion-exchange column using the AKTA FPLC apparatus (GE Healthcare, Marlborough, MA). Fractions containing the MBP fusion proteins were concentrated to 1 mg/ml by using Amicon Ultra centrifugal filter units (EMD Millipore, Billerica, MA), and proteins were aliquoted and stored at −80°C until use.

Immunoblotting and immunoprecipitation assays

For immunoblotting of whole-cell lysate, cells were lysed in non-denaturing lysis buffer [NDLB; 100 mM Tris-HCl pH 7.5, 500 mM NaCl, 5 mM EDTA, 1% (v/v) Triton X-100 and 1 mM PMSF], centrifuged at 16,000 ***g*** for 10 min at 4°C, and supernatants were collected for SDS-PAGE. Imaging was performed with c-DIGIT (LI-COR, Lincoln, NE) and X-ray film. For immunoblotting of fractionated cells, cells were lysed and fractions collected as previously described prior to SDS-PAGE (Thorne et al., 2010). For immunoprecipitation assays, cells were lysed in NDLB plus ubiquitin aldehyde (250 ng/µl) for samples expressing HA–TLE3 and MYC–XIAP constructs. For all other samples, 1 mM PMSF, 1× PhosSTOP (Roche), 1 mM NaF and 1 mM Na_3VO_4 were added. Lysates were centrifuged at 16,000 ***g*** for 10 min at 4°C, and anti-MYC agarose beads (Sigma-Aldrich, St Louis, MO), anti-XIAP antibody (Novus Biologicals) or anti-MYC antibody (Bethyl, Montgomery, TX) was added to the supernatant and incubated overnight at 4°C. For anti-XIAP and anti-MYC antibody samples, protein G beads (NEB, Ipswich, MA) were added and samples incubated for 1 h at 4°C. Beads were washed five times with 10× bead volumes of NDLB, bound proteins were eluted with sampler buffer and samples were processed for SDS-PAGE/immunoblotting.

Immunofluorescence

HEK293STF cells were grown on coverslips coated with fibronectin, fixed in 4% formaldehyde and permeabilized. Samples were then incubated with primary antibody followed by secondary antibodies conjugated to Alexa Fluor 488 (goat anti-mouse IgG H+L Alexa Fluor 488, cat. no. A-11001, ThermoFisher Scientific). Samples were mounted in ProLong Gold with DAPI (Invitrogen, Carlsbad, CA), and cells were visualized using a Cascade 512B camera mounted on a Nikon Eclipse TE2000-E confocal microscope.

In vitro phosphorylation assay

For the radioactive kinase assay, 100 ng MBP–XIAP was incubated with 100 ng TEV protease plus 250 units of GSK3 (NEB), 5 mM of cold ATP and 5 µCi of [γ^{32}P]ATP in 1× kinase reaction buffer [50 mM Tris-HCl pH 7.5, 10 mM $MgCl_2$, 5 mM dithiothreitol (DTT)]. Reactions were incubated at 30°C for 1 h on a TOMY shaker and terminated with sample buffer. For CK1 potentiation assays, 20 µl of MBP–XIAP (~1 mg/ml) bound to amylose beads in 1× protein kinase buffer (NEB) containing ATP (1.5 mM) was incubated in the absence or presence of 110 ng recombinant CK1α (Thermo Fisher Scientific). Reactions were incubated at 30°C for 1 h on a TOMY shaker. Beads were then washed three times with 1× kinase reaction buffer prior to the GSK3 radioactive kinase assay.

Mass spectrometry analysis

A kinase reaction was performed as described for the *in vitro* phosphorylation reaction except that radioactive ATP was not added. Reactions were subjected to SDS-PAGE followed by staining with Coomassie Brilliant Blue. The band corresponding to XIAP was then excised and cut into 1 mm^3 pieces prior to in-gel digestion and analysis by liquid chromatography-coupled tandem mass spectrometry. The gel pieces were treated with 45 mM DTT and available cysteine residues were carbamidomethylated with 100 mM iodoacetamide. After destaining the gel pieces with 50% MeCN in 25 mM ammonium bicarbonate, proteins were digested with trypsin (10 ng/µl) in 25 mM ammonium bicarbonate overnight at 37°C. Peptides were extracted by gel dehydration (60% MeCN and 0.1% TFA), the extract was dried by speed vac centrifugation, and peptides were reconstituted in 0.1% formic acid. The peptide solutions were then loaded onto a capillary reverse phase analytical column (360 µm outer diameter ×100 µm internal diameter) using an Eksigent NanoLC HPLC and autosampler. The analytical column was packed C18 reverse phase resin (Jupiter, 3 µm beads, 300 Å, Phenomenox), directly into a laser-pulled emitter tip. Mobile phase solvents consisted of 0.1% formic acid, 99.9% water (solvent A) and 0.1% formic acid, 99.9% acetonitrile (solvent B). A 90-min gradient was performed, and eluting peptides were mass analyzed on an LTQ Orbitrap mass spectrometer (Thermo Scientific), equipped with a nanoelectrospray ionization source. The instrument was operated using a data-dependent method with dynamic exclusion enabled. Full scan (*m/z* 400–2000) spectra were acquired with the Orbitrap spectrometer, and the top five most abundant ions in each MS scan were selected for fragmentation via collision-induced dissociation (CID) in the LTQ. An isolation width of 2 *m/z*, activation time of 30 ms and 35% normalized collision energy were used to generate tandem mass spectra. Dynamic exclusion duration was set to 60 s. For identification of peptides, tandem mass spectra were searched with Sequest (Thermo Fisher Scientific) against a human subset database created from the UniprotKB protein database (www.uniprot.org). Variable modifications of +57.0214 on Cys (carbamidomethylation), +15.9949 on Met (oxidation), and +79.9663 on Ser, Thr and Tyr (phosphorylation) were included for database searching. Search results were assembled using Scaffold 4.3.2 (Proteome Software).

TOPFlash reporter assay

HEK293STF cells stably transfected with a luciferase-based Wnt reporter were incubated with Wnt3a-conditioned or control medium at 24 h post transfection. After 48 h, cells were lysed with 1× Passive Lysis Buffer (Promega) and luciferase activity determined with the Steady-Glo reagent following the manufacturer's instructions (Promega). CellTiter-Glo (Promega) was used to normalize luciferase activities. Statistical analysis was performed using a Student's *t*-test (one-tailed) in PRISM. A value of $P<0.05$ was considered statistically significant.

Xenopus axis duplication assay and immunoblotting embryos

Xenopus embryos were *in vitro* fertilized, de-jellied, cultured, and injected with mRNA as previously described (Peng, 1991). Embryos were assessed for complete or partial duplication, and statistical analyses were performed using Fisher's exact test with Bonferroni correction. A value of $P<0.05$ was considered statistically significant. For immunoblotting, sample buffer was added to pooled embryos from each condition and processed for SDS-PAGE. All animal studies were approved by the Institutional Animal Care and Use Committee (IACUC) at Vanderbilt University and were in accordance with their policies.

Ubiquitylation assays

In vitro ubiquitylation assays were carried out using the ubiquitin thioester/conjugation initiation kit (Boston Biochem, Cambridge, MA). Briefly, an E1 ubiquitin-activating enzyme (1 µg), E2 UbcH5a (1 µg), ubiquitin (1 µg), XIAP or XIAP^{T180A} (1 µg) and HA–TLE3 (2 µl, generated from an *in vitro* transcription-translation reaction, Promega) were assembled in a 20 µl reaction, and samples were incubated on a TOMY shaker at 30°C for 90 min. Reactions were terminated by addition of sample buffer, and ubiquitylated TLE3 products subjected to SDS-PAGE followed by immunoblotting for HA (Muratani and Tansey, 2003). For cell-based ubiquitylation assays, HEK293STF cells were transfected with plasmids encoding HA–TLE3, MYC–XIAP (or MYC–XIAP^{T180A} or MYC–XIAP$^{H467A/F495A}$) and His$_6$–ubiquitin, and treated with 100 µM MG132 for 4 h prior to the assay. The assays were performed using the His-tagged ubiquitin method as previously described (Salghetti et al., 1999).

Flow cytometry

HeLa cells were transfected with vector only, or MYC–XIAP or MYC–XIAP^{T180A}. Medium [DMEM (CellGro-Corning, MT10013CV) plus 10% FBS] was changed 24 h post transfection, and cells were incubated with 100 ng/ml recombinant Fas ligand (Sigma-Aldrich) for 24 h. Cells were released into the medium and adherent cells were counted, pelleted at 400 ***g*** and resuspended in ice-cold 1× staining medium (1× PBS, 2% BSA and 0.1% sodium azide). Cells (1×10^6) were then washed 2× in ice-cold 1× staining medium, resuspended in 200 µl of Annexin V-binding buffer (BioLegend, San Diego, CA) and stained with 2.5 µl Annexin V (BioLegend) plus 0.5 µl propidium iodide (1 mg/ml) for 15 min in the dark at room temperature. An additional 300 µl of Annexin V-binding buffer was added prior to analysis on a BD Fortessa cell analyzer. Data were analyzed with FlowJo software and PRISM.

Acknowledgements

The authors would like to thank the Tansey lab, the Lee lab and the Vanderbilt Mass Spectrometry Research Center Proteomics Core for helpful discussions.

Competing interests

Ethan Lee is cofounder of StemSynergy Therapeutics Inc., a company that is currently developing inhibitors of the Wnt pathway as potential chemotherapeutic agents.

Author contributions

Conceptualization: V.H.N., B.I.H., E.L.; Methodology: V.H.N., B.I.H., L.M.S., L.R.N., E.E.C., K.L.R., A.Z., E.L.; Validation: V.H.N., B.I.H., E.E.C., K.L.R.; Formal analysis: V.H.N., B.I.H., L.R.N., E.E.C., K.L.R., A.Z.; Investigation: V.H.N., B.I.H., L.M.S., L.R.N., E.E.C., K.L.R., T.M.P., A.Z., E.L.; Resources: W.P.T., E.L.; Data curation: V.H.N., B.I.H.; Writing - original draft: V.H.N., E.L.; Writing - review & editing: V.H.N., L.A.L., S.H., E.L.; Visualization: V.H.N., B.I.H., L.M.S., L.R.N., K.L.R.; Supervision: W.P.T., E.L.; Project administration: E.L.; Funding acquisition: E.L.

Funding

V.H.N. was supported by the National Institutes of Health Microenvironment Influences in Cancer Training Grant (T32 CA00959228). L.R.N. was supported by the Training Program in Stem Cell and Regenerative Developmental Biology (T32 HD007502). T.M.P. and W.P.T. are supported by the National Institutes of Health (CA200709). S.S.H. is supported by the National Institutes of Health (R01DK078640). E.L. is supported by the National Institutes of Health (R01GM081635, R01GM103926 and R35GM122516). Deposited in PMC for release after 12 months.

Supplementary information

Supplementary information available online at
http://jcs.biologists.org/lookup/doi/10.1242/jcs.210575.supplemental

References

Ashkenazi, A. and Dixit, V. M. (1998). Death receptors: signaling and modulation. *Science* **281**, 1305-1308.

Barkett, M., Xue, D., Horvitz, H. R. and Gilmore, T. D. (1997). Phosphorylation of IκB-α Inhibits Its Cleavage by Caspase CPP32 in Vitro. *J. Biol. Chem.* **272**, 29419-29422.

Beurel, E., Grieco, S. F. and Jope, R. S. (2015). Glycogen synthase kinase-3 (GSK3): regulation, actions, and diseases. *Pharmacol. Ther.* **148**, 114-131.

Cole, A. R., Knebel, A., Morrice, N. A., Robertson, L. A., Irving, A. J., Connolly, C. N. and Sutherland, C. (2004). GSK-3 phosphorylation of the Alzheimer epitope within collapsin response mediator proteins regulates axon elongation in primary neurons. *J. Biol. Chem.* **279**, 50176-50180.

Damgaard, R. B., Nachbur, U., Yabal, M., Wong, W. W.-L., Fiil, B. K., Kastirr, M., Rieser, E., Rickard, J. A., Bankovacki, A., Peschel, C. et al. (2012). The ubiquitin ligase XIAP recruits LUBAC for NOD2 signaling in inflammation and innate immunity. *Mol. Cell* **46**, 746-758.

Daniels, D. L. and Weis, W. I. (2005). Beta-catenin directly displaces Groucho/TLE repressors from Tcf/Lef in Wnt-mediated transcription activation. *Nat. Struct. Mol. Biol.* **12**, 364-371.

Galbán, S. and Duckett, C. S. (2010). XIAP as a ubiquitin ligase in cellular signaling. *Cell Death Differ.* **17**, 54-60.

Gyrd-Hansen, M., Darding, M., Miasari, M., Santoro, M. M., Zender, L., Xue, W., Tenev, T., da Fonseca, P. C. A., Zvelebil, M., Bujnicki, J. M. et al. (2008). IAPs contain an evolutionarily conserved ubiquitin-binding domain that regulates NF-kappaB as well as cell survival and oncogenesis. *Nat. Cell Biol.* **10**, 1309-1317.

Hanson, A. J., Wallace, H. A., Freeman, T. J., Beauchamp, R. D., Lee, L. A. and Lee, E. (2012). XIAP monoubiquitylates Groucho/TLE to promote canonical Wnt signaling. *Mol. Cell* **45**, 619-628.

Heasman, J. (2006). Patterning the early Xenopus embryo. *Development* **133**, 1205-1217.

Holley, C. L., Olson, M. R., Colón-Ramos, D. A. and Kornbluth, S. (2002). Reaper eliminates IAP proteins through stimulated IAP degradation and generalized translational inhibition. *Nat. Cell Biol.* **40**, 439-444.

Hornbeck, P. V., Zhang, B., Murray, B., Kornhauser, J. M., Latham, V. and Skrzypek, E. (2015). PhosphoSitePlus, 2014: mutations, PTMs and recalibrations. *Nucleic Acids Res.* **43**, D512-D520.

Laible, M. and Boonrod, K. (2009). Homemade site directed mutagenesis of whole plasmids. *J. Vis. Exp.* **27**, e1135.

Liu, C., Li, Y., Semenov, M., Han, C., Baeg, G.-H., Tan, Y., Zhang, Z., Lin, X. and He, X. (2002). Control of beta-catenin phosphorylation/degradation by a dual-kinase mechanism. *Cell* **108**, 837-847.

Macfarlane, M., Merrison, W., Bratton, S. B. and Cohen, G. M. (2002). Proteasome-mediated degradation of Smac during apoptosis: XIAP promotes Smac ubiquitination in vitro. *J. Biol. Chem.* **277**, 36611-36616.

Mertins, P., Mani, D. R., Ruggles, K. V., Gillette, M. A., Clauser, K. R., Wang, P., Wang, X., Qiao, J. W., Cao, S., Petralia, F. et al. (2016). Proteogenomics connects somatic mutations to signalling in breast cancer. *Nature* **534**, 55-62.

Muratani, M. and Tansey, W. P. (2003). How the ubiquitin–proteasome system controls transcription. *Nat. Rev. Mol. Cell Biol.* **4**, 192-201.

Peng, J. (1991). Appendix A: Solutions and Protocols. Methods in Cell Biology. In *Xenopus laevis: Practical Uses in Cell and Molecular Biology*. Elsevier BV.

Saito-Diaz, K., Chen, T. W., Wang, X., Thorne, C. A., Wallace, H. A., PAGE-Mccaw, A. and Lee, E. (2013). The way Wnt works: components and mechanism. *Growth Factors* **31**, 1-31.

Salghetti, S. E., Kim, S. Y. and Tansey, W. P. (1999). Destruction of MYC by ubiquitin-mediated proteolysis: cancer-associated and transforming mutations stabilize MYC. *EMBO J.* **18**, 717-726.

Sharma, K., D'souza, R. C. J., Tyanova, S., Schaab, C., Wiśniewski, J. R., Cox, J. and Mann, M. (2014). Ultradeep human phosphoproteome reveals a distinct regulatory nature of Tyr and Ser/Thr-based signaling. *Cell Rep.* **8**, 1583-1594.

Sun, M., Meares, G., Song, L. and Jope, R. S. (2009). XIAP associates with GSK3 and inhibits the promotion of intrinsic apoptotic signaling by GSK3. *Cell. Signal.* **21**, 1857-1865.

Suzuki, Y., Nakabayashi, Y. and Takahashi, R. (2001). Ubiquitin-protein ligase activity of X-linked inhibitor of apoptosis protein promotes proteasomal degradation of caspase-3 and enhances its anti-apoptotic effect in Fas-induced cell death. *Proc. Natl Acad. Sci. USA* **98**, 8662-8667.

Thorne, C. A., Hanson, A. J., Schneider, J., Tahinci, E., Orton, D., Cselenyi, C. S., Jernigan, K. K., Meyers, K. C., Hang, B. I., Waterson, A. G. et al. (2010). Small-molecule inhibition of Wnt signaling through activation of casein kinase 1alpha. *Nat. Chem. Biol.* **6**, 829-836.

Veeman, M. T., Slusarski, D. C., Kaykas, A., Louie, S. H. and Moon, R. T. (2003). Zebrafish prickle, a modulator of noncanonical Wnt/Fz signaling, regulates gastrulation movements. *Curr. Biol.* **13**, 680-685.

Wu, D. and Pan, W. (2010). GSK3: a multifaceted kinase in Wnt signaling. *Trends Biochem. Sci.* **35**, 161-168.

Zeng, X., Tamai, K., Doble, B., Li, S., Huang, H., Habas, R., Okamura, H., Woodgett, J. and He, X. (2005). A dual-kinase mechanism for Wnt co-receptor phosphorylation and activation. *Nature* **438**, 873-877.

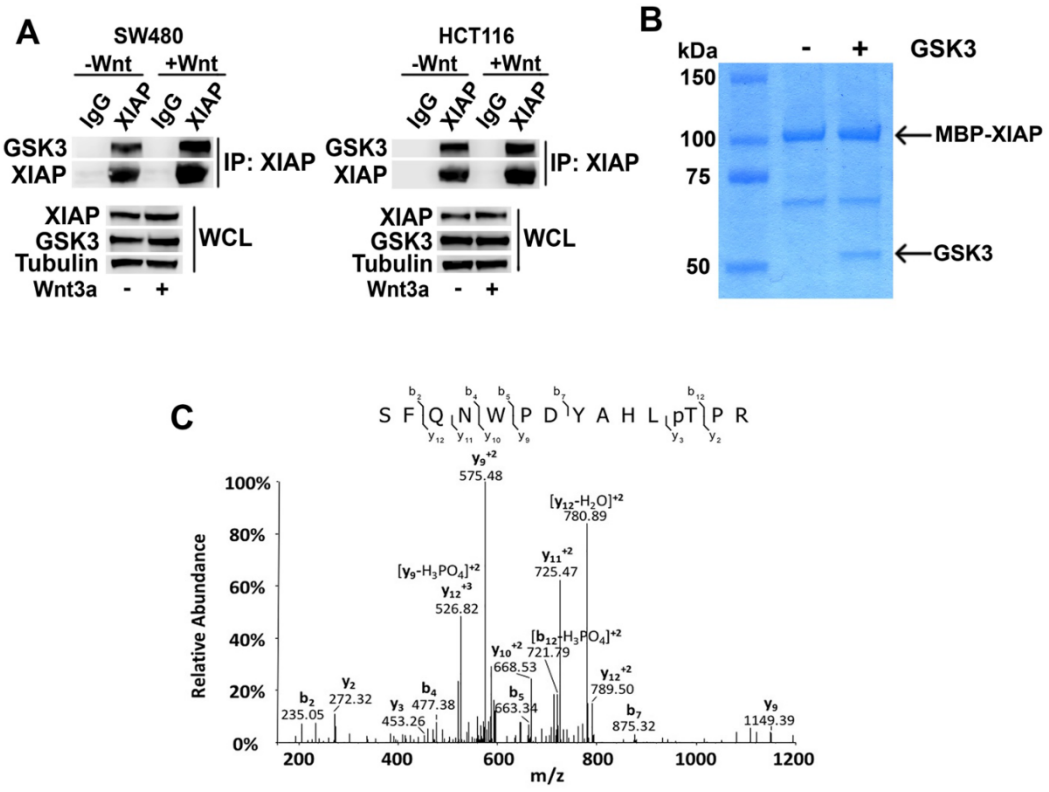

Supplementary Figure 1. GSK3 binds and phosphorylates XIAP at threonine 180. (A) Endogenous XIAP co-immunoprecipitates with endogenous GSK3 from SW480 and HCT116 colorectal cancer cell lines. Cell were incubated in the absence or presence of Wnt3a, lysed, and immunoprecipitation performed. WCL = whole cell lysates. IP = immunoprecipitation. (B) Coomassie showing equal loading of MBP-XIAP from the *in vitro* kinase assay (Fig. 1B) demonstrating equivalent amounts of XIAP protein in the reactions. (C) Mass spectrometry from an *in vitro* kinase reaction containing purified XIAP and GSK3 identifies phosphorylated threonine 180 on XIAP. The peptide sequence is shown above the spectrum with corresponding b and y ion splits with pT being the phosphorylated T180 site.

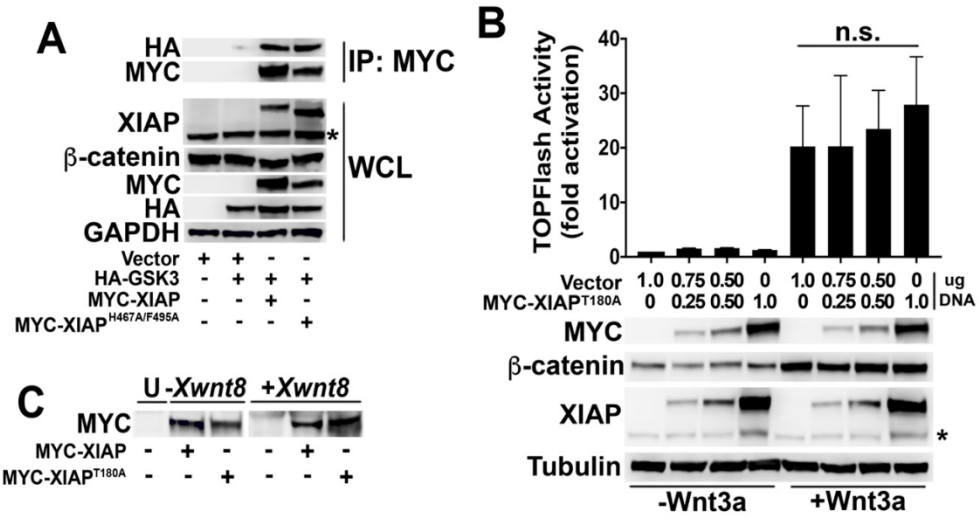

Supplementary Figure 2. The XIAP^{T180A} mutant does not potentiate Wnt signaling in contrast to XIAP. (A) The ligase mutant, XIAP$^{H467A/F495A}$, interacts with GSK3 to a similar extent as wild-type XIAP. HEK293STF cells were transfected as indicated, lysates collected, and immunoprecipitation performed. Asterisk indicates endogenous XIAP. WCL = whole cell lysates. IP = immunoprecipitation. (B) Injected XIAP and XIAP^{T180A} mRNAs are expressed at similar levels in *Xenopus* embryos. Sample buffer was added to pooled embryos from each condition and immunoblotting performed. U = uninjected. (C) Overexpression of XIAP^{T180A} fails to alter Wnt signaling. No statistically significant (as assessed by the student's t-test) increase or decrease in TOPFlash activity was detected even when XIAP^{T180A} is expressed at high levels. Lysates were collected and immunoblotted as indicated. Asterisk indicates endogenous XIAP.

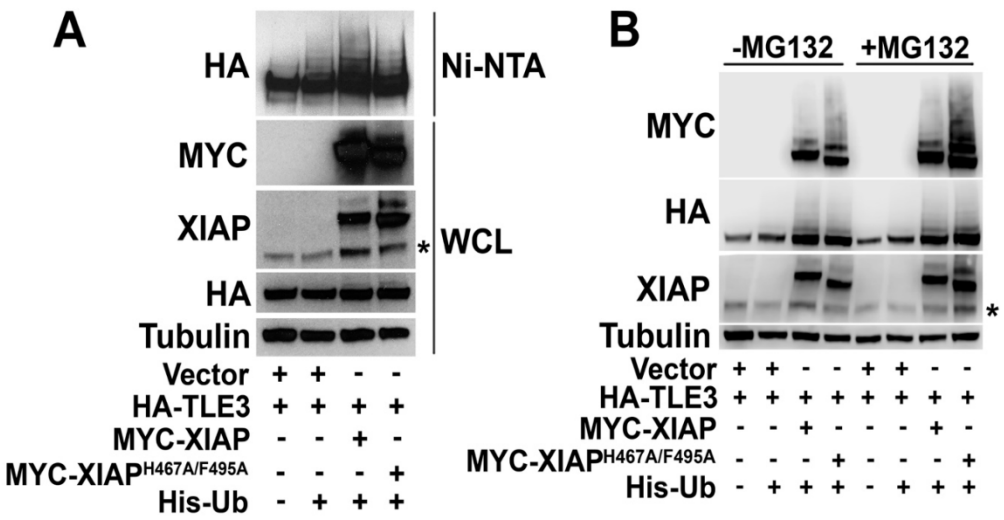

Supplementary Figure 3. The ligase mutant, XIAP$^{H467A/F495A}$, shows decreased ubiquitination of TLE3 and is rapidly turned over in cultured mammalian cells. (A) XIAP$^{H467A/F495A}$ is impaired in its capacity to ubiquitinate TLE3. HEK293STF cells were transfected as indicated, lysed under denaturing conditions, and His-Ub modified proteins isolated by nickel affinity chromatography. Transfected XIAP and TLE3 were detected by immunoblotting with anti-MYC and anti-HA antibodies, respectively. Asterisk indicates endogenous XIAP. (B) Treatment with the proteasomal inhibitor, MG132, indicate enhanced ubiquitination of XIAP$^{H467A/F495A}$. HEK293STF cells were transfected as indicated, and cells incubated in the absence or presence of MG132. Cells were then collected and immunoblotting performed. Transfected XIAP and TLE3 were detected by immunoblotting with anti-MYC and anti-HA antibodies, respectively. Asterisk indicates endogenous XIAP.